STRUCTURAL VIBRATION TRANSMISSION IN SHIPS USING STATISTICAL ENERGY ANALYSIS

BY

Terence Connelly

CEng BEng MSc MIMechE

This thesis is submitted in accordance with the requirements of Heriot-Watt University for the degree of Doctor of Philosophy

Department of Building Engineering and Surveying

Heriot-Watt University

December 1999

CONTENTS **Page**
No

List of Figures

List of Tables

LIST OF ABBREVIATIONS

ALD Acceleration Level Difference

B&K Bruel and Kjaer

CLF Coupling Loss Factor

ELD Energy Level Difference

FFT Fast Fourier Transform

I Inline Joint

IEEE Institute of Electrical and Electronic Engineers

ILF Internal Loss Factor

L Corner Joint

SEA Statistical Energy Analysis

T Tee Joint

TLF Total Loss Factor

X Cross Joint

LIST OF SYMBOLS

A	Area of beam	(m^2)
B	Bending stiffness for a beam	(Nm)
	Bending stiffness per unit width for a plate	(Nm)
E	Young's Modulus	(N/m^2)
E_i	Energy of i^{th} subsystem	(J)
F_{xi}	Force in x direction per unit width on plate i	(N/m)
F_{yi}	Force in y direction per unit width on plate i	(N/m)
F_{zi}	Force in z direction per unit width on plate i	(N/m)
G	Shear Modulus	(N/m^2)
J	Torsional Stiffness	
L_{ij}	Joint length	(m)
L_p	Sound pressure level	(dB re 20 μPa)
L_a	Acceleration level	(dB re 10^{-6} m/s^2)
L_v	Velocity level	(dB re 10^{-9} m/s)
L_E	Energy level	(dB re 10^{-12} W)
M	Modal overlap	
M_{yi}	Moment about y axis on plate i	(Nm/rad)
N	Predicted statistical mode count	
R_{ij}	Transmission loss	(dB)
S_i	Surface area plate i	(m/s^2)
T_{60}	Reverberation time	(s)

T_{bi}	Amplitude of bending wave on plate i	(m)
T_{ni}	Amplitude of nearfield bending wave on plate i	(m)
T_{li}	Amplitude of longitudinal wave on plate i	(m)
T_{ti}	Amplitude of transverse wave on plate i	(m)
U	Perimeter length of a plate	(m)
V	Volume	(m^3)
W_{in}	Input Power	(Watts)
W_{id}	Power lost internally	(Watts)
W_{ij}	Power flow from subsystem i to j	(Watts)
$\overline{W_{ij}}$	Net power flow from subsystem i to j	(Watts)
a	acceleration	(m/s^2)
c_o	Speed of sound in fluid	(m/s)
c_b	Bending wave speed	(m/s)
$c_b^{'}$	Thick plate bending speed	(m/s)
c_g	Group speed	(m/s)
$c_g^{'}$	Thick plate group speed	(m/s)
c_l	Longitudinal wave speed	(m/s)
c_t	Transverse wave speed	(m/s)
e	Exponential	
f	Frequency	(Hz)
f_c	Critical radiation frequency	(Hz)
h	Plate thickness	(m)

i	$\sqrt{-1}$	
k_b	Bending wave number	(rad/m)
k_l	Longitudinal wave number	(rad/m)
k_n	Nearfield bending wave number	(rad/m)
k_t	Transverse wave number	(rad/m)
k_x	Wave number in the x-direction	(rad/m)
k_y	Wave number in the y-direction	(rad/m)
l_x, l_y, l_z	dimensions	(m)
m	Mass	(kg)
	Radiation multiplier	
n,m,o	Positive integers	
n	Modal density	(modes/Hz)
p	Pressure	(N/m^2)
v	Velocity	(m/s)
x,y,z	Cartesian co-ordinates	
λ	Wavelength	(m)
γ	Ratio of c_b/c_t	
Δf	Frequency bandwidth	(Hz)
ρ	Density - material	(kg/m^3)
ρ_s	Density - surface	(kg/m^2)
ρ_o	Density - fluid	(kg/m^3)
ω	Radian frequency	(rad/s)

τ_{ij}	Transmission coefficient	
$\overline{\tau_{ij}}$	Average angular transmission coefficient	
$\tau_{ij}(\theta)$	Transmission coefficient at angle theta	
σ	Radiation efficiency	
η_i	Displacement normal to plane of plate *i*	(m)
ξ_i	Displacement normal to plane of plate *i*	(m)
ζ_i	Displacement normal to plane of plate *i*	(m)
η_i	Total loss factor for subsystem *i*	
η_{id}	Internal loss factor for subsystems *i*	
η_{ij}	Coupling loss factor from subsystem *i* to *j*	
θ	Angle of travelling waves on plate i	(rad)
ϕ_i	Rotational displacement field of plate *i*	(rad)
μ	Poisson's ratio	
ln	Log_e natural logarithim	
log	Log_{10} logarithm to base 10	
Re()	Real Part of imaginary number	

ACKNOWLEDGEMENTS

In this work a number of experimental studies were undertaken in the mechanical engineering laboratory at Heriot-Watt University and also at Yarrow Shipbuilders in Glasgow. The author would like to thank Mr Alistair Macfarlane for his diligence and hard work through 1997-98 in gathering experimental data which is used extensively throughout this work and Dr. Michael Platten for his efforts in gathering experimental data at Yarrows over several weekends. I would also like to thank Mr. David Calderwood who provided technical support for the project, in particular for his efforts in altering the water tank geometry, preparing material for the construction of test joints and for constructing the speakers used in the fluid loading section of this thesis.

In particular I would like extend my most sincere thanks to my project supervisors Professor R.J.M Craik and Dr J.A.Steel for their guidance, advice and support throughout this research project. I would also like to thank the UK Marine Technology Directorate who provided the funding for this project.

I would also like to thank Mr. John Sadden of Yarrow Shipbuilders, Glasgow, without whose support the case studies used in chapter six of this work would not have been possible, and Mr. Paul Macfarlane of Yarrows who acted as technical liaison.

Finally I would like to thank Jacqueline, my wife, without who none of this would have been possible. She has gave me the encouragement to do this from day one and has been unstinting in her support throughout this, tolerating the long hours and absences with good spirits.

ABSTRACT

This thesis presents the results of an investigation into the application of statistical energy analysis (SEA) to predict structure-borne noise transmission in ship structures. The first three chapters introduce the problems of noise and vibration in ships; the previous research on the application of SEA to ships; the basic theory of SEA and the experimental measurement techniques and procedures used to gather data

The main body of this thesis presents a wave transmission model for the hull frame joint which is commonly encountered on the hull, bulkheads and deck plates of ship structures. The wave model allows the transmission coefficients to be calculated for hull frame joints which can be used in the coupling loss factor equations of SEA models. The joint model has been verified against measured data taken on a simple two subsystem single joint laboratory structures and a large complex 38 plate test structure with multiple joints intended to represent a $1/10^{th}$ scale model of a hull section. In addition to the laboratory structures, the SEA modelling of sections of a ship is presented for a large ribbed deck plate, a section of the ship superstructure and a section of the ships hull. The results from the SEA models are compared with measured attenuation data taken on the respective ship sections. A large amount of damping data has been gathered on the test and ship structures and an equation for the internal steel based on data gathered by other researchers has been verified.

It has been shown in this thesis that SEA can be applied to ships. Better agreement is found with real structures in contrast to the poor results presented for SEA when applied to simple one dimensional structures. The level of detail of the model is important as a coarse model yields better predictions of vibration level. As with all models the results are sensitive to the damping level and it is necessary to include bending, longitudinal and transverse wave types in any SEA model to obtain the best prediction. It was also found that the flange plates can be neglected from the frame joint model without compromising the accuracy.

Chapter One

Introduction

1.1 Noise and Vibration in Ships

The development of methods for the prediction of noise and vibration levels aboard ships and offshore structures has been of considerable interest in the previous thirty years. This is due to increased awareness of the health risk and nuisance that are caused by exposure to high noise and vibration levels. Ships and offshore structures pose particular problems as they provide both workplace and living environment for onboard personnel who can be exposed to high noise and vibration levels for extended periods of time. It is therefore important to have the capability to predict noise and vibration levels during the design phase and ensure that noise levels are minimised . This obviates the need for expensive and costly remedial work on a completed vessel.

The problems posed by noise and vibration have been recognised by most ship classification societies who are responsible for approving ship design and construction (e.g. Lloyds for the United Kingdom, Det Norske Veritas for Norway, American Bureau of Shipping for the United States). In 1978 the International Maritime Organisation (IMO) started development of a noise code setting the maximum noise levels throughout a ship structure and permissible exposure times. This came into existence as the 'Code on Noise Levels Onboard Ships' in 1982 [1] for all new vessels (except fishing vessels) above 1600 gross tonnes and has subsequently been adopted by several

maritime countries as the minimum statutory requirement (e.g. Liberia, Netherlands) that all new vessels must achieve.

The IMO code for ship noise has been established with the following problems as the principal targets:

(a) Reduction and elimination of hearing damage;

(b) Minimisation of disturbance to sleep and rest;

(c) Reduction of interference with onboard speech communications;

(d) Ensuring that all-warning signals are clear and audible;

Ship vibration levels are covered by ISO 6954 [2] which came into effect in 1984, seven years after the first draft proposal on the subject was produced. This standard sets out the adverse and acceptable vibration levels for structural elements such as decks and bulkheads in accommodation and working spaces. The standard is based upon measurements collected from a series of different ship hulls.

It is also important to recognise that for vessels such as oceanographic survey ships and warships there are other requirements which are not covered in the general design requirements of ISO 6954 and IMO XII. The principal requirement is for low noise emission from the hull to the water. For surface warships this is particularly important as the acoustic signature allows detection by submarines and minimising underwater noise is extremely important. These types of vessel require more detailed consideration of the noise and vibration levels on the structure.

While the aforementioned noise and vibration codes specify the criteria that a ship design should achieve, they do not provide guidance on how the design criteria should be assessed at the design stage. It is particularly difficult to perform noise and vibration assessment for ships as they are large complex structures with different structure-borne and airborne noise sources located throughout the structure. The principal noise sources

are typically the main engine(s), auxiliary engine(s) and the propeller(s). This thesis does not consider the character and nature of the ship noise sources but instead focuses on the prediction method for structure-borne noise throughout the ship structure.

1.2 Aims of Thesis

The aims of this thesis are to investigate the application of statistical energy analysis to the prediction of structural vibration transmission in ships. The previous SEA work on ship structures is discussed in more detail in chapter two however the following observations can be made about the previous published research work that is available.

(a) Much of the work available is restricted to laboratory models intended to be representative of parts of the ship structure or small scale models of parts of a ship. While useful these do not present any insight into how a *real* ship structure should be modelled.

(b) The application of SEA to periodic and near-periodic structures has been studied by a number of researchers. It has been assumed that because of the stiffening present on decks, hull and bulkheads etc., that ships can be classified as near-periodic structures and as such the problems associated with periodicity render classical SEA useless. More sophisticated techniques such as wave intensity analysis have been proposed as a possible solution to the problem of periodicity however no work has been undertaken on a real ship to justify this assumption.

(c) The main joint type found in ship construction is the frame joint which is found on the decks, bulkheads and the hull which is formed from a steel T section welded to a plate. No work has been presented on the transmission characteristics of this type of joint and if classical SEA is to be successfully applied to a ship, then this joint is important for modelling ships

(d) The internal damping of real ship structures has not been rigorously investigated. The effect of the plate stiffeners welded fittings on damping have not been investigated. The most frequently used damping relationship has been taken from measurements on flat steel plates.

This thesis addresses the aforementioned problems with the principle aim of providing guidance on how a real ship structure can be analysed. This is achieved by a structured combination of laboratory experiments, surveys aboard parts of a real ship structure and theoretical developments that allow the typical steel ribbing found in ship structures to be modelled. The SEA modelling of simple and complex laboratory structures is presented along with sections detailing the modelling of sections of a real ship. Comparisons of predicted and measured vibration levels are presented. The predicted vibration levels are compared with experimental measurements.

1.3 Thesis Layout

Chapter two commences with a review of the problems of predicting noise transmission in ships and the techniques available. A review of the historical development of SEA as an analytical tool is presented. The important SEA parameters such as energy, coupling loss factor, internal loss factor and total loss factor are defined along with the use of power balance equations to determine the power flow. The importance of the mode count and modal overlap is introduced along with the problems of predicting the variation from the mean response.

Chapter three outlines the experimental techniques and equipment used to provide the measured data for this thesis. The measurement procedures in the laboratory and on the ship structures are discussed in detail and the statistical accuracy of the data and its importance is discussed at the end of the chapter.

Chapter four introduces the basic joint types used in the modelling of a ship. The theoretical analysis of the hull-frame stiffener setting out the basic equations and the solution methods is described. The results of a parametric study on two of the hull-frame joint configurations is presented to identify the key features of stiffener design on wave transmission characteristics.

In chapter five a comparison of the results from SEA models and experimental measurements are presented to confirm the integrity of the joint models. Initially the SEA modelling of simple two subsystem models utilising the previously developed hull-frame stiffener is presented. The results from the SEA models are compared with laboratory measured data to prove the accuracy of the theoretical model. A large ship-like tank structure used in the laboratory is then described as this forms the second part of the experimental work. The structure is complex, periodic and is constructed from a variety of joint types representative of those found in a real ship. The results of experimental measurements are compared with the results from SEA models of the structure to test the applicability of the joint models developed in chapter four to a large complex structure.

Chapter six investigates the analysis of real ship structures. The first part of the chapter presents the results of the investigation into the damping of the steel structure. The internal loss factor measurements taken from common ship structural elements such as steel ribbed deck plates, ribbed bulkheads, curved ribbed hull plating are presented along with measurements from hull plating with applied damping treatment. The SEA modelling of ribbed plates is investigated to identify the best modelling practices when studying ships. A detailed investigation of a large ribbed deck plate is presented using the hull-frame joint developed in chapter 4. Comparison between measurements taken on the real structure and SEA predictions from different model representations are given. The analysis of a ship superstructure unit which has a variety of different joint types i.e. L, T, X and hull–frame joints is presented. The final analysis presented is a large section of the ship hull which has a variety of different joint types e.g. parallel

plate joint and hull–frame joints. The SEA modelling of the superstructure unit and hull are discussed in detail along with the measurement strategy and comparison of the measured and predicted vibration levels are presented.

Chapter seven presents a general discussion of the theoretical and experimental studies presented in this thesis and the conclusions about the suitability of applying SEA to large welded structures that can be drawn from the work. The chapter finishes with suggestions for future research work that should be undertaken to progress the field of ship acoustics.

Chapter Two

Literature Review And Theory Of Statistical Energy Analysis

2.1 Introduction

Statistical energy analysis (SEA) is an analytical technique that allows the flow of power through structures to be predicted for broad band noise sources. SEA has evolved from a theoretical investigation of the power flow between coupled single degree of freedom oscillators to a method that allows the prediction of the vibration transmission in complex structures such as aircraft, automotive vehicles and buildings. The technique is called SEA because the model is statistical and does not represent a single unique structure but the mean of a population of structures with similar geometry and properties and energy is the variable that describes the system state. In theory an SEA model can be used to predict the standard deviation, but in practice studies are currently limited to the mean properties. An SEA model aims to predict the response of the population mean to an excitation and it also necessary to predict the deviation of the sample from the mean.

In section 2.2 of this chapter a review of the different methods available to predict shipboard noise and vibration levels is presented summarising their relative strengths and weaknesses. Section 2.3 reviews the development of SEA and introduces the SEA variables of energy, coupling loss factor, internal loss factor, total loss factor and the power balance equations. In section 2.4 a review of the problems of establishing the low

frequency limits of SEA is presented along with the important parameters of the statistical mode count and modal overlap. Section 2.5 presents a brief discussion of the problems in SEA associated with predicting the deviation of the response from the mean. Section 2.6 reviews the basic relationships between energy and other response variables.

2.2 Methods For The Prediction Of Ship Noise and Vibration Levels

The different analytical methods available to predict noise and vibration levels in ships are reviewed in this section.

2.2.1 Finite Element Methods

The finite element method (FEM) evolved in the early 1960's from the matrix-structural methods of the 1950's and is now a design tool used in the analysis of a wide range of structural problems. The finite element method is used to solve boundary value problems which allows it be applied to stress analysis, heat transfer, eigenvalue problems, electromagnetic and fluid-structure interaction problems.

In ship design, FEM is used to predict the global response of the ship hull and superstructure. A typical example of the use of FEM in ship vibration analysis is given in the work of Jantunen *et al* [3] where the finite element analysis of a 21,000 tonne cruise liner is discussed. Jantunen discusses the use of sub-structuring in building and analysing FE models of each deck and extracting the eigenvalues. The deck substructures are combined to produce an overall model of the ship aft structure and modal synthesis is used to combine the first 85 modes of the substructures. A separate model for the water was created to include the mass loading provided by the fluid-structure interaction. Measurements were taken aboard the vessel during fitting out and sea trials and comparison with the FE results discussed but no results were presented.

Similar work is outlined by Nagamoto *et al* [4] in applying FEM to determine the first 20 global modes of the superstructure of a liquid natural gas carrier and the effects of a local engine mounting details on the response of the aft structure. A comparison of ten measured and predicted natural frequencies is presented with a difference of less than 10% however no modal comparison is presented to verify that the correct modes are being compared.

In using FEM, ship designers are principally concerned in ensuring that the running speed of the main and auxiliary engines, reduction gearboxes, propeller and shaft are not coincident with the global modes of the ship superstructure. It is not possible however to use FEM to predict the structure-borne noise transmission is ships for the following reasons:

(a) To use FEM to predict structure-borne noise transmission would require an extremely large model, with the number of degrees of freedom in the order of several million;

(b) The resonant frequencies and mode shapes are extremely sensitive to the local geometry and manufacturing tolerances. It would not be possible to model to this level of detail. The results of the finite element model are also sensitive to the type of dynamic solution routine used (e.g. subspace iteration, Guyan reduction) ;

(c) The computing effort required to generate the ship finite element model and solve would be prohibitive. The number of resonant frequencies and mode shapes would be extremely large and the post-processing would be impossible;

2.2.2 Empirical Noise Prediction Methods

Empirical methods offer a simple and quick technique for predicting airborne and structure-borne noise levels at the preliminary design stage. Typically the various methods available are based on measurement data collected from existing vessels. The noise levels are then related via regression analysis to important design features such as the number of decks, the engine power, the engine running speed, the propeller and the reduction gear box.

The first empirical method proposed for the preliminary design phase was by Janssen and Buiten [5]. Janssen's model allows the vibration levels due to the diesel engine, the reduction gear box, the screw propellers and bow thrusters to be determined from which the vibration level in the hull and the cabin noise levels can be predicted in octave bands.

Plunt [6,7,8] conducted an extensive survey of 14 vessels of different designs, collecting large quantities of measurements which allowed the development of empirical calculation procedures. The developed formulae for vibration prediction covered the following:

- Main engines: prediction of the vibration levels at the foundations of rigidly mounted diesel engines with two speed ranges;
- Auxiliary engines: prediction of vibration levels for rigidly mounted and flexibly mounted diesel engines with two speed ranges;
- Propellers: the prediction formulae of Janssen and Brown were used;
- Hull plating: two formulae for different propeller shaft speeds were presented for the prediction of the vibration levels in hull plating ;
- Reduction gears: formulae were presented for predicting the vibration level in octave bands at the tooth meshing frequency of the gearbox ;

Another octave band noise technique was proposed by Szczerbicki and Szuwarzynski [9]. The prediction method was based on measurements taken aboard 15 cargo vessels and then verified against 5 other vessels. Szczerbicki employed multiple regression theory to develop the mathematical model however no comparison of measured and predicted data is included The method is based purely upon statistical evaluation of measured data and thus eschews the approaches of Buiten and Plunt who considered the different noise sources and their relative magnitudes.

Calcagno *et al* [10] presented two statistical prediction methods for predicting the A-weighted octave band noise levels on ship superstructures. The first method is based on the multiple regression method employed by Szczerbicki and the second method extends the Optimal Linear Parameter Estimation (OLPE) theory. Calcagno sought to show that the OLPE theory was superior to the regression method. Measurements taken aboard 18 vessels in a total of 913 cabins were the basis for the statistical model. Calcagno concluded that the OLPE method with a mean standard deviation of ± 5 dB was more accurate than the regression method with a standard deviation of between ± 6 dB and ± 8 dB.

The main advantage of empirical methods is that they are simple and can work well if the ship being analysed is similar in design and construction to those of the reference vessels from which the empirical rules have been developed. This is particularly useful in the early design stages as it can give the designer a feel for the noise levels without the need for complex calculations. If the requirements for similarity are not met, the predictions obtained have a greatly increased uncertainty. The problems with empirical methods can be summarised as follows:

- they take a simplistic and coarse approach to the ship design;
- they do not give any information about transmission paths through the ship;
- they do not permit the effects of structural design changes on sound transmission to be assessed;
- they are of limited use when novel features are included in the ship design;

2.2.3 Wave Guide Models

The wave guide model was first utilised by Fahy and Lindqvist [11] to study structure-borne noise transmission in ship hull-frame structures. The model developed was based on a hull plate bounded by two parallel frames. The purpose of the analysis was to determine the effectiveness of damping treatments applied to the hull plate. The analytical model revealed that the hull frames provided a flanking path that rendered the damping layers on the hull plate ineffective.

In a similar approach Nilsson [12] studied the propagation of structure-borne noise in the hull-frame structure by modelling the plates of the frame and the hull as a one-dimensional Timoshenko beam model. This was used to predict the transmission of structure-borne noise in the vertical direction. The Fahy and Nilsson frame models are shown in figures 2.1 and 2.2.

Nilsson [13] took the waveguide approach further by developing a model for the prediction of vibration levels in a ship superstructure. This mathematical model was based on a method developed by Heckl [14] for studying grillage structures. In this structural model the parallel frames are considered to act as a waveguides constraining the structure-borne noise to propagate in the vertical direction (for hull and superstructure plates) and the transverse direction (for deck plates) i.e. there is no transmission past the frame members. A diagram of the waveguide model is shown in figure 2.3. Nilsson [15] tested this conceptual model experimentally by constructing a 1/20th scale model to match the mathematical model which allowed comparison of predictions and measurements. For the scale model, excellent agreement was found between the measured and predicted vibration levels. Nilsson [16] further refined the model to improve the accuracy of the low frequency predictions and to allow for a loss of energy longitudinally past the frames by incorporating the empirical rules developed by Janssen [5].

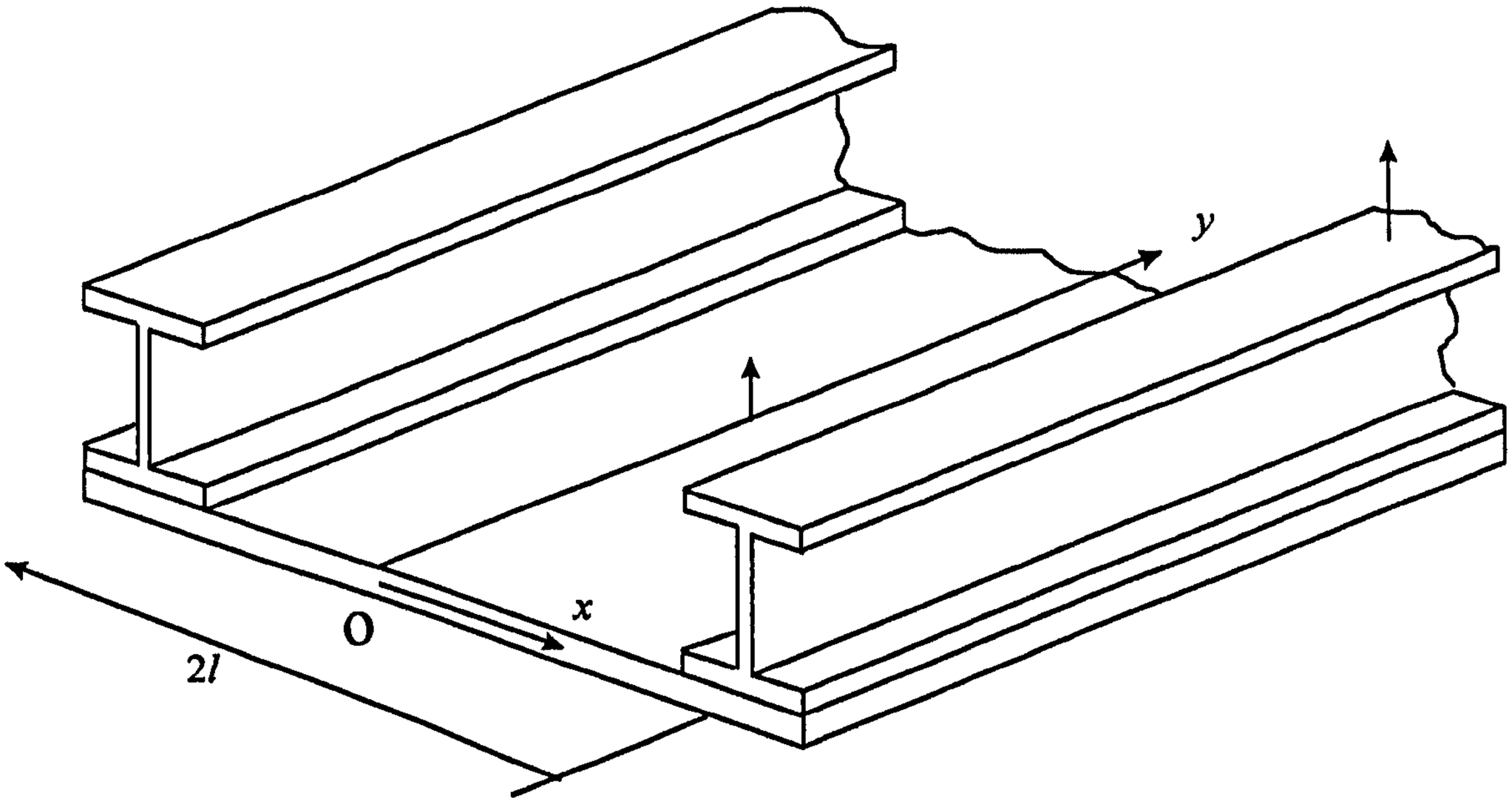

Figure 2.1 Fahy and Lindqvist frame model

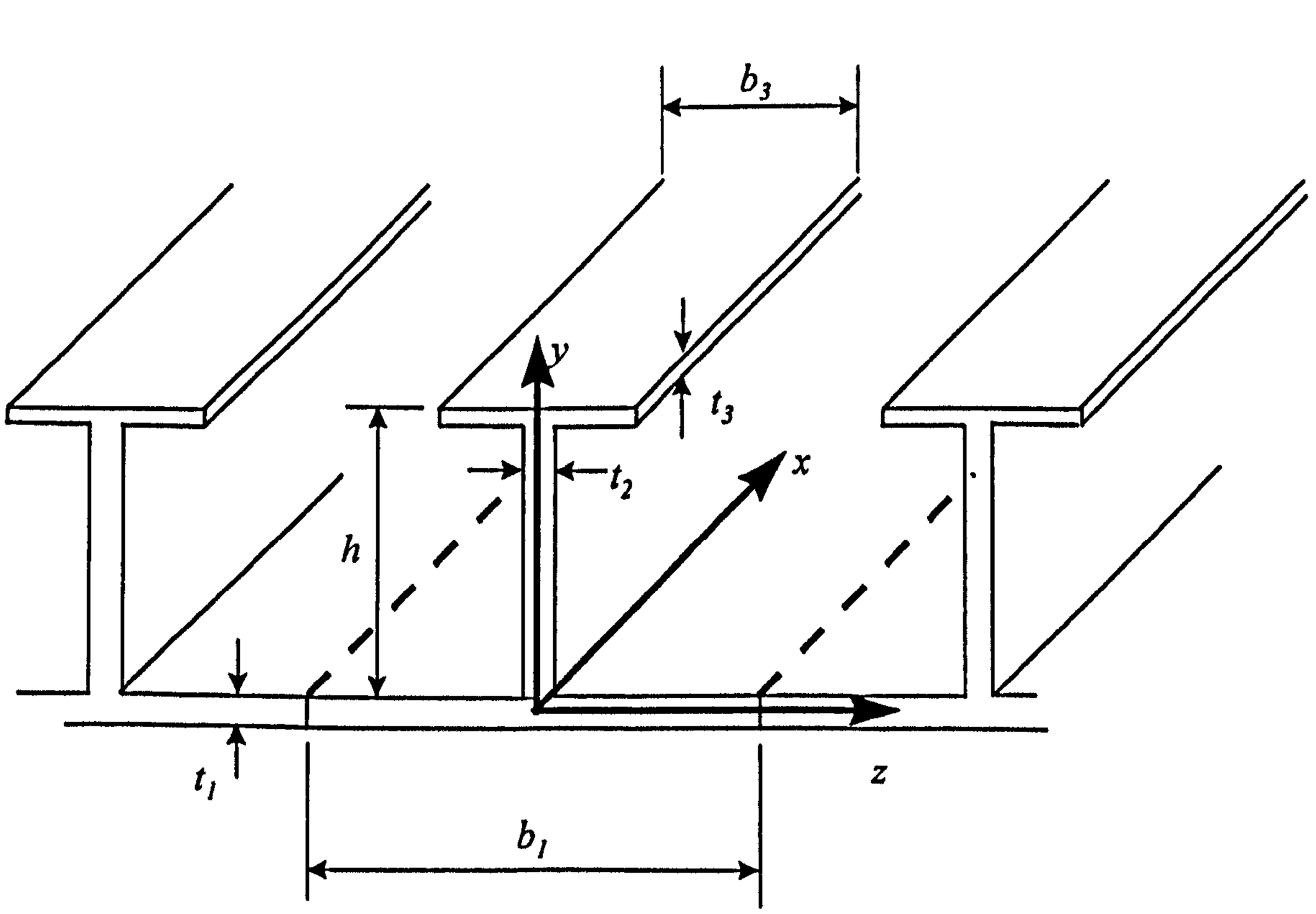

Figure 2.2 Nilsson frame model

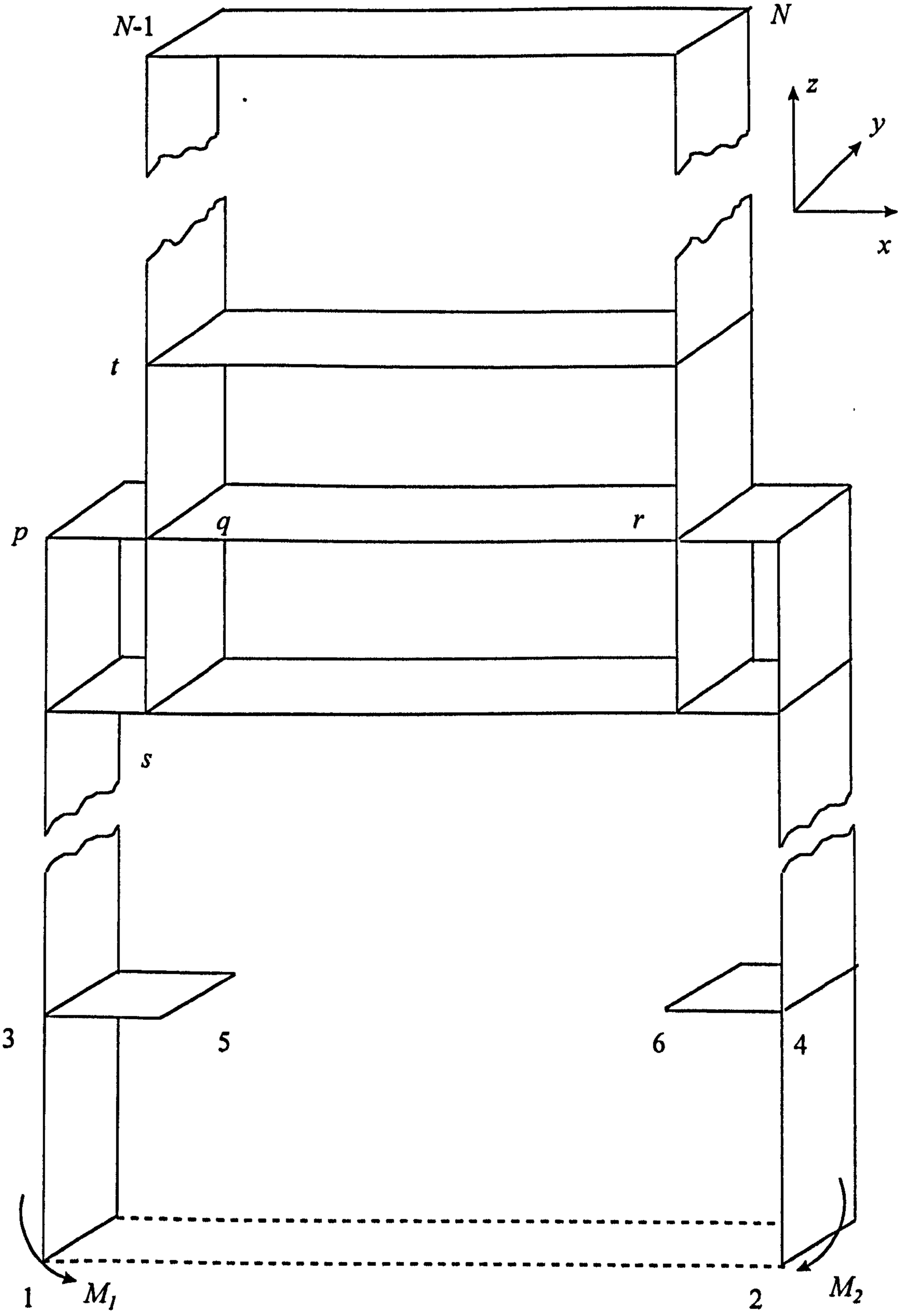

Figure 2.3 Nilsson waveguide model:

vertical section of a ship structure

The waveguide model is a more refined method for predicting noise levels than empirical methods since it considers the design of the structure. Computerised it offers a simple and quick modelling approach, however the experimental and measured data used to verify the model are for a particular ship construction to which the wave guide model is well suited. Typically this is a cargo vessel with superstructure above the engine room at the aft of the ship. The waveguide model has not been proven with published data for any other design of vessel.

2.2.4 Statistical Energy Analysis

There are a number of SEA studies of ships, ship like structures and parts of ship structures that have been published in the past twenty-five years and these are reviewed in more detail in this section

The first SEA analysis of a vessel was a theoretical study undertaken by Sawley [17]. The vessel studied had a length of 22 m and was constructed from steel. The deck house of the vessel was located directly above the engine room. The objective of the work was to identify the importance of the different transmission paths from the engine room to the deckhouse. This would allow the appropriate noise control measures to be identified to reduce the airborne noise level in the deck house below NC75. The comparison of the predicted and measured vibration level show good agreement, however because the vessel was small, the distance between the source and receiving subsystems was such that significant errors were not introduced.

Chernjawski and Arcidiacono [18] presented a theoretical study of the vibration transmission characteristics of a cross joint formed from the intersection of four semi-infinite plates at a rigid mass. A model for the transmission characteristics of infinite stiffened plate and of a plane structure was also presented. The investigation of the plane structure was based on Heckl's [14] grillage study but constructed from plates and beams. No experimental work was included to validate any of the theoretical models.

Jansen [19,20] presented the results of an investigation into the application of SEA to ship structures. A 1/5th scale model of a section through a bulk carrier was presented. The SEA model of the structure consisted of 27 bending wave subsystems with L,T and X joints. Measurements were taken on an undamped model and damped model where an additional constrained damping layer was applied. Jansen concluded that the poor agreement between the heavily damped prediction and measurements was due to the absence of in-plane flanking paths in the SEA model.

Irie and Takagi [21] examined the application of SEA for two scale laboratory models. The first model was a steel box (2 m x 1.74 m x 1.8 m) with 148 panels and 547 joints The second model was a 1/10th scale model of an engine room and accommodation space of a 36,000 tonne bulk carrier with 337 subsystems and 1317 joints. Both models consisted of 4 basic joint types covering L, T, X and inline joints. The measured and predicted results appear to show good agreement.

Fukuzawa and Yasuda [22] created an SEA model of the structure-borne noise in a 16650 tonne ship superstructure after taking onboard measurements of the vibration levels and the sound pressure level. Measurements were taken before and after noise and vibration countermeasures were installed. The modelling of the ship structure was performed in an unusual manner. Fukuzawa assumed symmetry to reduce the model and then further reduced the SEA model to a two-dimensional model in longitudinal and vertical directions. Thus the ship model was reduced to only 67 subsystems and 375 joints. Results are presented comparing the predicted and measured vibration levels, however the validity of the assumptions underlying the two-dimensional model approach are not discussed in any detail.

Plunt [23] in part II of his major study of ship noise examined the application of SEA to predicting structure-borne noise in ships. Plunt developed an SEA code, SEACAL1 and studied the following structural elements:

(a) A T-junction with different loss factors for the individual plates was analytically;

(b) Three T-junctions in series was investigated analytically. This was intended to represent the hull plate with deck plates;

(c) A steel plate reinforced with periodic stiffeners was studied analytically. The bending wave transmission characteristics of the stiffeners were based on Heckl's [14] model;

(d) A honeycomb structure intended to represent the double bottom structure of a ship was studied analytically and experimentally. The effect of different loss factor assumptions on the vibration levels was also investigated.

Plunt then went on to generate SEA models of the aft section of two of the reference ships from part I of his ship study. The results presented by Plunt generally show good agreement with the measured data over most of the frequency spectrum.

Yoshikai *et al* [24] outline the development of an SEA package for predicting ship cabin noise levels. Measurements were taken onboard an 84,000 tonne bulk carrier and a 15,000 tonne chemical carrier. The ship structures were excited by a tapping machine and airborne and structure borne noise levels were measured at locations throughout the ship. The reported difference between the predicted and measured airborne levels is within ±3 dB for approximately 78% of the results for both vessels. For the structure borne noise levels a ±3 dB difference is reported for 75% of the results on the bulk carrier and 58% of the results on the chemical carrier. Yoshikai also proposed a measure for the power levels on structural elements called the structural temperature level which would be directly comparable with the airborne sound pressure level.

Irie and Nakamura [25] presented a general paper outlining the general theory and equations of SEA with application to ship structures. Examples of the application of

SEA to laboratory models and scale models are given. The scale models discussed are the same as those previously presented by Irie [21]. Irie also presented an equation for the internal loss factor of steel plates based on experimental measurements.

Lyon and Tratch [26] and Tratch [27] used SEA to study the structure-borne sound transmission from machinery foundations to the bedplate and hull plate. Tratch constructed four experimental models of increasing complexity, the most important being the seven and twelve plate models and compared the results with SEA models. Tratch concluded that the in-plane contribution could not be ignored. The test structure studied by Tratch is shown in figure 2.4.

Shimomura and Lyon [28,29] studied sound transmission in oil storage tanks aboard a ship. The experimental part of this work was performed on a small water filled tank with offset plates as shown in figure 2.5. This was intended to represent a 1/10th scale model of an oil tank between decks where the offset plates represent the deck levels. Shimomura examined the effect of the water on the sound transmission between the offset plates. The effect of the fluid loading on the joint transmission characteristics was incorporated by interpolating a mass loading term from the experimental results and applying this to the joint coupling loss factors. Because of the geometry of the tank construction only corner (L) joints were studied in the analysis.

Iino and Honda [30] outline the development and structure of a software package for predicting the noise levels aboard passenger cruise ships utilising SEA for predicting the structure borne noise and normal calculations for the airborne noise. An example of the predicted noise levels for a 49,000 tonne passenger vessel are presented with 1647 subsystems and 7,500 joints. The difference between the airborne noise predictions and the measured data is indicated to be less than 3dB for approximately 80% of the predictions.

Taroudakis *et al* [31] studied the modelling of plate stiffeners on ship structures. The approach adopted by Taroudakis was to model the stiffeners as beam subsystems and as

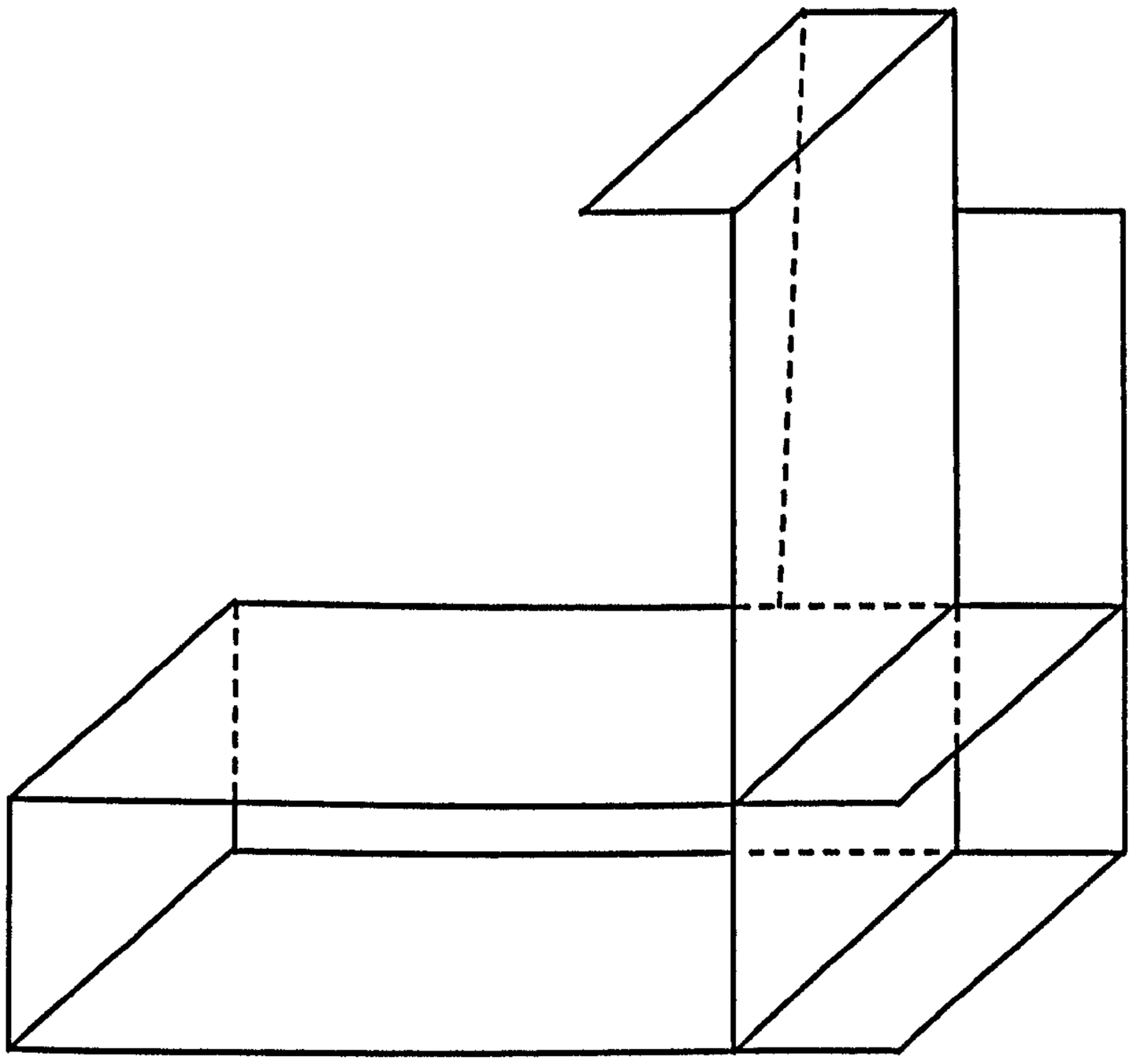

Figure 2.4 Test structure used by Tratch [27]

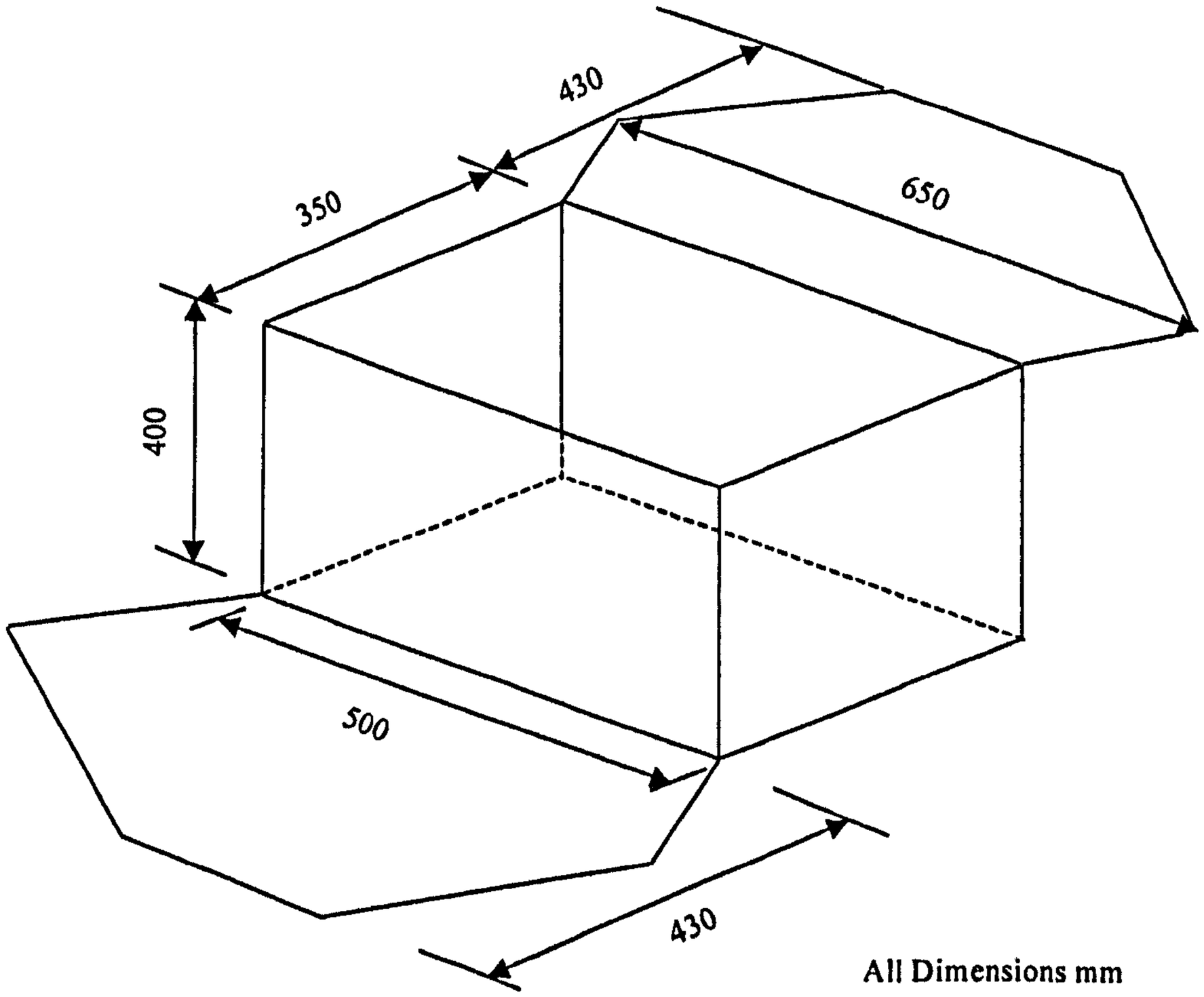

Figure 2.5 Tank structure used by Shimomura [28]

plates. The predicted results for the velocity and sound pressure level in the engine room of a 56 m patrol vessel are given. These indicate there is no significant difference in modelling the stiffeners as plates and beams over most of the frequency range.

Kim *et al* [32] studied the effects of bending wave transmission in multi-connected plates for a box-like test structure constructed from thirteen 0.1m^2 plates. The box structure consisted exclusively of T and L joint types. The separated mode method was used to predict the transmission across the structure for a harmonic force. The temporal and spatial velocities for each plate were averaged to produce a prediction of the root mean square vibration level. These were then compared to predictions obtained from an SEA model of the structure.

Kang *et al* [33] investigated the problem of modelling a ship structure and reducing the amount of input data required at the design stage. Kang investigated two SEA models of a cubic structure constructed from 5 mm thick steel plate intended to represent 4 decks with intermediate bulkheads. The first model included all joints which yielded 108 plate subsystems and 27 room subsystems. The second model used ' extended ' coupling types which reduced the model to 98 subsystems. These ' extended ' coupling types allowed one deck to be represented as a single subsystem since they only permit transmission from the deck to the internal bulkheads. Predicted results presented for this approach show good agreement from which Kang concluded that this was an efficient method of reducing the complexity of the model. Kang also reported work on the modelling of cabin linings which concluded that neglecting the noise radiated from false ceilings and lining panels did not significantly affect the SEA predictions.

Kim *et al* [34] outlines the development of an SEA package NASS for the prediction of structure borne noise. The code converts a finite element model of the ship to an SEA model. Results for the aft parts of a bulk carrier (320 subsystems) and a container carrier (719 subsystems) are presented. Comparisons of the predictions and measurements for a bulk carrier modelled from 320 subsystems and of the aft part accommodation of a container ship with 719 subsystems. Comparisons between the predicted and measured

sound pressure level from the engine room, control room and a cabin show good agreement across the frequency range. Kim attributes the better agreement for the container ship to more sophisticated modelling of the double hull structure.

Hynna *et al* [35] outlined the adaptation of a finite element pre-processor to reduce the labour in modelling a full ship structure. Results from a hydro-graphic echo sweeping vessel, a timber container carrier and a passenger cruise vessel are presented. The SEA models created were large, for instance the cruise vessel consisted of 5143 subsystems. To determine the input power levels, the vibration level adjacent to the resilient mounts on the main and auxiliary engines were measured and then converted to power the point mobility of the bedplate. Results are presented for the difference between the measured and predicted sound pressure level.

2.2.5 Summary of Previous work

In the previous sections, the methods available to predict structure borne noise levels in ships have been reviewed. The finite element method is suitable for predicting the low frequency global modes (1 to 30 Hz) of the ship structure, but as the frequency range of interest increases, the number of degrees of freedom required in the model rapidly increases requiring powerful computing resources. In addition the time expended in modelling renders the finite element unfeasible for the higher order frequencies.

Empirical methods give formulae that allow the designer a simple and quick technique to predict vibration and noise levels, however they are relatively coarse and crude, dependant on the design of the ships from which the experimental data was gathered and make assumptions about the layout of the structure. Empirical methods provide little or no information on transmission paths and how changes in the structure affect the structure borne noise levels.

The more sophisticated waveguide approach developed by Nilsson models a section through a ship and allows the transverse and vertical transmission to be predicted. This

is a simple modelling approach that gives a designer a 'feel' for vibration levels but because the waveguide model assumes that the rib stiffeners, which define the boundary of the model, are of infinite impedance, then longitudinal transmission is not adequately accounted for. In practice the rib stiffeners are of finite impedance and therefore longitudinal transmission will be important.

SEA is the most practical solution for the prediction of structure borne noise levels in ships since it will allow the prediction in the transverse, longitudinal and vertical directions. SEA also allows the impact of structural changes on vibration levels to be assessed and is flexible allowing the analyst to choose the complexity and detail of the SEA model as required. The problem with the work to date on the application of SEA to ships is that it has progressed in a piecemeal, uncoordinated approach over a period of thirty years. Much of the work has either concentrated on laboratory structures intended to represent scaled parts/sections of ship structures or on the development of internal SEA codes by shipbuilders. This is not intended as direct criticism since it is difficult to obtain owner/operators permission to access a ship to perform on-board measurements and much of the laboratory work does give some insight structure-borne noise mechanisms. The fact remains though, that in practice a ship is large, complex structure and very little data is available to allow an engineer creating an SEA model to make informed decisions about the modelling process.

2.3 Statistical Energy Analysis

The basic review of the key elements of SEA theory is presented in this section. A more detailed review can be found in the texts of Lyon and DeJong [36] and Craik [37].

2.3.1 The Development of Statistical Energy Analysis

SEA has evolved from the initial research by Lyon and Madianik [38] into the power flow between coupled linear oscillators excited by a broad band noise. This initial study was followed by a series of papers. Smith [39] investigated the application of SEA to

the problem of sound-structure interaction while Scharton [40] investigated the significance of light coupling. Lyon and Eichler [41] and Lyon [42] sought to develop some initial theories for predicting response variance. Lyon and Scharton [43] and Eichler [44] investigated the problem of three systems connected together.

The derivation of the fundamental relations has continued as an area of research. Maidanik [45,46,47] and Brooks and Maidanik [48] developed a general formalism for the basic SEA equations. Woodhouse [49] investigated the basic SEA equations by applying Rayleigh's classical approach for a system with a finite number of degrees of freedom. Dimitriadis and Pierce [50] derived a rigorous solution to the power flow between two perpendicular coupled plates to examine the basic SEA hypothesis particularly the strong coupling limitation. Manning [51] used a mobility approach to define all the basic SEA parameters while Langley [52,53] produced a general derivation of the basic SEA equations and the coupling loss factor. Mace [54,55] has reassessed the basic relations for coupled one dimensional subsystems and investigated the consistency relationship. Kishimoto *et al* [56] developed an energy flow model for deterministic connected structures to investigate the basic SEA model. Pinnington and Lednik [57,58] have investigated the extension of SEA to transient energy flow between coupled oscillators. A numerical study of the power flow between two coupled beams was presented and good agreement found with an exact wave solution. Sun *et al* [59] developed a model for three coupled oscillators. Sun determined that the power flow consists of direct power flow between the directly coupled oscillators and an indirect power flow between the unconnected oscillators.

The problem of indirect coupling, also referred to as 'tunnelling', has been investigated by Langley and Bercin [60]. Langley proposed the wave intensity technique to account for the directional dependency of a wave field. This is a phenomenon that can be found in structures that are spatially periodic. Heron [61] investigated a more general method for incorporating indirect coupling and applied it to a beam model.

Fahy [62,63] has reviewed the development of SEA to identify current weaknesses where further research is required. Particular aspects of basic SEA theory have been recently been investigated. Mace [64] has investigated the basic assumption that the vibration field within subsystems is incoherent and concluded that this is only valid in lightly coupled subsystems and that coherence is a measure of coupling strength. Beshara and Keane [65] have investigated the problem of non-conservatively connected subsystems and proposed the introduction of damping in joints to account for the additional energy dissipation.

From this work the following are the fundamental assumptions underpinning SEA.

(a) The input power spectra to any subsystem is approximately flat and considered to be a broad band source.

(b) If there are multiple power sources then they are statistically independent.

(c) The subsystem dynamic response is linear and the system is conservative.

(d) Within a subsystem, the modes are statistically independent and have equal mean energy.

(e) Power flows from the subsystem with the higher uncoupled modal energy to the subsystem with the lower uncoupled modal energy.

(f) The modal response within subsystems is considered to be incoherent.

2.3.2 Energy and Subsystems

In SEA a structure is subdivided into parts termed *subsystems* which are related to the physical components that the structure is constructed from i.e. beams, columns, plates etc. A subsystem however is not a physical component but a group of resonant modes of a similar nature that store energy. A plate can support bending, longitudinal and transverse wave types and can therefore be represented by three subsystems, with each subsystem representing the energy stored by a particular wave type. A beam can support bending, longitudinal and torsion waves and can be represented by four subsystems

since a beam can support bending in two directions. Each of the four subsystems represents the energy stored in the beam by a particular wave type.

Energy is the variable used in SEA to describe the state of a subsystem. The advantage in choosing energy as the state variable is that it permits the physical distinction between subsystems to be removed. Once a solution has been obtained the subsystem energy can be converted into any convenient variable that describes the subsystem response. Examples of variables that describe system response are the sound pressure level in a room or the vibration of a plate which can be described in terms of the acceleration, velocity or displacement. Other variables such as strain and stress can also be used if necessary.

For an acoustic subsystem with an acoustic impedance $\rho_o c_o$, the relationship between the energy E and sound pressure level is given by Craik [37] as

$$E = \frac{V\langle p^2 \rangle}{\rho_o c_o^2} \tag{2.1}$$

where V is the subsystem volume and $\langle p^2 \rangle$ is the mean square pressure level. For a structural subsystem the energy is related to the velocity by the following equation.

$$E = m\langle v^2 \rangle = m\frac{\langle a^2 \rangle}{\omega^2} \tag{2.2}$$

where m is the subsystem mass, $\langle v^2 \rangle$ is the mean square velocity level and $\langle a^2 \rangle$ is the mean square acceleration level.

The exchange of energy between two subsystems can be considered from a modal or wave viewpoint. In the wave approach, the vibration field is considered to be created by the superposition of travelling waves and the wave field throughout the subsystem is

assumed to be diffuse and uncorrelated. The wave energy is determined only by the dynamic properties of the medium through which the waves propagate and is essentially independent of the subsystem boundary conditions i.e. the wave representation requires no consideration of natural frequencies, mode shapes or assumptions about the boundary conditions.

The modal approach has traditionally been used in the development of the fundamental SEA theory and the assumptions that underlie the method. In the modal approach the equations governing the dynamic behaviour of the individual subsystems are described in terms of modal mass, stiffness and damping and the solution is expressed in terms of eigenvectors and eigenvalues. The modal approach is satisfactory for studies of coupled resonators but does not lend itself to the analysis of more complex coupled structures. Consequently it is the wave approach that is adopted when considering structure-borne noise transmission.

2.3.3 Coupling Loss Factor

The *coupling loss factor* represents the energy lost from one subsystem to another subsystem and is denoted by the term η_{ij}. The subscripts denote that energy flows from subsystem i to j. The coupling loss factor is defined as the energy loss per radian cycle thus the power flowing from subsystem i to j is given by

$$W_{ij} = E_i \omega \eta_{ij} \tag{2.3}$$

The amount of power transferred from subsystem i to j is dependent upon a number of variables such as the type of subsystem, the subsystem medium, and the type of connection between the subsystems.

Structure to Structure Coupling

As discussed in section 2.3.2 the energy in the system may be considered from a modal or wave viewpoint. In considering structure to structure coupling, the wave approach is the most frequently used for predicting the power transfer. The wave approach assumes that for an incident wave upon a joint that some of the wave energy is transmitted across the joint and some is reflected. It is assumed that for any joint model that energy is conserved, therefore the sum of the transmitted and reflected wave power must equal the incident power upon the joint. The transmission coefficient τ can be then be defined as

$$\tau_{transmitted} = \frac{W_{transmitted}}{W_{incident}} \tag{2.4}$$

For two coupled plates, the power transmitted from subsystem i to subsystem j is given by Craik [37] as

$$W_{ij} = E_i \frac{c_{gi} L_{ij} \tau_{ij}}{S_i \pi} = E_i \omega \eta_{ij} \tag{2.5}$$

where S_i is the surface area of the source plate, L_{ij} is the joint length and c_{gi} is the speed of energy transportation in the source subsystem. For plates the group and phase velocity of longitudinal and transverse waves is the same whilst the group velocity of flexural waves is twice that of the phase velocity. Equation *2.5* can be rearranged to give the general expression for the structural coupling loss factor as follows.

$$\eta_{ij} = \frac{c_{gi} L_{ij} \tau_{ij}}{2 S_i f \pi^2} \tag{2.6}$$

From the above equations it is clear that the structural coupling loss factors can only be predicted if the transmission coefficient is known. In SEA the angular average transmission coefficient is used since a diffuse wave field is assumed for all subsystems.

The angular average transmission $\overline{\tau_{ij}}$ coefficient can be determined by integrating over all angles of incidence and is given by Cremer et al [66] as follows.

$$\overline{\tau_{ij}} = \int_0^{\frac{\pi}{2}} \tau(\theta)\cos(\theta)d\theta \tag{2.7}$$

The transmission characteristics of different structural joint designs have been investigated and these are briefly reviewed here. The most frequently studied joint is the X joint which can be simplified to a T or L joint by omission of certain plates. This was first studied by Cremer et al [66] for an incident bending wave. Kihlman [67] extended the model to include in-plane waves for the source and coplanar plate. Craven and Gibbs [68,69] and Wohle et al [70,71] extended the model to include in-plane waves on all plates. Mees and Vermeir [72] investigated the cross joint for the presence of an elastic interlayer at the centre of the joint. Steel [73] developed the cross joint to include an integral beam/column at the intersection of the plates while Bosmans et al [74] investigated the cross joint for orthotropic plates.

The transmission characteristics of two parallel plates separated by a beam have been researched by Battachayra [75], Sullivan [76], Wilson [77] and Smith [78]. Langley and Heron [79] developed a general method for predicting the transmission characteristics of any plate-beam joint configuration in the dynamic stiffness matrix method. Langley [80] further extended this method to calculate the transmission characteristics of joints formed from beams and singly curved panels.

The joint transmission models for X, T, L and two parallel plates separated by a beam have been developed and these joint types are all found in ship structures. However the most commonly found joint in a ship is the hull frame stiffener which is found reinforcing deck plates, bulkheads and the ship hull. These stiffeners have been assumed to be extremely important in the prediction of structure borne noise in ships as the assumption has been made that these are usually periodic/near-periodic and therefore

pose unique problems. In particular it has been proposed that the periodic/near-periodic arrays of stiffeners act as wave filters with discrete stop and pass bands with the result that the classical SEA approach of defining a unique joint for each stiffener will not give accurate predictions and the more advanced methods such as dynamic stiffness matrix approach or wave intensity analysis will be required.

In chapter four of this thesis a specific transmission model is developed for the types of rib stiffener commonly encountered in ship construction which will then be used in all of SEA models of laboratory and ship structures presented in this thesis. The dynamic stiffness matrix could also be used to model the rib stiffeners but the development of a specific transmission model is a simpler and more straightforward task than developing the software code for the dynamic stiffness matrix.

Structure to Fluid Coupling

Structure to fluid coupling is an important transmission mechanism and will occur in most real situations and is determined from consideration of the power radiated by a plate or a wall. The power radiated is a function of the radiation efficiency which is defined as the ratio of the power radiated by the plate to that of a piston with the same area and velocity. For a plate the power radiated, W_{rad}, is given by

$$W_{rad} = \langle v^2 \rangle \rho_o c_o S \sigma \tag{2.8}$$

where S is the plate area, $\langle v^2 \rangle$ is the spatial averaged mean square velocity of the plate surface ρ_o is the fluid density, c_o is the acoustic wave speed of the fluid and σ is the radiation efficiency. By equating the radiated power predicted by the SEA and classical approaches, the coupling loss factor for a plate can be expressed in the following terms, as given by Craik [37] .

$$\eta_{12} = \frac{\rho_o c_o \sigma}{2\pi f \rho_s} \tag{2.9}$$

The prediction of the structure-fluid coupling loss factor is therefore dependent on being able to determine the radiation efficiency of a finite plate. Radiation efficiency is not a simple function and the response changes at a critical frequency f_c where the wave speed of the fluid and the plate are the same. The equation for critical frequency f_c is given by Craik [37] as

$$f_c = \frac{\sqrt{3}\, c_o^2}{\pi h\, c_l} \tag{2.10}$$

At and above the critical frequency the plate is an efficient radiator and couples strongly with the acoustic field. This process is illustrated in figure *2.6* for radiation from an infinite plate. It can be seen that efficient radiation is only possible when $\sin\theta = \lambda_o/\lambda_b < 1$. Below the critical frequency, the plate is an inefficient radiator due to the speed of the plate bending waves being lower than that of the fluid wave speed. This results in sideways motion of the fluid which cancels the pressure fluctuations due to the plate wave speed. Below the critical frequency acoustic radiation occurs due to edge and corner modes which arise because of incomplete cancellation of waves at the plate edges. Figure *2.7* illustrates different standing wave configurations that arise on a plate below f_c.

Methods for predicting the radiation efficiency of plates have been investigated by a number of researchers. Maidanik [81] determined asymptotic expressions for the radiation efficiency based on studies of a ribbed plate while Wallace [82] used the plate individual modal responses to calculate the radiation efficiency.

Leppington *et al* [83] investigated the prediction of the radiation efficiency over the full frequency spectrum and arrived at the following asymptotic expressions for describing the radiation efficiency which are used in this work. These are summarised as follows.

$$f < f_c \qquad \sigma = \frac{Uc_o}{4\pi^2\sqrt{f}\sqrt{f_c}S\left(\mu^2-1\right)}\left[\ln\left[\frac{1+\mu}{1-\mu}\right]+\frac{2\mu}{\mu^2-1}\right] \tag{2.11}$$

$$f = f_c \qquad \sigma = \left[\frac{2\pi f}{c_o}\right]\sqrt{l_x}\left[0.5-0.15\frac{l_y}{l_x}\right] \tag{2.12}$$

$$f > f_c \qquad \sigma = \left[1-\frac{f}{f_c}\right]^{-0.5} \tag{2.13}$$

where l_x and l_y are the plate dimensions, U is the perimeter length i.e. $2\left(l_x+l_y\right)$ and μ is a non-dimensional frequency ratio given by the equation $\mu = \sqrt{f/f_c}$

Equation *2.13* is the same as derived by Maidanik [81] but equation *2.11* the asymptotic approximation for the radiation efficiency below the critical frequency and equation *2.12* for radiation at the critical frequency are different to those of Maidanik.

The equations above were derived for a simply supported finite plate within an infinite baffle and radiating into free space. Further research by Leppington *et al* [84] into more realistic boundary conditions for a plate found that the effect of most types of clamped boundary conditions is to increase the radiation efficiency by a factor of 2. Similarly the effect of a perpendicular baffle at the plate boundary is to increase the radiation efficiency by a factor of 2. In real plates the transition in the radiation efficiency at the critical frequency is generally found to be smooth. Leppington [85] also proposed a smoothing function to remove the sharp transition at the critical frequency and this is given by the following equation.

$$m-(m-1)\left(\frac{f}{f_c}\right)^4 \tag{2.14}$$

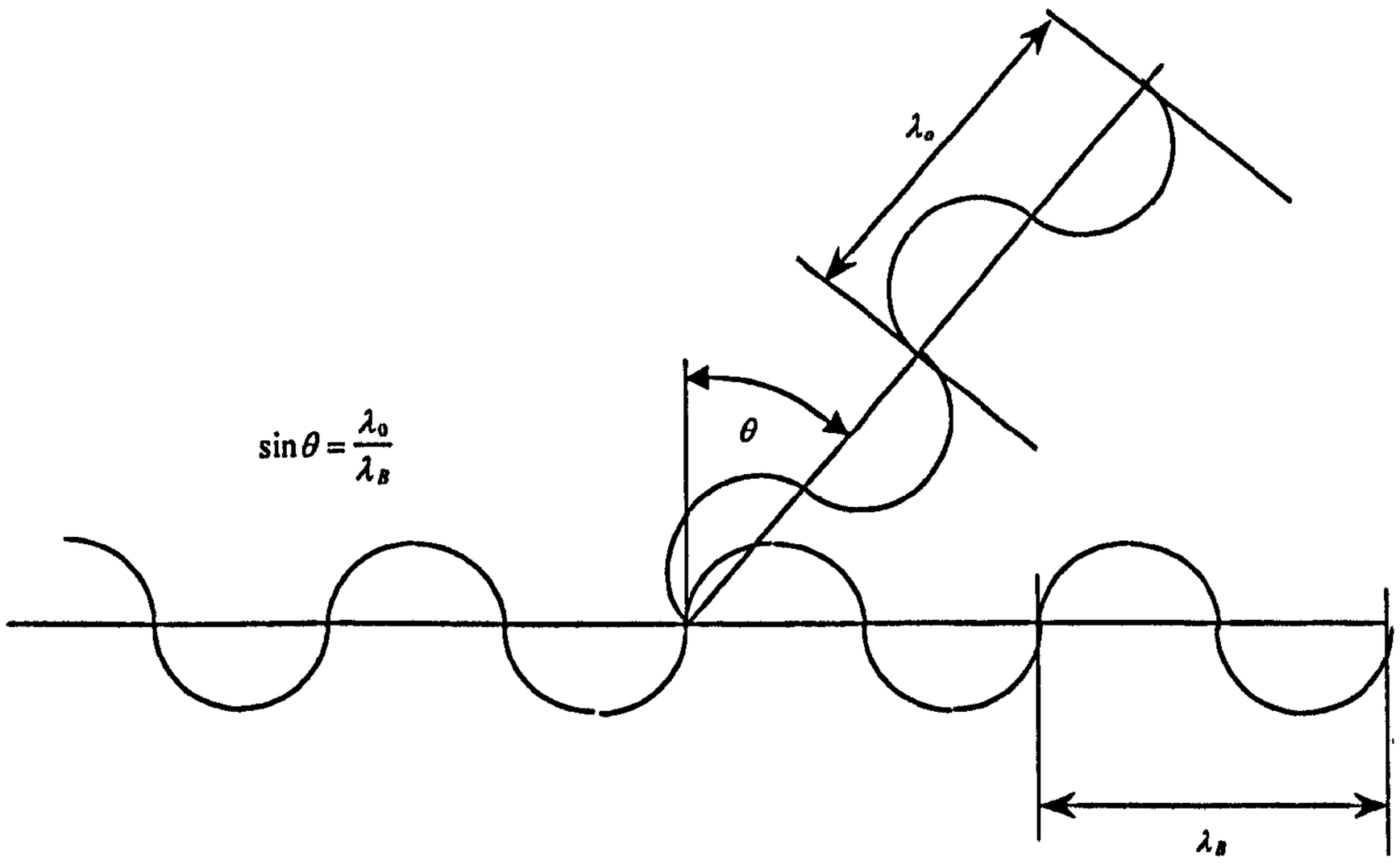

Figure 2.6 Radiation from a plate above the critical frequency

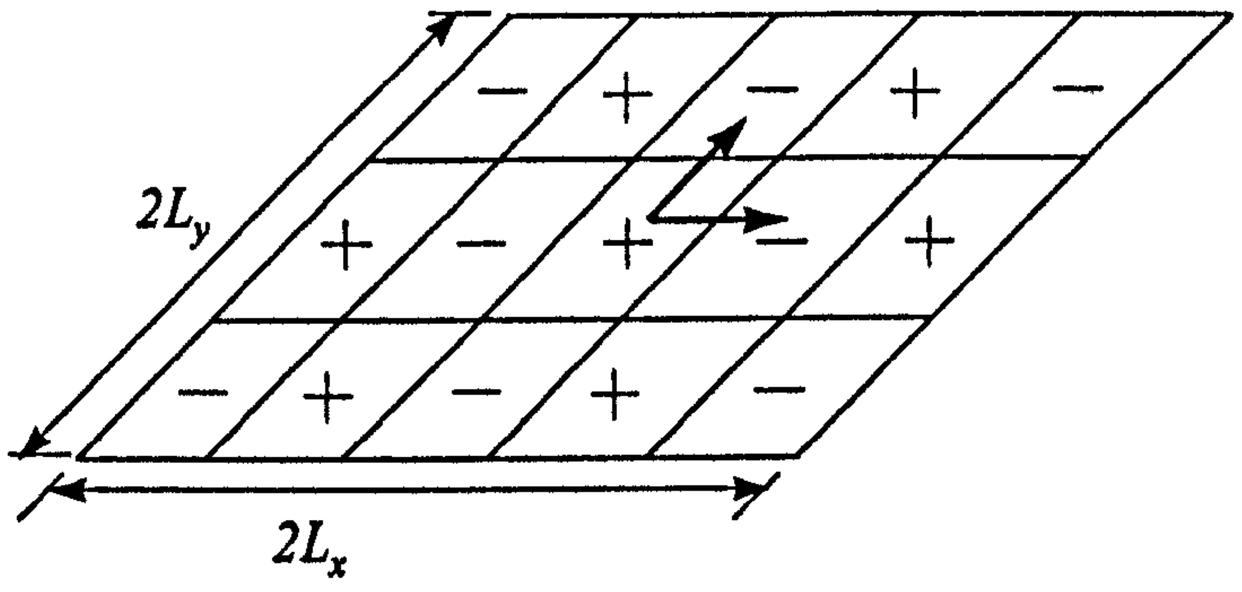

Odd-odd standing wave configuration

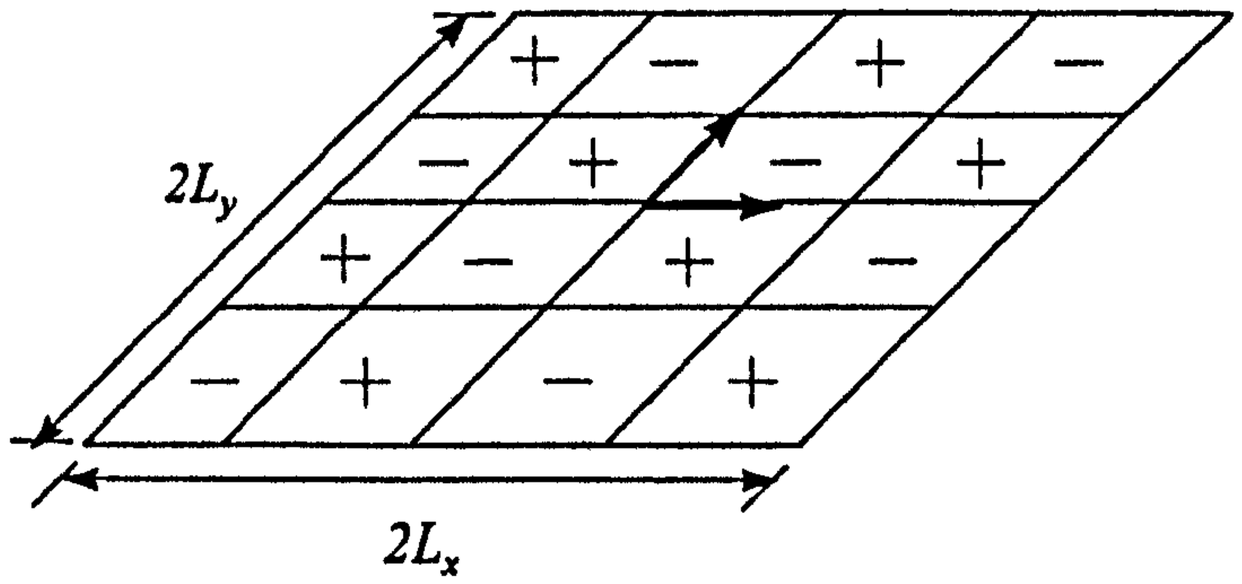

Even-even standing wave configuration

Figure 2.7 Radiation from a plate

where m is the radiation correction factor for the boundary condition effects described above.

It is not possible to directly calculate the coupling loss factor from a room to a plate. Coupling is calculated indirectly by using the consistency relationship which is valid for all coupling loss factors and defined as follows,

$$n_i \eta_{ij} = n_j \eta_{ji} \tag{2.15}$$

where n_i is the modal density of subsystem i and n_j is the modal density of the subsystem j. The coupling loss factor for a room to a plate is given by Craik [37]

$$\eta_{ij} = \frac{\rho_o c_o^2 S_i f_c \sigma}{8\pi V_i \rho_{s2} f^3} \tag{2.16}$$

Equations *2.9* and *2.16* have been used successfully to predict the coupling loss factor for air as the fluid medium. For a ship there will be radiation into the air and into the water.

2.3.4 Total Loss Factor

The *total loss factor* η represents the total energy lost from a subsystem by all loss mechanisms. For a subsystem i the total loss factor is represented by η_i which can be expressed in the following form.

$$\eta_i = \sum_{j=1}^{n} \eta_{ij} + \eta_{id} \tag{2.17}$$

The *internal loss factor* η_{id} denotes the energy lost from the subsystem by damping processes. The internal loss factor is discussed in section 2.3.5. The term $\sum_{j=1}^{n} \eta_{ij}$ represents the sum of the coupling loss factors of subsystem i which gives the

total energy flowing from subsystem *i* to all other subsystems to which it is physically connected.

2.3.5 Internal Loss Factor

The *internal loss factor* of a subsystem represents the energy lost from the subsystem due to damping. The internal loss factor is an unknown and dependent on a number of factors and can not be readily calculated from theory. The internal loss factor can be obtained from experimental measurements in the laboratory or in-situ by measuring the reverberation time of the subsystem.

The use of measured internal loss factor published in journals and text books requires caution. Measurements of reverberation time taken on a sample of the subsystem material will give the internal loss factor of the material itself where energy is dissipated in the form of heat and radiated sound waves to the environment. If the measurements are taken on the subsystem in-situ i.e. where it is connected to other subsystems then additional dissipation effects occur such as friction losses at bolted joints and welds, gas pumping at interfaces, sound radiation from free edges. These are often more efficient at dissipating energy than the material losses and consequently the measured internal loss factor in-situ can be significantly higher as a consequence. The only significant attempt to develop a theoretical model for internal losses has been performed by Maidanik [86] who investigated gas-pumping at interfaces.

As a consequence, in the experimental work, the internal loss factor is measured for all structures tested in the laboratory and on the ship structures surveyed and where appropriate a line fit will be applied to the experimental data to obtain an equation that can be used to predict the internal loss factor for the materials used.

2.3.6 The Power Balance Equations

In the previous section the basic terms have been defined. To outline the use of power balance equations, consider the example shown in figure 2.8 of two cabins separated by a common bulkhead. To analyse the power flow from cabin 1 to cabin 2 the structure has been broken down into 5 subsystems, consisting of the two cabins, the bulkhead and the deck of each cabin. The ceiling and other bulkheads have been omitted to increase clarity, but they could be included if desired. Only bending waves have been considered so that each structural element is modelled as a single subsystem.

To determine the power flow through the structure, the power balance equations for each individual subsystem must be formed. These are determined on the assumption that the principle of the conservation is energy is maintained i.e. the power flow in to a subsystem equals the power flow out. Figure 2.9 illustrates the power flow relationships between the 5 subsystems. Even for this simple 5 subsystem model the transmission paths are actually quite complex and as the number of subsystems increases then the number of transmission paths rapidly increase.

Initially the power balance equations can be written for each of the 5 subsystems as follows. The non-resonant transmission between subsystems 1 and 2 is not included.

$$W_{1,in} + W_{31} + W_{51} = W_{13} + W_{15} + W_{1d} \tag{2.18}$$

and subsystem 2

$$W_{2,in} + W_{42} + W_{52} = W_{24} + W_{25} + W_{2d} \tag{2.19}$$

and subsystem 3

$$W_{3,in} + W_{13} + W_{43} + W_{53} = W_{31} + W_{34} + W_{35} + W_{3d} \tag{2.20}$$

and subsystem 4

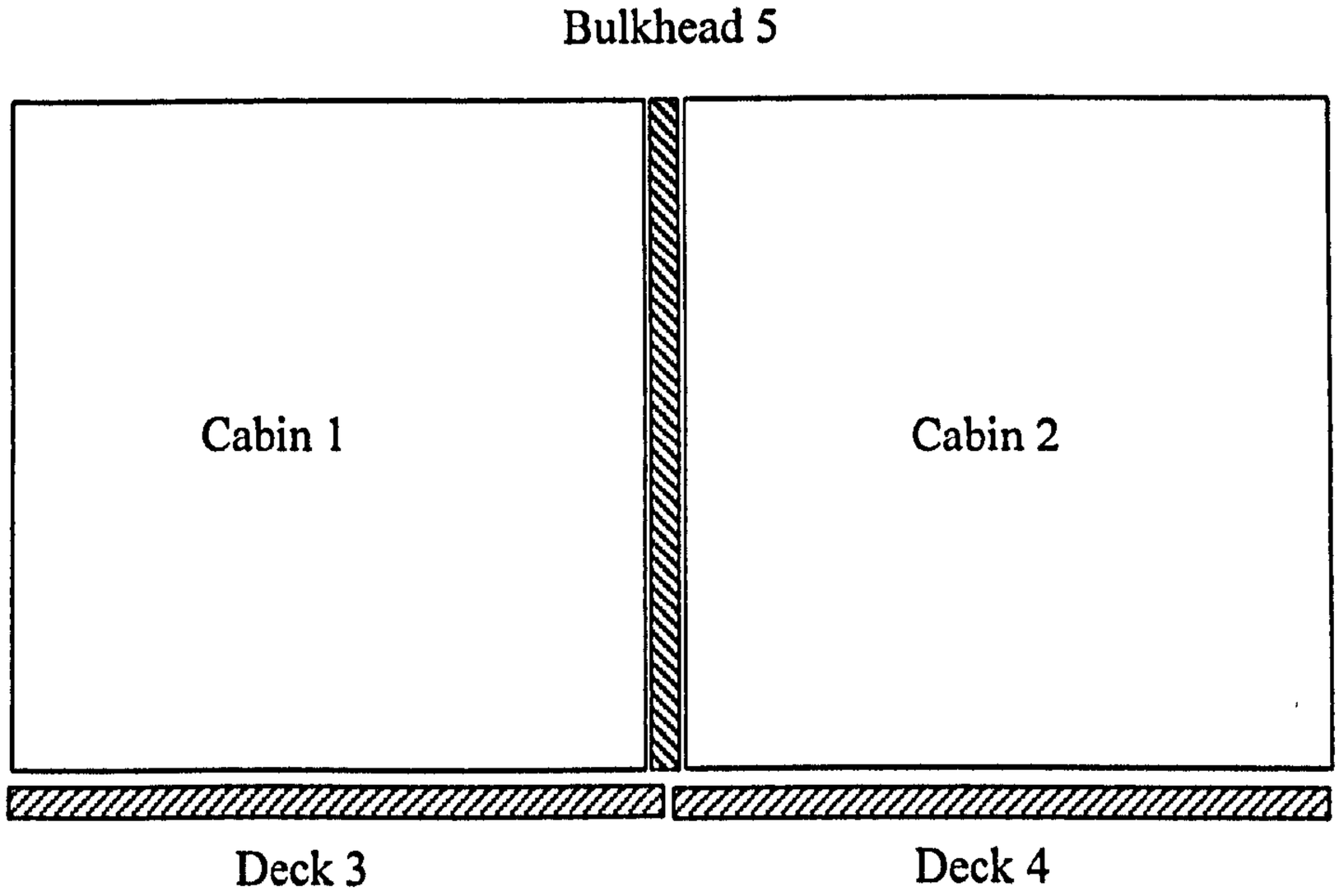

Figure 2.8 – Cabins separated by bulkhead.

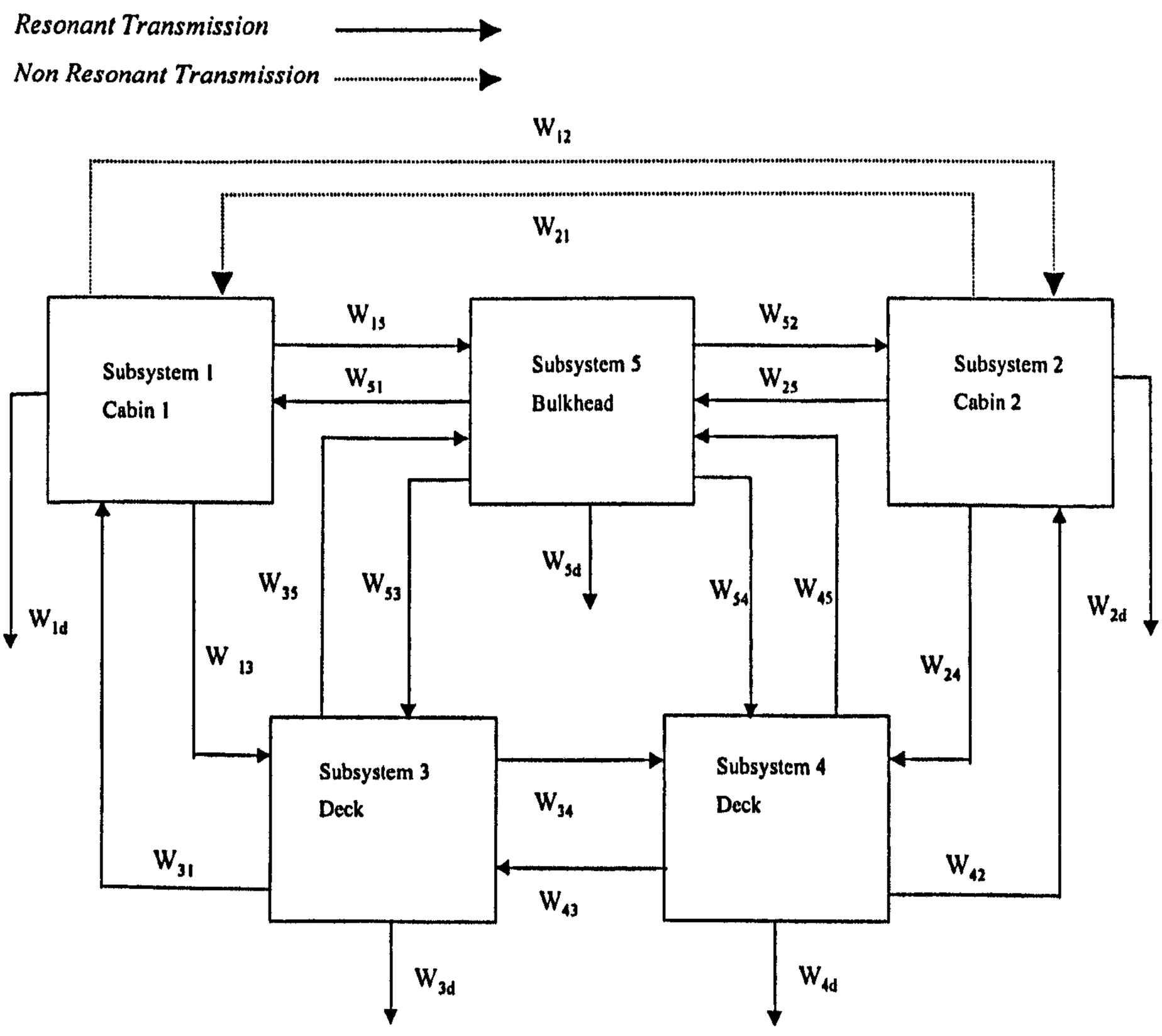

Figure 2.9 Five subsystem SEA representation of two cabins separated by common bulkhead

$$W_{4,in} + W_{24} + W_{34} + W_{54} = W_{42} + W_{43} + W_{45} + W_{4d} \tag{2.21}$$

and subsystem 5

$$W_{5,in} + W_{15} + W_{25} + W_{35} + W_{45} = W_{51} + W_{52} + W_{53} + W_{54} + W_{5d} \tag{2.22}$$

generally for a subsystem *i* the following equation can be written

$$W_{i,in} + \sum_{j=1,i\neq j}^{n} W_{ji} = \sum_{j=1,i\neq j}^{n} W_{ij} + W_{id} \tag{2.23}$$

where $W_{i,in}$ is the power input to subsystem *i* from an external source. If no external source is present then this term is zero. The summation term on the left hand side represents the total power flow into subsystem *i* from the *n* subsystems connected to it.

On the right hand side the summation term represents the total power flow out of subsystem *i* to the *n* subsystems to which it is connected and W_{id} is the power lost from subsystem *i* due to damping. The power flow between two subsystems W_{ij} is given by the following equation

$$W_{ij} = E_i \omega \eta_{ij} \tag{2.24}$$

and the power lost from subsystem *i* due to damping is given by W_{id} and can be determined from the following equation

$$W_{id} = E_i \omega \eta_{id} \tag{2.25}$$

Substituting equations *2.24* and *2.25* into equations *2.18* to *2.23*, the equations for each subsystem can be rewritten and the system of equations describing the power balance can be further simplified by recognising that the right hand side of each equation

represents the total energy lost by the subsystem and thus can be expressed as a function of the total loss factor as defined in equation *2.17*.

Thus equations *2.18* to *2.23* to be can be reduced, reordered and expressed in matrix format as follows:

$$\begin{bmatrix} \eta_1 & 0 & -\eta_{31} & 0 & -\eta_{51} \\ 0 & \eta_2 & 0 & -\eta_{42} & -\eta_{52} \\ -\eta_{13} & 0 & \eta_3 & -\eta_{43} & -\eta_{53} \\ 0 & -\eta_{24} & -\eta_{34} & \eta_4 & -\eta_{54} \\ -\eta_{15} & -\eta_{25} & -\eta_{35} & -\eta_{45} & \eta_5 \end{bmatrix} \begin{bmatrix} E_1 \\ E_2 \\ E_3 \\ E_4 \\ E_5 \end{bmatrix} = \begin{bmatrix} W_1/\omega \\ W_2/\omega \\ W_3/\omega \\ W_4/\omega \\ W_5/\omega \end{bmatrix} \tag{2.26}$$

Thus for an SEA model with n subsystems the following general equation can be written for a subsystem i as follows,

$$W_{i,in} + \sum_{\substack{j=1 \\ i \neq j}}^{n} E_i \omega \eta_{ji} = E_i \omega \eta_i \tag{2.27}$$

where the term on the right hand side of equation *2.27* is simply the total power lost from subsystem i and the summation term on the left hand side represents the total power flow into subsystem i from connected subsystems. A more general matrix form of equation *2.27* can be expressed for a system with n subsystems as follows

$$\begin{bmatrix} \eta_1 & -\eta_{21} & \cdots & -\eta_{(n-1)1} & -\eta_{n1} \\ -\eta_{12} & \eta_2 & \cdots & -\eta_{(n-1)2} & -\eta_{n2} \\ \cdots & \cdots & \cdots & \cdots & \cdots \\ -\eta_{1(n-1)} & -\eta_{2(n-1)} & \cdots & \eta_{n-1} & -\eta_{n(n-1)} \\ -\eta_{1n} & -\eta_{2n} & \cdots & -\eta_{(n-1),n} & \eta_n \end{bmatrix} \begin{bmatrix} E_1 \\ E_2 \\ .... \\ E_{n-1} \\ E_n \end{bmatrix} = \begin{bmatrix} W_1/\omega \\ W_2/\omega \\ \cdots \\ W_{n-1}/\omega \\ W_n/\omega \end{bmatrix} \tag{2.28}$$

Where there is no connection between subsystems the off diagonal coupling loss factor terms in the loss factor matrix above are zero resulting in a sparsely populated matrix. The power balance matrix can be solved simply by using standard matrix solution

techniques such as Gaussian elimination. In the case of large models the matrix equation can be solved by iterative methods as discussed by Craik [37].

2.4 The Low Frequency Limit of SEA

SEA is limited in it's application by the number of resonant modes available in a frequency band to store energy. If the number of modes available is low, then the vibration response can no longer be considered incoherent and the energy stored distributed equally between modes. It is therefore important to determine the low frequency limit of SEA.

2.4.1 Mode Count

The mode count for typical structural elements can be established from standard equations which are useful in determining where the first resonant frequencies occur and aid in the selection of subsystems. Table 2.1 gives the equations for determining the resonant frequencies of different types of subsystems.

2.4.2 Statistical Modal Count

In SEA the statistical mode count N is more important the actual mode count. This can be calculated for frequency bands as the product of the bandwidth and the modal density as follows.

$$N = n(f).\Delta f \tag{2.29}$$

where $n(f)$ is the modal density, $\Delta f = 0.23 f_c$ for 1/3 octave bands or $\Delta f = 0.707 f_c$ for 1/1 octave bands

The statistical mode count will be a real number, whilst the actual mode count will be an integer. It is however physically meaningful to consider the statistical mode count as the modal response can be spread over more than one frequency band. The modal densities of typical subsystems are given in table 2.2.

2.4.3 Modal Overlap

The previous sections allow the modal properties of a subsystem to be established, however these in themselves do not allow the low frequency limit of an SEA model to be definitively established. There have been several suggested limits for the minimum number of modes required in a particular frequency band for an SEA model to be valid (e.g. Cremer has suggested a minimum of six). One measure that has been suggested is the modal overlap factor M which is defined as the ratio of the half power bandwidth to the average frequency spacing. This gives the modal overlap as follows.

$$M = f\eta n \tag{2.38}$$

where f is the frequency, η is the total loss factor of the subsystem and n is the subsystem modal density. The modal overlap represents the proportion of the frequency spectrum that is controlled by resonant modes. If M is greater than 1, then the subsystem response is damping controlled and if $M < 1$ then the response is not damping controlled. For metal structures this is a useful limit, as there may be a reasonable number of modes at low frequencies to justify an SEA model but the low damping of metal prevents the modal overlap condition being satisfied. This is different from a building structure where there can be a low mode count but high damping which allows the modal overlap condition to be satisfied.

Table 2.1- Resonant frequency relationships.

Subsystem Type	Frequency	Equation Number
Beam/Column (In Bending)	$f_n = \frac{\pi}{4\sqrt{3}} h c_l \left[\frac{n^2}{l^2}\right]$	(2.30)
Plate (In Bending)	$f_n = \frac{\pi}{4\sqrt{3}} h c_l \left[\frac{n^2}{l_x^2} + \frac{m^2}{l_y^2}\right]$	(2.31)
Volume	$f_n = \frac{c_o}{2}\left[\frac{n^2}{l_x^2} + \frac{m^2}{l_y^2} + \frac{o^2}{l_z^2}\right]$	(2.32)

Where l_x , l_y and l_z are the structural dimensions and n, m and o are positive integers (0,1,2,3...).

Table 2.2 - Modal density relationships

Subsystem Type	Modal Density	Equation No.
beams / columns (In Bending)	$n(f) = \frac{l}{c_g} = \frac{\sqrt[4]{3}}{\sqrt{\pi}} \frac{1}{\sqrt{c_l h f}}$	(2.33)
Plates (bending waves)	$n(f) = \frac{\sqrt{3} S}{h c_l}$	(2.34)
Plates (longitudinal waves)	$n(f) = \frac{l}{c_g} = \frac{\sqrt[4]{3}}{\sqrt{\pi}} \frac{1}{\sqrt{c_l h f}}$	(2.35)
Plates (transverse waves)	$n(f) = \frac{l}{c_g} = \frac{\sqrt[4]{3}}{\sqrt{\pi}} \frac{1}{\sqrt{c_l h f}}$	(2.36)
Volume	$n(f) = \frac{4\pi f^2 V}{c_o^3} + \frac{\pi f S}{2 c_o^2} + \frac{L}{8 c_o}$	(2.37)

Where V is the volume of the room, S is the total surface area and L is the total perimeter length.

2.5 The Predicted Variation of SEA

As stated in the introduction, the SEA model of a structure represents the mean of a population of similar structures with the same general properties. It is therefore desirable to predict the standard deviation, probability distribution and the confidence levels. Currently this is an area where SEA requires further work and there are no general theoretical models available that permit the prediction of the variation of the response. Craik *et al* [87] have derived upper and lower confidence intervals based upon the variations in the point mobility of the receiving subsystems. This has been found to give good agreement for the coupling between two structural elements in the low part of the frequency spectrum where there are few modes in a frequency band. The upper limit given by Craik [37] is

$$L_{upper} = 10\log_{10}\left(\frac{1}{N}\right) \tag{2.39}$$

where N is the statistical mode count. This expression is valid only when $N < 1$. The lower limit is given by the following expression.

$$L_{lower} = 10\log_{10}\left(\frac{4f\eta n}{\pi}\right) = 10\log_{10}\left(\frac{4M}{\pi}\right) \tag{2.40}$$

Equation *2.40* is valid for $4M < \pi$. These equations are only valid for a two subsystem model or where a structure can be approximated to two subsystems.

2.6 Conversion From Energy To Response Variables

The result from an SEA model is a prediction of the energy level within the individual subsystems. This is not directly comparable with any measured scalar quantity and it is therefore necessary to convert the energy to a more meaningful response variable. The

relation between energy and sound pressure level was given in equation *2.1*. It is more convenient to express the relationship in dB and this can be expressed as follows:

$$L_p = L_E - 10\log_{10}(V) - 10\log_{10}\left(\frac{p_{ref}^2}{E_{ref}\rho_o c_o^2}\right) \tag{2.41}$$

where the sound pressure level is given by $L_p = 10\log_{10}\left(\langle p^2\rangle / p_{ref}^2\right)$ and the energy level is given by $L_E = 10\log_{10}\left(E/E_{ref}\right)$. For air the reference sound pressure level p_{ref} is $20\mu Pa$ and for water p_{ref} is $1\mu Pa$. The reference energy level E_{ref} is $1x10^{-12}$ J. Thus equation *2.41* can be reduced to

for air $$L_p = L_E - 10\log_{10}(V) + 25 \quad \text{dB re } 20\mu Pa \tag{2.42}$$

for water $$L_p = L_E - 10\log_{10}(V) + 93 \quad \text{dB re } 1\mu Pa \tag{2.43}$$

The relation between energy and vibration was given in equation *2.2*. This can be expressed in dB as a vibration level L_v with a velocity reference, v_{ref}, of $1x10^{-9} ms^{-1}$ or an acceleration level L_a with a reference, a_{ref}, of $1x10^{-6} ms^{-2}$ .Thus it can be shown that

$$L_v = L_E - 10\log_{10}(m) - 60 \quad \text{dB re } 1x10^{-9} ms^{-1} \tag{2.44}$$

$$L_a = L_E - 10\log_{10}(m) \quad \text{dB re } 1x10^{-6} ms^{-2} \tag{2.45}$$

2.7 Conclusions

This chapter has presented a review of the previous work on predicting noise transmission in ship structures using FEM, empirical methods, waveguide models and SEA. The previous work on SEA for ships has focused on the application to laboratory models and scale models of sections of ship structures. Where published work has been performed on real ship structures the tendency has been to use it to illustrate work on the

development of SEA software for ship analysis. SEA has been successfully applied to other large structures such as buildings where SEA has been proven to be a well developed and robust modelling approach even though the fundamental theory has only been developed for 2 or 3 coupled resonators.

The chapter also reviewed the development of SEA and introduced the basic variables of energy, power flow, loss factors, power balance equations and discussed the limitations of the SEA method.

CHAPTER THREE

Measurement and Experimental Procedures

3.1 Introduction

This chapter covers the experimental and measurement procedures used in gathering data for this work. The two basic techniques are the level difference measurement and loss factor measurement and these are covered in sections 3.2 and 3.3 for laboratory and shipboard measurements. In section 3.3 the interpretation of the measured loss factor data for the steel test structure and real ship structures and previous work on this is discussed. The calibration of the different measurement techniques employed is discussed in section 3.4 and the accuracy of the measurement procedures discussed in section 3.5. The chapter concludes with a general discussion of the measurement techniques employed.

3.2 The Level Difference Measurement Method.

The level difference measurement is the fundamental measurement technique and used in the laboratory on all test structures for structure-to-structure coupling and for structure-to-fluid coupling. On the sections of the ship structure surveyed only structure-to-structure coupling measurements were taken. The measurement process and the variations employed in the laboratory and on the sections of the ship structures are discussed in more detail in the following sections.

3.2.1 Laboratory Structure-to-Structure Measurements

The basis of the level difference measurement technique is as follows. Consider two coupled subsystems one and two, with a power input to subsystem one. The response in terms of the acceleration level of both subsystems is measured simultaneously and by comparing the response on subsystem two with the source level, the measurements are normalised to give an acceleration level difference that is independent of source strength. This measured acceleration level difference can then be related to the energy level difference or energy ratio as shown in equation *3.1*.

$$\frac{E_2}{E_1} = \frac{m_2}{m_1} \cdot \frac{\langle a_2^2 \rangle}{\langle a_1^2 \rangle} \tag{3.1}$$

where E_2/E_1 is the ratio of subsystem energies, $\langle a_2^2 \rangle / \langle a_1^2 \rangle$ is the ratio of subsystem acceleration levels between the two subsystems and m_2/m_1 is the ratio of the subsystem masses. For each measurement position, the acceleration level is measured on the subsystems for a short period of time, which gives a temporally averaged acceleration level. A number of measurement positions are used on each subsystem to give a spatial average of the acceleration level. Using the above relationship, the measured acceleration levels can be related to the mean energy level difference or energy ratio.

The experimental set up for level difference measurements is shown in figure 3.1. The vibrations are detected on the plate surface by an accelerometer. Typically a Bruel and Kjaer (B&K) type 4500 cubic accelerometer was used and attached to the plate surface by a thin layer of beeswax. The measured vibration level from each accelerometer was channelled via B&K type 2135 charge amplifiers to a dual channel B&K type 2148 real time frequency analyser to be recorded and then down loaded to a 286 personal computer via an IEEE-488 bus.

To obtain a measurement, the source was excited by randomly tapping the surface area with a plastic headed hammer for 15 seconds at a rate of 2 to 3 hits per second which approximates a spatially distributed white noise source for most of the frequency range. A linear averaging time of 16 seconds was used for every measurement, at the end of which the vibration level was recorded and downloaded. The accelerometers were then moved to new positions and the process repeated. As the measurements were stored on the computer, the 95% confidence level for the sample was calculated assuming a normal distribution of dB levels. The measurement process continued until the maximum confidence level within any frequency band was less than 2.5 dB between 125 Hz and 10 kHz. Before the measuring process began the background noise level of each subsystem was recorded. If the measured vibration level within any frequency band at any position was less than 8 dB above the background noise then the measurement in that particular band was discarded otherwise the correction was always for background noise. Typically 15 to 20 measurement positions were used for each test.

In practice it is normal to use the positive acceleration level difference ($L_{a1} - L_{a2}$) using the following relationship,

$$L_{a1} - L_{a2} = -10 log_{10}\left(\frac{a_2^2}{a_1^2}\right) \tag{3.2}$$

Calculated from the mean of the ratio of a_2^2/a_1^2.

3.2.2 Shipboard Structural Measurements

Measuring the vibration level differences aboard a ship structure is essentially identical to that of the laboratory except for some refinements to the measurement procedure due to the difficulties encountered in measuring vibration levels aboard a large structure. The equipment set up for ship measurement is shown in figure 3.2. The excitation was provided by tapping the surface of the source subsystem with a plastic headed hammer.

The main problem with this technique is that the power input to the structure by this method is limited and the vibration level attenuates rapidly with distance due to the presence of the plate stiffeners. As the distance between the source and receiving subsystems lengthened the gain of the charge amplifier at the receiving subsystem was increased. To facilitate this a calibrated peak level meter was used at the source subsystem to compare the strength of the two accelerometer signals. If the signal at the receiving subsystem was deemed low, then the gain was increased at the charge amplifier. The measurements were then corrected during processing. The use of the communications circuit allowed the operator at the control point to co-ordinate the measurement process. Because of the time constraints and the need to maximise the coverage of the structure tested it was decided to limit the number of measurements to ten positions for each subsystem rather than the 2.5 dB requirement for the 95% confidence level used in the laboratory. Typical confidence intervals are given at the end of the chapter in figure 3.12 and 3.14.

In practice the measurement surveys on the ship sections are considerably slower than on laboratory structures. These are due to a number of practical difficulties that can be encountered in performing the survey, examples of which are as follows:

1. The source subsystem may be remote from where suitable power supplies for the frequency analyser and PC are located, therefore a team of three engineers is required, one at the analyser/PC, one at the source subsystem and one at the receiving subsystem.

2. The survey team requires to be in constant communication so that the progress of the survey can be co-ordinated e.g. when to move accelerometers, when measurements start and stop etc. Technical difficulties also can be immediately reported back e.g. an accelerometer falling off, abortive tests due to overload. The operator may not permit the use of radios so it is advantageous to have a dedicated communications system allowing

the members of the team to talk to each other. The use of headsets with in-built microphones is particularly useful as they allow hands free use.

3. To minimise cable usage it is ideal to use multi core cables to carry the signal from the charge amplifier(s), the headphones and microphones, rather than a series of individual cables which are time consuming to route and present a significant tripping hazard. If a multi core cable is used then it must have adequate shielding to prevent cross talk between the vibration signal and the audio signals.

4. It is advantageous to have a level meter to allow the strength of the source and receiving signals to be compared. As the distance between the source and receiving subsystems increases it is necessary to increase the gain at the receiving subsystem and this allows the operator at the source subsystem to identify when the gain at the receiving subsystem requires to be increased.

5. Some practice in the laboratory before going onboard is advisable so that the equipment set-up and communications can be checked and a dry run of the survey procedures can be performed to ensure everyone is familiar with the equipment and what is expected of them.

3.3 Damping Measurements

The measurement of subsystem damping was obtained by measuring the subsystem reverberation time. The equation relating the loss factor and reverberation time is given by Cremer [66] as follows:

$$\eta = \frac{2.2}{f T_{60}} \tag{3.3}$$

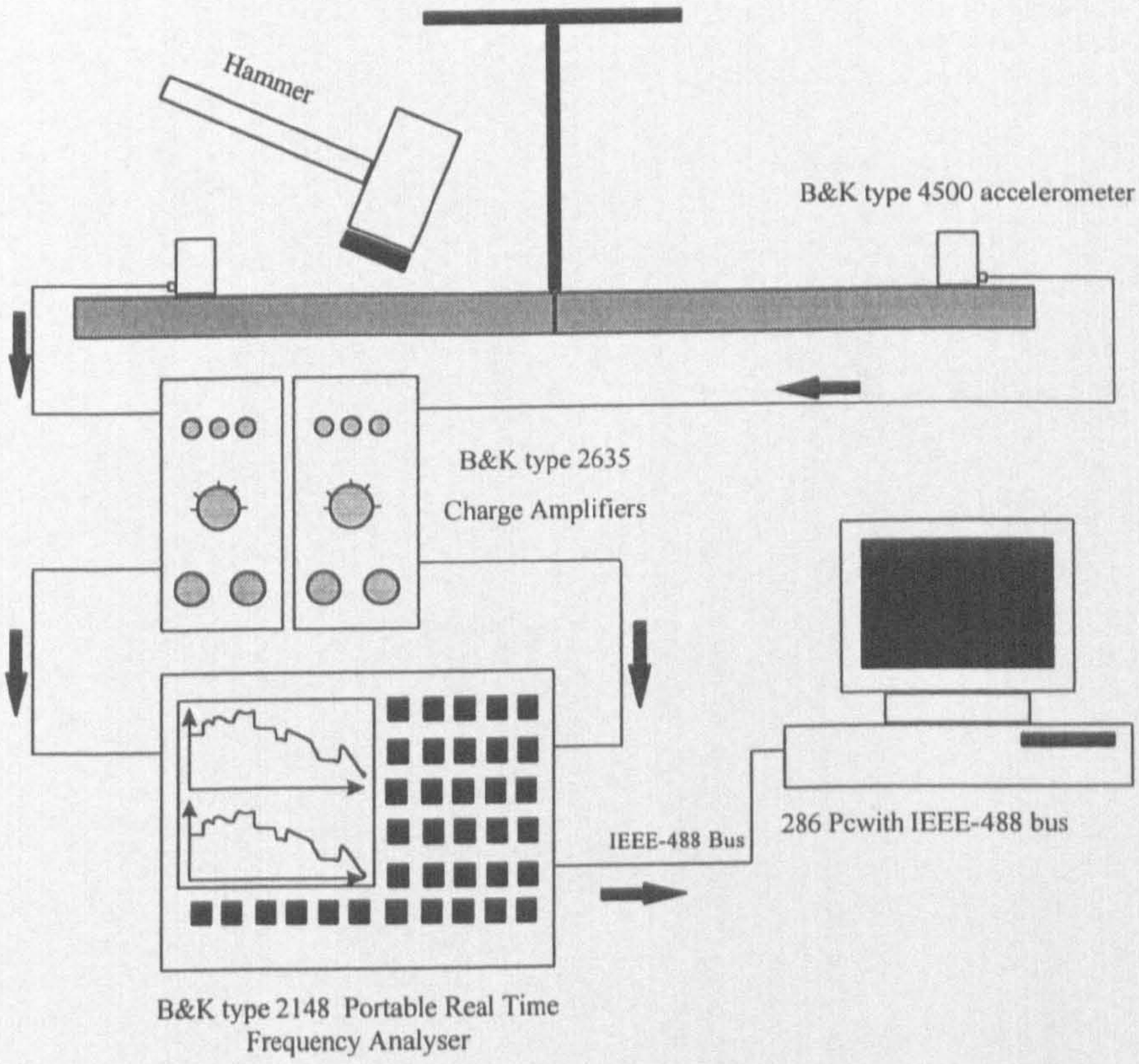

Fig 3.1 Acceleration level difference measurement setup

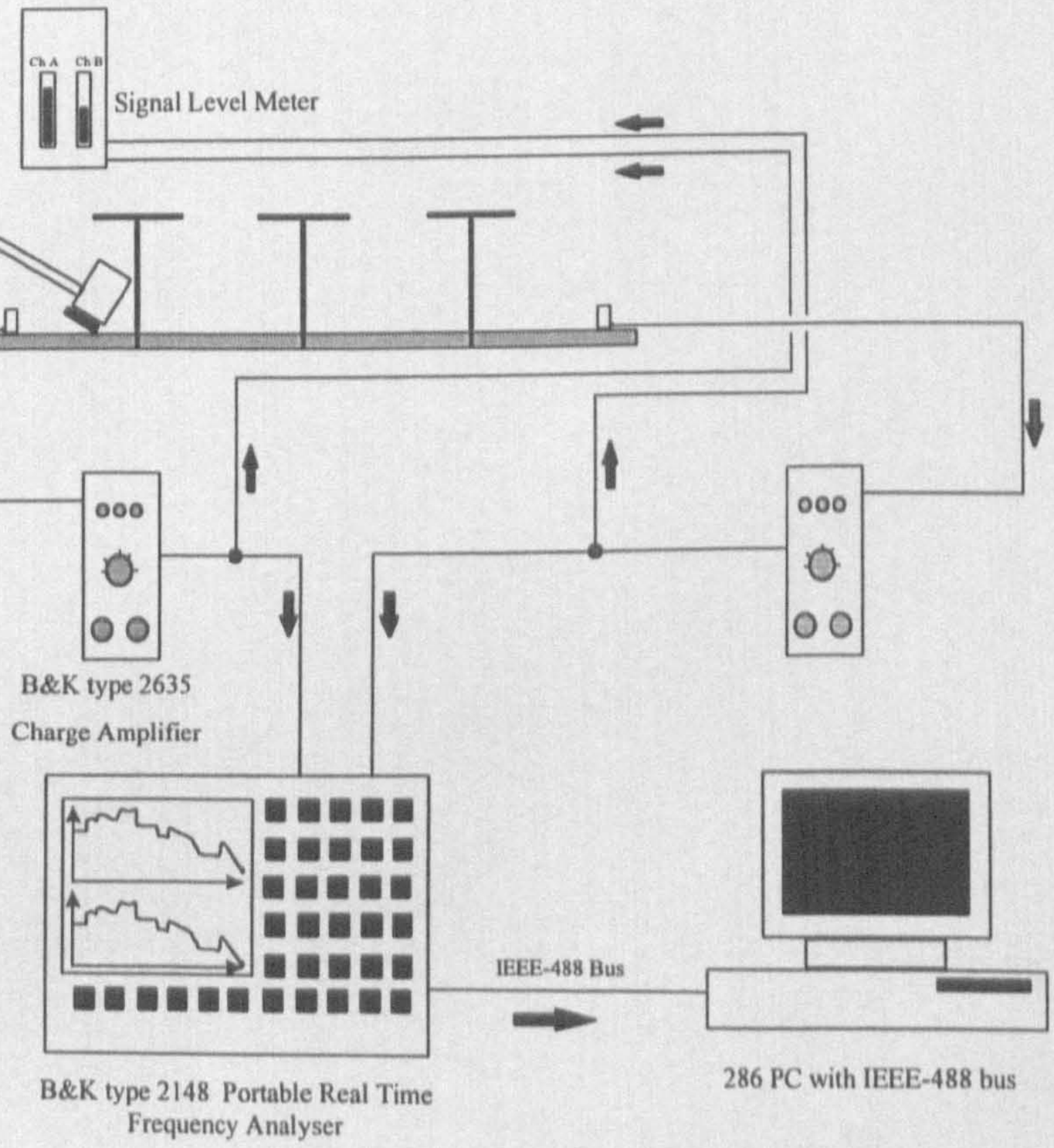

Fig 3.2 Ship measurement setup

where f is frequency and T_{60} is the reverberation time of the subsystem. Reverberation time is a standard acoustic measure and is defined as the time for a signal to fall to one millionth of the original signal level which is equal to 60 dB as a logarithmic value. With damping measurements, the main problem is to determine what exactly has been measured, the internal loss factor of the total loss factor. The interpretation of the measurements will discussed in section 3.3.3.

3.3.1 Laboratory Measurements

For structural subsystems a single accelerometer is mounted on the surface of the subsystem. Measurements were taken in-situ on the simple and complex laboratory structures and the laboratory set-up is shown in figure 3.3. An impulse is applied by hitting the plate surface with a plastic-headed hammer and measuring the vibration decay with time. The accelerometer detected the vibration level of the plate surface and the time-history of the vibration level was stored on a B & K type 2148 portable frequency analyser in 1/3-octave bands. The time histories of the vibration decay were subsequently downloaded to a PC where they were separated into individual frequency bands and the reverberation time of each frequency band determined. The reverberation time was measured by using a best-fit curve to the decay curve 5 dB above the noise floor and 5 dB below the peak vibration level. The loss factor was then determined across the frequency spectrum. Five measurement positions would typically be used and the measurements averaged.

Using the portable frequency analyser it was necessary to record two measurements at every accelerometer position. The first measurement had a sampling time step of 10 milliseconds to allow the low frequency vibration decay to be captured. The second measurement had a shorter sampling time step of 2 milliseconds to allow the high frequency vibration decay to be captured. Typically 100 spectra would be recorded for each measurement. The results from the 10 ms and 2 ms measurements would then be combined to give the overall damping curve.

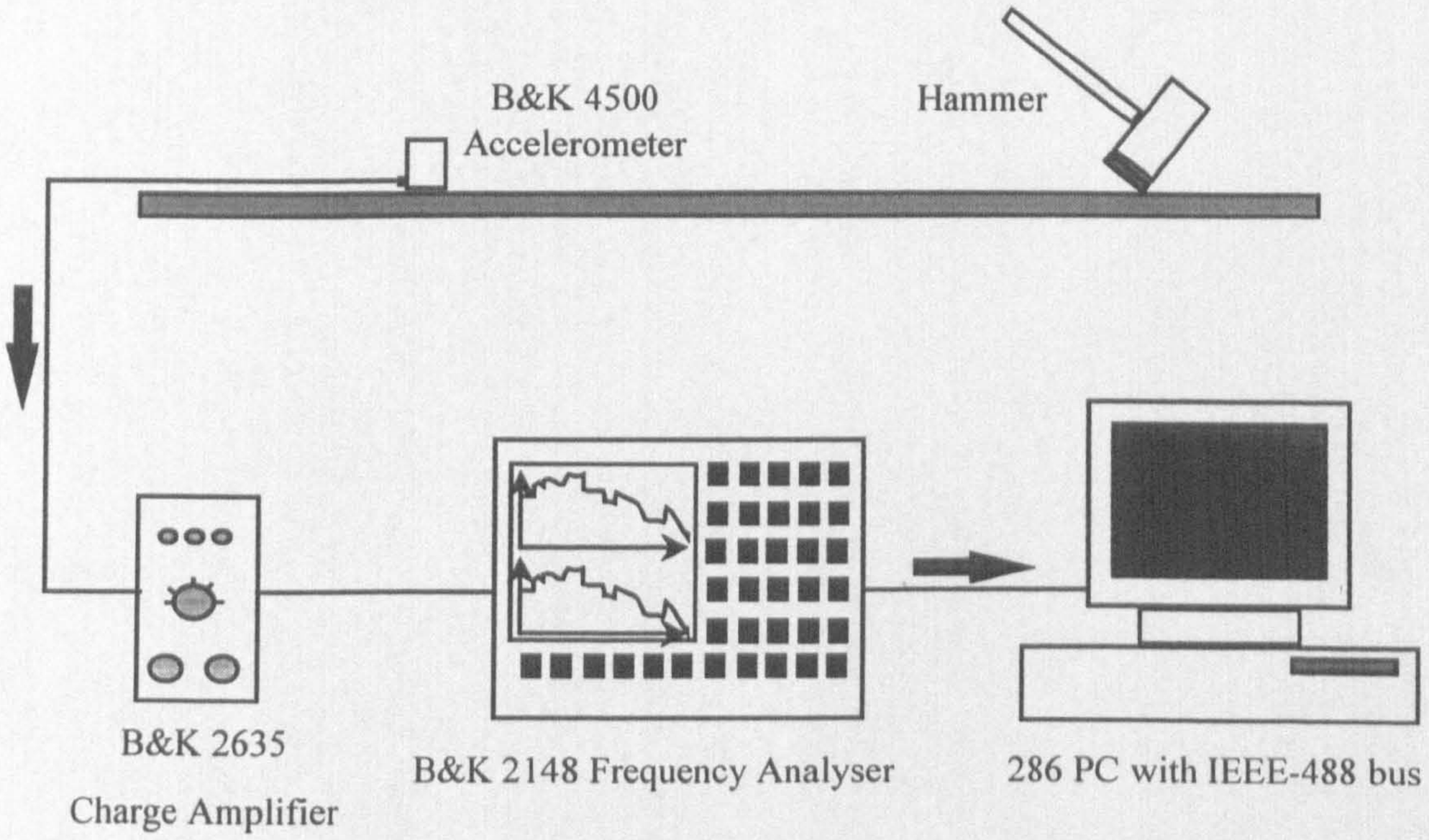

Fig 3.3 Laboratory damping measurement setup

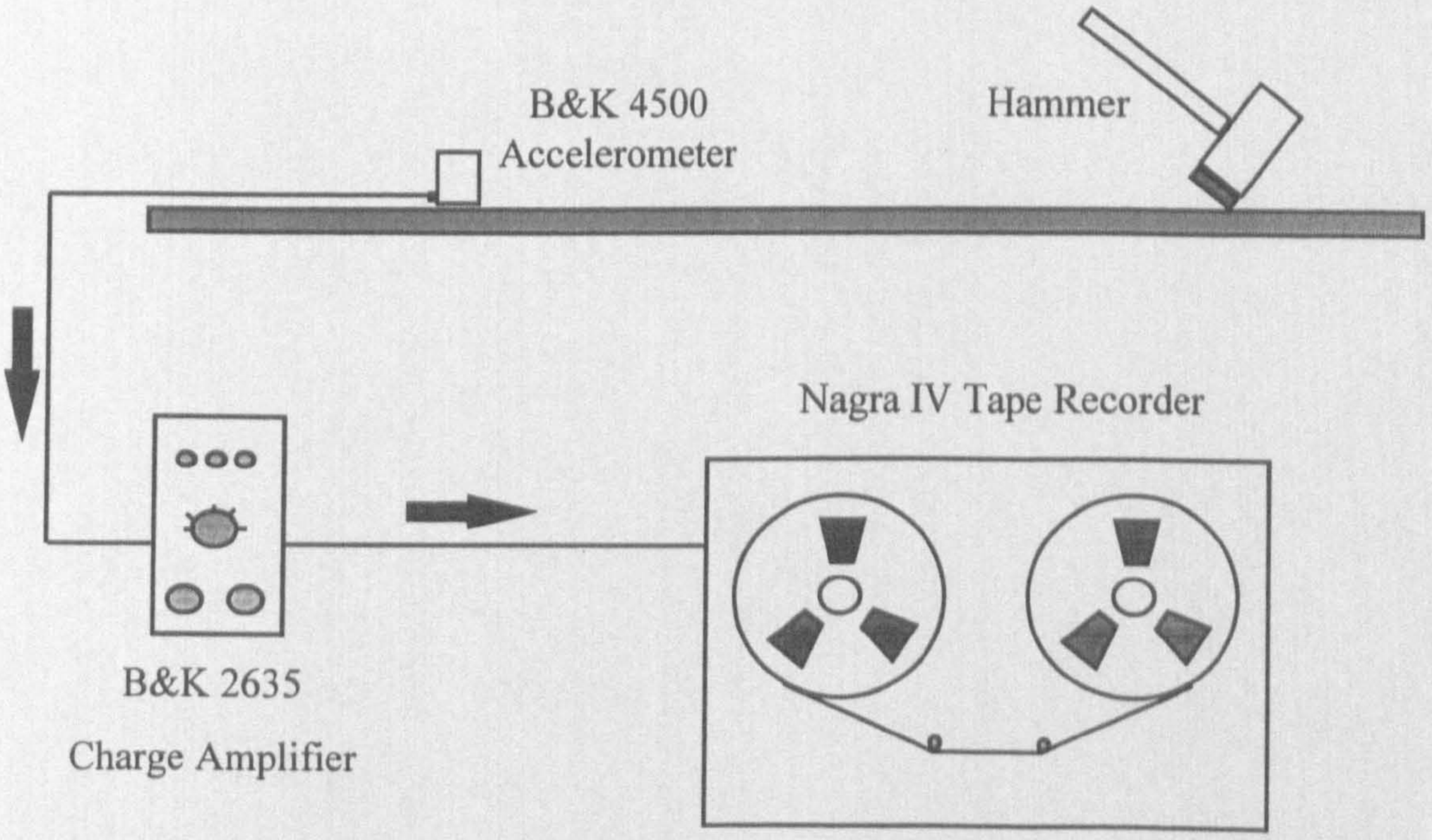

Fig 3.4 Ship damping measurement set-up

3.3.2 Shipboard Measurements

To measure the damping aboard the ship structures, the method used in the laboratory is too cumbersome and time consuming due to the limited storage capacity of the portable B&K frequency analyser and the need to download data to the PC or store data on floppy disk. Instead of the portable frequency analyser a Nagra IV three channel tape recorder was used. This allowed rapid collection of data on site which could then be processed in the laboratory. The vibration signal is recorded on channel one and the details of the structure being tested, position number and impact number recorded on audio channel three. As with the laboratory procedure, five measurement positions were used for each structural element. Because the tape recorder allows continuous measurement, ten hits were recorded for each measurement position, to allow for the variation in the input power and possible overload. The experimental set up is shown in figure 3.4.

Approximately 1500 structural damping measurements were recorded on the sections of the ship structures. Because of the large quantity of damping data gathered on the ship structures it was decided to process the result from one impact per measurement position and these were randomly selected for analysis. If the quality of the recorded decay from the selected impact was found to be of poor quality, another impact for the same measurement location was used. The pre-recorded signals from the Nagra were analysed in the laboratory with the equipment set-up as shown in figure 3.5.

3.3.3 Measured Loss Factor

Before reviewing the measured results it is important to discuss the interpretation of the damping results which can be interpreted as the material, internal or total loss factor.

To measure the internal loss factor of a material, a suspended plate with a free-free boundary condition in a vacuum is required and this is the only experimental set-up that will yield the material internal loss factor. If this experimental set-up is not utilised the

measured loss factor will then be a combination of the material loss factor and the coupling losses from the plate to the environment. To obtain the material internal loss factor, the predicted coupling loss of the plate must be subtracted from the measured loss factor. The use of a free-free boundary condition is important since it removes any ambiguities introduced by damping caused by edge effects due to boundary conditions. If a free-free boundary condition does not exist for the plate, then the edge effects such as dry friction and gas pumping will increase the damping of the plate. The material loss factor of steel is quoted by Cremer [66] as being between 0.0002 (83 dB re 10^{-12}) and 0.0006 (87.8 dB re 10^{-12}).

The in-situ loss factor for steel decking has been measured and estimated by other researchers for ship structures. Jensen [20] estimates the internal loss factor of stiffened deck plates to be of the order of 0.001 to 0.005. Jensen and Holm [88] estimate the loss factor for an 8 mm thick stiffened deck plate the loss factor to be between 0.06 and 0.002. Nilsson [14,15,16] estimates the internal loss factor of steel to be between 0.02 at 100 Hz and 0.006 at 4 kHz. Kihlman and Plunt [89] estimate the internal loss factor to be between 0.01 and 0.001 and quote Soviet sources as giving the internal loss factor as between 0.002 and 0.003, while Plunt [23] has measured the loss factor from laboratory and ship structures. Irie and Nakamura [25] has published a formula for the *internal* loss factor of steel based on measured data and this was utilised by Hynna et al [35] in their SEA models. The following relationship was derived by Irie from fitting a line to the experimental data,

$$\eta_{id} = 0.41 f^{-0.7} \tag{3.4}$$

where η_{id} is the internal loss factor of subsystem i and f is the frequency. This equation represents the internal loss factor and does not include the energy lost by radiation from the plate to the environment. Though not explicitly stated by Irie, the radiation loss factor must have been subtracted from the measured data before the formula was derived or assumed to be negligible. This gives the internal loss factor as 0.013 at 125

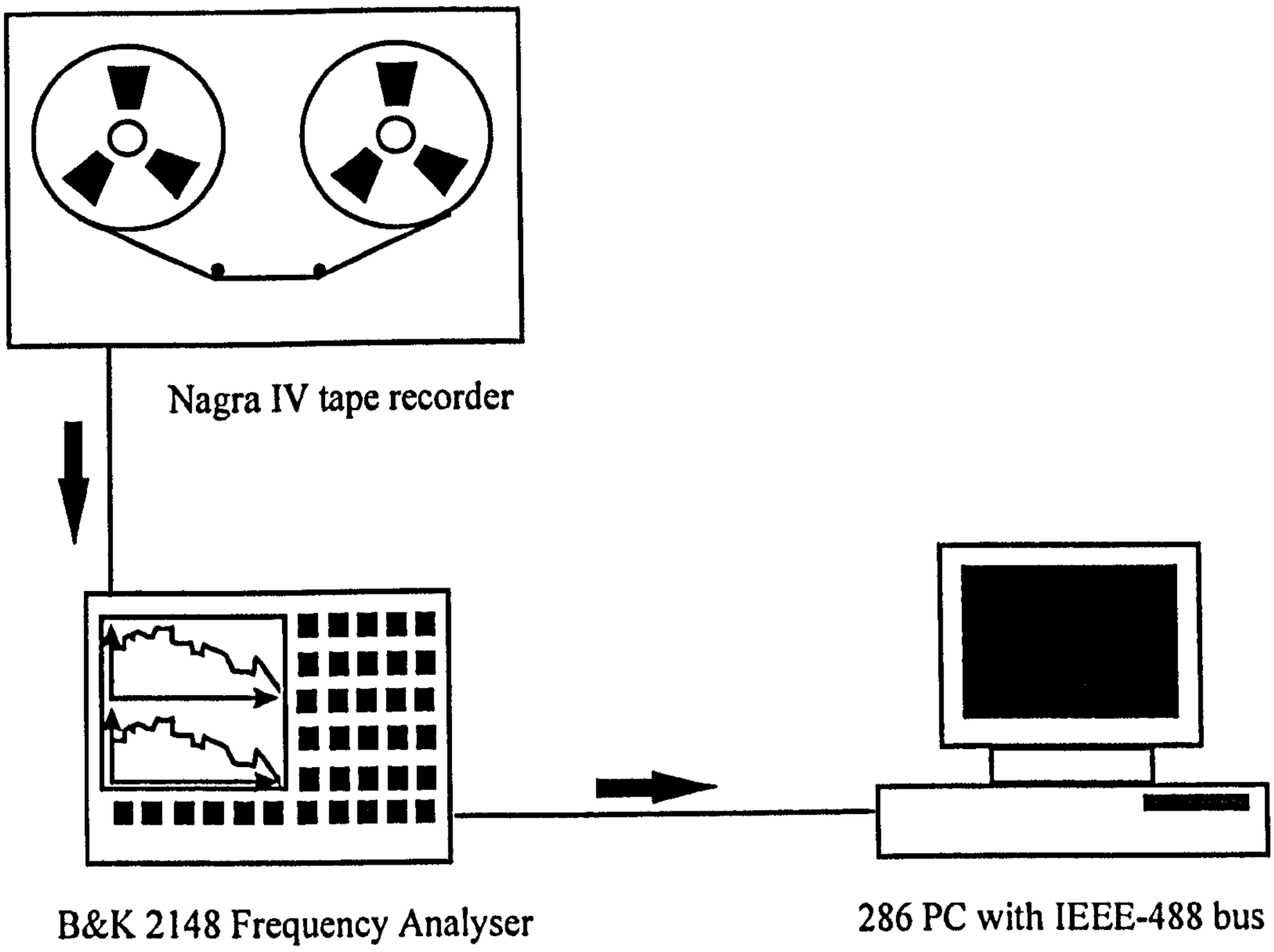

Fig 3.5 Laboratory processing set-up

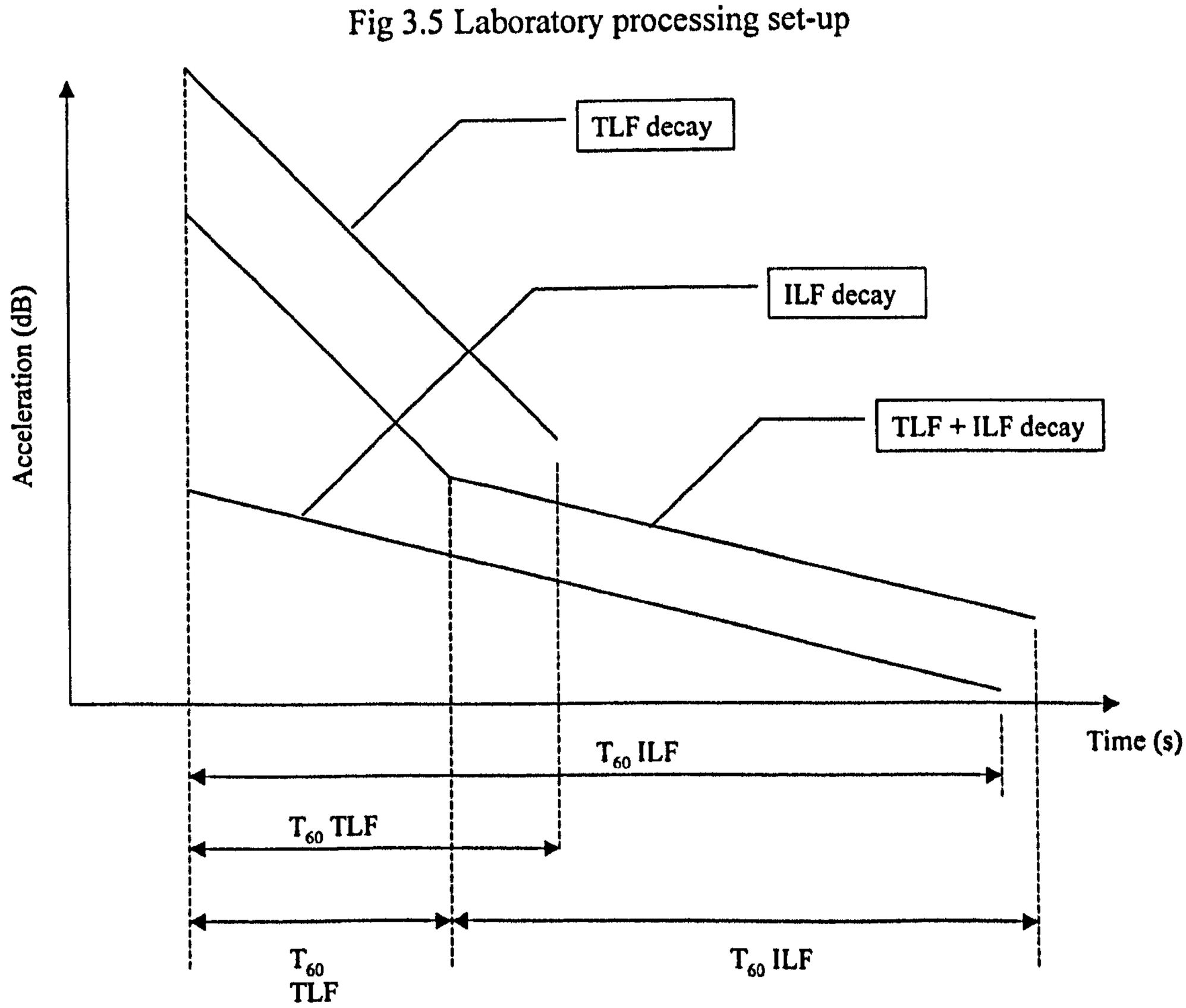

Fig 3.6 Comparison of decay time histories

Hz and 0.0012 at 4 kHz. Irie does not give any details of the measurement process, test set-up or the structure on which the measurements were taken. It can be seen that from the previous work there is a significant variation in the estimates of internal loss factor for steel plates in ships.

Figure 3.6 illustrates the decay in acceleration level with time for a total loss factor measurement, internal loss factor measurement and a combination of both. Comparing the total loss and internal loss factor decays it can be seen that there is a difference in the gradient but in practice the combined decay curve is a more realistic visualisation. The important features in determining the measured damping quantity are the amplitude of the impulse, the length of the internal and total loss factor T_{60} intervals, the sampling rate and the time step. In practise it is difficult with a single hammer impact to input sufficient power to record a full 60 dB decay. Instead 30 to 35 dB is more normal and since the analysis discards the first 5 dB of the decay top and bottom the analysis range is reduced further. Typically 100 samples were recorded at time steps of 0.01s and 0.002s.

For an excitation and response measured on the same subsystem, if the internal loss factor is higher than the sum of the coupling loss factors, then more energy is dissipated in the subsystem than lost to coupled subsystems and consequently the total loss factor will be measured and the decay will be similar to the T_{60} TLF shown in figure 3.6. If the sum of the coupling loss factors is higher than the internal loss factor then more energy from the hammer impact is lost to other subsystems than dissipated and the decay of the resonant subsystem response is measured which is due to the internal loss factor. If the excitation is applied to a different subsystem from where the vibration response is measured and the two locations are far apart then it is the internal loss factor that is measured.

In figure 3.7 the measured loss factor for different sized steel plates on the laboratory test structure reviewed in chapter 5. The excitation was applied to the same subsystem on which the response was measured. Also shown in the figure is the predicted internal

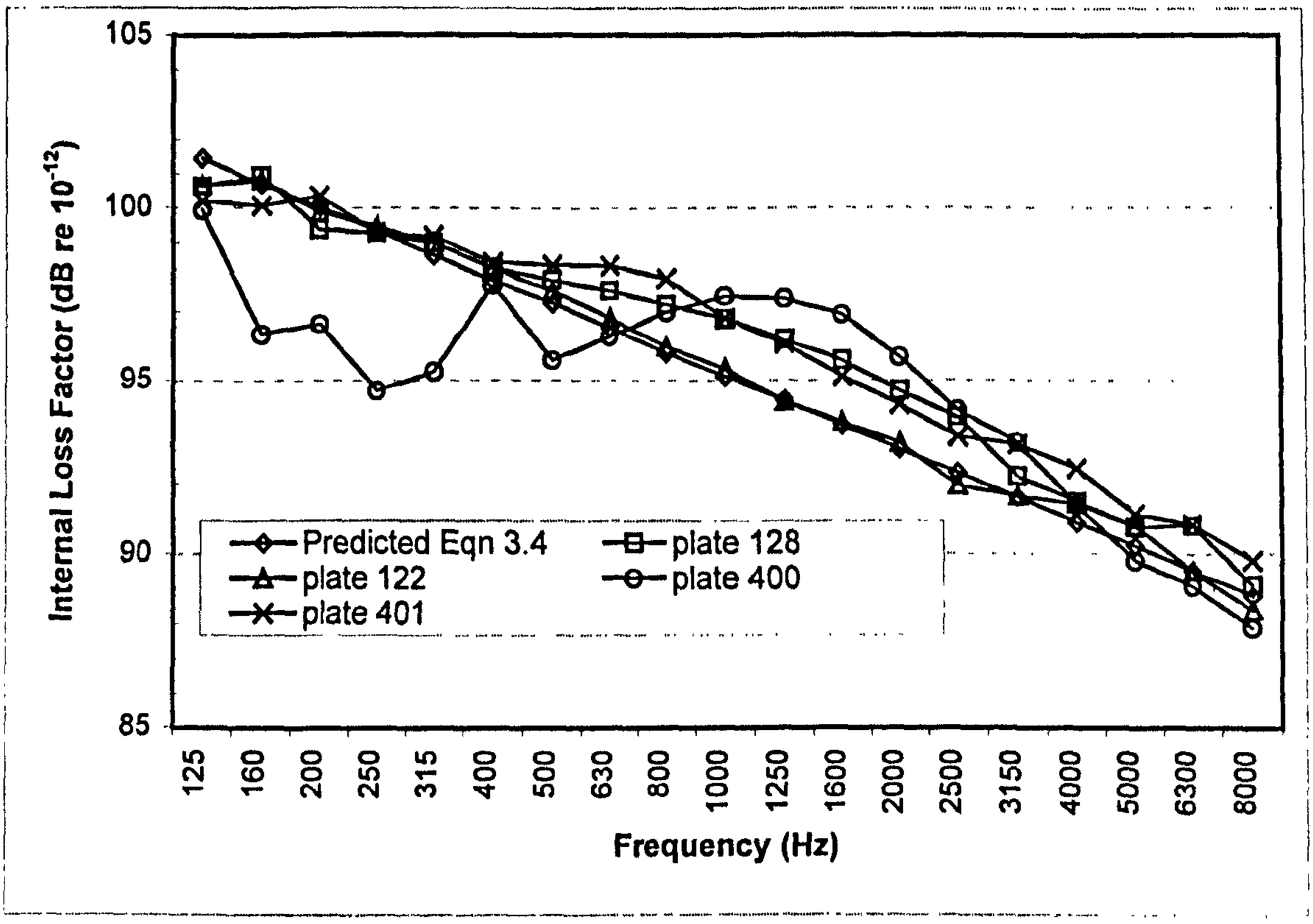

Figure 3.7 Comparison of measured internal loss factor of steel plates

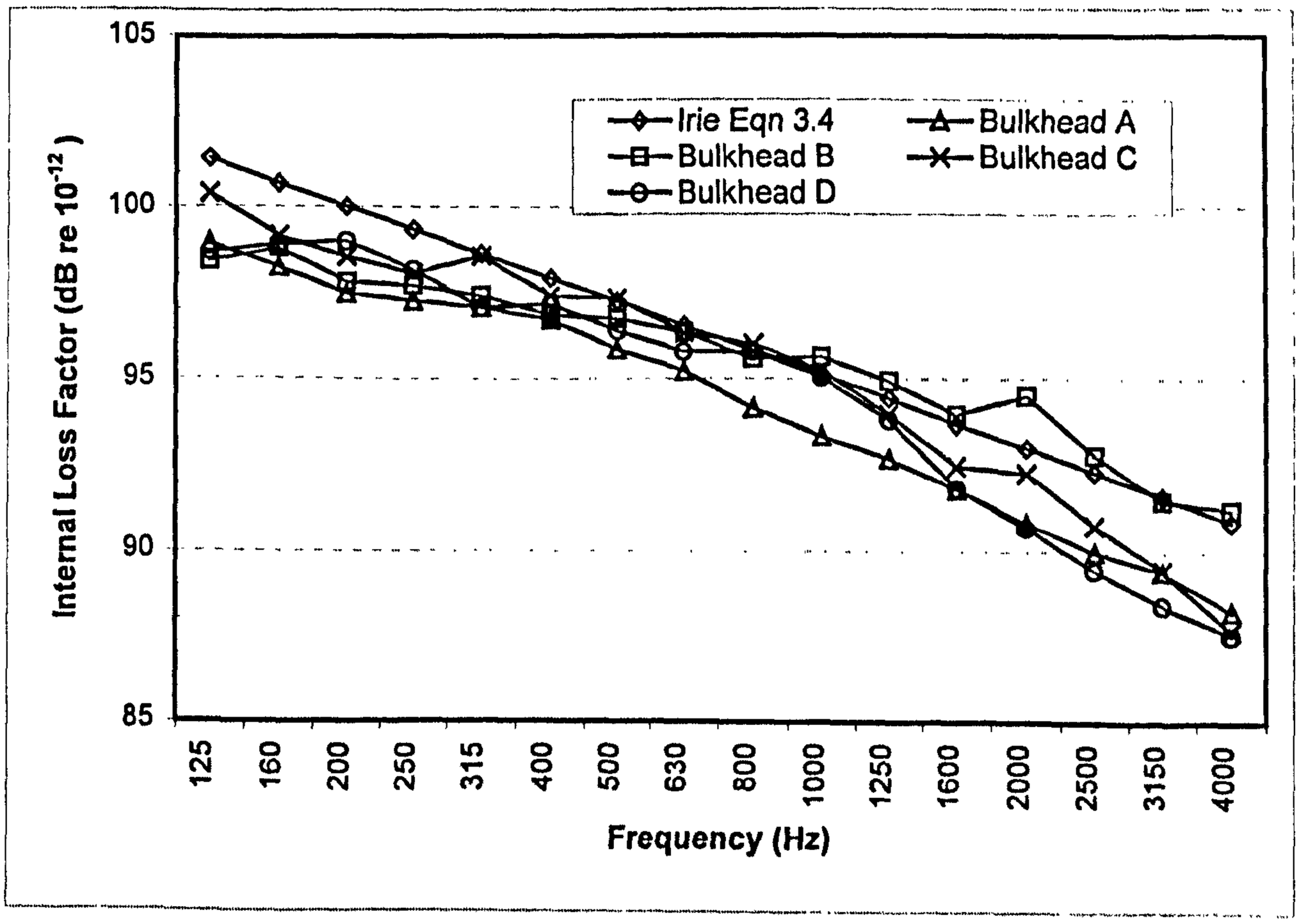

Figure 3.8 Measured internal loss factor: ship bulkheads

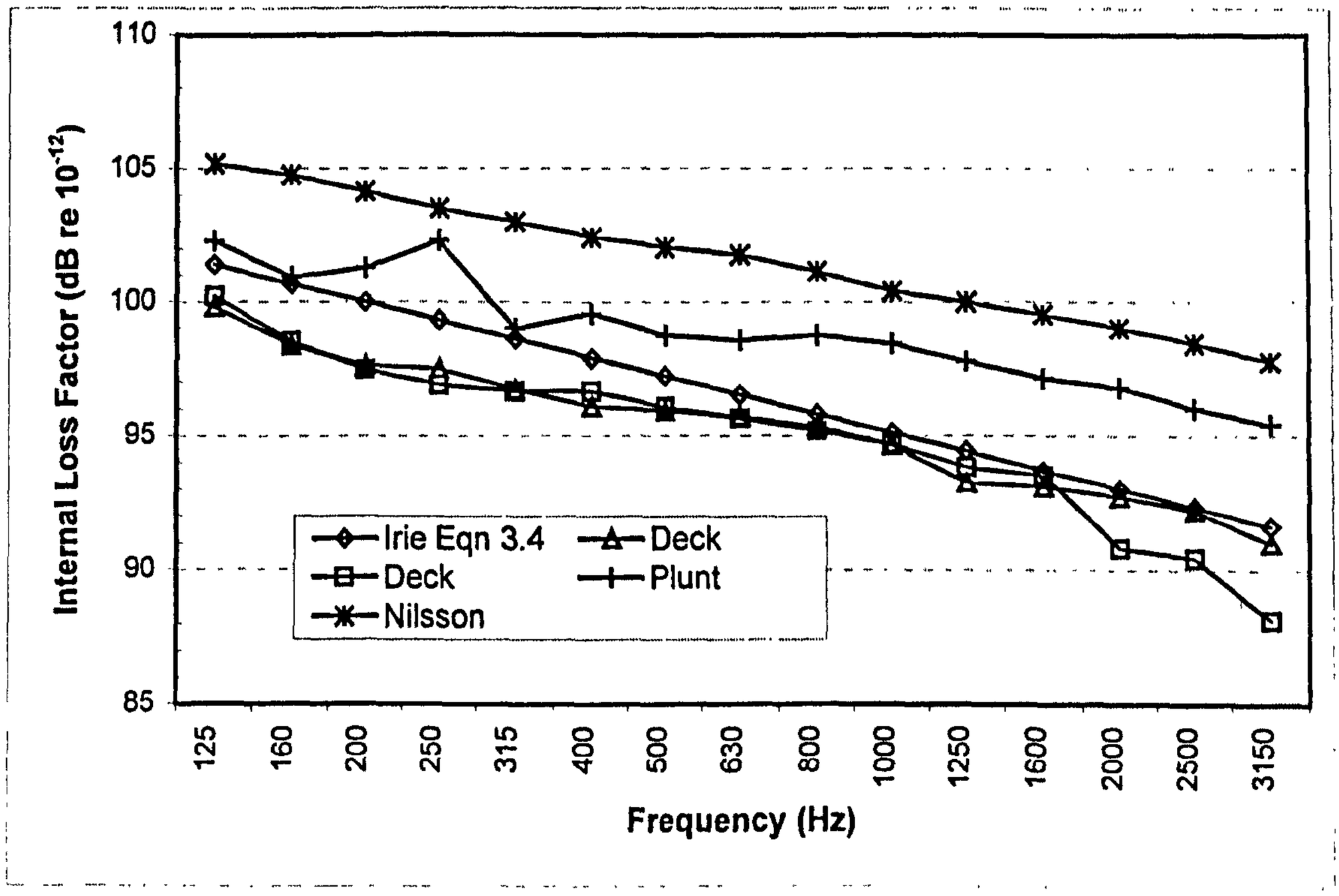

3.9 Measured internal loss factor: superstructure deck plates

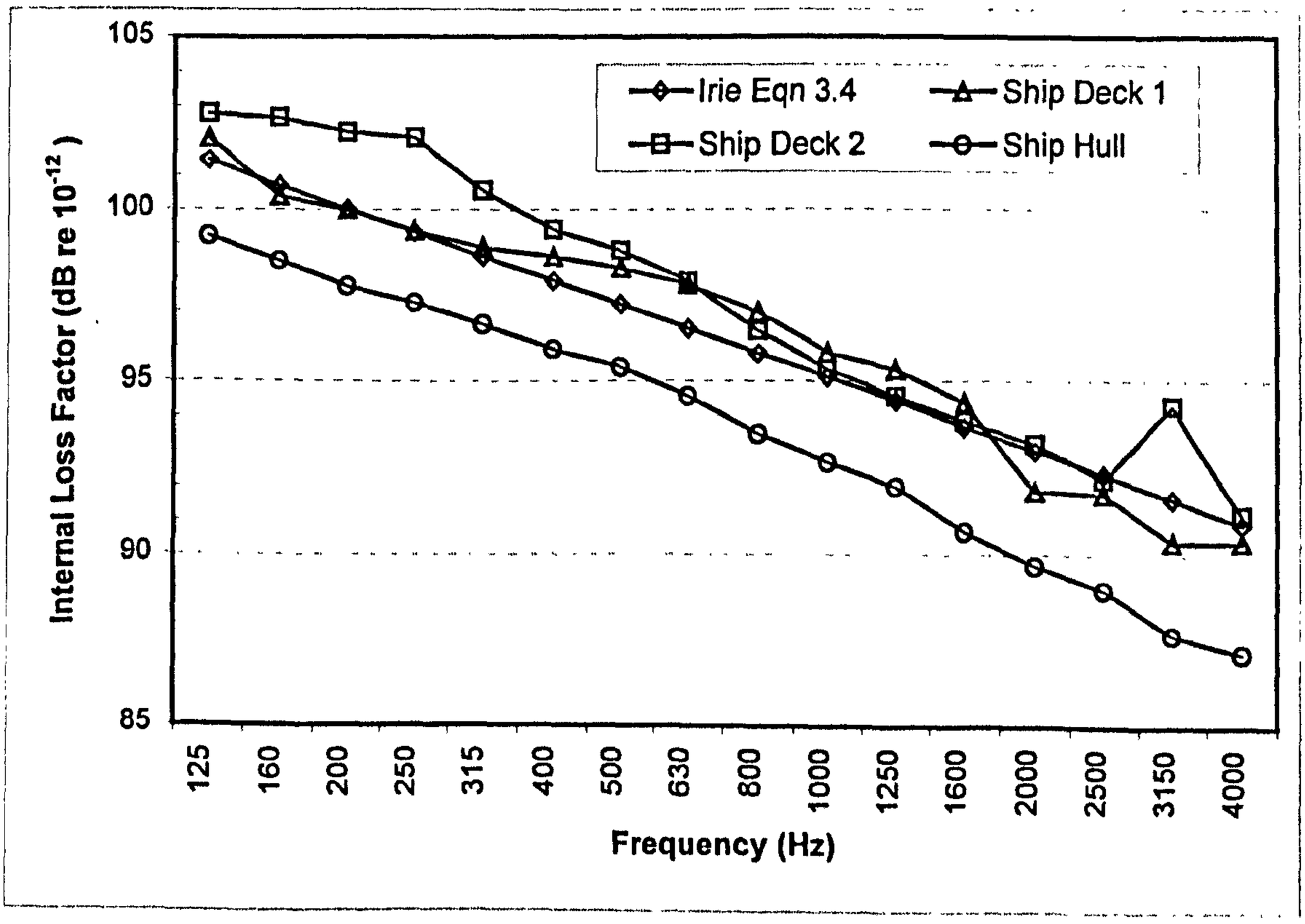

Figure 3.10 Measured internal loss factor: ship decks and hull

loss factor by the Irie equation. It can be seen that the measured loss factor and predicted internal loss factor show good agreement.

In figure 3.8 the measured loss factor measured on four steel bulkheads from the ship structures tested is plotted in the 125 Hz to 4 kHz frequency bands and the predicted internal loss factor from the Irie equation *3.4*. The excitation was applied to the same subsystem on which the response was measured. The measurements are in good agreement with the prediction but it can be seen that between 125 Hz to 630 Hz and 1.25 kHz and 4 kHz for bulkhead A, that the measured internal loss factor is 2 to 3 dB lower than predicted in most frequency bands.

In figure 3.9 the loss factor measured in-situ on large ribbed steel deck plates of two superstructure units is shown. The excitation was applied far away from the point at which the response was measured. Comparing the measurements with the prediction using the Irie formula, it can be seen that the measurements and predictions are in good agreement over most of the frequency spectrum. As with the results for the bulkhead measurements shown in figure 3.7 the measured internal loss factor is 2 to 3 dB lower in the 125 Hz to 630 Hz frequency bands. Above the 630 Hz band there is better agreement with the Irie prediction. Also shown is the measured loss factor for a ship deck measured by Plunt [23] and the loss factor used by Nilsson [14,15,16]. The measured loss factor from Nilsson appears to be significantly higher than that for Plunt or this work, however Nilsson in his analysis models multipliers of 0.7 and 0.35 are applied to the internal loss factor to account for the variation in loss factor.

In figure 3.10 the measured loss factor taken for two deck levels of a complete ship and a curved section of the ships hull are plotted against the Irie prediction. The excitation was applied far away from the point at which the response was measured. It can be seen that the internal loss factor of the deck measurements from the complete ship structure are marginally higher than the Irie prediction in most frequency bands. In contrast the internal loss factor measurement from the hull is lower than the Irie prediction by 3 to 4 dB in most frequency bands.

For all the measurements on the laboratory and ship structures it can be seen that the measured loss factor shows good agreement with the prediction from the Irie formula independent of the distance between the excitation and response locations. It is therefore taken that the measured loss factor is in fact the internal loss factor of steel including all the edge damping effects. The measured values also show reasonably good agreement with the measured loss factor given by other researchers.

The Irie formula can therefore be taken as the equation for the prediction of the internal loss factor of steel plates in SEA models.

3.4 Calibration

Before each new experiment the equipment would be calibrated to verify it's operation and accuracy. This was also performed at the start and end of every day to verify the functionality of the equipment set up. To calibrate the accelerometers a B&K type 4294 vibration calibrator was used. This produces a standard r.m.s vibration level of 140 dB (10 ms^{-2} ref. 10^{-6} ms^{-2}) at a frequency of 160.2 Hz.

3.5 Accuracy of Measurements

In taking measurements there is always a degree of uncertainty regarding the accuracy due to the limited time available to gather measurements and the variation that occurs in nominally identical structures. As the number of measurements increase the degree of uncertainty reduces and therefore it is necessary to find a balance between the allowable degree of uncertainty and the number of measurements required. To assess the accuracy of the measured data a suitable statistical model for the distribution of the data is required. Craik [90] studied this problem in building structures and found that the standard deviation and 95% confidence level airborne data could be well estimated assuming a normal distribution of dB levels. The following expressions for determining the accuracy were used in this work.

The arithmetic mean was calculated after converting the data from dB to absolute units. With the mean calculated it was then converted back to dB. For any single variable measurement x, the mean m, of n measurements is given by [91],

$$m = \frac{\sum x}{n} \tag{3.7}$$

For the level difference measurements it is not x but a_2/a_1 that is averaged. Craik [90] found that the standard deviation sd and 95% confidence interval can be calculated in dB from the measured data and that it is unnecessary to convert to absolute units. The standard deviation is given by Spiegel [91] as

$$sd = \sqrt{\frac{\sum x^2 - \frac{(\sum x)^2}{n}}{n-1}} \tag{3.8}$$

and the 95% confidence interval is given by Spiegel [91],

$$95\%CC = \frac{sd(dB)}{\sqrt{v}} t_{v,0.975} \tag{3.9}$$

The term $t_{v,0.975}$ is the value taken from the students t distribution for a 95% confidence interval of a measurement sample with v degrees of freedom where v equals n-1. For large values of n the students t distribution closely approximates the normal distribution.

Figures 3.11 and 3.14 show typical standard deviation and 95% confidence intervals in third octave band measurements for structural level difference measurements from the laboratory and real ship structures. Typically 20 measurements were used in the laboratory and 10 measurements for the ship structures. The 95% confidence interval is less than 2 dB for all frequencies except in frequency bands below 160 Hz for the laboratory structure. For the ship structure the 95% confidence level is less than 2 dB for

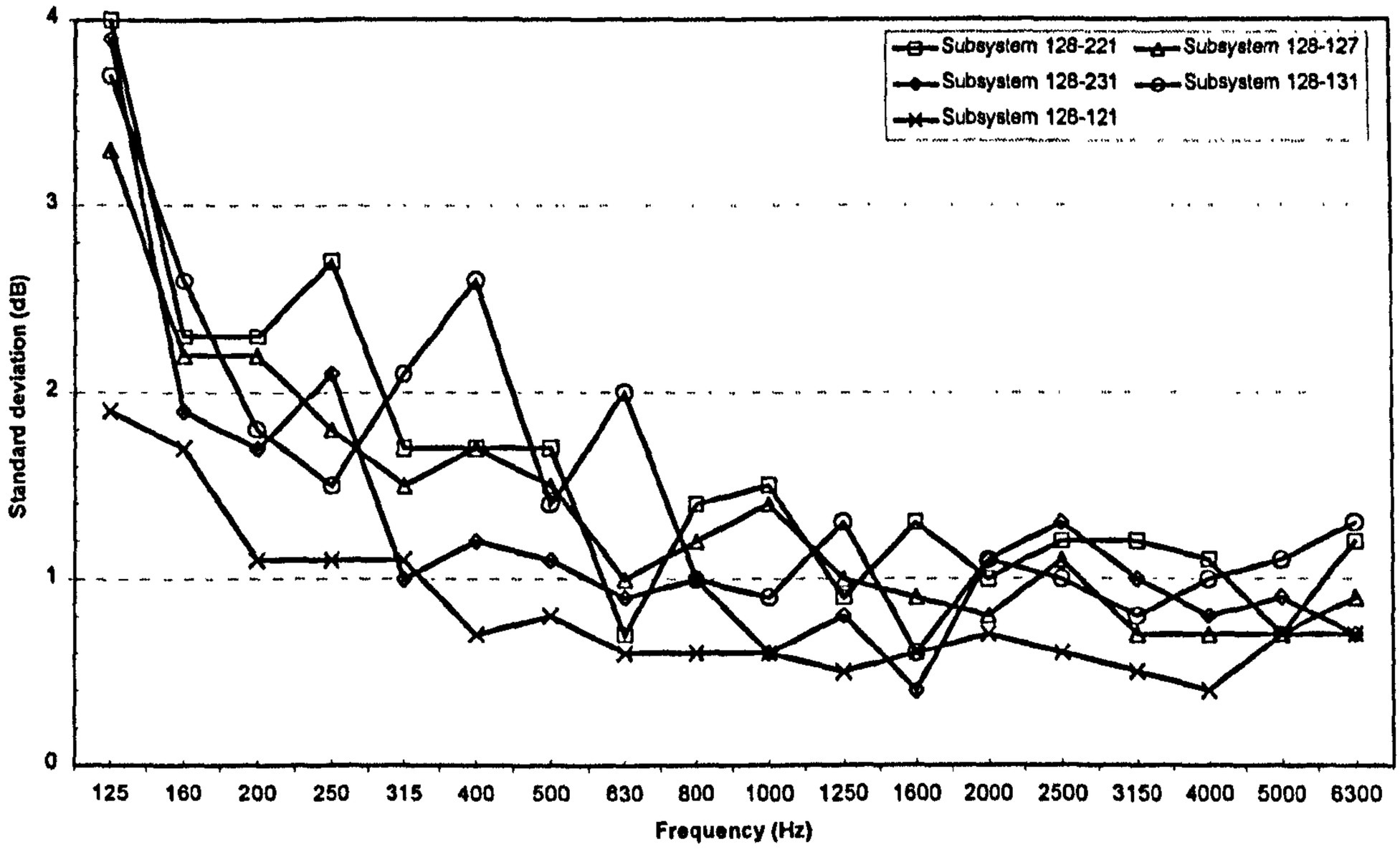

Figure 3.11 Typical laboratory structure measurement standard deviation

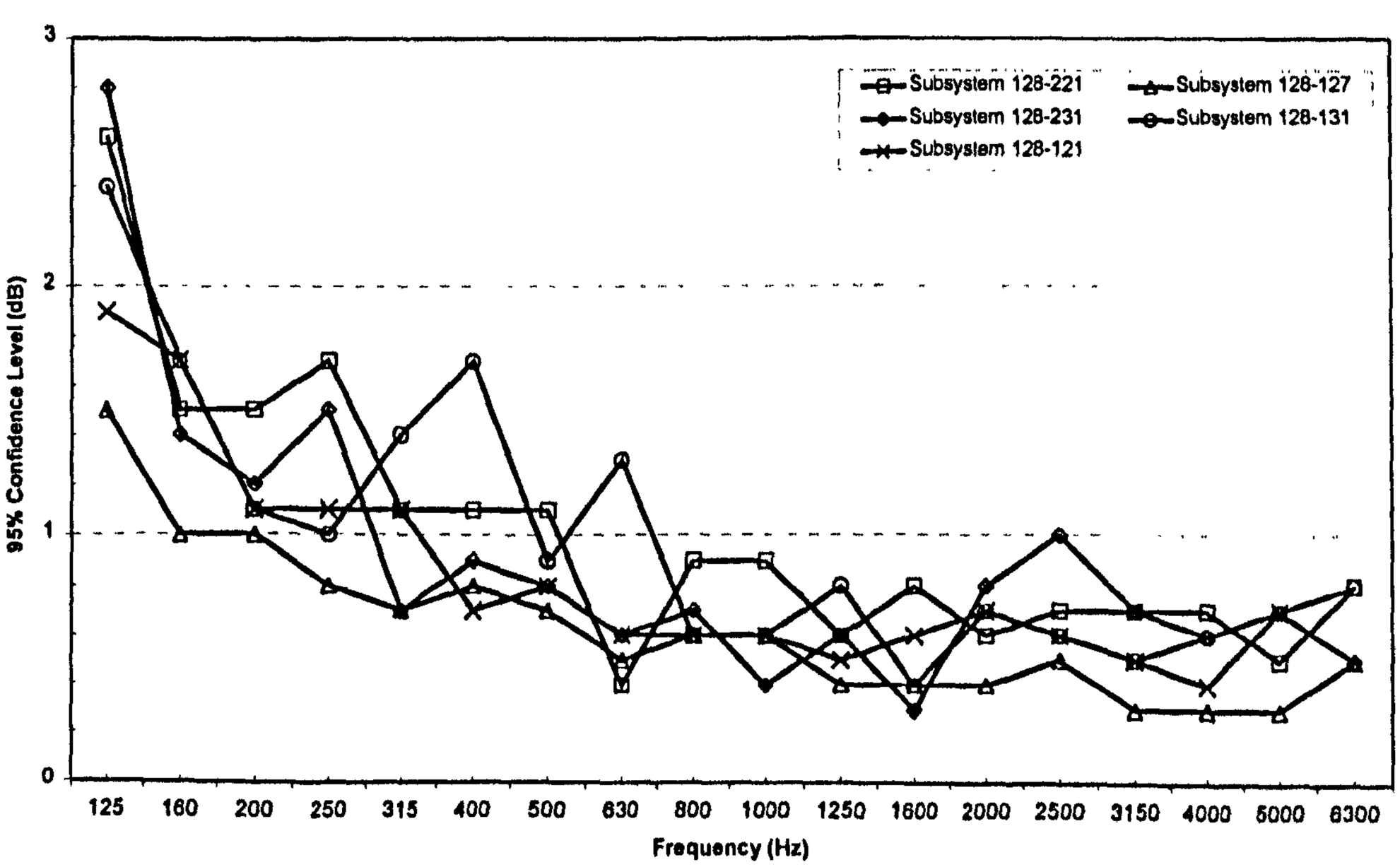

Figure 3.12 Typical laboratory structure measurement 95% confidence levels

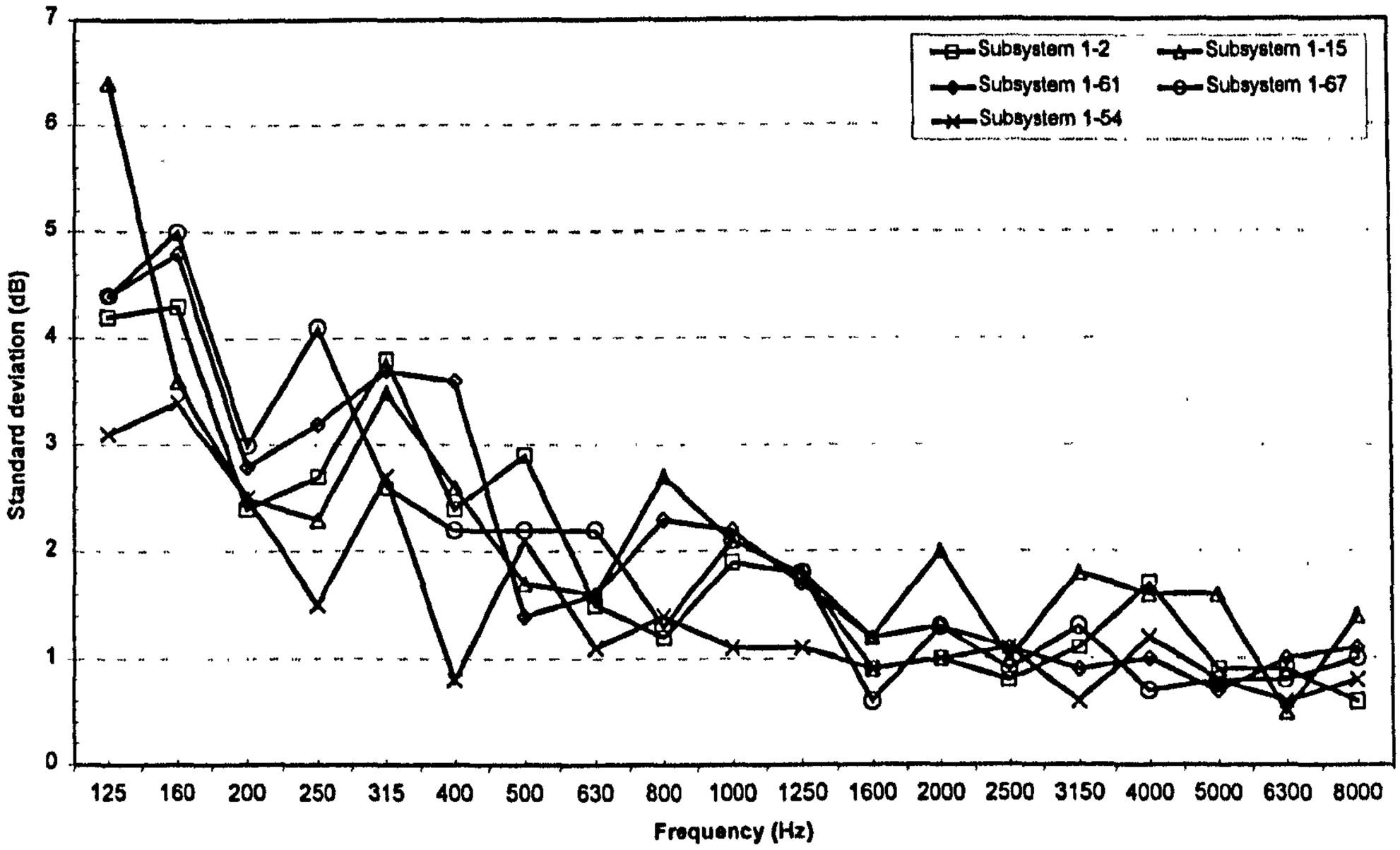

Figure 3.13 Typical ship measurement standard deviation

Figure 3.14 Typical ship measurement 95% confidence levels

measurements above 500 Hz and less than 3 dB for measurements above 200 Hz. This is a consequence of the 10 measurement position limit set when surveying the ship structures. Clearly the confidence limits would have been lower if the number of measurement positions had been increased however the overall coverage of the ship structure would have been greatly reduced.

3.6 Discussion of Measurement Techniques

The basic measurement techniques presented in this section have been used by a number of researchers although the exact implementation has been different. For the acceleration level differences measurements researchers such as Lyon [36], Shimomura [28], Tratch [27] use an electromagnetic shaker driven by a noise generator for the noise source. This has the advantage of allowing an input power to be specified and controlled. To overcome the problem of locating the shaker at a node point in the lower frequency bands and not exciting specific modes three excitation locations are typically used. An irregularly shaped source plate rather than a rectangular plate was used on laboratory structures to ensure an incoherent wave field.

There are however advantages to using a hand held hammer to input power into the test and ship structures. Advantages include the fact that using a hammer is simple and non-destructive and the equipment required is minimised since the shaker requires a noise generator and power amplifier. Before attaching the shaker, some preparation is also required as it is necessary to drill holes to allow the shaker to be fixed to the structure. This may be satisfactory for a laboratory structure but it would not be acceptable for a ship since the operators would not permit permanent damage to parts of the structure such as the hull. The hammer therefore is the best solution in practice and by normalising the measured acceleration level difference as described in section 3.1 the variation in power input with the hammer is not an issue between measurements.

The acceleration level difference measurement is a well proven and robust procedure but there are potential problems if care is not taken. The positioning of the

accelerometers is important as they must not be located near to plate/joint boundaries because nearfield waves are created at the boundary, which would affect the measured acceleration level. The other potential problem is that of mass loading caused by the accelerometer. On thin steel plates, the use of metal accelerometers with a magnet to attach the accelerometer can significantly reduce the upper measurement frequency. The problem of mass loading can be checked by calculating the impedance of the plate and accelerometer/magnet assembly. Mass loading was not a problem with any of the measurements in this work because the accelerometers chosen were lightweight 3 gram modal accelerometers and the limiting upper measurement frequency is above 10 KHz.

The measurement of the loss factor by the reverberation time decay is a standard measurement technique. It is widely used since it can measure the loss factor over a large part of the frequency spectrum. There are other alternative techniques such as the half-power bandwidth and power balance method which could be used and the reasons for rejecting these is discussed in the following paragraphs.

The half power bandwidth is one of the possible techniques that could have been used to measure damping. This technique relies on being able to excite a specific resonant mode of a structure and then calculate the damping of the mode and is described by Cremer [66] and Lyon and DeJong [36]. The limitation of this technique is that it can only be applied at low frequencies if the resonant modes are well separated and cannot reveal any information about damping in the higher frequency bands. Lyon gives the relationship between the modal spacing Δf and the upper frequency limit of the method in the following equation.

$$\Delta f < 3\eta f \tag{3.5}$$

If the modal spacing criteria above is met then the half power bandwidth can no longer be used. The other problem with the half power method is that where there is low

damping, the bandwidth of resonant peak in the response is very narrow and it can be difficult to obtain sufficient resolution to reliably determine the damping.

The other technique that could be used is the power balance method. The power input and the response is measured and this allows the damping to be calculated. This technique works well for a test structure that is a single subsystem or can be equated to a single subsystem but the problem comes when applying it to a coupled structure. As all measurements are taken on the source subsystem, but there will be power flow from the other coupled subsystems back to the source subsystem and this makes the calculation of the damping difficult.

These are the alternative measurement techniques available to measuring the damping of a structure and it was judged that the reverberation decay method is the most practical technique to measure the structural damping.

3.7 Conclusions

This chapter described the basic measurement techniques and equipment used in the laboratory and aboard the ship structures to acquire the experimental data for this work. The level difference measurement and damping measurement were discussed in detail, in particular the variations employed when moving from the laboratory to real ship structures. The results of the measured loss factor on the steel laboratory structure and ship sections were presented and the Irie damping model has been adopted for the SEA models. The calibration methods used to verify the functionality of the test equipment was presented and discussed. The chapter ended with a discussion of the accuracy of the measurement procedure and the use of the normal distribution to assess the variance of the measurements from the mean. Results from one of the laboratory test structures and a ship structure were presented to show how the standard deviation and confidence levels vary across the frequency spectrum. The different measurement techniques and the alternative procedures available for measurement were also discussed.

Chapter Four

Structural Vibration Transmission in Hull Frames

4.1 Introduction

This chapter introduces the theory of structural vibration transmission in hull frame structures typically found in ship construction and the parametric studies performed to determine the behaviour of the basic model. In section 4.2 the basic theoretical model of the hull frame structure is outlined and the equations for predicting the transmission coefficients are developed. A parametric study of the variation of the basic geometric parameters is presented in section 4.3 to identify what features of the frame have significant effect on the noise transmission across hull frame structures. The conclusions about the performance of the basic hull-frame joint are given in section 4.4.

4.2 Hull Frame Transmission Model.

4.2.1 Introduction

In this first section the basic theoretical model for predicting the wave transmission coefficients necessary for calculating the coupling loss factor in SEA models is developed. The model must be able to predict the wave transmission characteristics of the different type of stiffeners commonly found in ship construction. In the reviews of ship design by Taggart [92] and Cetena [93] it can be seen that there are five common types of stiffener encountered in practice and these are shown in figure 4.1. The model developed for predicting the wave transmission coefficients must be capable of analysing these different stiffener variations.

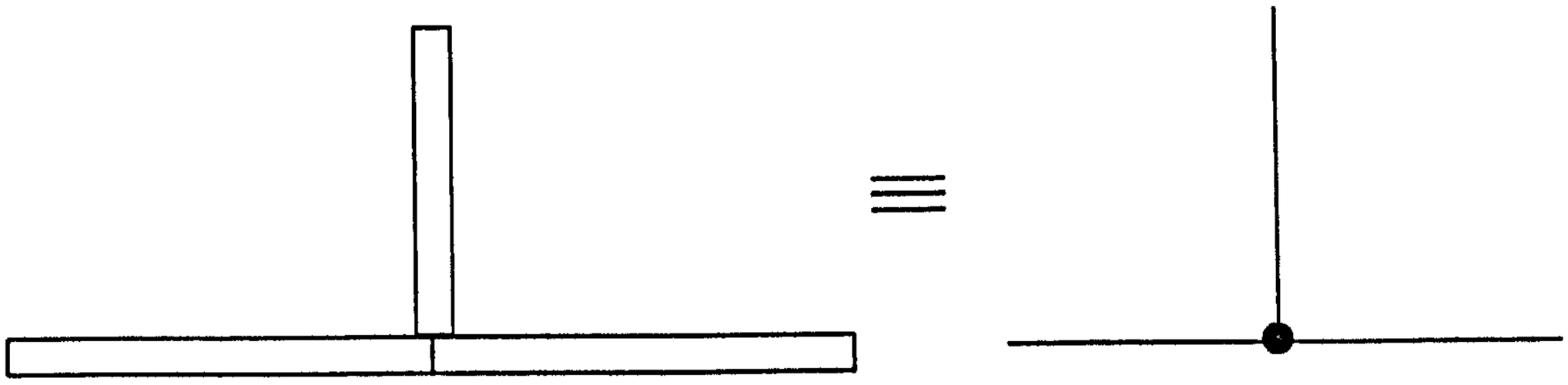

Flat bar stiffener

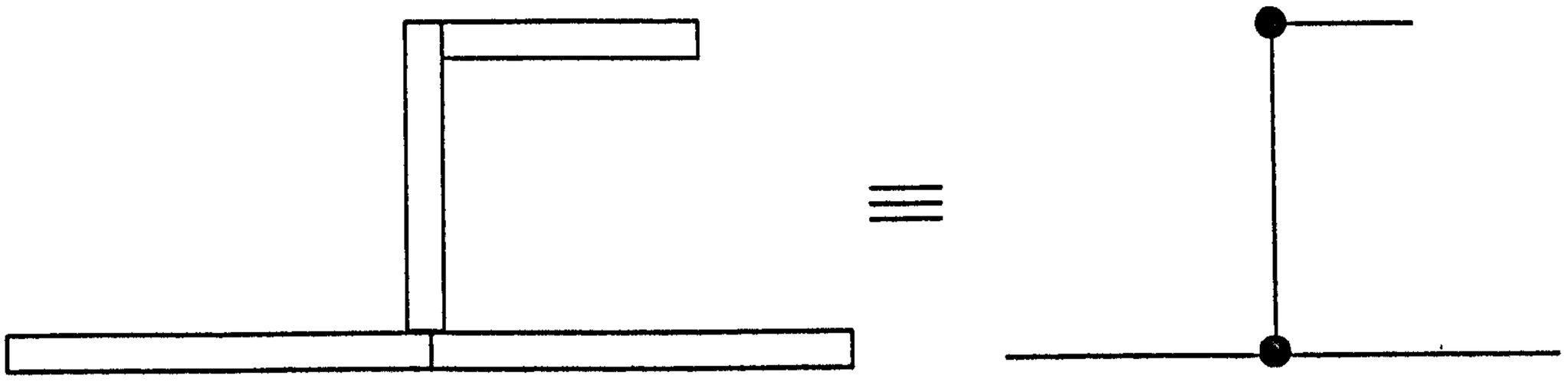

Angle stiffener

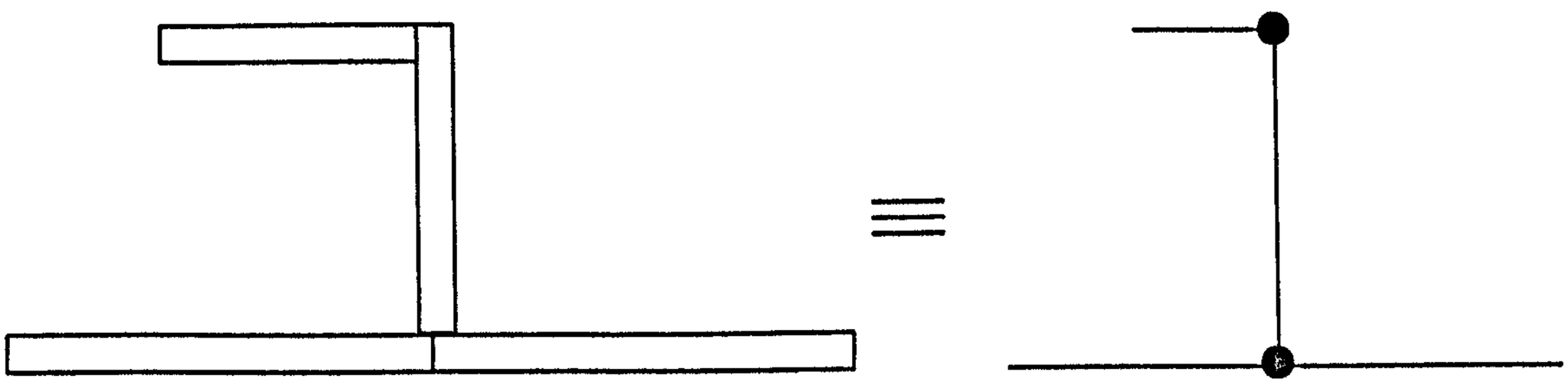

Angle stiffener

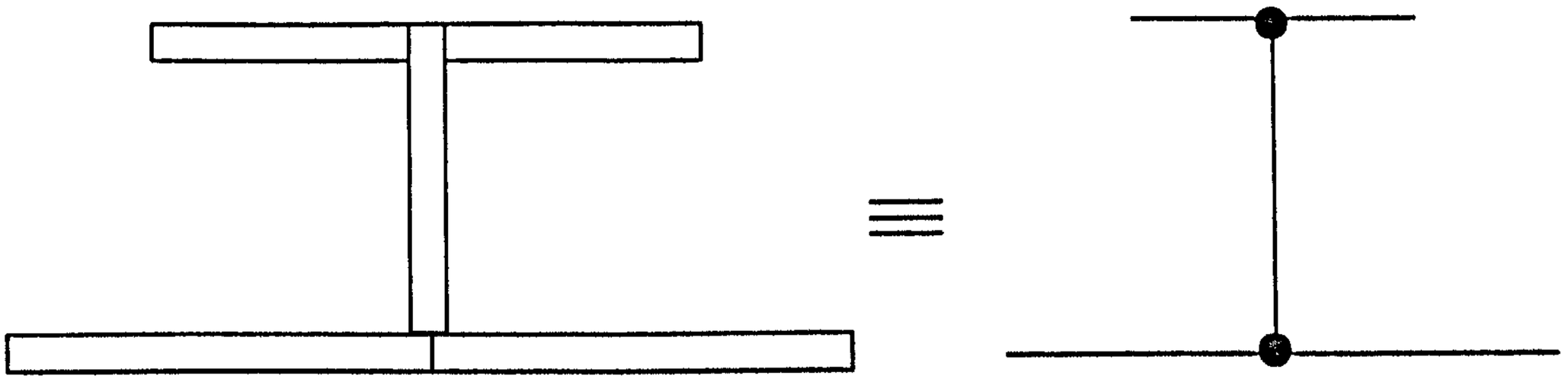

Hull frame stiffener

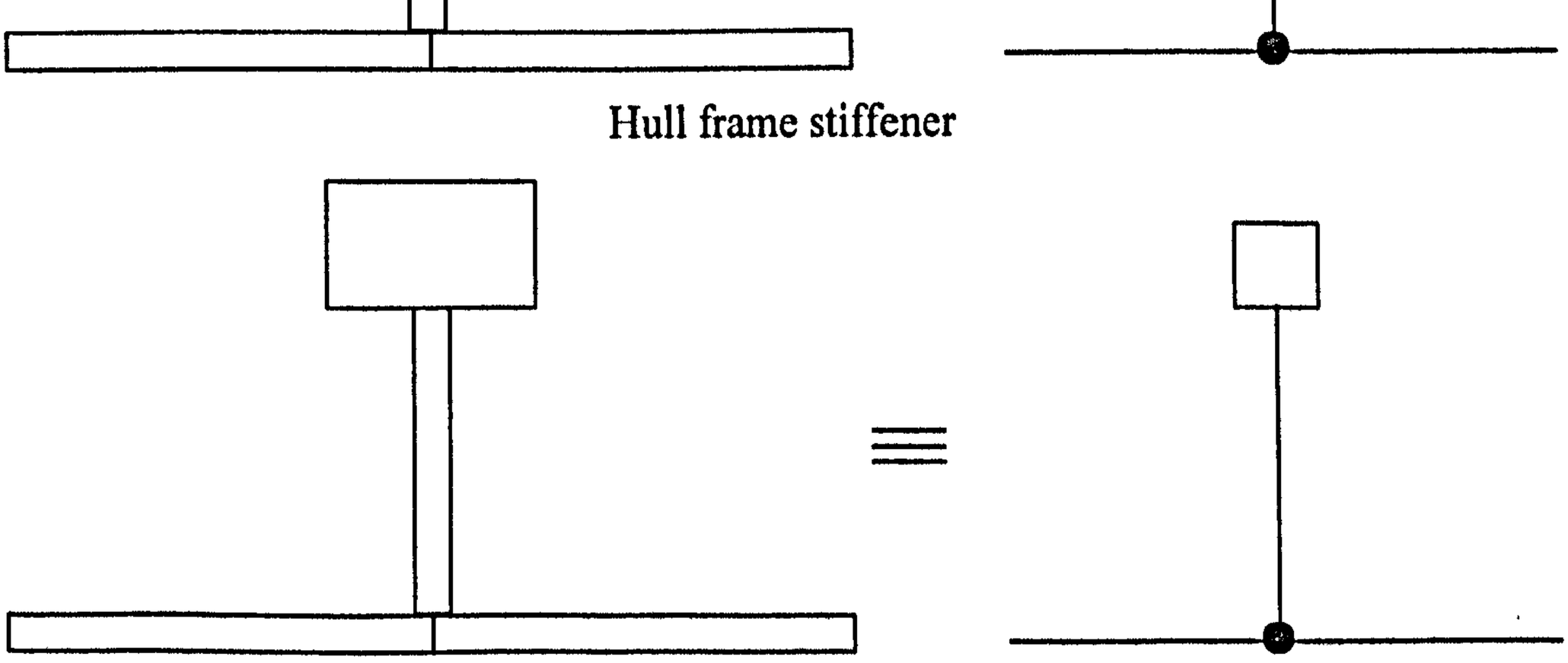

Bulb plate stiffener

Figure 4.1 Stiffener designs found in ship construction

4.2.2 Wave Types and Properties

Before considering the model of the hull-frame structure it is important to consider the properties of structure-borne sound waves which have been studied in detail by Cremer et al [66]. The basic properties of structure-borne sound waves required in the development of the transmission model are summarised in this section.

The different types of structure-borne sound wave may be classified according to the structure upon which they travel. Structural elements such as beams, columns and rods are considered one dimensional since the two cross sectional dimensions are assumed to be smaller than a wavelength and can support bending waves in two directions, longitudinal and torsion waves. Structures such as flat plates and cylindrical shells are classified as two-dimensional structures because the thickness is much less than a wavelength. Flat plates can support bending, longitudinal and transverse wave types and cylindrical shell structures can support longitudinal, circumferential and radial wave types. Figure 4.2 indicates the direction of propagation and displacements of the different wave types on beam structures and figure 4.3 on plate structures, as these are the principle areas of interest for this work.

Cremer [66] has shown that for the different wave types the following relations between the physical properties and wave properties exist. For all wave types the following wavespeed equation is valid. The frequency f is related to the wavelength λ and wave speed c and the wavenumber k as shown in equation 4.1. This is the basic definition of phase velocity which is the speed at which deformations are transported through a structure.

$$f = c\lambda = c\frac{2\pi}{k} \tag{4.1}$$

The energy is transported at a velocity termed the group velocity, c_g, which is defined as follows,

$$c_g = \frac{\partial \omega}{\partial k} \tag{4.2}$$

(a) Bending waves

The bending wave speed c_b is given by Cremer [66] as follows

$$c_b = \sqrt[4]{\frac{B\omega^2}{\rho_s}} \tag{4.3}$$

This is applicable to beams and thin plates where B is the bending stiffness and ρ_s is the mass per unit length of a beam or the mass per unit area of a plate and ω is the cyclic frequency in radians per second. For a plate the bending stiffness is given by equation *4.3a* and for a beam the bending stiffness B_{xx} and B_{zz} are about the principal axis of the beam are given by equation *4.3b*

$$B = \frac{E h^3}{12\left(1-\mu^2\right)} \tag{4.3a}$$

$$B_{zz} = \frac{E d\, b^3}{12}, B_{xx} = \frac{E b\, d^3}{12} \tag{4.3b}$$

where E is the modulus of elasticity, h is the plate thickness, μ is the Poisson ratio in equation *4.3a* and b and d are the breadth and depth of the beam section as appropriate. The group velocity as defined in equation *4.2* is different from the phase velocity and the relationship between them is given by Cremer [66] as follows,

$$c_b = 0.5 c_g \tag{4.4}$$

Equation *4.3* and *4.4* has been derived from the thin bending wave equation which is based on the assumption that the bending wavelength is large compared to the thickness of the plate. Bending wavelength decreases as the frequency increases and there is a transition frequency at which the bending wavelength can no longer be considered large

relative to the cross-sectional dimensions of the beam or thickness of the plate. At this transition frequency it is more appropriate to use the thick bending wave equation. Cremer [66] has shown that the thick bending wave solution is appropriate if the bending wavelength λ_b is less than the value given in equation *4.5*,

$$\lambda_b \leq 6h \tag{4.5}$$

where h is the thickness of a plate or the cross sectional dimension of a beam. There is not an abrupt change in the phase speed but rather a gradual increase in error as the wavelength reduces. The maximum error introduced in the phase speed does not exceed 10% until the bending wavelength equals the value given in equation *4.5* and for thick plates the phase speed c_b can be calculated from the following equation given by Craik [37].

$$\frac{1}{c_b'^3} = \frac{1}{c_b^3} + \frac{1}{\gamma^3 c_T^3} \tag{4.6}$$

where c_T is the transverse wave speed and γ is the ratio of the bending wave speed c_b over the transverse wave speed c_T. The thick plate group speed c_g' can be found from the equation *4.7* given by Craik [37]. The equation is an approximate solution for c_g' and is accurate to within 10%.

$$\frac{1}{c_g'} = \frac{c_b'^2}{c_g c_b^2} + \frac{c_b'^2}{\gamma^3 c_T^3} \tag{4.7}$$

(b) Longitudinal waves

The longitudinal wave speed c_L, is given by Cremer [66] as follows:

For a beam $$c_L = \sqrt{\frac{E}{\rho}} \tag{4.8}$$

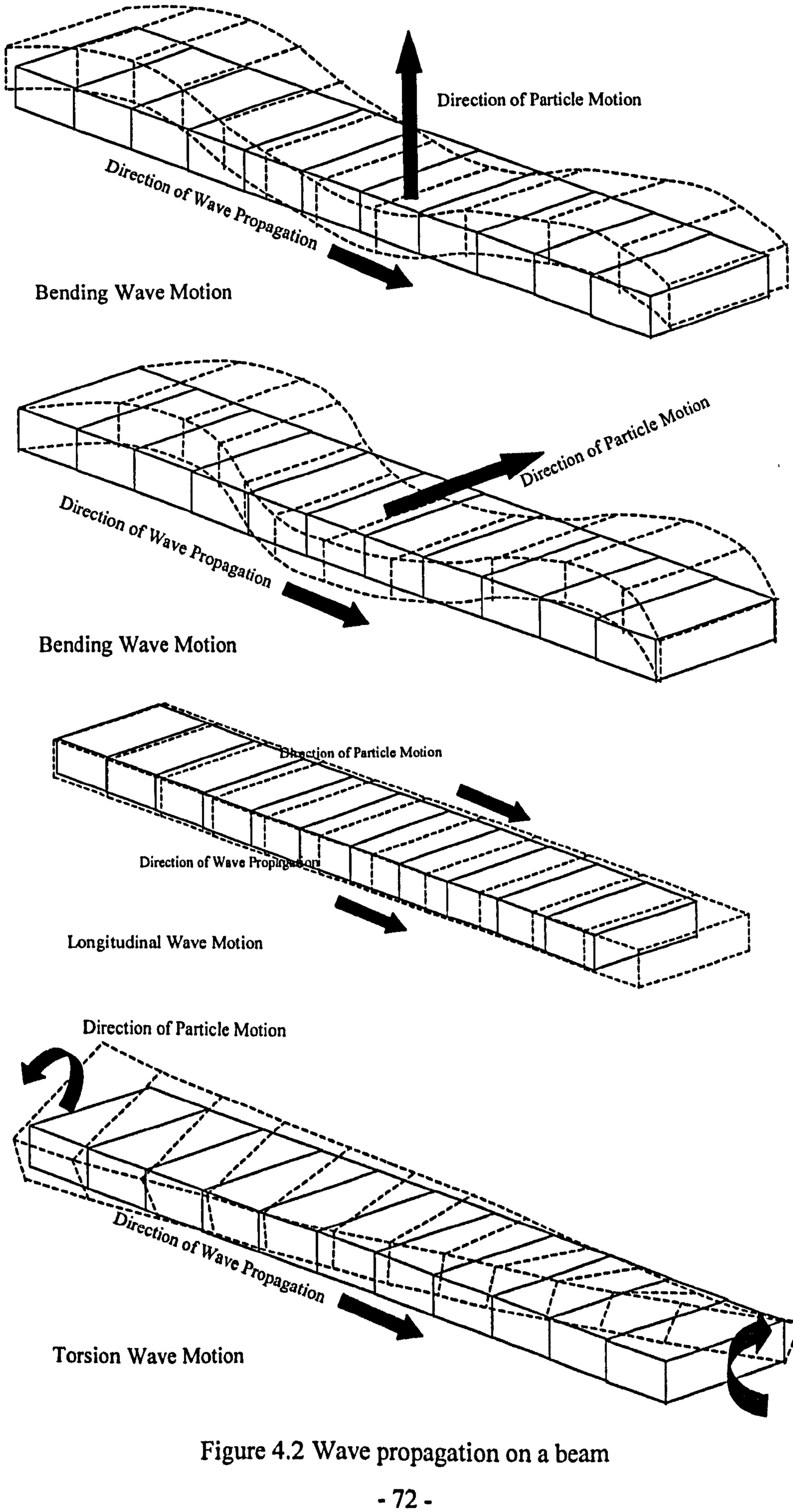

Figure 4.2 Wave propagation on a beam

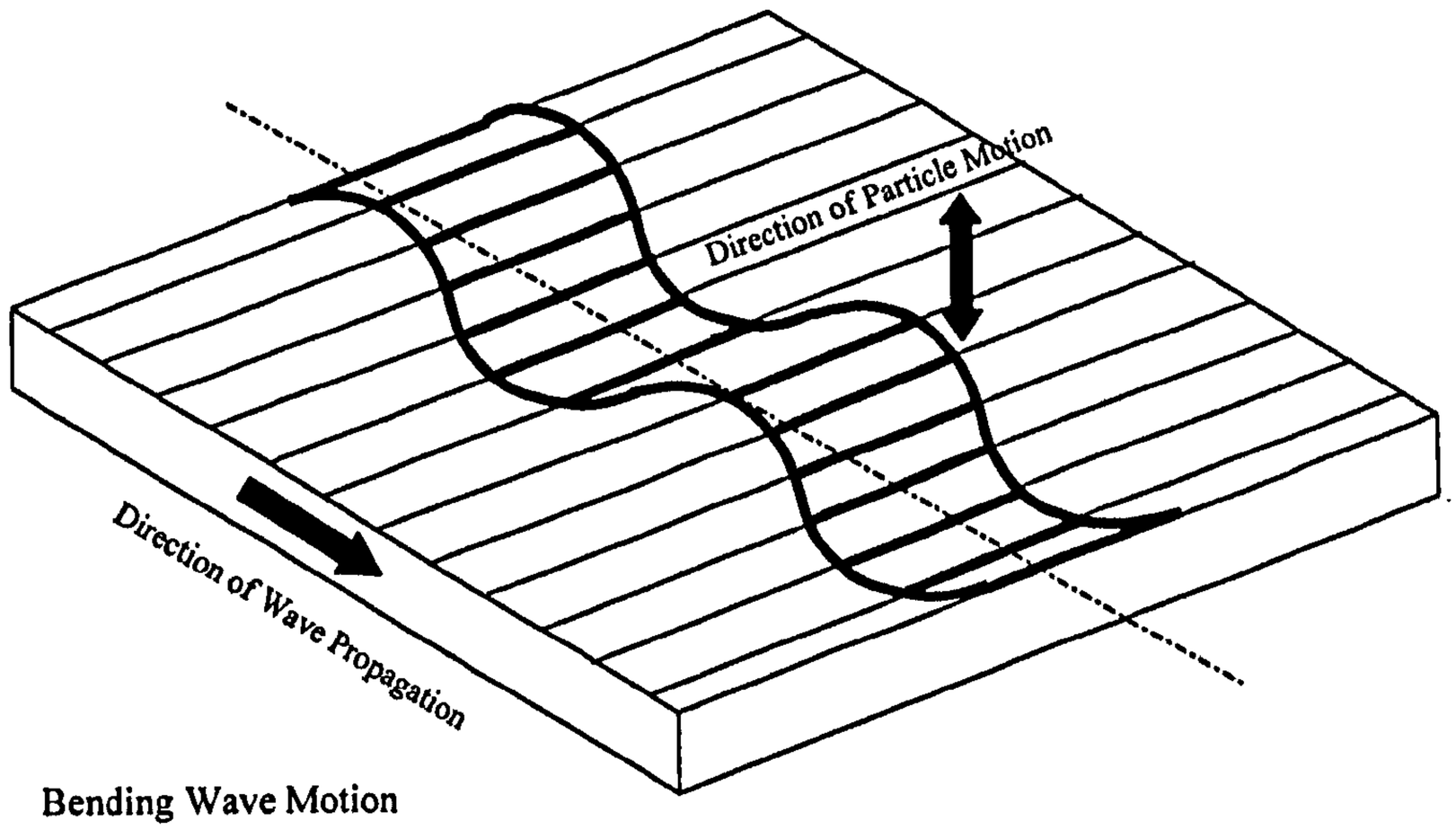

Bending Wave Motion

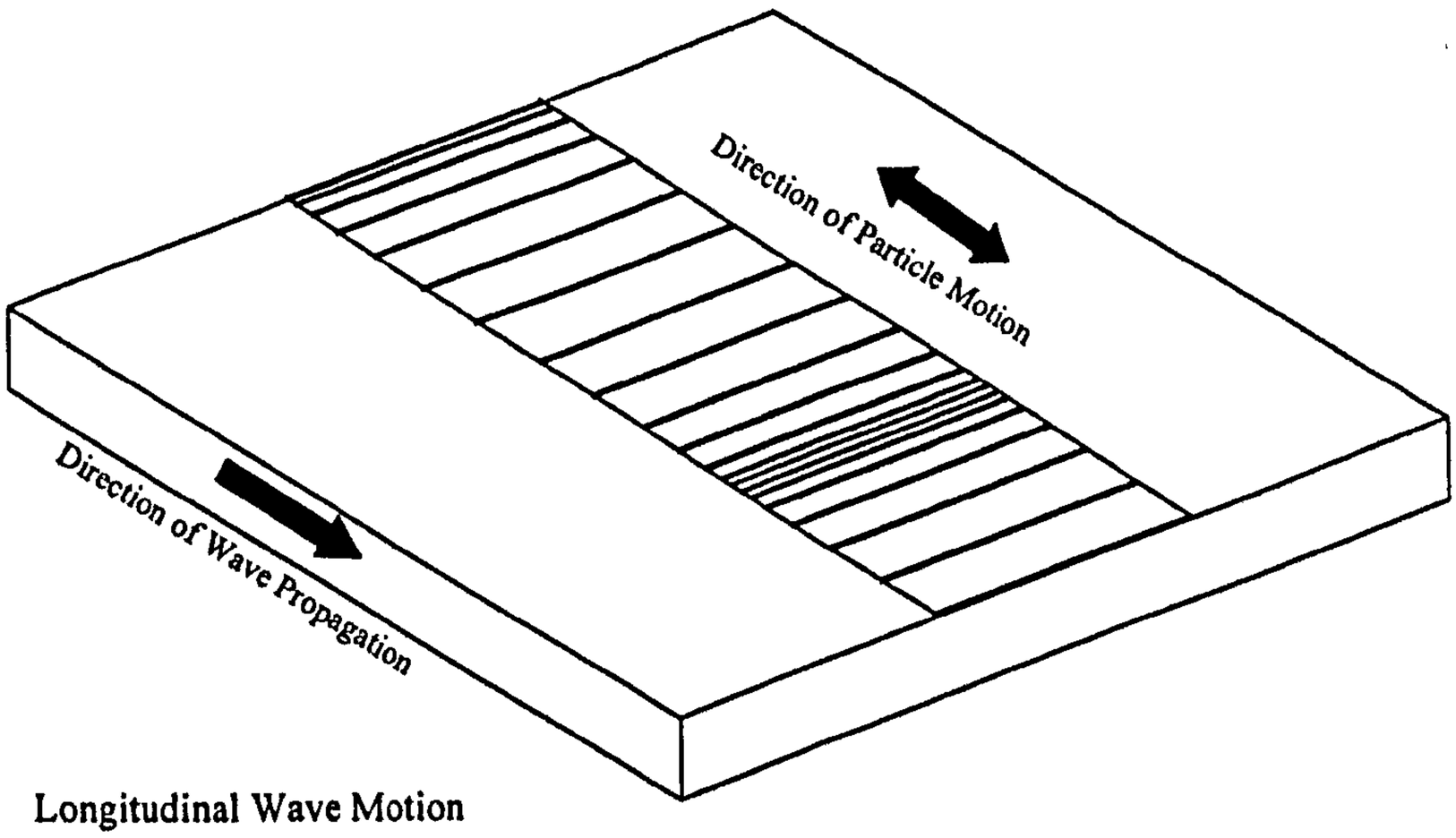

Longitudinal Wave Motion

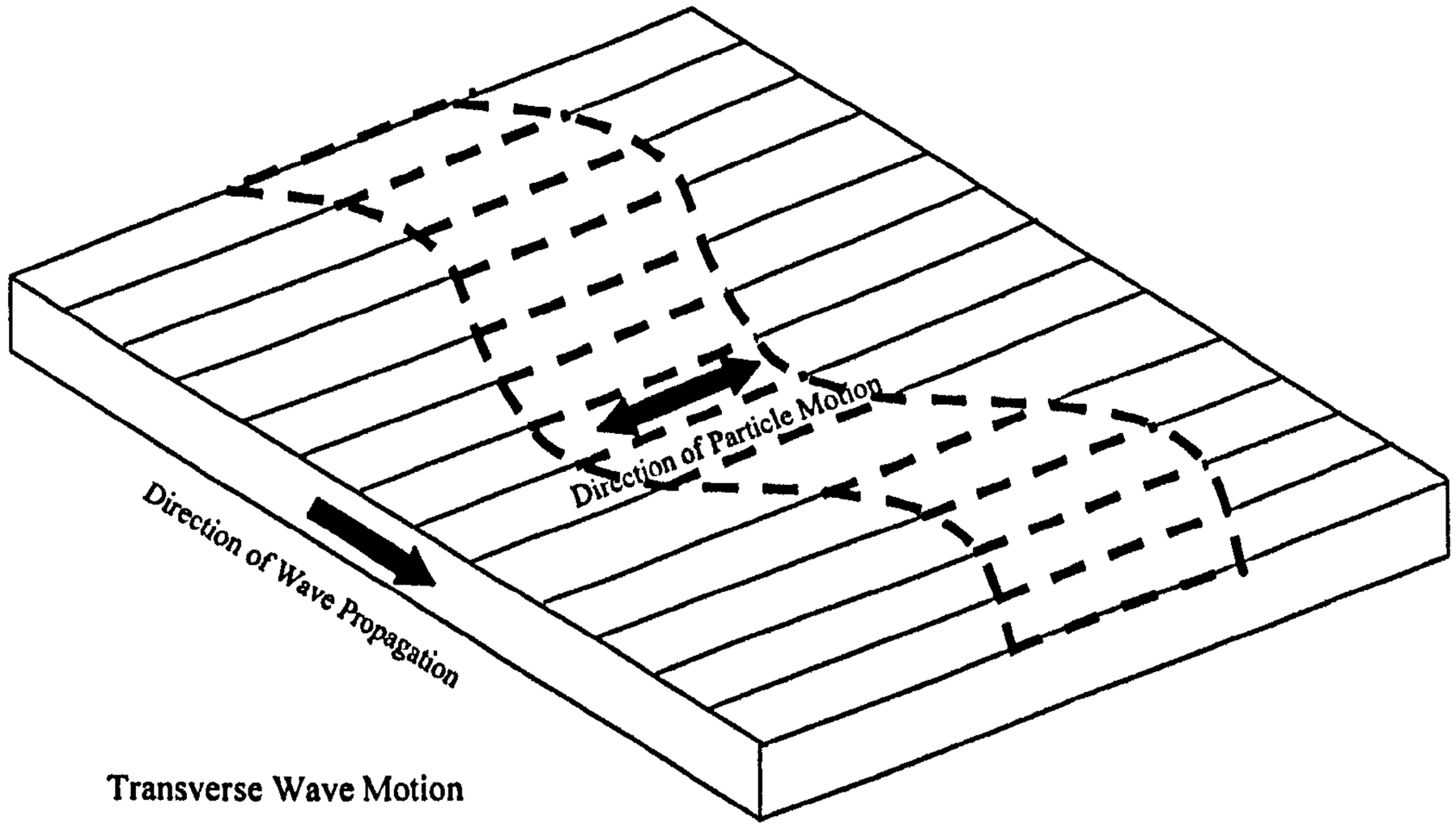

Transverse Wave Motion

Figure 4.3 Wave propagation on a plate

For a plate
$$c_L = \sqrt{\frac{E}{\rho(1-\mu^2)}} \tag{4.9}$$

where E is Young's modulus, ρ is the density of the material and μ is the Poisson ratio of the material. For longitudinal waves the group and phase speed are the same.

(c) Transverse waves

The transverse wave speed c_T, is given by Cremer [66] as follows:

$$c_T = \sqrt{\frac{G}{\rho}} \tag{4.10}$$

where G is the shear modulus and ρ is the density of the material. For transverse waves the group and phase speed are the same. The shear modulus is related to Young's modulus E by the following classical relationship.

$$G = \frac{E}{2(1+\mu)} \tag{4.11}$$

4.2.3 Hull Frame Geometry

The theory presented in this section develops the mathematical model for predicting the wave transmission coefficients of typical hull-frame structures encountered in ship construction. The basic geometry of the hull frame structure under consideration is shown in figure 4.4

The mathematical model is constructed from five plates where plates 1 and 2 are semi-infinite and plates 3, 4 and 5 are finite. Plate 1 extends from $x = -\infty$ to $x = 0$ and plate 2 extends from $x = 0$ to $x = +\infty$ and can be considered as representing a section of hull plate, deck plate or a bulkhead. Plates 3 and 4 represent the flange plates of the stiffener

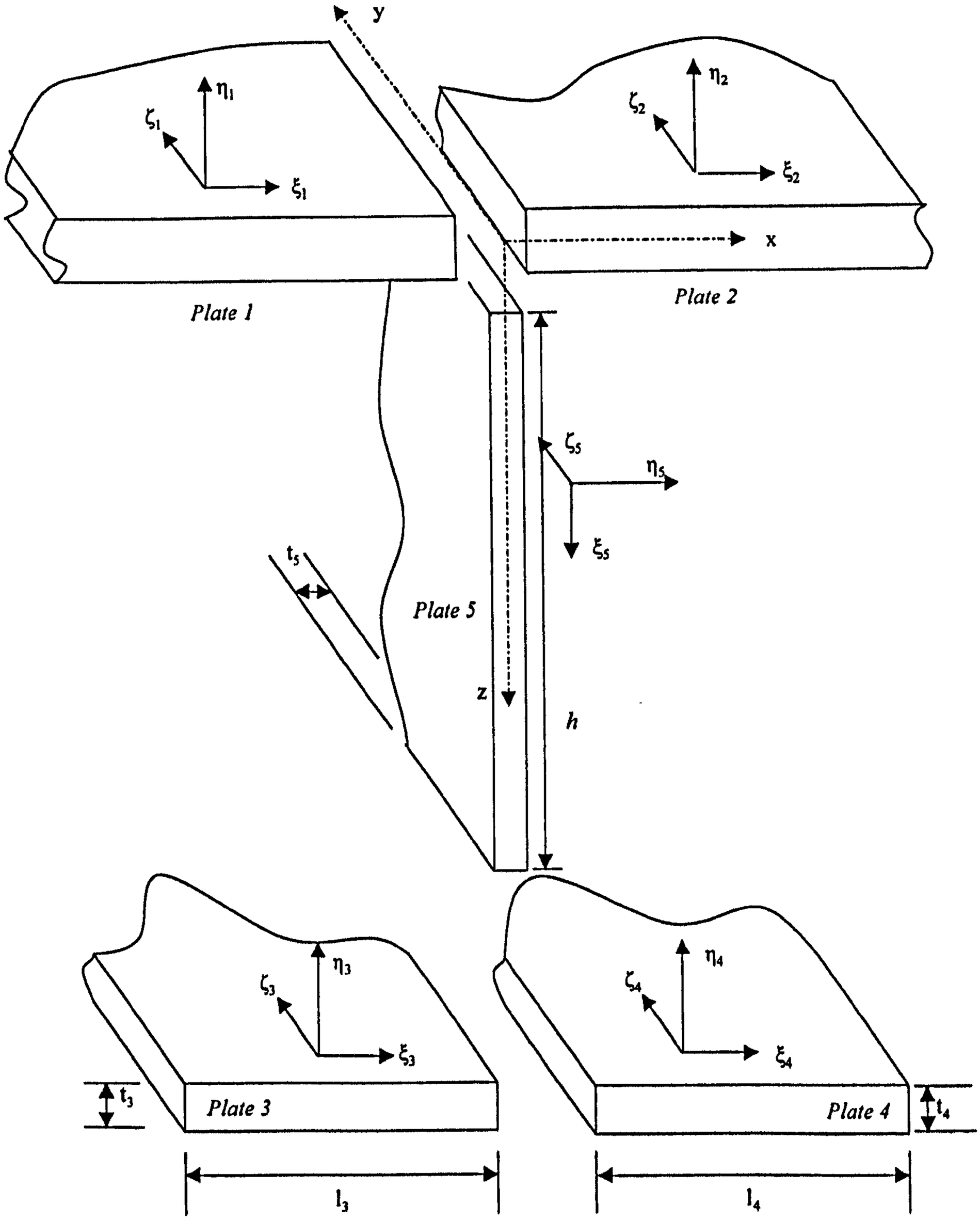

Figure 4.4 Hull plate stiffener model

of width l_3 and l_4 and thickness t_3 and t_4 respectively while plate 5 represents the web plate of the stiffener with depth h and thickness t_5. In section 4.2.1 the variation of stiffener designs encountered in ship construction was briefly discussed and the model developed can be used to analyse stiffener types 1 to 4 shown in figure 4.1 by omission of the relevant plates e.g. the flat bar stiffener (type 2) can be modelled by setting the dimensions of plates 3 and 4 to zero. The bulb plate stiffener (type 5) is a special case and the adjustments to the theory for this are discussed in the next section.

In the model it assumed that the joints formed by the intersection of plates 1, 2 and 5 at $x = 0$, $y = 0$, $z = 0$ and of plates 3, 4 and 5 at $x = 0$, $y = 0$, $z = h$ are rigid. The displacements are specified as follows for each plate i:

$\eta_i =$ The displacement normal to the plane of plate due to propagation of bending waves;

$\xi_i =$ The displacement parallel to the x-direction on plates 1 to 4 of due to in-plane waves. On plate 5 the displacement is parallel to the z direction;

$\zeta_i =$ The displacement parallel to the y direction on plates 1 to 5 due to in-plane waves;

To develop the model it is first necessary to describe the wave types that are generated on plates 1 to 5. The approach used in this section of describing the wave equations for each plate to predict the wave transmission coefficients has become a standard method and used in other joint models e.g. Craik [37], Steel [73], Bosmans [74]. An incident bending wave of unit magnitude travelling on plate 1 impinging at the intersection of plates 1,2 and 5 provides the excitation as shown in Figure 4.5. The bending wave can be incident on the joint from any angle θ, hence the displacement field due to the incident bending wave $\eta_{incident}$ can be expressed as follows after Craik [37],

$$\eta_{incident} = e^{-ik_1 \cos\theta_1 x} e^{-ik_1 \sin\theta_1 y} e^{i\omega t} \tag{4.12}$$

Equation *4.12* represents a bending wave travelling in the positive k_x and k_y directions. The reflected bending wave $\eta_{reflected}$ field on plate 1 contains two components, a travelling wave of amplitude T_{b1} and an evanescent wave of amplitude T_{n1} that can be described as follows:

$$\eta_{reflected} = \left(T_{b1} e^{ik_{b1}\cos\theta_{b1}x} + T_{n1} e^{k_{n1}x}\right) e^{-ik_1 \sin\theta_{b1} y} e^{i\omega t} \tag{4.13}$$

Equation 4.13 represents a bending wave travelling in the negative k_x and k_y directions and because it is due to the incident wave it has the same harmonic dependency and wave component in the y direction since these components are unaffected by the reflection. The total bending wave field on plate 1 can be written as the sum of the incident and reflected bending wave fields given in equations *4.12* and *4.13*:

$$\eta_1 = \left(e^{-ik_{b1}\cos\theta_{b1}x} + T_{b1} e^{ik_{b1}\cos\theta_{b1}x} + T_{n1} e^{k_{n1}x}\right) e^{-ik_1 \sin\theta_{b1} y} e^{i\omega t} \tag{4.14}$$

On plate 2, the bending wave field is constructed from a travelling wave component of amplitude T_{b2} and an evanescent wave component of amplitude T_{n2} caused by the incident-bending wave. The bending wave field is given by equation *4.15*;

$$\eta_2 = \left(T_{b2} e^{-ik_{b2}\cos\theta_{b2}x} + T_{n2} e^{-k_{n2}x}\right) e^{-ik_{b2} \sin\theta_{b2} y} e^{i\omega t} \tag{4.15}$$

Because the wave field on plate 2 is generated by the incident wave on plate 1 it therefore has the same harmonic dependency. This is true for all plates of the model and therefore the $e^{i\omega t}$ term can be removed from all further wave equations as it is a common term. The angle θ_{b2} of the travelling waves can be determined from Snell's law of refraction, which requires that waves transported across a boundary have the same trace wavelength, i.e.

$$k_1 \sin\theta_1 = k_i \sin\theta_i \tag{4.16}$$

Rearranging equation *4.16* we obtain the following important equation

$$sin\theta_i = \frac{k_1}{k_i} sin\theta_1 \tag{4.17}$$

The equation *4.17* allows the angle of incidence θ_i of the wave leaving plate i to be calculated. There can be conditions where $sin\theta_i$ is greater than one and when this occurs there is no travelling wave on plate i, instead a second evanescent wave is generated which causes some local deformation at the joint but no power transmission.

Because plates 3, 4 and 5 are finite the bending wave equations have two travelling wave components and two evanescent wave components. Considering web plate 5 as an example, the incident-bending wave on plate 1 generates a travelling and an evanescent wave of amplitude T_{b5} and T_{n5} which propagate in the y-z plane. When the travelling wave reaches $z = h$ some of the energy of the wave is transmitted to plates 3 and 4 and some is reflected back from the junction. The amplitude of the reflected travelling and evanescent waves is given by T_{b6} and T_{n6} respectively. Thus the wave field is composed of waves originating from junction 1 and reflected from junction 2 and the bending wave field for plate 5 is given in equation *4.18*.

$$\eta_5 = \left(T_{b5} e^{-ik_{b5}cos\theta_{b5}z} + T_{n5} e^{-k_{n5}z}\right) e^{-ik_{b5}sin\theta_{b5}y} + \left(T_{b6} e^{ik_{b6}cos\theta_{b6}z} + T_{n6} e^{k_{n6}(z-h)}\right) e^{-ik_{b6}sin\theta_{b6}y} \tag{4.18}$$

In a similar manner for flange plate 3 the bending wave field equation η_3 can be written where T_{b3} and T_{n3} represent the travelling and evanescent waves from junction 2 and T_{b7} and T_{n7} represent the reflected travelling and evanescent waves from the edge of the flange.

$$\eta_3 = \left(T_{b3} e^{ik_{b3}cos\theta_{b3}x} + T_{n3} e^{k_{n3}x}\right) e^{-ik_{b3}sin\theta_{b3}y} + \left(T_{b7} e^{-ik_{b7}cos\theta_{b7}x} + T_{n7} e^{-k_{n7}(13+x)}\right) e^{-ik_{b7}sin\theta_{b7}y} \tag{4.19}$$

Similarly manner for flange plate 4 the bending wave field equation η_4 can be written where T_{b4} and T_{n4} represent the travelling and evanescent waves from junction 2 and T_{b8} and T_{n8} represent the reflected travelling and evanescent waves from the edge of the

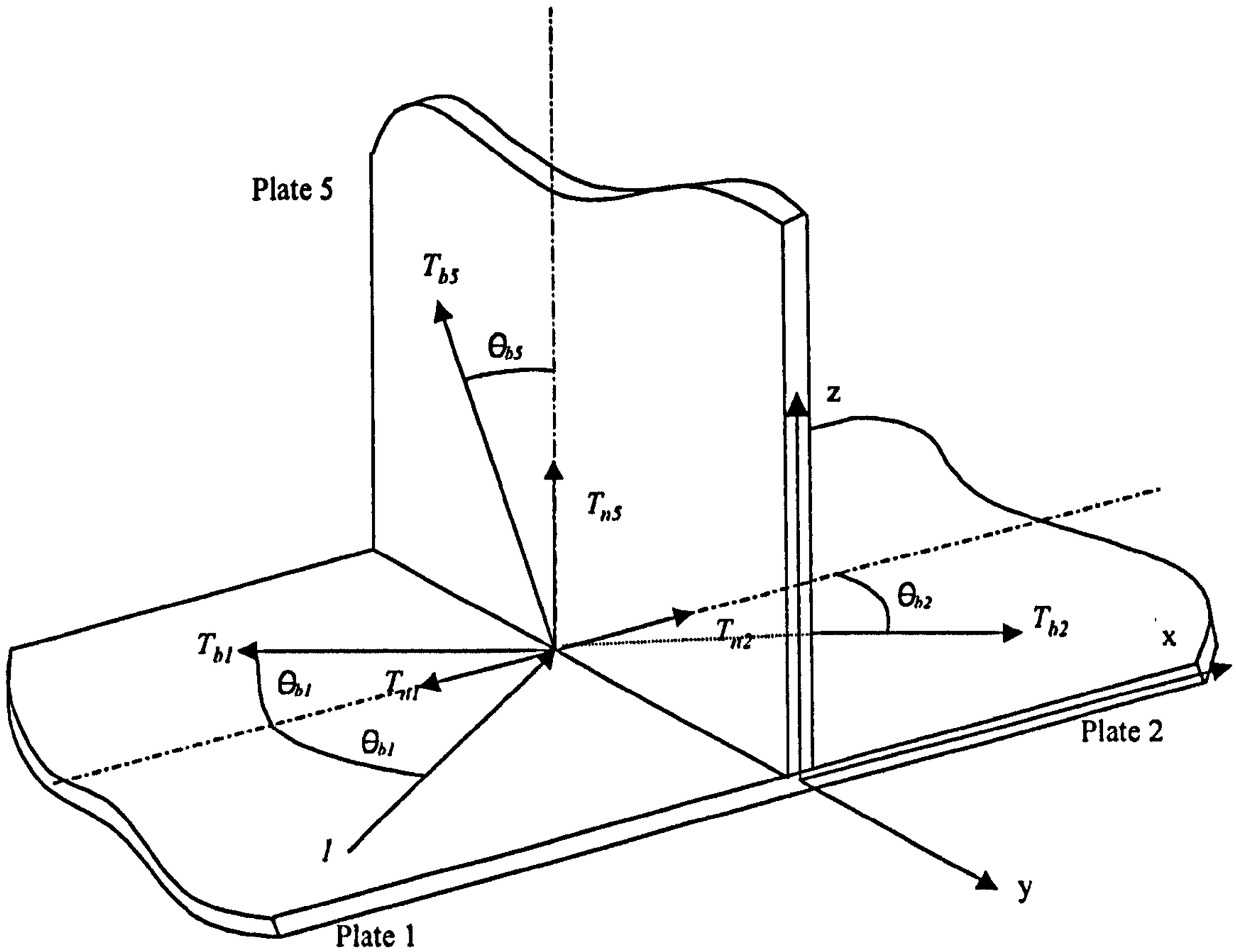

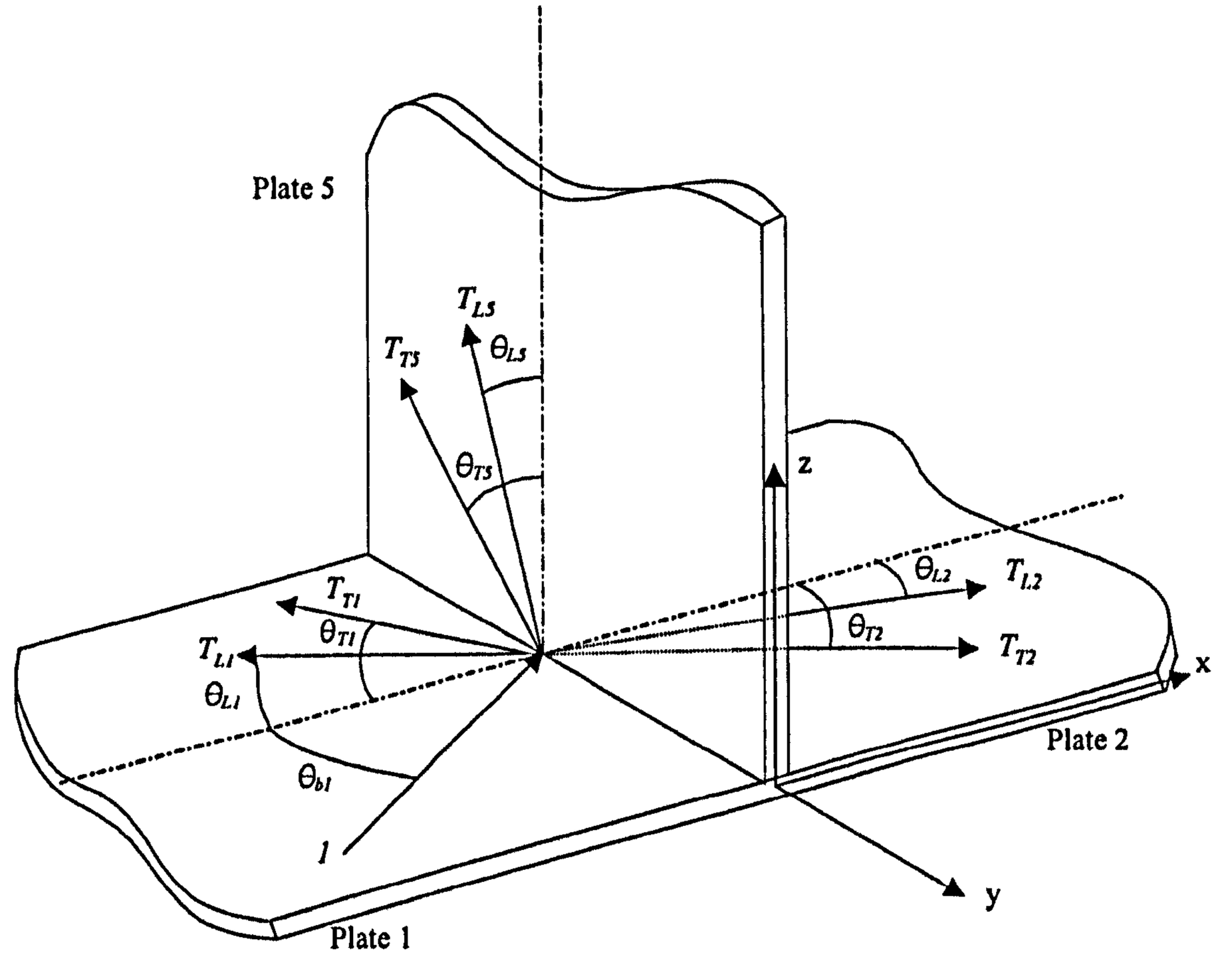

Figure 4.5 – Incident bending wave on plate 1 flange

$$\eta_4 = \left(T_{b4}e^{-ik_{b4}\cos\theta_{b4}x} + T_{n4}e^{-k_{n4}x}\right)e^{-ik_{b4}\sin\theta_{b3}y} + \left(T_{b8}e^{ik_{b8}\cos\theta_{b8}x} + T_{n8}e^{k_{n8}(x-l4)}\right)e^{-ik_{b8}\sin\theta_{b8}y} \quad (4.20)$$

Because the stiffener is eccentric to plates *1* and *2* of the joint the incident bending wave on plate 1 causes in-plane waves to be generated. This process is illustrated in figure *4.5* where the in-plane displacements ξ and ζ are functions of the longitudinal and transverse wave fields. For plate 1 the longitudinal wave field ξ_{L1} is given by

$$\xi_{L1} = T_{L1}e^{-ik_{L1}\cos\theta_{L1}x}e^{-ik_{L1}\sin\theta_{L1}y} \quad (4.21)$$

And the transverse wave field equation ξ_{T1} is given by

$$\xi_{T1} = T_{T1}e^{-ik_{T1}\cos\theta_{T1}x}e^{-ik_{T1}\sin\theta_{T1}y} \quad (4.22)$$

For plate 1 the in-plane displacement wave field in the x direction is given from the summation of the trigonometric components of the longitudinal and transverse waves given in equations *4.21* and *4.22*.

$$\xi_1 = \left(-T_{L1}\cos\theta_{L1}e^{ik_{L1}\cos\theta_{L1}x}\right)e^{-ik_{L1}\sin\theta_{L1}y} - \left(T_{t1}\sin\theta_{t1}e^{ik_{t1}\cos\theta_{t1}x}\right)e^{-ik_{t1}\sin\theta_{t1}y} \quad (4.23)$$

Similarly for plate 2 the in-plane wave field in the x direction is given by summing the trigonometric components of the longitudinal and transverse waves given in equations *4.21* and *4.22*.

$$\xi_2 = \left(T_{L2}\cos\theta_{L2}e^{-ik_{L2}\cos\theta_{L2}x}\right)e^{-ik_{L2}\sin\theta_{L2}y} - \left(T_{t2}\sin\theta_{t2}e^{-ik_{t2}\cos\theta_{t2}x}\right)e^{-ik_{t2}\sin\theta_{t2}y} \quad (4.24)$$

The in-plane wave field in the x-direction on plates 3,4 can be described in a similar manner but as with the bending equations, the finite boundary of the flange plates again result in the generation of reflected wave components. For plates 3 and 4 this gives,

$$\xi_3 = \left(-T_{L3}\cos\theta_{L3}e^{ik_{L3}\cos\theta_{L3}x}\right)e^{-ik_{L3}\sin\theta_{L3}y} - \left(T_{t3}\sin\theta_{t3}e^{ik_{t3}\cos\theta_{t3}x}\right)e^{-ik_{t3}\sin\theta_{t3}y} + \left(T_{L7}\cos\theta_{L7}e^{-ik_{L7}\cos\theta_{L7}x}\right)e^{-ik_{L7}\sin\theta_{L7}y} - \left(T_{t7}\sin\theta_{t7}e^{-ik_{t7}\cos\theta_{t7}x}\right)e^{-ik_{t7}\sin\theta_{t7}y} \quad (4.25)$$

$$\xi_4 = \left(T_{L4}\cos\theta_{L4}e^{-ik_{L4}\cos\theta_{L4}x}\right)e^{-ik_{L4}\sin\theta_{L4}y} - \left(T_{t4}\sin\theta_{t4}e^{-ik_{t4}\cos\theta_{t4}x}\right)e^{-ik_{t4}\sin\theta_{t4}y} - \left(T_{L8}\cos\theta_{L8}e^{ik_{L8}\cos\theta_{L8}x}\right)e^{-ik_{L8}\sin\theta_{L8}y} - \left(T_{t8}\sin\theta_{t8}e^{ik_{t8}\cos\theta_{t8}x}\right)e^{-ik_{t8}\sin\theta_{t8}y} \quad (4.26)$$

The in-plane wave field in the z-direction on plate 5 can be described in a similar manner to plates 3 and 4.

$$\xi_5 = \left(T_{L5}\cos\theta_{L5}e^{-ik_{L5}\cos\theta_{L5}z}\right)e^{-ik_{L5}\sin\theta_{L5}y} - \left(T_{t5}\sin\theta_{t5}e^{-ik_{t5}\cos\theta_{t5}z}\right)e^{-ik_{t5}\sin\theta_{t5}y} - \left(T_{L6}\cos\theta_{L6}e^{ik_{L6}\cos\theta_{L6}z}\right)e^{-ik_{L6}\sin\theta_{L6}y} - \left(T_{t6}\sin\theta_{t6}e^{ik_{t6}\cos\theta_{t6}z}\right)e^{-ik_{t6}\sin\theta_{t6}y} \quad (4.27)$$

Considering the in-plane displacement wave field in the *y* direction on plate 1, the wave field can be constructed from equation *4.21* and *4.22* in a similar manner to equation *4.23*. Thus the in-plane displacement wave field in the y direction on plate 1 is given by:

$$\zeta_1 = \left(T_{L1}\sin\theta_{L1}e^{-ik_{L1}\cos\theta_{L1}x}\right)e^{-ik_{L1}\sin\theta_{L1}y} - \left(T_{t1}\cos\theta_{t1}e^{-ik_{t1}\cos\theta_{t1}x}\right)e^{-ik_{t1}\sin\theta_{t1}y} \quad (4.28)$$

And the in-plane displacement wave field in the y direction on plate 2 is given by

$$\zeta_2 = \left(T_{L2}(\sin\theta_{L2})e^{ik_{L2}\cos\theta_{L2}x}\right)e^{-ik_{L2}\sin\theta_{L2}y} + \left(T_{t2}\left(\cos\theta_{t2}\right)e^{ik_{t2}\cos\theta_{t2}x}\right)e^{-ik_{t2}\sin\theta_{t2}y} \quad (4.29)$$

The in-plane displacement wave field in the *y* direction on plate 3 is given by

$$\zeta_3 = \left(T_{L3}(\sin\theta_{L3})e^{ik_{L3}\cos\theta_{L3}x}\right)e^{-ik_{L3}\sin\theta_{L3}y} - \left(T_{t3}\cos\theta_{t3}e^{ik_{t3}\cos\theta_{t3}x}\right)e^{-ik_{t3}\sin\theta_{t3}y} + \left(T_{L7}(\sin\theta_{L7})e^{-ik_{L7}\cos\theta_{L7}x}\right)e^{-ik_{L7}\sin\theta_{L7}y} + \left(T_{t7}\cos\theta_{t7}e^{-ik_{t7}\cos\theta_{t7}x}\right)e^{-ik_{t7}\sin\theta_{t7}y} \quad (4.30)$$

In a similar manner for plate 4 the in-plane displacement wave field in the *y* direction:

$$\zeta_4 = \left(T_{L4}\sin\theta_{L4}e^{-ik_{L4}\cos\theta_{L4}x}\right)e^{-ik_{L4}\sin\theta_{L4}y} + \left(T_{t4}\cos\theta_{t4}e^{ik_{t4}\cos\theta_{t4}x}\right)e^{-ik_{t4}\sin\theta_{t4}y} + \left(T_{L8}\sin\theta_{L8}e^{ik_{L8}\cos\theta_{L8}x}\right)e^{-ik_{L8}\sin\theta_{L8}y} - \left(T_{t8}\cos\theta_{t8}e^{ik_{t8}\cos\theta_{t8}x}\right)e^{-ik_{t8}\sin\theta_{t8}y} \quad (4.31)$$

And finally for plate 5

$$\begin{aligned}\zeta_5 = &\left(T_{L5}\sin\theta_{L5}e^{-ik_{L5}\cos\theta_{L5}z}\right)e^{-ik_{L5}\sin\theta_{L5}y} + \left(T_{t5}\cos\theta_{t5}e^{-ik_{t5}\cos\theta_{t5}z}\right)e^{-ik_{t5}\sin\theta_{t5}y} \\ &+\left(T_{L6}\sin\theta_{L6}e^{ik_{L6}\cos\theta_{L6}z}\right)e^{-ik_{L6}\sin\theta_{L6}y} - \left(T_{t6}\cos\theta_{t6}e^{ik_{t6}\cos\theta_{t6}z}\right)e^{-ik_{t6}\sin\theta_{t6}y}\end{aligned} \tag{4.32}$$

From consideration of the wave field equations *4.16* to *4.32* above there are 32 unknown wave amplitudes as follows:

$$\left\{\begin{matrix}T_{b1}, T_{b2}, T_{b3}, T_{b4}, T_{b5}, T_{b6}, T_{b7}, T_{b8}, T_{n1}, T_{n2}, T_{n3}, T_{n4}, T_{n5}, T_{n6}, T_{n7}, T_{n8}, \\ T_{L1}, T_{L2}, T_{L3}, T_{L4}, T_{L5}, T_{L6}, T_{L7}, T_{L8}, T_{T1}, T_{T2}, T_{T3}, T_{T4}, T_{T5}, T_{T6}, T_{T7}, T_{T8},\end{matrix}\right\} \tag{4.33}$$

A solution for these unknowns requires 32 equations which can be determined from consideration of the requirements of displacement continuity and the force/moment equilibrium equations at the plate junctions. The joint can be subdivided into 4 nodes as indicated in figure 4.6. From the requirements of the displacement continuity we can determine that at node 1 *(x = 0, y = 0, z = 0)* we have the following conditions:

$$\eta_1 = \eta_2 \quad (4.34), \qquad \eta_1 = -\xi_5 \quad (4.35), \qquad \xi_1 = \xi_2 \quad (4.36)$$

$$\xi_1 = \eta_5 \quad (4.37), \qquad \zeta_1 = \zeta_2 \quad (4.38), \qquad \zeta_1 = \zeta_5 \quad (4.39)$$

The assumption of a rigid connection between plates 1, 2 and 5 requires that rotational displacements are equal which gives the following conditions,

$$\phi_1 = \phi_2 \quad (4.40), \qquad \phi_1 = \phi_5 \quad (4.41)$$

where the rotational displacement is given by $\phi_1 = \frac{\partial \eta_1}{\partial x}$, $\phi_2 = \frac{\partial \eta_2}{\partial x}$ and $\phi_5 = \frac{\partial \eta_5}{\partial z}$

At node 2 *(x = 0, y = 0, z = h)* a similar set of boundary conditions can be specified for translation displacements as those for node 1:

$$\eta_3 = \eta_4 \ (4.42), \qquad \eta_3 = -\xi_5 \ (4.43), \qquad \xi_3 = \xi_4 \quad (4.44)$$

$$\xi_3 = \eta_5 \quad (4.45), \qquad \zeta_3 = \zeta_4 \quad (4.46), \qquad \zeta_3 = \zeta_5 \quad (4.47)$$

and for the rotational displacements based on the assumption of a rigid connection we have

$$\phi_3 = \phi_4 \quad (4.48), \qquad \phi_3 = \phi_5 \quad (4.49)$$

where the rotational displacement is given by $\phi_3 = \frac{\partial \eta_3}{\partial x}$, $\phi_4 = \frac{\partial \eta_4}{\partial x}$ and $\phi_5 = \frac{\partial \eta_5}{\partial z}$

Consideration of the displacement continuity requirements provides sixteen of the required thirty-two equations. The remaining sixteen equations come from consideration of the joint equilibrium requirements. Figure 4.6 illustrates the free body diagram of the joint. Summation of the forces and moments at node 1 gives:

$$\sum F_x = 0 \Rightarrow F_{x1} - F_{x2} - F_{x5} = 0 \quad (4.50), \quad \sum F_y = 0 \Rightarrow F_{y1} - F_{y2} - F_{y5} = 0 \quad (4.51)$$

$$\sum F_z = 0 \Rightarrow F_{z1} - F_{z2} + F_{z5} = 0 \quad (4.52), \quad \sum M_y = 0 \Rightarrow M_1 - M_2 - M_5 = 0 \quad (4.53)$$

And similarly at node 2,

$$\sum F_x = 0 \Rightarrow F_{x3} - F_{x4} + F_{x5} = 0 \quad (4.54), \quad \sum F_y = 0 \Rightarrow F_{y3} - F_{y4} + F_{y5} = 0 \quad (4.55)$$

$$\sum F_z = 0 \Rightarrow F_{z3} - F_{z4} - F_{z5} = 0 \quad (4.56), \quad \sum M_y = 0 \Rightarrow M_3 - M_4 + M_5 = 0 \quad (4.57)$$

And at node 3 the following,

$$\sum F_x = 0 \Rightarrow F_{x3} = 0 \quad (4.58), \quad \sum F_y = 0 \Rightarrow F_{y3} = 0 \quad (4.59)$$

$$\sum F_z = 0 \Rightarrow F_{z3} = 0 \quad (4.60), \quad \sum M_y = 0 \Rightarrow M_3 = 0 \quad (4.61)$$

And at node 4 the following,

$$\sum F_x = 0 \Rightarrow F_{x4} = 0 \quad (4.62), \quad \sum F_y = 0 \Rightarrow F_{y4} = 0 \quad (4.63)$$

$$\sum F_z = 0 \Rightarrow F_{z4} = 0 \quad (4.64), \quad \sum M_y = 0 \Rightarrow M_4 = 0 \quad (4.65)$$

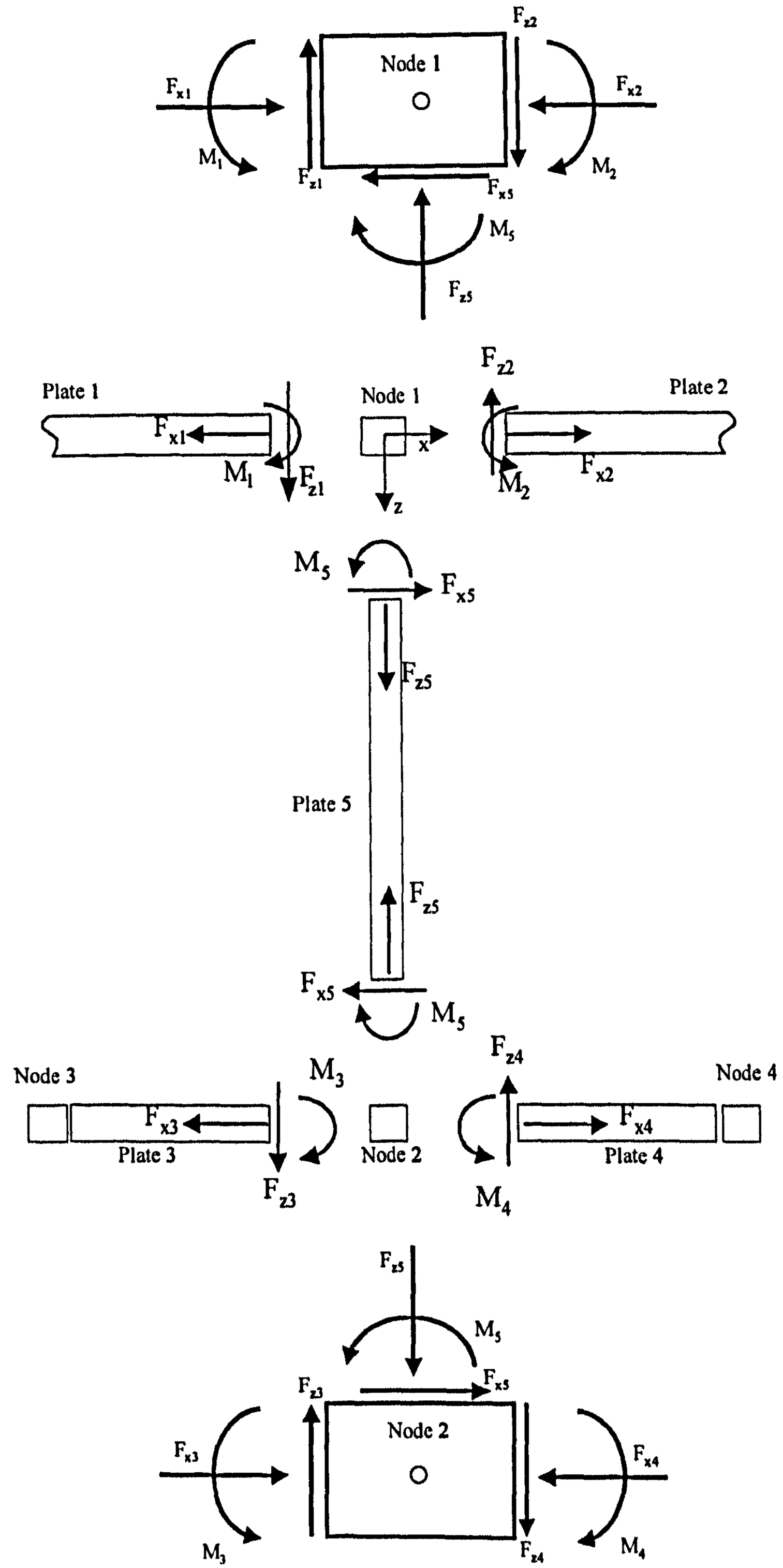

Figure 4.6 Free body diagram of hull frame joint

The moment M_i is related to the bending wave displacement η_i of plate i by the following equation from Cremer [66]. For plate 5, the x term in the 2nd order partial derivative is replaced by a z term:

$$M_i = -B_i\left\{\frac{\partial^2 \eta_i}{\partial x^2} + \mu_i \frac{\partial^2 \eta_i}{\partial y^2}\right\} \tag{4.66}$$

The relationship between the transverse shear forces F_{z1}, F_{z2}, F_{z3}, F_{z4}, F_{x5} and the respective bending wave displacements is given by equation *4.67* from Cremer [66]. The x terms are replaced with z terms for plate 5:

$$F_{zi} = B_i\left[\frac{\partial}{\partial x}\left\{\frac{\partial^2 \eta_i}{\partial x^2} + (2-\mu_i)\frac{\partial^2 \eta_i}{\partial y^2}\right\}\right] \tag{4.67}$$

The in-plane longitudinal forces F_{x1}, F_{x2}, F_{x3}, F_{x4} and F_{z5} for plates 1 to 5 are related to the in-plane wave displacements by the following equation given by Langley [79]. As with equation *4.66* the x terms are replaced with z terms for plate 5:

$$F_{xi} = \frac{-E_i h_i}{(1+\mu_i^2)}\left\{\frac{\partial \xi_i}{\partial x} + \mu_i \frac{\partial \zeta_i}{\partial y}\right\} \tag{4.68}$$

In equation *4.69* given by Langley [79] the in-plane shear force in the y direction, F_{yi} for any plate i is related to the in-plane wave displacements. As with equation *4.66* the x terms are again replaced with z terms for plate 5:

$$F_{yi} = \frac{-E_i h_i}{2(1+\mu_i)}\left\{\frac{\partial \xi_i}{\partial y} + \frac{\partial \zeta_i}{\partial x}\right\} \tag{4.69}$$

Using the wave and force/moment equations previously outlined, the 32 continuity and equilibrium equations can be expressed in matrix format which can be solved

numerically by standard methods such as Gauss elimination in terms of the unknown wave amplitudes T_{bi}, T_{ni}, T_{Li} and T_{Ti}.

With the wave amplitudes determined it is necessary to calculate the wave transmission coefficients. The power leaving a joint depends on the amplitude of the wave and the angle of incidence. The wave transmission coefficient is defined for plate *1* and *2* as

$$\tau_{12} = \frac{Power\ transmitted\ across\ the\ joint\ to\ plate\ 2}{Power\ incident\ on\ the\ joint\ at\ plate\ 1} \tag{4.70}$$

For an incident bending wave on plate 1, the bending wave transmission coefficient is given by Cremer [66] as

$$\tau_{1b2b} = \left[\frac{2\rho_{s2}\cos\theta_{b2}}{k_{b2}}\left|T_{2b}\right|^2\right]_{transmitted}\left[\frac{k_{b1}}{2\rho_{s1}\cos\theta_{b1}}\right]_{incident} \tag{4.71}$$

The transmission coefficient for conversion from bending waves on plate 1 to longitudinal waves on plate 2 is given by

$$\tau_{1b2L}\left[\frac{\rho_{s2}\cos\theta_{L2}}{k_{L2}}\left|T_{L2}\right|^2\right]_{transmitted}\left[\frac{k_{b1}}{2\rho_{s1}\cos\theta_{b1}}\right]_{incident} \tag{4.72}$$

The transmission coefficient for conversion of bending waves to transverse waves from plate 1 to plate 2 is given by

$$\tau_{1b2T}\left[\frac{\rho_{s2}\cos\theta_{T2}}{k_{t2}}\left|T_{2T}\right|^2\right]_{transmitted}\left[\frac{k_{b1}}{2\rho_{s1}\cos\theta_{b1}}\right]_{incident} \tag{4.73}$$

For incident longitudinal and transverse wave types, the incident power is given by Langley and Heron [79] and can be substituted for the bending wave incident power

term in equations *4.71* to *4.73*. In SEA the wave field is assumed to be diffuse and therefore all angles of incidence are considered equally probable. It is normal to consider the average angular transmission coefficient at for each frequency which is calculated by integrating the transmission coefficient over the angle of incidence as follows:

$$\tau_{ave} = \int_0^{\pi/2} \tau(\theta) \cos\theta d\theta \tag{4.74}$$

The above equation is solved numerically since the determination of the wave transmission amplitude matrix is not possible by direct methods. All of the wave equations and transmission coefficients presented in this chapter have been derived on the basis of an incident bending wave on plate 1. Solution for incident transverse and longitudinal waves can be achieved by removing the incident bending wave term in equation *4.15* and substituting a unit incident longitudinal or transverse wave term into equations *4.23* and *4.28* as appropriate.

The validity of the solution can be checked by ensuring that the power flow out of the joint equals the power flow in since the model is conservative. This is expressed as follows:

$$\tau_{1b1b} + \tau_{1b1L} + \tau_{1b1T} + \tau_{1b2b} + \tau_{1b2L} + \tau_{1b2T} = 1 \tag{4.74}$$

where τ_{1b1i} are the reflection coefficients and τ_{1b2i} are the transmission coefficients where $i=b,L,T$.

The model has been validated by comparing with results from other previously defined models e.g. Smith [78] and Fraser [94].

4.2.4 Plate – Beam Model

The other type of stiffener design encountered in ship construction is the offset bulb plate as discussed previously. The theoretical model developed in the previous section does not cover the bulb plate stiffener, but with a few simple modifications the theory can be adapted to include this type of construction.

The basic geometry of the joint is shown in figure 4.7. The model is similar to that shown in figure 4.4 except that the flange plates 3 and 4 have been replaced by a beam element. For the joint described there are 16 unknown transmission coefficients as follows:

$$\{T_{b1}, T_{b2}, T_{b5}, T_{b6}, T_{n1}, T_{n2}, T_{n5}, T_{n6}, T_{L1}, T_{L2}, T_{L5}, T_{L6}, T_{T1}, T_{T2}, T_{T5}, T_{T6}\} \quad (4.75)$$

Using the previously defined wave equation for plates 1, 2 and 5 and the displacement continuity and force/moment equilibrium equations for the intersection of plates 1, 2 and 5 at node 1 will provide twelve of the sixteen equations required to determine the transmission coefficients. The remaining four equations are provided by consideration of the equilibrium requirements at the junction of the web plate 5 and the beam as shown in the free body diagram in figure 4.8.

It is therefore only necessary to consider the interface of plate 5 at $z=h$ and the beam stiffener. Considering the equilibrium the joint at node 2, the plate force and moments are resisted by the beam element, which permits the following equilibrium equations to be written.

$$M_5 = M_{beam} \quad (4.76), \quad F_{x5} = F_{x-beam} \quad (4.77)$$

$$F_{y5} = F_{y-beam} \quad (4.78), \quad F_{z5} = F_{z-beam} \quad (4.79)$$

Considering the beam forces in the x direction, the total resisting force is composed of a bending component and an acceleration term as defined in Cremer [66]. The total resisting force $F_{x\text{-}beam}$ is given by

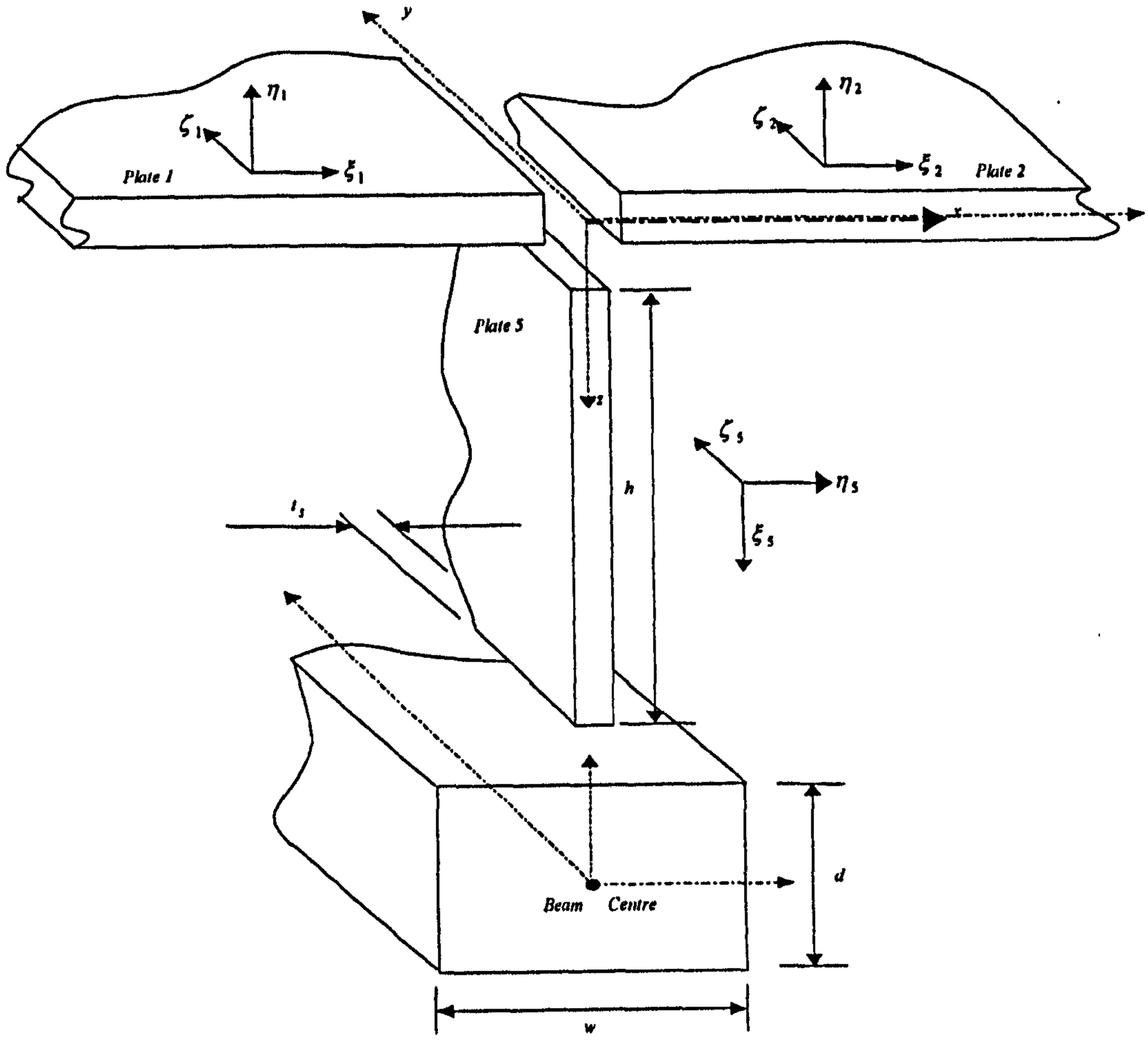

Figure 4.7 Geometry of plate-beam joint

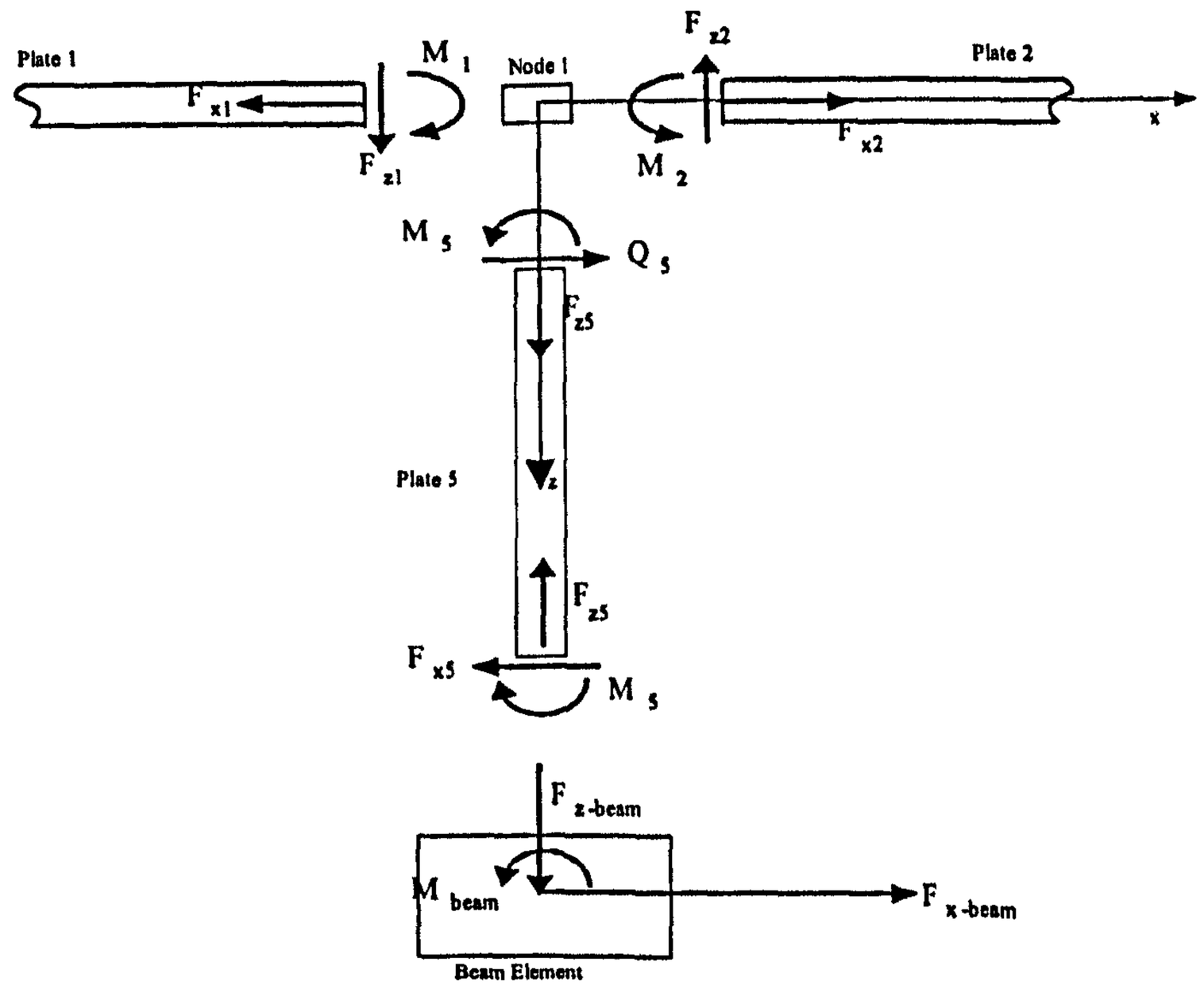

Figure 4.8 Free body diagram of plate-beam joint

$$F_{x-beam} = -B_z \frac{\partial^4 \eta_5}{\partial z^4} - \omega^2 \rho_l \eta_5 \tag{4.80}$$

Where B_z is the bending stiffness about z-axis and ρ_l is the mass per unit length of the beam. For a rectangular beam element the bending stiffness B_z is given by,

$$B_z = \frac{E h_b d^3}{12} \tag{4.81}$$

The total resisting force in the z direction is given by $F_{z\text{-}beam}$.

$$F_{z-beam} = -B_z \frac{\partial^4 \xi_5}{\partial z^4} - \omega^2 \rho_l \xi_5 \tag{4.82}$$

where B_x is the bending stiffness about the x-axis and ρ_l is the mass per unit length of the beam. For a rectangular beam element the bending stiffness B_x is given by

$$B_x = \frac{E d\, h_b^3}{12} \tag{4.83}$$

The total force in the y-direction is due to the compression and tension forces of the beam and the acceleration force of the beam which is given by

$$F_{y-beam} = -EA \frac{\partial^2 \zeta_5}{\partial y^2} - \omega^2 \rho_l \zeta_5 \tag{4.83}$$

where A is the cross-sectional area of the beam and E is Young's modulus.

The bending moment, at the plate edge is opposed by the torsion characteristics of the beam. Cremer [66] has shown that the moment transferred from a plate to a beam will result in a torsion moment and rotational acceleration of the beam as shown.

$$M_{beam} = -G\frac{\partial^2 \phi_5}{\partial y^2} - \omega^2 J \phi_5 \qquad (4.84)$$

Where J is the torsional stiffness of the beam element and G is the shear modulus of elasticity of the beam material. For a rectangular beam element the torsional stiffness is calculated from the following

$$J = \frac{E h_b d^3}{3} \quad if \quad h_b > d \text{ or } J = \frac{E d h_b^3}{3} \quad if \quad d > h_b \qquad (4.85)$$

Combining equations *4.76* to *4.85* above with the appropriate equation for plates *1*, *2* and *5* allows the transmission coefficients for the plate-beam model to be determined.

4.3 Parametric Design Study.

In the previous section a model was developed for the prediction of wave transmission coefficients in ship hull frame joints. In this section the wave transmission characteristics of hull frame joints are investigated in a numerical parametric study to identify what are the important features (if any) of joint design that determine the characteristics of the power transmitted across the joint.

In this parametric study two of the stiffener designs shown in figure 4.1 were selected for detailed analysis. The first joint (Type 1) is the flat bar stiffener which is the simplest of the possible hull frame variations since it consists of only three plates. Analysing the three-plate model first allows the effect of the web plate on the transmission characteristics to be isolated. The second joint to be analysed (Type 2) is the full five plate hull frame stiffener which will allow the effects of the flange plate and web plate on the overall transmission characteristics to be identified.

The parametric study has focused solely on variations in the stiffener geometric parameters. In all of the parametric models, the hull plate elements were chosen to have a constant thickness of 6 mm. The material chosen for the analysis models was plain

carbon steel as this is the most commonly used material in ship construction. The use of composite materials is considered to be outside the scope of this work.

The results of the parametric study present the variation in the joint transmission loss with frequency. The relation between the transmission loss R_{ij} and the transmission coefficient τ_{ij} is given by equation *4.86*.

$$R_{ij} = 10 log_{10}\left(\frac{1}{\tau_{ij}}\right) \tag{4.86}$$

The analysis of each joint has been performed with a full bending, longitudinal and transverse wave model, with the results presented for an incident bending wave source. The transmission loss has been calculated from 60 Hz to 7000 Hz at 20 Hz intervals as this provides a reasonable balance between accuracy and frequency range.

4.3.1 Web Plate Parametric Model

The parametric modelling has considered the effect the variation in the depth and thickness of the web plate on the transmission characteristics. The analysis results presented are for stiffeners of depth 200 mm and 800 mm and thickness of 4 mm and 8 mm as these are typical of the dimensions of stiffeners commonly found in ship construction. The hull plates 1 and 2 for all joints analysed are 6 mm thick steel plate.

The bending, longitudinal and transverse wave transmission loss curves are plotted in figure 4.9 for a 200 mm by 4mm web plate. It can be seen that the bending wave transmission loss curve consists of a series of shallow, broadening curves interspersed with a series of sharp peaks. As the frequency increases, the shallow curves lengthen and flatten while the amplitude of the sharp peaks increase. Examining the longitudinal and transverse wave transmission loss curves it can be seen that they are broadly similar in shape and frequency content. At low frequencies the transmission loss curves are sharp and pronounced, but as the frequency increases the peak-to-peak amplitude reduces and the curves broaden out. At higher frequencies it can be seen that there appear to be 'ripples' in the transmission loss curves.

The relationship between the bending, longitudinal and transverse wave TL curves can be explained by considering the web plate to be equivalent to a cantilevered beam. For a cantilever beam the first five resonant frequencies can be calculated from equation *4.87* [Ref. 95].

$$f_i = a_i \sqrt{\frac{B}{m'}} \frac{1}{l^2} \tag{4.87}$$

for $i = 1,2,3,4,5$ then $a_i = 0.56,\ 3.50,\ 9.82,\ 19.25,\ 31.83$. Where l is the web depth, B is the stiffness of the web plate and m' is the mass per unit area. The fundamental frequency of a cantilever is also given by Cremer [66].

The first five resonant frequencies calculated by assuming that the web plate behaves as a cantilever are predicted to occur at 86 Hz, 543 Hz, 1523 Hz, 2985 Hz, and 4938 Hz. In the bending wave transmission loss curve, there are five sharp peaks which agree well with the predicted bending frequencies of the web plate. The frequencies at which the peaks in the bending wave TL occur are not modes of the web plate since it is infinitely long in the y direction, rather the peaks are at frequencies where matching of the bending wavenumbers of plates 1 and 2 and the web plate occurs. This matching of bending wavenumbers results in an increase in the impedance mismatch due to the web plate at the joint and increases the transmission loss. The increase in the amplitude of the peak at the wave matching frequencies is due to the increase in the number of incident waves where wavenumber matching occurs resulting in the larger transmission loss.

In the longitudinal and transverse wave transmission loss curves it can be seen that the local minimum values in the transmission loss curve occur at approximately the resonant frequencies of the web plate. When the matching of the bending wavelength of the web and plates 1 and 2 occurs, the eccentricity of the web plate from plates *1* and *2* results in longitudinal and transverse waves being excited on hull plates *1* and *2*. The maximum peaks in the longitudinal and transverse wave transmission loss curves occur at the following frequencies; 240 Hz, 960 Hz, 2180 Hz, 3820 Hz and 6660 Hz which are

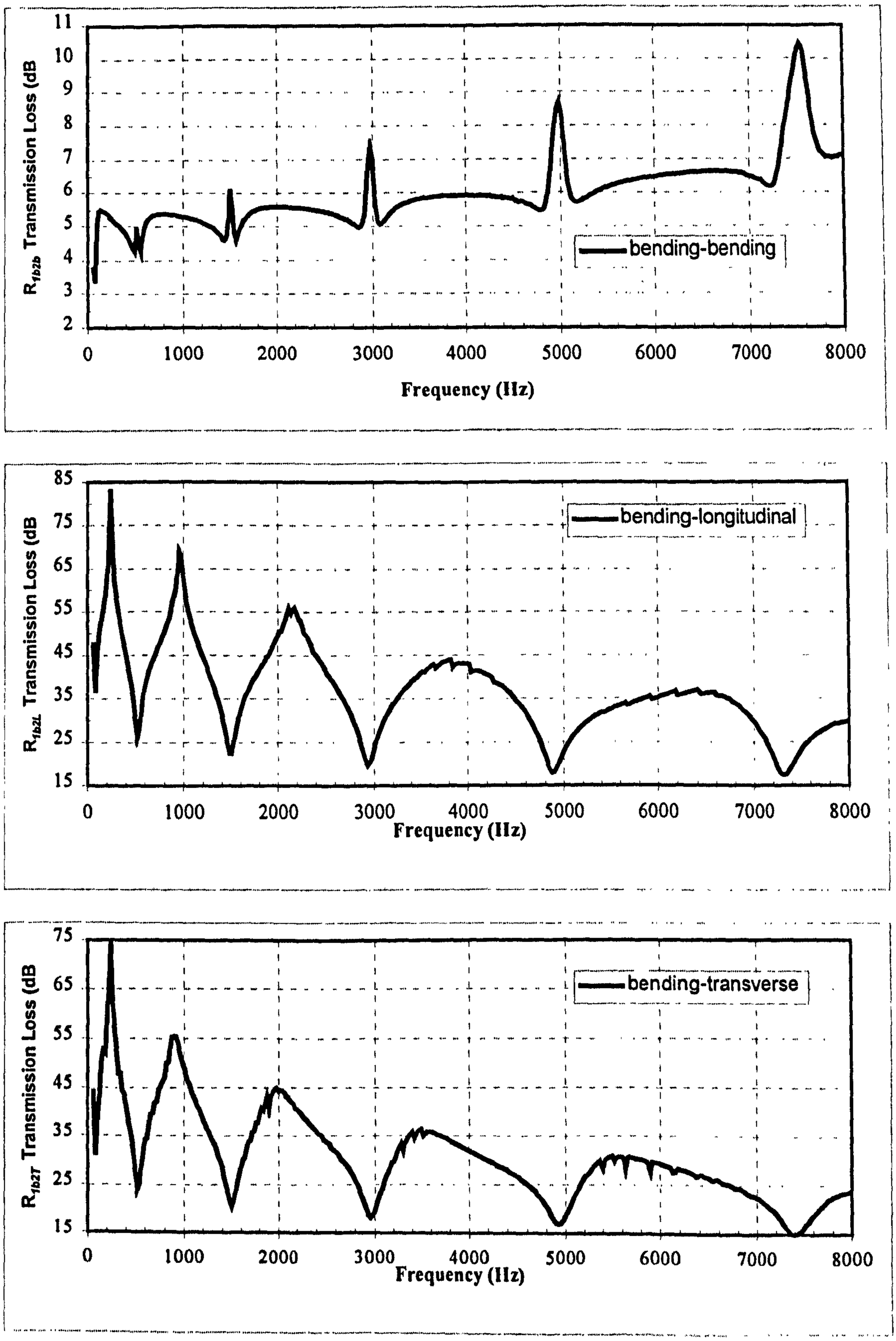

Figure 4.9 BLT Transmission loss curves for 4 mm x 200 mm web plate

frequencies where the wavelength is a multiple of half the web depth and does not excite in-plane waves.

With a 200 mm by 8 mm thick web plate a similar set of transmission curves is obtained as shown in figure 4.10. The bending wave transmission loss curve again consists of a series of curves that broaden and flatten as the frequency increases interspersed with four peaks that sharpen and increase in amplitude as the frequency increases. Treating the 8 mm by 200 mm web plate as a cantilever, the first four frequencies are predicted with equation 4.87 to occur at 173 Hz, 1086 Hz, 3046 Hz and 5975 Hz. The frequencies at which the peaks in the transmission loss curve occur are lower than the predicted frequencies and it is because the prediction using equation *4.87* is based on the assumption of a rigid boundary. The junction of plates 1, 2 and 5 is flexible and this reduces the wave matching frequencies. The difference is more obvious with the 8 mm thick web because of the increased bending stiffness of the web plate which is greater than that of plates 1 and 2.

The longitudinal and transverse wave transmission loss curves are again very similar in shape and frequency content, initially having sharp peaks that reduce in amplitude and broaden as the frequency increases. As with the 4 mm by 200 mm web the local minimum values in the transmission loss curve occur at approximately the same frequencies as the peaks in the bending wave transmission loss curve. This is for the reasons discussed previously.

One aspect that is clear is that the longitudinal and transverse wave transmission loss curves show large variations in the magnitudes with frequency. For SEA models it may therefore be prudent to average the transmission loss for a number of frequencies in each third octave frequency band rather than rely on the transmission loss calculated at the centre frequency of the band.

The bending, longitudinal and transverse transmission loss curves are shown in figure 4.11 for a 4 mm by 800 mm web plate. The bending wave curve transmission loss curve initially appears complex as there are a series of closely spaced 'damped' peaks with the

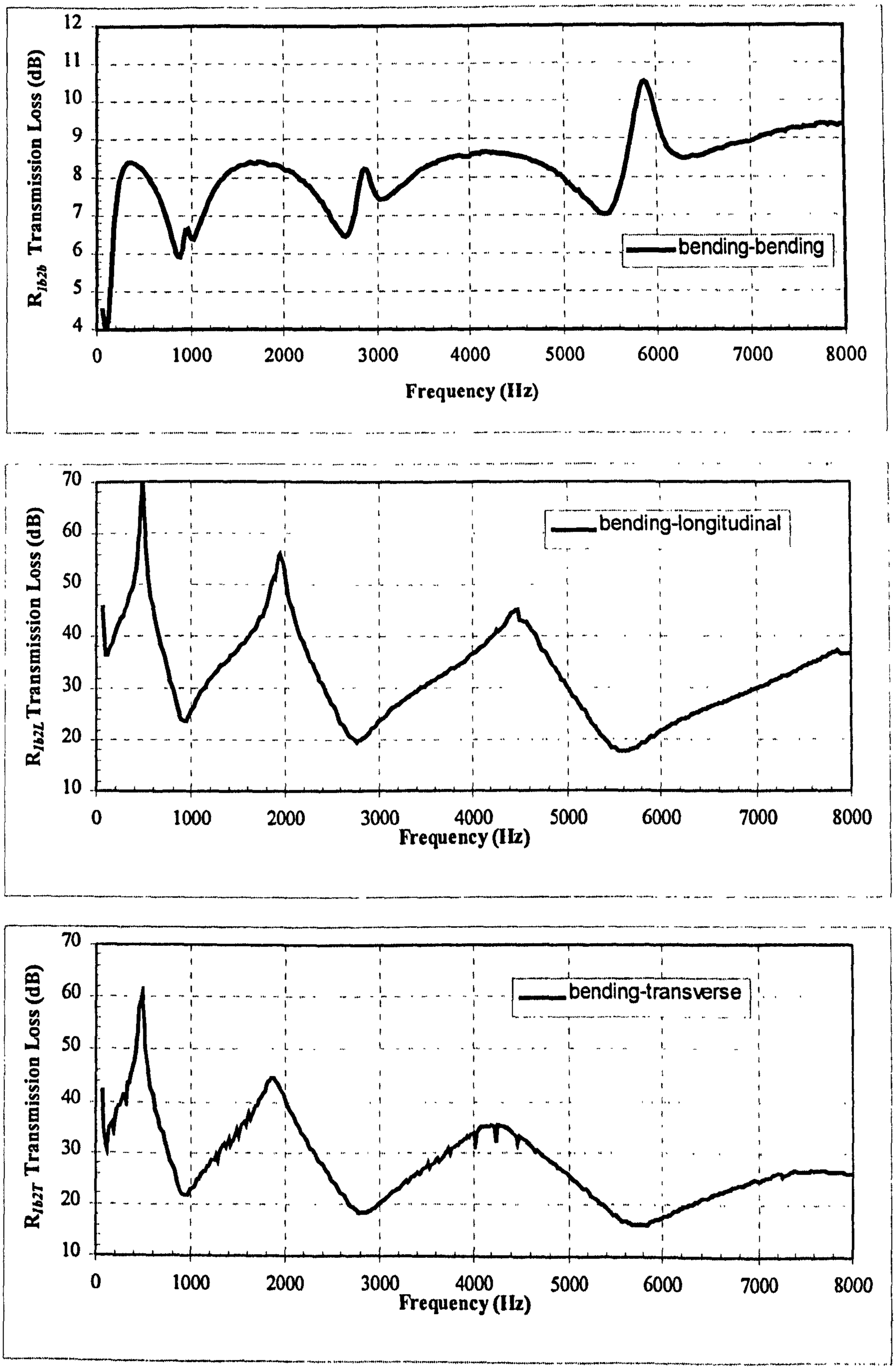

Figure 4.10 BLT Transmission loss curves for 8 mm x 200 mm web plate

transmission loss generally increasing until approximately 2800 Hz. Between 2800 Hz and 3000 Hz there is a transition in the transmission loss curve after which the curve is dominated by a series of sharp peaks.

For the longitudinal and transverse wave curves it can be seen that they are again very similar in shape and frequency content. The curves have a series of sharp peaks and as the frequency increases the peak-to-peak amplitude reduces and the curves broaden out. At approximately 2800 Hz both curves level off and the peak-to-peak amplitude remains constant at approximately 20 dB for the longitudinal wave curve and 10 dB for the transverse wave curve.

From the previous analysis of the 200 mm web results, the minimum value in the longitudinal and transverse transmission loss coincided approximately with the resonant frequencies of the web. Equation *4.87* gives the first five frequencies but for the higher frequencies, the bending wavenumbers match can be predicted from the equation *4.88* which is derived from equations *4.1* and *4.3*.

$$f_n = \frac{\pi}{8}\sqrt{\frac{B}{m'}}\frac{(2n-1)}{l^2} \quad \text{for } n = 1,2,3,4,5 \text{ etc} \tag{4.88}$$

For the fundamental frequency this equation is not particularly accurate when compared with equation *4.87*, but at higher frequencies the above equation is sufficiently accurate for the purpose of explaining the transmission loss curves. Tables 4.1 and 4.2 compare the predicted resonant frequencies from equations *4.87* and *4.88* for the web plate considered in this section.

Comparing the predicted frequencies for the 800 mm web with the frequencies at which the local minimum values of the longitudinal and transverse transmission loss curves occur it can be seen that there is good agreement. On the deeper web plates the matching of bending waves on plate 1,2 and the web results in the generation of in-plane waves as discussed previously. The major difference between the 200 mm and 800 mm web

	Web Plate Dimensions (Depth x Thickness)			
	200 x 4	**200 x 8**	**800 x 4**	**800 x 8**
ρ_s (kg/m^2)	*1201.5*	*9611.7*	*1201.5*	*9611.7*
B (N/m^2)	*31.2*	*62.4*	*31.2*	*62.4*
f_1 (Hz)	*86.9*	*173.8*	*5.4*	*10.9*
f_2 (Hz)	*543.1*	*1086.3*	*33.9*	*67.9*
f_3 (Hz)	*1523.3*	*3046.6*	*95.2*	*190.4*
f_4 (Hz)	*2987.6*	*5975.3*	*186.7*	*373.5*
f_5 (Hz)	*4938.2*	*9876.4*	*308.6*	*617.5*

Table 4.1 Predicted frequencies using equation *4.87* : web plate as a cantilever

	Web Plate Dimensions (Depth x Thickness)			
	200 x 4	**200 x 8**	**800 x 4**	**800 x 8**
ρ_s (kg/m^2)	*1201.5*	*9611.7*	*1201.5*	*9611.7*
B (N/m^2)	*31.2*	*62.4*	*31.2*	*62.4*
f_1 (Hz)	*60.9*	*121.8*	*3.8*	*7.6*
f_2 (Hz)	*548.3*	*1096.6*	*34.3*	*68.5*
f_3 (Hz)	*1523.1*	*3046.1*	*95.2*	*190.4*
f_4 (Hz)	*2985.2*	*5970.4*	*186.6*	*373.2*
f_5 (Hz)	*4934.7*		*308.4*	*616.8*
f_6 (Hz)	*7371.6*		*460.7*	*921.5*
f_7 (Hz)	*10295.9*		*643.5*	*1287.0*
f_8 (Hz)			*856.7*	*1713.4*
f_9 (Hz)			*1100.4*	*2200.8*
f_{10} (Hz)			*1374.6*	*2749.1*
f_{11} (Hz)			*1679.2*	*3358.4*
f_{12} (Hz)			*2014.3*	*4028.5*
f_{13} (Hz)			*2379.8*	*4759.6*
f_{14} (Hz)			*2775.8*	*5551.6*
f_{15} (Hz)			*3202.2*	*6404.5*
f_{16} (Hz)			*3659.2*	*7318.3*
f_{17} (Hz)			*4146.5*	*8293.1*
f_{18} (Hz)			*4664.4*	*9328.8*
f_{19} (Hz)			*5212.7*	*10425.2*
f_{20} (Hz)			*5791.5*	
f_{21} (Hz)			*6400.7*	
f_{22} (Hz)			*7040.4*	
f_{23} (Hz)			*7710.5*	
f_{24} (Hz)			*8411.5*	
f_{25} (Hz)			*9142.5*	

Table 4.2 Predicted frequencies using equation *4.88* : web plate as a cantilever

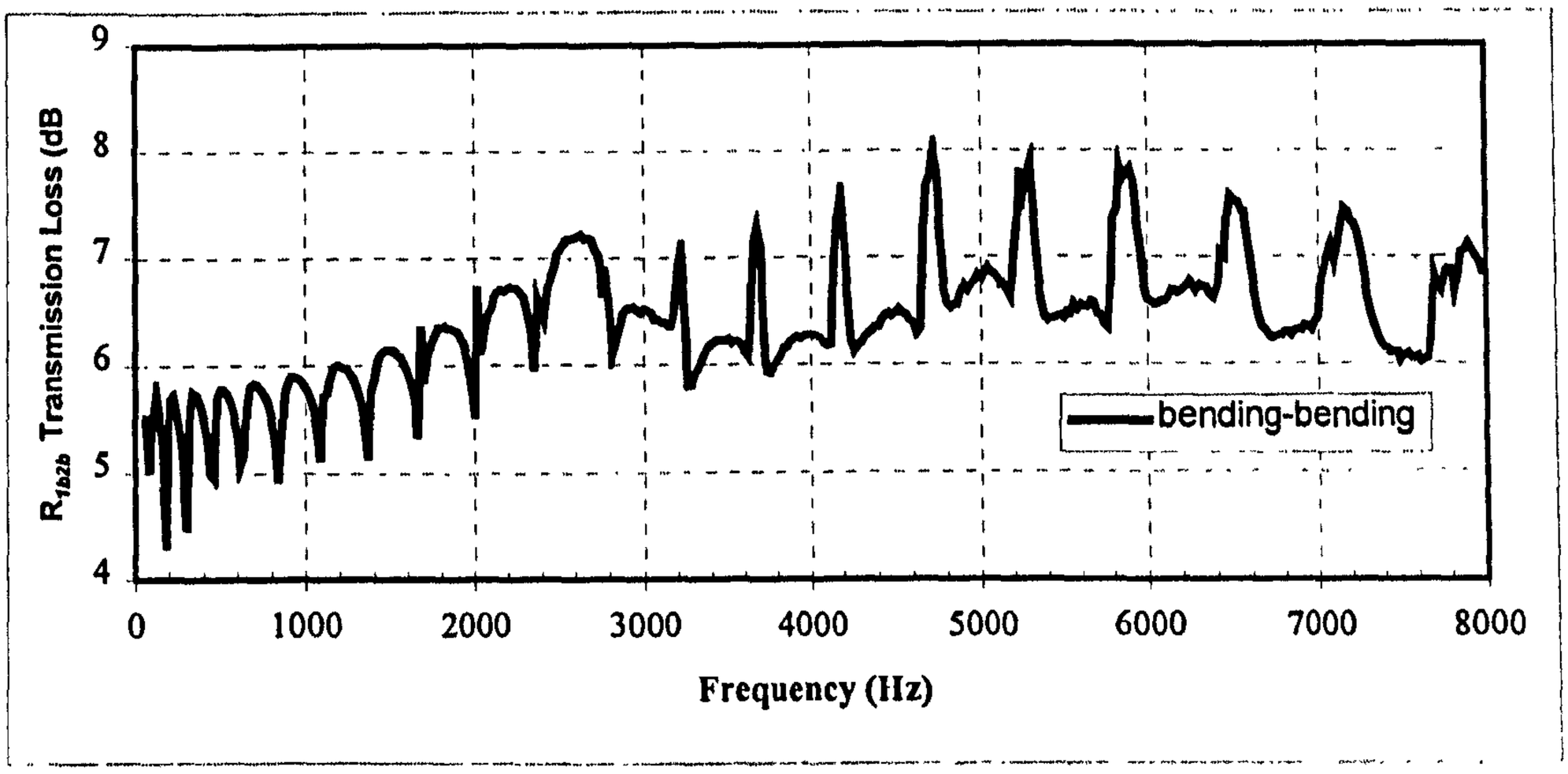

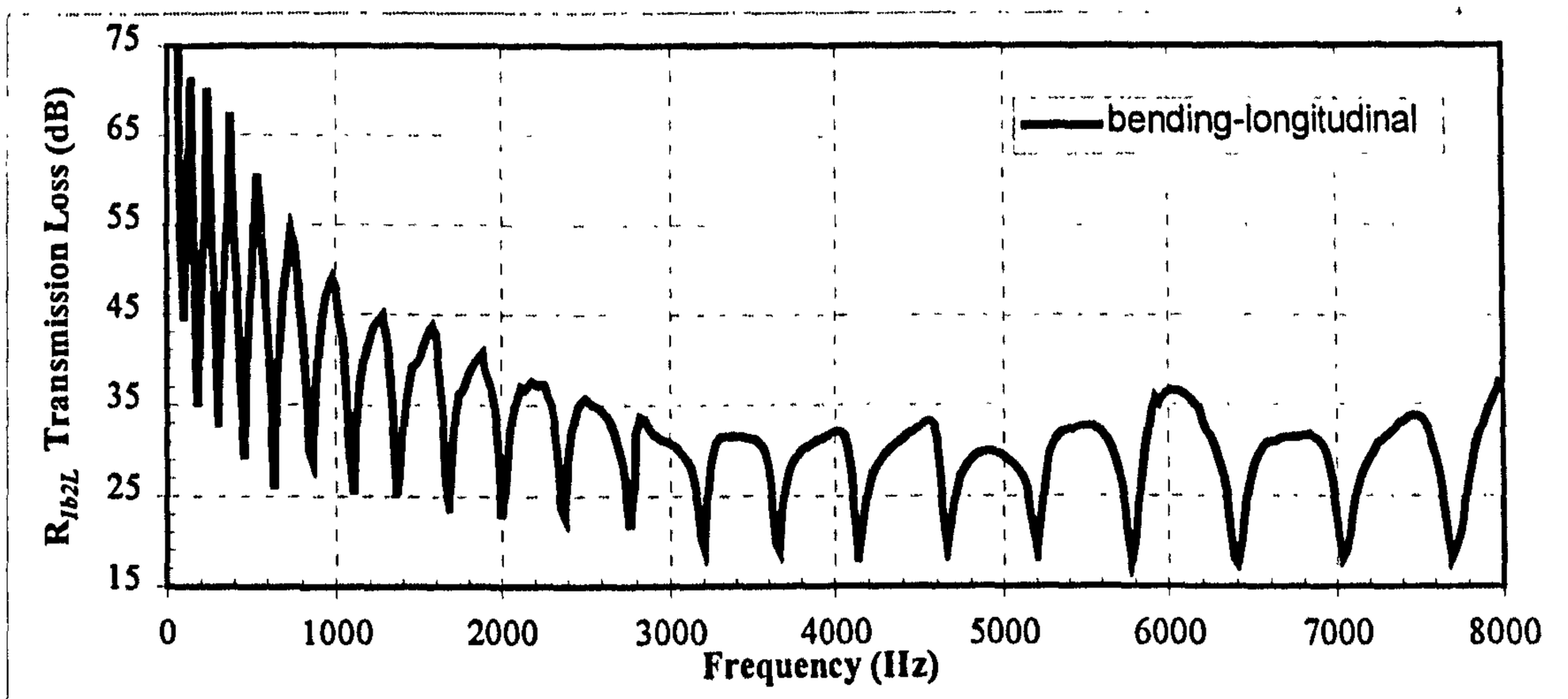

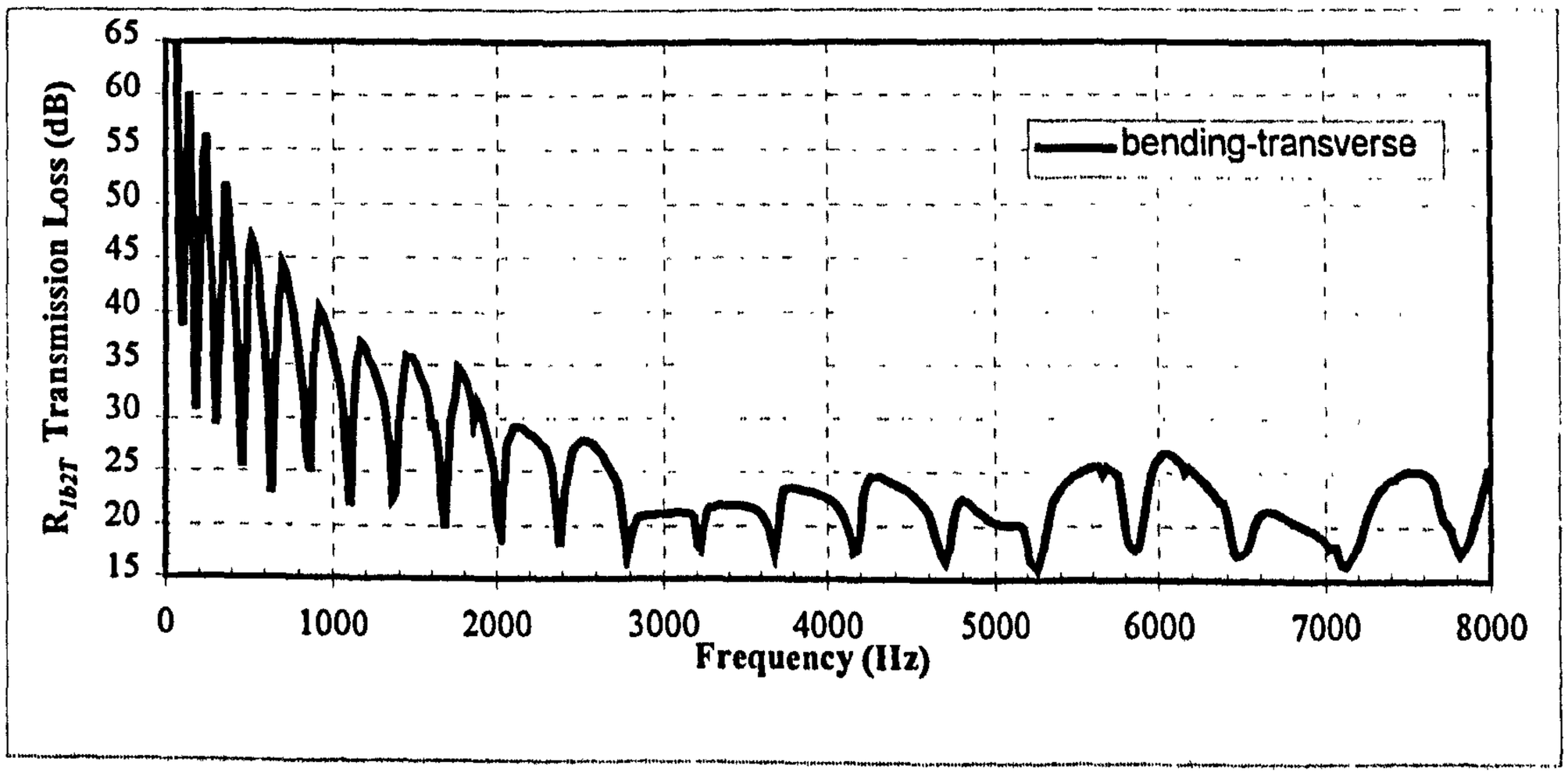

Figure 4.11 BLT Transmission loss curves for 4 mm x 800 mm web plate

results is the levelling off of the longitudinal and transverse transmission loss curves above 2800 Hz.

From the bending wave transmission loss curve it can be seen that there is a transition in the transmission loss curve at approximately 2800 Hz. Below this transition frequency there are a series of curves where the minimum transmission loss occurs at the frequencies of the web. At 1600 Hz, 2020 Hz, 2380 Hz and 2780 Hz it can be seen that there are sharp peaks that increase in amplitude and bandwidth as the frequency increases above 2800 Hz become dominant. These peaks are very close to the 11^{th}, 12^{th}, 13^{th} and 14^{th} frequencies of the web plate as listed in table 4.2. The peaks due to the first ten frequencies are present but are not obvious for two reasons.

The first reason is that the 20 Hz frequency resolution is insufficient on the deeper web plate to show the detail at low frequency. A more detailed analysis was undertaken around one of the lower wave matching frequencies with a 0.5 Hz interval which confirmed a narrow bandwidth peak in the bending wave transmission loss. The second reason is that at the lower frequencies there are fewer incident waves where the trace wavelength matches the web wavelength occurs. When the transmission coefficient is integrated over all angles of incidence the effect on the transmission loss is diminished. As the frequency increases, the number of incident waves where the trace wavelength matches the wavelength of the web increase and when the average transmission coefficient is calculated it reflects the increase in the impedance mismatch of the joint.

The transition above 2800 Hz is due partially to the development of in-plane wave of the web. The first transverse wave is predicted to occur at 2211 Hz and the first longitudinal wave is predicted to occur at 3359 Hz. The excitation of in-plane waves in the web plate results in a significant change in the joint dynamics The in-plane waves are reflected from the web-plate boundary, and the in-plane waves excite bending waves on plates 1 and 2 modifying the transmission loss curve. The sharp peaks that are seen in the bending wave transmission loss curve above 2800 Hz are due to the matching of the incident wave and the web-plate bending waves discussed previously. At the higher

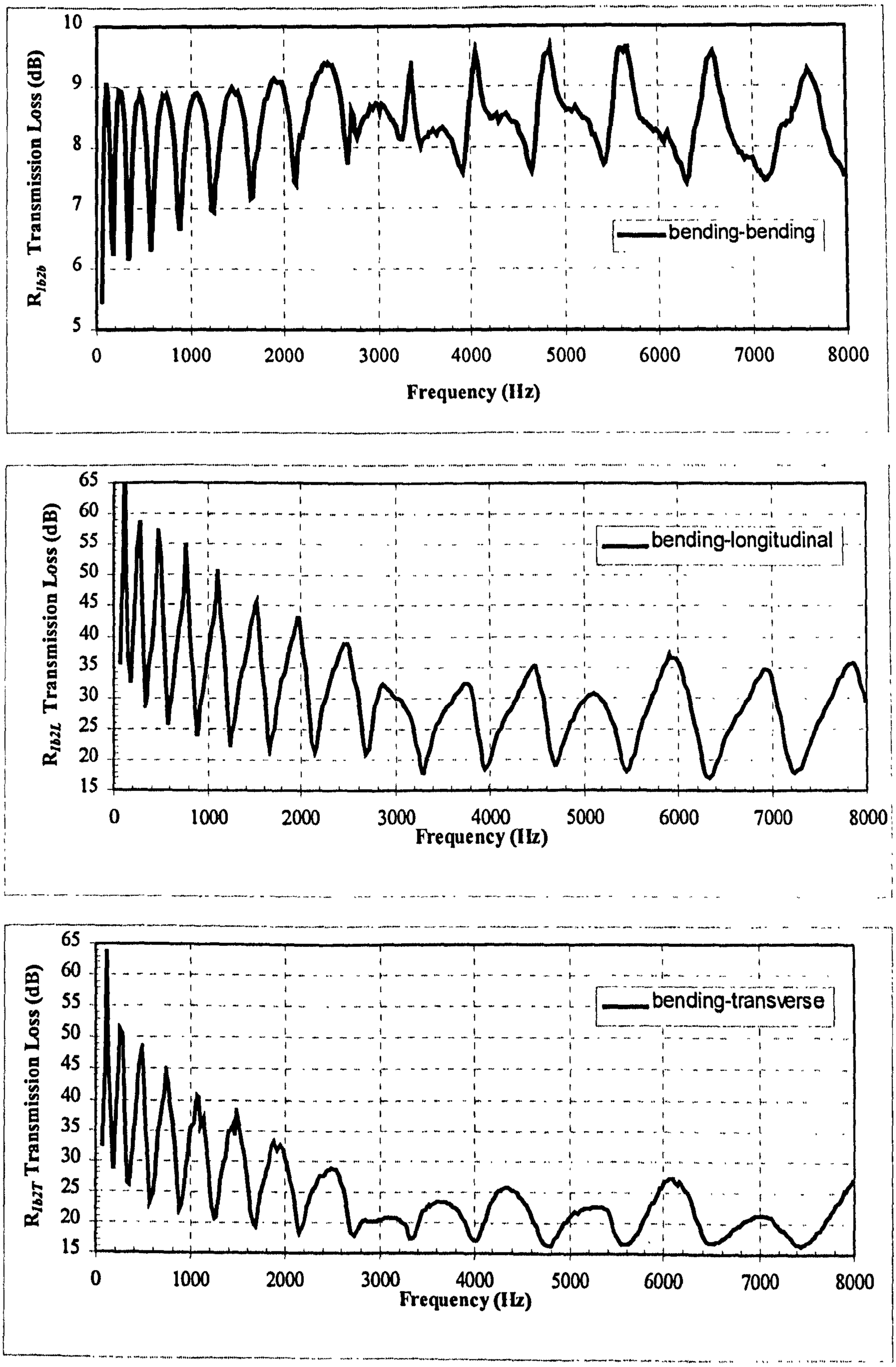

Figure 4.12 BLT Transmission loss curves for 8 mm x 800 mm web plate

frequencies there are many more incident waves which match and this becomes a dominant feature of the transmission loss curve. This results in the longitudinal and transverse transmission loss curves levelling off.

The transmission loss curves for a 8 mm x 800 mm web plate are shown in figure 4.12 and it can be seen that these are very similar to the 4 mm x 800 mm web transmission loss curves shown in figure 4.11. There are fewer peaks in the 8 mm curves due to the lower number of resonant modes of the web-plate. The transition in the bending wave transmission loss curve again occurs at approximately 2800 Hz and the longitudinal and transverse curves level off at this frequency. The transition frequency at 2800 Hz is unchanged since the in-plane longitudinal and transverse waves of the web plate are independent of the web thickness and determined by the depth of the web plate and the boundary conditions. As with the 200 mm x 8 mm thick web plate the flexibility of the junction of plates 1, 2 and 5 reduces the wave-matching frequencies of the web-plate when compared to the predicted frequencies in tables 4.1 and 4.2.

4.3.2 Hull-Frame Plate Parametric Model

In the previous section the parametric model of the web plate identified how the wave transmission characteristics changed as a function of the web depth and thickness. In this section the effect of the flanges on the transmission characteristics is investigated. The results are presented for 200 mm and 800 mm deep web plates with 4 mm and 8 mm thick webs The parametric models utilised the same thickness of flange plates on all models but with different widths combined with the different web depths and thickness. This is a limited number of variations but with five plates there are a large number of possible combinations that could be considered. The two flange lengths considered are 100 mm, which is typical of the dimensions encountered in practise, and 500 mm which is more extreme but will allow the effect of flange length to be determined. The transmission loss curves are analysed and compared with the results presented in the previous section.

Figure 4.13 show the bending, longitudinal and transverse transmission loss curves for a 4 mm by 200 mm deep web for 100 mm wide flange plates. Comparing these results with the transmission loss curves in figure 4.9 for the 200 mm by 4 mm web plate the results initially appear to be quite different and more complex. This is because the addition of the flange plates changes the web plate boundary condition and it can no longer be equated to a cantilever, instead it can be considered as equivalent to a pinned-pinned beam or a clamped-clamped beam. Equation *4.87* is still valid to predict the first five frequencies except the variable a_i changes. For the first five frequencies of a pinned-pinned beam a_i is 1.57, 6.28, 14.15, 25.15, 39.3 and for a clamped-clamped beam a_i is 3.501, 9.82, 19.26, 31.83, 47.46. Table 4.3 gives the predicted frequencies for the clamped-clamped boundary condition as it shows the best agreement.

From the web-plate analysis the first step was to identify the wave matching frequencies of the web plate and this is best achieved by correlating examining the frequency peaks in the bending wave transmission loss curve and the corresponding local minimum in the longitudinal and transverse transmission loss curves.

For the longitudinal and transverse waves it can be seen that they are similar in shape and frequency content when compared to the corresponding curves in figure 4.9 they are very different. The regular smooth in-plane transmission loss curves obtained for the web plate only are replaced by complex irregular transmission loss curves because of the change in the boundary conditions. The local minimum values in the transmission loss curves occur at the wave matching frequencies of the web-plate listed in table 4.3. For the 200 mm by 4 mm web plate the first five wave matching frequencies are predicted to occur 548 Hz, 1523 Hz, 2985 Hz, 4933 Hz and 7371 Hz and the minimum values in the in-plane transmission loss curves occur at approximately these frequencies. It can also be seen that there are dips in the curves at 120 Hz and 3300 Hz. The dip at 3300 Hz correlates to the first in-plane mode in the web plate predicted to occur at 3360 Hz. It is more difficult to find any correlation for the dip at 120 Hz and at this low frequency must be equivalent to a rigid body mode of the frame which because of it's eccentricity excites in-plane waves in plate 1 and 2.

	Web Plate Dimensions (Depth x Thickness)			
	200 x 4	**200 x 8**	**800 x 4**	**800 x 8**
ρ_s (kg/m^2)	*1201.5*	*9611.7*	*1201.5*	*9611.7*
B (N/m^2)	*31.2*	*62.4*	*31.2*	*62.4*
f_1 (Hz)	*543.1*	*1086.3*	*33.9*	*67.9*
f_2 (Hz)	*1523.3*	*3046.6*	*95.2*	*190.4*
f_3 (Hz)	*2987.6*	*5975.3*	*186.7*	*373.5*
f_4 (Hz)	*4938.2*	*9876.4*	*308.6*	*617.5*
f_5 (Hz)	*7362.9*	-	*460.2*	*920.4*

Table 4.3 Predicted frequencies using equation *4.87*:

web plate as a clamped-clamped beam

	Flange Plate Dimensions (Depth x Thickness)	
	100 x 8	**500 x 8**
ρ_s (kg/m^2)	*1201.5*	*9611.7*
B (N/m^2)	*31.4*	*62.4*
f_1 (Hz)	*695*	*27.8*
f_2 (Hz)	*4344*	*173.8*
f_3 (Hz)	*12175*	*487.0*
f_4 (Hz)		*955.7*
f_5 (Hz)		*1913.8*

Table 4.4 Predicted frequencies using equation *4.87*: flange plate as a cantilever

	Flange Plate Dimensions (Depth x Thickness)	
	100 x 8	**500 x 8**
ρ_s (kg/m^2)	*1201.5*	*9611.7*
B (N/m^2)	*31.2*	*62.4*
f_1 (Hz)	*60.9*	*19.5*
f_2 (Hz)	*487.4*	*175.5*
f_3 (Hz)	*4386.4*	*487.4*
f_4 (Hz)	*12184.5*	*955.3*
f_5 (Hz)		*1579.1*
f_6 (Hz)		*2358.9*
f_7 (Hz)		*3294.7*
f_8 (Hz)		*4386.4*
f_9 (Hz)		*5634.1*
f_{10} (Hz)		*7037.8*
f_{11} (Hz)		*8597.4*

Table 4.5 Predicted frequencies using equation *4.88* : flange plate as a cantilever

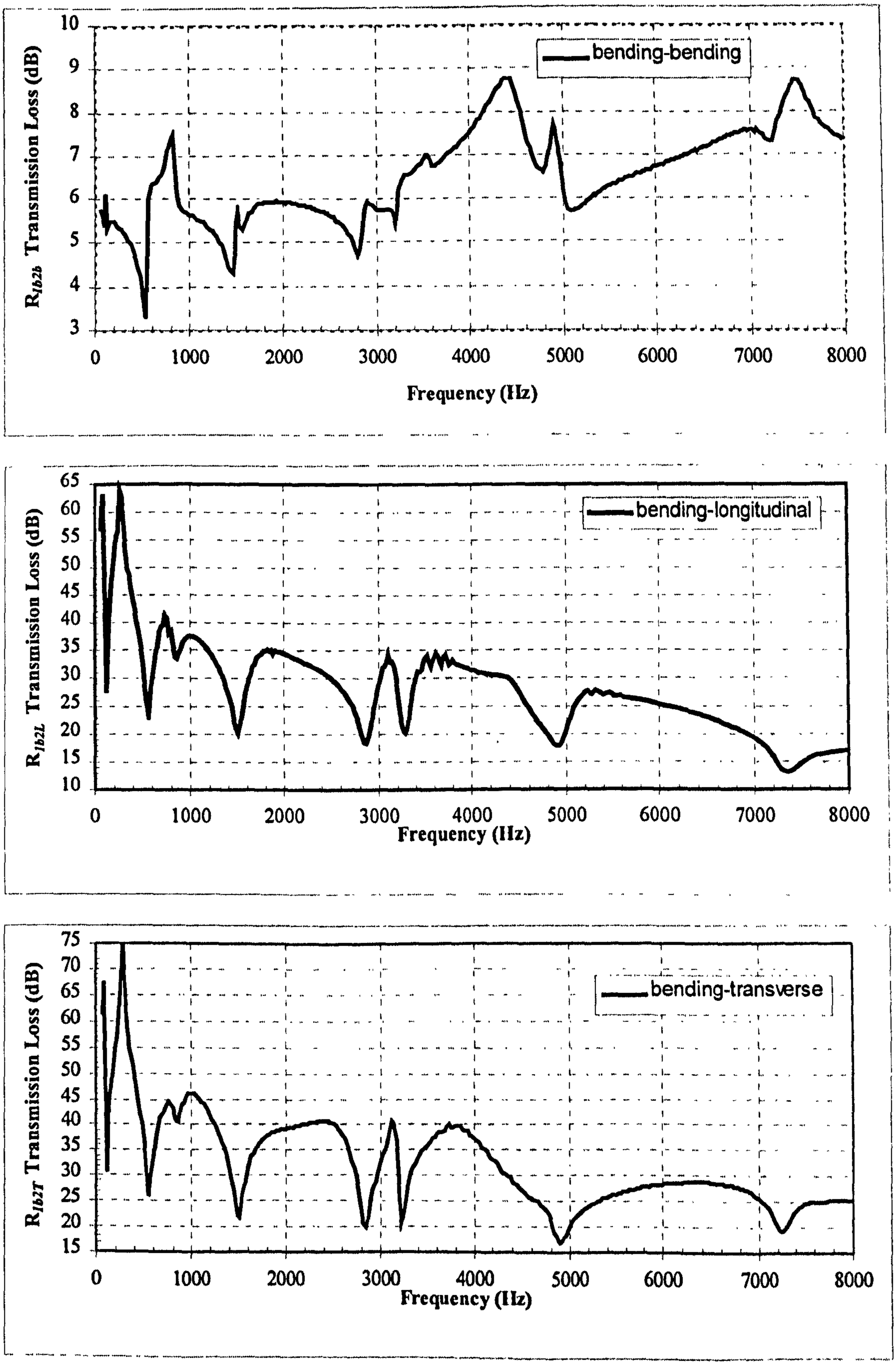

Figure 4.13 BLT Transmission loss curves for 200mm x 4 mm Web plate and 100 mm x 8 mm flange plates

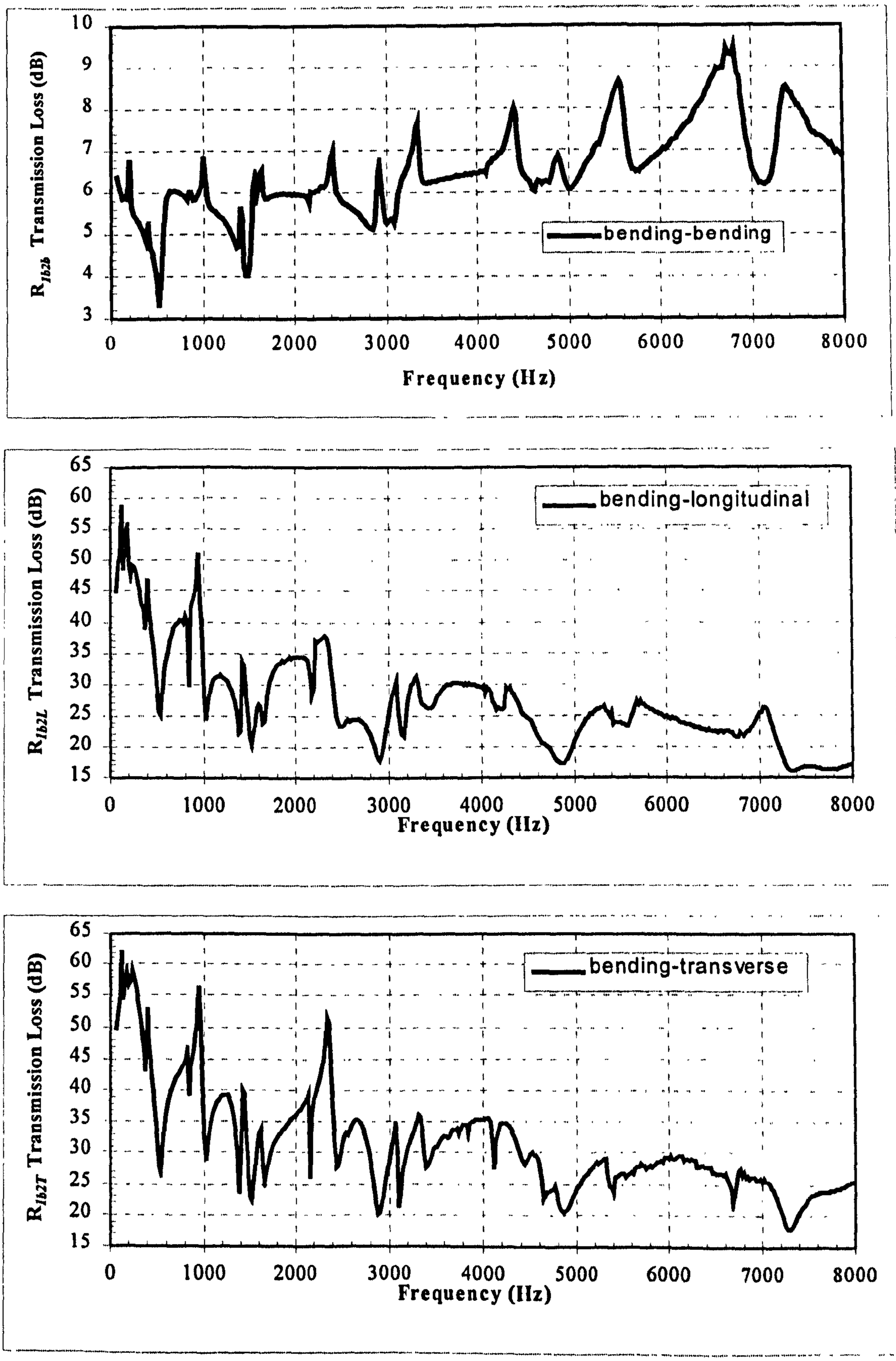

Figure 4.14 BLT Transmission loss curves for 200 mm x 4 mm Web plate and 500 mm x 8 mm flange plates

Assuming that the flange plates are cantilevers, the first two predicted resonant frequencies of the 100 mm flange plates using equation *4.87* occur at 695 Hz and 4344 Hz. It can be seen that the are two peaks in the bending wave transmission loss curve at 820 Hz and 4420 Hz and these are due to wave matching between the web plate and flange plates. The predicted wave matching frequency is based on the assumption of a rigid boundary condition between the flange and web plate hence the difference with the actual wave matching frequency.

Figure 4.14 show the bending, longitudinal and transverse transmission loss curves for a 4 mm by 200 mm deep web with 500 mm wide flange plates. Comparing the bending wave transmission loss curve for the 100 mm flange plates shown in figure 4.13 it can be seen that the general trend is similar but there are additional peaks. The wave matching frequencies of the web plate listed previously can be identified by their peaks in the bending wave transmission loss and the corresponding local minimum values in the in-plane transmission loss curves. The other peaks in the bending wave transmission loss are found to coincide with the predicted wave matching frequencies for the flange plates shown in tables 4.4 and 4.5. For example the 4^{th} mode of the flange plate is predicted to occur at 955 Hz and the 6^{th} mode is predicted to occur at 2359 Hz and corresponding peaks can be observed in the bending wave transmission loss curve near to these frequencies. The effect of the wider flange plates and change in boundary conditions on the in-plane transmission loss however is to change the transmission loss graphs because of the more complex wave interaction between the five plates .

In figure 4.15 the bending, longitudinal and transverse transmission loss curves are shown for a 200 mm by 8 mm web-plate for the 100 mm wide flange plates. Comparing the 100 mm flange plate results in figure 4.15 with the web only results in figure 4.8 it can be seen that there is a similarity in the trend between the curves but the flange plates change the transmission characteristics. In the longitudinal and transverse wave curves there are a series of dips in the transmission loss which correlate to the dips in the bending wave transmission loss curve. For the 200mm by 4 mm web plate results in figure 4.13 the peaks in the bending wave transmission loss correlate to the dips in the in-plane transmission loss graphs. As discussed in the web plate results the peaks are

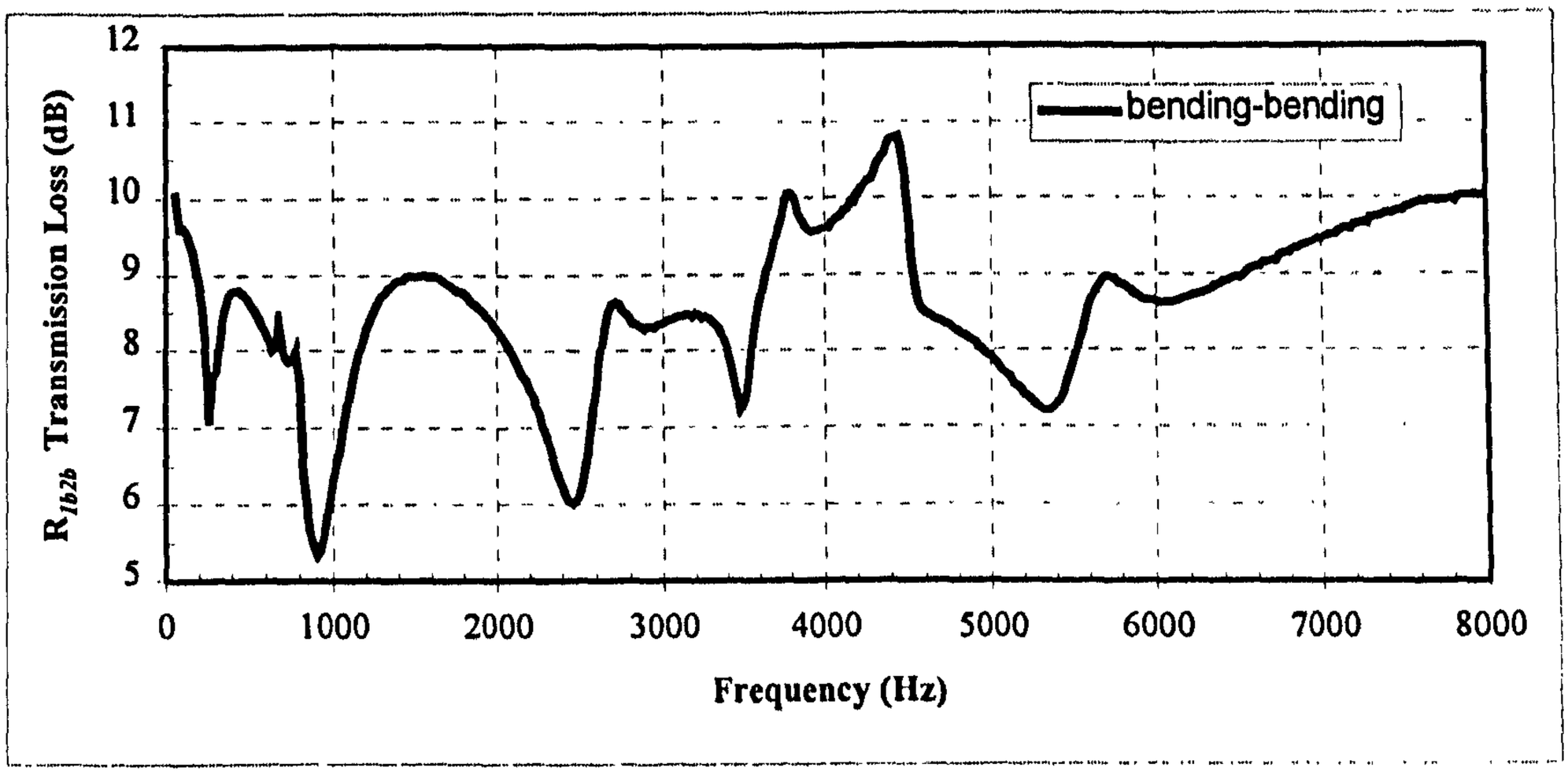

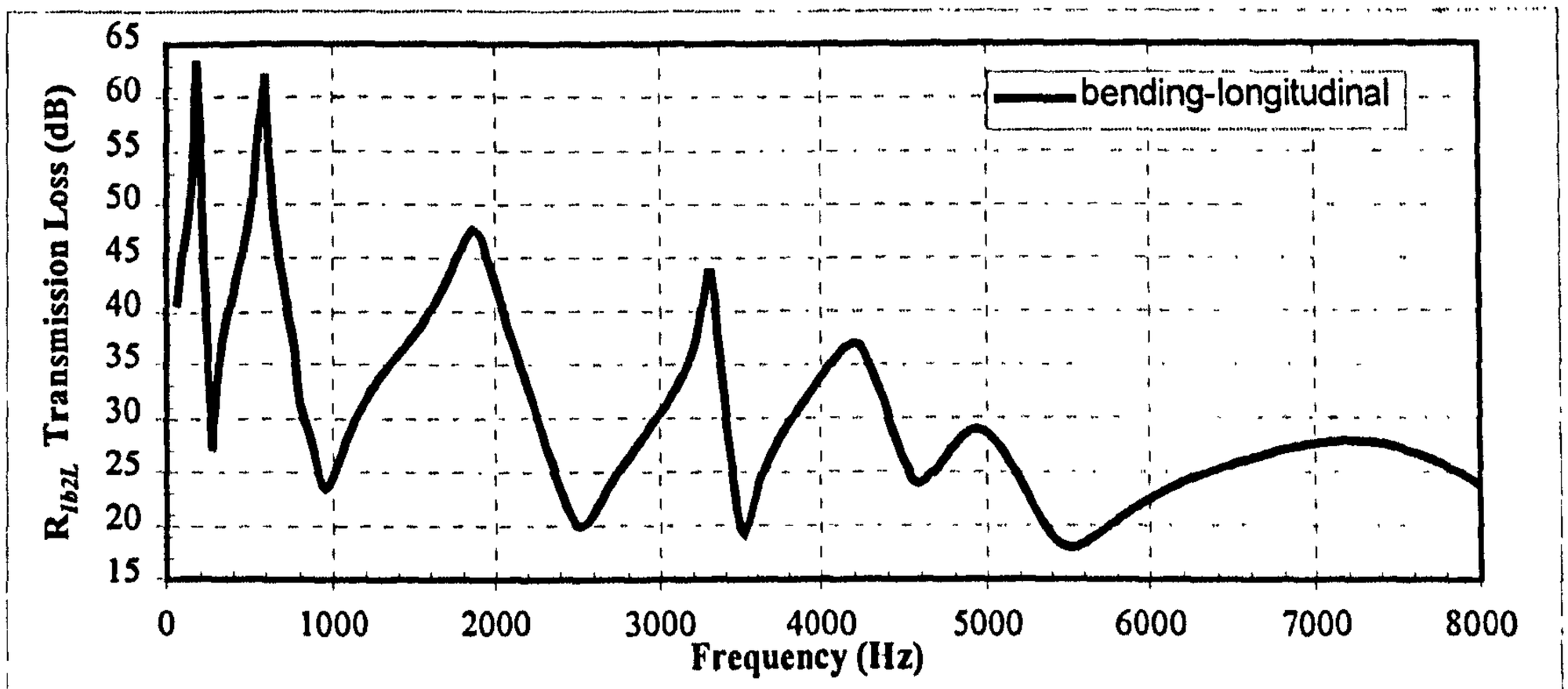

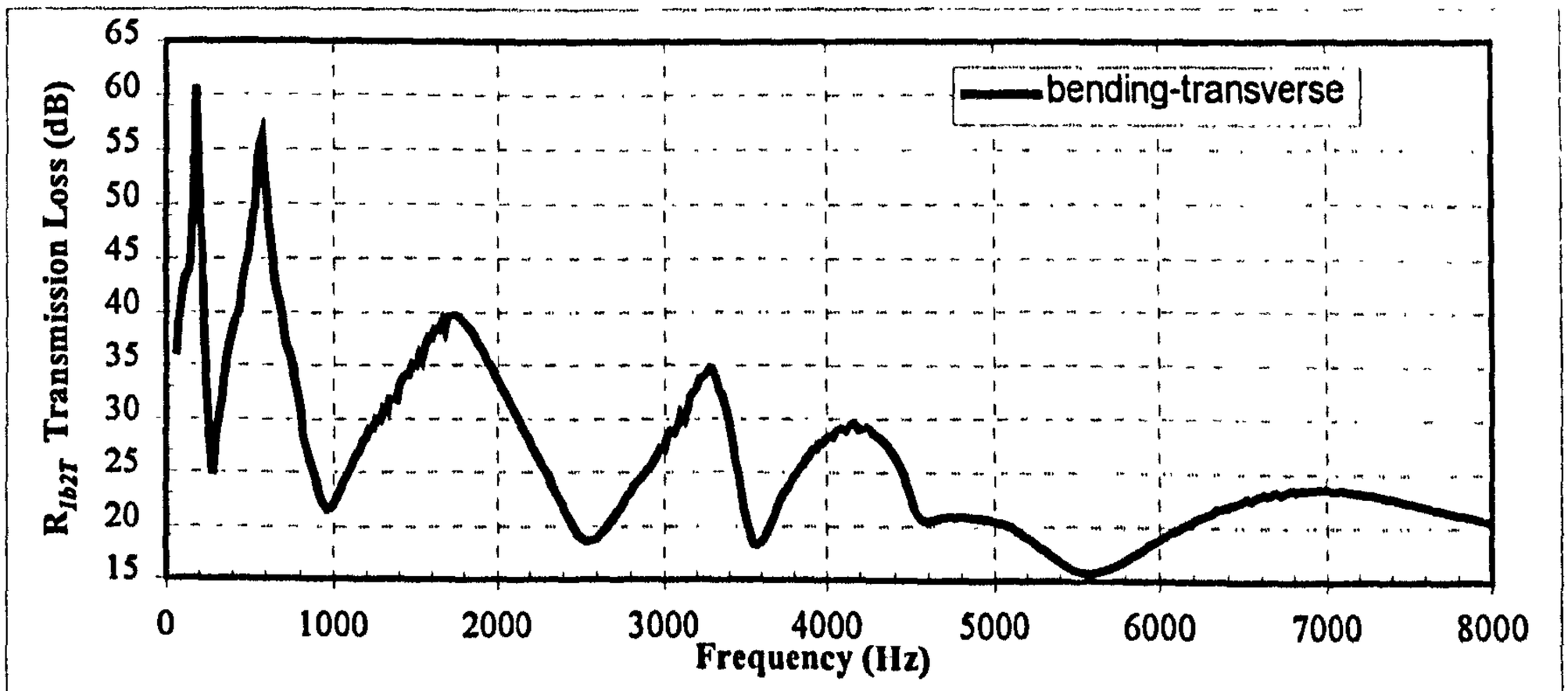

Figure 4.15 BLT Transmission loss curves for 200mm x 8 mm Web plate and 100 mm x 8 mm flange plates

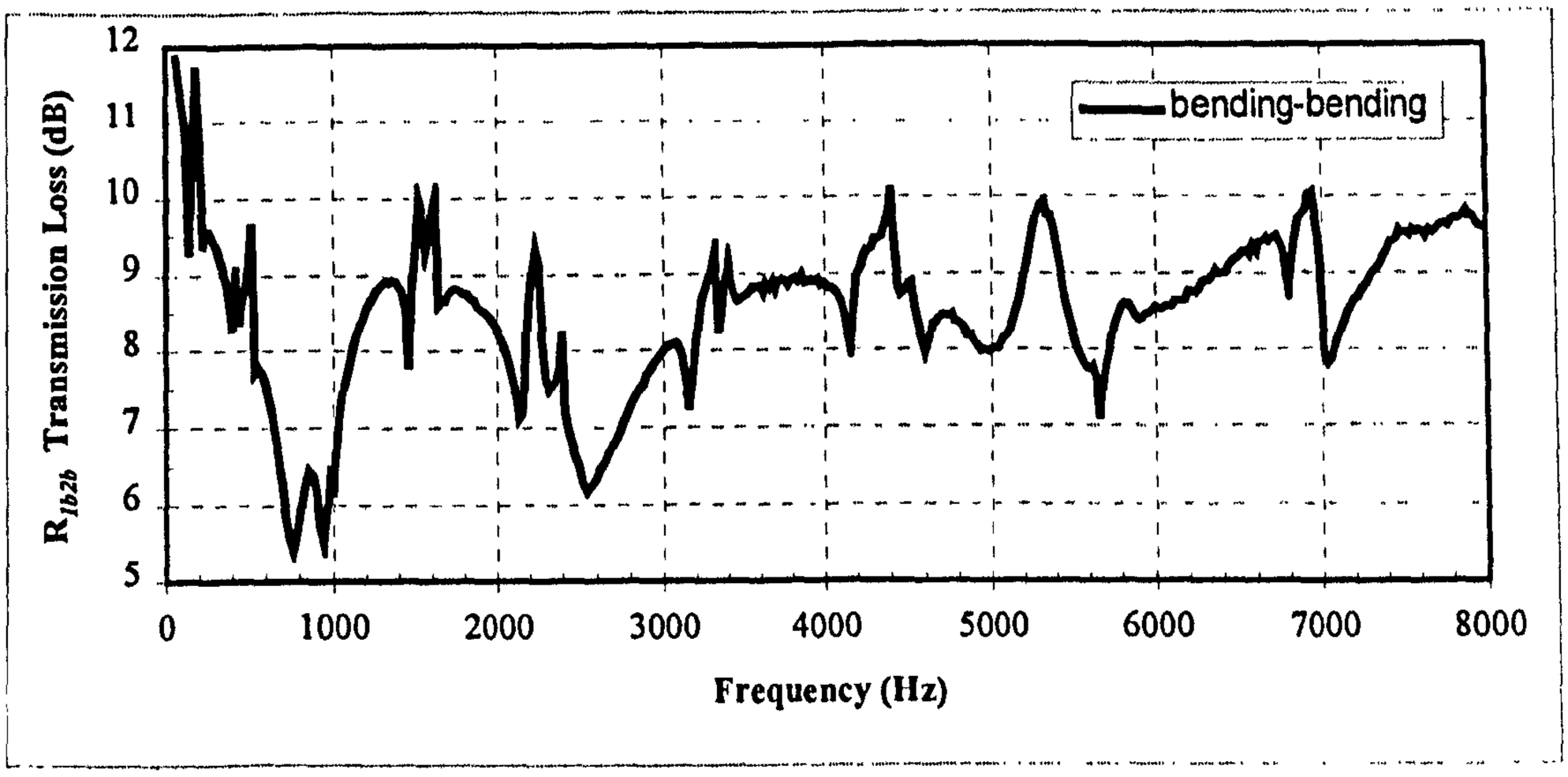

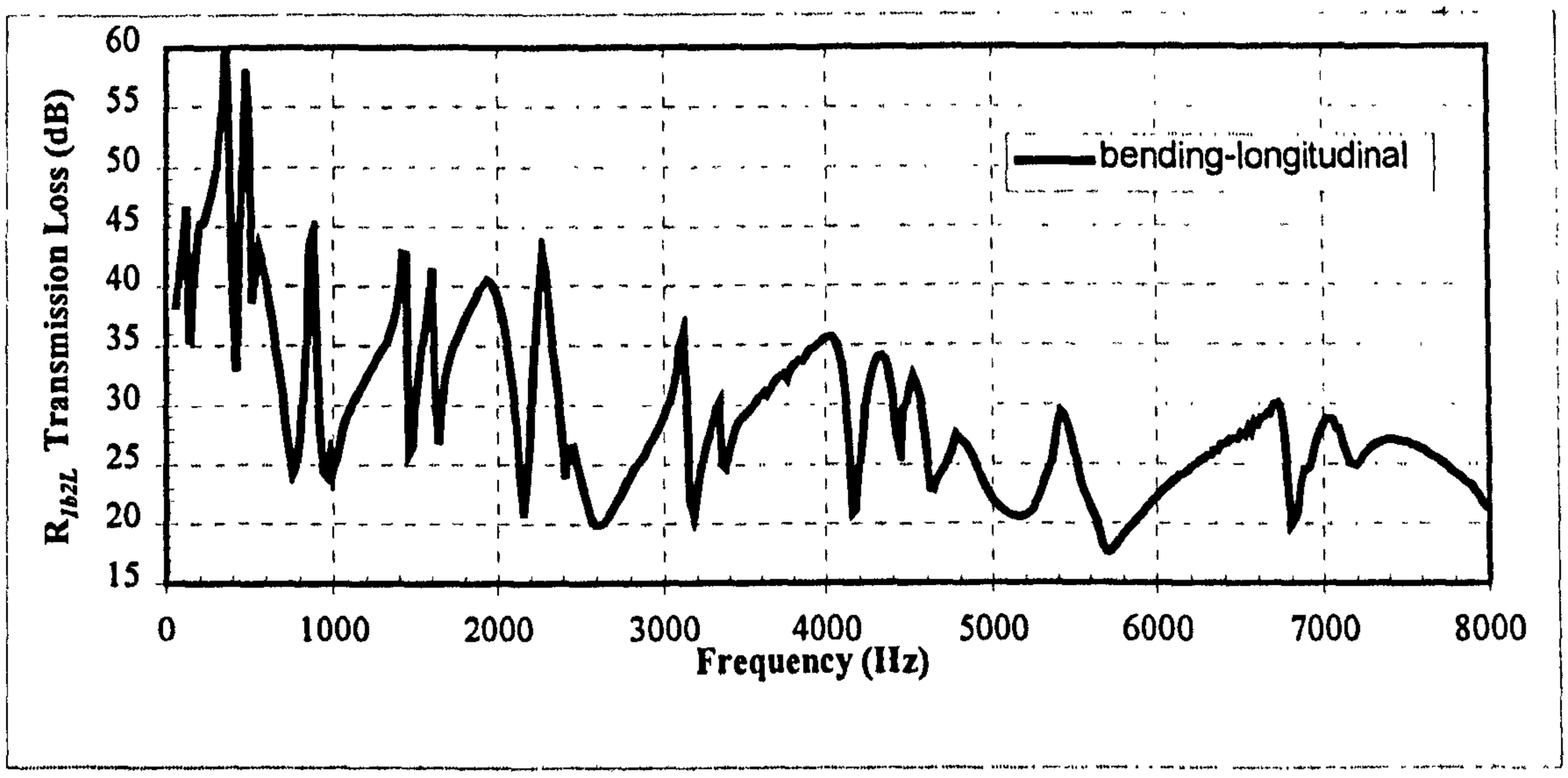

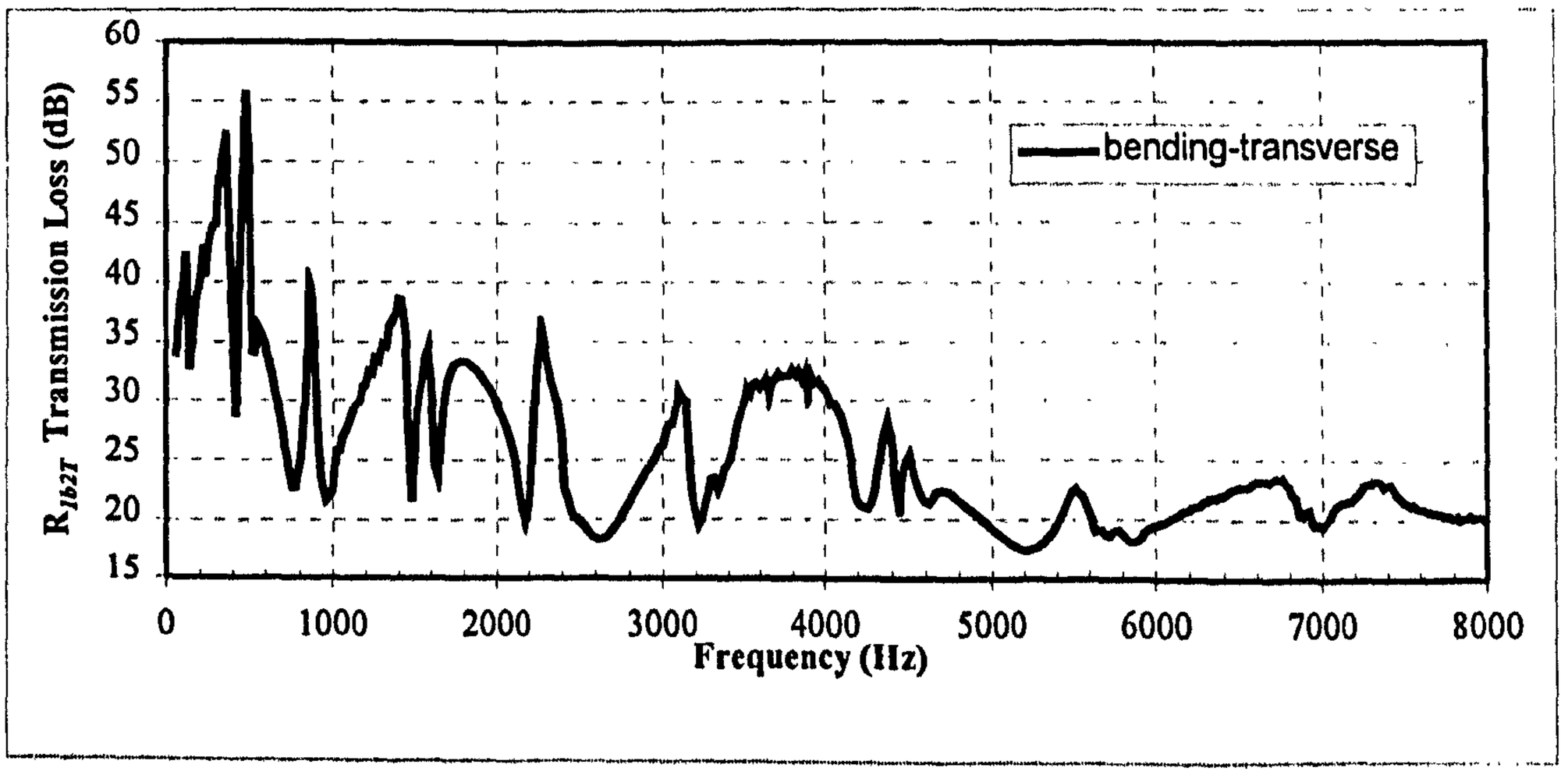

Figure 4.16 BLT Transmission loss curves for 200mm x 8 mm Web plate and 500 mm x 8 mm flange plates

present in the 8 mm web plate bending wave graph but the resolution of the analysis is insufficient to bring them out.

In figure 4.16 the bending, longitudinal and transverse transmission loss curves are shown for a 200 mm by 8 mm web-plate for 500 mm wide flange plates. The 500 mm flange plate results shown in figure 4.16 it can be seen that the bending wave transmission loss curve follows the same trend as the 100 mm flange plate results but there are many more sharp peaks in the curve. These peaks occur close to the predicted frequencies of the flange plates given in tables 4.4 and 4.5. The additional peaks in the longitudinal and transverse wave loss curves are found to coincide with peaks in the bending wave transmission loss curve, which coincide with frequencies of the flange plate as with the 200 mm by 4 mm results in figure 4.14.

The transmission loss curves for the 800 mm by 4 mm web plate with 100 mm wide flange plates are shown in figure 4.17 Comparing the bending wave transmission loss curve results for the 100 mm wide flanges plate with those obtained from the corresponding web-plate parametric model shown in figure 4.11 the curves are very similar. The main obvious difference is between 3000 Hz and 4000 Hz where there are 3 peaks in the transmission loss. The peaks at 3120 Hz is the 14^{th} resonant mode of the web plate predicted to occur at 3200 Hz and the peak at 3700 Hz is the 15^{th} resonant mode of the web plate predicted to occur at 3659 Hz. The peak at 3300 Hz is due to the excitation of the first longitudinal mode of the web plate which is predicted to occur at approximately 3358 Hz. Examining the longitudinal and transverse transmission loss curves it can be seen that they are broadly similar to the transmission loss curves shown in figure 4.11.

The transmission loss curves for the 800 mm by 4 mm web plate with 500 mm wide flange plates are shown in figure 4.18. It can be seen that the trend is very similar to the 100 mm flange plate results but the spectrum has more peaks in the bending wave transmission loss curve and local minimum in the in-plane transmission loss curves. As with the 100 mm web-plate results these additional peaks coincide with the resonant modes of the flange plates. For example it can be observed that there are peaks at 500

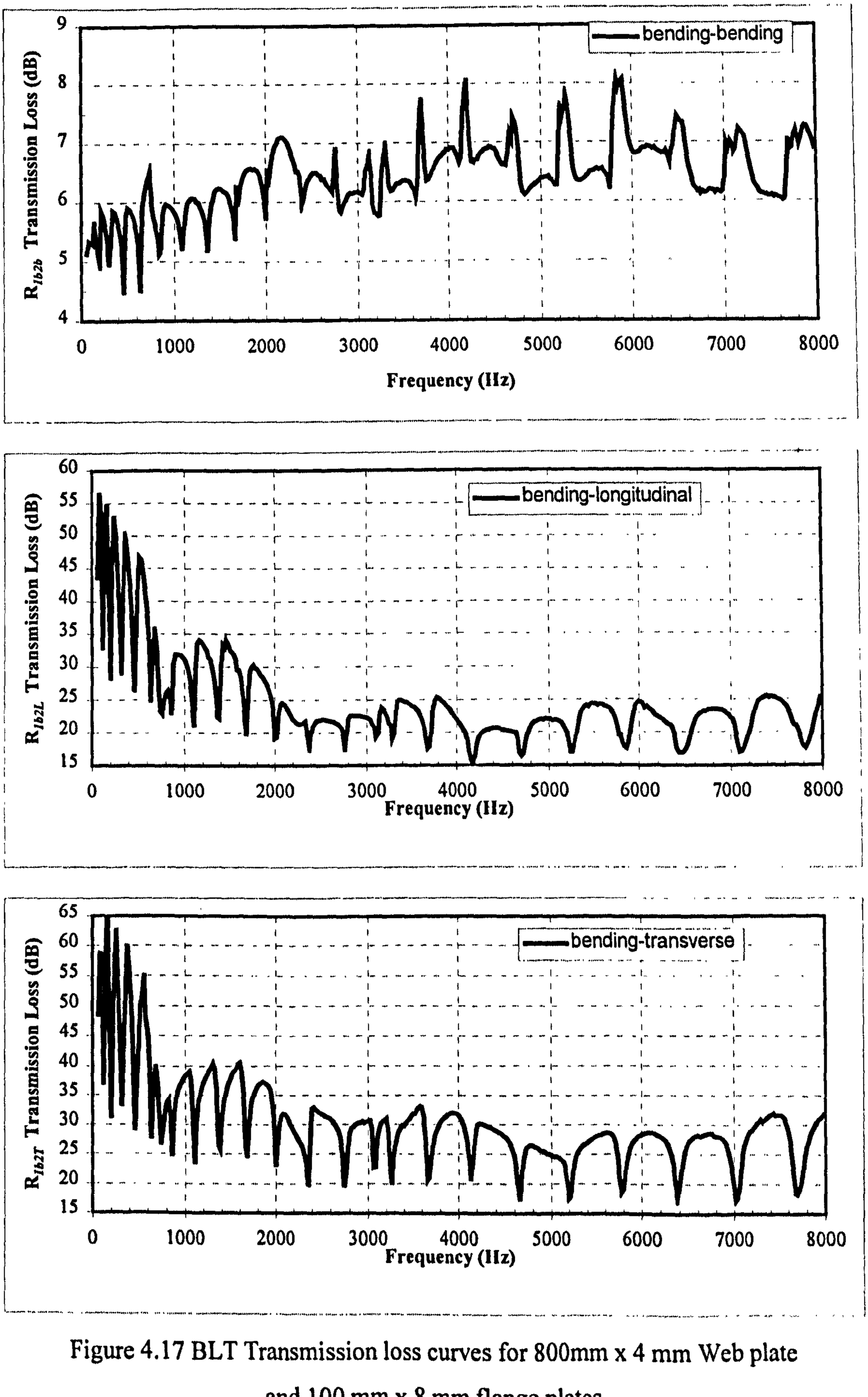

Figure 4.17 BLT Transmission loss curves for 800mm x 4 mm Web plate and 100 mm x 8 mm flange plates

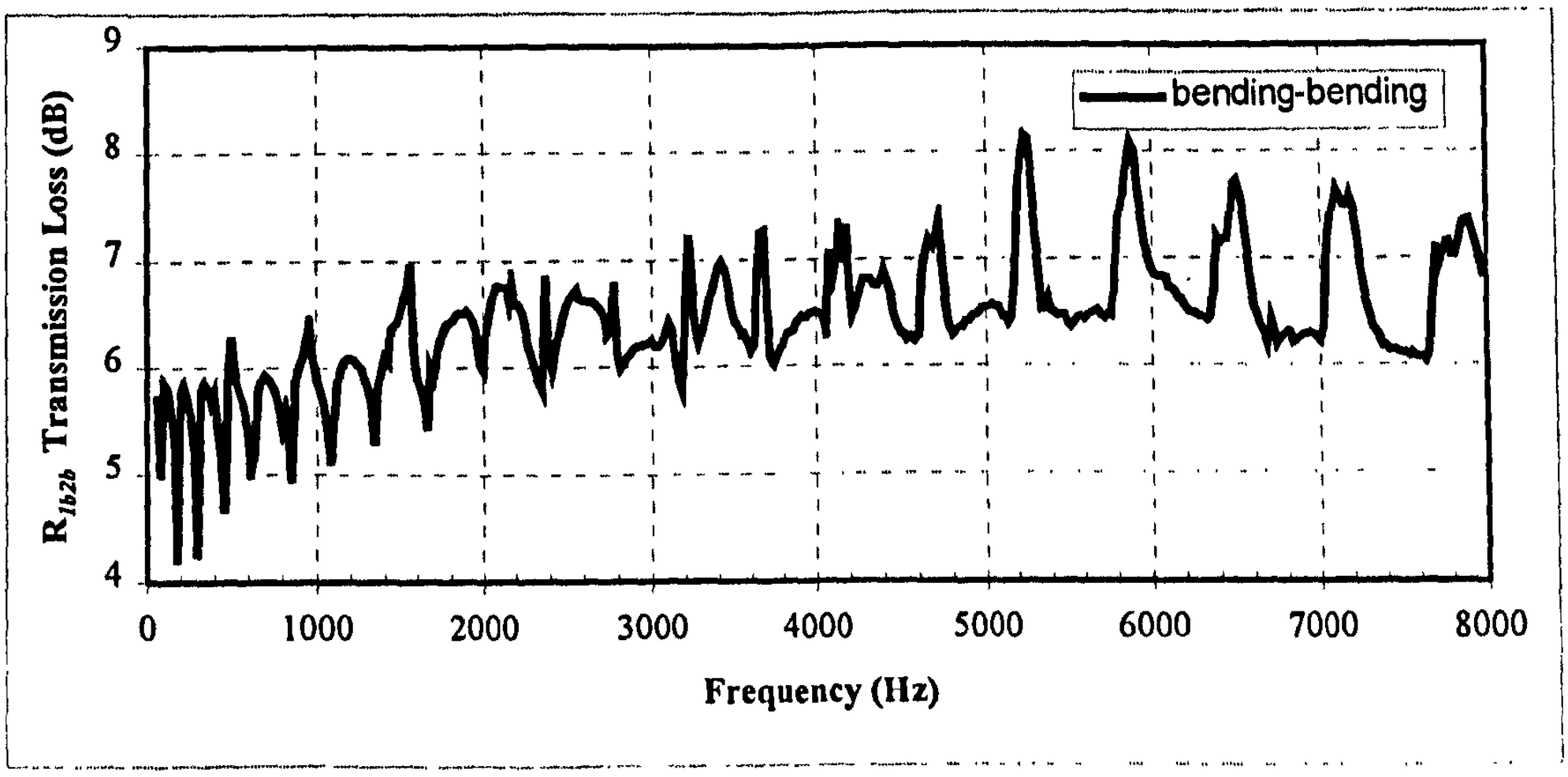

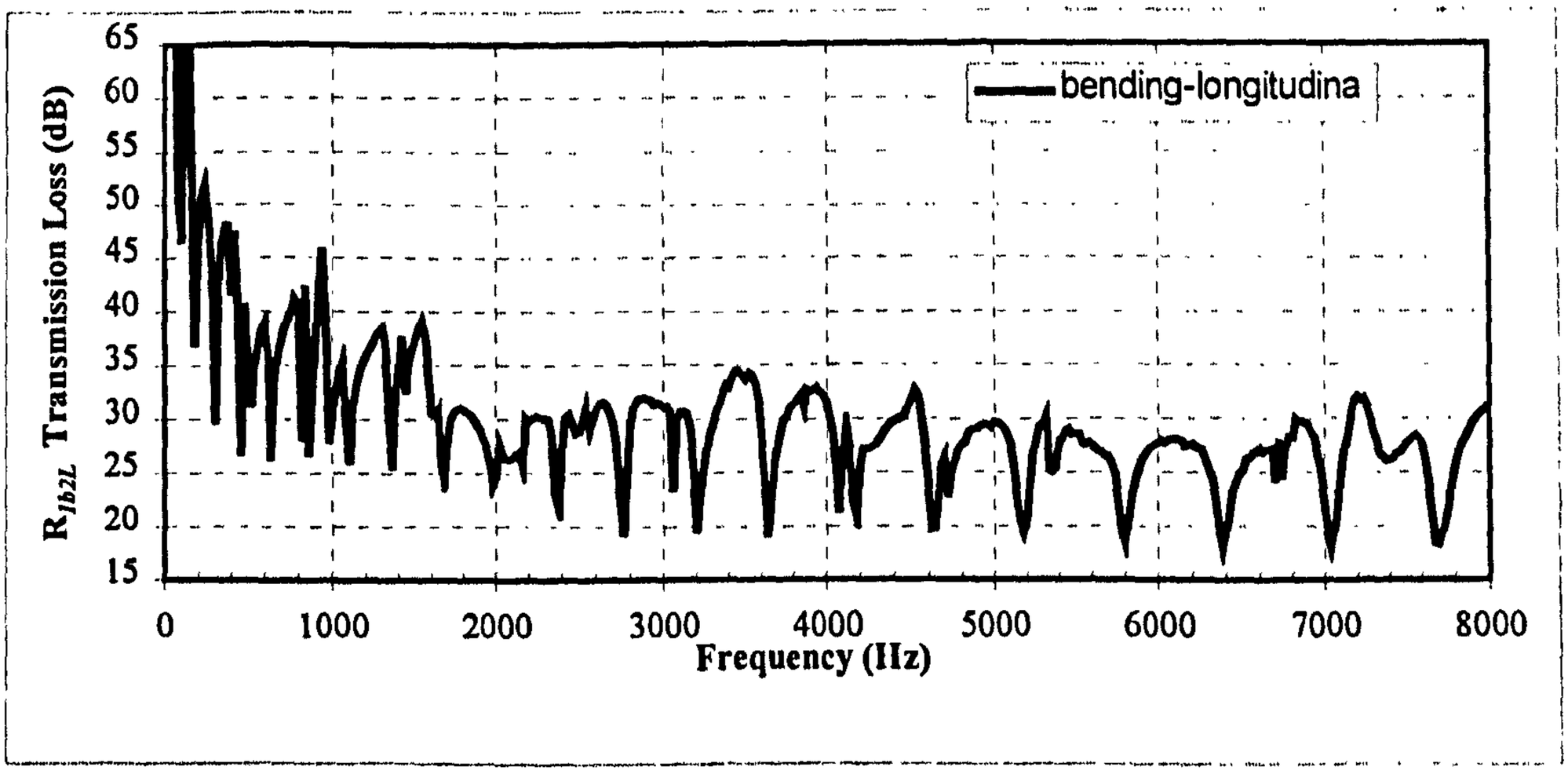

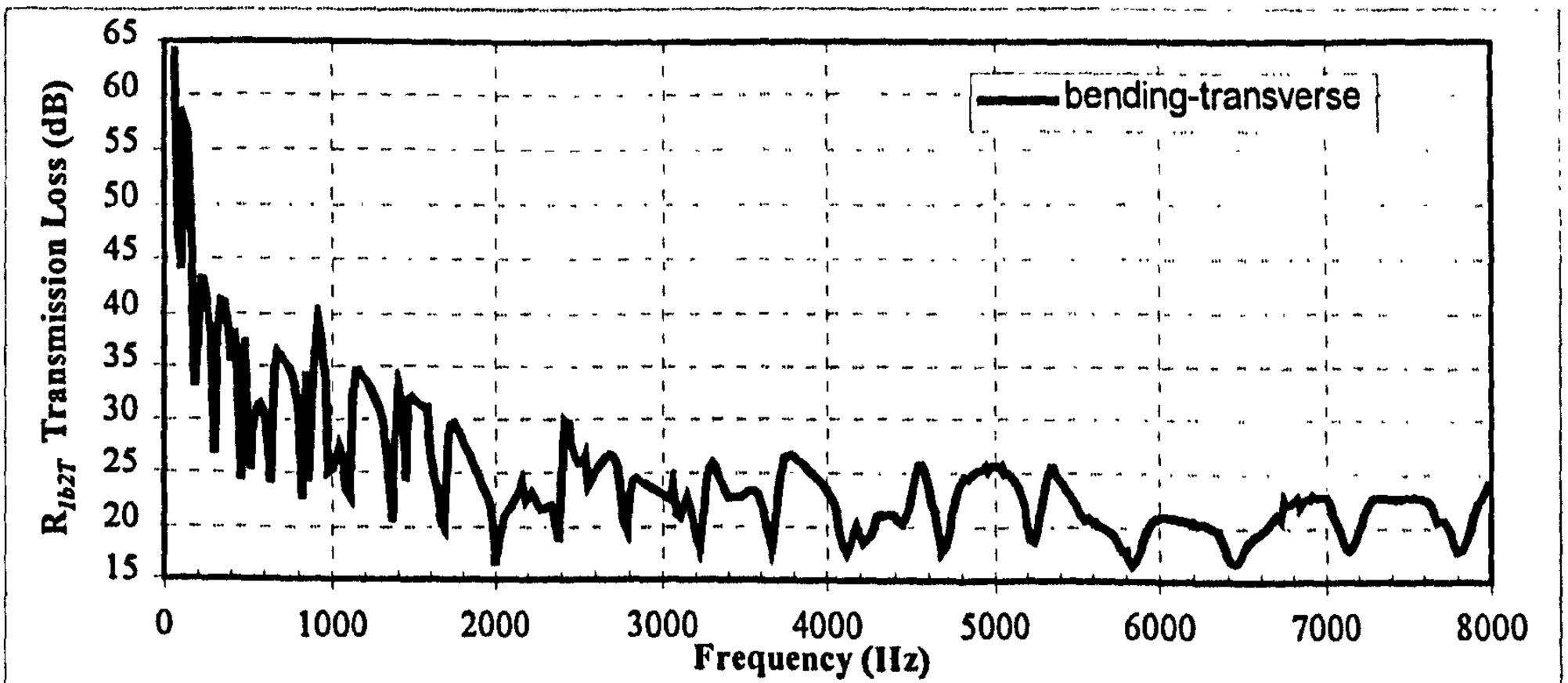

Figure 4.18 BLT Transmission loss curves for 800mm x 4 mm Web plate and 500 mm x 8 mm flange plates

Hz, 960 Hz, and 1560 Hz which are close to the 3rd mode (487 Hz), 4th mode (955 Hz) and the 5th mode (1579 Hz) of the 500 mm flange plates.

The longitudinal and transverse wave transmission loss curves have the same general trends as the 100 mm flange plates and tend to level off at a mean value although the general appearance of the curves is 'noisier'. The combination of deep web and flange plates gives very similar transmission loss curves to the web only result. This is because for the short web plates, the flanges give an approximate a clamped-clamped boundary for the web plate. As the web plate increases in depth the flexibility of the flange/web junction increases and tends towards a clamped-free boundary. This is why the transmission loss curves for narrow and deep flanges for the 800 mm deep web plate resemble the web only results. The bending, longitudinal and transverse transmission loss curves for an 800 mm by 8 mm thick web plate with 100 mm wide flange plates are shown in figure 4.19. Comparing the 100 mm flange plate results in figure 4.19 with the transmission loss results for the 800 mm deep by 8 mm thick web-plate results shown in figure 4.12 it can be seen that the bending wave transmission loss curve is extremely similar. The peak at 800 Hz is again observed in the bending wave transmission loss due to wave matching between the web plate and the flange plates and a corresponding change in the in-plane transmission loss. The other difference is that between 3000 Hz and 4000 Hz there are two peaks at 3200 Hz and 3659 Hz. From the results in figure 4.17 and 4.19 it can be concluded that the small flange plates on a deep web plate are generally insignificant because of their low mode count and do not effect the wave transmission characteristics to any significant degree and can be ignored.

The bending, longitudinal and transverse transmission loss curves for an 800 mm by 8 mm thick web plate with 500 mm wide flange plates are shown in figure 4.20. Examining the 500 mm wide flange plate results it be can seen that there are additional peaks in the bending wave transmission loss curves due to the flange plates. Again the peaks in the bending wave transmission loss due to the matching of bending waves on the web plate occur at the same frequencies at which the local minimum values in the longitudinal and transverse wave curves occur. Where the peaks in the bending wave

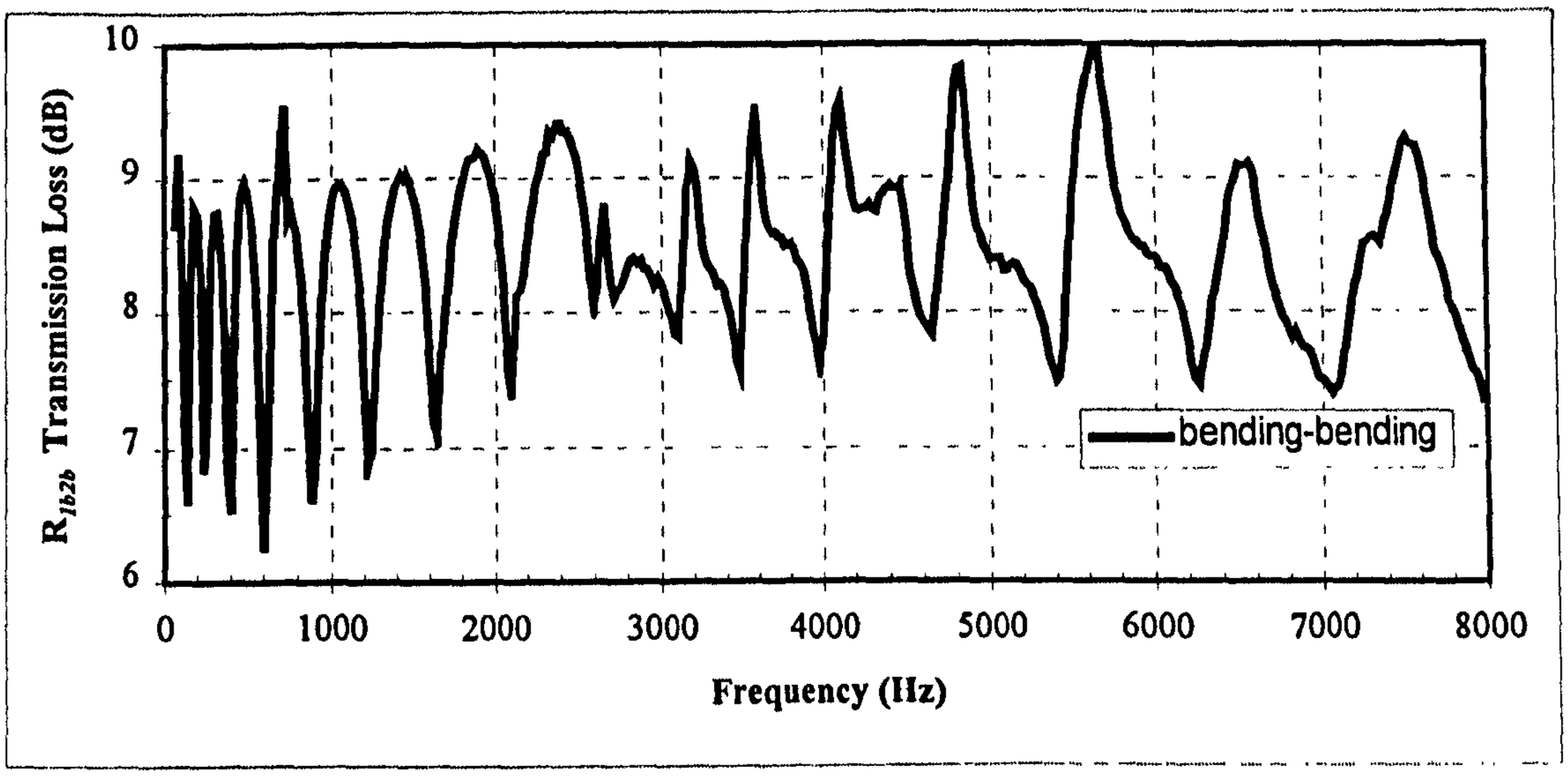

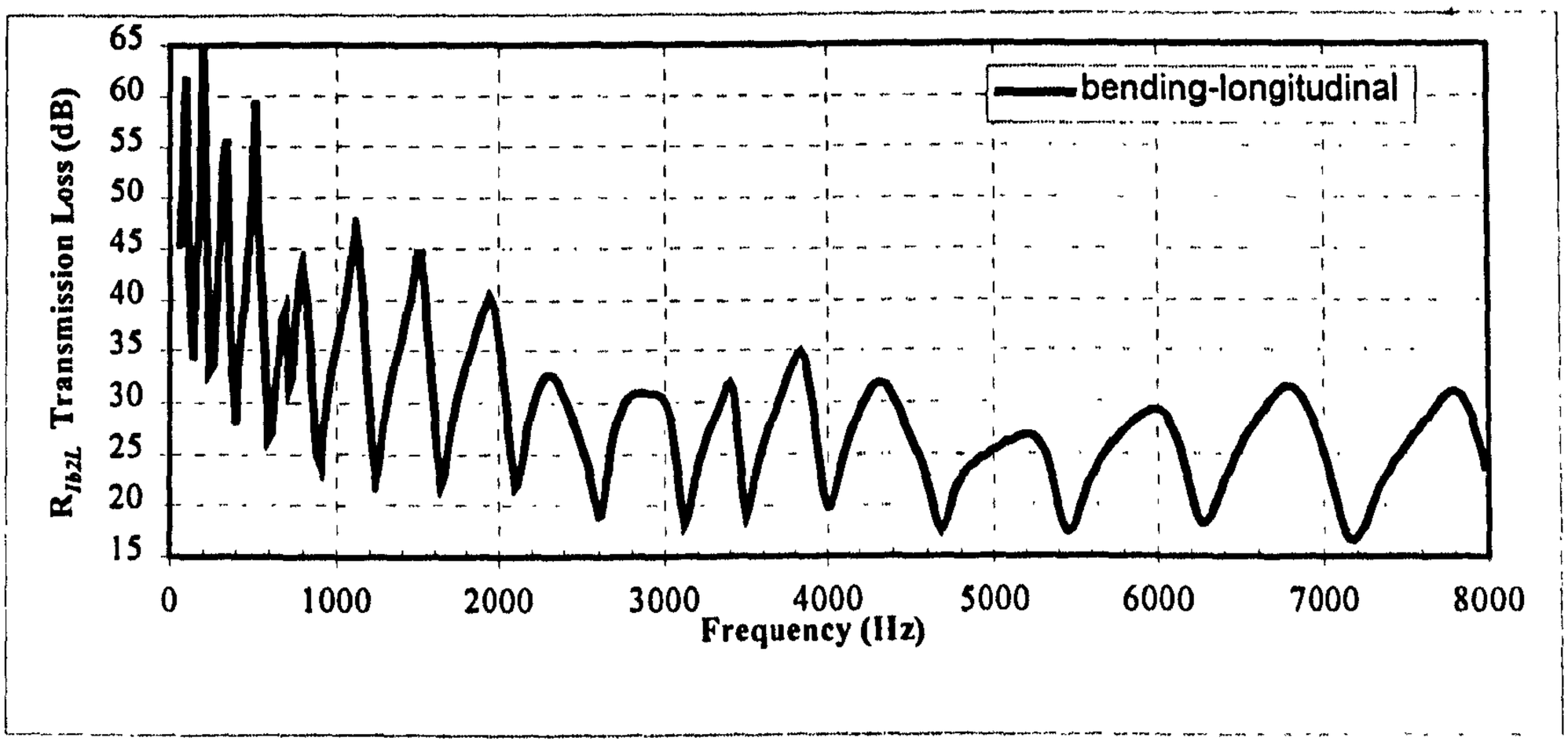

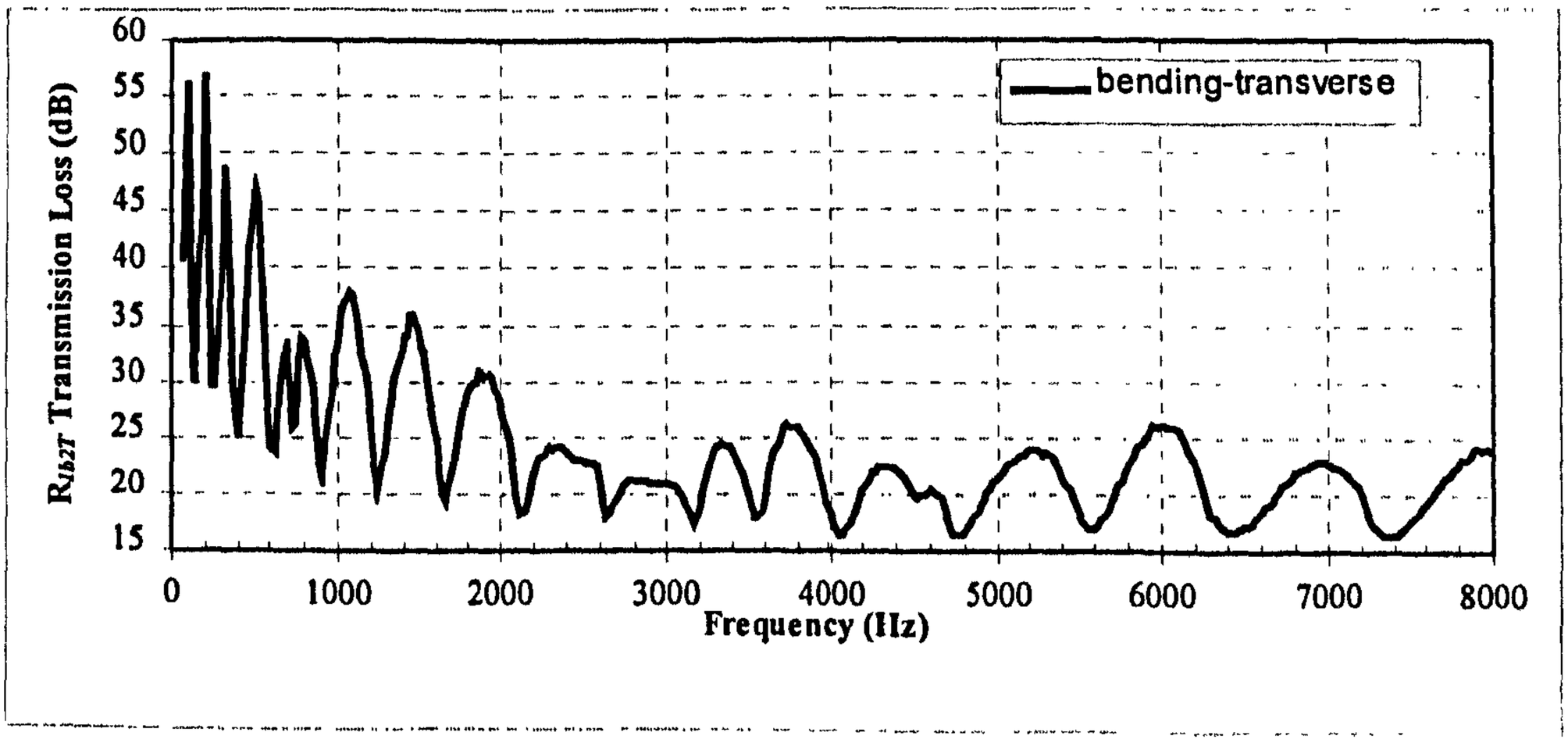

Figure 4.19 BLT Transmission loss curves for 800mm x 8 mm Web plate and 100 mm x 8 mm flange plates

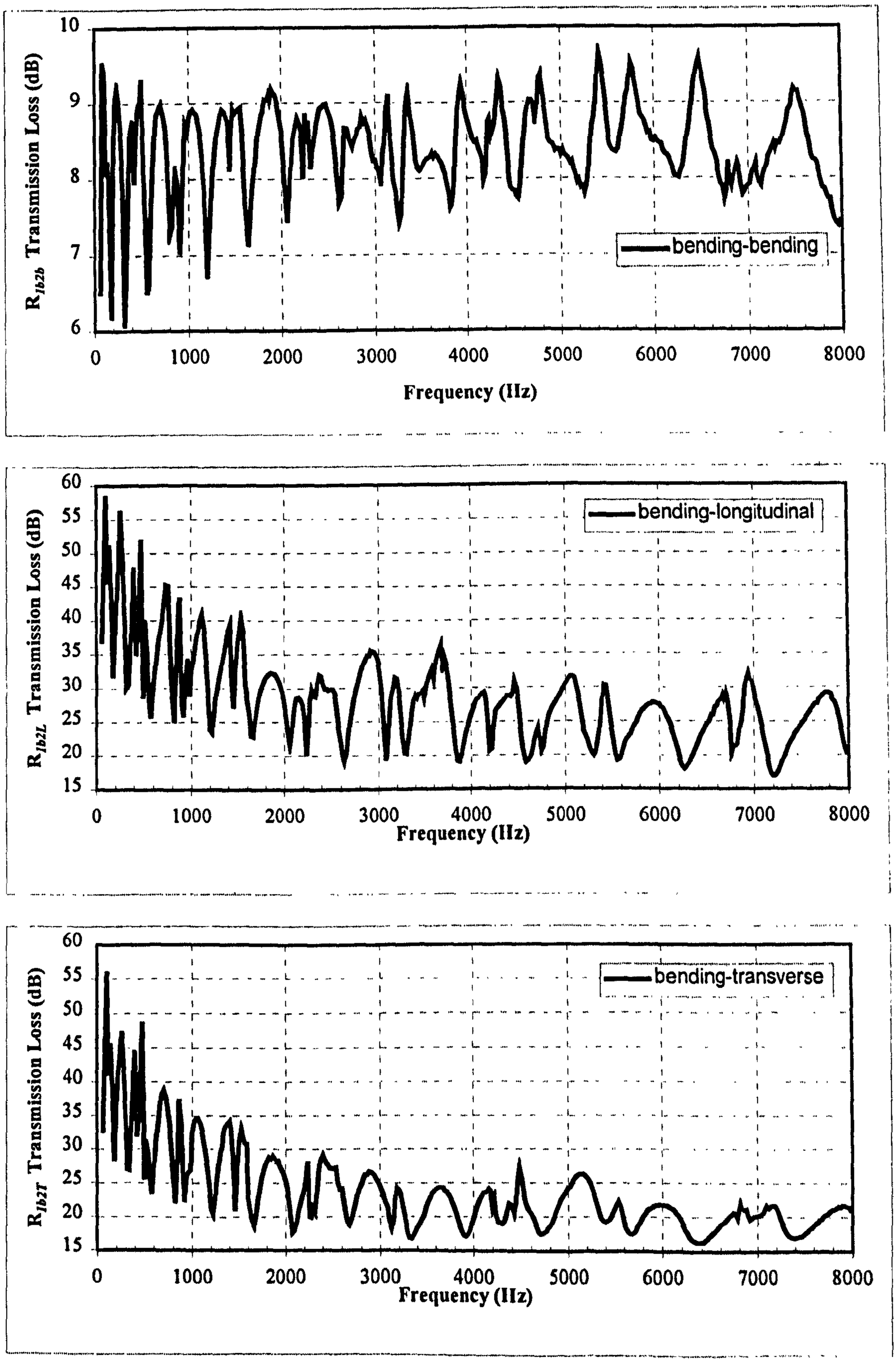

Figure 4.20 BLT Transmission loss curves for 800mm x 8 mm Web plate and 500 mm x 8 mm flange plates

transmission loss curves are due to wave matching between the web plate and the flange plates then they can be correlated to events in the in-plane transmission loss curves.

4.4 Discussion

The results for the parametric survey presented in section 4.3 of this chapter have provided some insight into the transmission characteristics. It can be seen that for the 800 mm web results with 100 mm and 500 mm flange plates are very similar when compared to the corresponding web plate only results presented in section 4.3.1. For deep web plates it appears that the addition of web plates does not have any significant effect on the bending, longitudinal and transverse transmission loss curves. Figure 4.21 shows the bending wave transmission loss for the 800 mm by 8 mm web plate with no flange plate, 100 mm flanges and 500 mm flanges. It can be seen that the predicted transmission loss is very similar apart from localised differences due to the flanges, therefore the flanges do not have any significant effect on the overall transmission loss.

In figure 4.22 the bending to longitudinal transmission loss is also plotted for the 800 by 8 mm web plate. It can be seen that the flange plates do not significantly effect the transmission loss as the curves are all very similar. Therefore for deep web plates it is reasonable to assume that neglecting the flange plates will not adversely change the power transmission across the joint. This would simplify the modelling of joints by reducing the input data required to define the joint. It would also reduce the computation time for solution of the wave transmission characteristics since only a 16 by 16 matrix requires to be solved to a web only model instead of a 32 by 32 matrix for the full frame model.

In figure 4.23 the bending wave transmission loss R_{1b2b} for the 200 mm by 4 mm web plate is shown. It can be seen that transmission loss curves for the three different parametric models are similar but there is a small but significant difference between the results in comparison to the deep web results. It can be seen that there are differences of up to 2-3 dB in the transmission loss between the web only results and the flanged results. For small frames the decision to model the flange plates could be significant. A

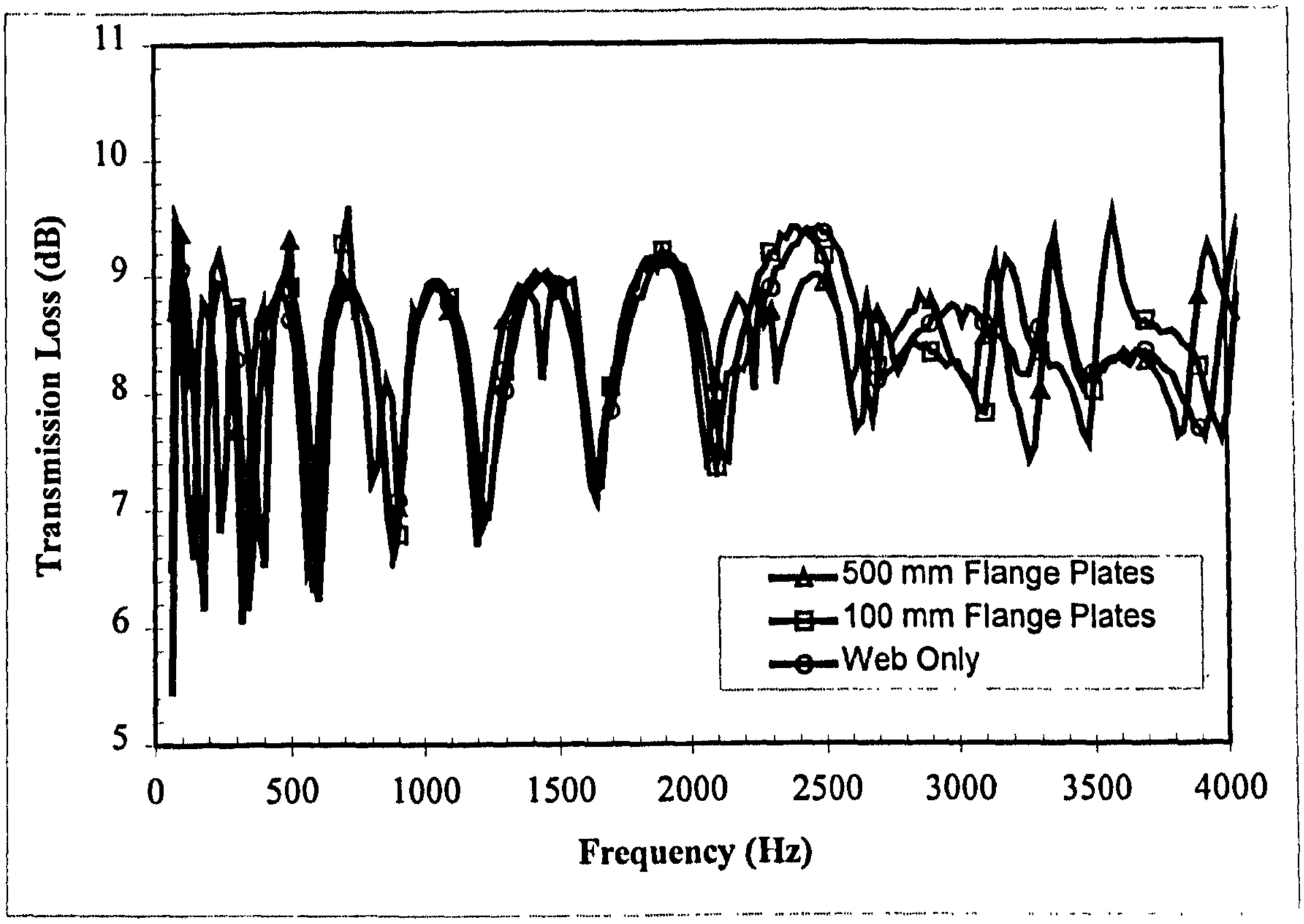

Figure 4.21 Comparison of 800 x 8 mm web plate – different boundary conditions

R_{1b2b} bending to bending transmission loss

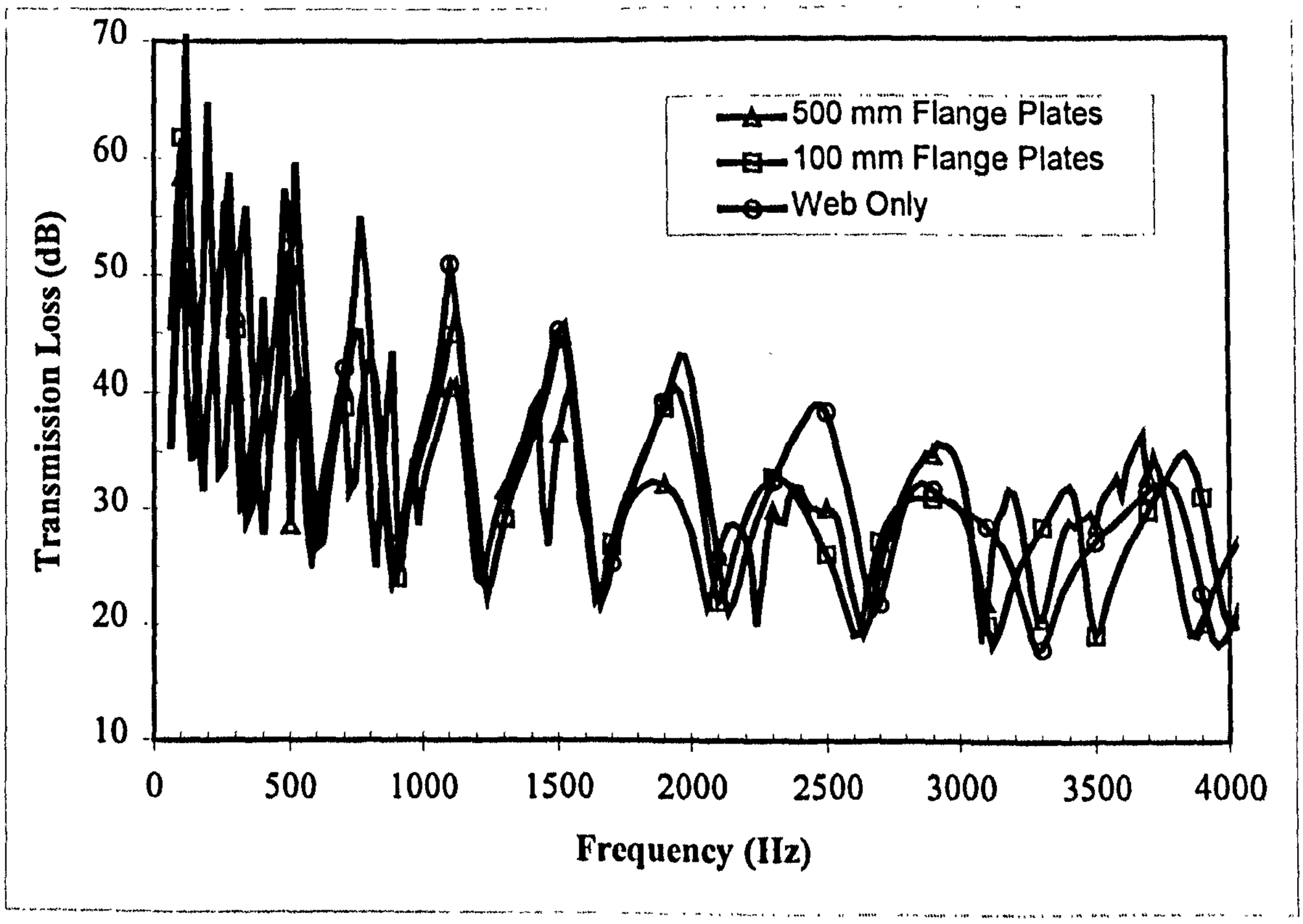

Figure 4.22 Comparison of 800 x 4 mm web plate – different boundary conditions

R_{1b2L} bending to longitudinal transmission loss

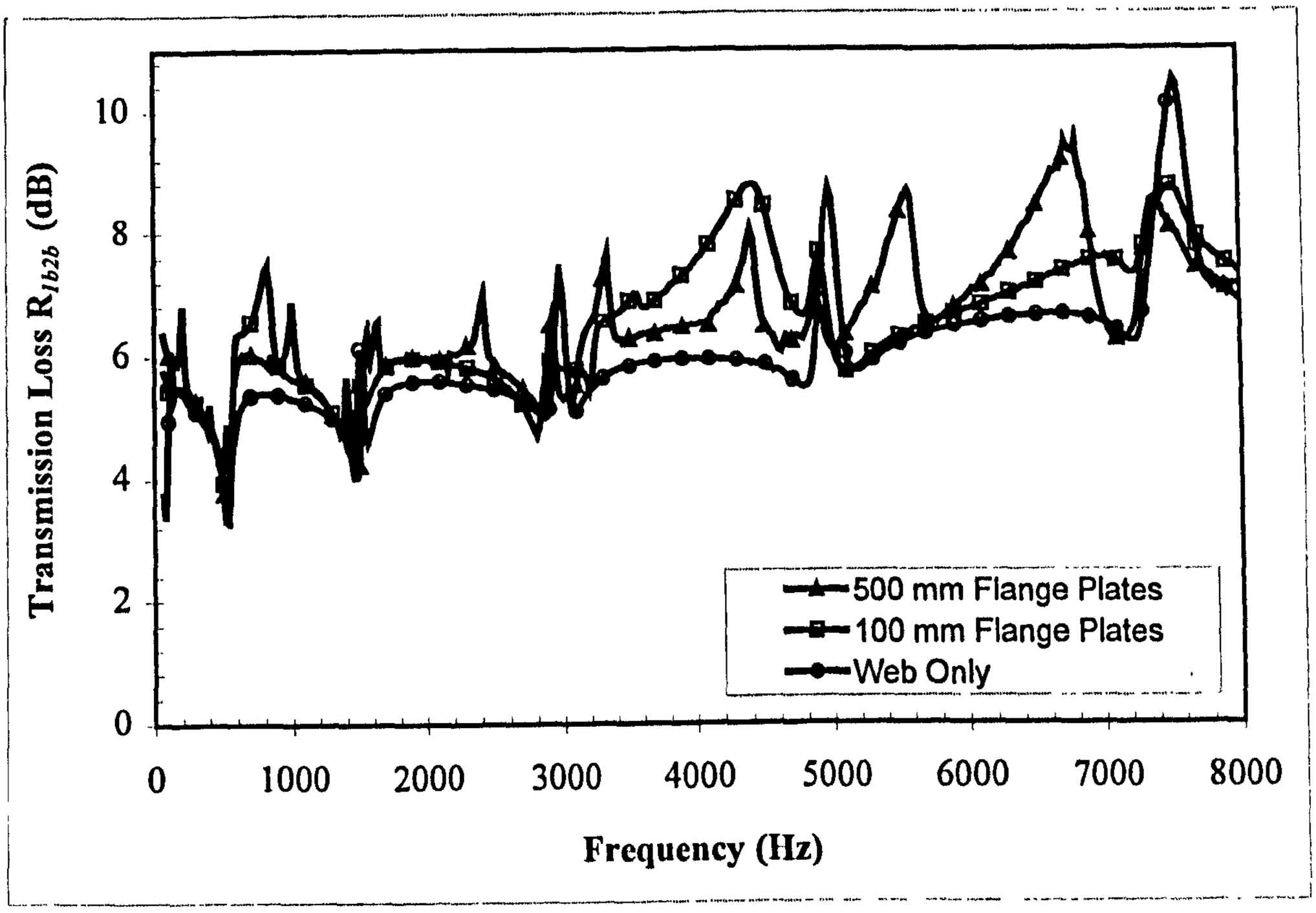

Figure 4.23 Comparison of 200 x 4 mm web plate – different boundary conditions
R_{1b2b} bending to bending transmission loss

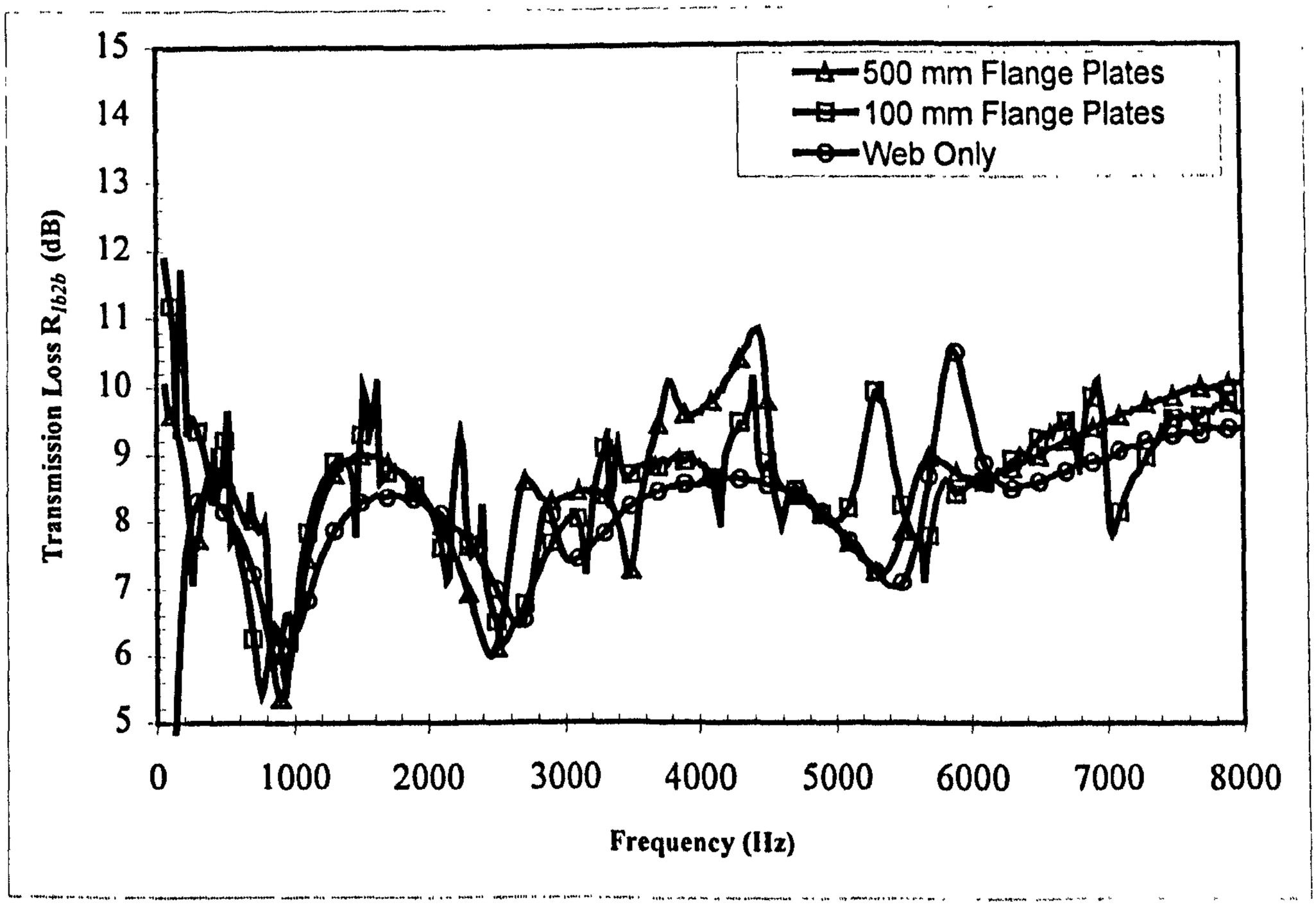

Figure 4.24 Comparison of 200 x 8 mm web plate – different boundary conditions
R_{1b2b} bending to bending transmission loss

difference of 2-3 dB in the transmission loss for one joint may not appear significant, but in a ship where the structure is near periodic and the joint configuration is repeated, a difference of 2dB can be extremely important. For every joint crossed the difference between the predicted structure borne noise by the two modelling approaches will accumulate. Only experimental studies of the joint will determine the more accurate of the two modelling approaches. It would be anticipated at this stage that the full frame model would be the more accurate as it models full behaviour of the frame.

In figure 4.24 the bending wave transmission loss R_{1b2b} for the 200 mm by 8 mm web plate is shown. It can be seen that transmission loss curves for the three different parametric models are similar but again there is a small but significant difference between the results.

4.5 Conclusions

In this chapter the design of hull frame stiffeners and the variations were introduced. A transmission model and the important equations have been described that will permit the wave transmission characteristics of the basic stiffener designs commonly found in ships to be predicted. The method utilised has been established by other researchers for other joint configurations and the results of a parametric analysis have been presented which allow the effects of the different elements of the frame stiffener (i.e. web-plate, flanges) on the transmission characteristics to be determined.

The depth of the web-plate is important as this determines the number of wave matching frequencies of web plate. In the absence of flange plates the web-plate can be approximated to a cantilever and the maximum transmission loss across the stiffener occurs when the incident wave is an integer multiple of the ¼ wavelength of the web-plate. Flange plates can affect the transmission characteristics but this depends on the web-plate to which they are connected. For a deep web it has been shown that wide and narrow flanges have no significant effect on the transmission characteristics and can be neglected. If the web-plate is small then flange plates can be significant. Flange length is also important as it determines how significant a role the flange plays by increasing

the number of wave-matching frequencies between the flanges and web plate. The parametric survey has shown that small frames can give a difference of 2 to 3 dB in the predicted transmission if the flanges are omitted. This is important in a ship context given the near-periodic arrangement of frames on the structure, as any small differences in modelling will be amplified with each joint crossed. It is believed that the full frame should be more accurate as it models the complete joint.

The longitudinal and transverse transmission loss curves show large variations in the magnitudes with frequency. For SEA models it may therefore be prudent to average the transmission loss for a number of frequencies in each third octave frequency band rather than rely on the transmission loss calculated at the centre frequency of the band.

Chapter Five

SEA Modelling of Laboratory Test Structures

5.1 Introduction

In chapter two the basic methodology of SEA was introduced to the reader whilst in chapter three the experimental measurement techniques were reviewed and in chapter four a theoretical model was developed to predict the power transmitted across hull frame structures. In this chapter all of the elements previously developed are brought together as a series of experimental structures are used to validate the theoretical joint model developed in chapter four. Initially a series of simple hull-frame structures are reviewed to verify the accuracy of the basic frame model and then a larger more complex laboratory test structure with an array of frames elements is reviewed to verify the performance of the joint.

5.2 Simple Laboratory Structures

To verify the mathematical model developed, a series of laboratory measurements were made on simple experimental hull frame structures. In this section the results from the laboratory measurements are compared with predictions from SEA models of the test structure using the hull frame model developed in chapter four to calculate the average transmission coefficients.

The laboratory models were constructed in a reverberation chamber from two thin aluminium plates bolted to the flanges of a steel I-beam with M10 bolts. The free edges of the plates were supported above the chamber floor on foam lined battens. To prevent

equi-partition of energy occurring additional damping was applied to the plate designated as the receiving subsystem and this was applied by laying sand filled bags along the plate free edges to absorb some of the energy of the incoming waves to the plate edges. The laboratory test arrangement is shown in figure 5.1.

There are two aspects of the test structure that must be considered in relation to the mathematical model. To emphasise this, figure 5.2 illustrates the cross section of the laboratory structure and the mathematical model.

The first and most important difference is the use of bolts to connect the aluminium plates to the bottom flange of the I-beam. The theoretical model was developed with a continuous line contact assumed between the web plate of the frame and the hull plates (plates 1 and 2). In previous work by Smith (Ref. 78) on stud walls where plasterboard sheets were nailed to a wooden batten, the possibility of this joint type functioning in two different ways was highlighted. First the joint can behave as a continuous line contact or because of the nails, it can behave as a series of point contacts. The important relationship is the pitch of the fixings and the frequency at which a half bending wavelength is equal to the pitch of the fixings. Below this frequency the connection behaves as a line contact but above it behaves as a series of point contacts at the fixings.

To investigate if the use of bolts to connect the plates to the I-beam resulted in a continuous line contact or a series of point contacts a simple set of experiments were conducted. For the bolted configuration a set of acceleration level difference measurements were made using the procedures discussed in chapter three, section 3.2. Initially measurements were made with plate 1 as the source and plate 2 as the receiving subsystem. Damping measurements were taken on the receiving the subsystem using the reverberation time technique discussed in chapter three, section 3.3. Measurements were then taken with plate 2 as the source and plate 1 as the receiving subsystem after the additional damping treatment had been moved. The bolts were then removed and a thin layer of epoxy resin was applied to the edge of the aluminium plates to bond the

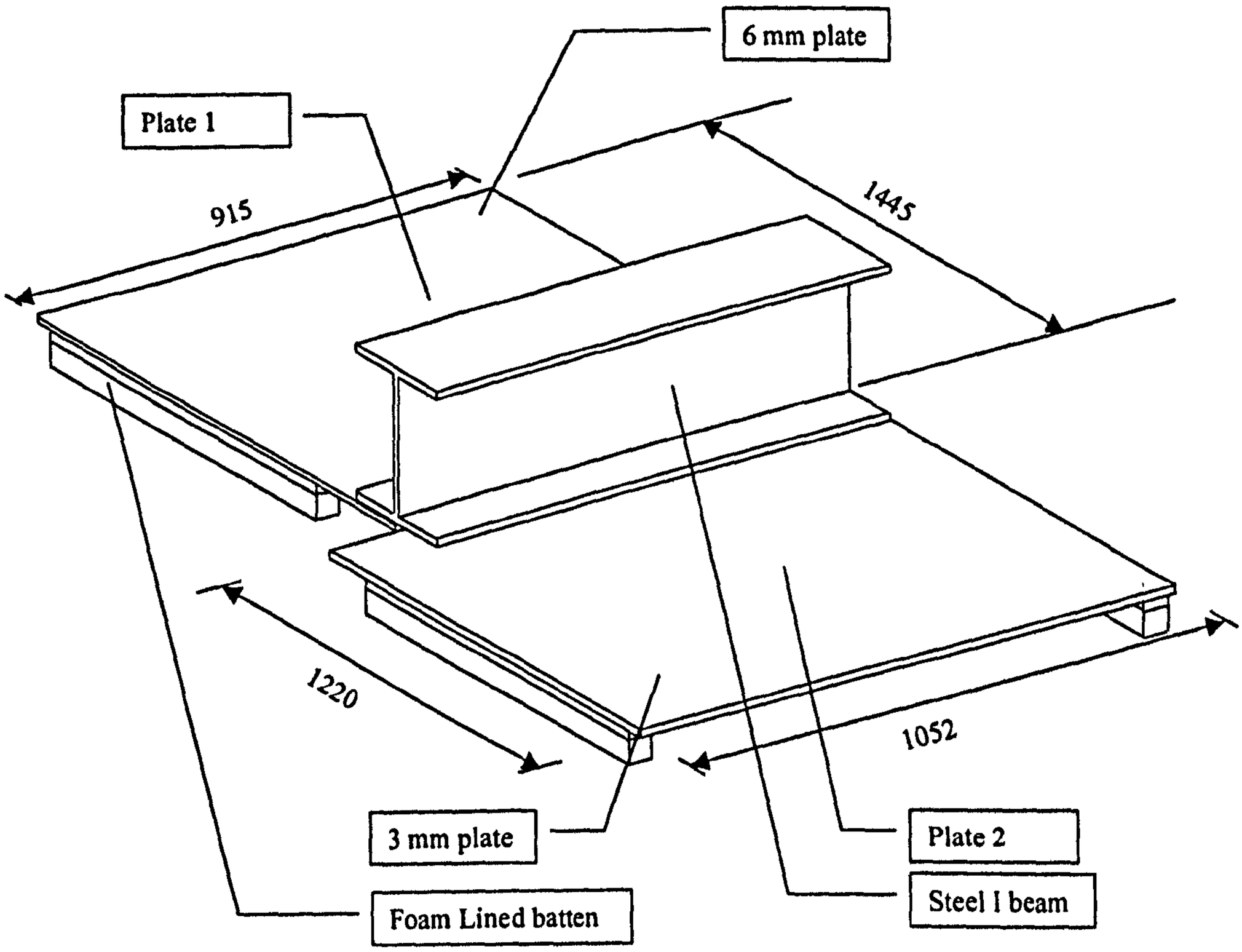

Figure 5.1 Simple laboratory test structure

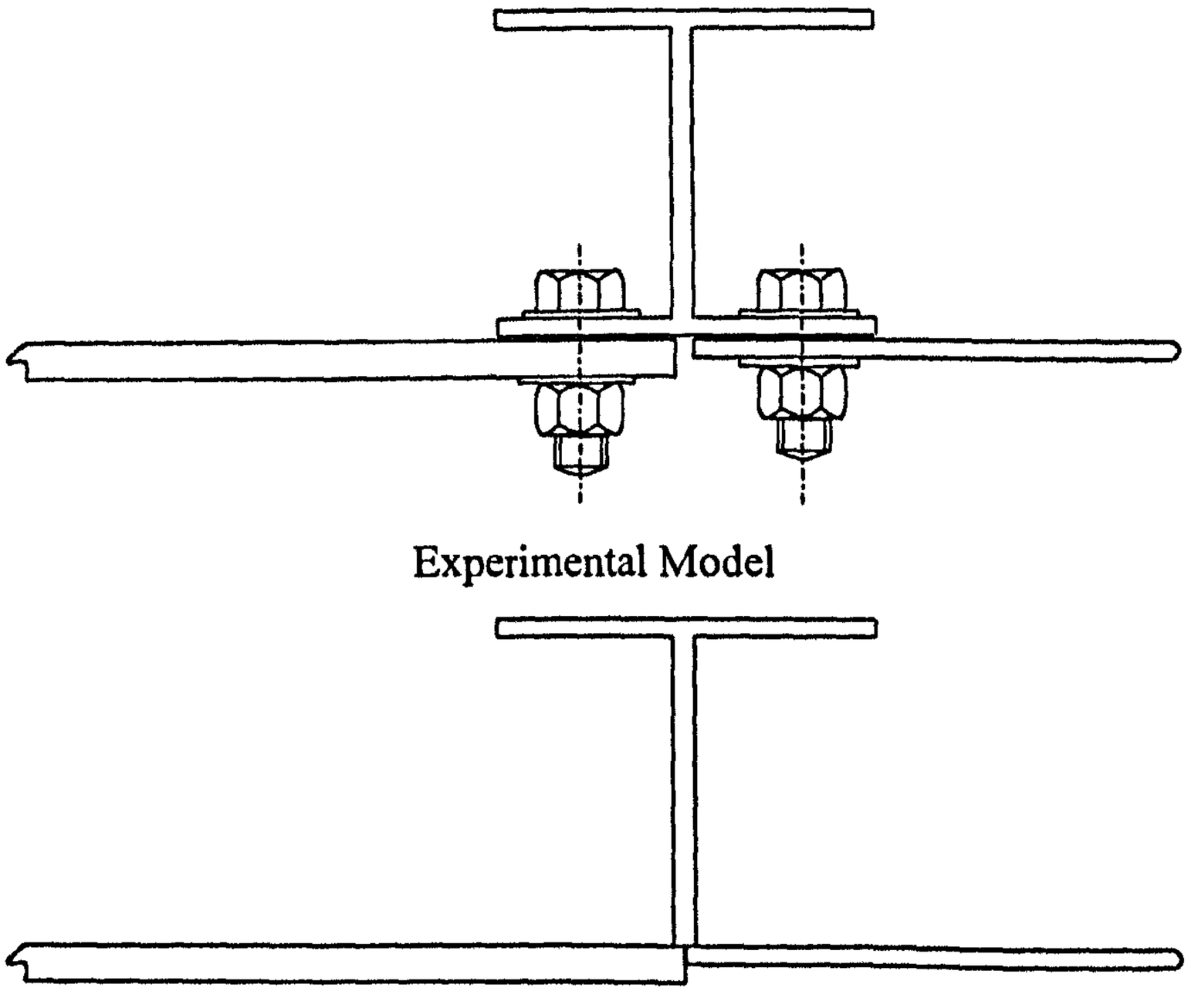

Experimental Model

Mathematical Model

Figure 5.2 Comparison of cross-sectional details

plate to the flange of the I-beam to give a line contact. After allowing the resin bond to cure, the measurements were repeated.

In figure 5.3 the measured acceleration level difference is shown for the bolted and bonded joints for power input to plate 2. It can be seen that the two curves show the same variation with frequency. The bolted result is consistently higher than the bonded result but the difference is within the range of experimental error for the measured data. In figure 5.4 the measured total loss factor for plate 1, η_1, is plotted for the bolted and bonded joints and it can be seen that the total loss factor for the bonded plate is marginally higher, probably due to the additional damping provided by the epoxy resin of the joint. Using the measured acceleration level difference and the total loss factor, and correcting for the masses of the subsystems, the measured coupling loss factor can be calculated. Figure 5.5 shows the measured coupling loss factor for the bolted and bonded joints and it can be seen that the CLF η_{21} for both joints is very similar across the frequency spectrum proving that the bolted joint behaves as a continuous line contact. Similar results were found when comparing the coupling loss factor η_{12} for the bonded and bolted joints.

The reason for the bolted joints behaving as a continuous line contact rather than a series of point contacts at the bolts is due to the clamping effect of the bolts and the compression of the flange and plate between the nut and bolt head. As mentioned, the work by Smith [Ref. 78] was on party wall constructions where the plates were nailed to a batten, this is in fact similar to the riveted joint construction found in aerospace structures. These types of nailed/riveted construction do not produce the same magnitude of compression load on the plate between the fixing and the batten as a bolt and nut and hence the pitch and number of the fixings becomes important in determining if the joint behaves as a continuous line contact or a series of point contacts at the fixings.

The second difference between the experimental and theoretical model is the presence of the bottom flange of the I-beam because in the joint model the web plate of the stiffener is connected directly to the hull plates. There are several reasons for using the

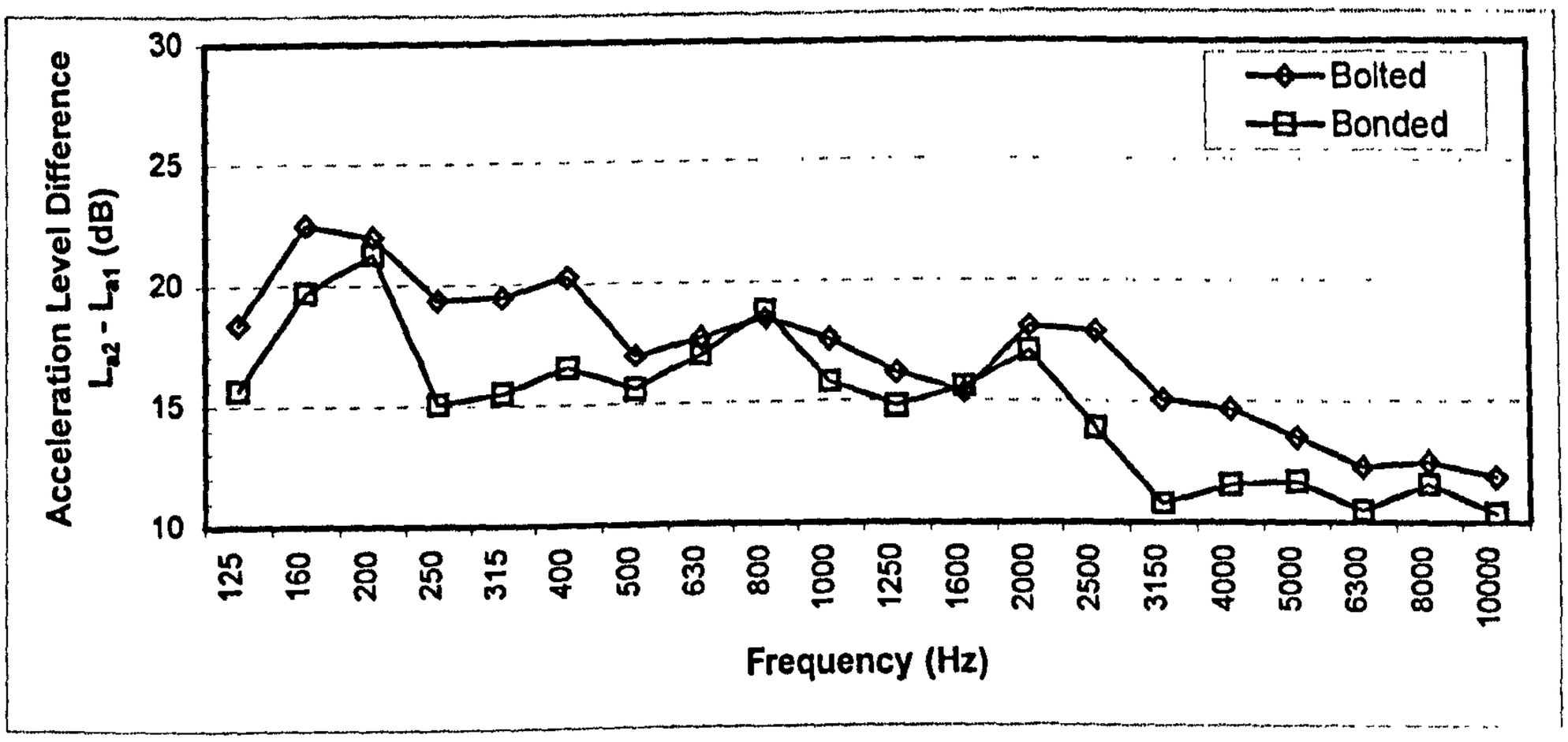

Figure 5.3 Comparison of measured ALD for bolted and bonded joints

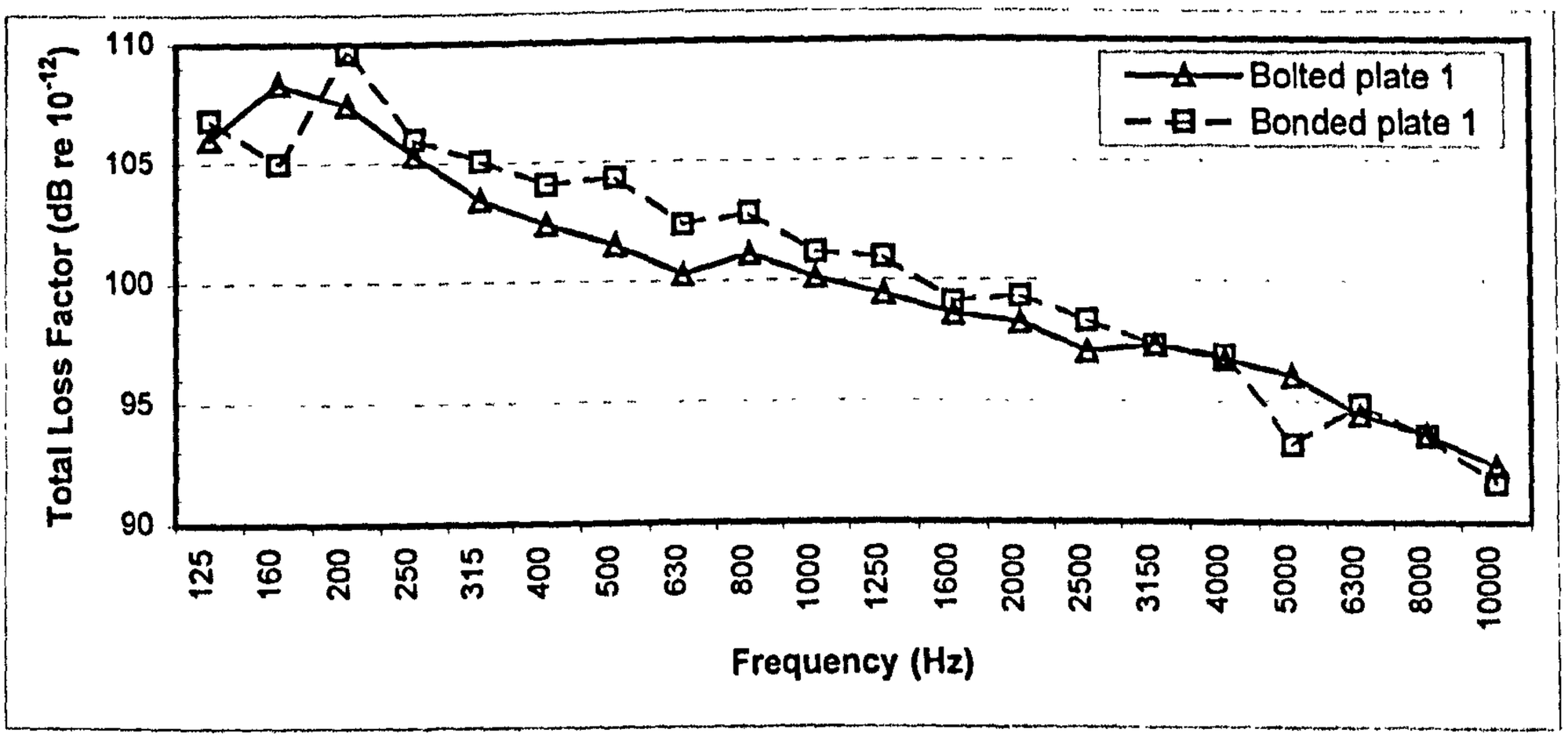

Figure 5.4 Comparison of measured TLF η_1 for bolted and bonded joints

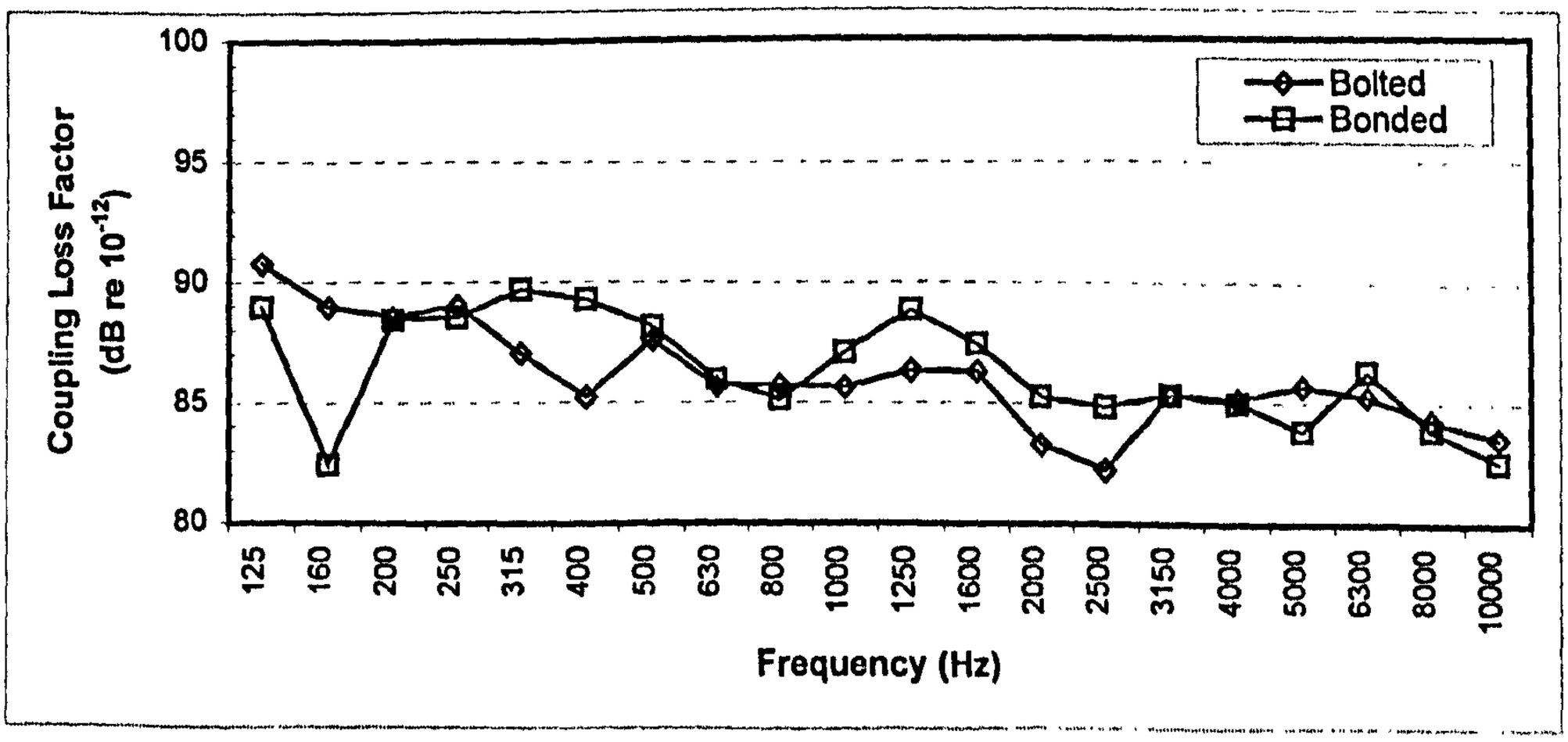

Figure 5.5 Comparison of measured CLF η_{21} for bolted and bonded Joints

experimental model employed here. The first is the use of the bolted connections allows different I-beam section sizes to be employed with the same plates minimising material consumption while the use of aluminium plates reduces the weight of the test structure allowing it too be easily assembled and handled. The material properties of aluminium are approximately one-third those of steel and therefore the plates will be more flexible and have a higher mode count. The joints were constructed so that the aluminium plates were not in contact along their common edge thus the structure-borne sound waves are transmitted between the plates via the flanges. The bottom flange therefore acts as part of the aluminium plates and does not have any adverse effect upon the experimental model apart from producing a localised stiffening effect where the flange and plate overlap. To prove this a dynamic stiffness matrix model which included the bottom flange plates was analysed and it was found that the difference in the transmission loss is approximately 1 dB across the entire frequency spectrum. The effect of the bottom flange is considered to be insignificant and can be neglected.

The experimental measurements were undertaken with three different I-beam section sizes which are listed in table 5.1.

Table 5.1 *I*-Beam Section Sizes

Nominal Section Size	*Web Depth (mm)*	*Web Thickness (mm)*	*Flange Width (mm)*	*Flange Thickness (mm)*	*Mass (kg/m)*
127 x 76	127	5.6	76.4	9.6	16
203 x 133	203	5.4	133.4	7.6	25
406 x 178	402.6	7.6	178	10.9	54

The size of the I-beams selected for the experimental work are representative of the range of typical hull frame stiffeners found in ship construction. A series of measurements were taken for each section size used. Acceleration level difference measurements between the source and receiving subsystem in both directions for the bending and in–plane waves were undertaken on the test structure as discussed in

chapter three. In addition damping measurements were made on each receiving subsystem with the plates connected and the reverberation time of the chamber and acceleration-sound pressure level difference were also measured in each test series.

5.3 SEA Modelling of Simple Laboratory Structures

For the purposes of the analysis three joint approaches are used in the SEA models to predict the structure-borne noise transmission which are then compared with the measured acceleration level differences. The three modelling approaches used are as follows:

(a) Frame Model: the full frame model developed in the previous section is used to predict the average angular transmission coefficient.

(b) Web model: the full frame model is simplified by omitting the flange plates of the stiffener. For real ship structures this would greatly reduce the data input for the joints.

(c) Eccentric beam model: the stiffener is modelled as a beam subsystem rather than an assembly plates. This is a commonly used modelling approach for ship structures used by other researchers. A previously developed plate-beam model by Smith [Ref. 78] is used in the analysis.

In addition to the three different joint models employed for the prediction of the average angular wave transmission coefficients, a series of different SEA models were created for the analysis of the power flow. The SEA software code used to perform the analysis is PPC, an in-house analysis code developed at Heriot Watt University.

The 7 subsystem SEA model of the test structure in figure 5.1 is shown in figure 5.6. where each plate is modelled as supporting bending, longitudinal and transverse wavetypes, with each wavetype modelled as a subsystem. For plate 1, the bending wave subsystem is 1, the longitudinal wave subsystem is 1001 and the transverse wave

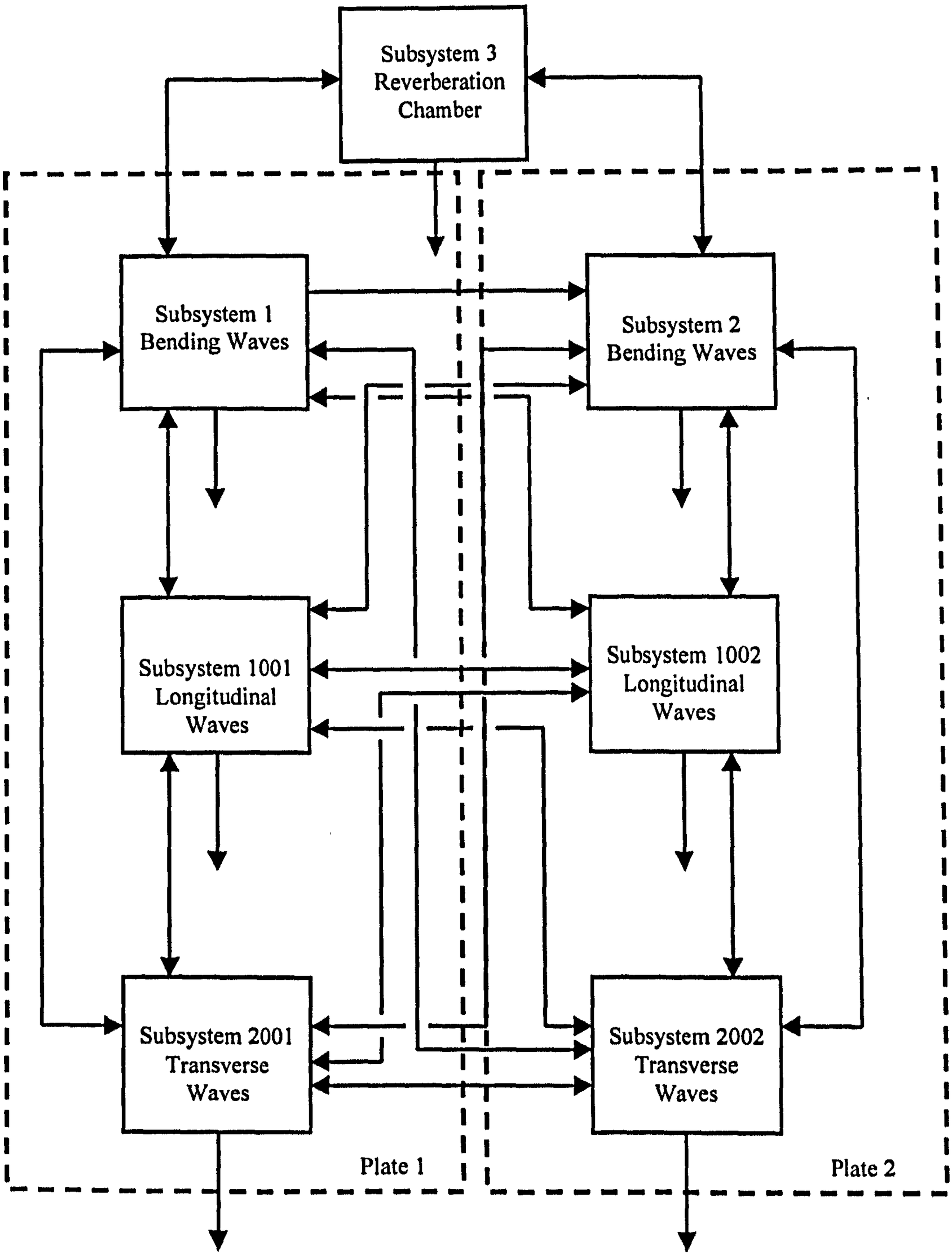

Figure 5.6 7 Subsystem SEA model of two plate test structure shown in figure 5.1

subsystem is 2001 and the subsystems on plate 2 are numbered in a similar manner. The reverberation chamber (subsystem 3) is only coupled to the bending wave subsystems 1 and 2 and the radiation efficiency and coupling loss factor from the plate to the chamber were calculated using equations *2.11*, *2.12* and *2.13*. As discussed in chapter 2, the radiation efficiency is based on the assumption of simply supported boundary conditions with multipliers for built-in edges. There will also be coupling between the longitudinal subsystem and the reverberation chamber subsystem due to the Poisson effect however this will be at least an order of magnitude lower than the coupling between the bending wave subsystems and the chamber subsystem and can be neglected. There will also be some nearfield radiation due to the hammer impacting on the plate, however this was calculated to be insignificant and is neglected.

Because the plate edges are supported on foam lined battens, the boundary conditions are assumed to be simply supported rather than clamped and the radiation multiplier, m, is assumed to be 1. Also, the plates are supported approximately 50 mm above the floor of the reverberation chamber and it is assumed that only one side of the plate is radiating to the reverberation chamber.

The 7 subsystem SEA model in figure 5.6 initially appears quite complex, however by removing the appropriate coupling terms between subsystems it can easily be reduced to a 2 subsystem or 3 subsystem model as required. For example to reduce the model to a 3 subsystem model all the coupling terms between the bending wave subsystems and the in-plane wave subsystems are removed leaving just the power flow between the bending wave subsystems 1 and 2 and the reverberation chamber 3.

5.3.1 Comparison of Predicted Coupling Loss factor

Before considering the experimental results the predicted coupling loss factor from the different modelling approaches will be discussed. In figure 5.7 the predicted coupling loss factor η_{12} is plotted in third octave frequency bands for the 406 x 178 beam for the three different modelling approaches. It can be seen that the full model and web model are in close agreement in most frequency bands. In contrast the predicted coupling loss

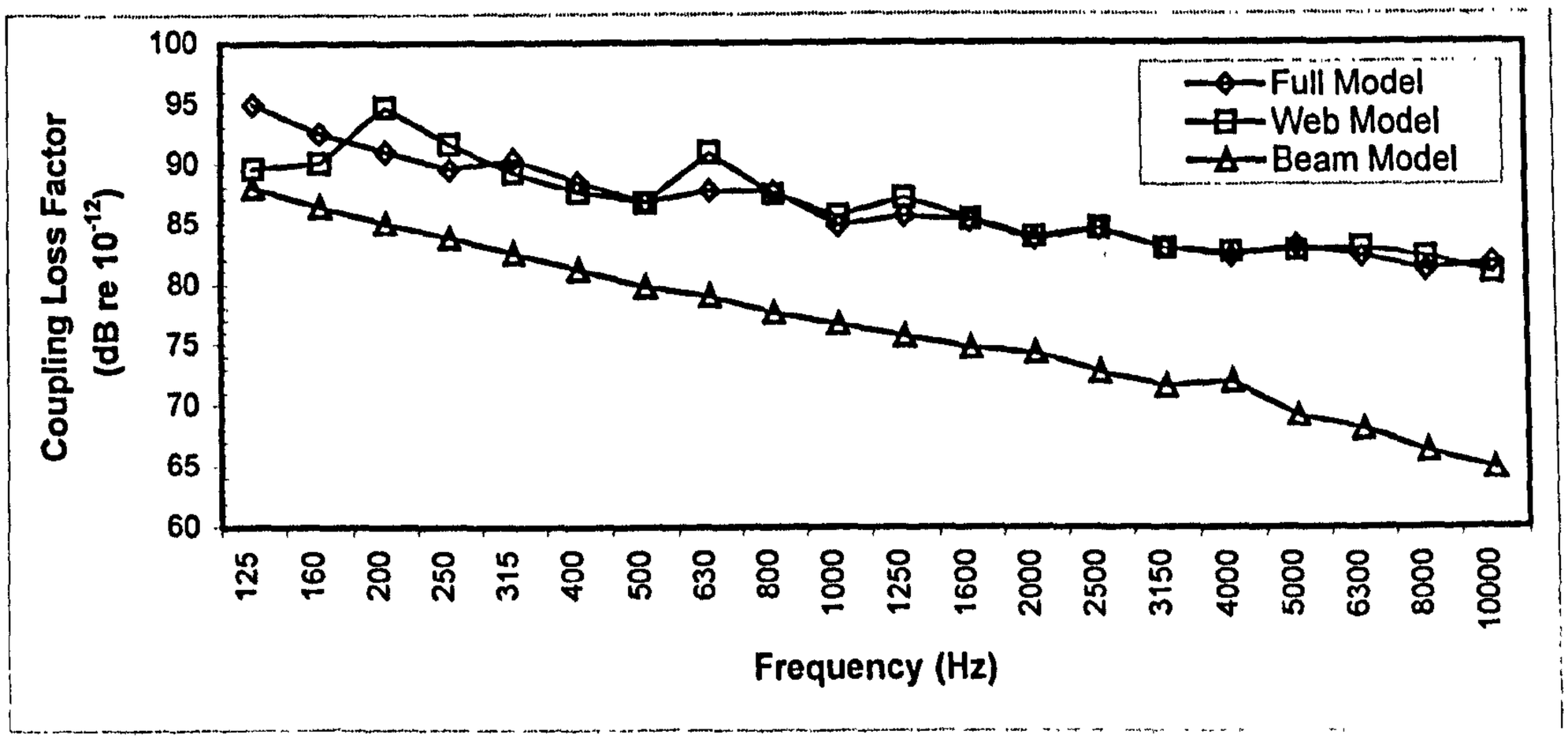

Figure 5.7 Predicted CLF η_{12} by different modelling approaches for 406 x 178 I-beam

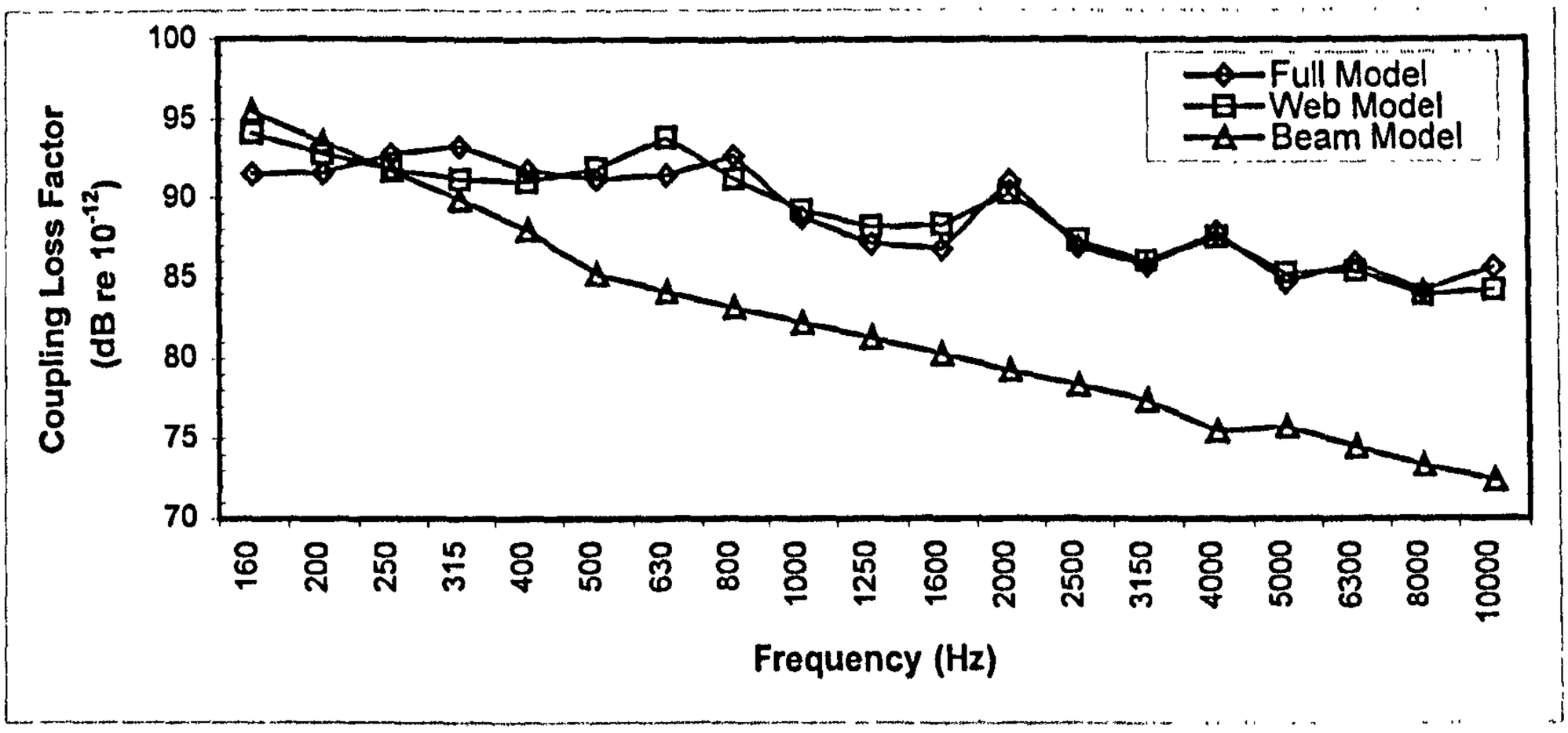

Figure 5.8 Predicted CLF η_{12} by different modelling approaches for 203 x 133 I-beam

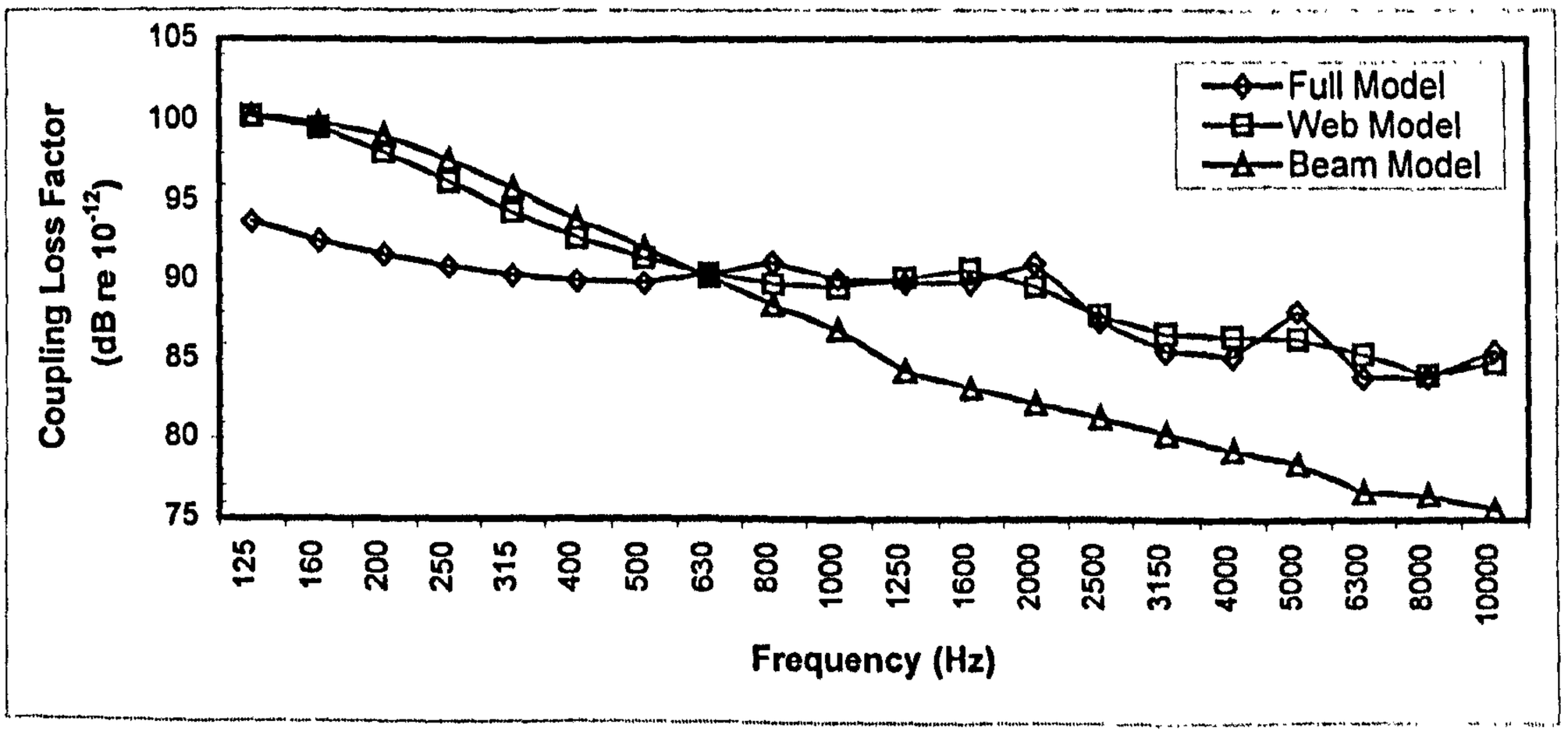

Figure 5.9 Predicted CLF η_{12} by different modelling approaches for 127 x 76 I-beam

factor from the beam model is significantly lower than the full frame model e.g. approximately 9 dB in the 125 Hz band and 19 dB in the 10 kHz band.

In figure 5.8 the predicted coupling loss factor η_{12} for the 203 x 133 I-beam is plotted for the three different modelling approaches. Again it can be seen that the full model and the web plate model are in good agreement over most of the frequency spectrum except at low frequencies. Between the 125 Hz band and the 315 Hz frequency bands the web plate model coupling loss factor shows agreement with the predicted coupling loss factor from the beam model. Above the 315 Hz frequency band, the predicted coupling loss factor from the beam model again diverges from the predicted coupling loss factor of the full model and the web plate model.

Figure 5.9 shows similar results for the 127 x 76 I-beam for the three different modelling approaches. For this small beam size it can be seen that the full model agrees with the web plate model between the 630 Hz and the 10 kHz frequency bands. However between the 125 Hz and 630 Hz frequency bands, the web model is very similar to the predicted coupling loss factor from the beam model.

There are two important points that arise from the modelling approach. The first is that the web model exhibits a clearly defined transition frequency above which it behaves as a plate, but below the transition frequency the web model behaves as a beam model. The second point is the flange plates are clearly shown to be significant and that the web plate model will not model the full behaviour of the frame. In figure 5.8, the transition frequency for the 203 x 133 I-beam occurs in the 315 Hz frequency band and if the frequency band results were extended below 125 Hz the transition frequency for the 406 x 178 I-beam would be found. When comparing the predicted acceleration level difference results the beam model results need only be considered for the small 127 x 76 I-beam size.

5.3.2 Subsystem Properties

In this section the basic subsystem properties of damping, statistical mode count and modal overlap are investigated for the bending wave subsystems of the two aluminium plates.

To prevent equi-partition of energy occurring the damping of the receiving subsystem in the tests was artificially increased by the addition of sand filled bags at the plate edges. Because of this the damping must be measured to allow a value of total loss factor to be added to the receiving subsystem. Figure 5.10 shows the measured internal loss with and without damping treatment on the plates, and it can be seen that the addition of the sand bags significantly increases the total loss factor of plate 1 and 2. The total loss factor of the undamped aluminium plates was measured in an anechoic chamber, and therefore the total loss factor is due to the internal damping of the aluminium plates and the power radiated to the environment. The increase in the 3 mm and 6 mm curves at 2 kHz and 4 kHz coincides with the critical radiation frequency for the 6 mm plate predicted to occur at 2015 Hz and at 4030 Hz for the 3 mm plate. It can be seen that the effect of the sandbags is to increase the low frequency damping of the aluminium plates by 10 to 17 dB in the 125 Hz to 1600 Hz frequency bands. A line fit was applied to the total loss factor of the damped aluminium plates for input to the SEA models.

Figure 5.11 shows the predicted statistical bending mode count N for the 6 mm plate and the 3 mm plate using equations *2.29* and *2.34* from chapter two. Plate 2 being thinner has the twice the number of modes of plate 1 and the mode count on plate 1 is between 2 and 6 modes per frequency band below 500 Hz. As discussed in chapter 2 a reasonable mode count is not sufficient to guarantee the low frequency limit of the SEA model.

Using the total loss factor and equation *2.38* from chapter two, the modal overlap M for plates one and two has been calculated. The modal overlap M is plotted between the 125 Hz and 10 KHz third octave frequency bands for the two plates in figure 5.12 and

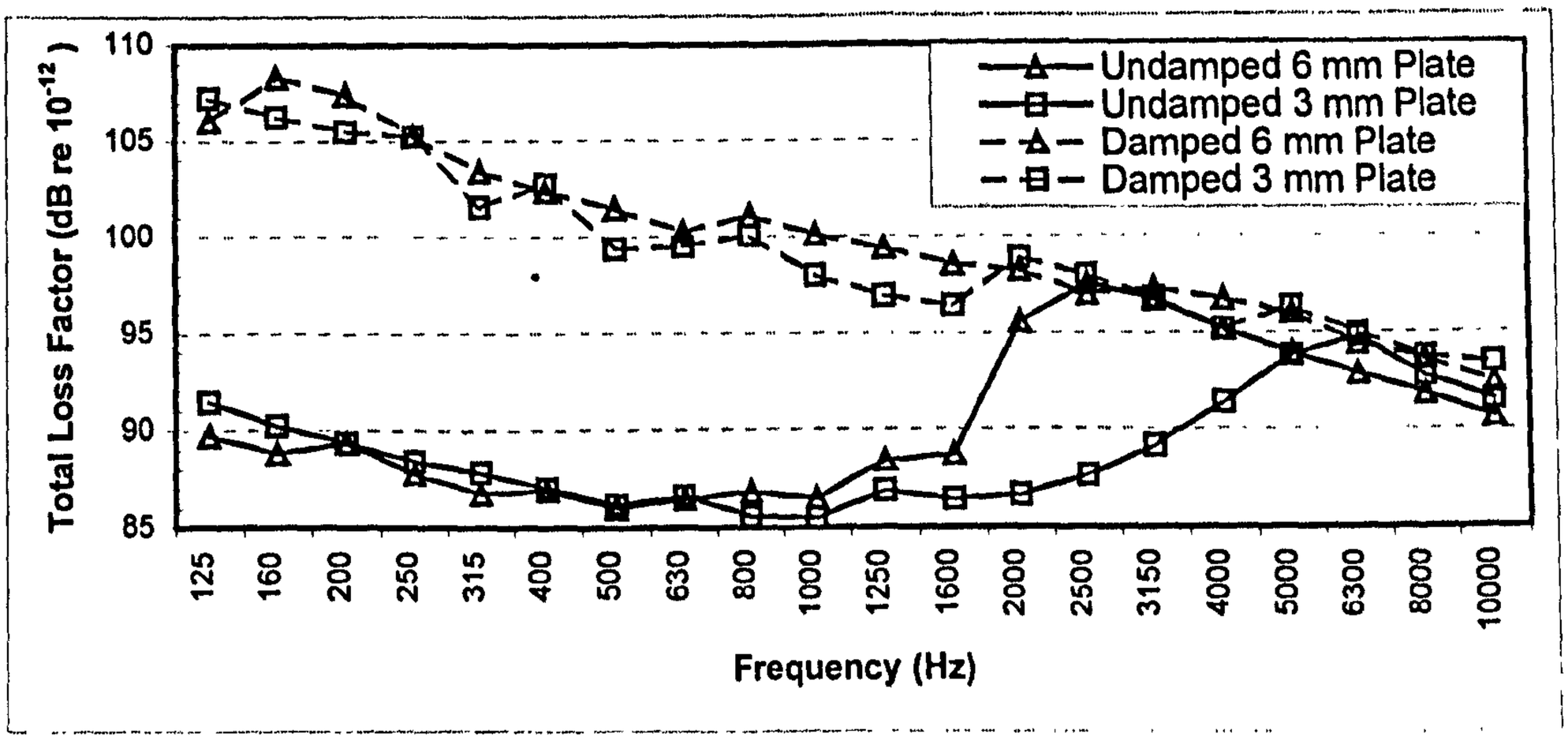

Figure 5.10 Comparison of measured damped and undamped TLF of plates 1 and 2

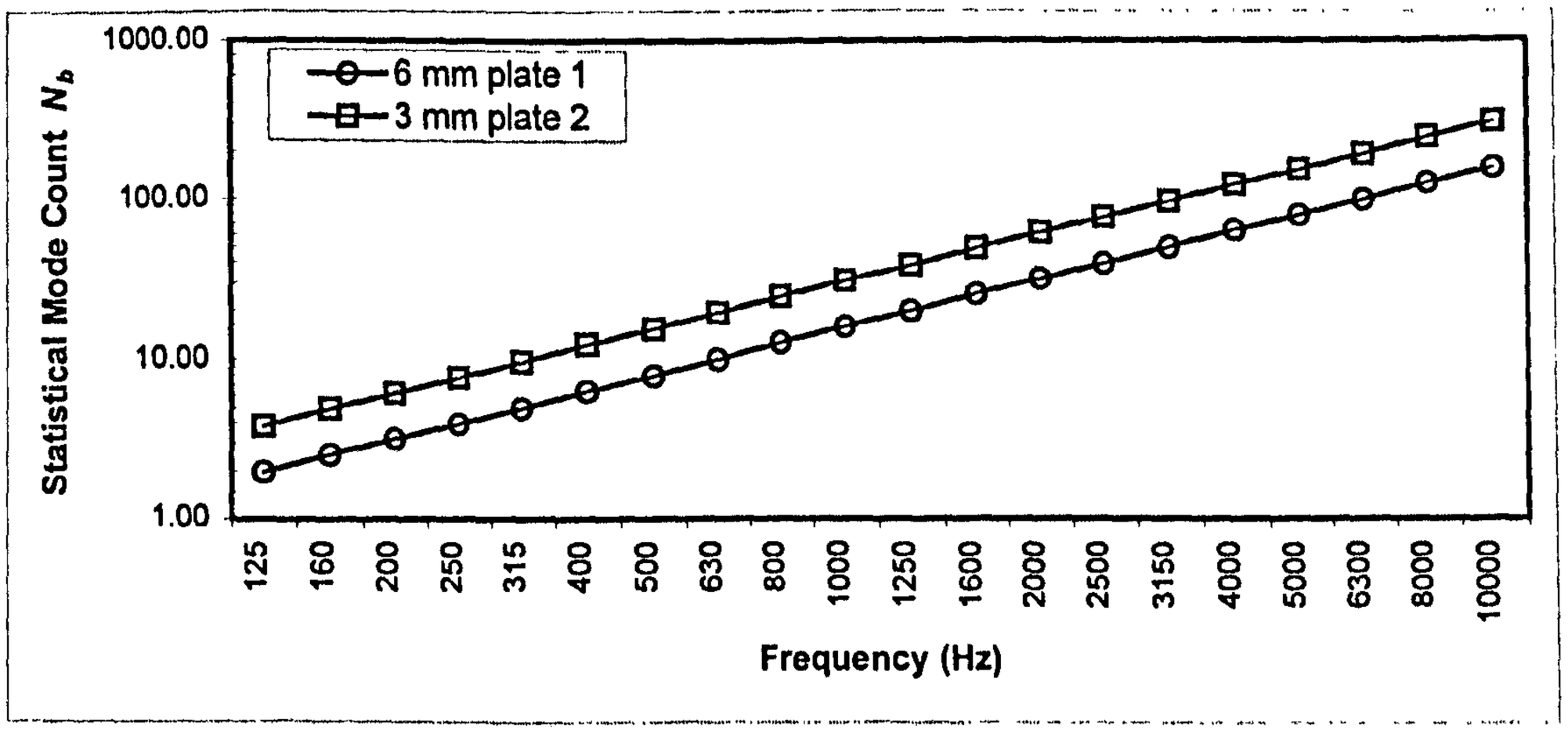

Figure 5.11 Predicted statistical mode count – plate 1 and plate 2

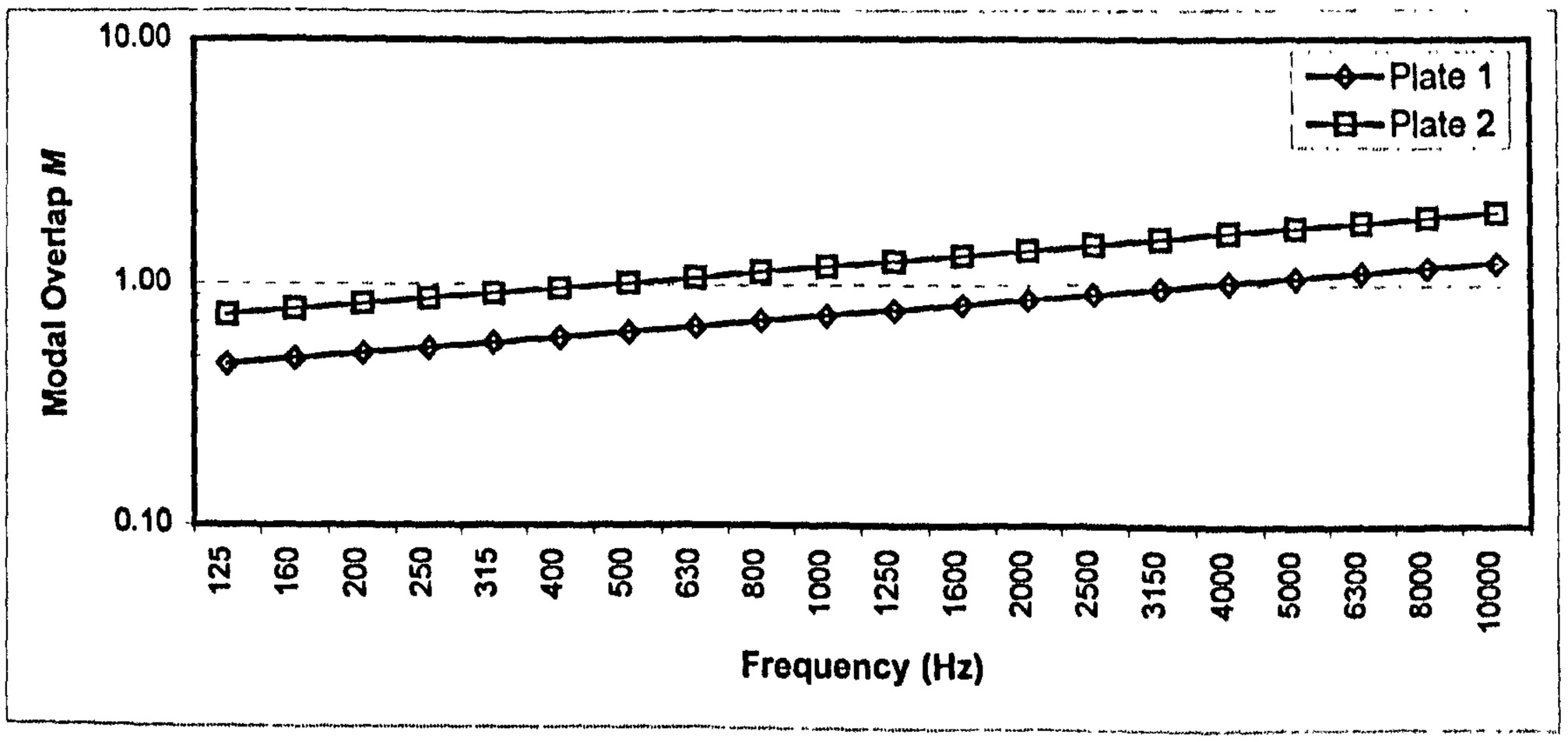

Figure 5.12 Predicted modal overlap plate 1 and plate 2

it can be seen that for plate two the modal overlap is above unity in the 400 Hz frequency band but for plate 1 the modal overlap does not rise above unity until the 4000 Hz frequency band. As discussed in chapter two, section 2.3, the modal overlap provides a measure of the low frequency limit for the SEA prediction and as M decreases below unity the accuracy of the SEA model decreases. The problem here is that even with a reasonably high number of resonant number of modes per frequency band, the low level damping of the aluminium and low modal density results in a low modal overlap, which is the problem with plate 1. This is different to building structures where there can be a low number of resonant modes per frequency band but the higher damping of building materials results in satisfaction of the modal overlap condition. Craik [Ref. 37] for instance has shown that two modes per frequency band in building structures is all that is required to achieve modal overlap of unity. It is therefore expected that because of the low modal overlap that the accuracy of the SEA predictions will show poorer agreement with the measured acceleration level difference in the low frequency bands.

5.3.3 Comparison of Predicted and Measured Acceleration Level Difference

In figure 5.13 the predicted and measured acceleration level difference for the 127 x 76 I-beam is shown for power input to plate 1 and in figure 5.14 for power input to plate 2. The predicted acceleration level differences are from the full plate model, the web model and the beam model. It can be seen that the predicted acceleration level difference from the full plate model shows good agreement with the measured results from 125 Hz to the 10 kHz frequency band. As predicted from the examination of the coupling loss factors the acceleration level differences for the web plate model shows good agreement with the full plate model between 630 the Hz and 10 kHz frequency bands but from 125 Hz to 630 Hz the web plate model and the beam model give poor agreement. At all frequencies it can be seen that the beam model gives very poor agreement and it can be discounted as a modelling approach for I-beams.

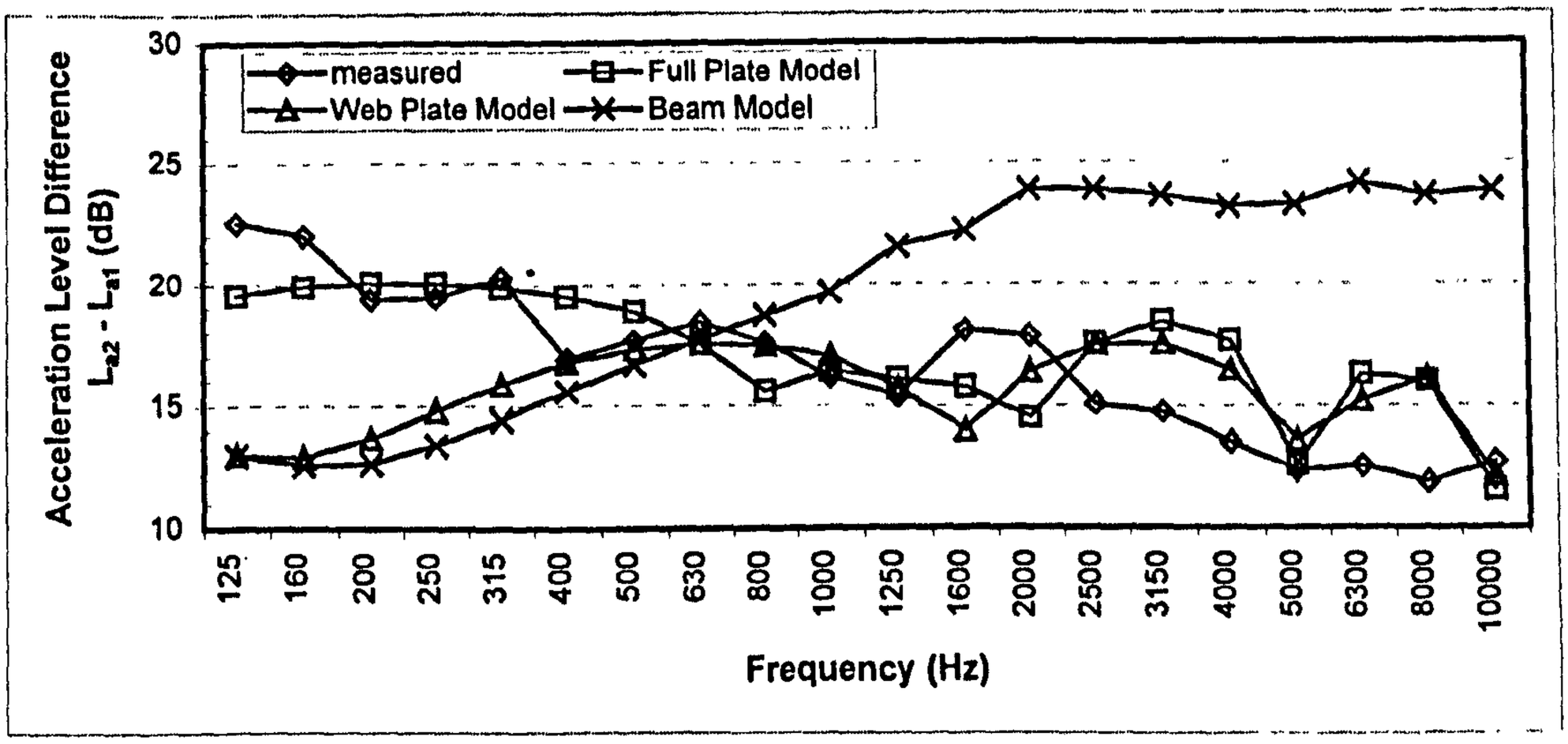

Figure 5.13 Comparison of predicted and measured ALD for 127 x 76 beam

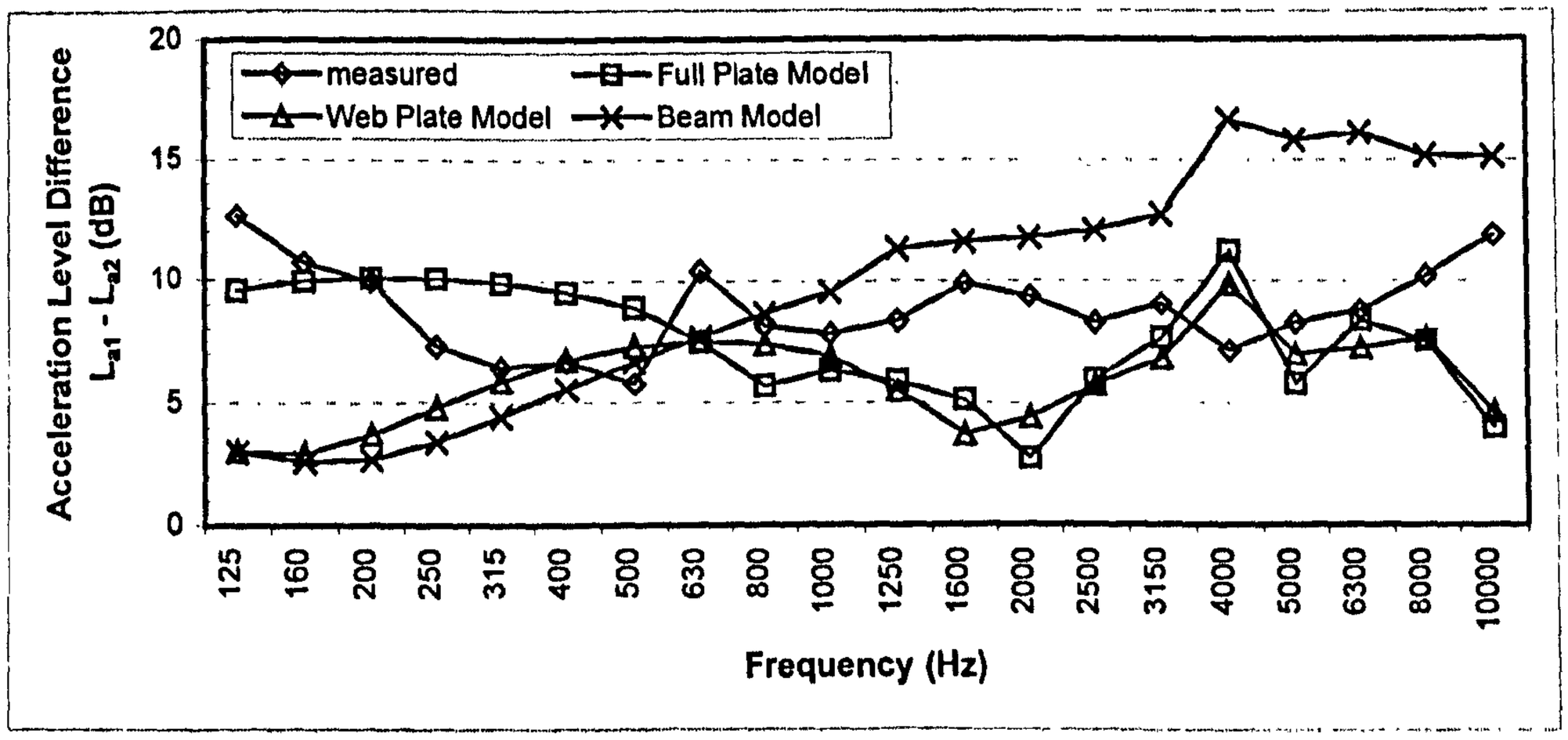

Figure 5.14 Comparison of predicted and measured ALD for 127 x 76 beam

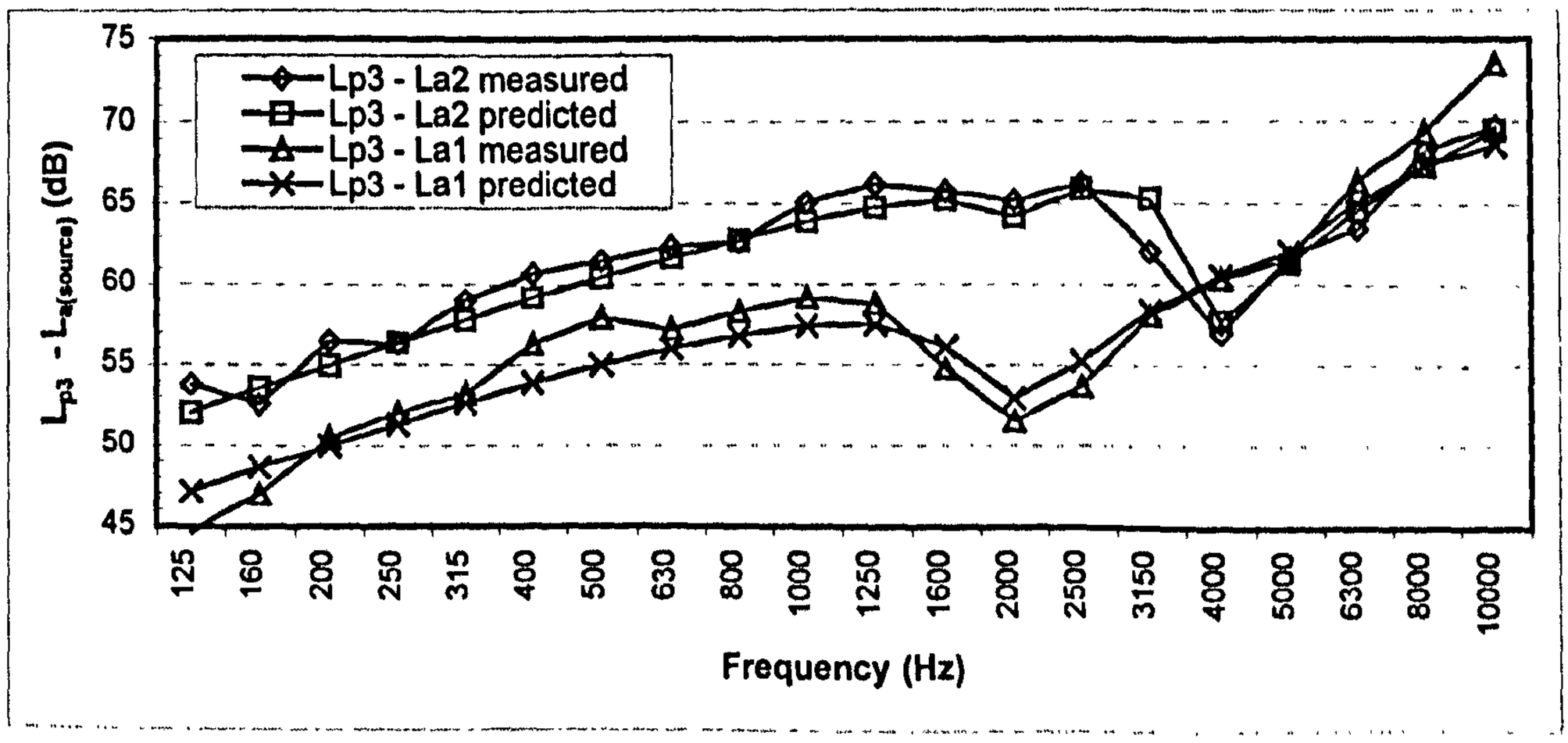

Figure 5.15 Comparison of the predicted and measured difference between the sound pressure level and the acceleration level for the 127 x 76 beam

In figure 5.15 the predicted and measured difference between the sound pressure level (L_p *dB re 20μPa)* of the reverberation chamber and the acceleration level (L_a *dB re* 10^{-6} ms^{-2}) of the plate is shown. The results are presented for plate 1 and for plate 2 as the source subsystem. It can be seen that the predicted and measured results show excellent agreement over the frequency spectrum which shows that the assumptions made regarding the plate boundary conditions, the radiation multiplier and the surface area coupled to the reverberation chamber are correct. The acoustic coupling loss factor is of a similar order of magnitude as the structural coupling loss factor.

In figure 5.16 the predicted and measured acceleration level difference for the 203 x 133 I-beam is shown for power input to plate 1 and in figure 5.17 for power input to plate 2. The predicted results for the full plate model and web model are in close agreement over the frequency spectrum however when compared with the measured results in the 125 Hz to 315 Hz frequency bands the agreement is poorer. The dips in the predicted acceleration level difference in the 630/800 Hz, 2 kHz, 4 kHz and 6.3 kHz frequency bands are where wave matching is predicted to occur for the 203 x 133 beam as discussed previously in chapter four.

In Figure 5.18 the predicted and measured difference between the sound pressure level, (L_p *dB re 20 μPa)*, of the reverberation chamber and the acceleration level (L_a *dB re* 10^{-6} ms^{-2}) of the plate is shown. The results are presented for plate 1 and for plate 2 as the source subsystem. Again it can be seen that the predicted and measured results show excellent agreement over the frequency spectrum indicating the assumptions regarding the coupling between the plates and the chamber are correct.

In figure 5.19 the predicted and measured acceleration level difference for the 406 x 178 I-beam is shown for power input to plate 1 and in figure 5.20 for power input to plate 2. The predicted results for the full plate model and web plate model are in close agreement over the entire frequency spectrum. The effect of the excitation of the wave matching with the I-beam is not so obvious as seen previously in the 127 x 76 and 203 x 133 I-beams. This is because the 406 x 178 beam has many more wave matching frequencies and consequently the effect of the wave matching on the transmission does

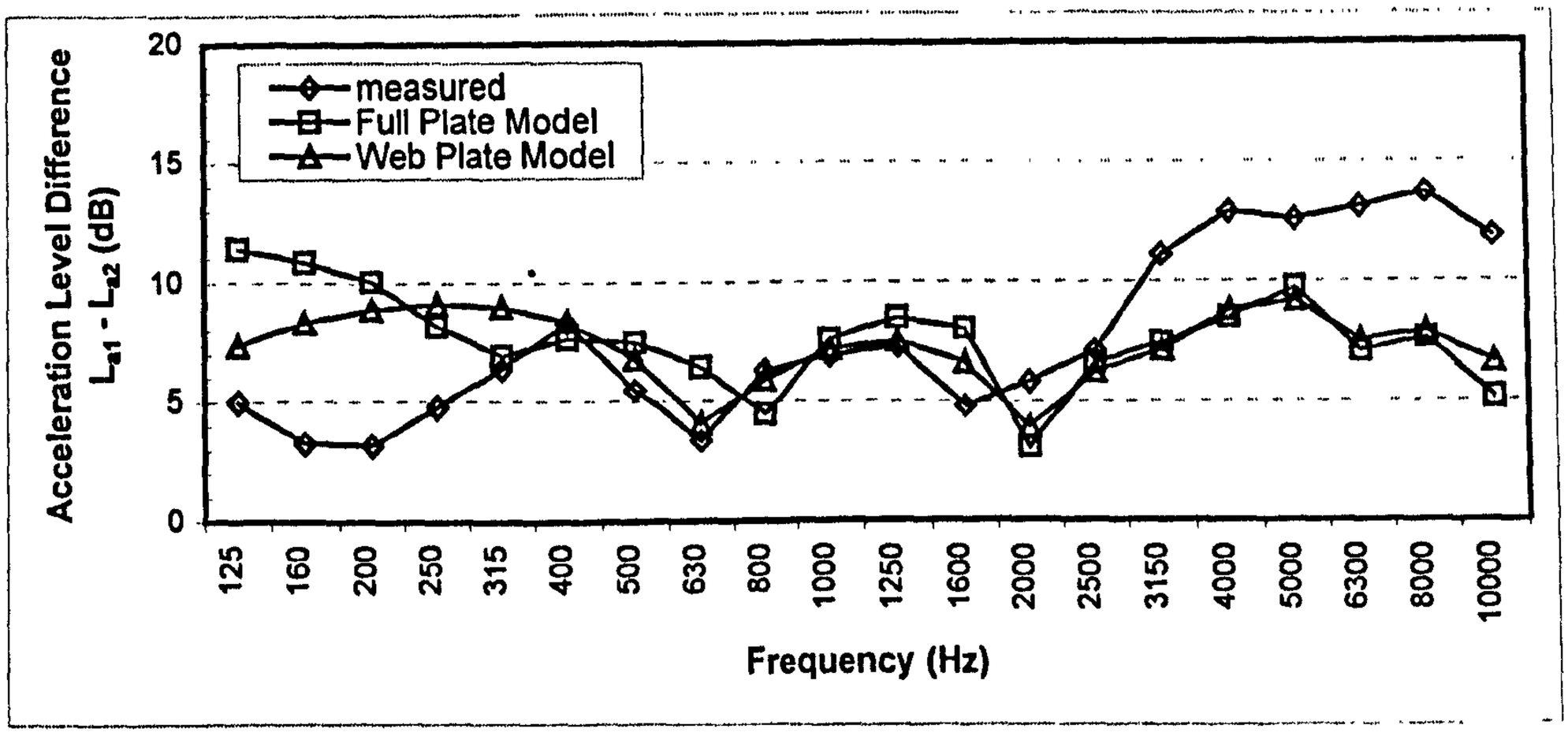

Figure 5.16 Comparison of predicted and measured ALD for 203 x 133 beam

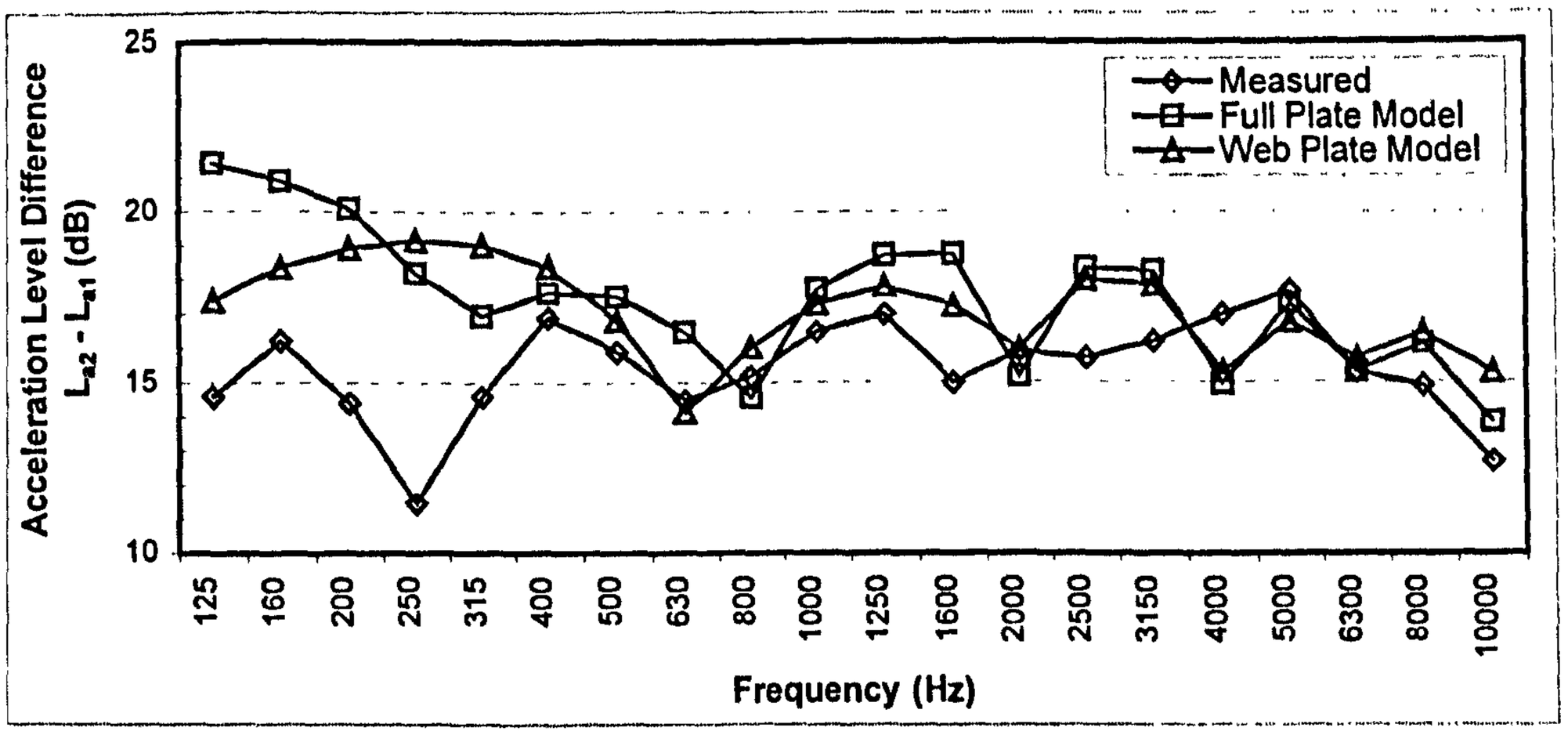

Figure 5.17 Comparison of predicted and measured ALD for 203 x 133 beam

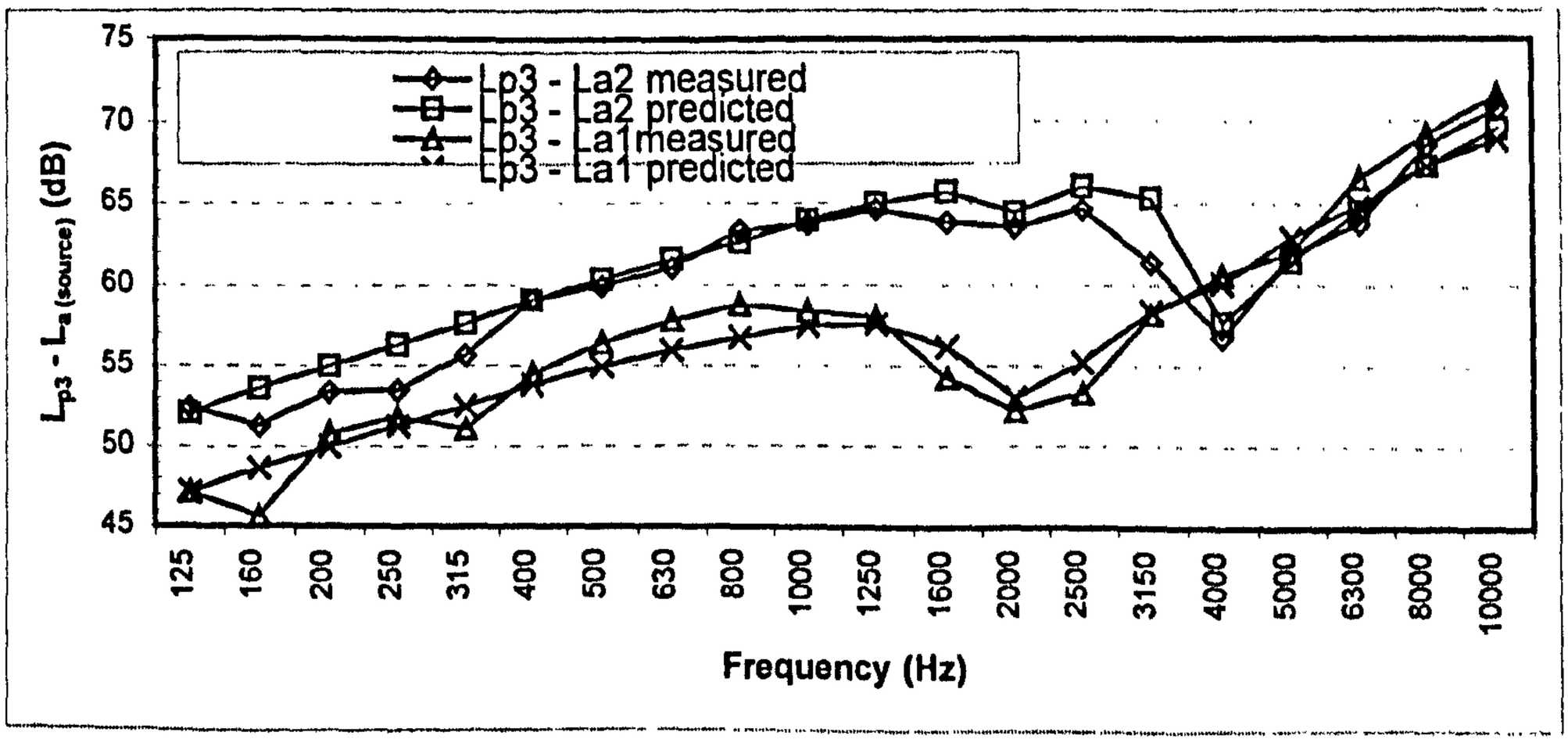

Figure 5.18 Comparison of the predicted and measured difference between the sound pressure level and the acceleration level for the 203 x 133 beam

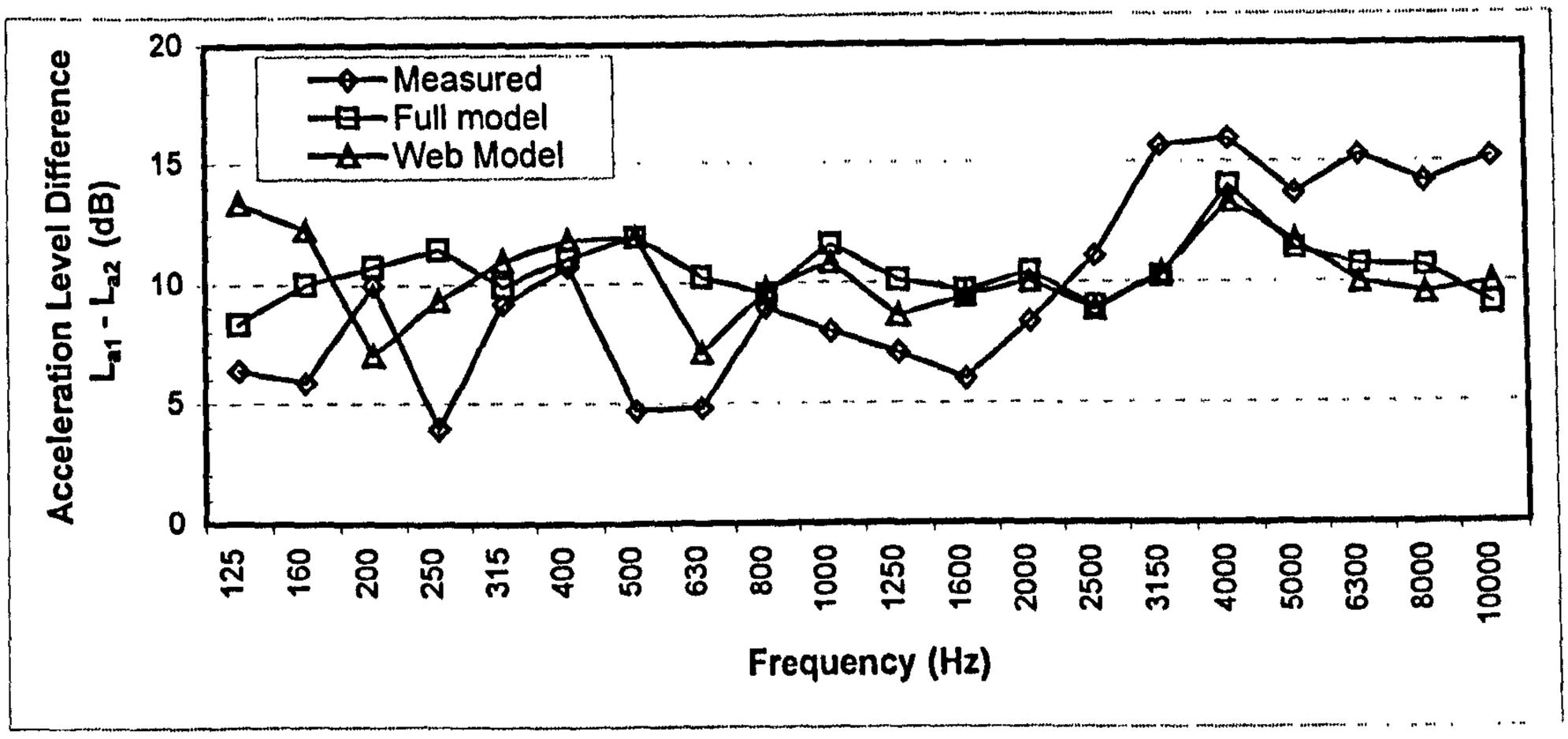

Figure 5.19 Comparison of predicted and measured ALD for 406 x 178 beam

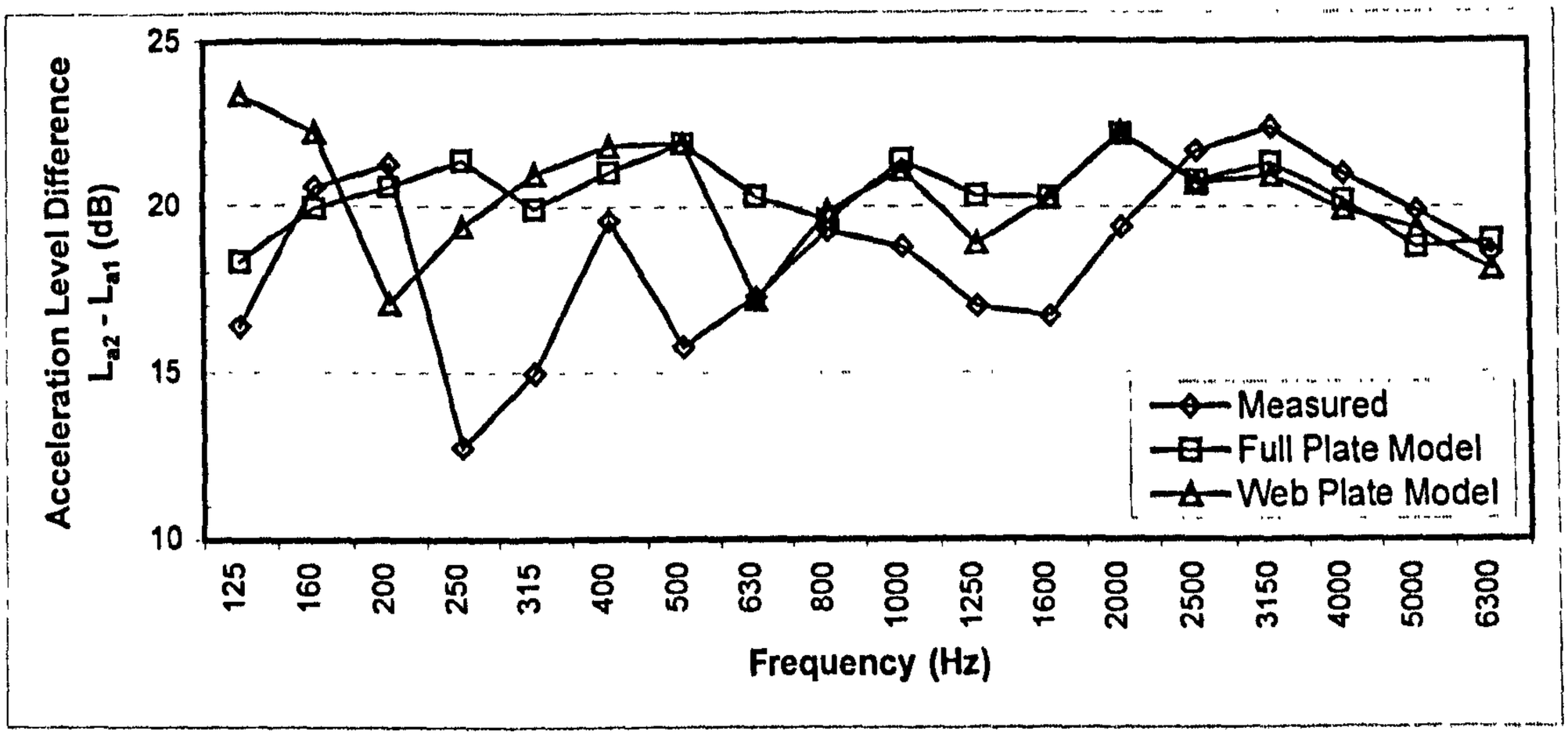

Figure 5.20 Comparison of predicted and measured ALD for 406 x 178 beam

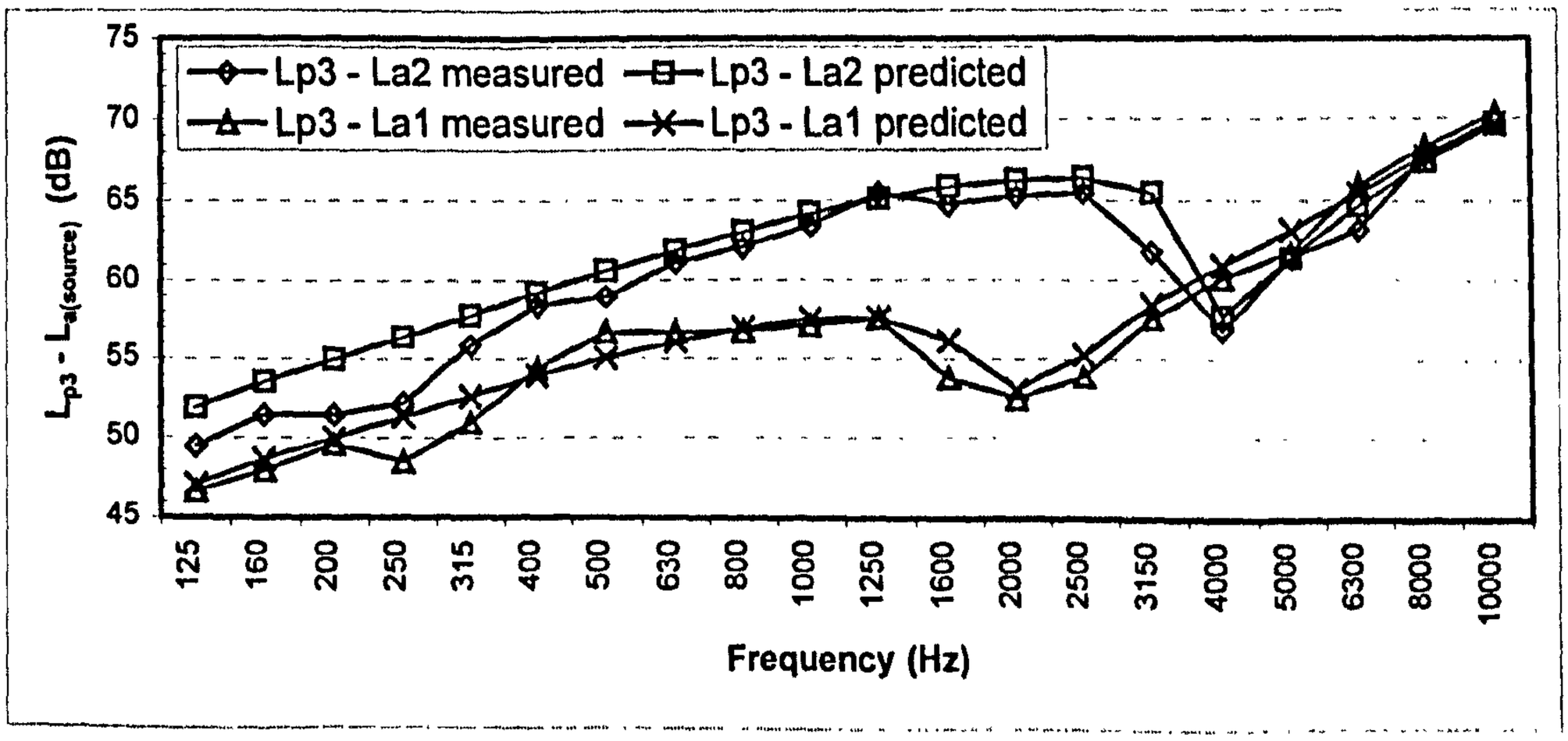

Figure 5.21 Comparison of the predicted and measured difference between the sound pressure level and the acceleration level for the 406 x 178 beam

not stand out. This is confirmed from the coupling loss factor curves in figure 5.9 and it can be seen that there are no distinct peaks. The predicted and measured acceleration level differences show reasonably good agreement over most of the frequency spectrum except in the 125 Hz to 500 Hz frequency bands where the low modal overlap exists.

In figure 5.21 the predicted and measured difference between the sound pressure level, L_p, of the reverberation chamber and the acceleration level of the plate is shown. The results are presented for plate 1 and for plate 2 as the source subsystem. It can be seen that the predicted and measured results show excellent agreement over the frequency spectrum.

5.3.4 Discussion

For the results presented here it is possible to conclude at this point that the use of a beam subsystem to represent the frame stiffener is inappropriate and a plate representation is more accurate. It is however not possible to determine at this stage which of the two modelling approaches, full plate or web plate model give the more accurate prediction, though it would be expected that the full model would be better.

From the SEA models of the different beam sizes it can be seen that good agreement is generally seen between the measured and predicted vibration level above the 400 Hz frequency band. This is the frequency where the modal overlap of the bending wave subsystem rises above unity for plate 2. Below 400 Hz it can be seen that there can be quite large fluctuations in the measured vibration level with which the SEA models do show good agreement. The large fluctuations in the vibration level are indicative that the experimental structure is not truly multi-modal in these frequency bands and therefore the modal overlap is a good indicator of the low frequency limit, in this instance 400 Hz.

For the 203 x 133 and 406 x 178 beams it can be seen in figures 5.17 and 5.20 for the source on plate 1 that there is good agreement in the 2 kHz to 10 kHz frequency bands between the measured and predicted vibration level. For the source on plate 2 the results

in figure 5.16 and 5.19 are not quite as good in the 2 to 10 kHz frequency bands. For simplicity the measured internal loss factor from plate 2 was used in all SEA models and it is this that causes the poorer agreement in the results for the source on plate 2.

5.4 Complex Laboratory Structure

The previous section validated the accuracy of the theoretical model developed in section 4.2 for predicting the structure borne noise transmission across simple hull frame structures by comparison with simple experimental models. Whilst the ability to predict structure borne noise transmission across one joint is useful, a ship is a large complex structure with thousands of joints and a number of different joint types e.g. tee joint, corner joint, cross joint etc. It is therefore much more important to be able to predict vibration transmission for this situation and this is the ultimate objective. The next stage then is to examine a larger structure, with a variety of joint types and a large number of joints and subsystems but in a controlled laboratory environment.

An isometric view of the large experimental structure used in the laboratory is shown in figure 5.22. The structure is a large steel tank originally designed as a water filled wave tank to test models of offshore structures. The tank is constructed from plates bolted to steel I-beams which are welded together to form frames which are distributed at regular intervals along the tank length. The tank is approximately 14 metres long, 2.4 metres high and 1.83 metres wide. The side plates are approximately 1.22 m x 2.4 m and the bottom plates are approximately 1.22 m x 1.83 m. and all are 6 mm thick steel plate. The internal steel bulkhead is 8 mm thick steel plate and has dimensions 1.83 m x 2.4 m. There are also two 10 mm thick polycarbonate plates which are approximately 1.22 m x 2.4 m and were originally installed as viewing windows. These are located on the south side of the tank as shown in figure 5.22. Each end of the tank has a hydraulic ram mechanism used to drive large hinged plate for the production of waves when the tank is filled with water, however during testing all wavemaking machinery was switched off.

Figures 5.23 shows an end elevation of the tank structure which is constructed from two plates. Figure 5.24 shows the front elevation and figure 5.25 shows a plan view of the

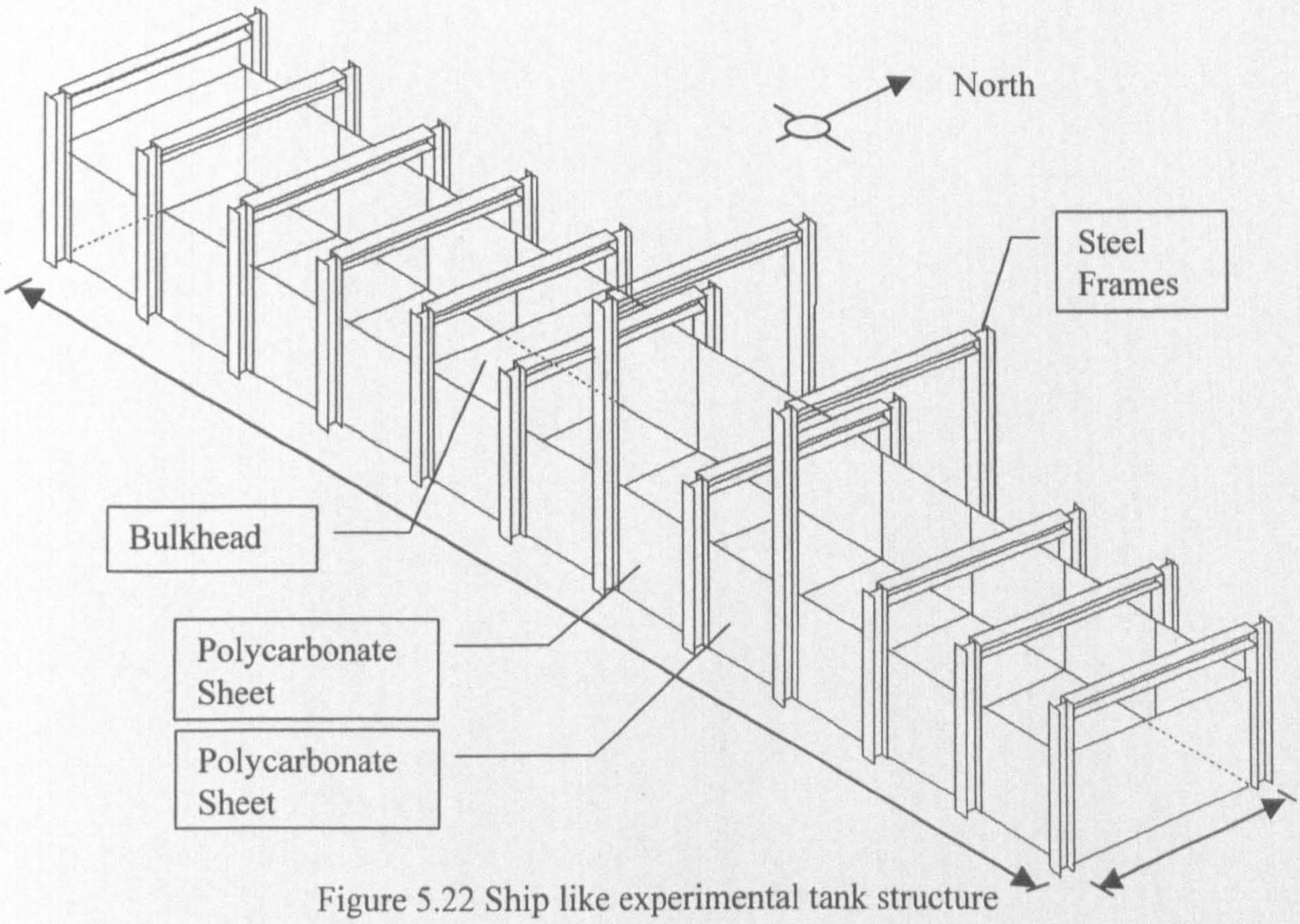

Figure 5.22 Ship like experimental tank structure

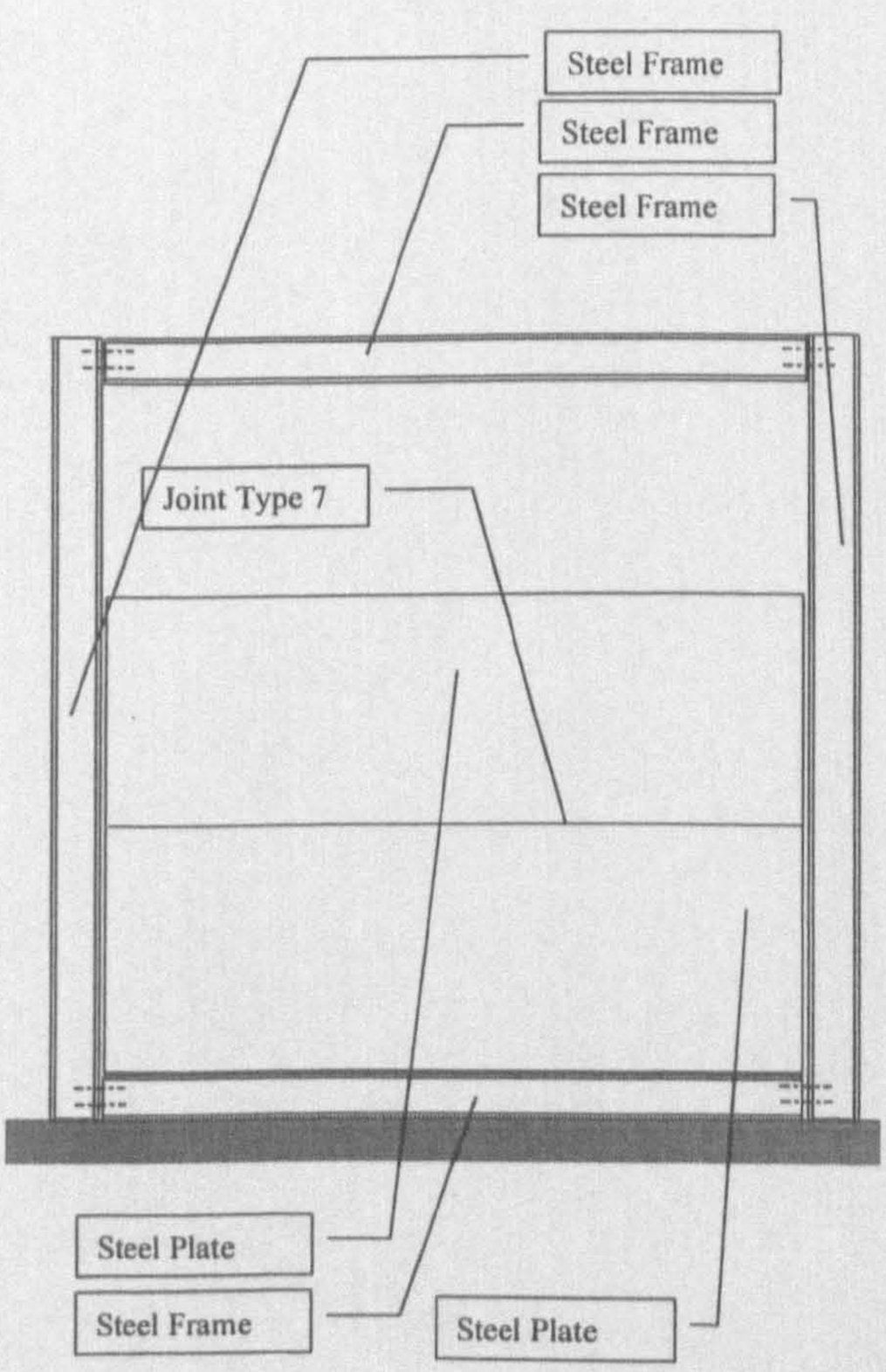

Figure 5.23 End elevation -tank end plates. View from west

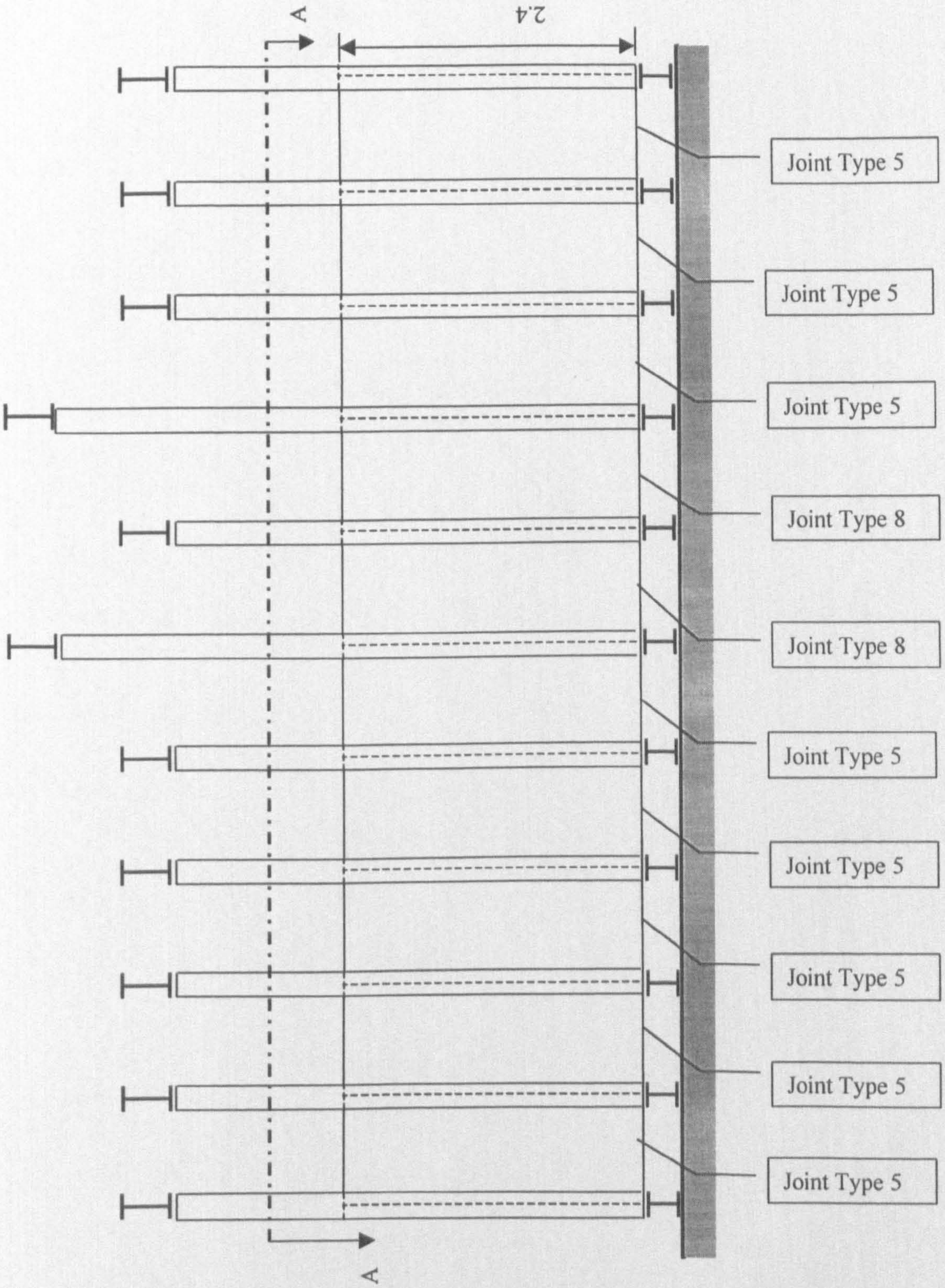

Figure 5.24 Front elevation: view looking north to tank structure

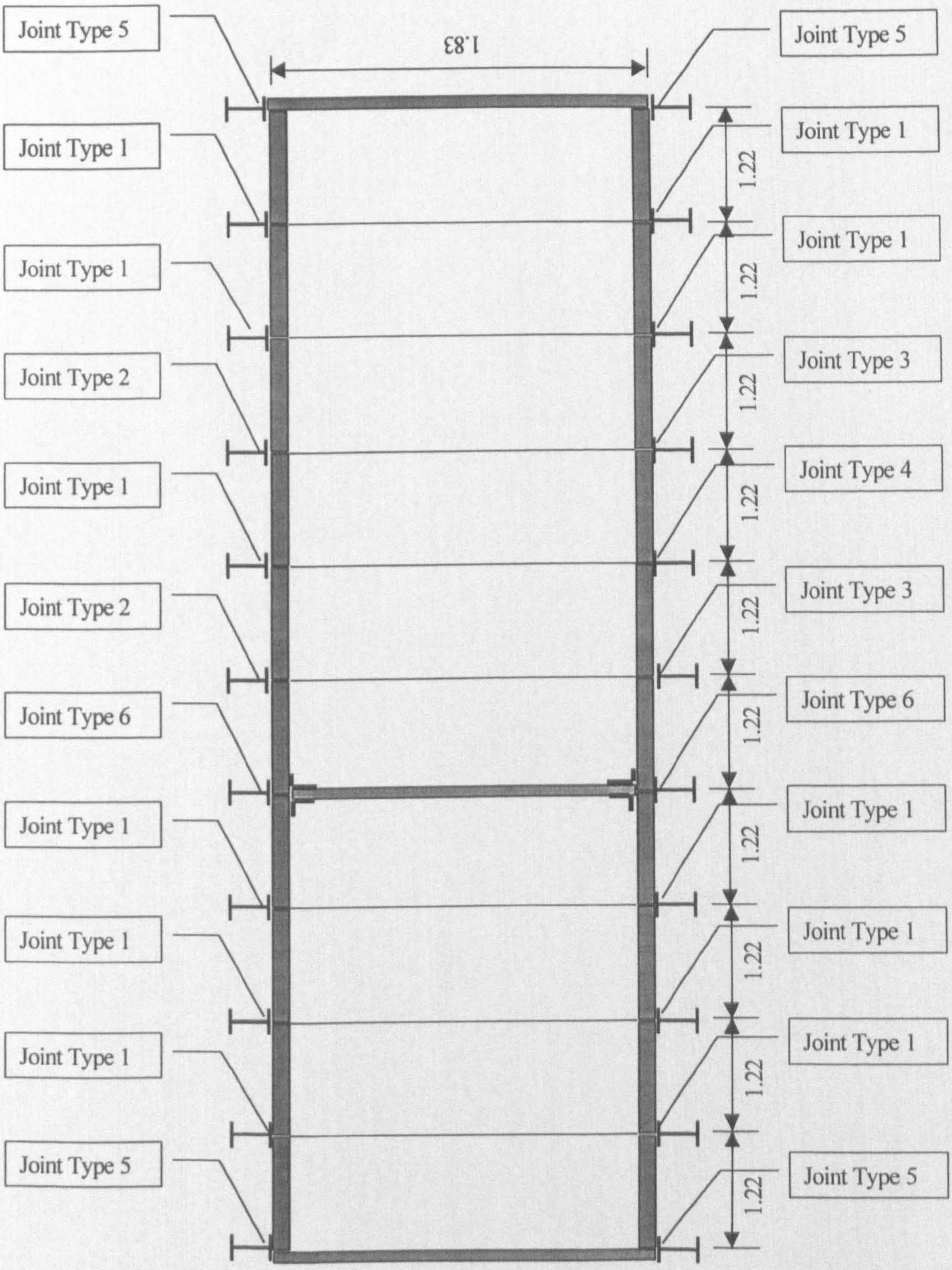

Figure 5.25 Tank structure: plan view on AA (Ref. Fig 5.24)

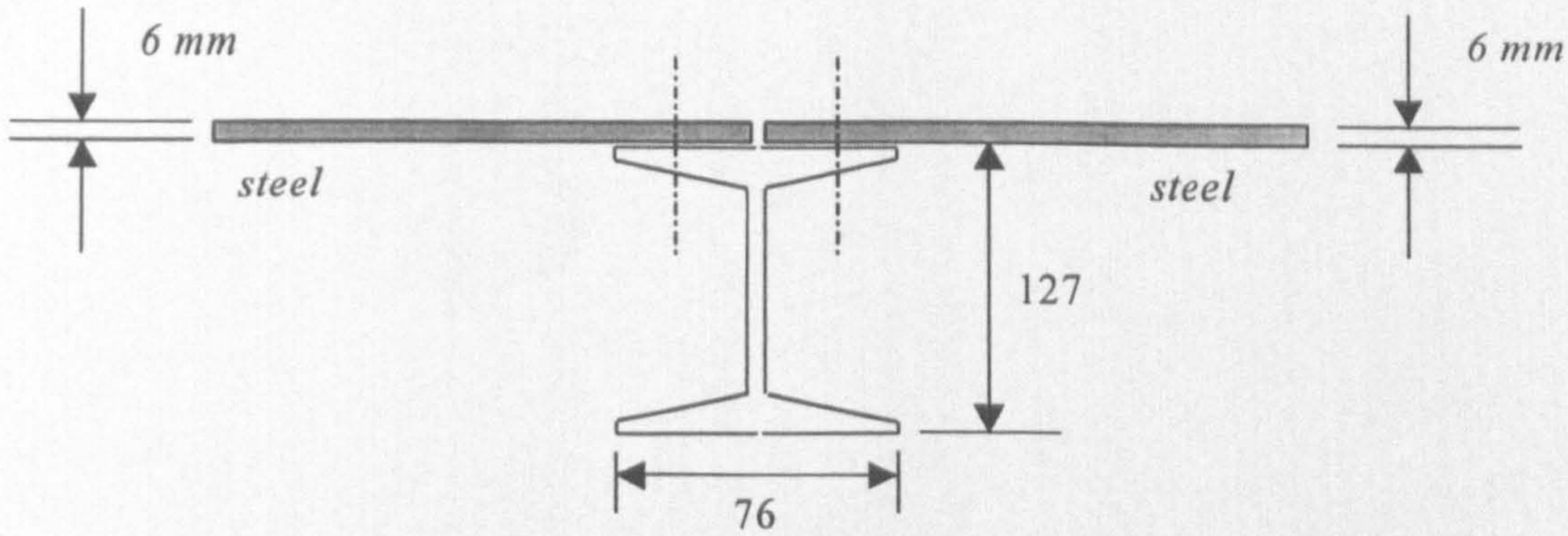

Joint type 1 - hull frame joint

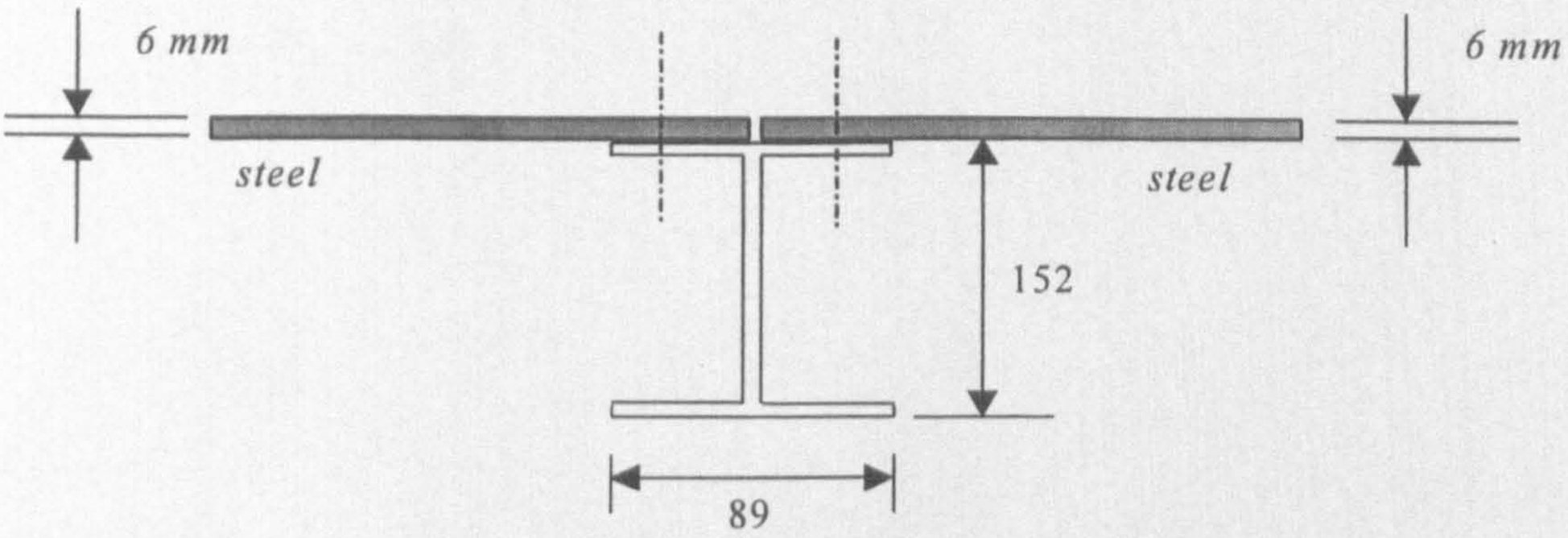

Joint type 2 - hull frame joint

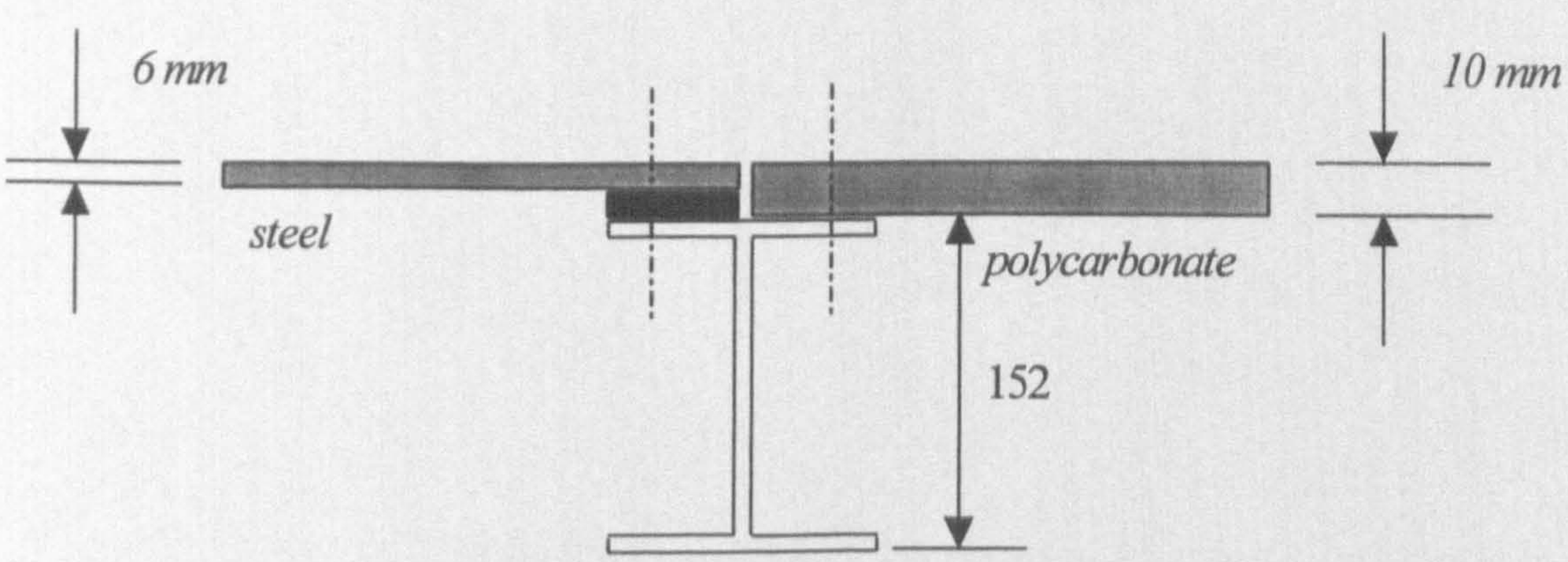

Joint type 3 - hull frame joint

Joint type 4 – hull frame joint

Figure 5.26 tank frame joint types

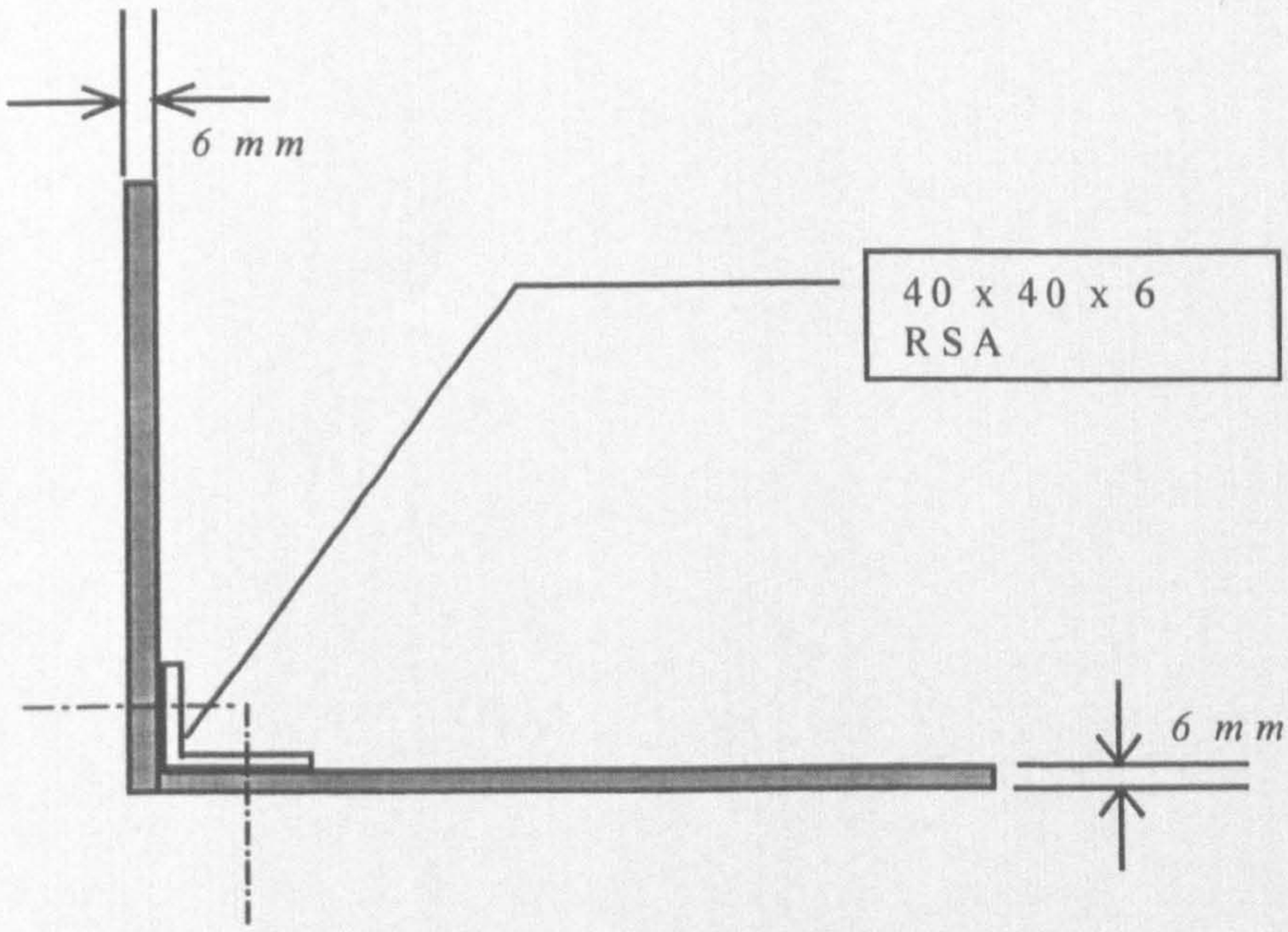

Joint type 5 – tank corner joint

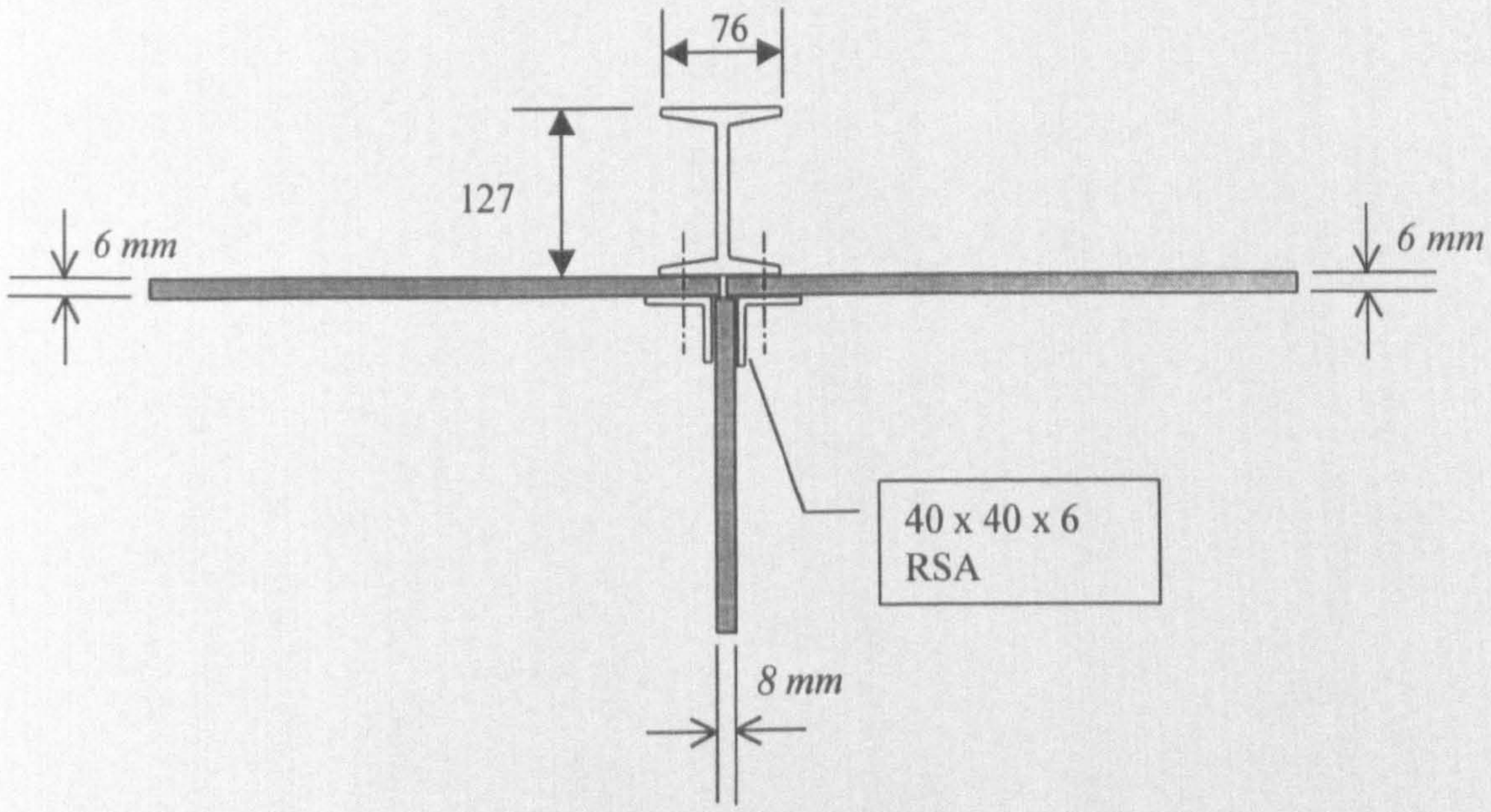

Joint type 6 – tee joint

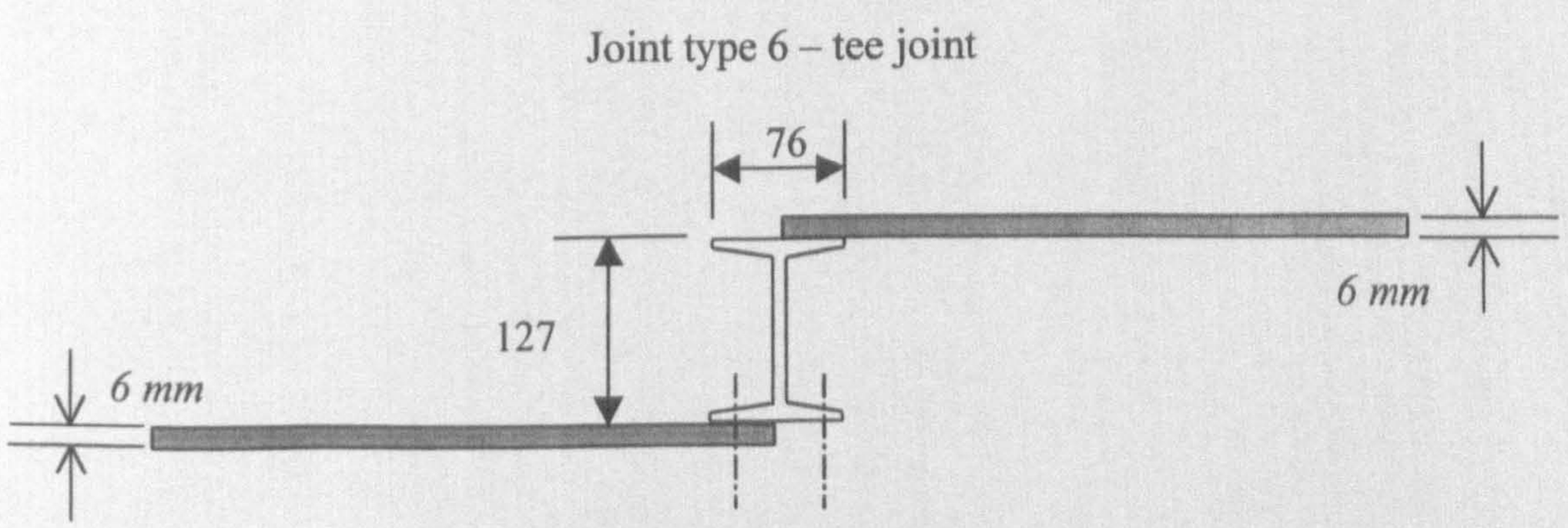

Joint type 7

Figure 5.27 tank joint types

tank structure. In figures 5.23 to 5.25 the different joint types used in the tank construction are identified i.e. Joint type 1, Joint type 2, etc. The joints of the tank can be classified into tee-joint, corner joint and hull frame joint which are representative of the joints found in ship construction. The details of the individual joint construction found in the tank structure are shown in figures 5.26 and 5.27. It can be seen that the hull frame joints shown in figure 5.26 are of the same construction as discussed in the previous section. The only difference is in joint type 3 where the two plates have a different thickness and a 4 mm thick steel packing plate has been inserted between the side plate and flange. However there are only two joints of this type in the tank structure and therefore this joint variation should not prove critical.

The tank is constructed from a total of forty three plates with seventy six joints. All frames of the tank are constructed with 127 x 78 RSJ sections to which the side and bottom plates are bolted except at the polycarbonate plates where 152 x 120 I beams are used. The bolt size was M10 with a 150 mm pitch and this is identical to that used in the simple laboratory tests with the aluminium plates. Because the polycarbonate plates do not have the bending strength of the steel plates, to withstand the hydrostatic pressure when the tank is filled with water a reinforcing steel frame was added to increase the bending stiffness of the plate. Details of the framework are not presented.

The corner joints between the side and bottom plates and the side and end plates are formed by bolting the plates to an RSA section. The behaviour of this bolted joint was verified using the aluminium plates and an RSA section in the procedure outlined previously in section 5.2. This was again done to verify that the bolted corner joint acted as a continuous line contact, rather than a series of point contacts at the bolted connections. Good agreement was found between the measured and predicted attenuation proving that the bolted joint behaved as a continuous line contact, though the results are not presented here.

5.5 Measurement Surveys of Complex Laboratory Structures

A large number of vibration measurement surveys were conducted on the tank structure and some of the results are presented in this section. Each plate of the structure was

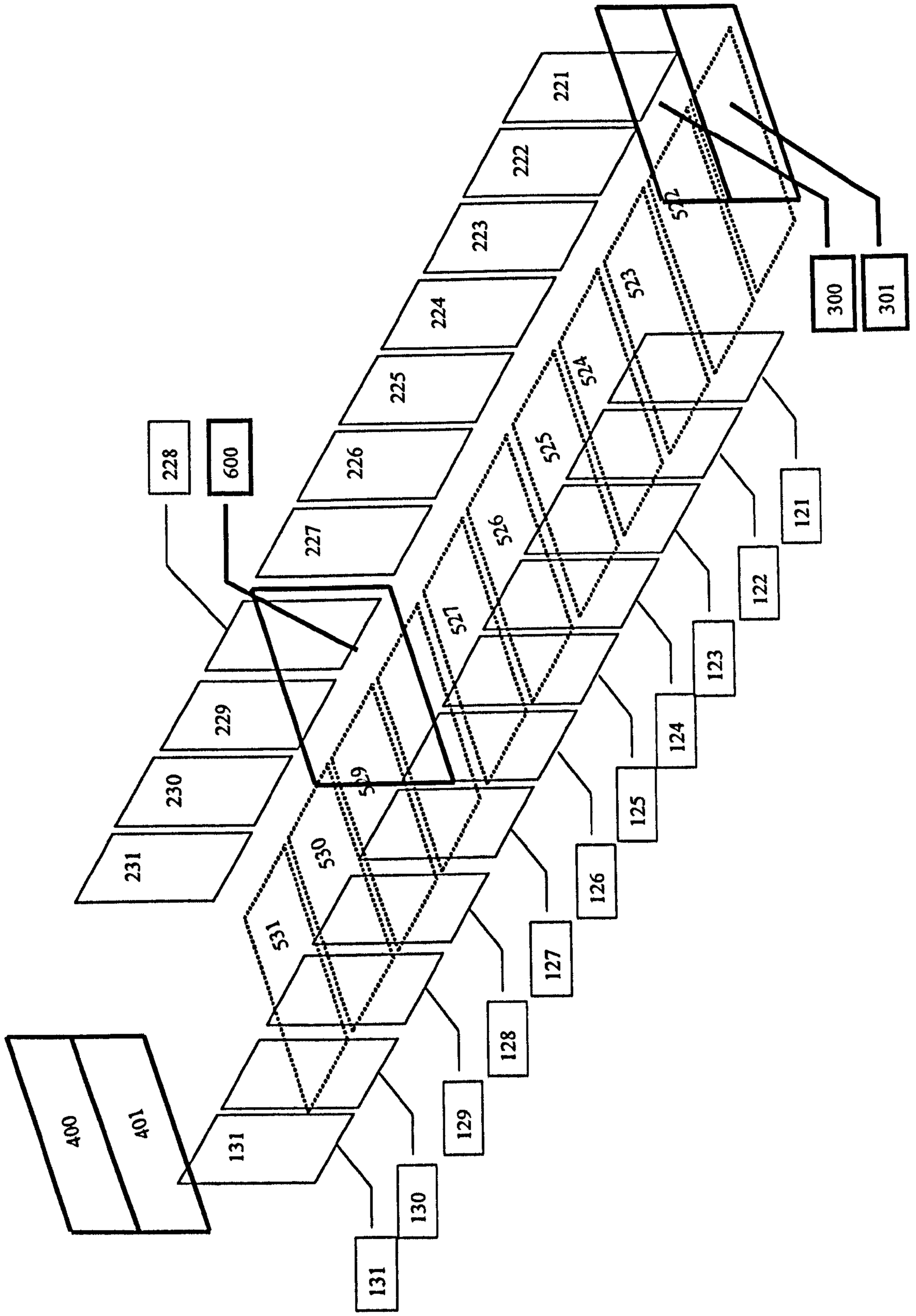

Figure 5.28 subsystem numbering of tank structure

given a unique identification number at the start of the experimental work which was used in all subsequent measurements surveys. Figure 5.28 shows the plate numbering system adopted for the experimental work which subsequently forms the basis of the SEA model subsystem numbering. The measurements were conducted in accordance with the procedures outlined in chapter three. When examining the results, it is instructive to refer back to this diagram.

5.6 SEA Modelling of Complex Laboratory Structures

The SEA modelling of the tank structure consists of two models, a bending wave model (B model) and a bending, longitudinal and transverse wave model (BLT model). For the bending wave model, the subsystem numbers are as shown in figure 5.28. For the BLT model, the bending wave subsystems are also the same as shown in figure 5.28 and the corresponding longitudinal wave subsystems numbers are incremented by 1000 and the transverse wave subsystems numbers are incremented by 2000 e.g. 122, 1122 and 2122 are the numbers of the bending, longitudinal and transverse wave subsystems of plate 122.

The results are presented by the comparison of the measured and predicted acceleration level differences in third octave frequency bands. The results presented are for the B and the BLT wave SEA models but it would be expected that the predictions from the BLT wave SEA should be better than the B wave model. As with the aluminium plate model, the frame joints will also be modelled in two different ways, thus giving four SEA models of the tank structure for which results will be presented.

(a) Frame Model: the full frame model developed in the chapter four is used to predict the average angular transmission coefficient.

(b) Web model: the full frame model is simplified by omitting the flange plates of the stiffener.

In chapter two the importance of the cross joint model was discussed and it this joint that is used for the tee and corner joints in the SEA model of the tank. The tee and

corner joints are formed by omitting the relevant plates from the joint formulation. The analysis software PPC includes the cross joint in it's joint libraries and the accuracy of the joint formulation has been verified by previous researchers who have used the code e.g. Craik [Ref. 37], Smith [Ref. 78].

5.6.1 Subsystem Properties

Before reviewing the results the subsystem properties such as the mode count and modal overlap will be considered. In figure 5.29 the statistical mode count N_b of the bending wave subsystems is shown plotted in the 100 Hz to 10 kHz frequency bands for a 6 mm thick steel side plate, the 8 mm thick steel bulkhead and the 10 mm thick polycarbonate plate. It can be seen that in the 100 Hz frequency band there are 8 modes per band for the polycarbonate plate but in the steel plates there are only four modes per band. The mode count for the steel plates reaches 10 by the 250 Hz frequency band

The predicted modal overlap of the bending wave subsystems, M_b, is shown in figure 5.30 and it can be seen that for the 6 mm and 8 mm steel plates is above unity in the 100 Hz frequency band, and in the 125 Hz frequency band for the polycarbonate plate. Therefore from figure 5.30 it can be seen that the low frequency limit can be taken as 100 Hz if necessary. This is in contrast to the modal overlap of the aluminium plates shown in figure 5.21 where the modal overlap was predicted to reach unity occur in much higher frequency bands. This difference in the low frequency limit is because the total loss factor of the aluminium plates only include one structural coupling, while the tank plates are coupled to at least three other subsystems thus increasing the total loss factor.

It is also important to consider the subsystem properties for the in-plane wave types. In figure 5.31 the longitudinal mode count N_L is plotted for the 6 mm steel plate, the 8 mm steel plate and the 10 mm thick polycarbonate plate. The statistical mode count was calculated using equations *2.40* and *2.47*. It can be seen that the statistical mode count for the steel plates is extremely low in comparison to the bending mode count N_b in figure 5.29. The first mode of the 6 mm steel plate is predicted to occur at 2 kHz and

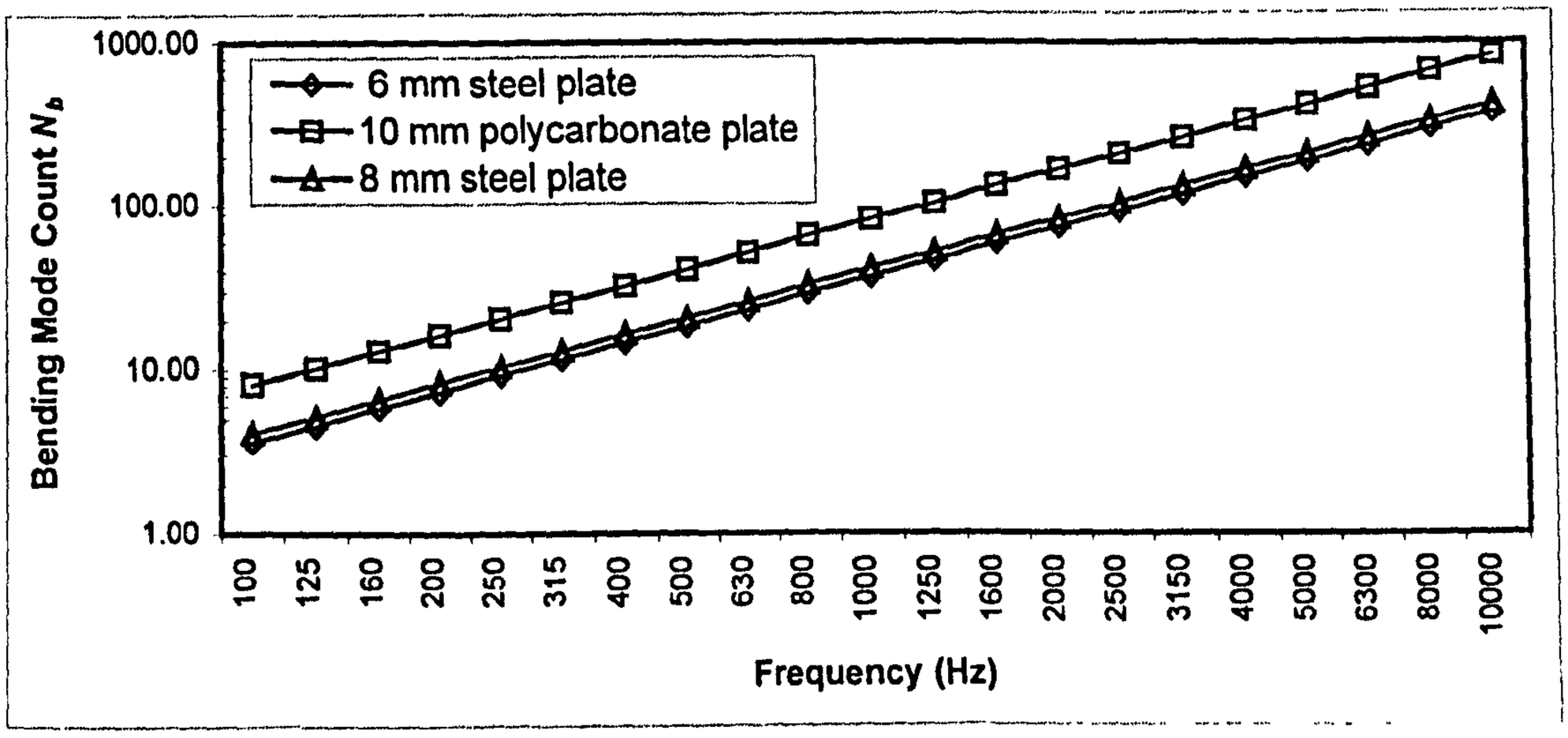

Figure 5.29 Predicted statistical mode count for bending wave subsystems.

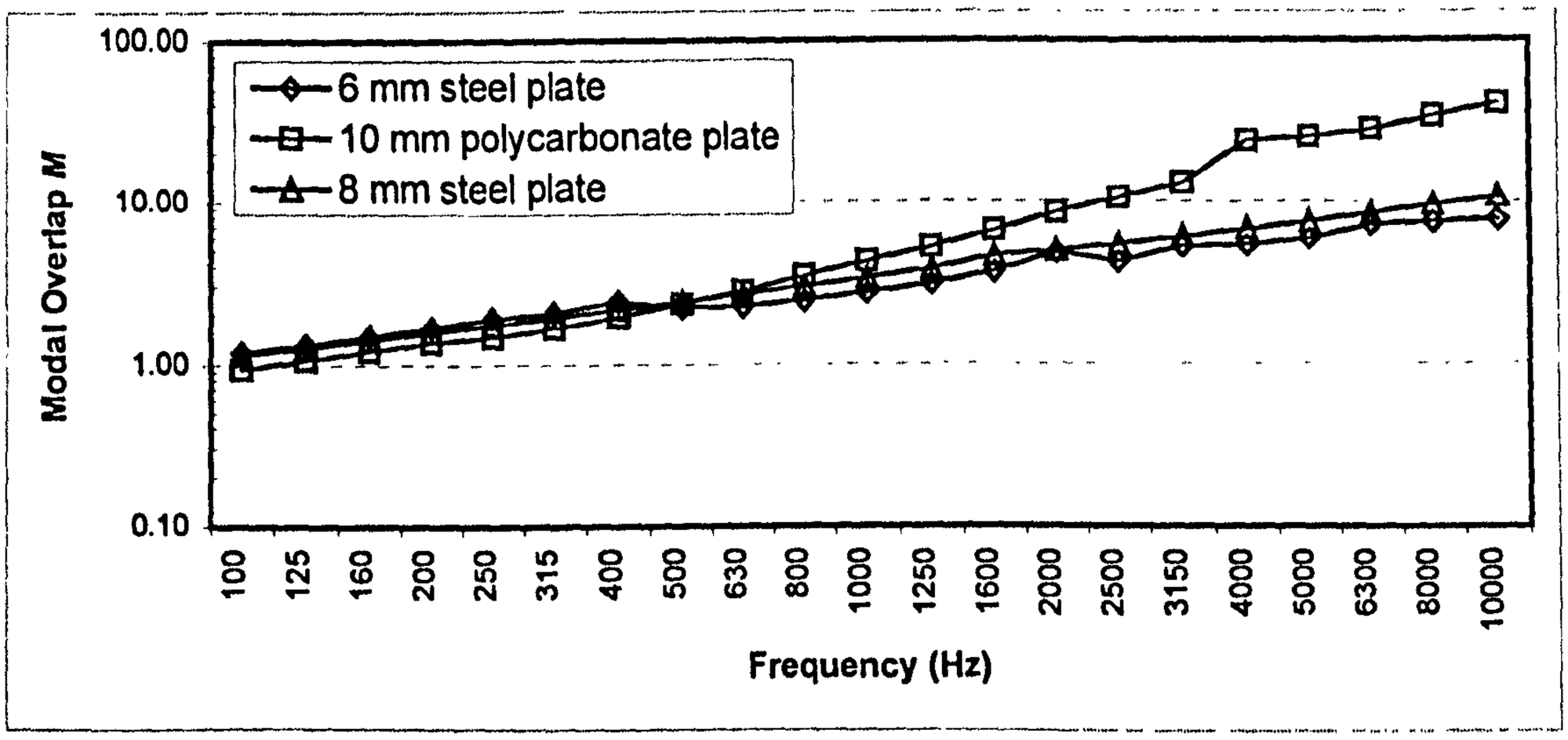

Figure 5.30 Predicted modal overlap for bending wave subsystems.

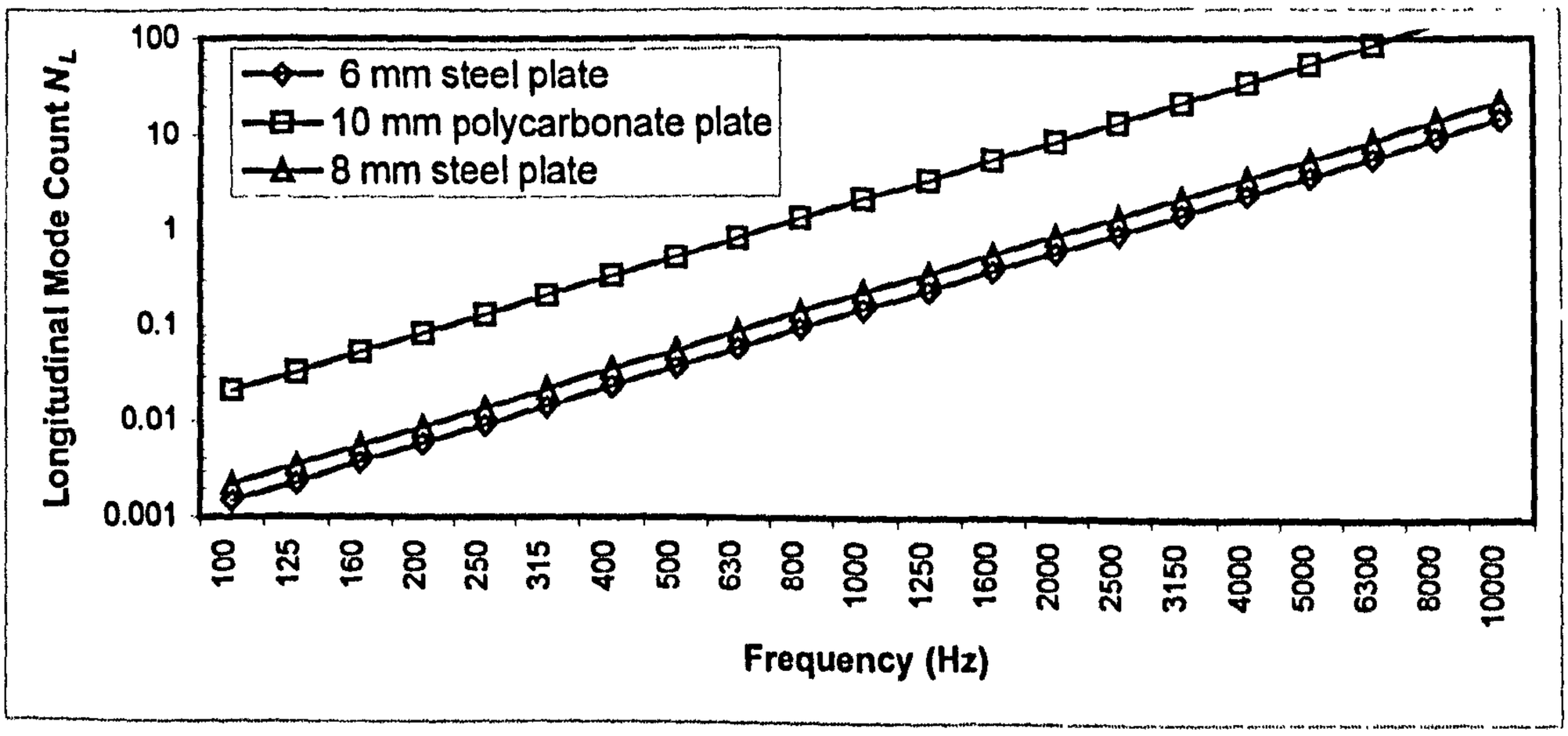

Figure 5.31 Predicted statistical mode count for longitudinal wave subsystems

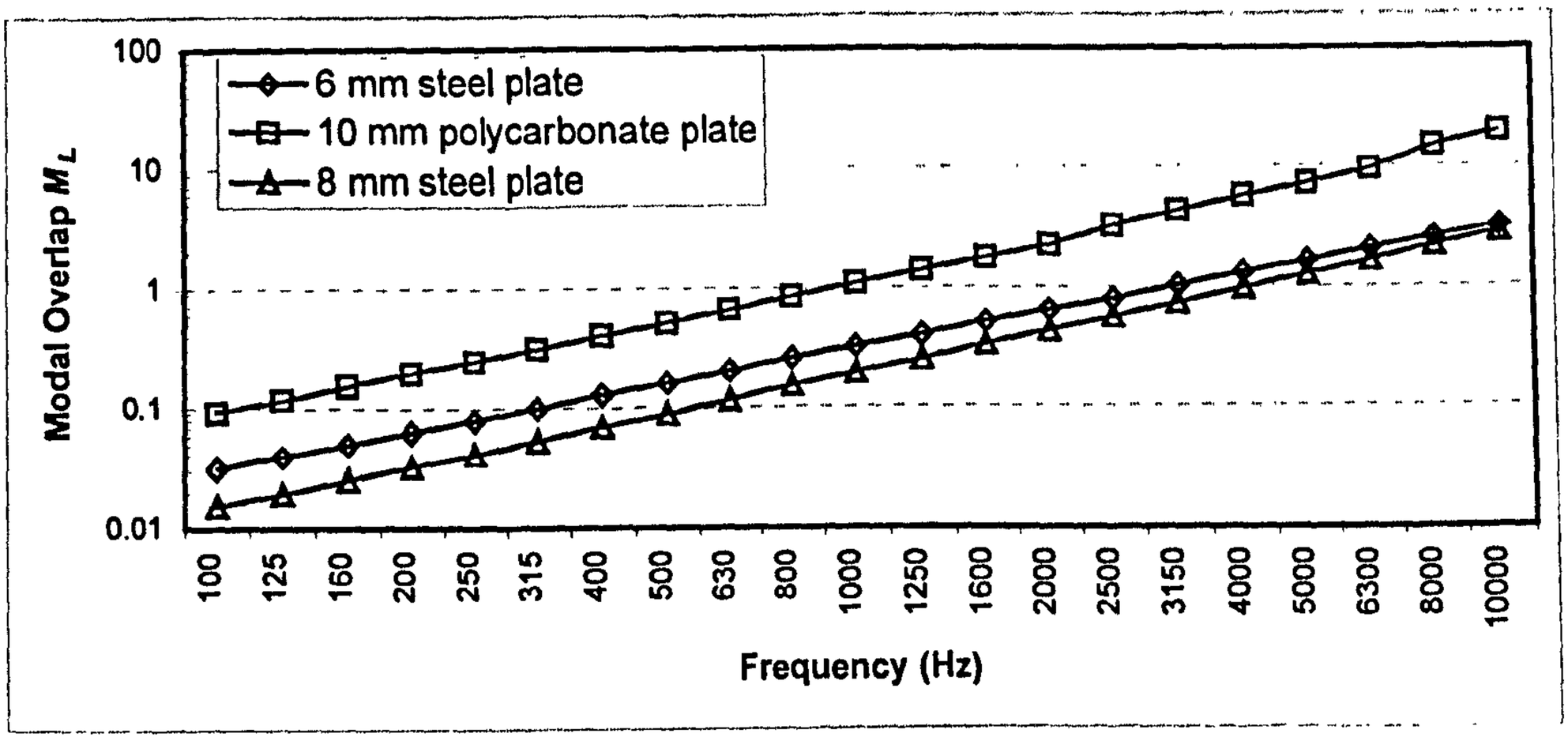

Figure 5.32 Predicted modal overlap for longitudinal wave subsystems.

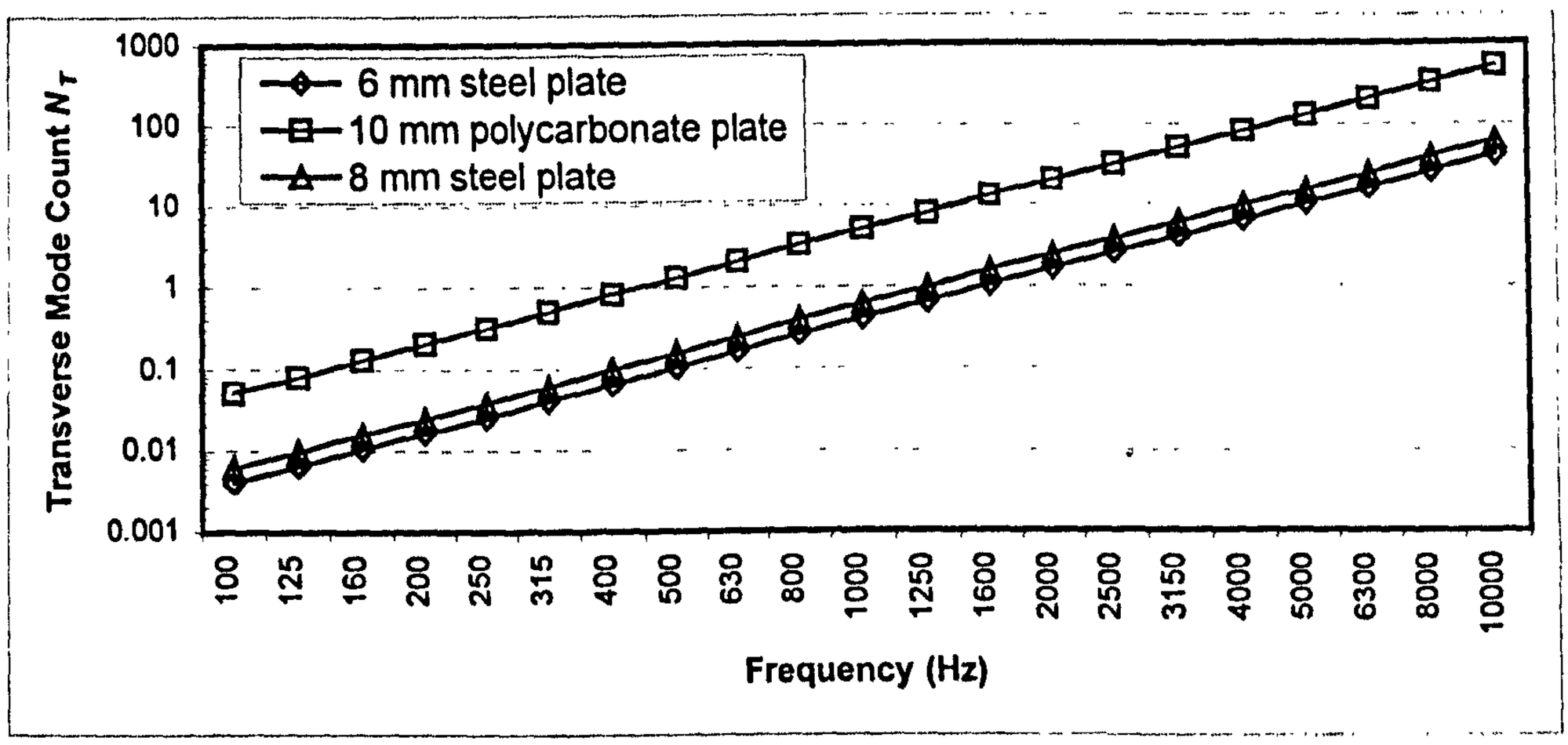

Figure 5.33 Predicted modal overlap for transverse wave subsystems

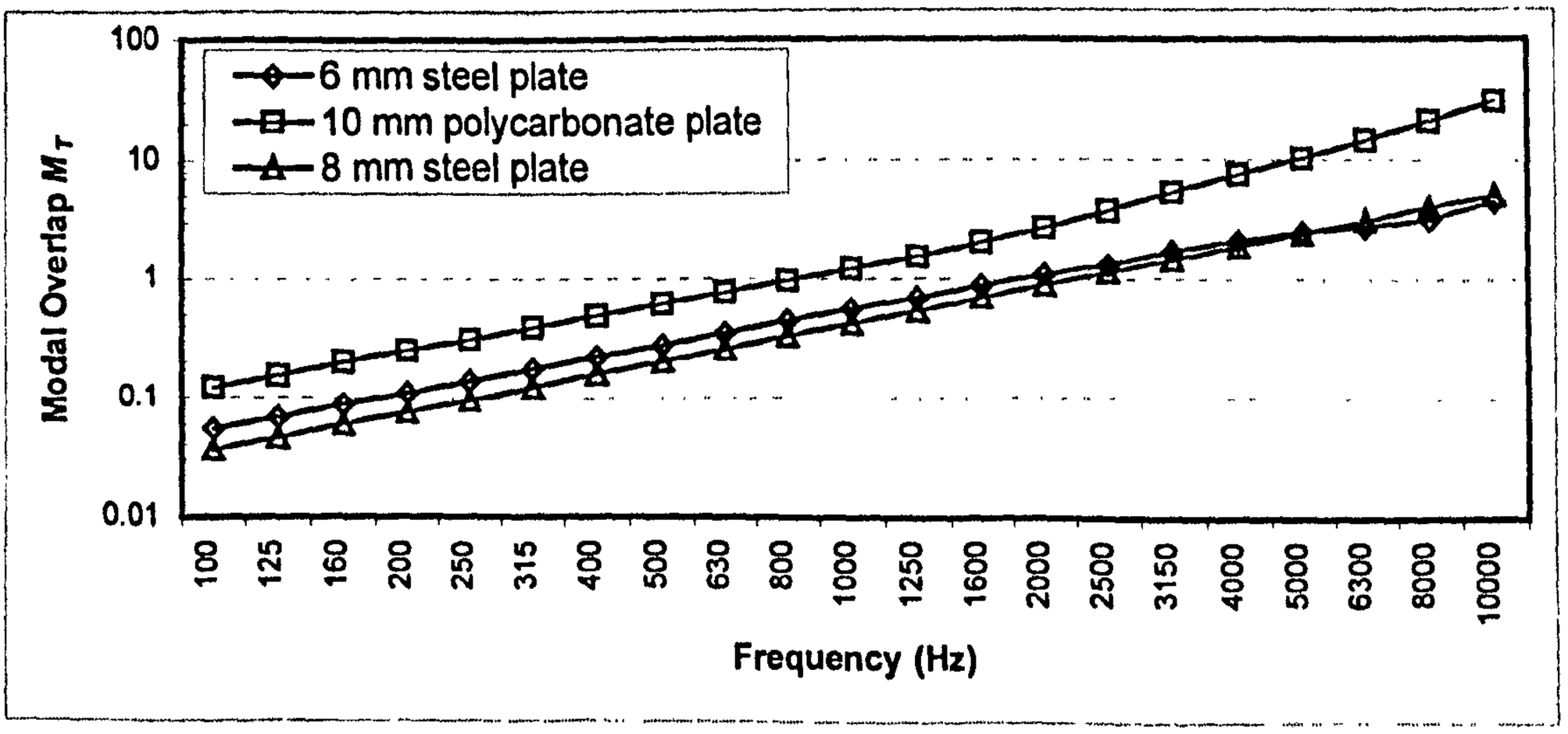

Figure 5.34 Predicted modal overlap for transverse wave subsystems

2.5 kHz for the 8 mm steel plate. In figure 5.32 the modal overlap is shown for the 6 mm and 8 mm steel plates and the 10 mm polycarbonate plate and was calculated using equations *2.35* and *2.40*. It can be seen that the modal overlap of steel plates does not rise above unity until the 2 kHz and 2.5 kHz frequency bands. It therefore can be concluded that the tank plates can be only be considered as supporting longitudinal wave subsystems at the higher end of the frequency spectrum and that the dominant transmission path will be through the bending wave subsystems.

In figure 5.33 the transverse mode count N_T is plotted for the 6 mm steel plate, the 8 mm steel plate and the 10 mm thick polycarbonate plate. The statistical mode count was calculated using equations *2.36* and *2.29*. It can be seen that the statistical mode count for the steel plates is extremely low in comparison to the bending mode count N_b in figure 5.29. The polycarbonate plate again has a much higher mode count. In figure 5.34 the modal overlap is shown for the 6 mm and 8 mm steel plates and the 10 mm polycarbonate plate. The modal overlap was calculated using equations *2.36* and *2.40*. It can be seen that the modal overlap of steel plates does not rise above unity until the 2 kHz and 2.5 kHz frequency bands, two frequency band down from the corresponding longitudinal subsystem. It therefore can be concluded that the tank plates can be only be considered as transverse wave subsystems at the higher end of the frequency spectrum. A more appropriate modelling strategy might be to combine the longitudinal and transverse wave subsystems into a single in-plane subsystem with the modal density added rather than consider them separately which would have the benefit of reducing the model data significantly.

5.6.2 Internal Loss Factor

Before reviewing the results it is important to discuss the internal loss factor of the tank materials to be used in the SEA models. The tank structure uses two materials in its construction, steel and polycarbonate, and it is important to measure the internal loss factor of the two materials to allow a value to be set in the SEA model. Obviously the measured internal loss factor of steel will be important when looking at ship structures. The internal loss factor of the two materials used in the tank construction has been measured using the reverberation decay method discussed in chapter three, section 3.3.

The internal loss factor of steel has been previously measured by Irie and Nakamura [25] and was utilised by Hynna et al [35] in their SEA models and the following relationship was derived by Irie by fitting a line to the experimental data,

$$\eta_{id} = 0.41 f^{-0.7} \tag{5.1}$$

where η_{id} is the internal loss factor of subsystem i and f is the frequency. Note that this equation represents the material internal loss factor and does not include the energy lost by radiation from the plate to the environment. The important feature is that the internal loss factor is not a constant value with frequency as quoted in Cremer [Ref. 66] but decreases with frequency. In figure 5.35 the measured internal loss factor from individual steel plates on the tank structure is plotted against the predicted internal loss factor from equation *5.1*. It can be seen that there is good agreement between the measured and predicted internal loss factor over the frequency spectrum.

The internal loss factor of the bending wave subsystems has been measured for both material used in the tank construction, however it is also necessary to specify the damping of the in-plane wave subsystems. It is extremely difficult to measure the damping of the in-plane waves because of the problems associated with exciting the in-plane waves independently of the bending waves. Therefore some assumption about the internal loss factor is required and in the analysis model it is assumed that the internal loss factor of the in-plane subsystems is the same as the internal loss factor of the bending wave subsystems.

Shown in figure 5.36 is the measured internal loss factor for a polycarbonate plate on the south side of the tank. Because polycarbonate is a polymer material, there is no readily available damping data for comparative purposes. The nearest material is plexiglass, for which Cremer [Ref. 66] gives the internal loss factor as between 103 dB and 106 dB re 10^{-12}. The measured internal loss factor is approximately 100 dB over most of the frequency spectrum, but reduces at higher frequencies. Consequently the measured internal loss factor has been used directly in all of the SEA models rather than the constant value given by Cremer [Ref. 66].

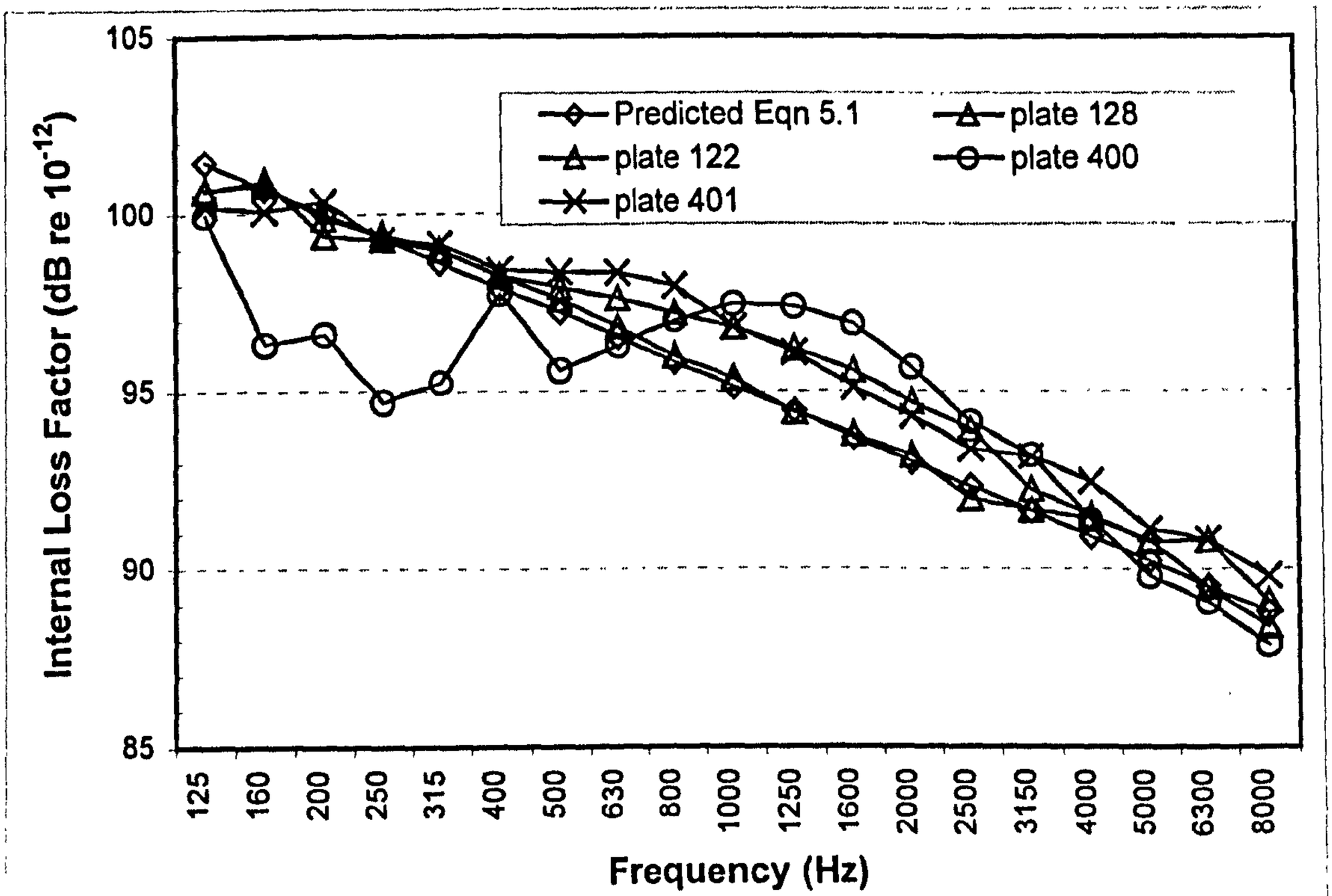

Figure 5.35 Comparison Of Measured Internal Loss Factor of Steel Plates And The Irie Equation 5.1

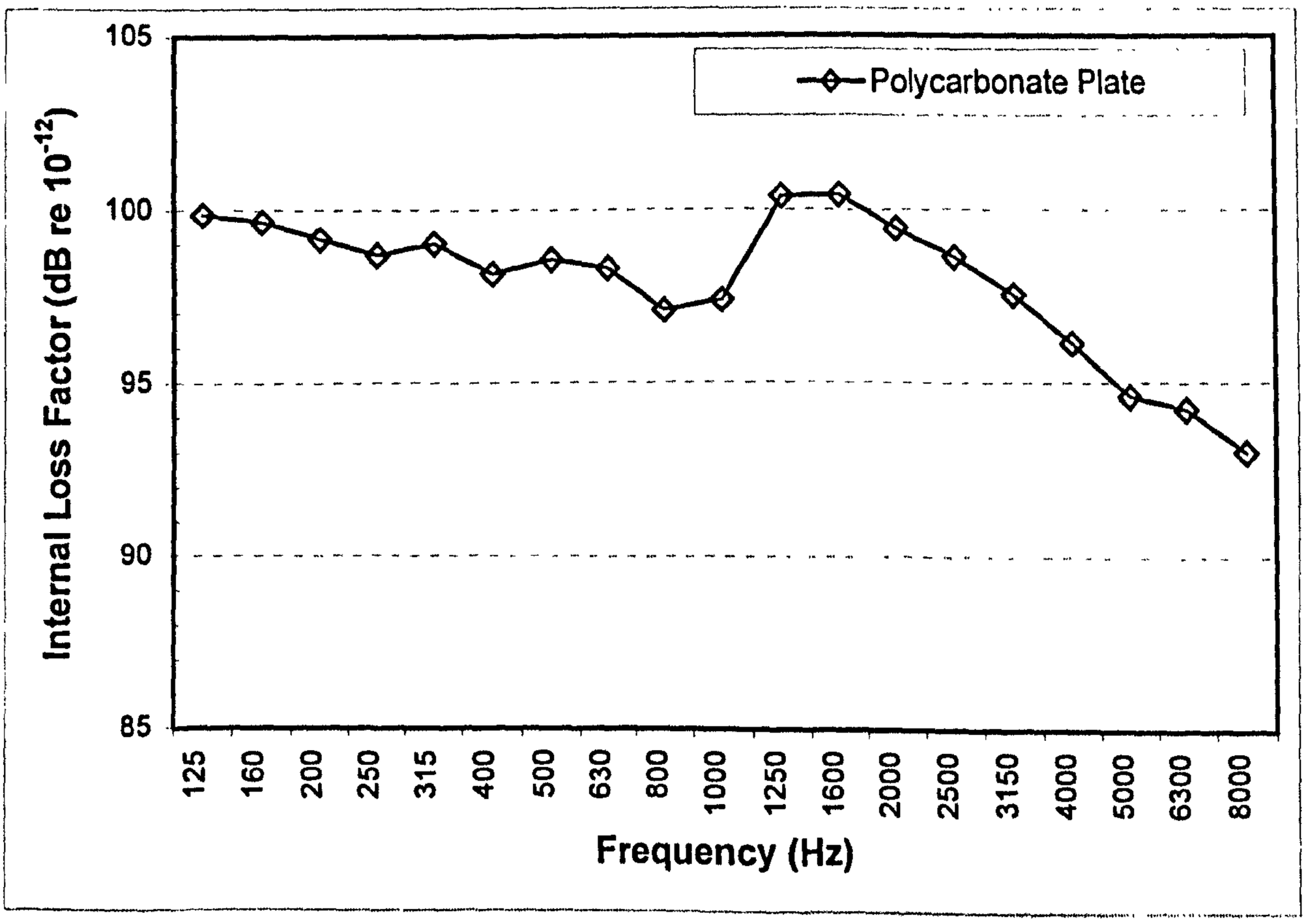

Figure 5.36 Measured Internal Loss Factor of Polycarbonate Plates

5.6.3 Predicted Attenuation With Distance

The first set of results presented are for a power input to subsystem 222 on the north side of the tank and illustrate the predicted attenuation with distance along the side of the tank. In figure 5.37 the predicted and measured acceleration level differences from subsystem 222 to 223 is shown for the full frame and web plate models with the B and BLT variations. It can be seen that for the predicted transmission across one joint that there is no significant difference between the B and the BLT variations in either the hull frame or web plate joint model. Both modelling approaches show good agreement with the measured results, with the full frame being marginally closer to the measured results.

In figure 5.38 the predicted and measured acceleration level difference from subsystem 222 to subsystem 226 is shown for the full frame and web plate models for the B and BLT wave SEA models. Results are only presented in the 125 Hz to 8 kHz frequency bands because insufficient power was injected above 8 kHz for the subsystem acceleration level to rise above the background noise level. It can be seen that for the predicted attenuation across 4 joints there is now a clear difference between the measurements and the predictions. Comparing the B and BLT wave SEA models it can be seen that there is no significant difference between the results below the 2000 Hz frequency band, however above 2000 Hz there is some variation but the difference does not exceed 2 dB. Examining the joint modelling approaches it can be seen that the predicted attenuation by the web plate model is approximately 3 to 4 dB above the measured attenuation over most of the frequency bands. In contrast the predicted attenuation from the full frame model is in very poor agreement with the measured attenuation in the 125 Hz to 500 Hz frequency bands. Above the 500 Hz band, the predicted attenuation from the full frame joint shows slightly better agreement than the web plate results.

In figure 5.39 the predicted and measured attenuation from subsystem 222 to 230 is again shown for the full frame and web plate joints for the B and BLT models. Results are only presented in the 125 Hz to 5 kHz frequency bands because insufficient power

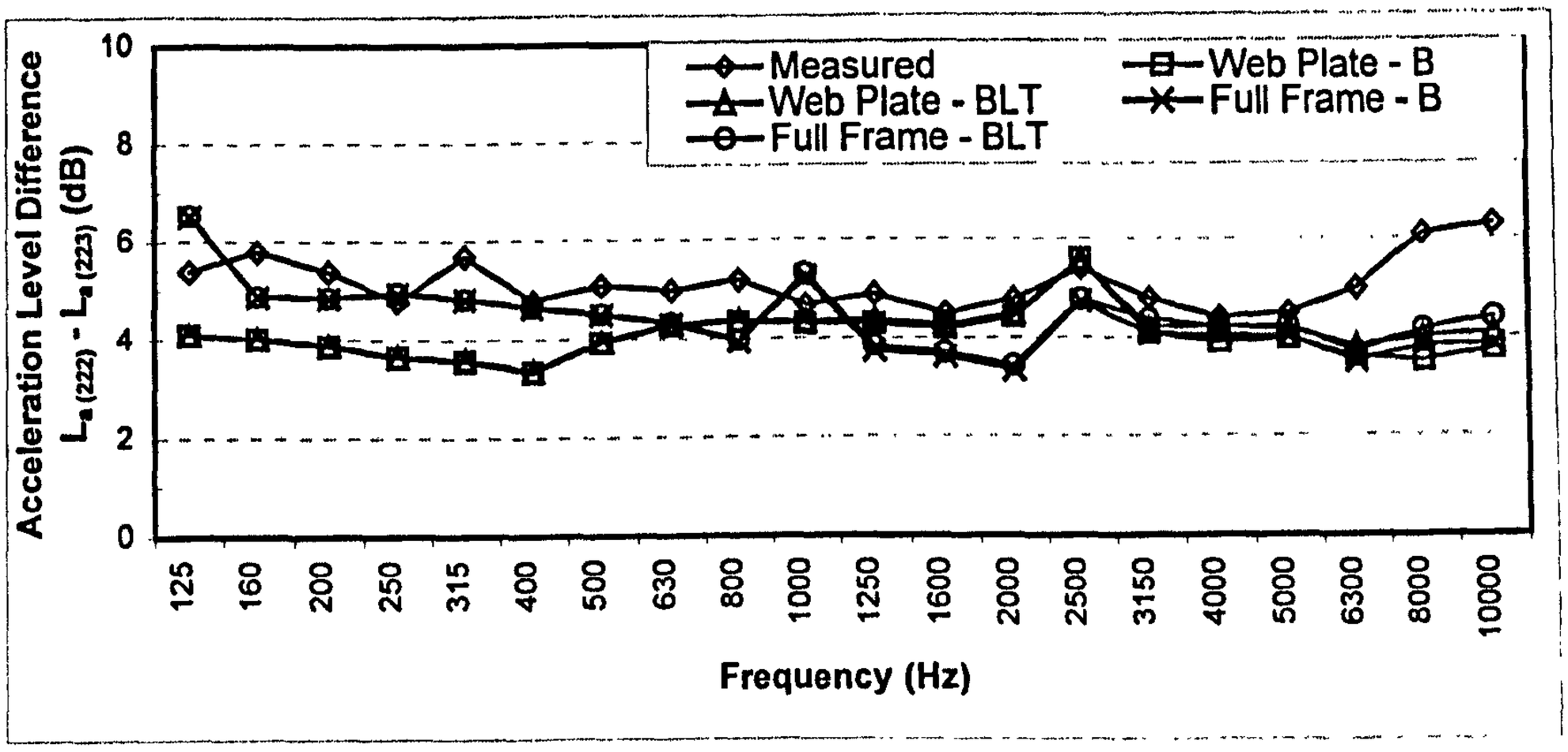

Figure 5.37 Predicted and measured attenuation from subsystem 222 to 223

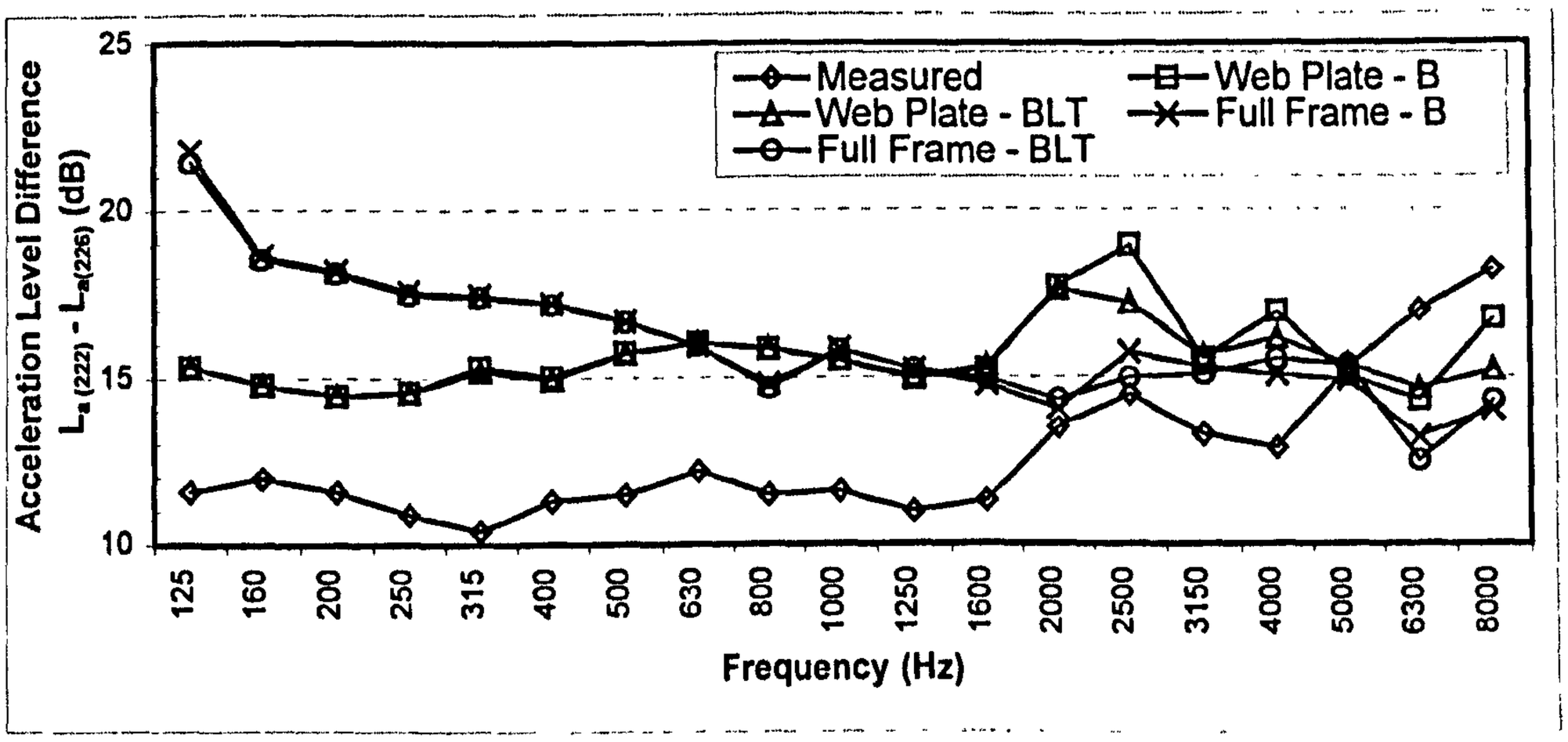

Figure 5.38 Predicted and measured attenuation from subsystem 222 to 226

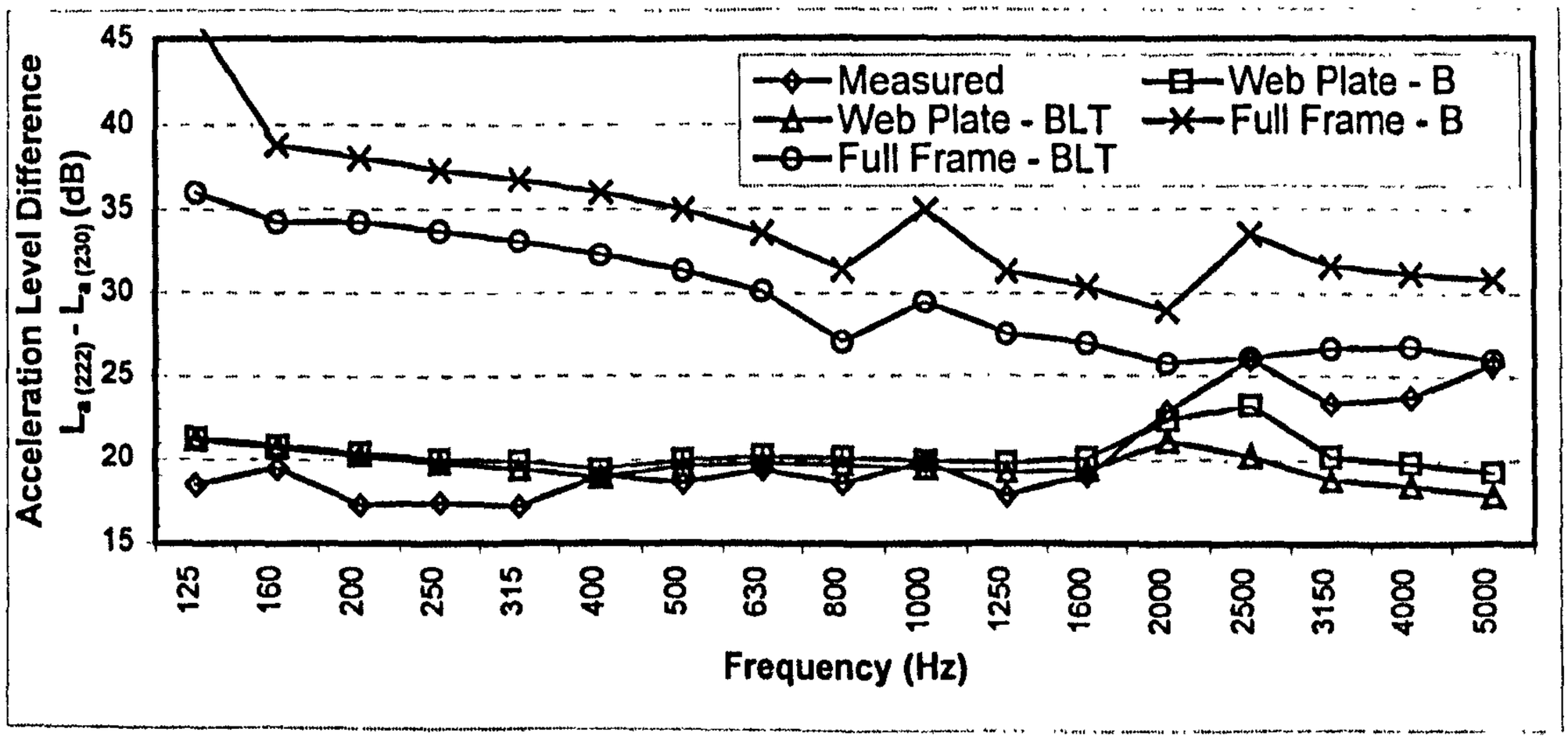

Figure 5.39 Predicted and measured attenuation from subsystem 222 to 230

was injected above 5 kHz for the subsystem acceleration level to rise above the background noise level. It can be seen that for the predicted attenuation across 8 joints there is now a significant difference between the predictions. It can be seen for the web plate joint model the predicted attenuation by the B and BLT wave SEA models is the same until the 2500 Hz frequency band and show good agreement with the measured attenuation where the difference is less than 3 dB. The predicted attenuation from the full frame joint models shows that the B model prediction is approximately 5 dB higher than that predicted by the BLT model. However both the B and BLT wave SEA models show poor agreement over most of the frequency bands. The BLT model only shows agreement with the measured attenuation above the 2000 Hz frequency band.

To illustrate attenuation with distance along the side of tank, the difference between the measured and predicted attenuation along the eleven plates of the north side on the tank is shown in figure 5.40 for subsystems 221 to 231 for the source on plate 222. Results are presented from the B and BLT model for the SEA model utilising the web plate joints. The results presented show the difference between the predicted and measured level difference for each subsystem i.e. + 3 dB indicates the predicted acceleration level difference is 3 dB above the measured level difference.

For the results presented it can be seen that the difference between the B model and the BLT model is typically no more than 0.5 dB in most of the subsystems. The difference between the predicted and measured attenuation is less then 3 dB across the first three joints but beyond the first three joints it can be seen that difference between the predicted and measured attenuation increases to between 4 dB and 7dB over the next three joints. It can also be seen that in the 2 kHz and 4 kHz frequency bands the results from the BLT model show better agreement. This is due to the energy being stored in the in-plane subsystems, which the analysis of the subsystem properties indicated would not be of any significance until the 2 kHz frequency band.

In contrast in figure 5.41 the same information is presented as in figure 5.40, but this time for the full frame model. It can be seen that as the number of joints increases, the difference between the predicted and measured attenuation increases for the B and BLT

-2.5	+3.0	+4.5	+6.5	+5	+4	+2	0	-1	W_{in}	-1
-2.5	+3.0	+4.5	+6.5	+5	+4	+2	0	-1	W_{in}	-1

blt

125 Hz

-0.5	+2.5	+4.5	5.5	+6.5	+4	+3	0.5	-1	W_{in}	+1
-0.5	+2.5	+4.0	4.5	+6.5	+4	+3	0.5	-1	W_{in}	+1

blt

250 Hz

-2	+1.5	+4	+6	+5.5	+4	+1.5	-0.5	-1	W_{in}	-1
-2.0	+1	+3.5	+5	+5.5	+4	+1.5	-0.5	-1	W_{in}	-1

blt

500 Hz

-4	0	+3	+6.5	+5.5	+4	+2	-0.5	0	W_{in}	0
-4	-0.5	+2.5	+4.5	+5.5	+4	+2	-0.5	0	W_{in}	0

blt

1000 Hz

-5.5	-0.5	+3.5	+6	+7	+4	+2	+0.5	0	W_{in}	0
-6.5	-2	+1.5	+0.5	+6.5	+4	+2	+0.5	0	W_{in}	0

blt

2000 Hz

-9.5	-4	-0.5	-2.0	+6	+4	1.5	+0.5	0	W_{in}	+2
-10	-5	-3	-0.5	+2.5	+3.5	+2	+1	0	W_{in}	+2

blt

4000 Hz

Figure 5.40 Attenuation with distance for source on subsystem 222. difference between measurements and predictions from web plate joint model in SEA B and BLT models. (All values in dB)

+31	+27.5	+21	+17	+14.5	+10	+7	+3	+1	W_{in}	+2
+16	+17.5	+15	+14	+13.5	+10	+7	+3	+1	W_{in}	+2

blt

125 Hz

+23.5	+20	+15.5	+12	+11	+6.5	+5.5	+1.5	+0.5	W_{in}	+2
+17	+16.5	+13.5	+10.5	+11	+6.5	+5.5	+1.5	+0.5	W_{in}	+2

blt

250 Hz

+20	+16.5	+12.5	+10	+7.5	+5	+2.5	0.0	-0.5	W_{in}	-1
+13.5	+13	+10.5	+8.5	+7	+5	+2.5	0.0	-0.5	W_{in}	-1

blt

500 Hz

+18.5	+15	+11.5	+8.5	+7	+4.5	+3	0.0	+0.5	W_{in}	+0.5
+10	+9.5	+8	+6.5	+6.5	+4	+3	0.0	+0.5	W_{in}	+0.5

blt

1000 Hz

+7.4	+6	+4	+3	+1	+0.5	-1	-1.5	-1.5	W_{in}	-1
+2.5	+3	+2	+1.5	+1	+1	-0.5	-1.0	-1.5	W_{in}	-1

blt

2000 Hz

+8.5	+7.5	+4.5	+3.0	+3.5	+2	+0.5	-0.5	-0.5	W_{in}	+2
+2	+3	+1.5	+1.0	+3.5	+2.5	+1.5	0.0	-0.5	W_{in}	+2

blt

4000 Hz

Figure 5.41 Attenuation with distance for source on subsystem 222. difference between measurements and predictions from full plate joint model in SEA B and BLT models. (All values in dB) models.

For the predicted attenuation for the full frame model it can be seen that the attenuation of the B model is the same as the BLT model over the first 5 joints. As the number of joints increases between the source and receiving subsystems, the predicted attenuation from the B model is significantly higher than that predicted from the BLT model. It is clear that between the 125 Hz and 1 kHz frequency bands the predicted attenuation shows increasingly poor agreement with each joint crossed, however in the 2 kHz and 4 kHz frequency bands the difference between the predicted and measured attenuation from the BLT wave SEA model over all subsystems is less than 3 dB.

5.6.4 Predicted Attenuation Throughout Structure

In the previous section results were presented for attenuation along the North side of the tank in subsystems 221 to 231 for power input to 222. In this section results are presented for power input to subsystem 128, which is adjacent to the internal bulkhead. The results are presented for attenuation throughout the entire tank structure. As previously the results are presented for the web plate and full frame joint models for SEA models using bending wave subsystems only (B model) and using bending, longitudinal and transverse wave subsystems (BLT model). The results are presented for the plates on the North side, the South side and the bottom of the tank by comparison of the predicted and measured acceleration level differences.

In figure 5.42 the predicted and measured attenuation across two joints from subsystem 128 to subsystem 130. The two joints are joint type 1 (Ref. fig 5.26) and it can be seen that the measured attenuation is approximately 5 to 7 dB over most of the frequency bands. The predicted attenuation from the full frame B and BLT models is identical over most of the frequency bands. The results from the B wave and BLT wave SEA models using the web plate joints are also very similar but it can be seen that the predicted attenuation is better than the frame model in the 125 Hz to 500 Hz frequency bands.

In figure 5.43 the predicted and measured attenuation across two joints from subsystem 128 to subsystem 126 is shown. It can be seen that the measured attenuation is approximately 10 dB across the two joints. This is higher than the measured attenuation

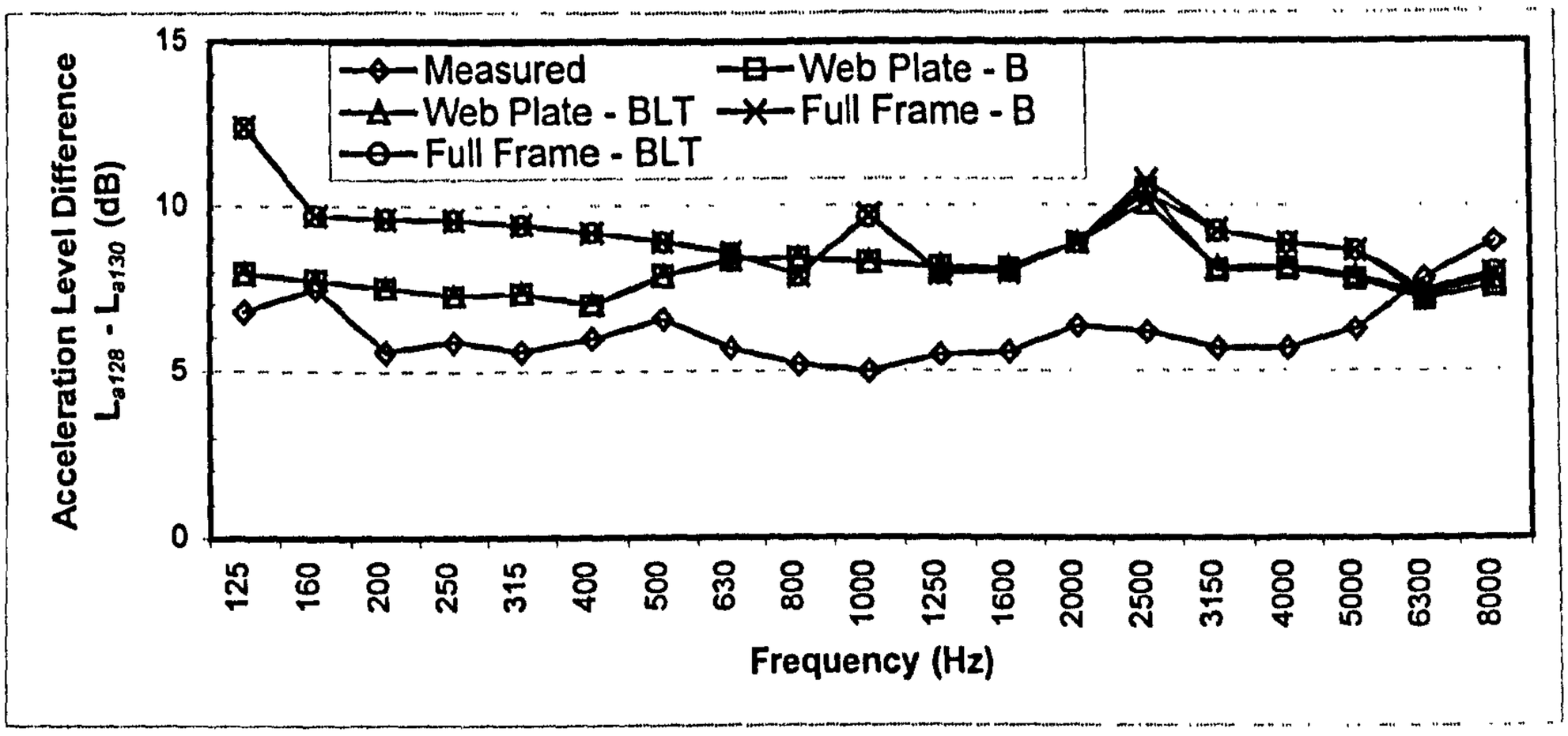

Figure 5.42 Predicted and measured attenuation from subsystem 128 to 130

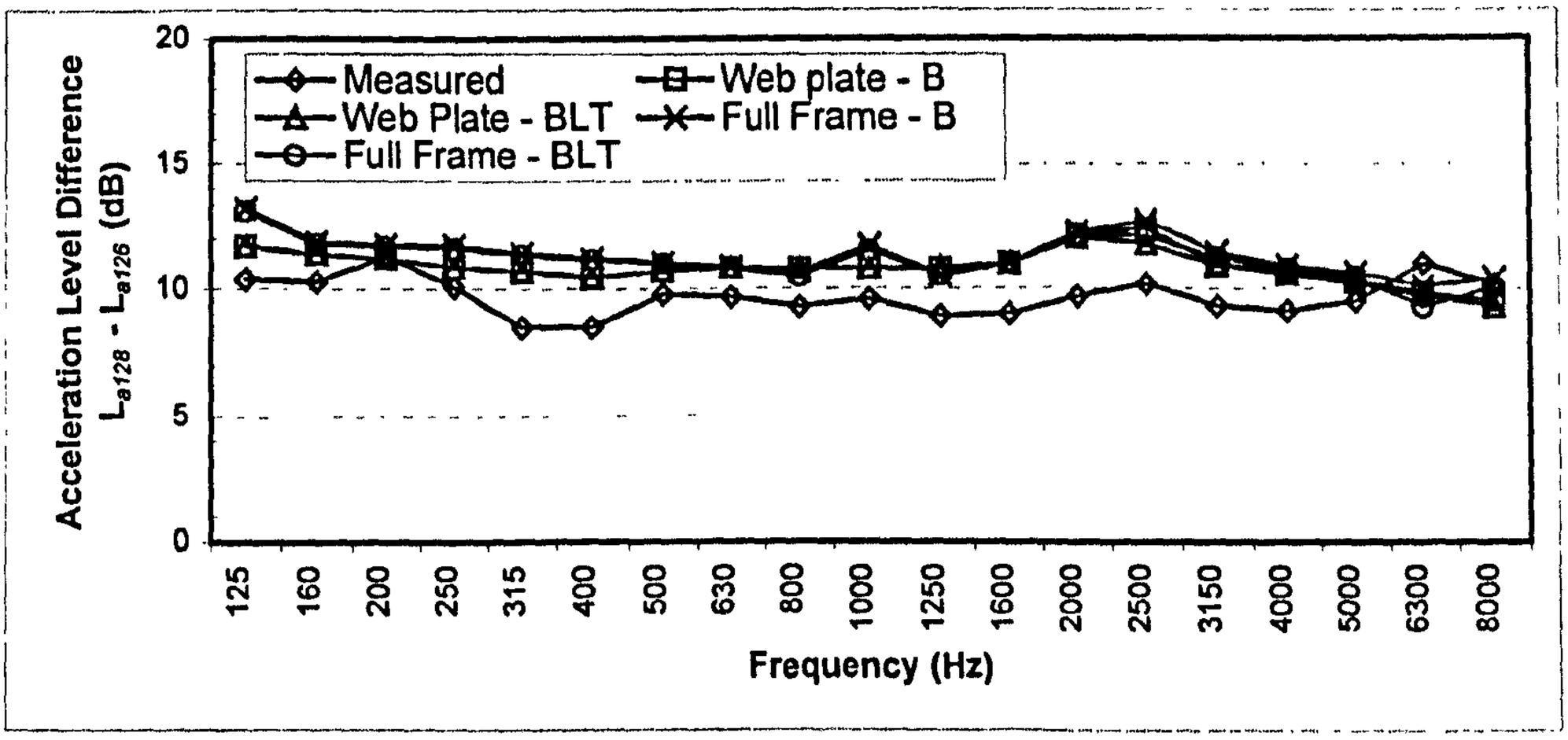

Figure 5.43 Predicted and measured attenuation from subsystem 128 to 126

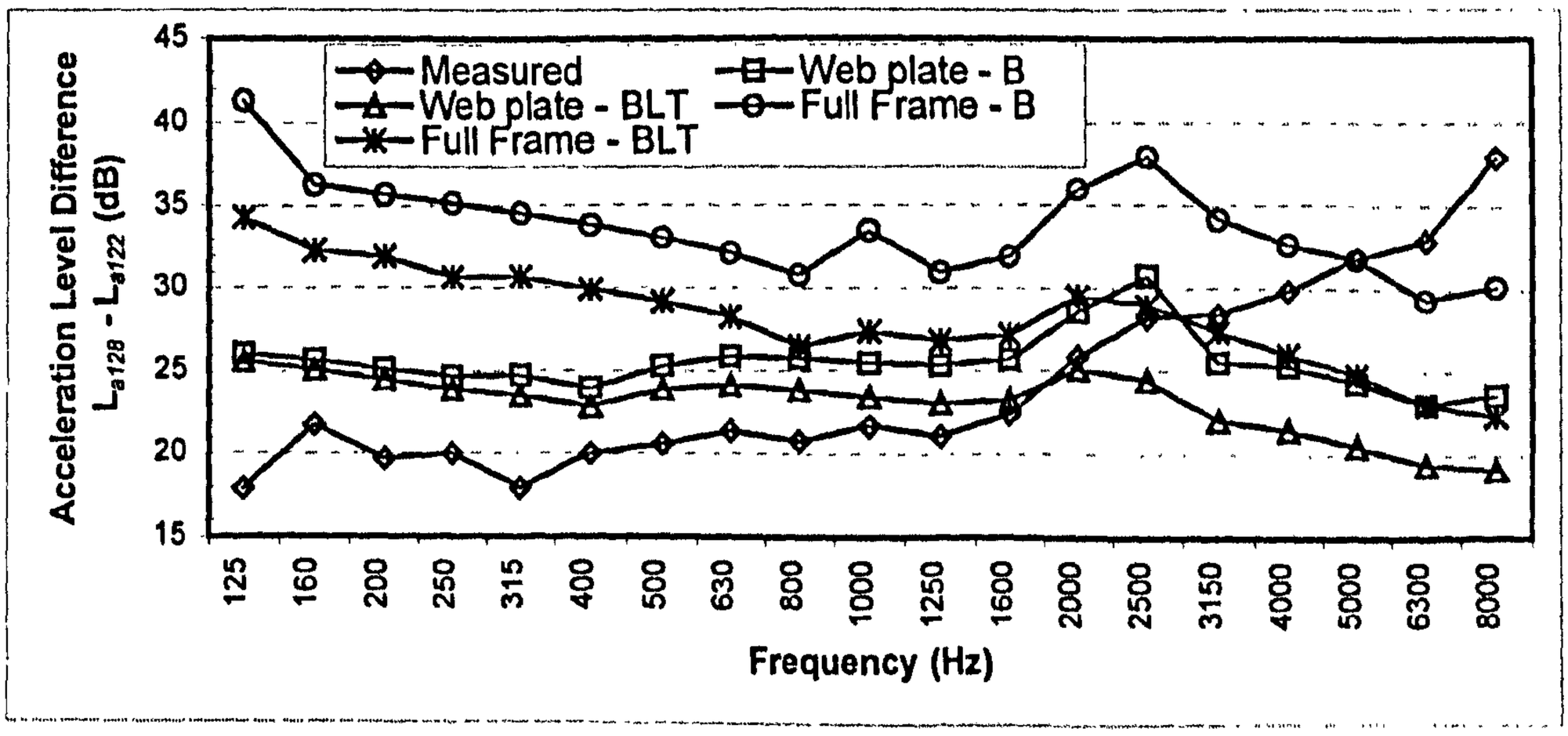

Figure 5.44 Predicted and Measured Attenuation From Subsystem 128 to 122

across two joints shown in figure 5.43. This is because the first joint is the tee joint formed between the bulkhead and the side plates and consequently energy is transmitted to the bulkhead 600 and side plate 128 . It can be seen that for the web-plate and hull-frame joint models, the B and BLT wave SEA models are almost identical but there is better agreement in the 125 Hz and 500 Hz low frequency bands between the measured and predicted attenuation from the web plate models.

In figure 5.44 the predicted and measured attenuation across six joints is shown. It can be seen that the measured attenuation is approximately 20 dB between the 125 Hz and 1600 Hz frequency bands, however between the 2000 Hz and 8000 Hz frequency bands the measured attenuation increases by approximately 16 dB. Examining the predictions it can be seen that there is clear difference between the SEA models. The predicted attenuation from the full frame joint B wave SEA model is much greater than the measured attenuation, varying by 10 to 20 dB in the 125 Hz to 2.5 kHz frequency bands. The most accurate prediction is from the web plate BLT wave SEA model. This shows a difference of approximately 1 to 4 dB over most of the frequency bands which is good agreement considering the 95% confidence levels. The largest errors are observed in the 3.15 kHz to 8 kHz frequency bands where the predicted and measured trends are different .

The change in the measured attenuation in the 3.15 kHz to 8 kHz frequency bands is believed to be a consequence of the polycarbonate plates The first effect to consider is that each polycarbonate plate has a reinforcing steel framework and this is not included in the SEA models. The steel framework is composed from small channel sections and at higher frequencies these break the polycarbonate plates down into a series of smaller plates and increases the number of joints. The result of this is seen in the increase in the measured attenuation. The second effect to consider is the construction of the steel-polycarbonate joint shown in figure 5.26. In practice the use of the 4 mm thick packing plate may change the joint dynamics at high frequencies because of the localised stiffening it produces on the bottom flange plate and therefore the joint is not being correctly modelled. The other effect to consider is that in the 6.3 kHz frequency band the bending wavelength on the polycarbonate plates is at the limit of thin plate theory.

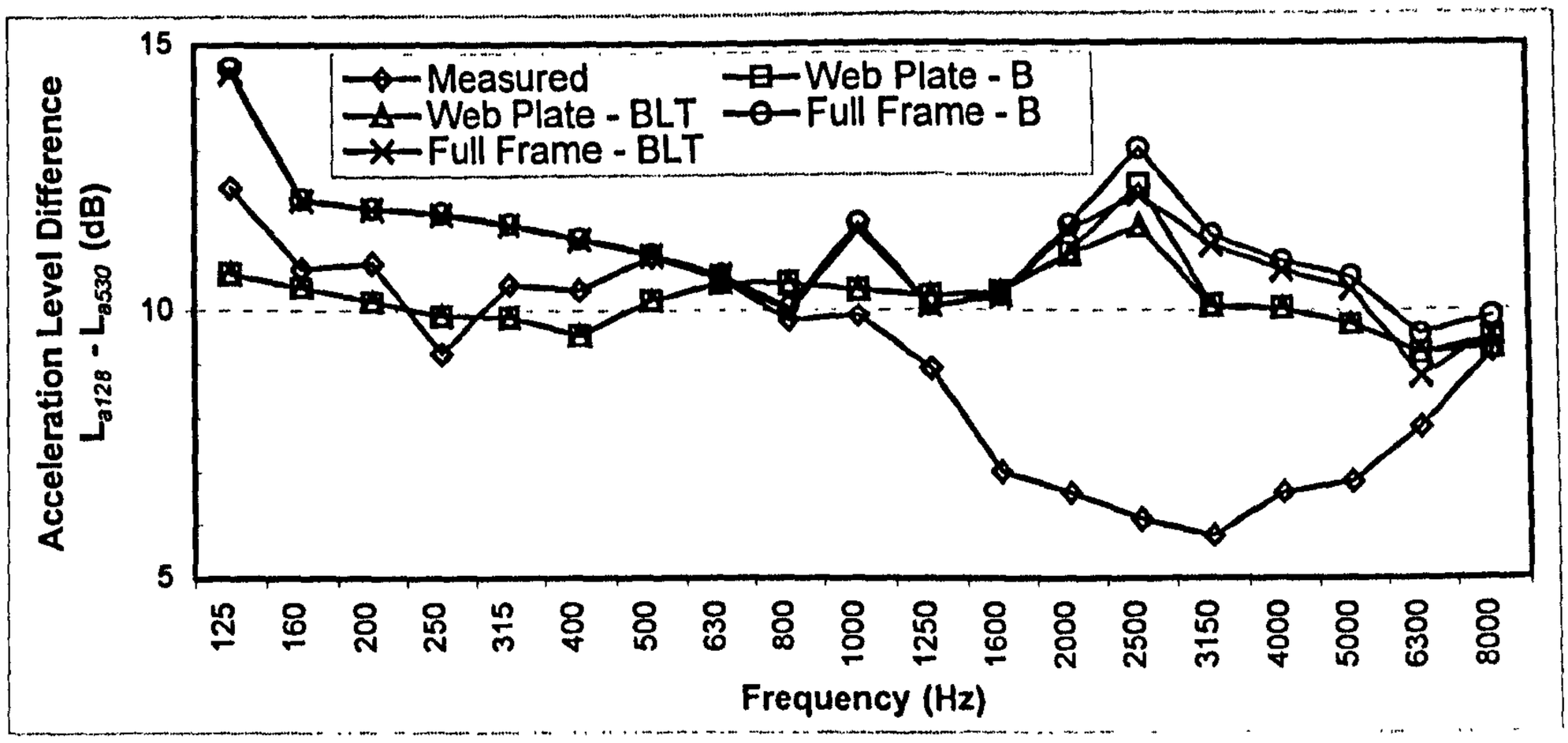

Figure 5.45 Predicted and measured attenuation from subsystem 128 to 530

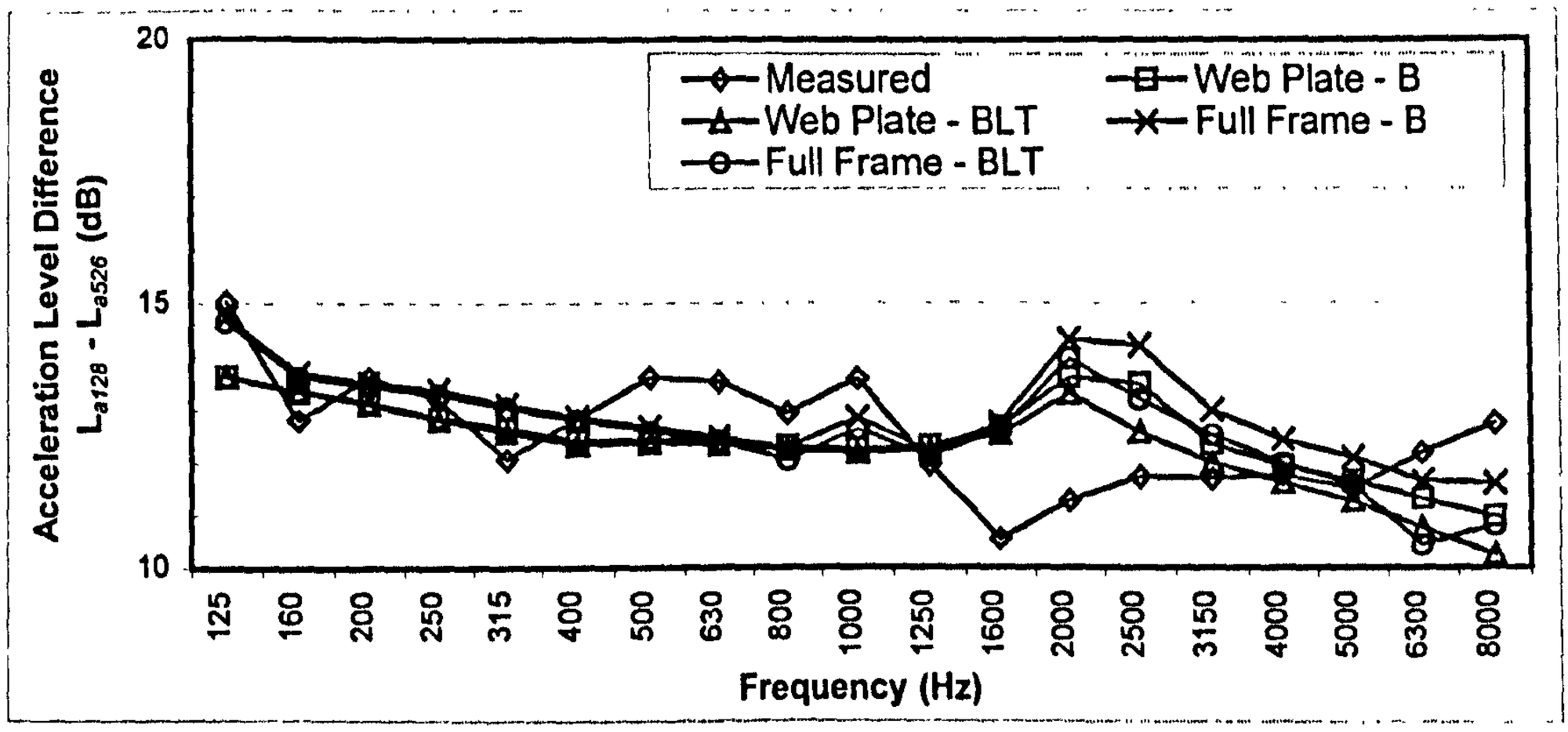

Figure 5.46 Predicted and measured attenuation from subsystem 128 to 526

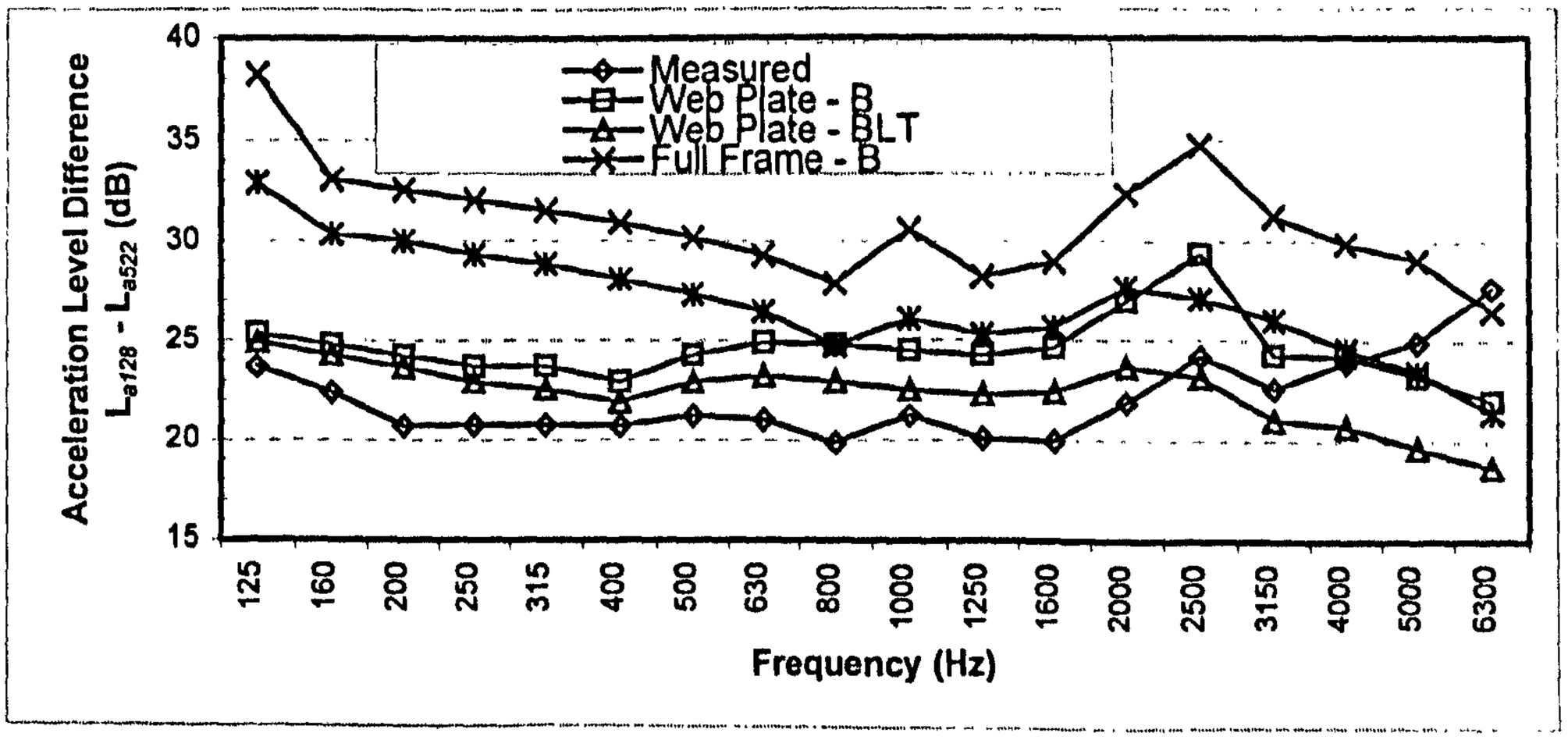

Figure 5.47 Predicted and measured attenuation from subsystem 128 to 522

In figure 5.45 the predicted and measured attenuation is shown for transmission from subsystem 128 to subsystem 530 on the bottom of the tank structure. As with the previous graphs, the predictions from all four SEA models are very similar. The web plate joint model shows better agreement with the measured attenuation between the 125 Hz and 500 Hz frequency bands. The predictions show excellent agreement with the measured attenuation between the 125 Hz and 1.25 kHz frequency bands but above the 1.25 kHz frequency band the measured attenuation reduces.

In figure 5.46 the measured and predicted attenuation from subsystem 128 to subsystem 526 on the bottom of the tank structure is shown. It can be seen that the measured attenuation is approximately 3 to 4 dB higher than that measured on the adjacent side plate 126. Examining the predicted attenuation it can be seen that the results from all the SEA models are very similar and in good agreement with the measured attenuation across the entire frequency spectrum.

In figure 5.47 the measured and predicted attenuation from subsystem 128 to subsystem 522 on the bottom of the tank is shown. It can be seen that the measured attenuation is approximately 20 dB between the 200 Hz and 1.6 kHz frequency bands, but above the 1.6 kHz band the attenuation rises by approximately 6 dB between the 2 kHz and 6.3 kHz frequency bands. It can be seen that this is similar to the measured trend observed in figure 5.44 except the attenuation between the 2 kHz and 6.3 kHz frequency bands is significantly lower. This is believed to be due to the attenuation in the flanking path transmission in these frequency bands due to the stiffening framework on the polycarbonate sheets discussed previously. The SEA predictions follow the same trend observed in figure 5.44 with web plate joint BLT wave SEA model giving excellent agreement with the measured attenuation between the 125 Hz and 3.15 kHz frequency bands. The predictions from the full frame B and BLT wave SEA models gives increasingly poor agreement as the attenuation with distance increases.

Figure 5.48 shows the predicted and measured attenuation from subsystem 128 on the South side to subsystem 230 on the North side of the tank structure. As was observed in figure 5.45 for the measured attenuation to subsystem 530, there is a reduction in the

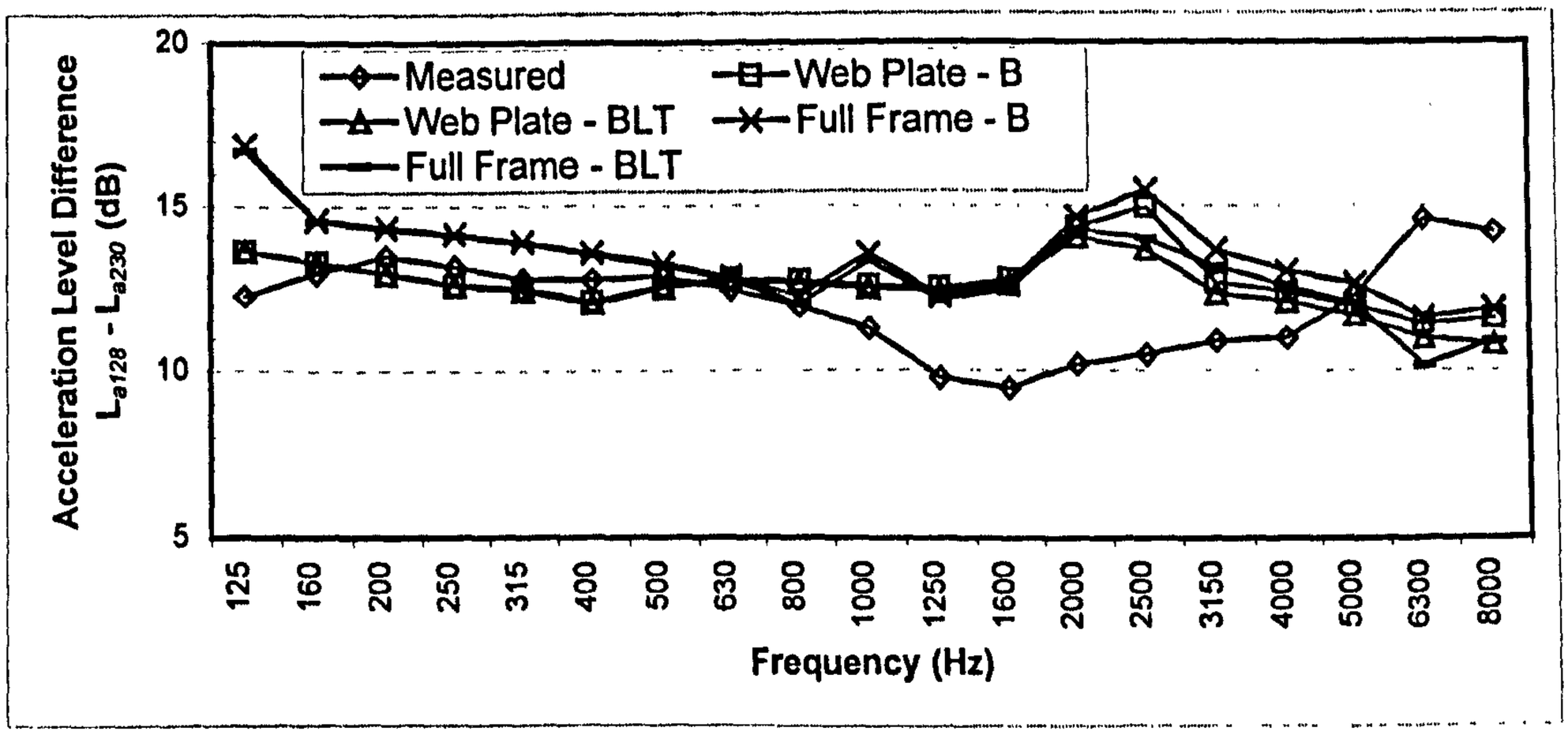

Figure 5.48 Predicted and measured attenuation from subsystem 128 to 230

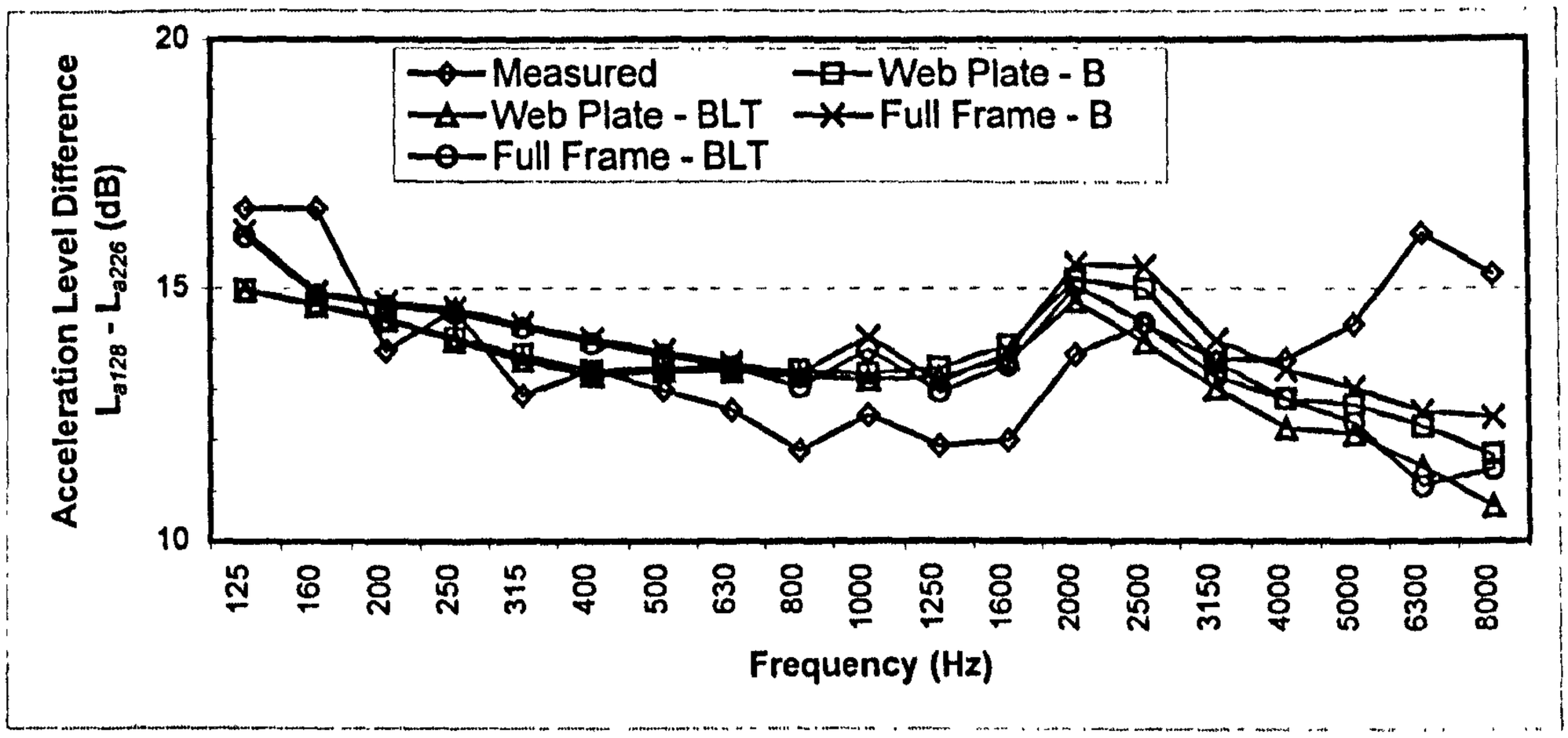

Figure 5.49 Predicted and measured attenuation from subsystem 128 to 226

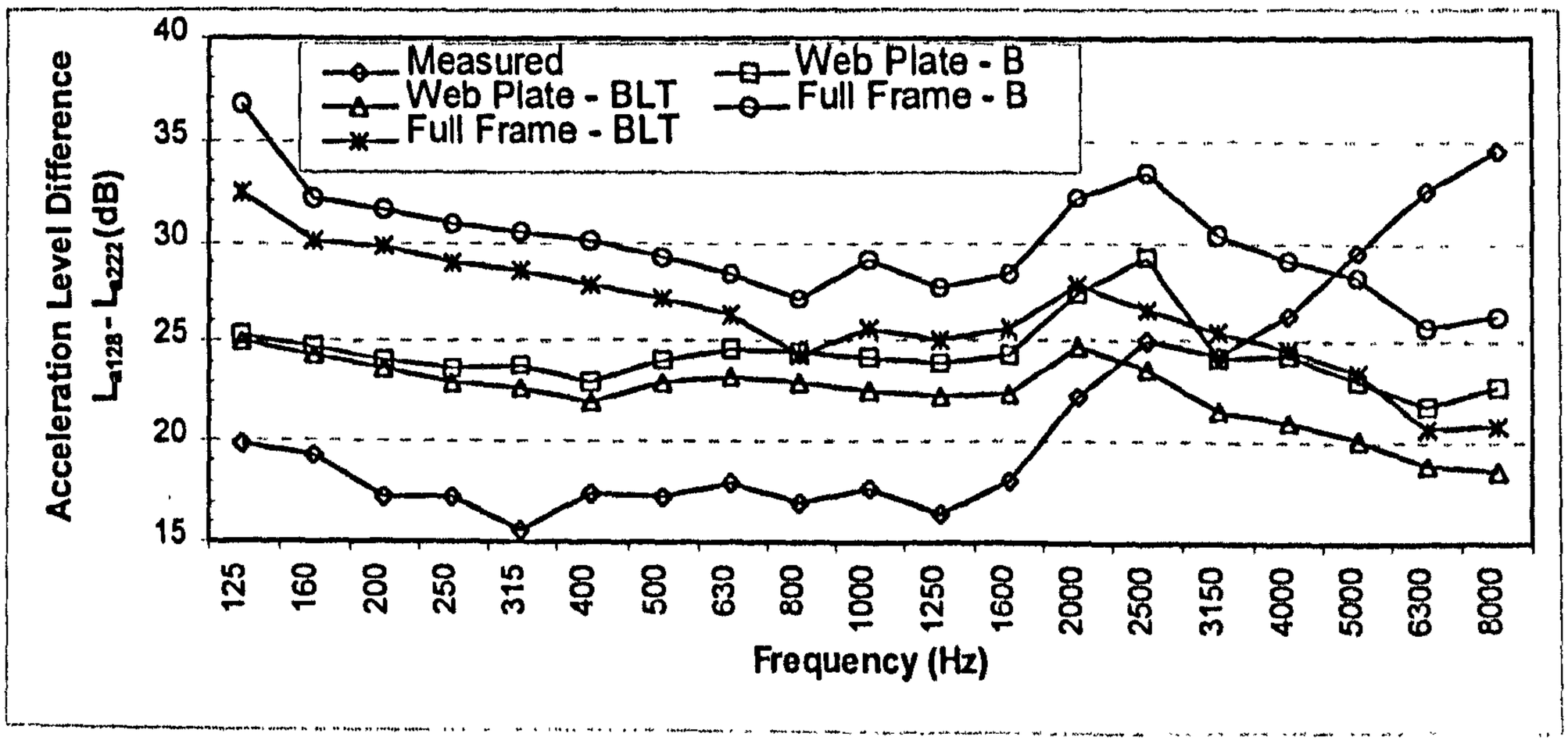

Figure 5.50 Predicted and measured attenuation from subsystem 128 to 222

attenuation between the 1.25 kHz to 5 kHz frequency bands. The measured attenuation is approximately 3 to 4 dB higher than measured on subsystem 530. The predicted attenuation for both joint modelling approaches is the same for the B and BLT wave in the lower frequency bands for the SEA models .

In figure 5.49 the predicted and measured attenuation from subsystem 128 to subsystem 226 on the North side of the tank is shown. It can be seen that the predictions from all 4 SEA models are very similar. Close to the source subsystem the joint modelling approach does not appear to have a significant effect on the predicted structure-borne transmission. Only in the 2.5 kHz to 8 kHz frequency bands does the predicted attenuation show any signs of divergence. This is consistent with the results previously presented for subsystems 530, 130, 230, 126 and 526.

In figure 5.50 the predicted and measured attenuation from subsystem 128 to subsystem 222 show the same trends observed for plate 122 on the opposite side of the tank and plate 522 on the bottom of the tank. It can be seen that the measured attenuation is approximately 17 dB in the 200 Hz to 1.6 kHz frequency bands, which is lower than 20 dB attenuation seen in plate 122 which is closer to the source subsystem 128.

In a similar manner to that shown in figures 5.40 and 5.41, the attenuation for the entire structure is shown in the 125 Hz and 250 Hz frequency bands in figure 5.51, figure 5.52 shows the attenuation in the 500 Hz and 1 kHz frequency bands and in figure 5.53 the attenuation in the 2 kHz and 4 kHz frequency bands is shown. Results are only shown for the web plate joint B and BLT wave SEA models as this was clearly the more accurate prediction method. The results are again presented in the form of the difference between the predicted and measured acceleration level difference. The results are presented in the form of an array for each frequency band. If the array is compared with the numbering diagram of the SEA model in figure 5.28, the end plates and internal bulkhead have been removed from the figure and the North and South sides of the tank have been 'folded' onto the same plane as the bottom plate subsystems. The comparison should then become obvious.

+6.0 B +5.5BLT	+1.5 B +1.0BLT	+1.5 B +1.5BLT	-0.5 B -0.5 BLT	-2.0 B -2.0 BLT	-1.5 B -1.5 BLT	+6.0 B +5.0BLT	+6.0 B +5.0BLT	+6.0 B +5.5BLT	+6.5 B +5.0BLT	+7.5 B +7 BLT
-1.5 B -2.0 BLT	-1.5 B -1.5 BLT	-1.0 B -1.0 BLT	-2.0 B -2.0 BLT	-3.0 B -3.0 BLT	-2.5 B -2.5 BLT	-2.5 B -2.5 BLT	+0.5 B +0.0BLT	+0.5 B +0.0BLT	+1.5 B +1.5BLT	
+3.0 B +2.0BLT	+1.5 B +1.0BLT	-0.5 B -0.5 BLT	↑ $W_{in,128}$	+4.0 B +4.0BLT	+1.5 B +1.0BLT	-1.0 B -1.0 BLT	+0.5 B +0.0BLT	+7.5 B +7.0BLT	+8.0 B +7.5BLT	+4.5 B +4.5BLT

North Side / Bottom / South Side

125 Hz

+3.0 B +2.0BLT	-0.5 B +1.0BLT	+0.5 B +0.5BLT	-1.0 B -1.0BLT	-2.5 B -3.0 BLT	-0.5 B -1.0 BLT	+2.0 B +0.5BLT	+4.0 B +4.0BLT	+6.5 B +6.0BLT	+7.0 B +6.0BLT	+4.0 B +3.5BLT
+1.5 B +1.0BLT	+0.5 B +0.5BLT	+1.0 B +1.0BLT	0.0 B 0.0BLT	+0.5 B +0.5BLT	-0.5 B -0.5 BLT	+0.5 B 0.0 BLT	+0.5 B 0.0 BLT	+3.5 B +2.0BLT	+3.0 B +2.0BLT	-1.5 B 0.0 BLT
+4.0 B +3.5BLT	+2.5 B +2.5BLT	+0.5 B +0.5BLT	↑ $W_{in,128}$	-2.5 B -2.5 BLT	+1.0 B +0.5BLT	-1.0 B -0.5 BLT	+2.0 B +1.0BLT	+6.0 B +5.0BLT	+4.5 B +4.0BLT	+2.0 B +1.5BLT

North Side / Bottom / South Side

250 Hz

Figure 5.51 Attenuation throughout structure for source on subsystem 128 difference between measurements and predictions from web plate joint model in SEA B and BLT models. (All values in dB)

+2.0 B +2.0BLT	-0.5 B 0.0 BLT	+0.5 B +0.5BLT	+1.0 B +0.5BLT	+0.5 B 0.0 BLT	+0.5 B +2.0BLT	+3.0 B +3.0BLT	+4.0 B +4.0BLT	+6.0 B +5.0BLT	+7.0B +6.0BLT	+6.0 B +4.5BLT	North Side
+0.5 B +1.0BLT	-1.0 B 0.0 BLT	-1.0 B -0.5 BLT	+2.0 B +2.0BLT	-1.0 B -1.0 BLT	-1.0 B -1.0 BLT	-1.0 B -1.0BLT	+1.0 B +0.0BLT	+3.0 B +2.0BLT	+3.0 B +2.0BLT	+0.5 B 0.0 BLT	Bottom
+4.0 B +4.0BLT	+1.5 B +2.0BLT	+1.0 B +1.5BLT	$W_{in,128}$ ↑	+2.5 B +2.0BLT	+1.0 B +1.5BLT	+1.0 B +1.0BLT	+6.0 B +4.5BLT	+9.0 B +7.5BLT	+5.0 B +3.5BLT	+2.5 B +1.5BLT	South Side

500 Hz

+3.5 B +3.0BLT	+1.5 B +1.0BLT	+1.5 B +1.5BLT	+1.5 B +1.5BLT	-0.5 B -0.5 BLT	+1.0 B +0.0BLT	+2.0 B +2.0BLT	+4.5 B +4.0BLT	+6.0 B +4.5BLT	+6.5 B +5.0BLT	+4.0 B +2.5BLT	North Side
+1.0B +0.5BLT	+0.5 B +0.5BLT	0.0 B 0.0 BLT	+2.0 B +2.0BLT	-1.5 B -1.5 BLT	-1.5 B -1.5 BLT	-0.5 B -0.5 BLT	+ B1.5 +1.0BLT	+3.0 B +2.0BLT	+3.5 B +4.0BLT	0.0 B 0.0 BLT	Bottom
+5.0 B +5.0BLT	+3.5 B +3.0BLT	+2.0 B +2.0BLT	$W_{in,128}$ ↑	+1.5 B +1.5BLT	+1.0 B +1.0BLT	+1.0 B +1.0BLT	+7.0 B +5.5BLT	+8.5 B +6.5BLT	+4.0 B +2.0BLT	+0.5 B +1.0BLT	South Side

1000 Hz

Figure 5.52 Attenuation throughout structure for source on subsystem 128 difference between measurements and predictions from web plate joint model in SEA B and BLT models. (All values in dB)

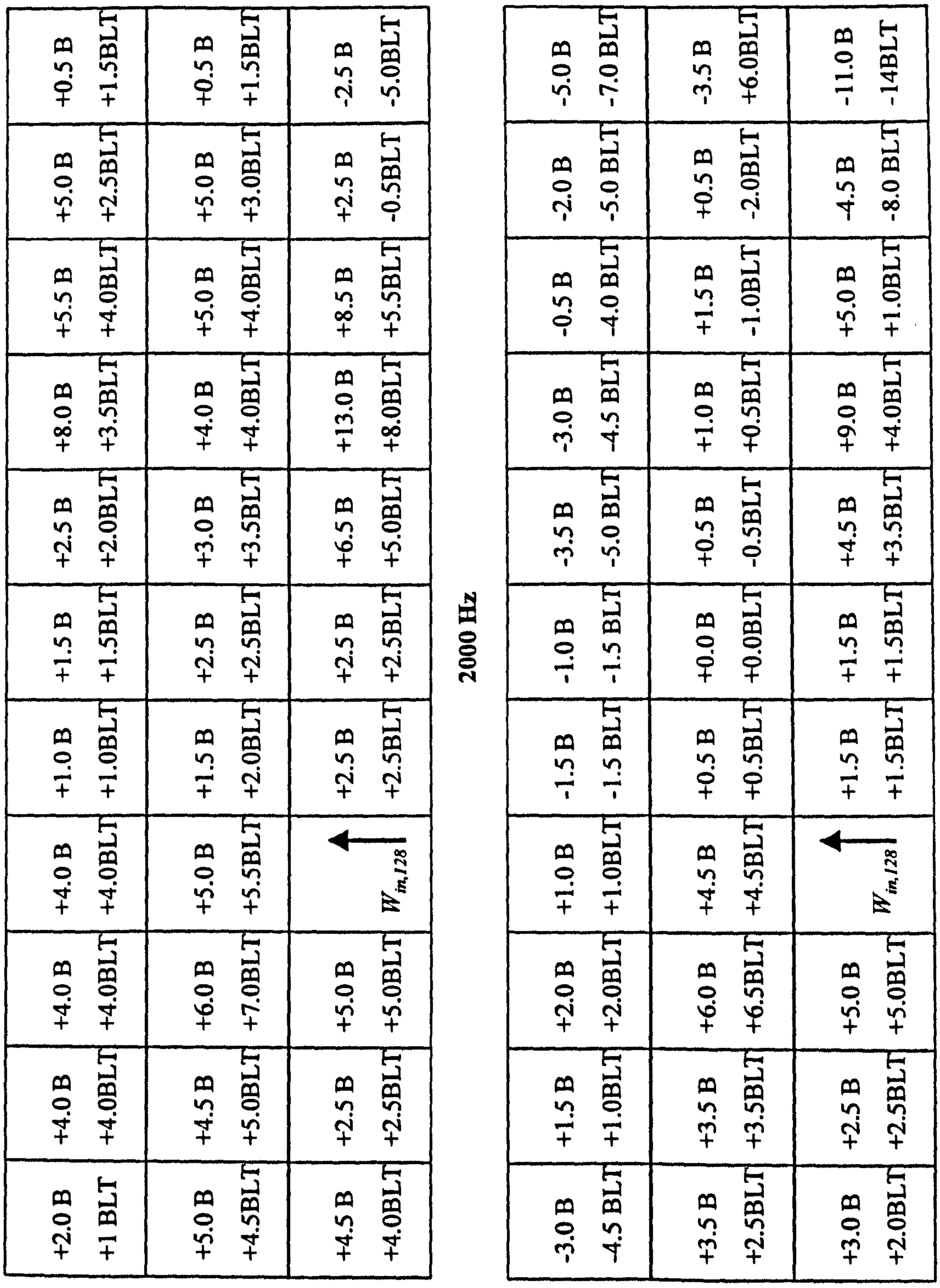

Figure 5.53 Attenuation throughout structure for source on subsystem 128 difference between measurements and predictions from web plate joint model in SEA B and BLT models. (All values in dB)

For the results in figure 5.51 for the 125 Hz and 250 Hz frequency bands it can be seen that for the majority of subsystems the difference between the predicted and measured attenuation is particularly good, generally less than ±3 dB for the BLT wave SEA model. The results along all the bottom plates of the tank are extremely good. It is only at the far end of the tank that the difference between B and BLT predictions become obvious. There is very little difference between the predictions until the far end of the structure is reached.

In figure 5.52 the difference between the predicted and measured attenuation throughout the structure are presented for the 500 Hz and 1 kHz frequency bands. It can be seen that over the majority of the structure the difference between the predicted and measured attenuation is less than ±3 dB in most subsystems. The results on the bottom of the tank again show very good agreement. As stated previously, there is very little difference between the B and BLT wave SEA models. It is only in the subsystems at the end of the structure that the difference between the models becomes apparent and it is the BLT wave SEA model that shows the better agreement

In figure 5.53 the difference between the predicted and measured attenuation is presented for the 2 kHz and 4 kHz frequency bands. In bottom plate subsystems 528 to 530 and side plate subsystems 228 to 230 the agreement is poorer than in the other frequency band results presented. This is due to the reduction in the measured attenuation seen in figures 5.45 and 5.48 between 2 kHz and 4 kHz which is also present in the listed subsystems. In contrast to the other frequency band results presented, the BLT wave results show better agreement in the subsystems remote from the input subsystem. This is due to the existence of in-plane modes on the plates and the conversion of bending wave energy to in-plane energy becomes important in these frequency bands. Therefore at higher frequencies the BLT wave SEA model is the more appropriate solution.

5.6.5 Discussion

In section 5.6.3 the results for the predicted attenuation along the North side of the tank structure were presented from four SEA models. The results presented showed that modelling the frames as a web plate and considering bending, longitudinal and transverse subsystems gave good agreement between the predicted and measured attenuation in 125 Hz to 2 kHz frequency bands. It could also be seen in the results (e.g. figures 5.37 and 5.38), that the web plate and full frame model were in close agreement in most frequency bands, however between the 125 Hz and 500 Hz frequency bands there was a consistent difference .

In figure 5.54 the predicted coupling loss factor is shown for joint type 1 for the full frame and web plate models. It can be seen that in the 630 Hz to 10 kHz frequency bands there is very close agreement between the two joint model, but in the 125 Hz to 500 Hz frequency bands the web plate coupling loss factor is approximately 2 to 3 dB higher than the full frame model. In the analysis of the transmission across one joint presented in section 5.2 it was found that the difference between the modelling approaches is because the web plate behaves as a beam model in these low frequency bands. This explains the difference observed in the attenuation with distance results. As the distance and number of joints between the source and receiving subsystem increases, the 2 to 3 dB difference in the coupling loss factors in the low frequency bands becomes important as the error accumulates with each subsystem. This is clear from the results shown in figures 5.37 to 5.39. The slight difference shown in the high frequency bands 3.15 kHz to 10 kHz also results in an accumulated error between the two modelling approaches but the difference is much smaller, less than 1 dB, the overall difference between the two modelling approaches is smaller.

In figure 5.55 the predicted coupling loss factor for joint type two is shown for the web plate and full frame joint models. It can be seen that the web plate exhibits beam like behaviour in between the 125 Hz and 315 Hz frequency bands because of the deeper web plate. It can be seen that in the 800 Hz and 10 kHz frequency bands that there are

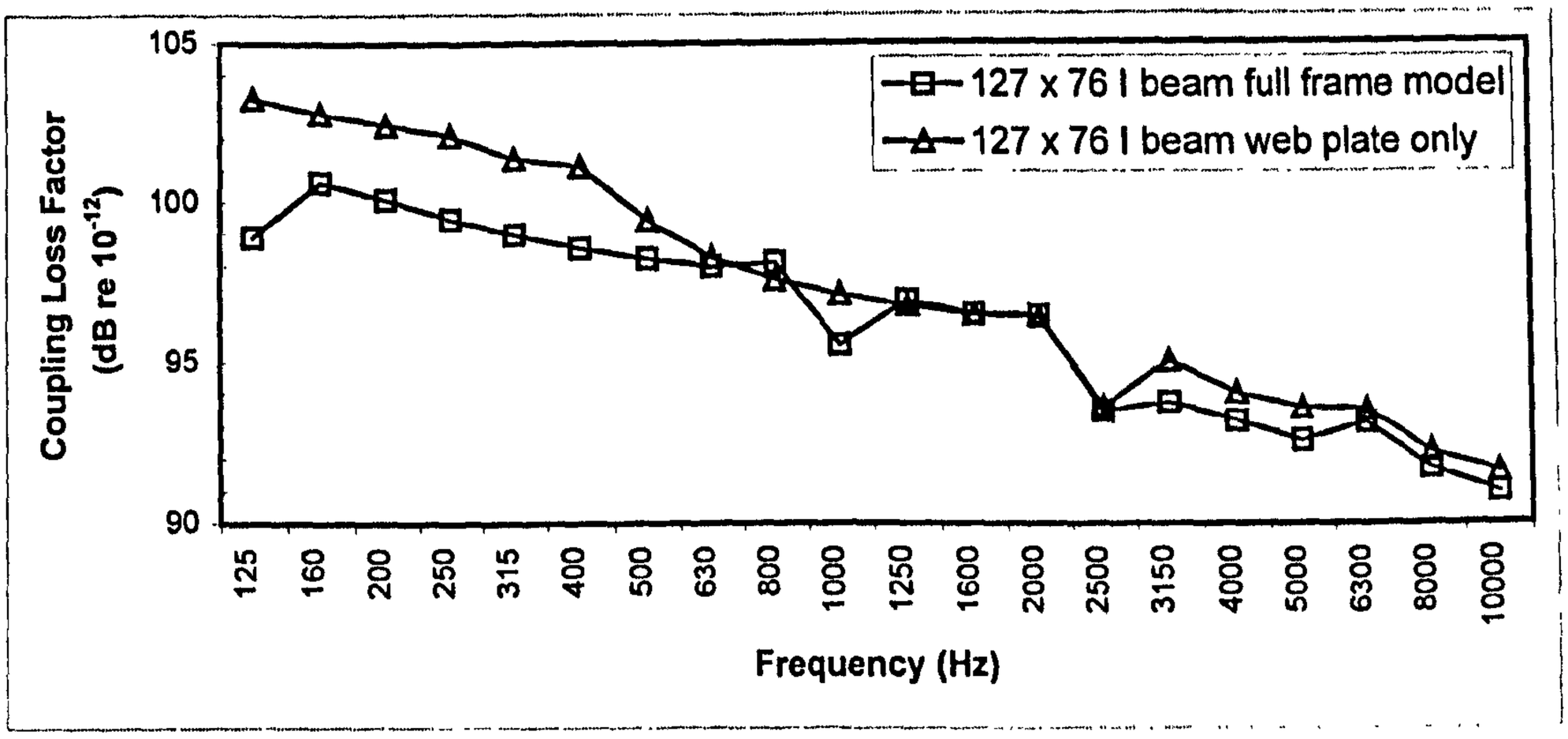

Figure 5.54 Comparison of CLF from full frame and web plate models, joint type 1

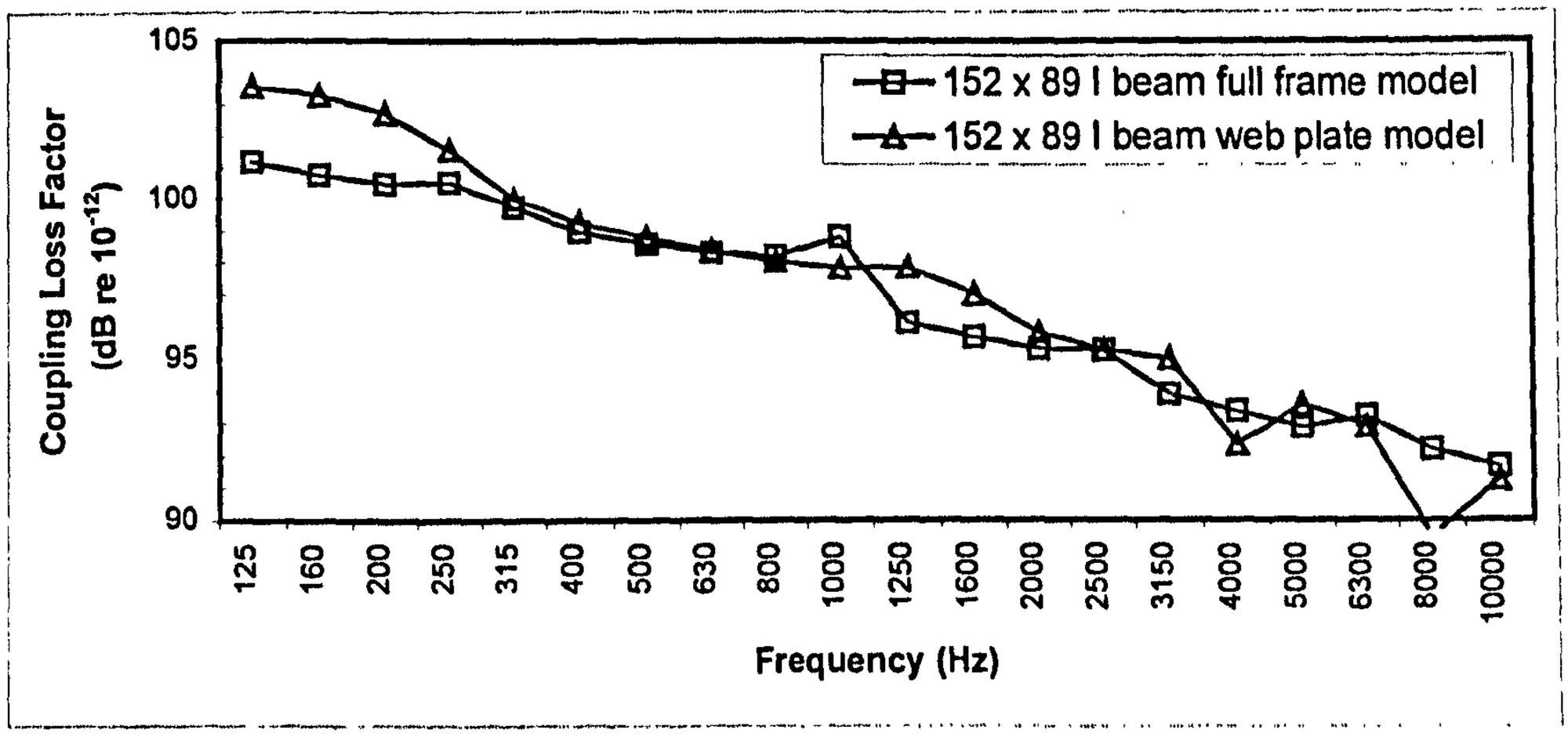

Figure 5.55 Comparison of CLF from full frame and web plate models, joint type 2

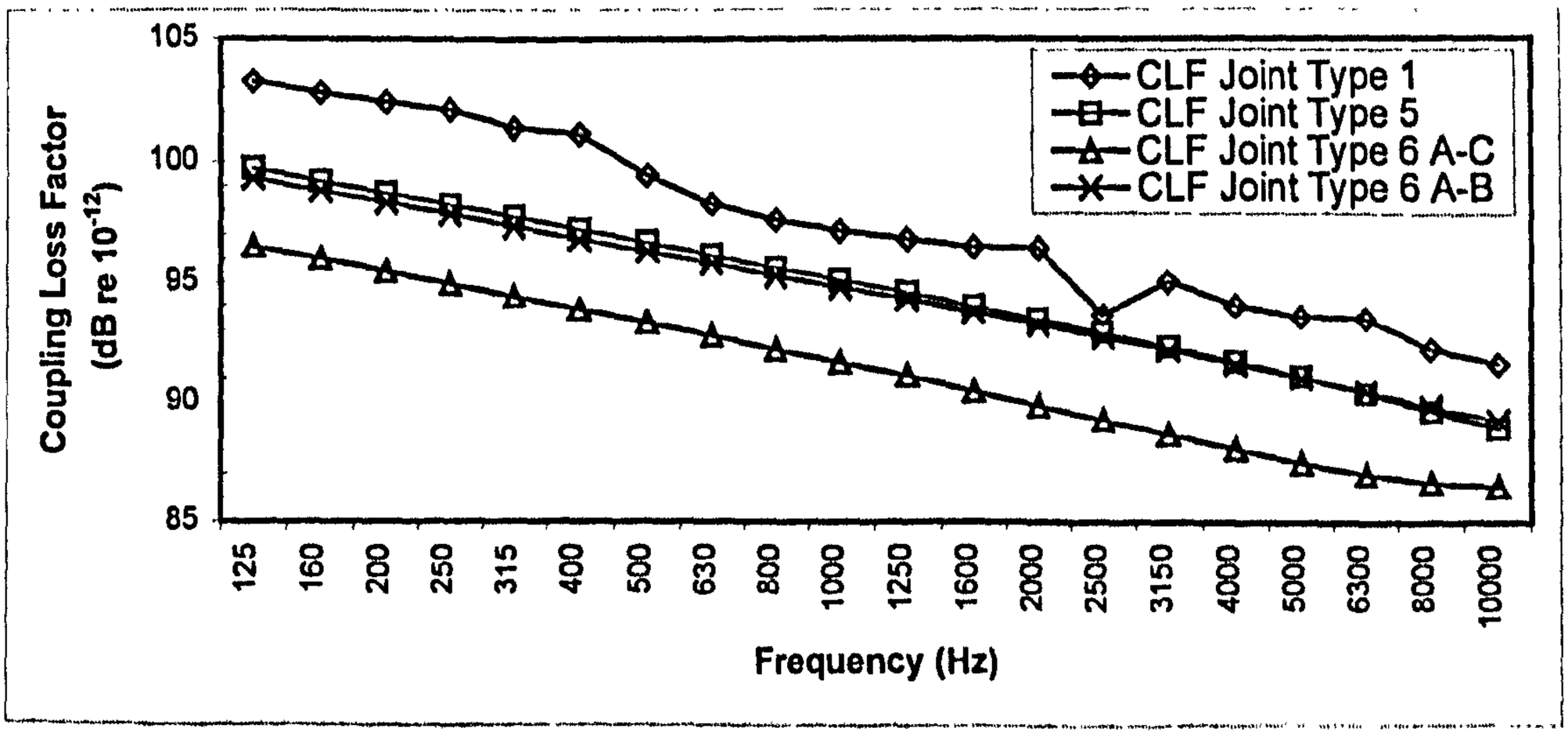

Figure 5.56 Comparison of predicted coupling loss factor of joints for subsystem 128

small differences in the predicted coupling loss factor which will contribute to the accumulated error with distance.

Considering the results presented in section 5.6.4 for the structure borne noise transmission throughout the structure for a power input to subsystem 128. It could be seen that the results presented showed good agreement with the measured attenuation. The reason for selecting subsystem 128 as the source is that the transmission path is more complex that of subsystem 222 which was coupled to two frame joints (type 1) and a corner joint (type 5). Subsystem 128 has one frame joint (type 1), one corner joint (type 5) and the tee joint (type 6).

Figure 5.56 presents a comparison of the bending wave coupling loss factor from subsystem 128 to connected subsystems. It can be seen that the coupling loss factor from subsystem 128 to 129 (joint type 1) is approximately 7 dB higher than that from subsystem 128 to 127 (joint type 6 A-C). The coupling loss factor from the side plate to bottom plate 8 (joint type 5) is almost the same as that from side plate 128 to bulkhead 600 (joint type 6 A-B). Consequently less power flows across the tee junction than to subsystem 129 which is entirely different to the power flow from subsystem 222.

The choice of joint modelling approach (i.e. web plate or full frame) is not significant close to the source subsystem. It is only at the remote subsystems where the difference between the joint modelling approach becomes apparent. The difference between the predictions in the attenuation with distance results were consistent with the observed variations in the coupling loss factor for the two joint modelling approaches discussed earlier in this section. In figure 5.57 the predicted transmission loss R_{1b2b} for the 127 by 76 I-beam for the web plate and full frame models is plotted and it can be seen that except for 1.25 kHz to 2.5 kHz there is a difference in the two modelling approaches.

In figure 5.58 the variation in the transmission coefficient τ_{1b2b} with the angle of incidence is plotted for the 250 Hz frequency band. It can be seen that because of the boundary conditions imposed by the flange plates in the full frame model there are only two narrow incident angles where total transmission occurs. In contrast for the web plate

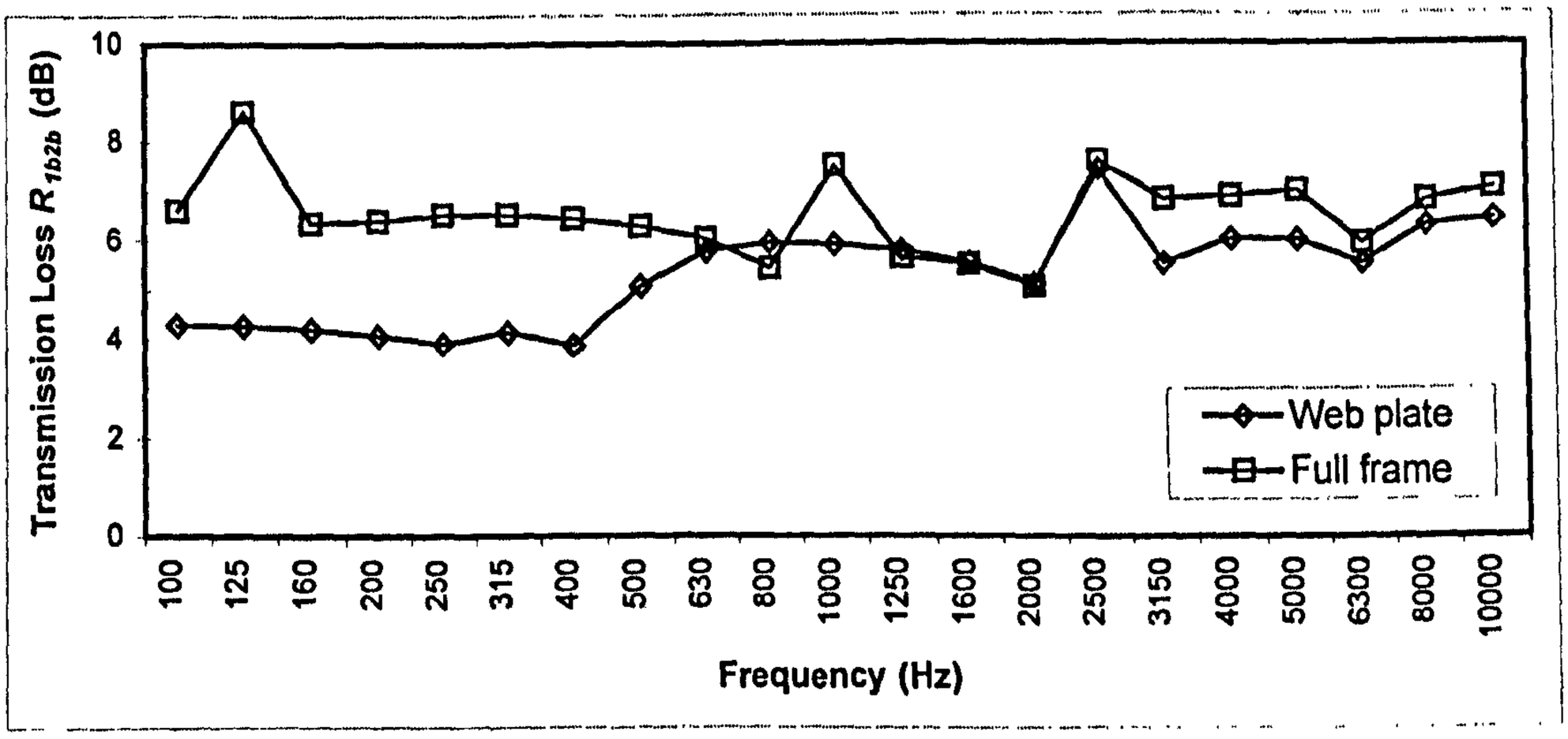

Fig 5.57 Comparison of predicted transmission loss 127 x 76 I beam

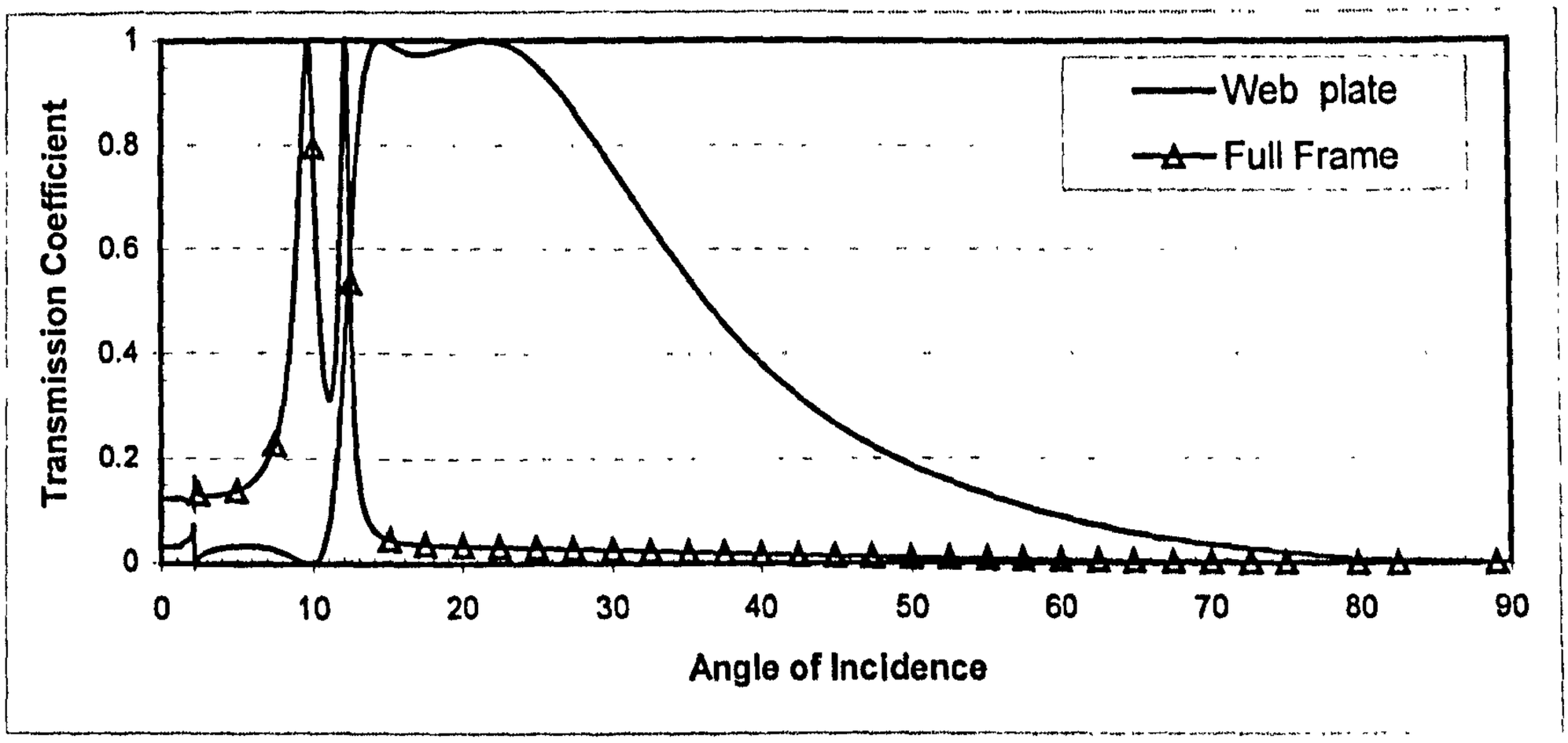

Fig 5.58 Transmission coefficient τ_{1b2b} vs. angle of incidence at 250 Hz

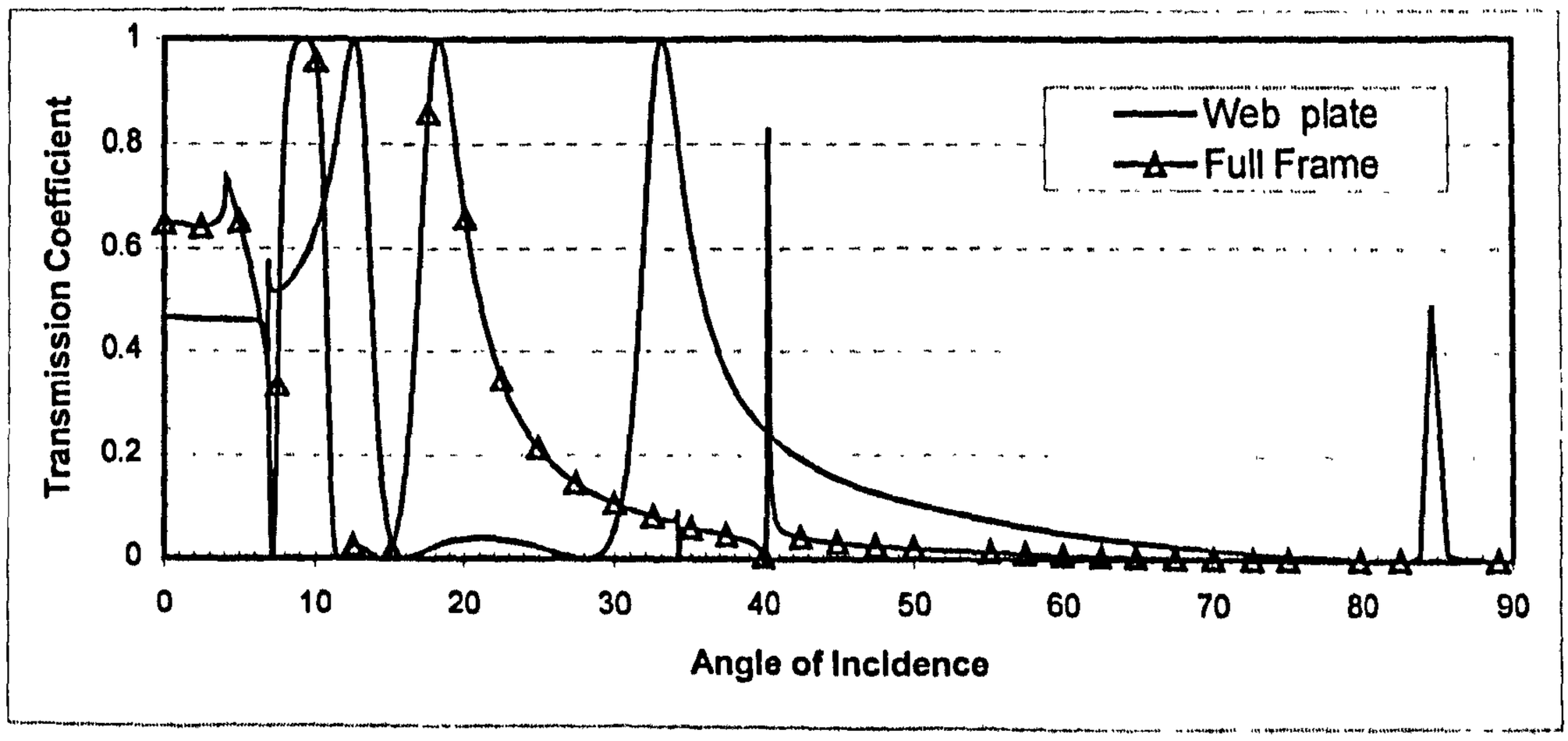

Fig 5.59 Transmission coefficient τ_{1b2b} vs. angle of incidence at 2500 Hz

model, which has been equated to a cantilever, it can be seen that there is a much wider range of incident wave angles which result in near total transmission. This is why the web–plate has the higher coupling loss factor and gives the better predicted attenuation with distance. Figure 5.59 shows the variation in the transmission coefficient τ_{1b2b} with the angle of incidence for the 2.5 kHz frequency band. Although the angles of incidence where total transmission occur are different for the two models, the overall shape of the two curves are very similar. When integrated over all angles of incidence the average transmission coefficient will be very similar and this is shown in the transmission loss figure 5.57 and this is why at higher frequencies the predicted attenuation from the full frame and web plate models shows better agreement.

The one aspect that has not been discussed regarding the tank structure is the nature of the tank itself. From figure 5.22 it can be seen that the tank structure is spatially periodic as defined by Cremer [Ref. 66] i.e. the frames are spaced uniformly. It is often stated in the literature that 'classical' SEA is unable to predict the attenuation in spatially periodic structures because it is unable to model the wave filtering characteristics. In practise a periodic structure acts as stop and pass band wave filter, i.e. stopping some wavelengths from propagating but passing other wavelengths unattenuated. In examples that have been presented by other researchers, 'classical' SEA models have been found to over predict the attenuation because it does not allow for the passing of unattenuated waves across the periodic structure. This is the reason that researchers in this field such as Heron [Ref. 60] and Langley [Ref. 59,79,80] have developed the techniques of wave intensity analysis and the dynamic stiffness matrix method. However the results presented in this chapter have shown that 'classical' methods can produce good agreement in a structure of a periodic nature. The modelling approach used in this thesis would be termed 'classical' SEA.

As an example a five plate model was analysed with four web joints, with the cross section of the structure shown in figure 5.60. The plates were given the dimensions of the steel side plate and the web plates given the dimensions of the joint type 1 (Ref. figure 5.26). The structure was modelled in two different ways, the first being the classical method where each plate is defined as a subsystem and each joint defined

individually. The second model was constructed using the dynamic stiffness matrix method, where plate one was defined as the source subsystem and plate five was defined as the receiving subsystem. One joint was defined consisting of plates two, three and four with the four web plates.

Figure 5.61 plots the predicted attenuation from plate one to plate five from 100 Hz to 10 kHz on a logarithmic scale. It can be seen that the 'classical' SEA approach renders a smooth attenuation prediction with two peaks which coincide with the wave matching frequencies of the web plate. The dynamic stiffness matrix curve has the same trend but there are peaks across the entire frequency spectrum. This is because the dynamic stiffness matrix model has three web plates there are now many more incident bending wavelengths which will match the bending wavelength of the web plates. Applying a line fit to the dynamic stiffness matrix results it can be seen that the difference between the classical SEA predictions and the line fit to the dynamic stiffness matrix prediction is approximately 3 to 4.5 dB.

The problem with the dynamic stiffness matrix model is that it only predicts attenuation in one dimension and therefore can not be used in a two dimensional structure. The tank is spatially periodic but is also a two dimensional structure, and consequently there will be flanking transmission paths. The dynamic stiffness matrix approach does not allow for flanking transmission, but because the SEA model of the tank includes the effect of the flanking transmission this improves the accuracy of the predicted attenuation.

In addition the tank is a real structure with nominally identical dimensions, but there are manufacturing and construction tolerances included which will result in variation throughout the structure from frame to frame. This is important for the wave filtering characteristics as the analytical model assumes a perfect structure to obtain wave filtering. However small deviations in practice can reduce the wave filtering effects by breaking up the stop and pass frequency bands.

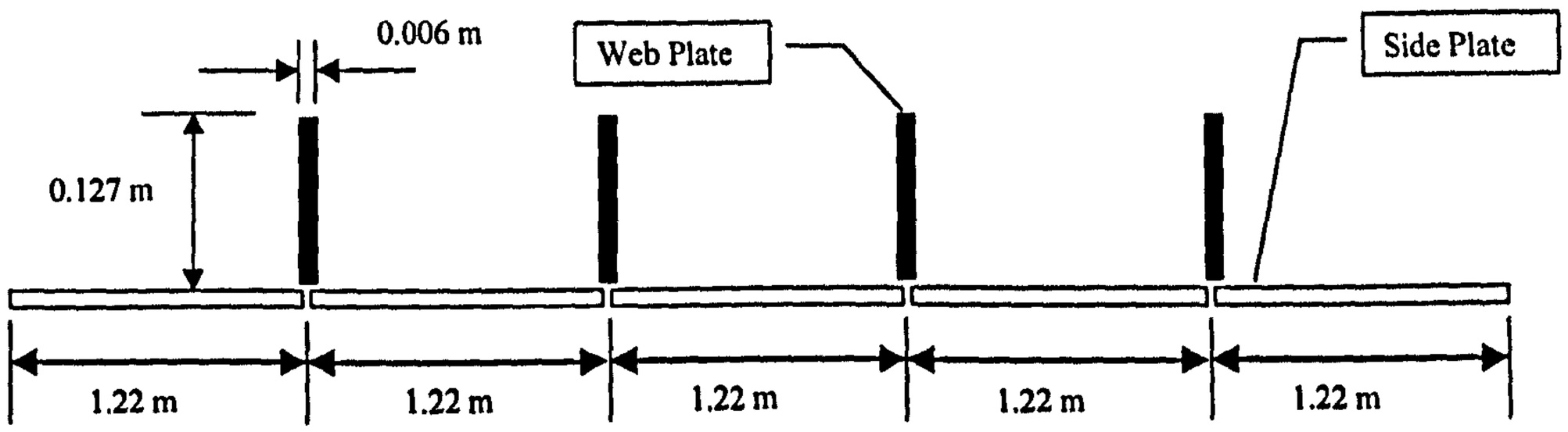

Fig 5.60 Four joint model

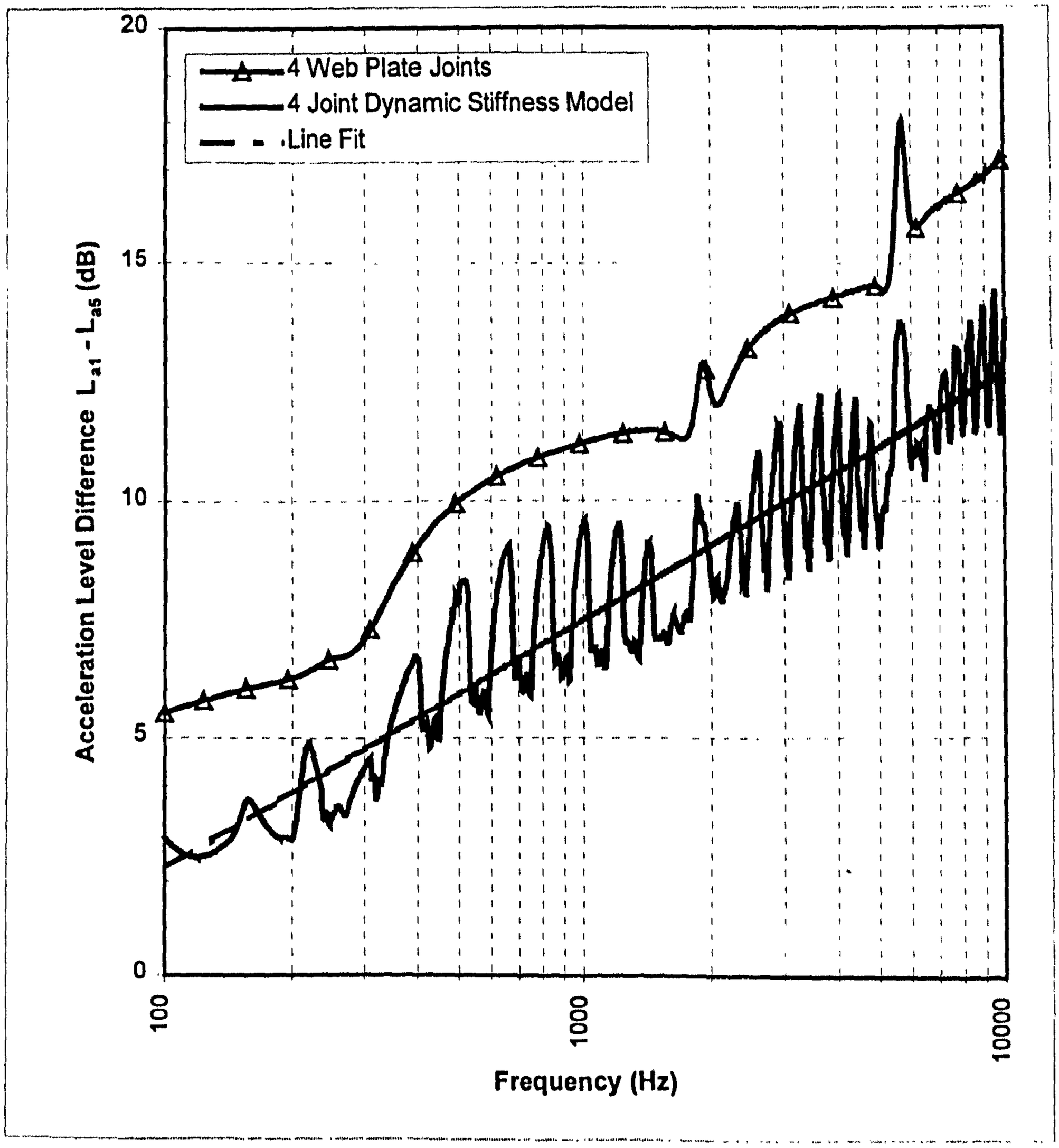

Figure 5.61 Comparison of predicted attenuation across 4 joints.

classical SEA vs dynamic stiffness method

5.7 Summary

In this chapter the theoretical model developed in chapter four has been used in the SEA models of the laboratory test structures. Results were presented from a simple two plate laboratory structure to verify the transmission across one joint using I-beams of different sizes. It was shown that the modelling the frames as an assembly of plates was appropriate for small, medium and deep frame sizes, however ignoring the flange plates and only considering the web plate also gave good agreement.

Results were presented for a large, ship-like laboratory structure constructed from steel plates and I-beams welded to make frames. Results were presented for power input into two different subsystems and good agreement was shown between the measured data and the predicted vibration levels. It was seen that for the small beam sizes used in the frames, that ignoring the effect of the flange plates resulted in better agreement in most frequency bands. This is because the web plate model gives higher average transmission coefficient than the full frame model.

The use of SEA models utilising bending and in-plane wave subsystems was found to give more accurate predictions at remote locations in the lower frequency bands. This is because in practise the test structures can support in-plane waves even though the SEA model subsystem properties indicate in-plane waves would be generated and supported.

5.8 Conclusions

It is concluded from the SEA modelling work presented that the theoretical joint developed in chapter four can be applied to simple single joints structures to give accurate predictions when the modal overlap of one of the subsystems is above unity. When applied to more complex multi-joint structures the full frame model over predicts the attenuation in the vibration level as the number of joints between the source and receiving subsystem increase. Better results are found when the flange plates are ignored and only the web plate is modelled. This conclusion could not be drawn from the single joint results.

Chapter Six

SEA Modelling of Ship Structures

6.1 Introduction

In the previous chapter the theoretical model developed in chapter four was applied to SEA models of simple and complex laboratory structures. Although the laboratory structures have allowed the application of SEA to be demonstrated, they are still relatively simple when compared to the complexity of a real ship structure. In this chapter the application of SEA to large parts of a ship structure is investigated and to accomplish this measurement surveys were performed on sections of a 4,500 tonne warship during it's construction at Yarrow Shipbuilders. Because the surveys were performed on a naval vessel, precise details of the ship construction such as plate thickness, stiffener dimensions, stiffener spacing etc., cannot be given in this chapter, instead general details such as overall dimensions and tonnage are presented.

The sections of the ship structure selected allow different aspects of SEA modelling to be investigated. The sections of the ship surveyed include the following:

(a) Large Ribbed Near-Periodic Deck Plate;

(b) Single Tier Unit of Ship Superstructure;

(c) Double Tier Unit of Ship Superstructure;

(d) Curved Section of Ship's Hull.

In addition to the vibration surveys undertaken on the ship sections, a large amount of damping data was gathered on the individual ship sections surveyed, and the complete

ship structure. The chapter begins with analysis of the internal loss factor data gathered on the different sections of the ship structure before a reviewing the SEA modelling of the different sections of the ship structure, commencing with the simplest structure surveyed and proceeding to increase the complexity of the structure.

6.2 Large Ribbed Deck Plate

In this section the analysis of vibration transmission across a large ribbed deck plate from a partially constructed unit is presented. The geometry and overall dimensions of the structure surveyed is shown in figure 6.1. It essentially consists of a large steel deck plate, with welded ribs consisting of an array of regularly spaced frame stiffeners in the x-direction and bulb plate stiffeners in the y-direction. In the x-direction there is a total of fourteen regularly spaced small flat bar stiffeners between the frame stiffeners, but these are not shown on the figure. Attached to the structure are two ribbed bulkheads and two ribbed side shells, one of which has been removed from the figure for clarity. As the structure was under construction at the time, the welding of the side shells was incomplete at their interface with the deck plate and tack welds were used to hold the side shells in position, however all other welding on the structure was complete. The source subsystem was as shown in figure 6.1.

The depth of the flat bar stiffeners is approximately one third of the frame stiffeners and the bulb stiffeners are approximately half the depth of the frame stiffeners. The size of the frame stiffeners is somewhere between that of the 203 x 133 and 406 x 178 I-beams analysed in chapter four. The modal density for the deck area is approximately 0.6 modes per Hertz and the modal overlap is above unity in the 125 Hz frequency band. After reviewing the geometry of the structure and considering the relative size of the ribs, it was decided to model the structure in two different ways. The first modelling approach discussed is a coarse model of the ribbed deck plate which is described in the following section. This is followed by a section in which a more detailed SEA model is described.

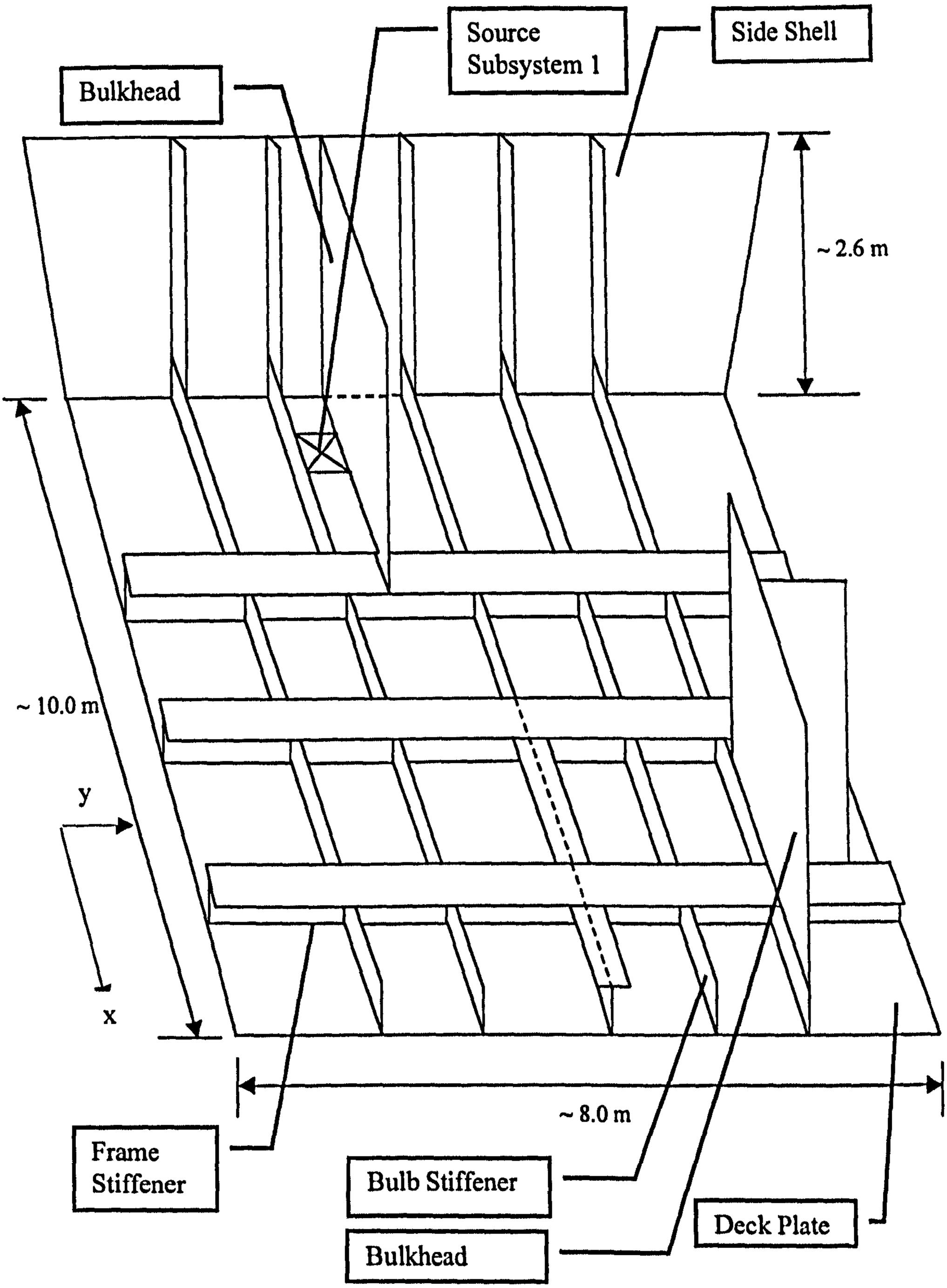

Figure 6.1 Large ribbed deck plate

6.2.1 Coarse SEA Model

In the coarse SEA model the small flat bar stiffeners running in the *y* direction on the deck plate were ignored and only the frame and bulb plate stiffeners were modelled. This approach was also applied to the bulkheads where small rib stiffeners were ignored but the side shell bulb plate stiffeners, which were the same size as those on the deck plate, were included. In figure 6.2 the coarse SEA model of the deck plate is shown with the corresponding subsystem numbers. The bulkheads and side shells are included in the model but no measured or predicted data is presented as transmission across the deck plate is the focus of the analysis. In practical terms the coarse model is the preferred modelling approach, since it would require the definition of fewer subsystems and joints. As with chapter four, the different joint modelling approaches are investigated to determine the most suitable approach.

(a) Model 1: The SEA model of the structure consists of bending, longitudinal and transverse wave subsystems. The frame stiffeners in the *x* and *y* directions are modelled with flange plates and all other rib stiffeners are modelled as web plate joints. The model has a total of 47 plate subsystems with 52 joints and 616 coupling loss factors.

(b) Model 2: The SEA model of the structure consists of bending, longitudinal and transverse wave subsystems. All rib stiffeners on the deck plate are modelled as web plate joints i.e. the flanges of the frame stiffeners are ignored.

(c) Model 3: The SEA model of the structure consists only of bending wave subsystems. All rib stiffeners are modelled as web plate joints, the flanges of the frame stiffeners are ignored. The model has a total of 47 subsystems with 52 joints and 136 coupling loss factors.

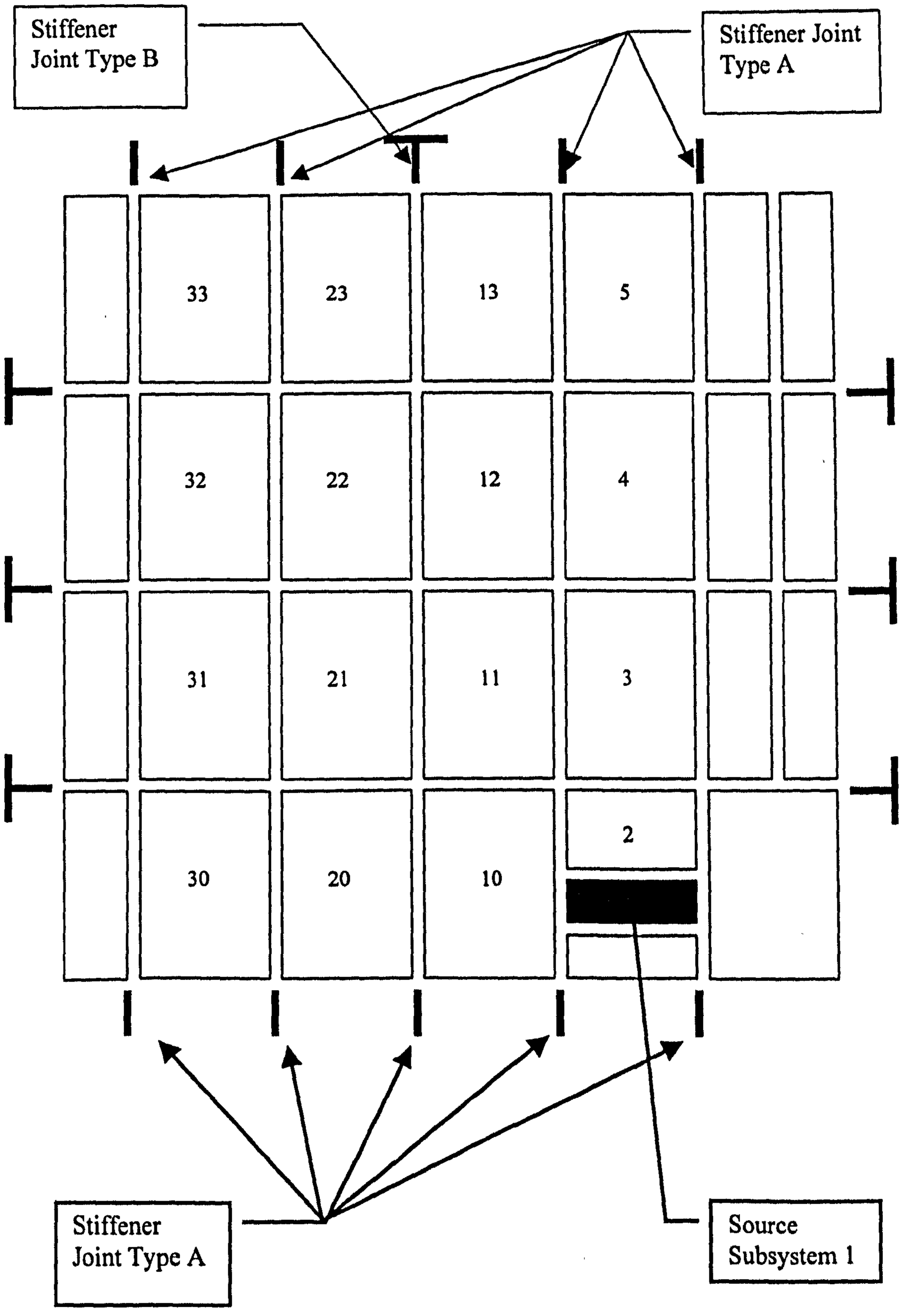

Figure 6.2 Coarse SEA model of large ribbed plate

6.2.2 Detailed SEA Model

The alternative approach for the SEA model of the ribbed deck plate, the bulkheads and side shells is to consider all the stiffeners of the structure. Each subsystem on the deck is defined as the section of deck plate contained within 4 stiffeners. As a consequence the number of bending wave subsystems increases from 52 in the coarse SEA model to 150 in the detailed SEA model and the number of joints in the BLT model increases from 112 in the coarse model to 529 in the detailed SEA model. It can be seen that even for a very small section of the ship structure, the change from a coarse to a detailed modelling strategy rapidly increases the complexity and size of the SEA model.

In figure 6.3 the detailed SEA model of the deck plate is shown with the corresponding subsystem numbers where measurements were taken. Comparing the coarse and detailed SEA models of the deck plate it can be seen that 3 to 4 stiffeners per subsystem were omitted in the coarse model. The same modelling strategy and designation is used as for the coarse model.

(a) Model 1: The SEA model of the structure consists of bending, longitudinal and transverse wave subsystems. The frame stiffeners in the x and y directions are modelled with flange plates and all other rib stiffeners are modelled as web plate joints. The number of subsystems is 172 and there are 257 joints. For the BLT model the total number of coupling loss factors is 2765.

(b) Model 2: The SEA model of the structure consists of bending, longitudinal and transverse wave subsystems. All rib stiffeners on the deck plate are modelled as web plate joints i.e. the flanges of the frame stiffeners are ignored. The number of coupling loss factors is the same as model 1.

(c) Model 3: The SEA model of the structure consists only of bending wave subsystems. All rib stiffeners are modelled as web plate joints, the flanges of

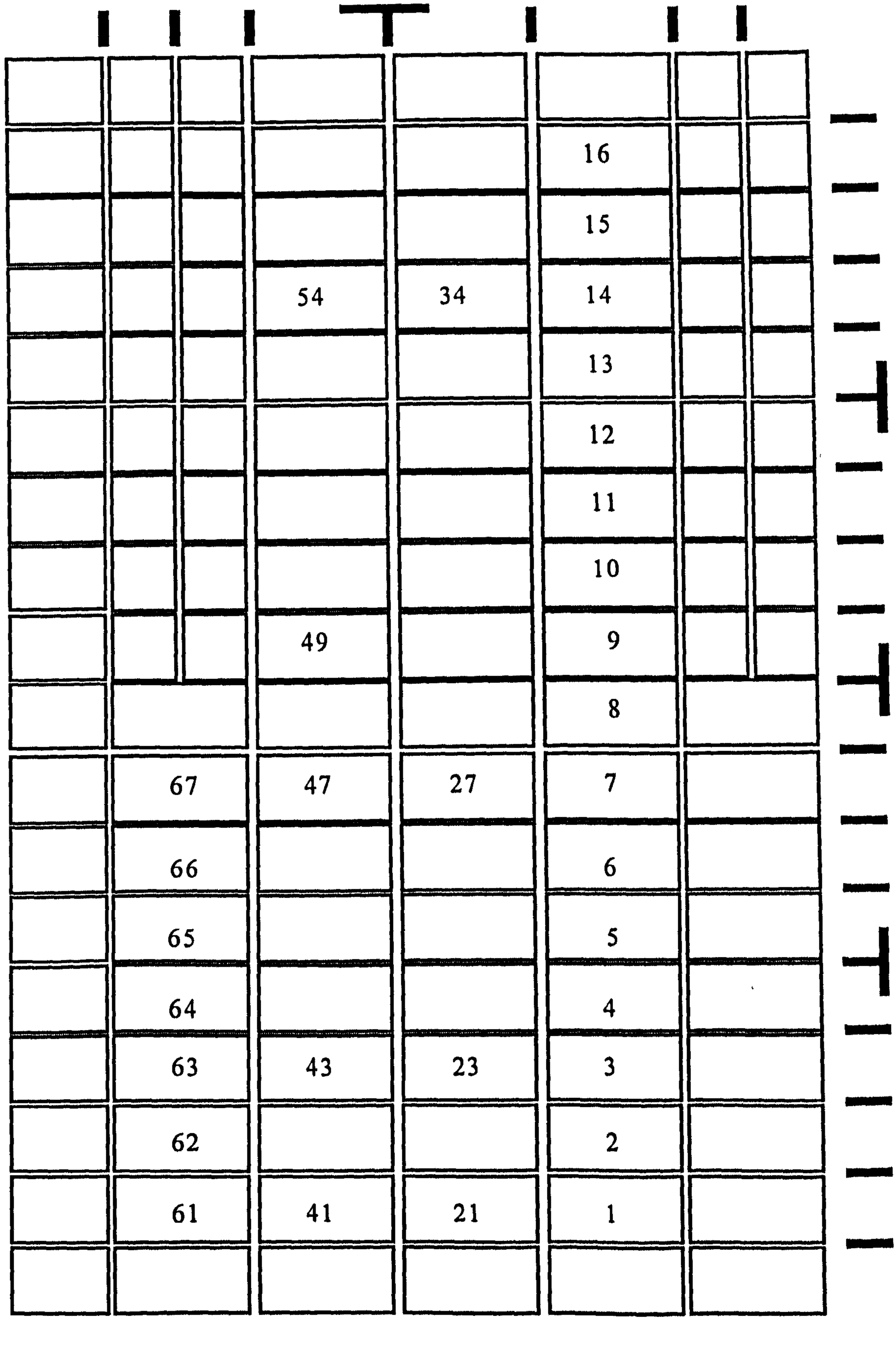

Figure 6.3 Detailed SEA model of large ribbed plate

(d) the frame stiffeners are ignored. The total number of coupling loss factors is 580.

Before reviewing the results from the two modelling approaches, the basic subsystem properties such as statistical mode count, modal overlap and coupling loss factors are reviewed in the next section for the coarse model.

6.2.3 Coarse SEA Model – Subsystem Properties

In figure 6.4 the statistical mode count for the bending wave subsystem 4, longitudinal wave subsystem 1004 and transverse wave subsystem 2004 is shown. The number of modes in the bending wave subsystems is higher than observed in figure 5.29 for the steel plates in the laboratory structure. The in-plane subsystems have no modes in the 100 to 1250 Hz frequency bands, but above the 1600 Hz frequency band the in-plane modes start to occur. The in-plane mode count however is based on the dimensions of the subsystem, but in practice there will be in-plane modes in the lower frequency bands that propagate across the entire deck plate, which will be relatively unattenuated by the rib stiffeners.

In figure 6.5 the modal overlap M of bending wave subsystem 4, longitudinal wave subsystem 1004 and transverse subsystem 2004 are shown. It can be seen that the predicted modal overlap of the bending wave subsystem is above unity in all frequency bands between the 100 Hz and 10 kHz frequency bands but in the laboratory structure this did not occur until the 160 Hz frequency band. The modal overlap M_T for the transverse wave subsystem and M_L for the longitudinal wave subsystem does rise above unity until the 5 kHz frequency band.

In figure 6.6 the predicted coupling loss factor for joint type A (see figure 6.2) from bending wave subsystem 3 to subsystem 11, $\eta_{3\text{-}11}$, is shown. Also plotted is the coupling loss factor for joint type B (see figure 6.2) from bending wave subsystem 3 to subsystem 4, $\eta_{3\text{-}4}$, for the web plate and full frame modelling approaches. It can be seen that the coupling loss factor $\eta_{3\text{-}11}$ is higher than $\eta_{3\text{-}4}$ across the entire frequency

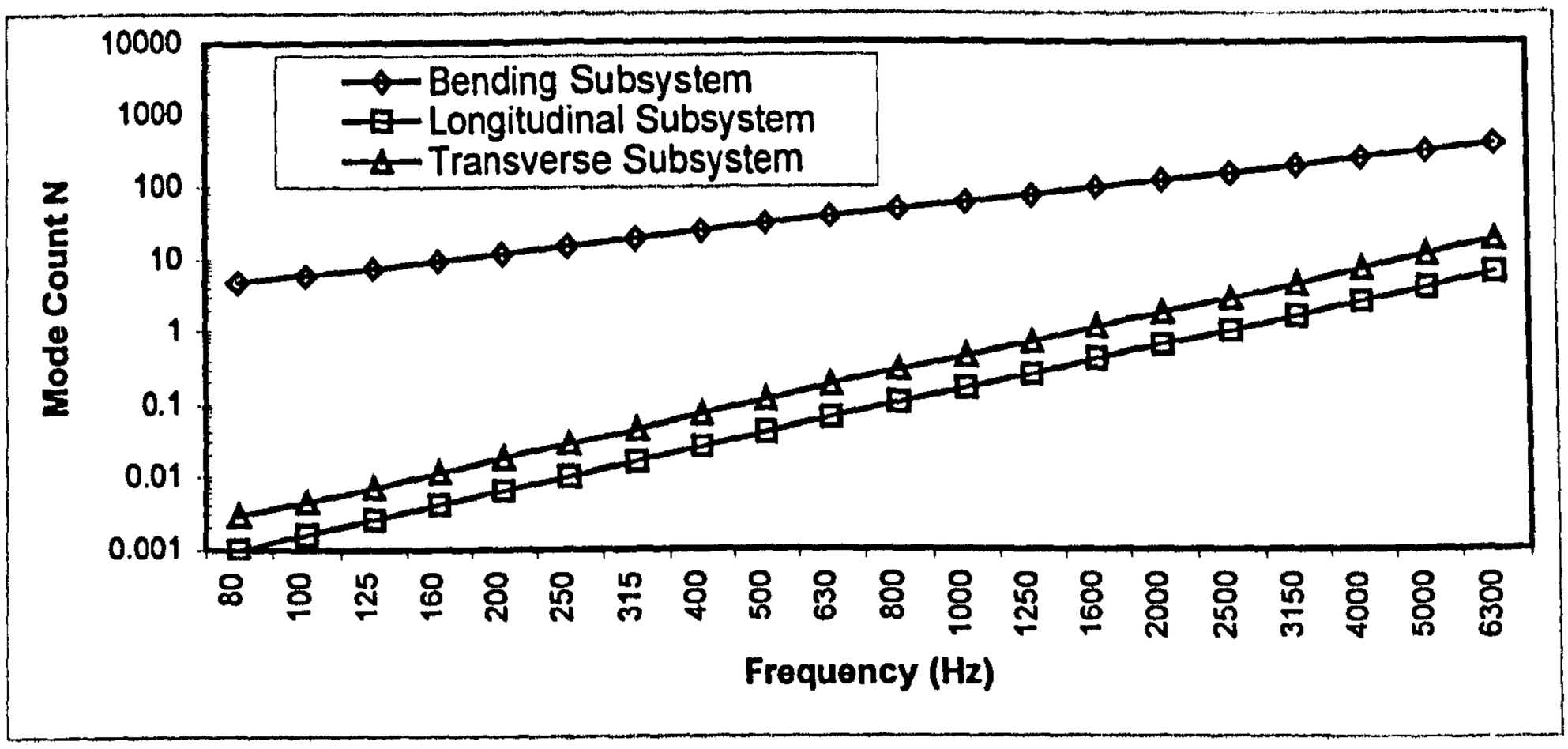

Figure 6.4 Comparison of statistical mode count for B L and T subsystems

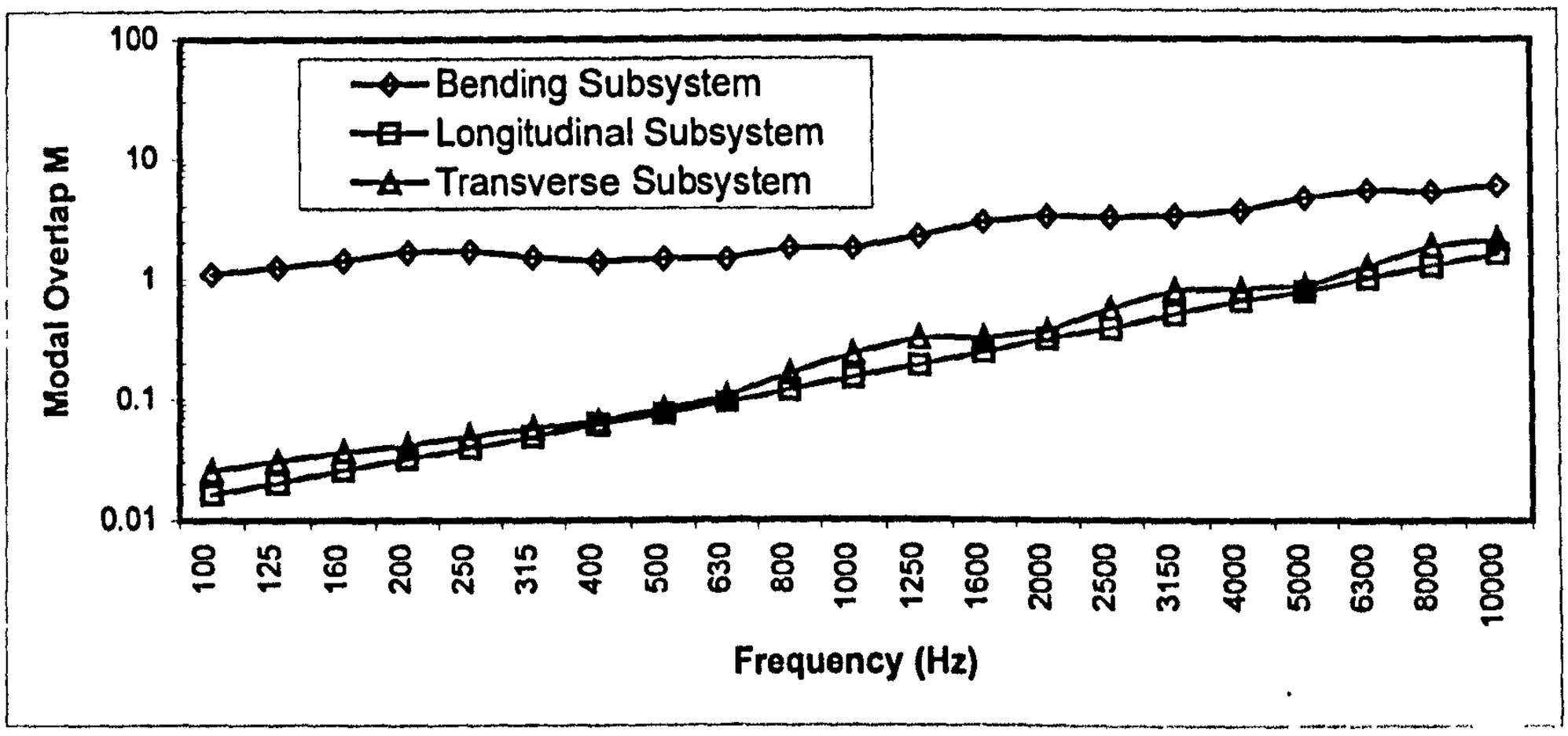

Figure 6.5 Comparison of predicted modal overlap for B L and T subsystems

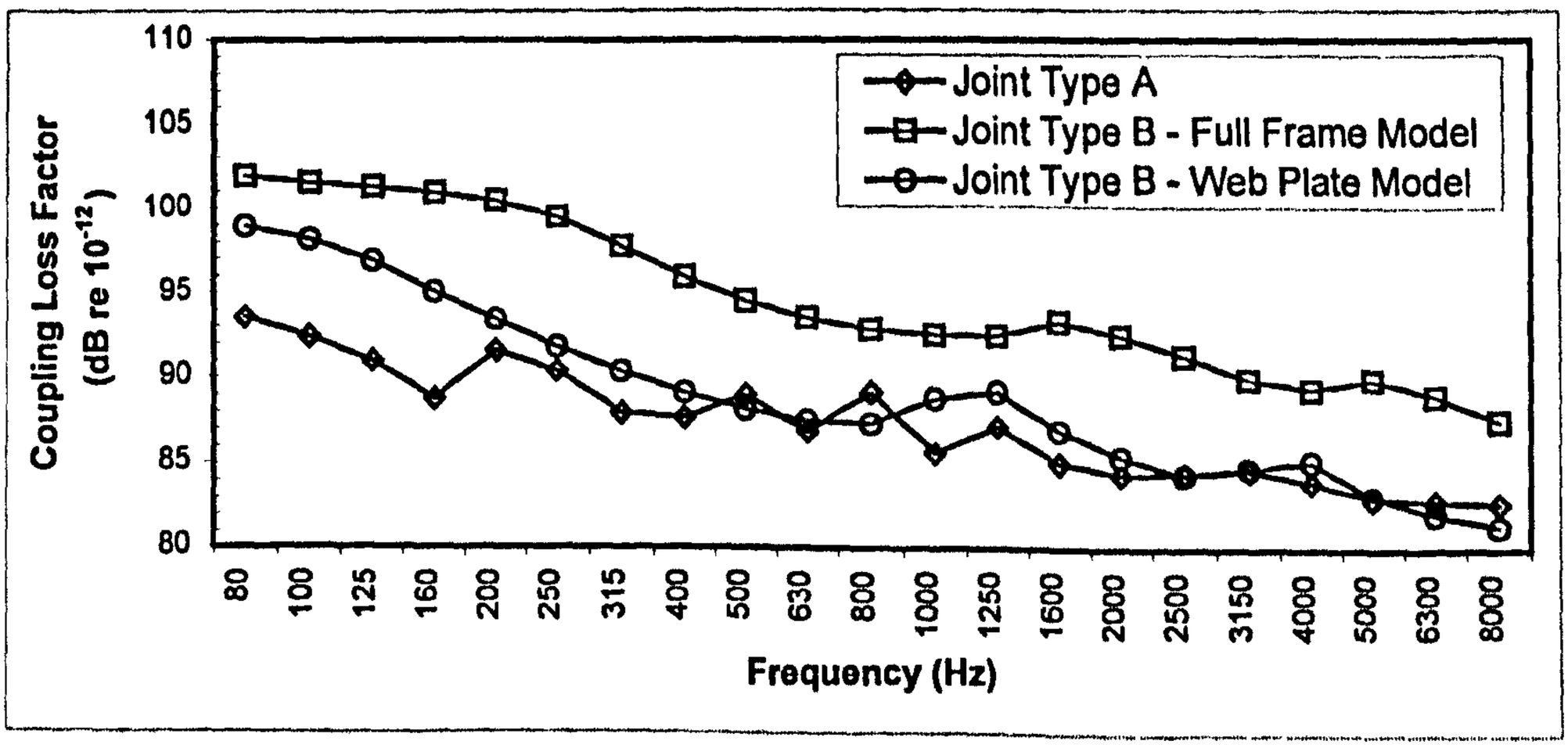

Figure 6.6 Comparison of coupling loss factor for deck plate

spectrum, therefore more power will be transmitted in the *y*-direction. For joint type B the web plate modelling approach gives a smooth curve as was observed in chapter 5 which is higher by 2 to 5 dB than the full frame model in the 100 Hz to 500 Hz frequency bands.

Above the 500 Hz frequency band, the full frame and web plate modelling approaches are similar but only in certain frequency bands is the predicted coupling loss factor from the two modelling approaches are identical e.g. 630 Hz, 2.5 kHz, 3.15 kHz etc.

6.2.4 Detailed SEA Model– Subsystem Properties

In figure 6.7 the predicted mode count for bending wave subsystem 7, longitudinal wave subsystem 1007 and transverse wave subsystem 2007 are shown. Because the subsystems are smaller than those in the coarse model, the mode count is lower. In particular the mode count for the in-plane wave subsystems is very low, only rising to 2 or 3 modes above the 4 kHz frequency band. The comments about the artificial nature of the statistical mode count for in-plane wave subsystems discussed in section 6.2.3 on the coarse subsystem properties are applicable to the detailed model.

In figure 6.8 the modal overlap is plotted for the bending wave subsystems, longitudinal wave subsystems and transverse wave subsystems. It can be seen that the modal overlap of the bending wave subsystem, M_b, rises above unity in the 200 Hz frequency band. Therefore despite the size of the detailed subsystems being one-quarter to one-fifth of the size of the coarse model subsystems, the modal overlap is above unity in most of the frequency bands and therefore the detailed model should be accurate down to 200 Hz. For the transverse and longitudinal wave subsystems the modal overlap M_T and M_L does not rise above unity until the 2.5 kHz and 4 kHz frequency bands.

In figure 6.9 the different bending wave coupling loss factors are plotted for subsystem 7. The coupling loss factor for joint type 1 is for the small web plate stiffeners shown in figure 6.6. It can be seen that this is much higher than any of the other coupling loss factors in all frequency bands, but it is common to all three SEA models. Also plotted is

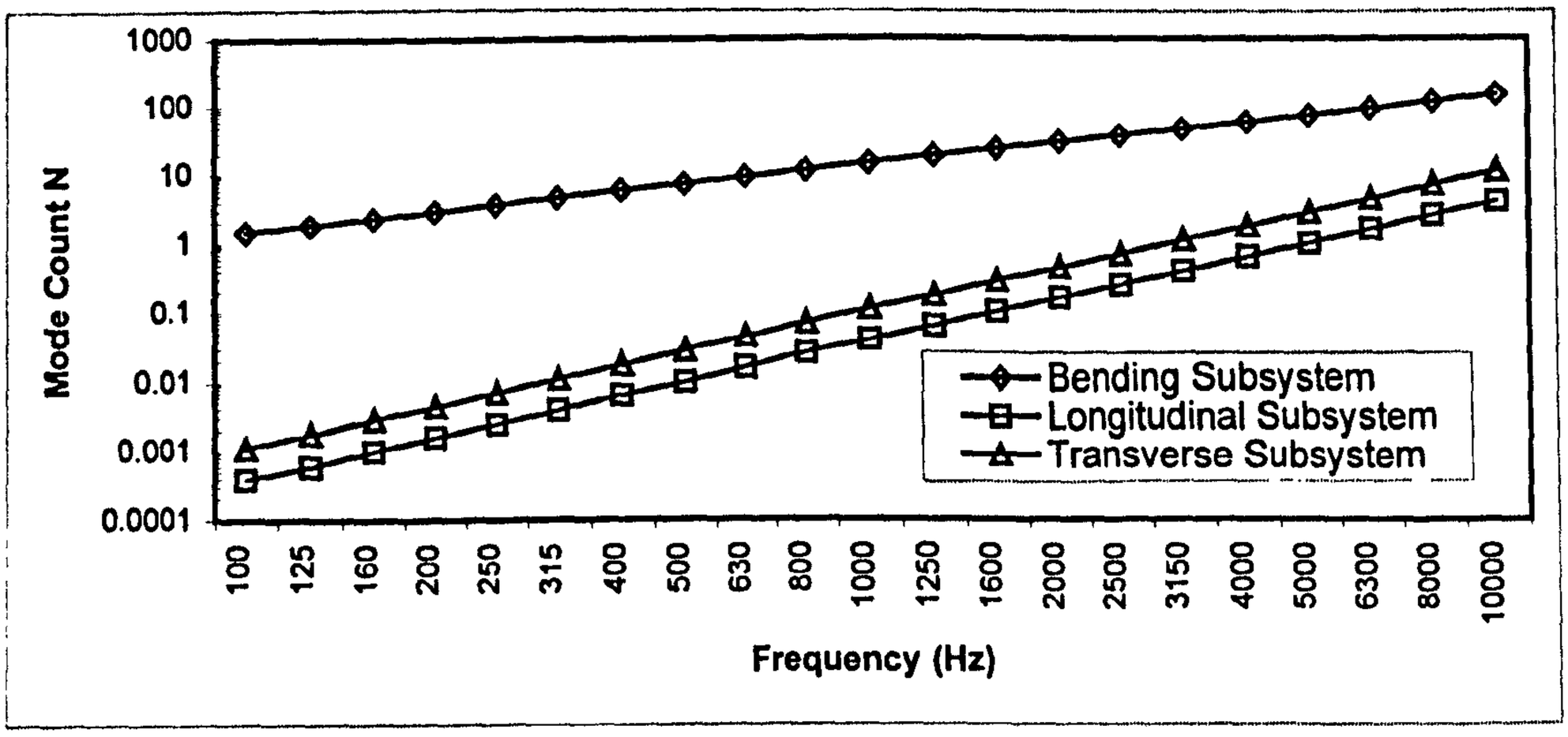

Figure 6.7 Comparison of statistical mode count for B L and T subsystems

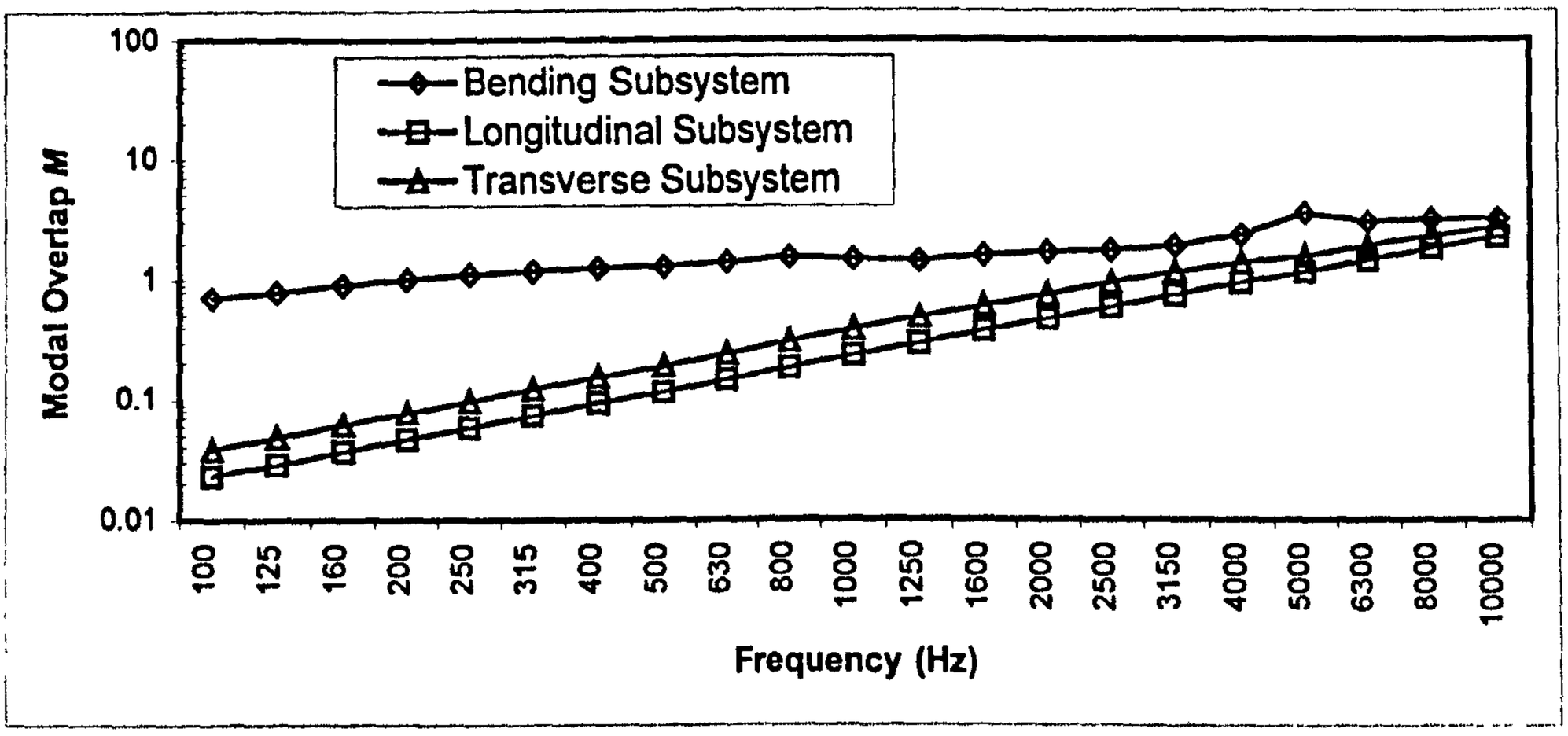

Figure 6.8 Comparison of modal overlap for B L and T subsystems

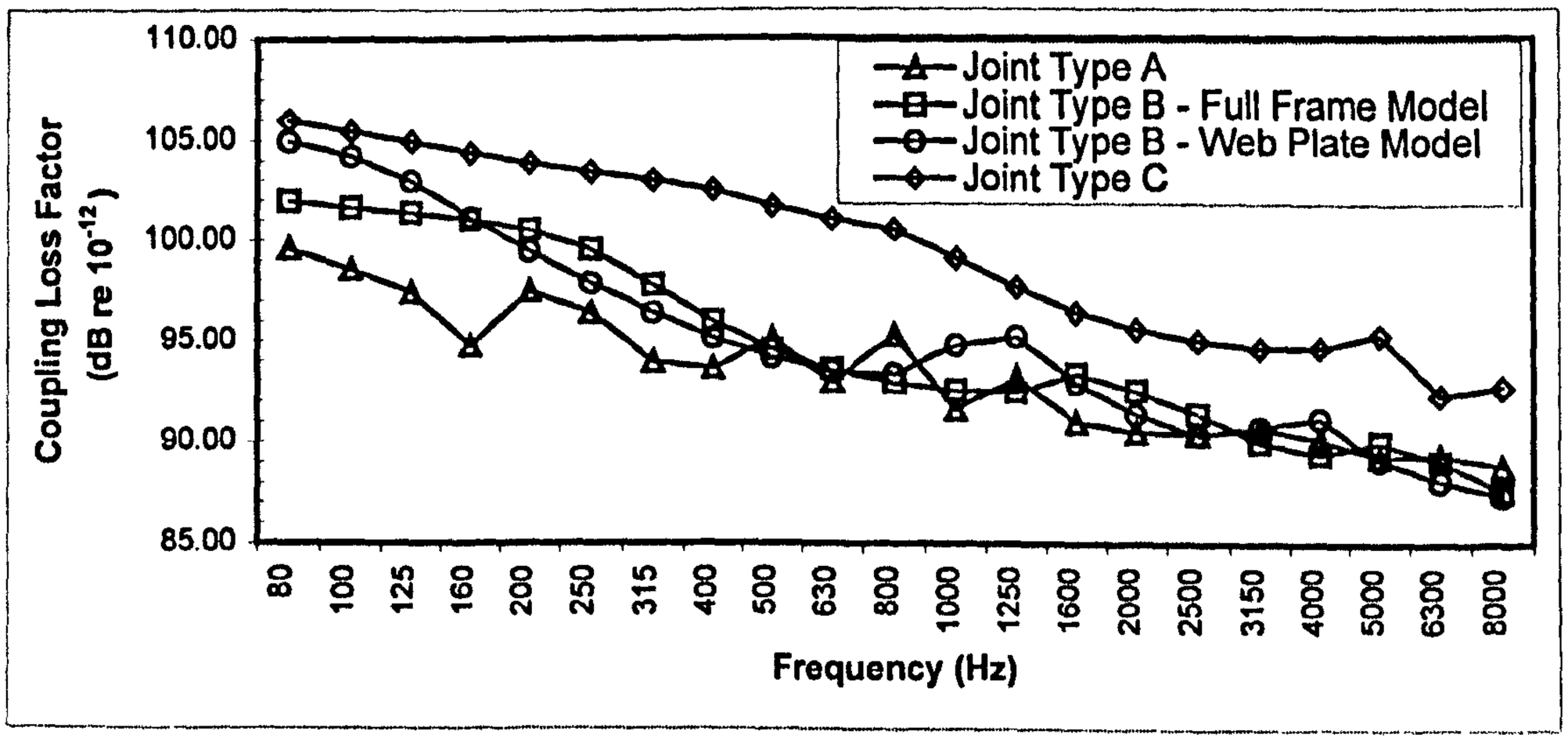

Figure 6.9 Comparison of bending wave coupling loss factor for deck plate

the coupling loss factor for joint type 2 for the longitudinal stiffeners in the *y* direction. It can be seen that this is much lower than joint 1 in the mid and high frequency bands. More power will be transmitted in the *x* direction than the *y* direction from each subsystem. The coupling loss factor for joint type 3 is plotted for the full frame joint model and for the web plate joint model. It can be seen that the difference in the coupling loss factor due to the modelling approach follows the trend observed in the coarse model and the laboratory structures i.e. at low frequencies the difference between the coupling loss factor is due to the web plate behaving as a beam.

6.2.5 Coarse SEA Model – Comparison Of Predicted And Measured Attenuation

In figure 6.10 the predicted attenuation from source subsystem 1 to subsystem 3 (see fig 6.2) across the first frame joint is shown. It can be seen that the measured and predicted attenuation shows good agreement in most frequency bands. The difference between model *2* (BLT wave web plate model) and model *3* (B wave web plate model) is very small across the first joint. It can be seen that the prediction from model *1* shows slightly better agreement with the measured attenuation between 200 Hz and 8 kHz.

In figure 6.11 the predicted attenuation from source subsystem *1* to subsystem *4* across two frame joints is shown. The model *1* results (the full frame model) show poor agreement in the low frequency bands, but do improve at the higher frequencies although the prediction does not follow the trend observed in the measured attenuation. The predicted attenuation from model *2* shows good agreement over most of the frequency spectrum and follows the trend of the measured attenuation. The prediction from model *3* shows good agreement with the measured attenuation between the 125 Hz and 1 kHz frequency bands, but above this the predicted attenuation increases.

In figure 6.12 the predicted attenuation form source subsystem *1* to subsystem *5* across three frame joints is shown. The prediction from model *2* shows good agreement with the measured attenuation in most frequency bands and follows the trend of the measured attenuation. The results from model *3* (the B- wave SEA model), show the same trend as the measured attenuation, however there is a significant difference

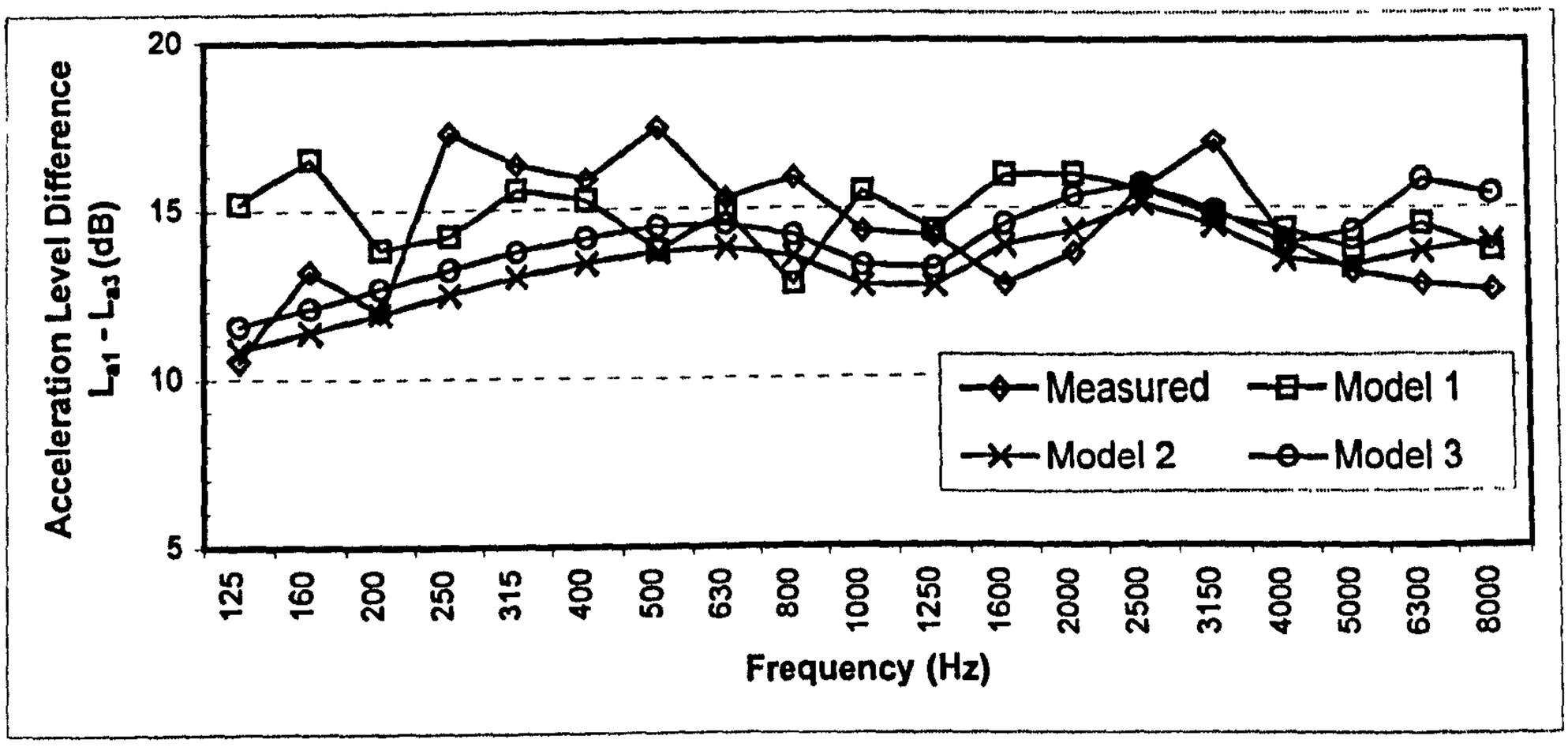

Figure 6.10 Comparison of measured and predicted attenuation L_{a1}-L_{a3}

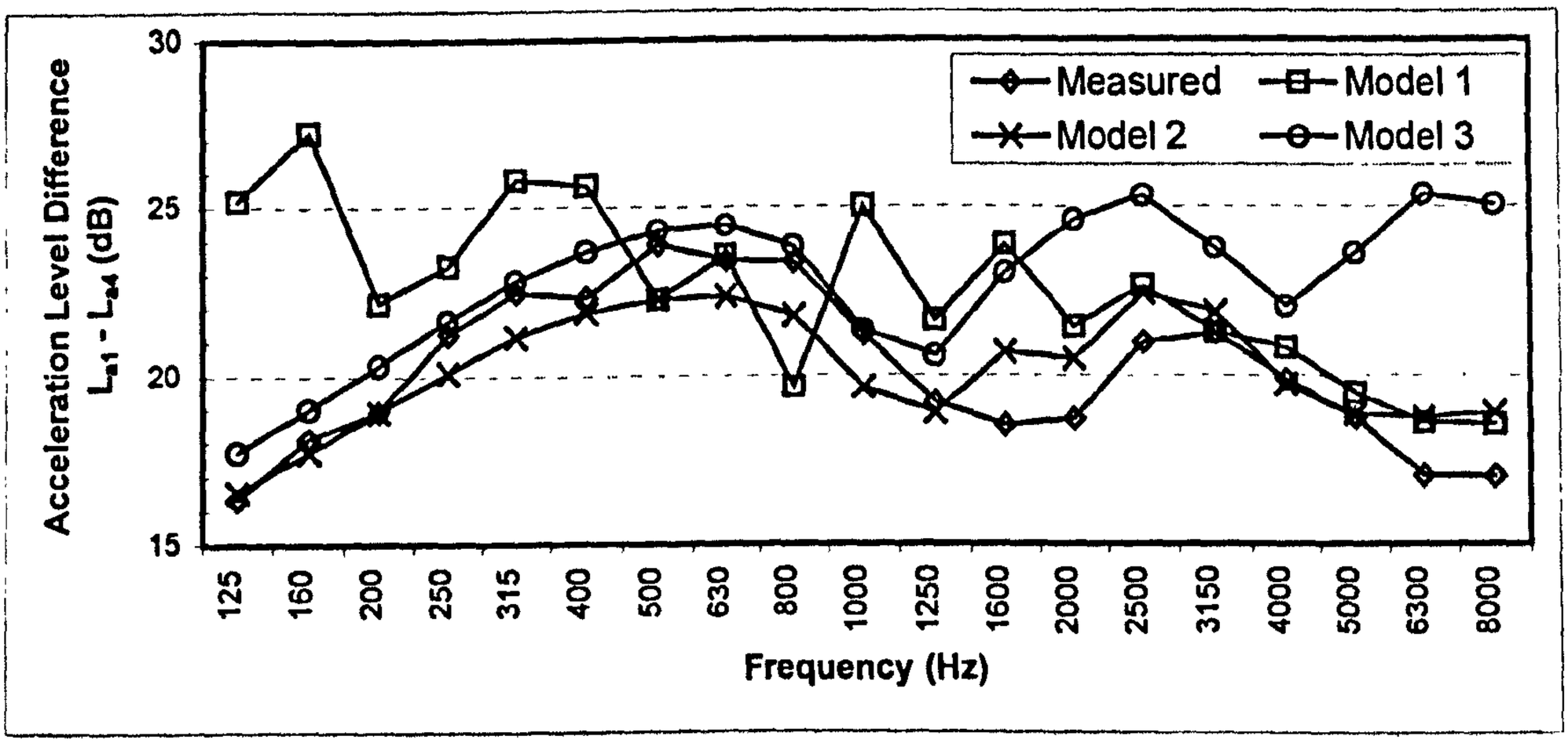

Figure 6.11 Comparison of measured and predicted attenuation L_{a1}-L_{a4}

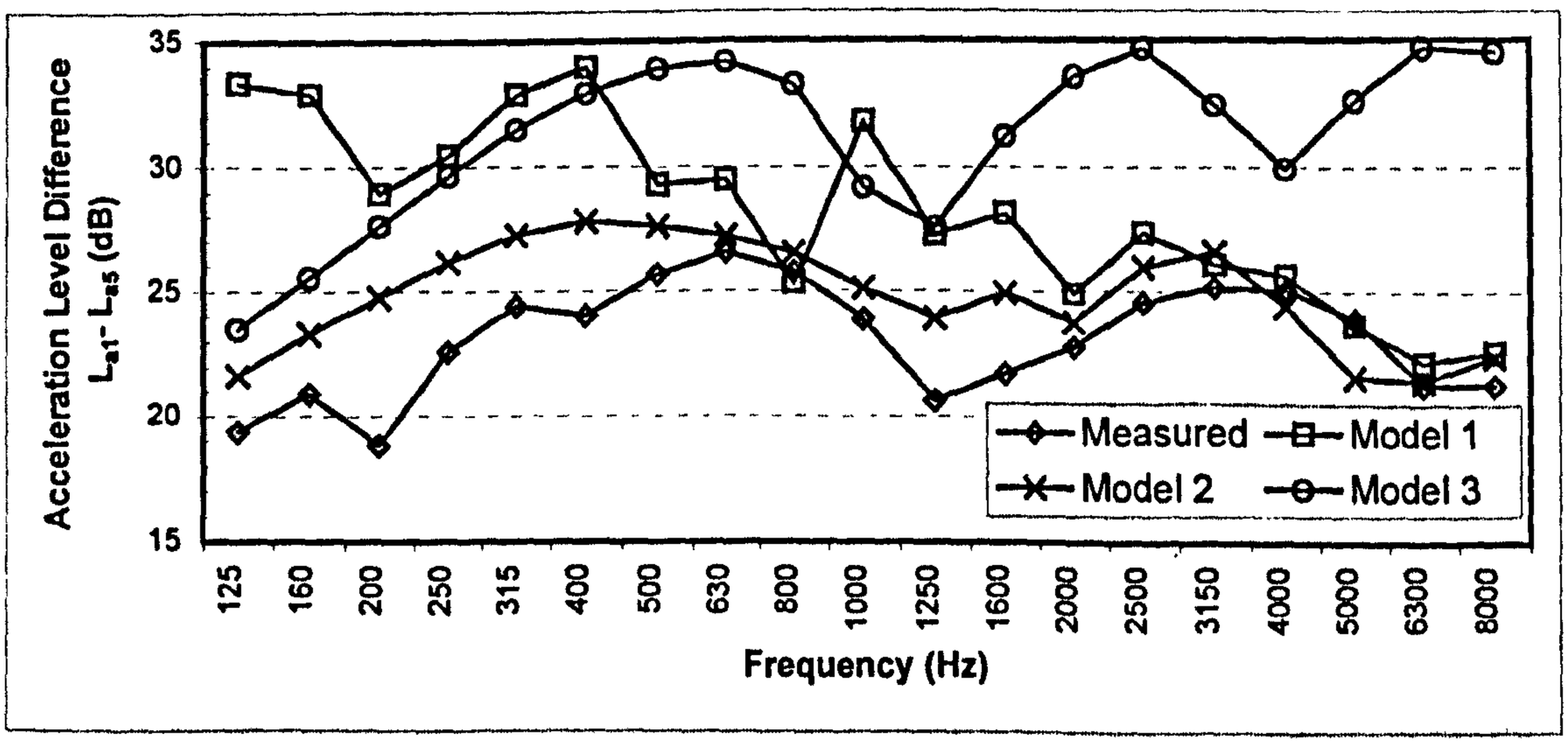

Figure 6.12 Comparison of measured and predicted attenuation L_{a1}-L_{a5}

between the predicted and measured attenuation that increases with frequency. The results for model *1* show poor agreement below 2.5 kHz with the measured attenuation.

In figures 6.13 the predicted and measured attenuation from subsystem *1* to subsystem *22* is shown. It can be seen that the predicted attenuation from model *2* shows the best agreement with the measured attenuation. As with the results shown in figures 6.10 to 6.12 the results from model *3* (the B-wave SEA model) shows the correct trend when compared to the measured attenuation, but the prediction is too high. For model *1*, the predicted attenuation shows poor agreement in the lower frequency bands but improves above the 400 Hz frequency band.

In figures 6.14 the predicted and measured attenuation from subsystem *1* to subsystem *23* is shown. The predicted attenuation from model *2* shows the best agreement with the measured attenuation between 250 Hz and 8 kHz. The results from model *3* (the B-wave SEA model) again show the correct trend when compared to the measured attenuation, but the prediction is too high. For model *1*, the predicted attenuation shows poor agreement in the lower frequency bands but improves above the 400 Hz frequency band.

In figure 6.15 the predicted and measured attenuation shows from subsystem *1* to subsystem *31* on the opposite side of the deck plate. The predicted results from model *2* again shows good agreement with the measured attenuation and the predictions from models *1* and *3* are very similar.

6.2.6 Detailed SEA Model – Comparison Of Predicted And Measured Attenuation

In figure 6.16 the predicted attenuation from source subsystem 1 to subsystem 5 (see fig 6.3) across three web plate stiffeners and the first frame joint is shown. The measured and predicted attenuation show good agreement in most frequency bands. The difference between model *2* (BLT wave web plate model) and model *3* (B wave web plate model) is very small across the four joints in the low frequency bands but in the 4 kHz to 8 kHz frequency bands there is a small difference between the predictions. The

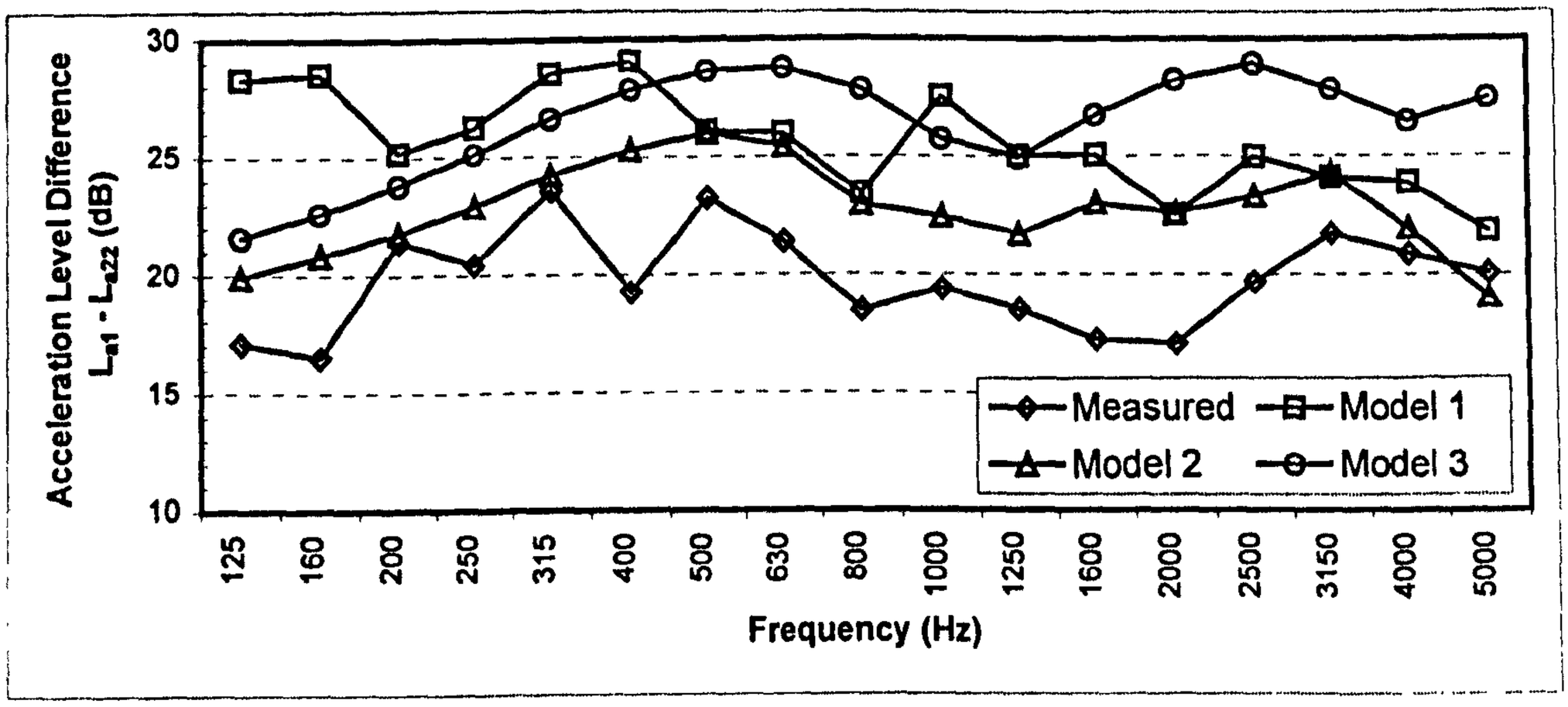

Figure 6.13 Comparison of measured and predicted attenuation L_{a1}-L_{a22}

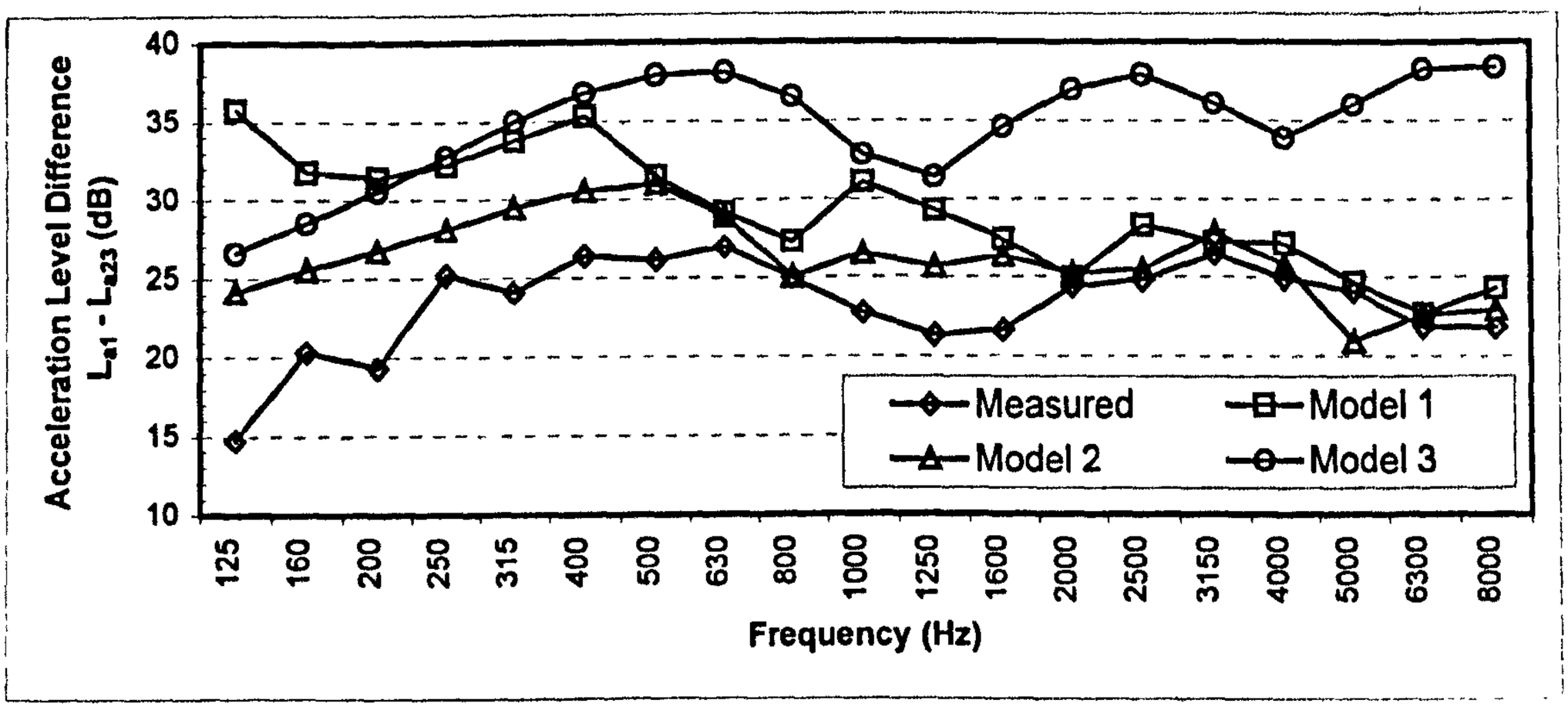

Figure 6.14 Comparison of measured and predicted attenuation L_{a1}-L_{a23}

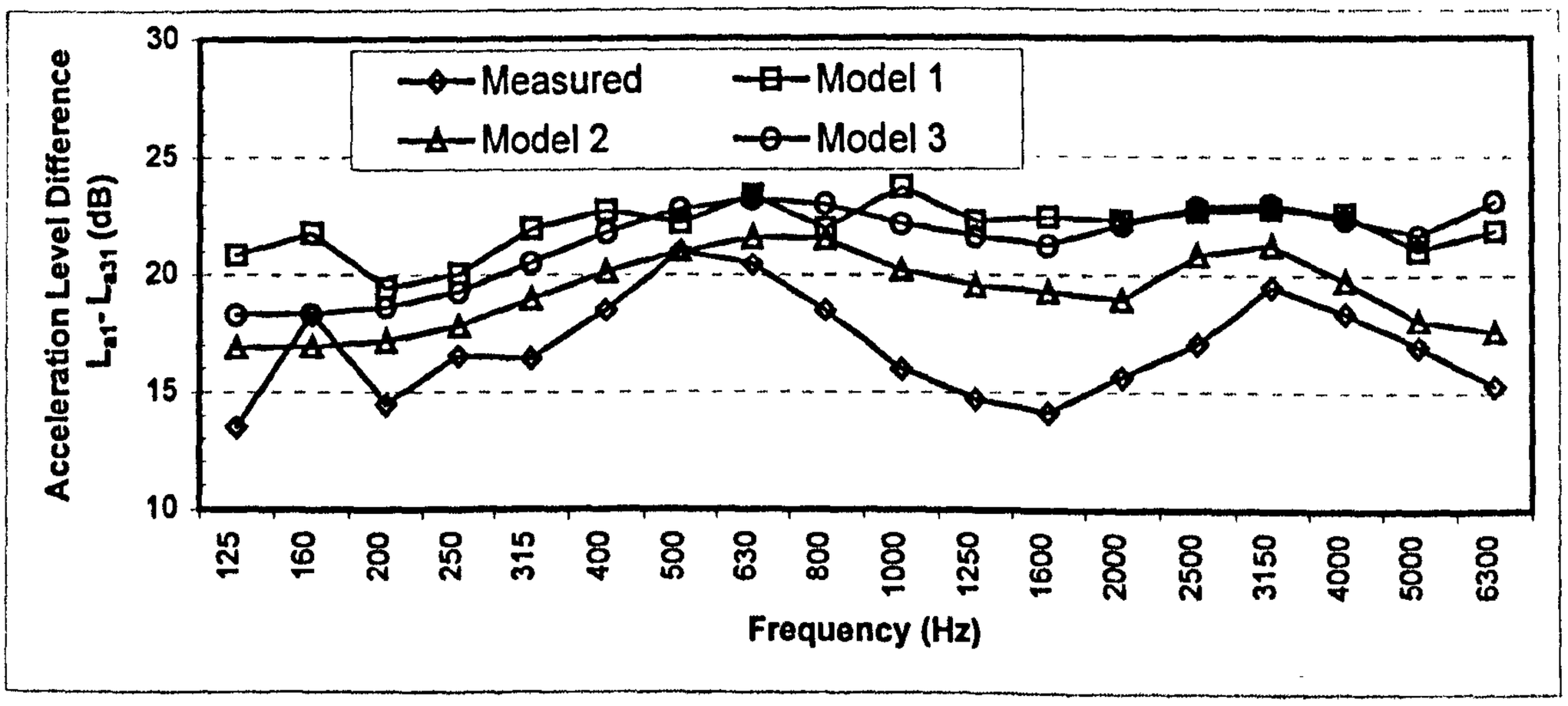

Figure 6.15 Comparison of measured and predicted attenuation L_{a1}-L_{a31}

prediction from the model *1* (BLT wave full frame) shows better agreement with the model *2* prediction above the 400 Hz frequency band.

In figure 6.17 the predicted attenuation is shown from source subsystem *1* to subsystem *10* across seven web plate joints and two frame joints. The results from model *1* (the full frame BLT model) shows poor agreement with the prediction from model *2* (web plate only BLT model) below the 400 Hz frequency band. The predicted attenuation from model *2* generally follows the trend of the measured attenuation but the prediction is between 3 to 8 dB higher than measured over most of the frequency spectrum and. The prediction from model *3* shows poor agreement with the measured attenuation as the frequency increases.

In figure 6.18 the predicted attenuation is shown from source subsystem *1* to subsystem *15* across three frame joints and eleven web plate joints. It can be seen that the prediction from model *2* is 6 to 12 dB higher than the measured attenuation in most frequency bands but follows the trend of the measured attenuation. The results for model *1* is in agreement with the predicted attenuation from model 2 except in the 125 Hz to 400 Hz frequency bands The results from model *3* (the B-wave SEA model), show the same trend as shown in figure 6.20 but the predicted attenuation is higher than measured.

6.2.7 SEA Model – Comparison Of Detailed and Coarse Results

In this section a comparison of the results from the coarse and detailed SEA modelling approaches is presented. It was found that the best results from each modelling approach were obtained from a model with bending, longitudinal and transverse subsystems and with all frame joints modelled as a web-plate and only these are shown. To compare the detailed SEA results, the energy of the subsystems between the frames and bulb stiffeners were combined to give the equivalent coarse subsystem energy and then the energy level difference was computed relative to the source subsystem. The energy level difference was corrected for the subsystem masses to give an acceleration level difference that could be compared with the coarse model results.

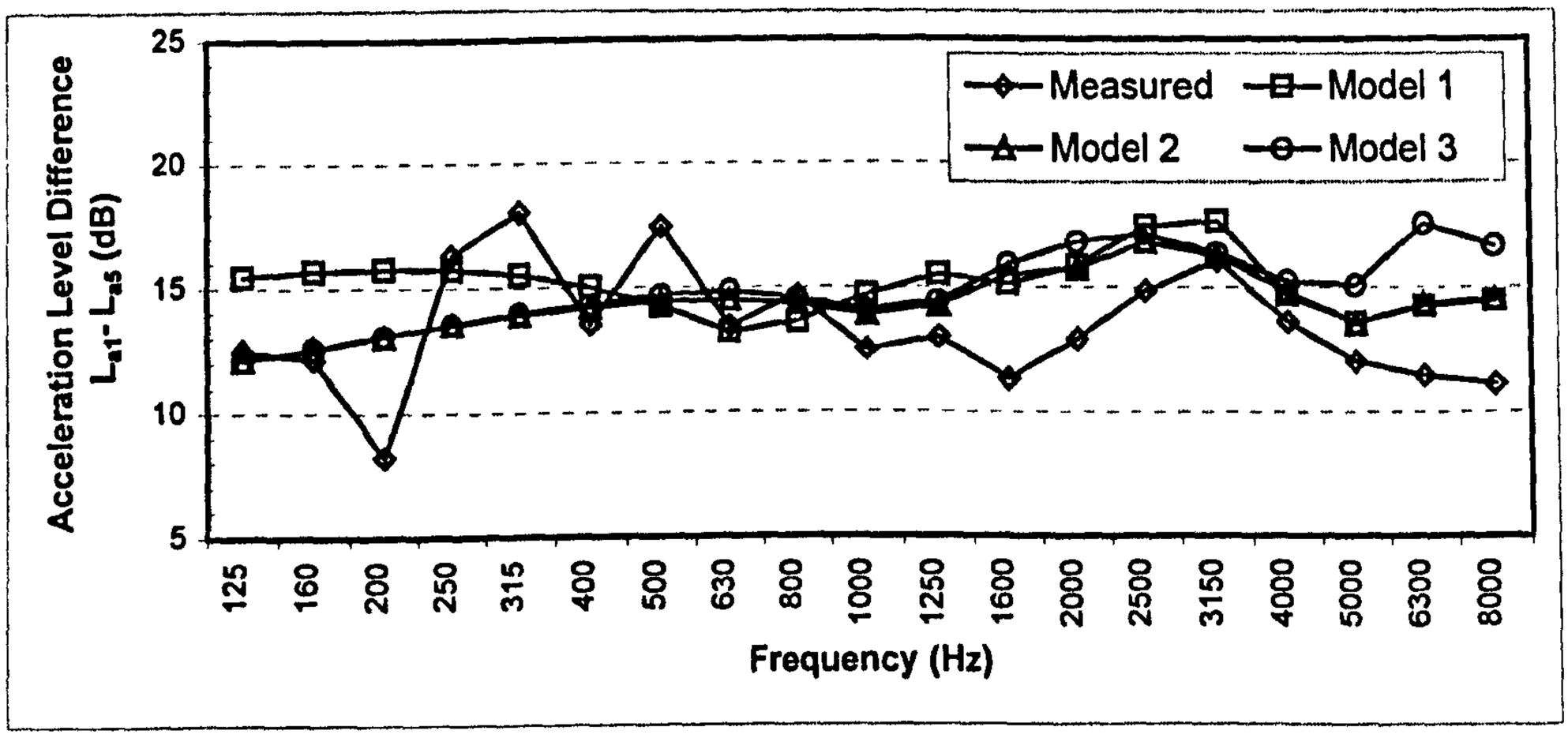

Figure 6.16 Comparison of measured and predicted attenuation L_{a1}-L_{a5}

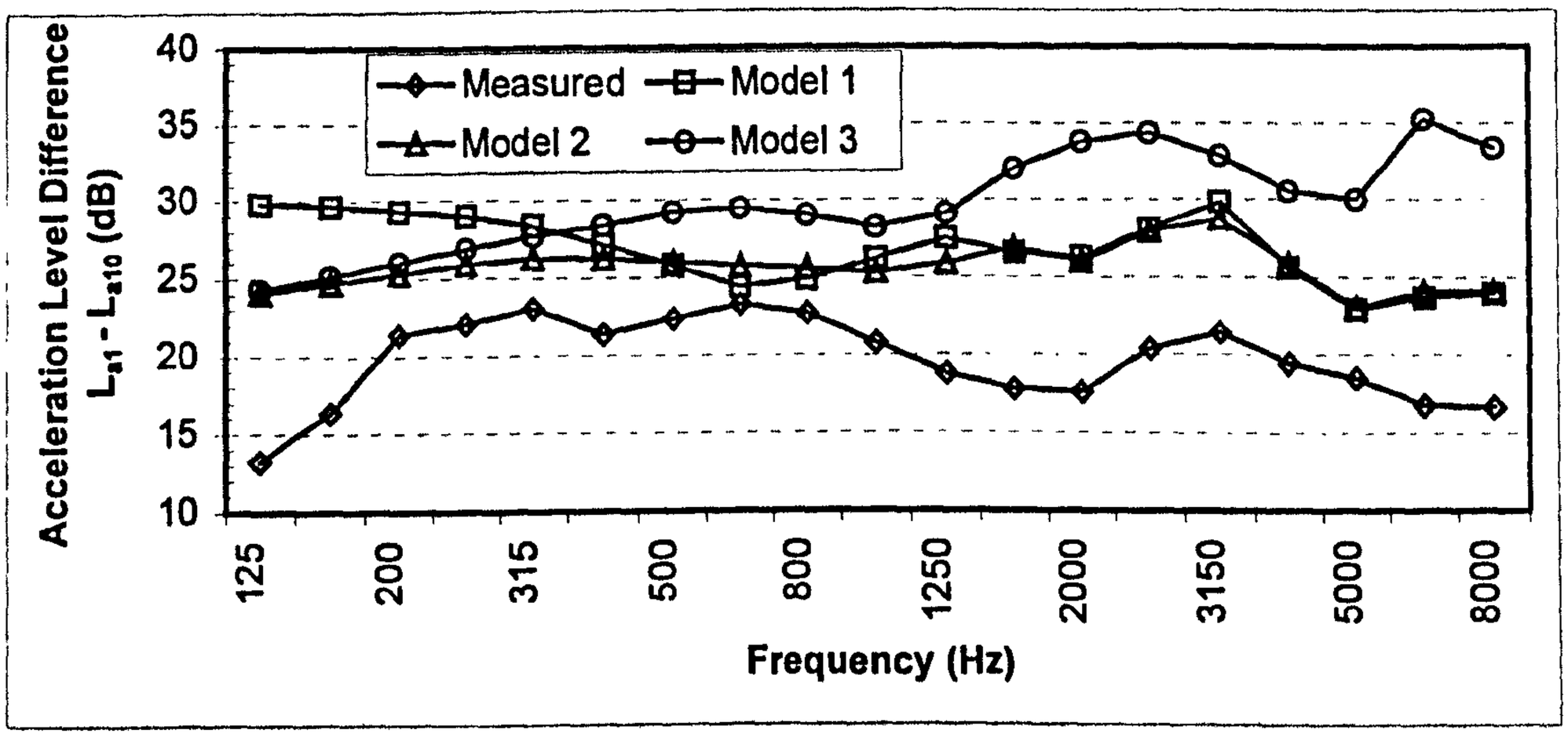

Figure 6.17 Comparison of measured and predicted attenuation L_{a1}-L_{a10}

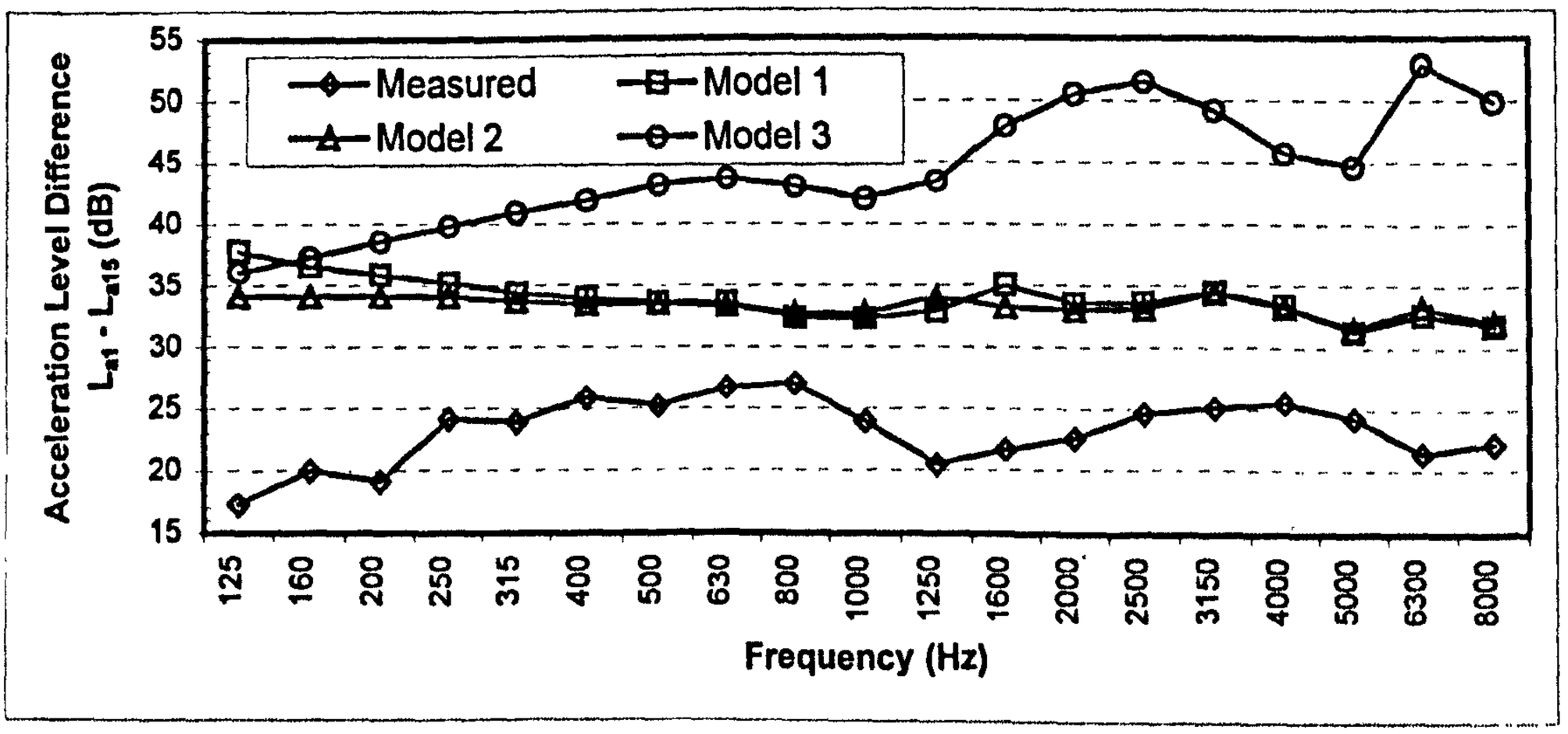

Figure 6.18 Comparison of measured and predicted attenuation L_{a1}-L_{a15}

In figure 6.19 the predicted and measured attenuation from subsystem 1 to subsystem 3 (see fig 6.2) is shown. The prediction from the coarse SEA model show very good agreement with the measured attenuation following the variation in the attenuation with frequency. The results from the detailed SEA modelling approach also shows better agreement in the lower frequency bands. The detailed model also follows the general trend for the measured attenuation but is consistently 4 dB above the coarse SEA prediction.

In figure 6.20 the predicted and measured attenuation from subsystem 1 to subsystem 4 (see fig 6.2) is shown. The prediction from the coarse SEA model shows very good agreement with the measured attenuation, the difference being typically less than 1 dB. The result from the detailed SEA modelling approach follows the general trend for the measured attenuation but the predicted attenuation is 8 to 9 dB higher than measured.

In figure 6.21 the predicted and measured attenuation from subsystem 1 to subsystem 5 (see fig 6.2) is shown. The prediction from the coarse SEA model shows very good agreement with the measured attenuation following the variation in the attenuation with frequency and a difference between 1 to 4 dB. The result from the detailed SEA modelling approach follows the general trend for the measured attenuation but the predicted attenuation is 6 to 12 dB higher than measured. The predicted attenuation from the detailed model also levels off and does show the variation with frequency seen in the measured attenuation.

In figure 6.21 the predicted and measured attenuation from subsystem 1 to subsystem 31 (see fig 6.2) is shown. The prediction from the coarse SEA model show good agreement in the low and high frequency bands with the measured attenuation following the variation in the attenuation with frequency. The agreement is not as good in the mid-frequency range with a difference of 4 to 5 dB between the measurements and predictions. The prediction from the detailed SEA modelling approach is similar to that from the coarse model of 0 to 3 dB higher across the frequency spectrum.

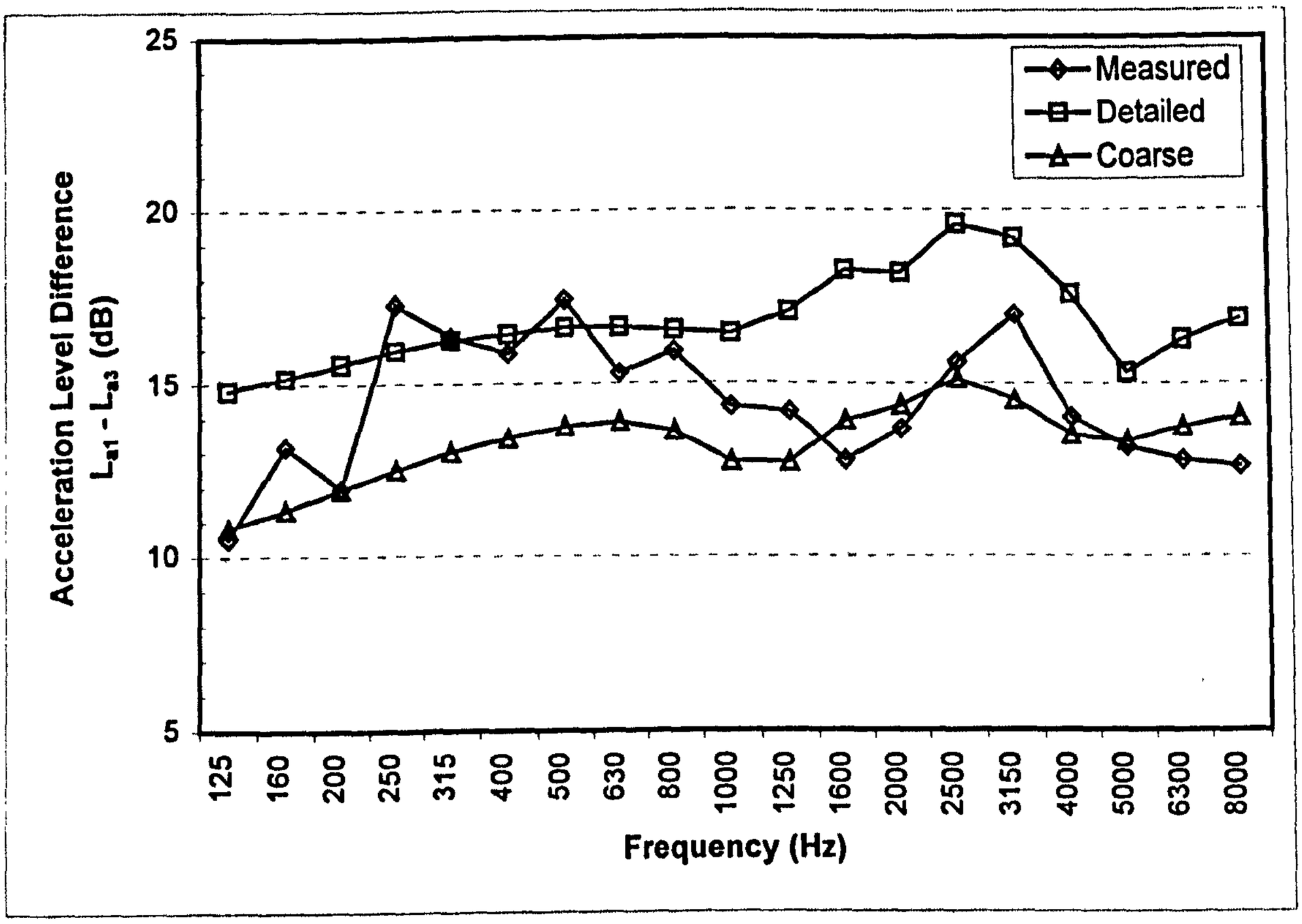

Figure 6.19 Comparison of measured and predicted attenuation L_{a1}-L_{a3}

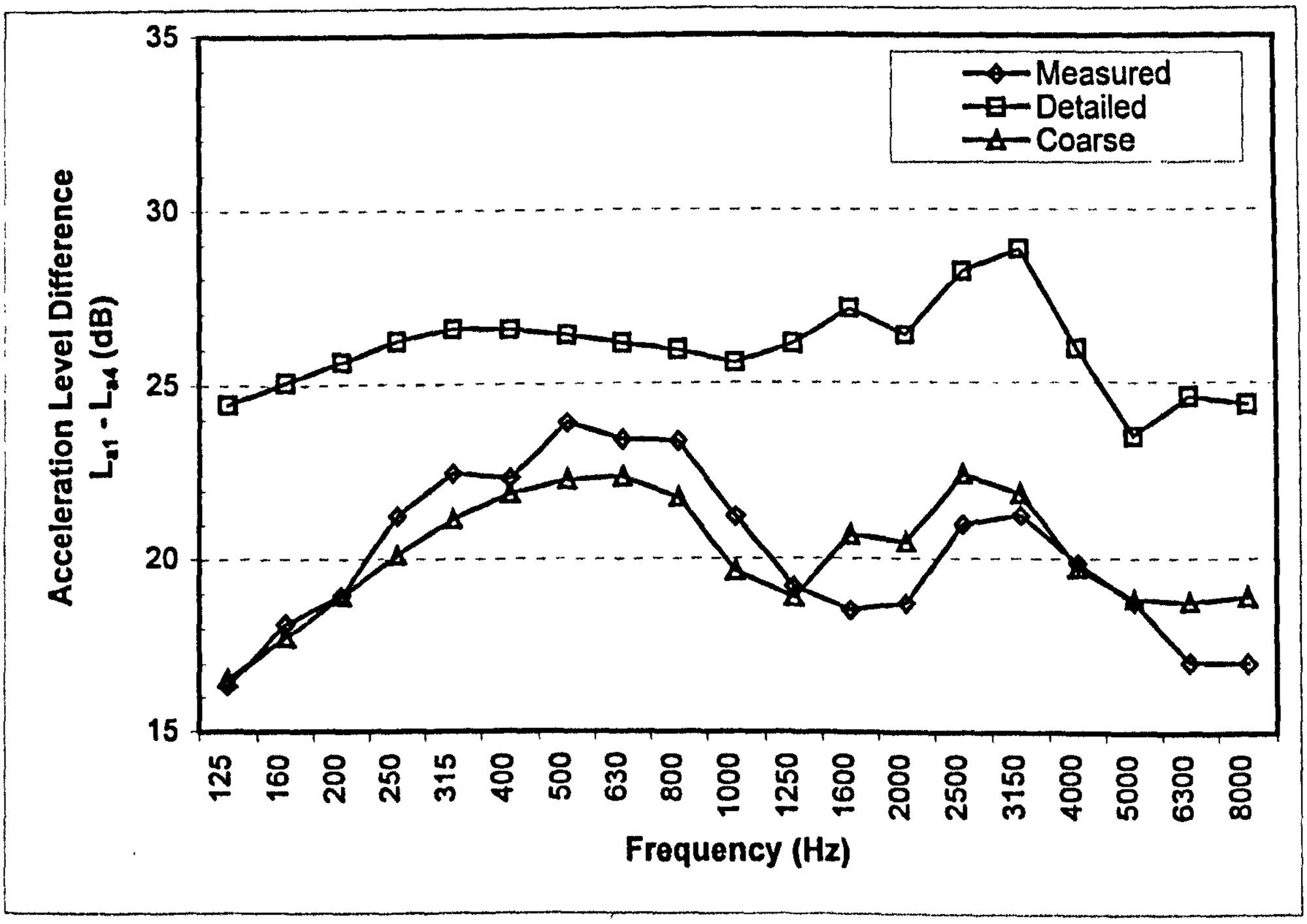

Figure 6.20 Comparison of measured and predicted attenuation L_{a1}-L_{a4}

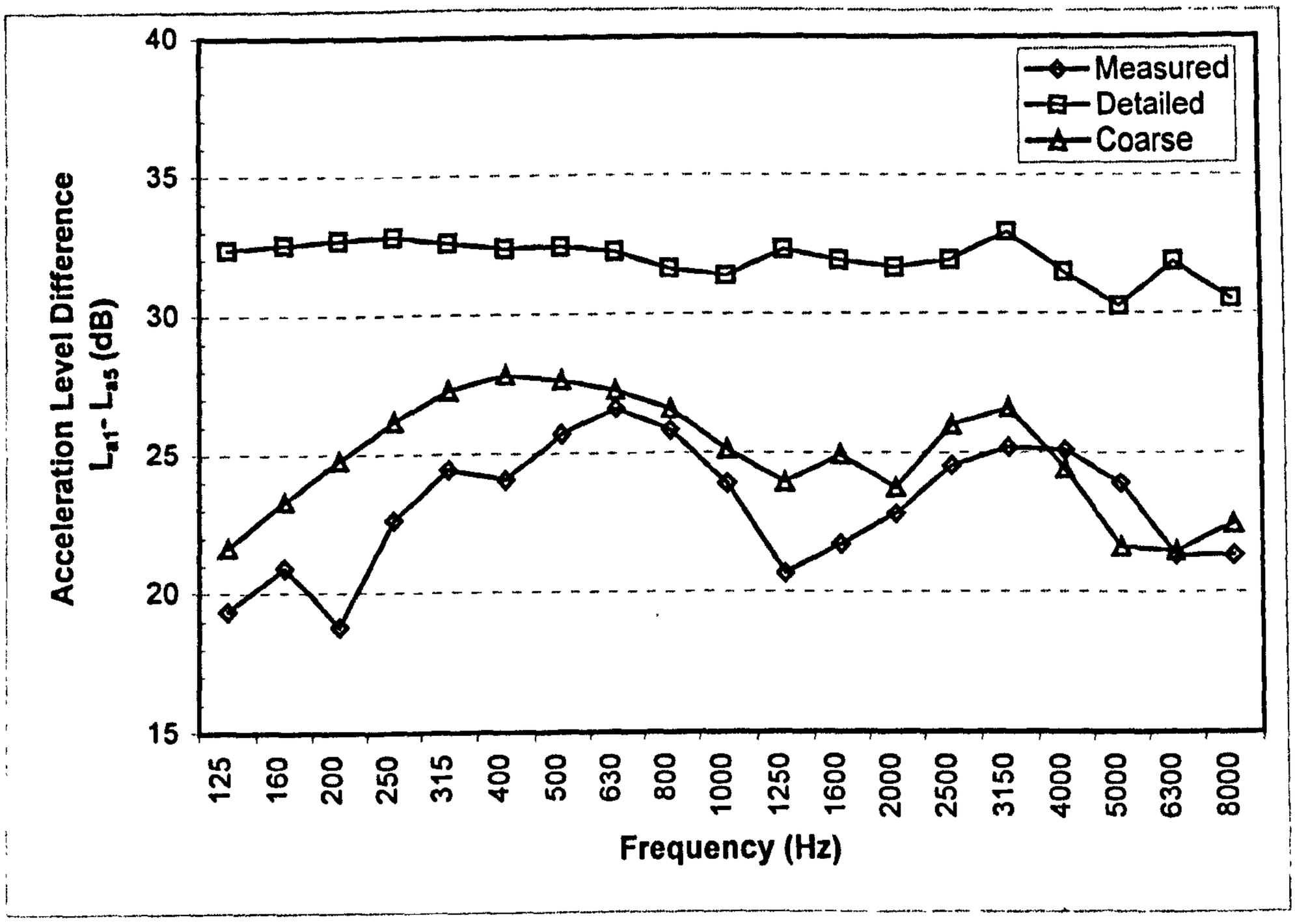

Figure 6.21 Comparison of measured and predicted attenuation L_{a1}-L_{a5}

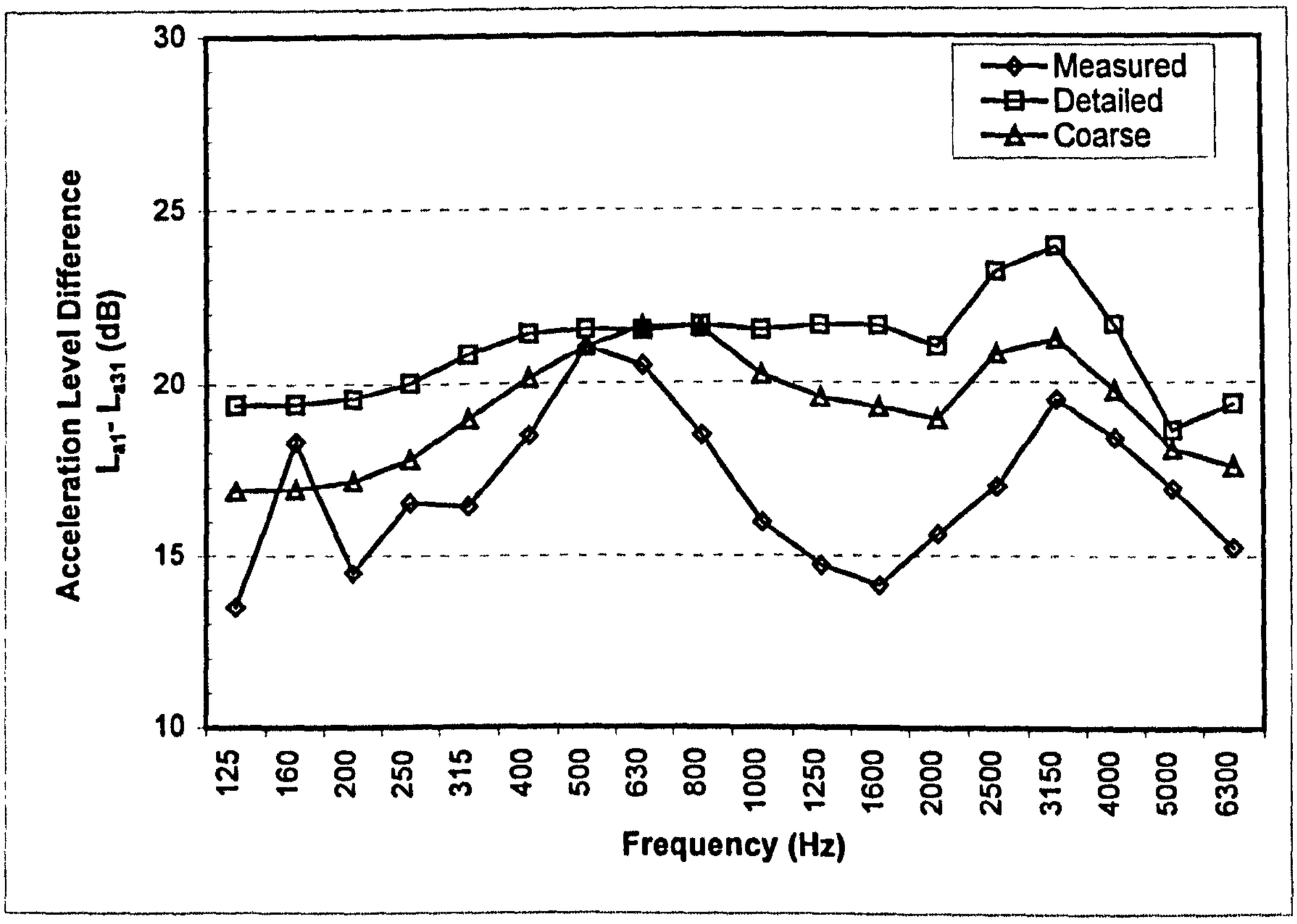

Figure 6.22 Comparison of measured and predicted attenuation L_{a1}-L_{a31}

From the results presented in this section it is could be concluded that the coarse modelling approach is the best modelling approach, however the results presented here are for an incomplete section. In the next section a complete superstructure unit is investigated.

6.3 Ship Superstructure Unit

In the previous section of this chapter, the SEA modelling of a complex ribbed section of ship structure was discussed. In this section the SEA modelling of a more conventional section of the ship superstructure is reviewed. The geometry of the superstructure section is shown in figure 6.23. The structure is symmetrical consisting of two side shells, a central bulkhead, a transverse bulkhead, a ribbed deck plate, a series of smaller front bulkheads and side pods. The structure as shown in figure 6.23 is considerably simplified, as the deck plate has ribs in the transverse direction, while the central bulkhead, side shells and front bulkheads all have stiffeners in the vertical direction. Figures 6.24 to 6.27 show the stiffening arrangements.

Figure 6.24 shows the stiffening arrangement of the side shell which has longitudinal frame stiffener and vertical rib stiffeners. Figure 6.25 shows the cross section details of the stiffener arrangement for the central bulkhead which interfaces with the transverse bulkhead. Figure 6.26 shows the cross section of the interface between the deck plate and the transverse bulkhead and the stiffeners running in the transverse direction. The deck plate on each side of the central bulkhead is also bisected by a frame stiffener in the longitudinal direction. Figure 6.27 shows a cross section through the side shells, centre and transverse bulkhead and the rib stiffeners.

The mass of the unit is approximately 5 tonnes with the approximate dimensions of 4 m x 8.5 x 4.5m. The modal density $n(f)$ of the deck plate is approximately 1.2 modes/Hz, for the centre bulkhead $n(f)$ is 1.35 modes/Hz and for the side shell $n(f)$ is 0.76 modes/Hz. As a consequence of the high modal density the modal overlap is above unity for most subsystems in the 125 Hz frequency band. The approximate sizes of the stiffeners in the structure are as follows. The bulb stiffeners are the same size of those

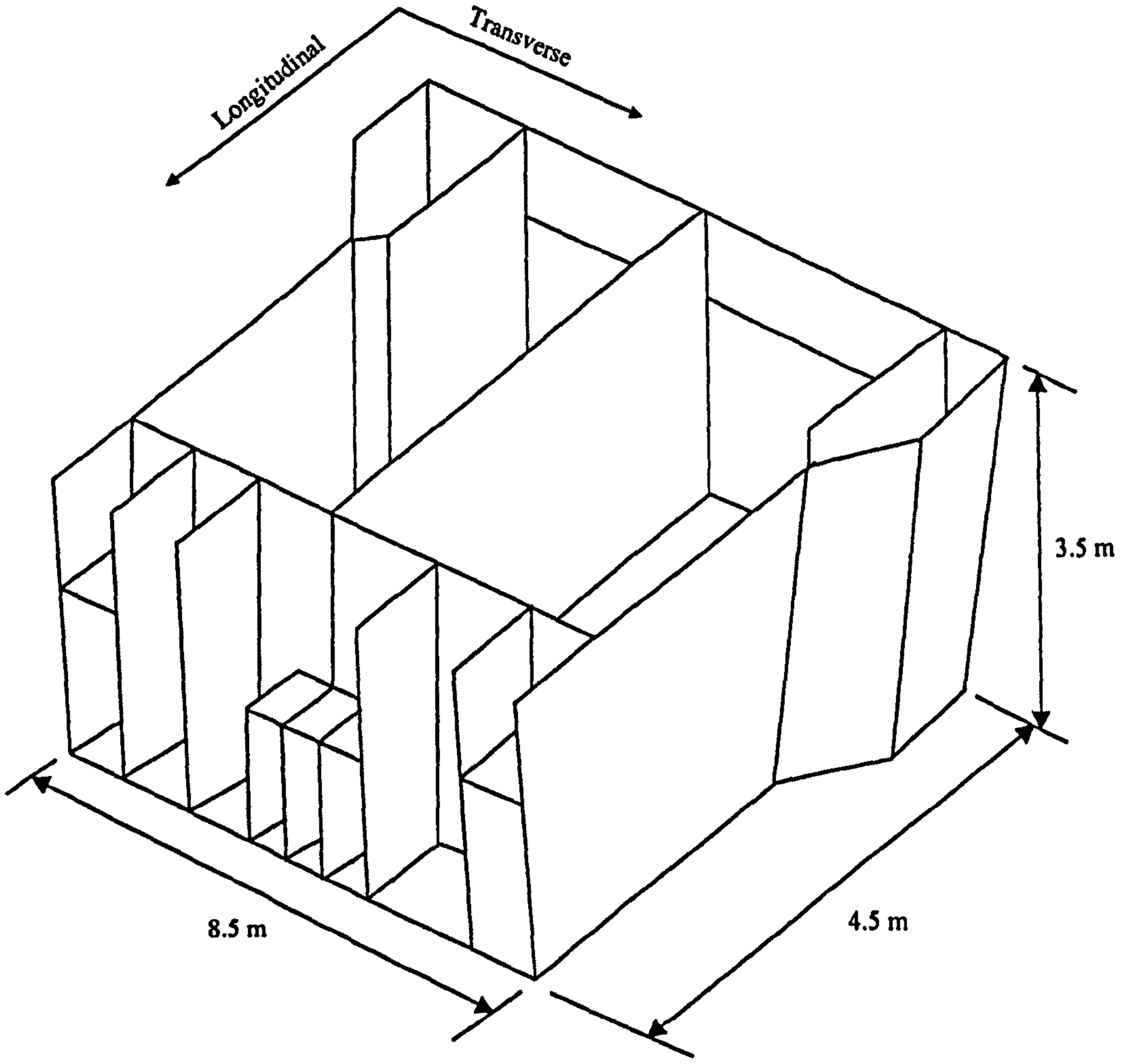

Figure 6.23 Isometric view of superstructure unit

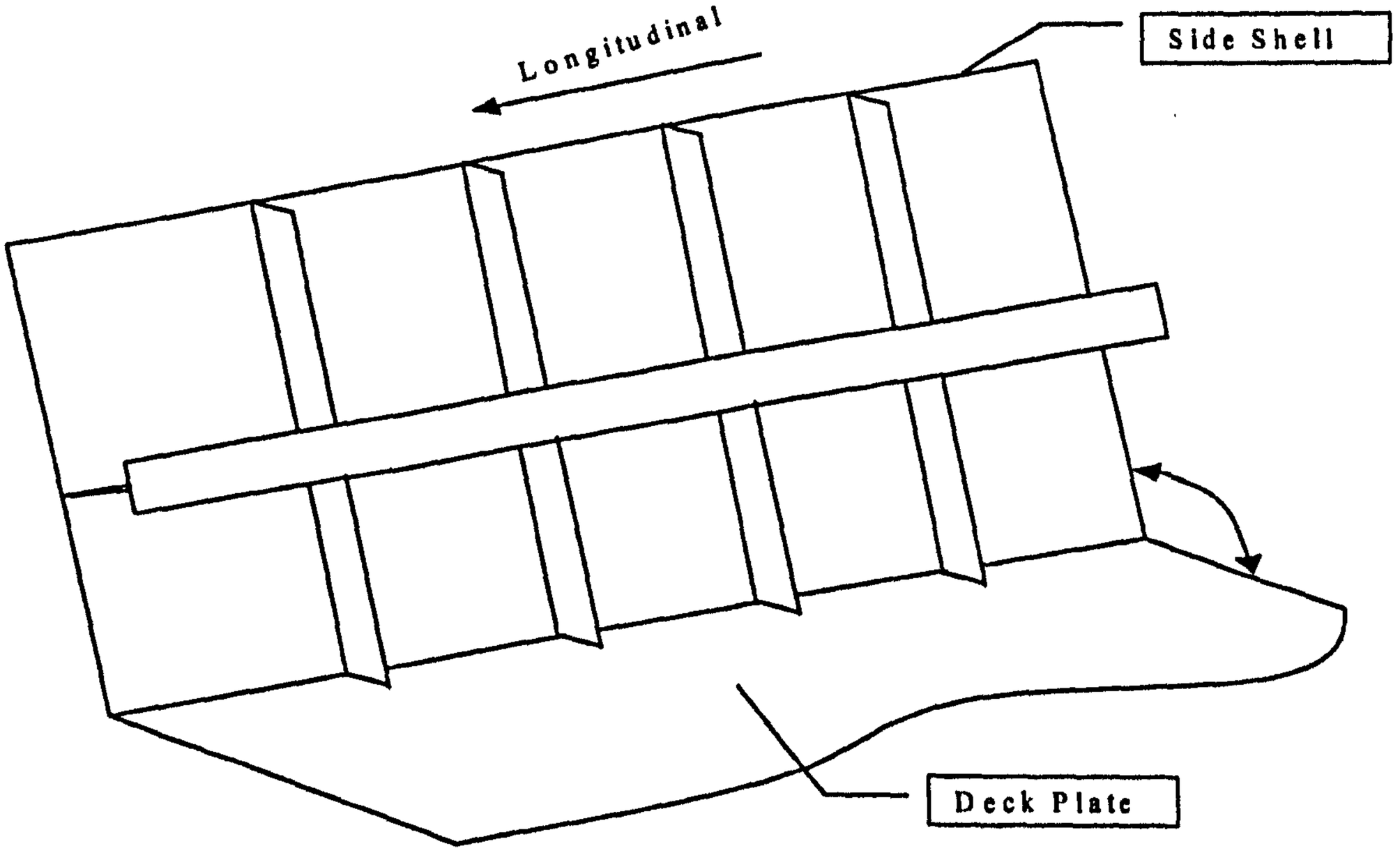

Figure 6.24 Cross sectional details of stiffeners on side plate

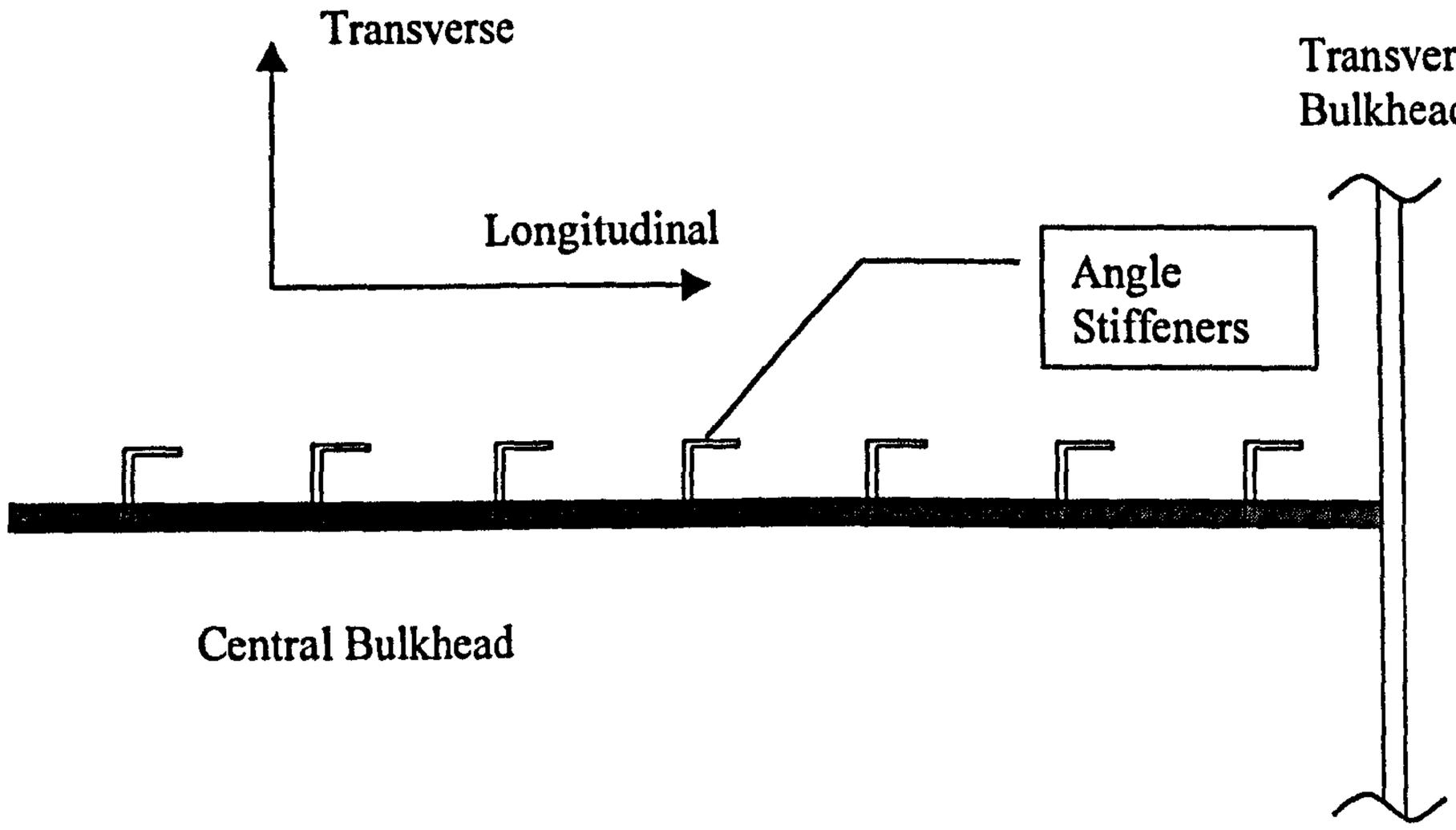

Figure 6.25 Plan views of stiffeners at centre bulkhead.

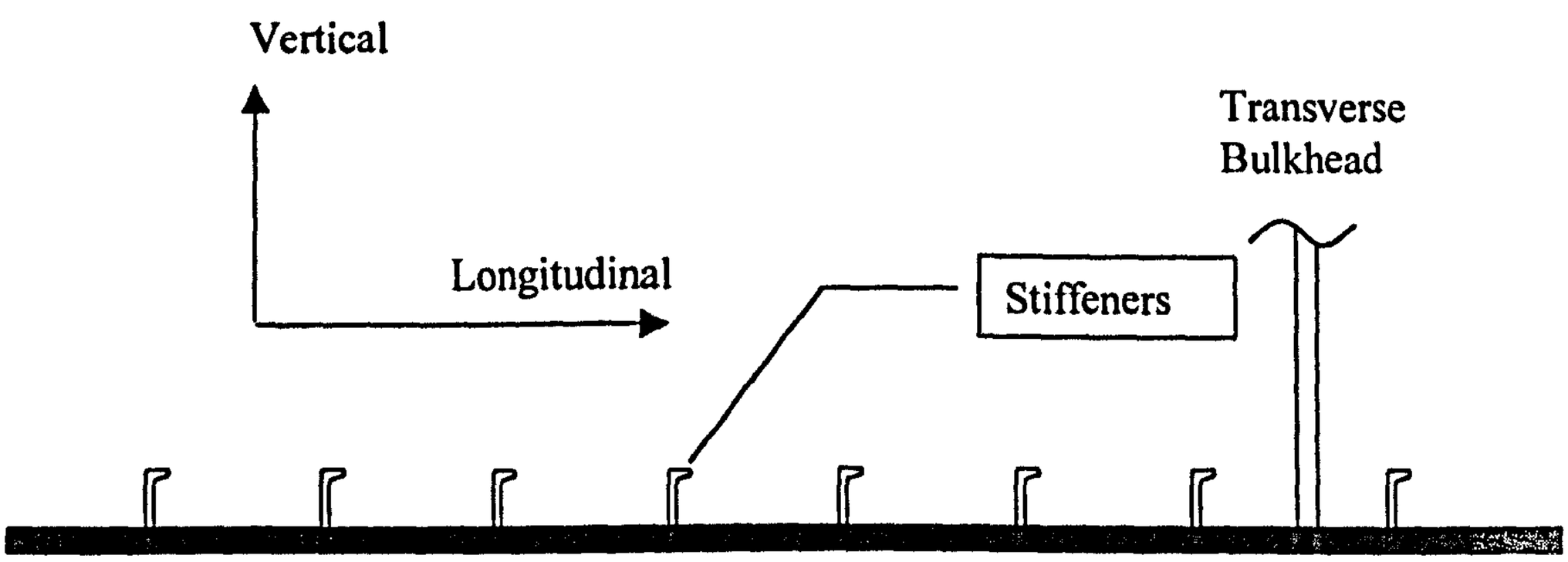

Figure 6.26 Cross sectional details of stiffeners on deck plate

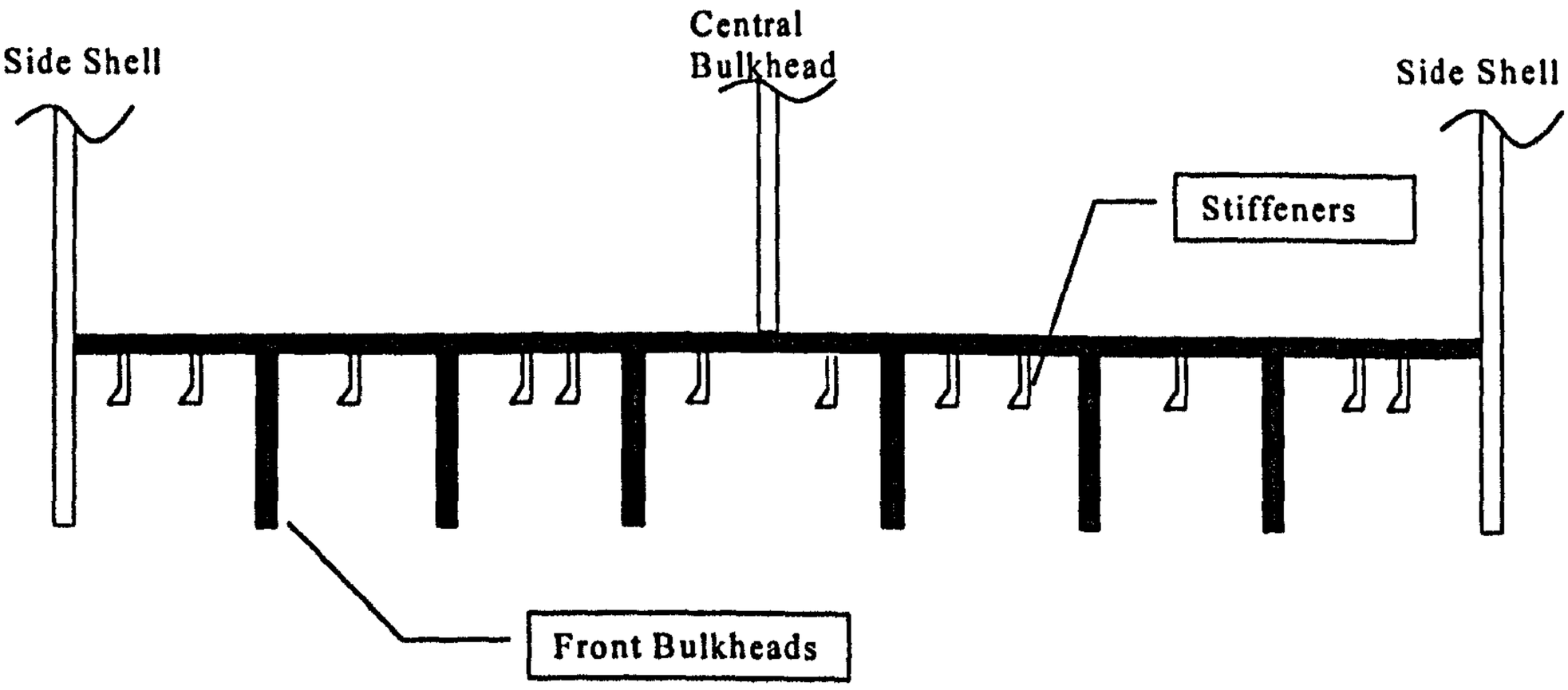

Figure 6.27 Cross sectional details of stiffeners on deck plate

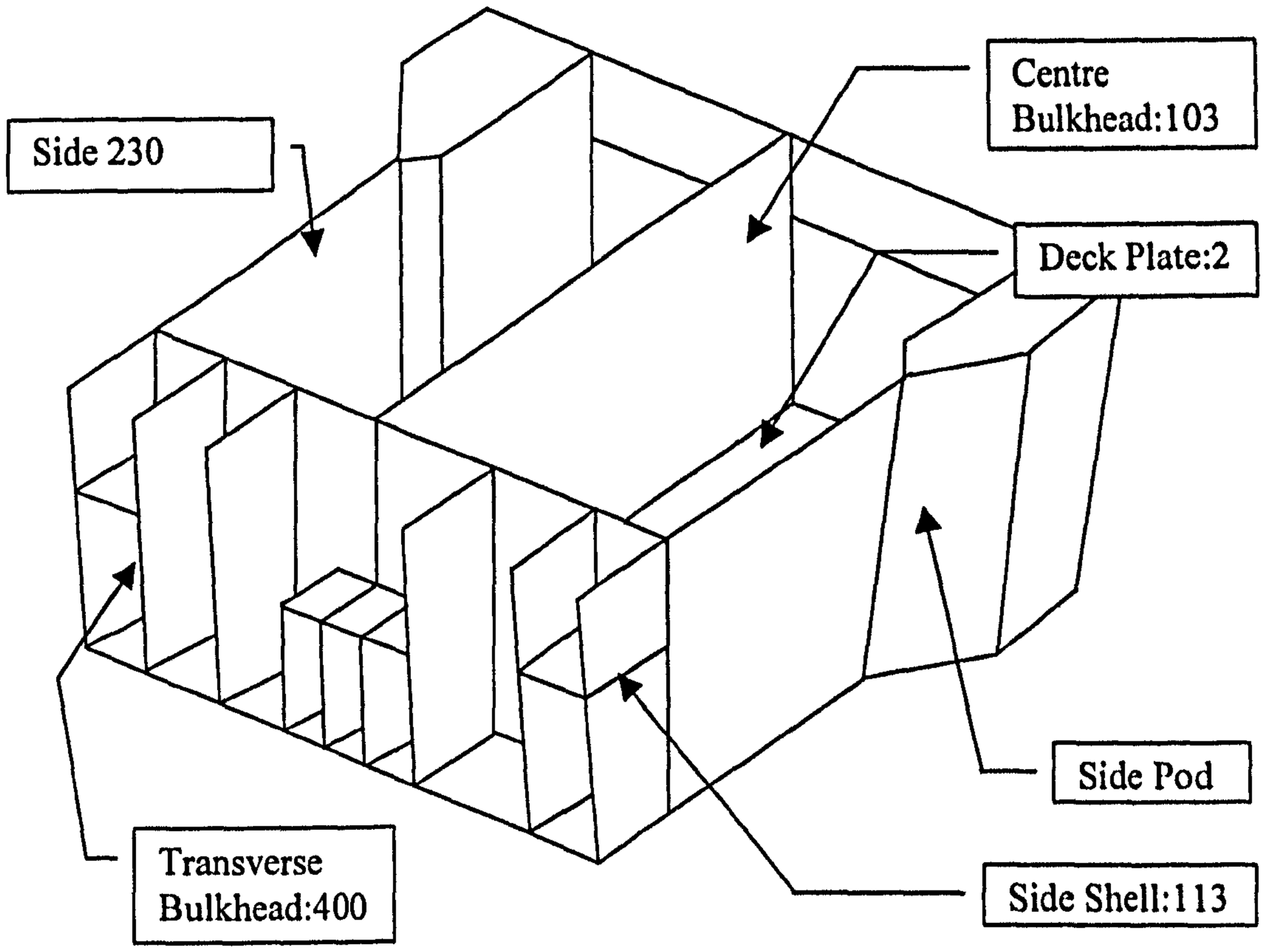

Figure 6.28 Superstructure SEA subsystem numbers

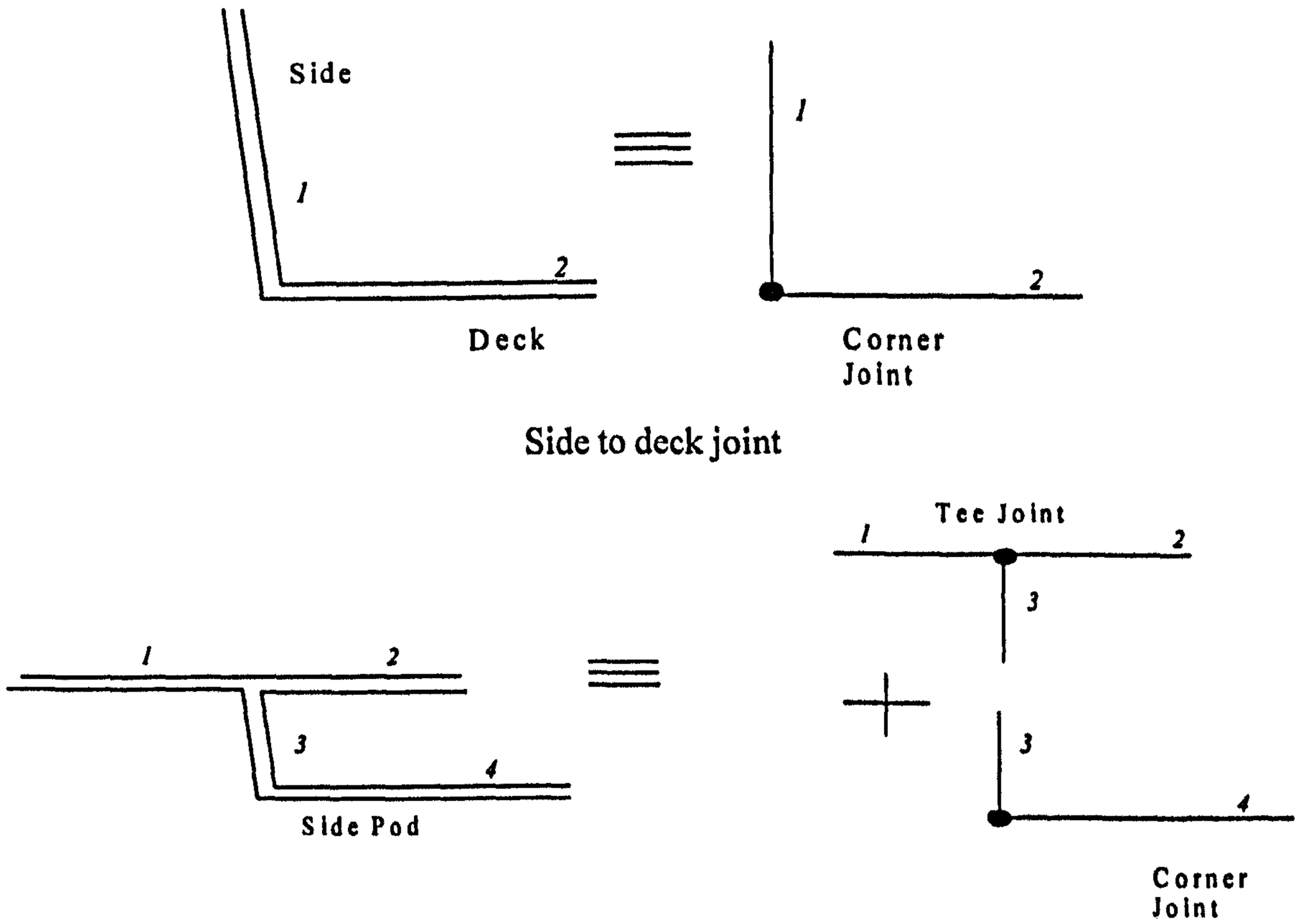

Figure 6.29 Side joint modelling

on the ribbed deck plate analysed previously and the angle stiffeners are also of a comparable size to the flat bar stiffeners of the ribbed deck plate. The frame stiffeners on the deck plate and side shell are smaller than the 203 x 133 I-beam analysed previously in chapter 5.

6.3.1 Coarse SEA Model

In the coarse SEA model the stiffening on the side shell, deck plate, central bulkhead and transverse bulkhead will be ignored and the structure will be considered simply as an assembly of flat plates. As the ship superstructure is generally remote from the principal noise sources on the ship, a coarse model would be the preferred modelling solution as it would simplify the modelling process. The results from coarse and detailed SEA modelling approach to the structure will again be presented to test this assumption.

Two coarse SEA model of the ship superstructure have been analysed to determine the most suitable modelling approach. Figure 6.24 to 6.27 show that even a relatively simple section of ship superstructure has a variety of different joint types. The SEA models of the superstructure are as follows:

(a) Model 1: The SEA model consists of bending, longitudinal and transverse wave subsystems. The damping of each subsystem is predicted with the Irie equation. The damping of in-plane subsystems is assumed to be identical to the bending wave subsystems. The SEA model consists of 150 subsystems, 52 joints and 2656 coupling loss factors.

(b) Model 2: The SEA model is identical to model 1 in construction but consists only of bending wave subsystems. The damping of each subsystem is predicted with the Irie equation *3.4*. The SEA model consists of 50 subsystems, 52 joints and 256 coupling loss factors.

Figure 6.28 shows the numbers of the SEA subsystems for which results are presented. Because of the symmetry of the structure the centre bulkhead was selected as the source subsystem. The excitation was applied by tapping randomly over the entire surface of the plate, between the stiffeners. The coarse SEA model consists of corner joints, tee joints and the cross joint, which have been used for example by Craik [37] to predict structure borne noise transmission in building structures, as indicated in figure 6.28. The other feature that is neglected is the joint between the side shell and deck plate, which is not perpendicular as the side shells have a slight taper and the joint angle is greater than 90° as indicated in figure 6.29.

6.3.2 Detailed SEA Model

The modelling strategy follows that of the coarse model and two detailed SEA models of the ship superstructure have been analysed to determine the most suitable modelling approach. The subsystems of the detailed model are defined by the stiffeners and plate boundaries. For example the section of side shell shown in figure 6.24 is defined as one subsystem in the coarse models but eight subsystems in the detailed models. The SEA models of the superstructure are as follows:

(a) Model 3: The SEA model consists of bending, longitudinal and transverse wave subsystems. The frame joints and bulb stiffeners are represented by the web plate joint. The damping of each subsystem is predicted with the Irie equation. The damping of in-plane subsystems is assumed to be identical to the bending wave subsystems. The SEA model consists of 150 subsystems, 52 joints and 2656 coupling loss factors.

(b) Model 4: The SEA model is identical to model 3 in construction but consists only of bending wave subsystems. The damping of each subsystem is predicted with the Irie equation. . The SEA model consists of 50 subsystems, 52 joints and 256 coupling loss factors.

Before reviewing the results from the models and the measurement survey, the basic subsystem properties such as statistical mode count, modal overlap and the coupling loss factors are reviewed in the next section.

6.3.3 SEA Subsystem Properties

In figure 6.30 the bending, longitudinal and transverse statistical mode count N_b, N_l and N_t for the smallest subsystem 113 on the side shell and the centre bulkhead 103 in the coarse SEA models are plotted. It can be seen that for bending wave subsystem 113, there are approximately 3 modes in the 100 Hz band and 10 bending modes in the 250 Hz frequency band. Bending wave subsystem 103 has approximately 25 modes in the 100 Hz frequency band and 78 modes in the 250 Hz band. For the bending wave subsystems the smallest subsystem in the SEA model has a reasonable number modes at 250 Hz to suggest that an accurate prediction can be obtained down to this frequency.

For the longitudinal subsystem 1103, the first mode occurs in the 1 kHz frequency band and by 4 kHz there are approximately 10 modes per band. For the transverse wave subsystem 2103 the first mode is predicted to occur in the 800 Hz frequency band and by 2.5 kHz there are approximately 10 modes per band. Above 2.5 kHz the in-plane subsystems on the centre bulkhead are expected become important as bending waves are converted to in-plane waves and energy is stored. For the small side shell subsystems, the first mode in the longitudinal wave subsystem 1113 is predicted to occur in the 3.15 kHz frequency band and by 8 kHz there are approximately 5 modes in the band. The first mode in the transverse wave subsystem 2113 is predicted to occur in the 2.5 kHz frequency band and by 8 kHz there are approximately 14 modes in the band. From examination of the mode count of the in-plane subsystems of the small side shell subsystem is therefore not expected become important until the 6.3 kHz to 8 kHz frequency bands.

In figure 6.31 the predicted modal overlap M_b, M_l and M_t is shown for the bending, longitudinal and transverse wave subsystems for 103 and 113 in the 100 Hz to 10 kHz frequency bands. It can be seen that for subsystem 113 the modal overlap of the bending

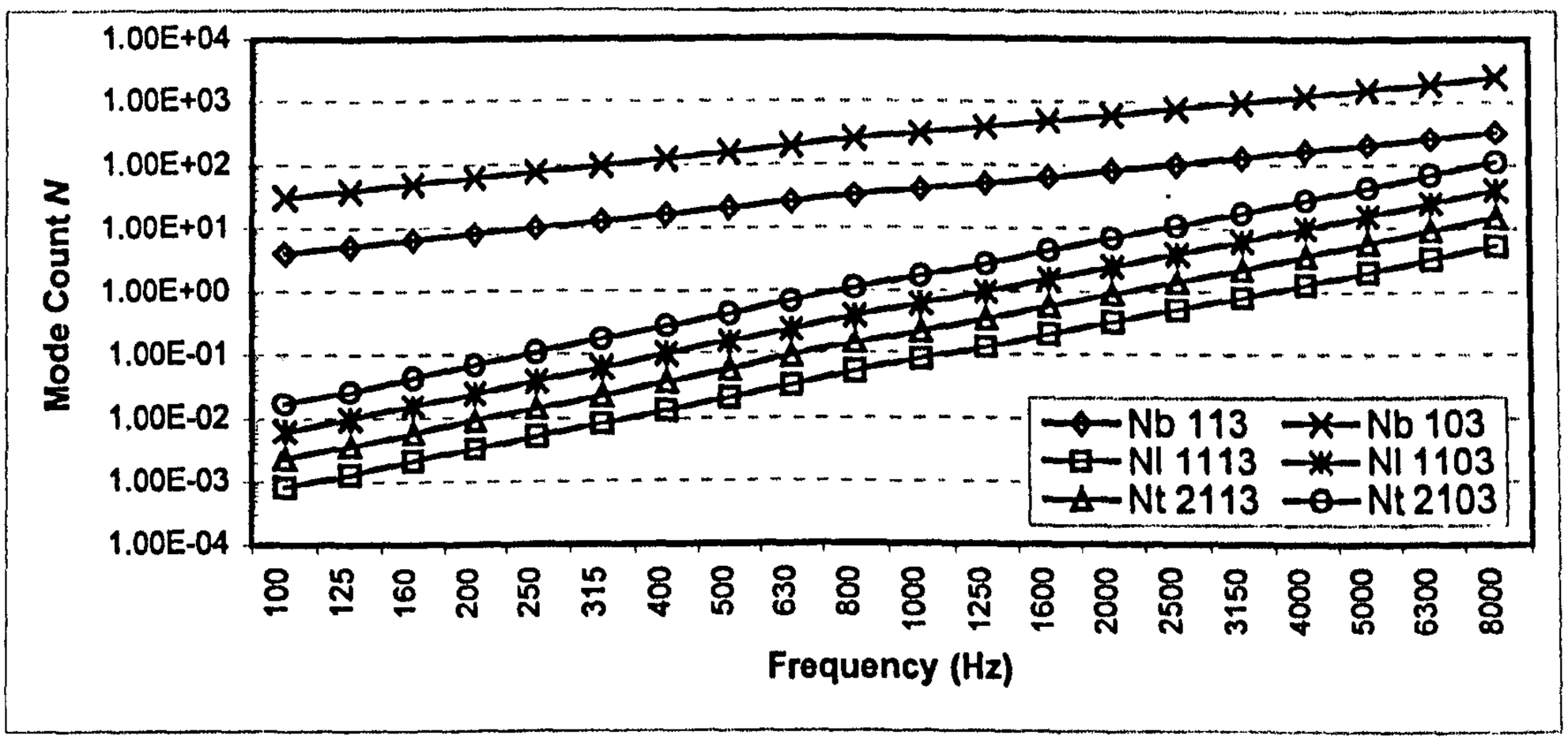

Figure 6.30 Comparison of statistical mode count – coarse model

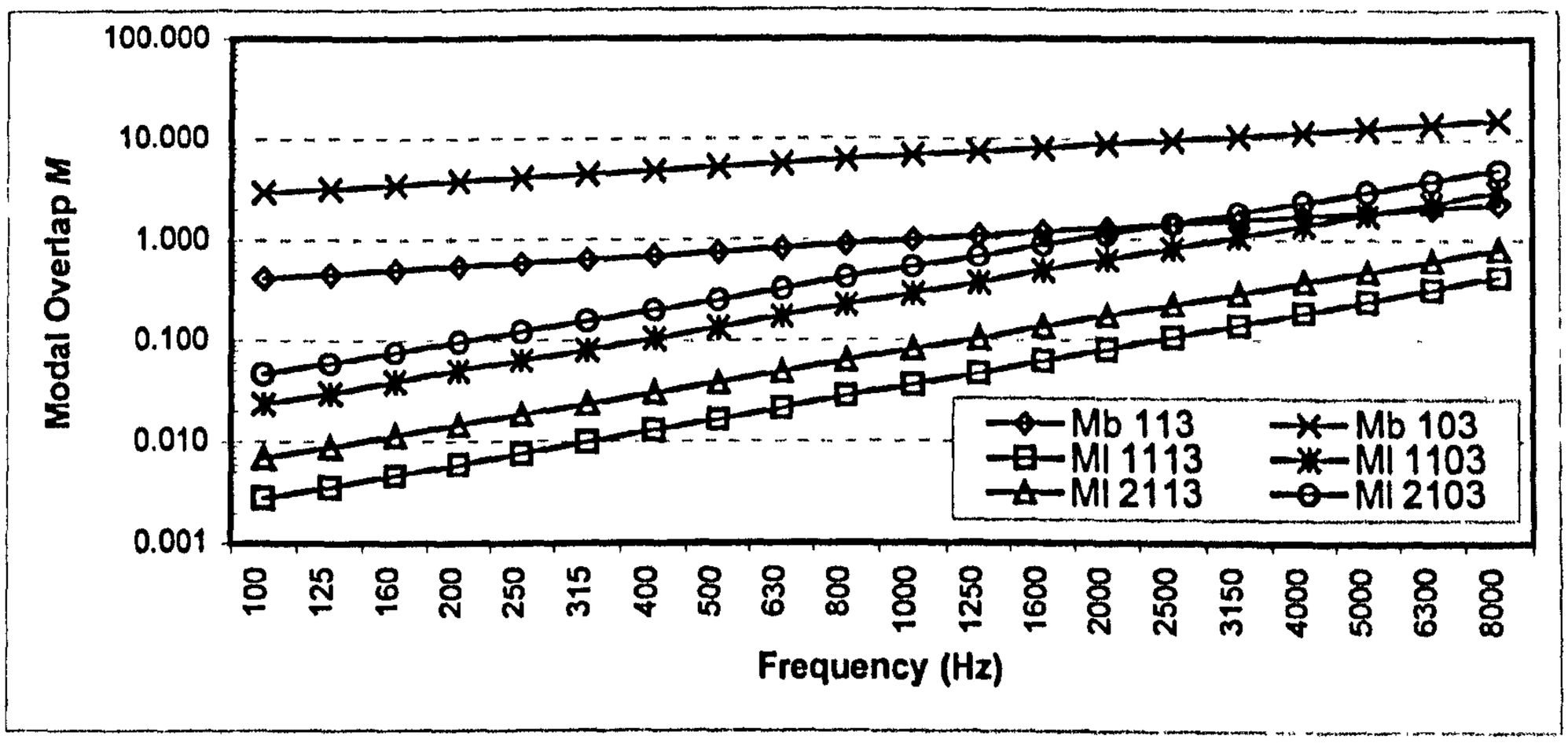

Figure 6.31 Comparison of predicted modal overlap – coarse model

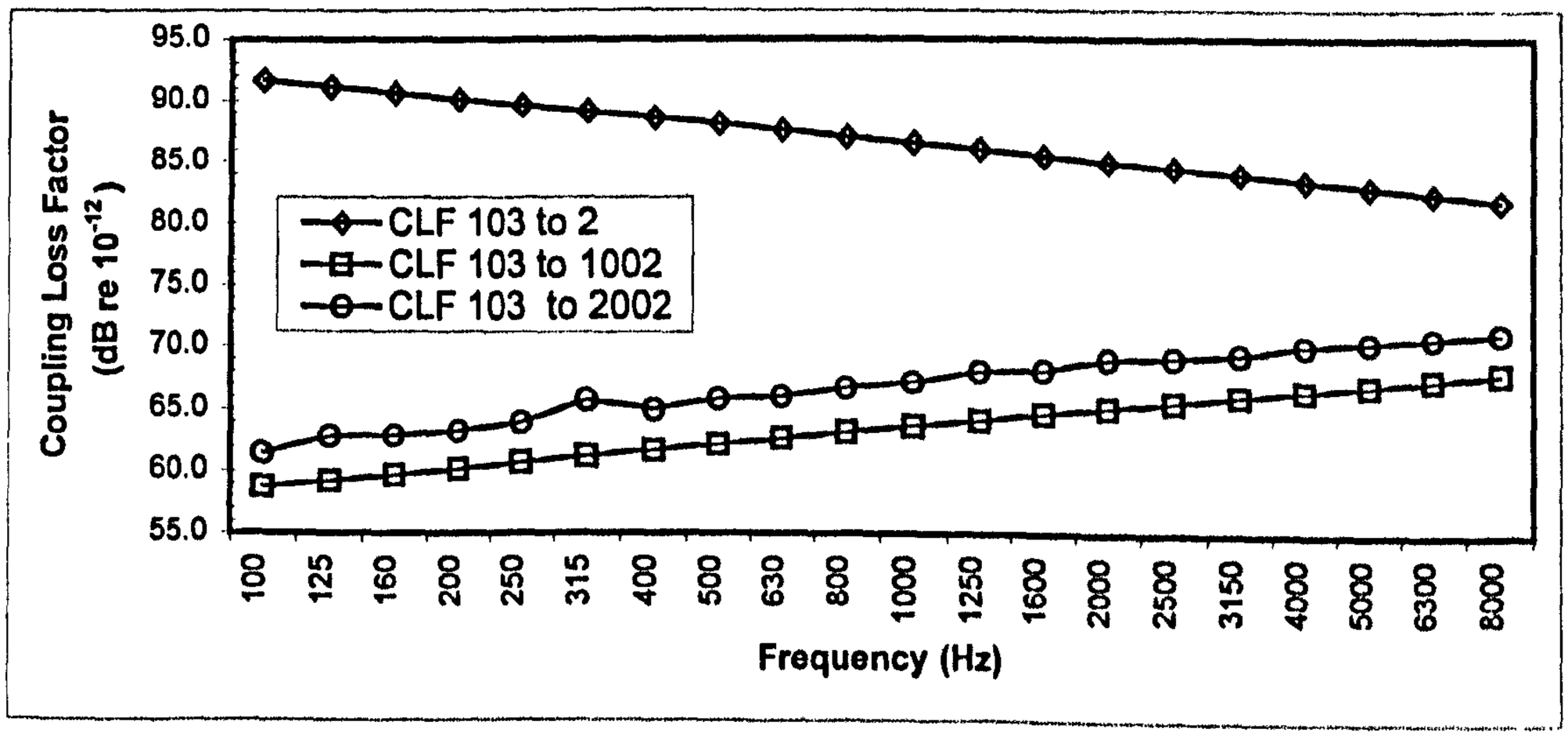

Figure 6.32 Comparison of predicted CLF's – bulkhead 103 to deck plate 2

wave subsystem 113 does not exceed unity until the 1 kHz frequency band. The modal overlap of the longitudinal and transverse wave subsystems 1113 and 2113 does not exceed unity in any of the frequency bands. Therefore the in-plane subsystems should not be of any significance for subsystem 113 and the predictions from the two SEA model should be the same. The modal overlap of the bending wave subsystem 103 is above unity in all frequency bands. The modal overlap does not exceed unity for the longitudinal wave subsystem until the 3.15 kHz frequency band and the 2 kHz frequency band for the transverse wave subsystem. Therefore the in-plane subsystems should not be of any significance until the 2 kHz frequency band for subsystem 103.

In figure 6.32 the predicted coupling loss factor from bending wave subsystem 103 to the deck plate bending subsystem 2, longitudinal subsystem 1002 and transverse wave subsystem 2002 is shown between the 100 Hz to 8 kHz frequency bands. It can be seen that the bending wave coupling loss factor decreases linearly with frequency while the bending to inplane coupling loss factors increase with linearly with frequency. The magnitude of the bending-inplane coupling loss factor is much lower than the bending-bending coupling loss factor, therefore the amount of power transmitted to in-plane subsystems will be small and the predictions from the BLT and B wave SEA models should be very similar.

6.3.4 SEA Model – Comparison Of Predicted And Measured Attenuation

In this section a comparison of the results from the coarse and detailed SEA modelling approaches with the measured attenuation is presented. To compare the results, the energy of the subsystems between the frames and bulb stiffeners were combined to give the equivalent coarse subsystem energy and the energy level difference was then computed relative to the source subsystem. The energy level difference was corrected for the subsystem masses to give an acceleration level difference that could be compared with the coarse model results.

Figure 6.33 shows the measured attenuation between the centre bulkhead subsystem 103 and the side shell subsystem 230 from the 125 Hz to 3.15 kHz frequency bands. No

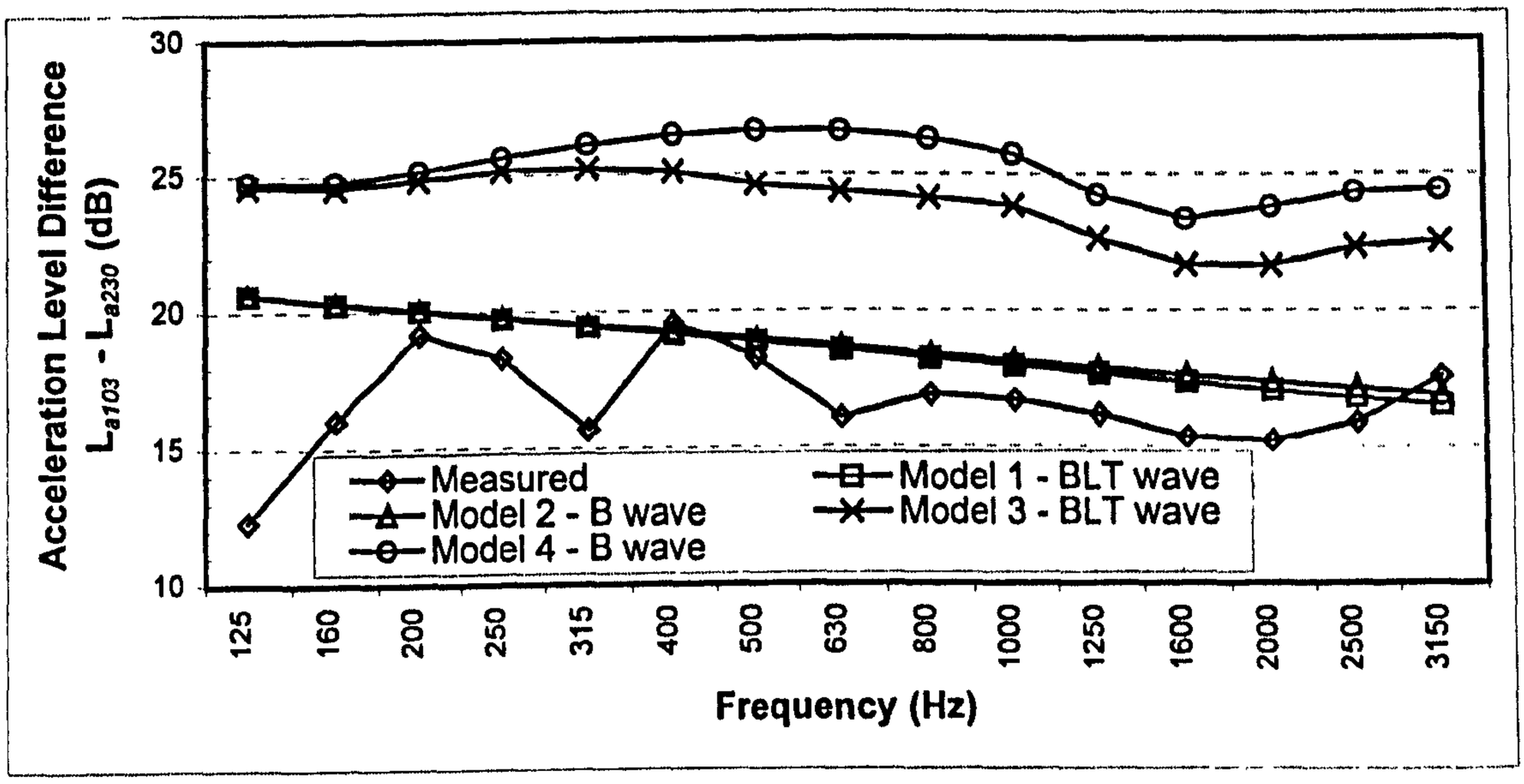

Figure 6.33 Comparison of predicted and measured attenuation L_{a103}-L_{a230}

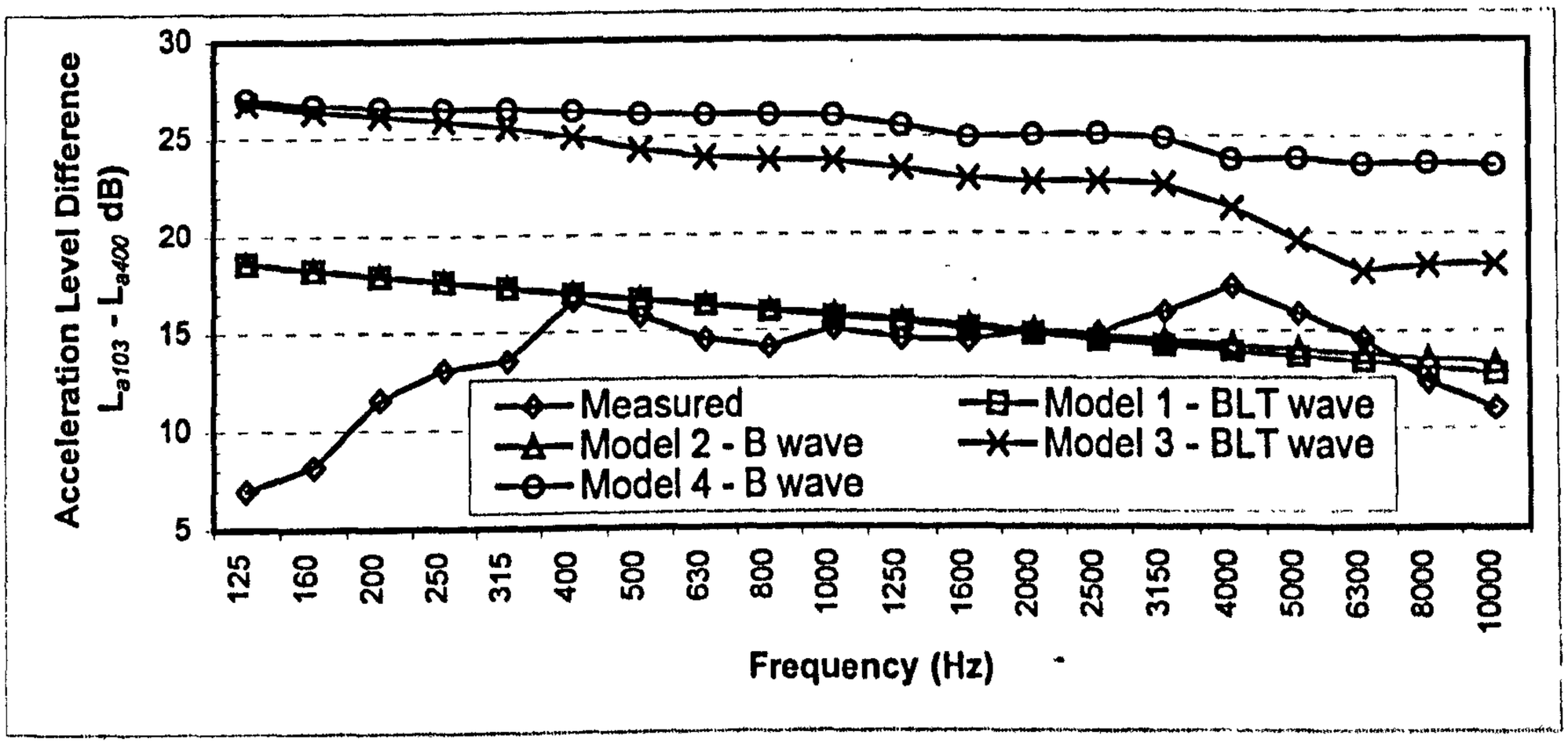

Figure 6.34 Comparison of predicted and measured attenuation L_{a103}-L_{a400}

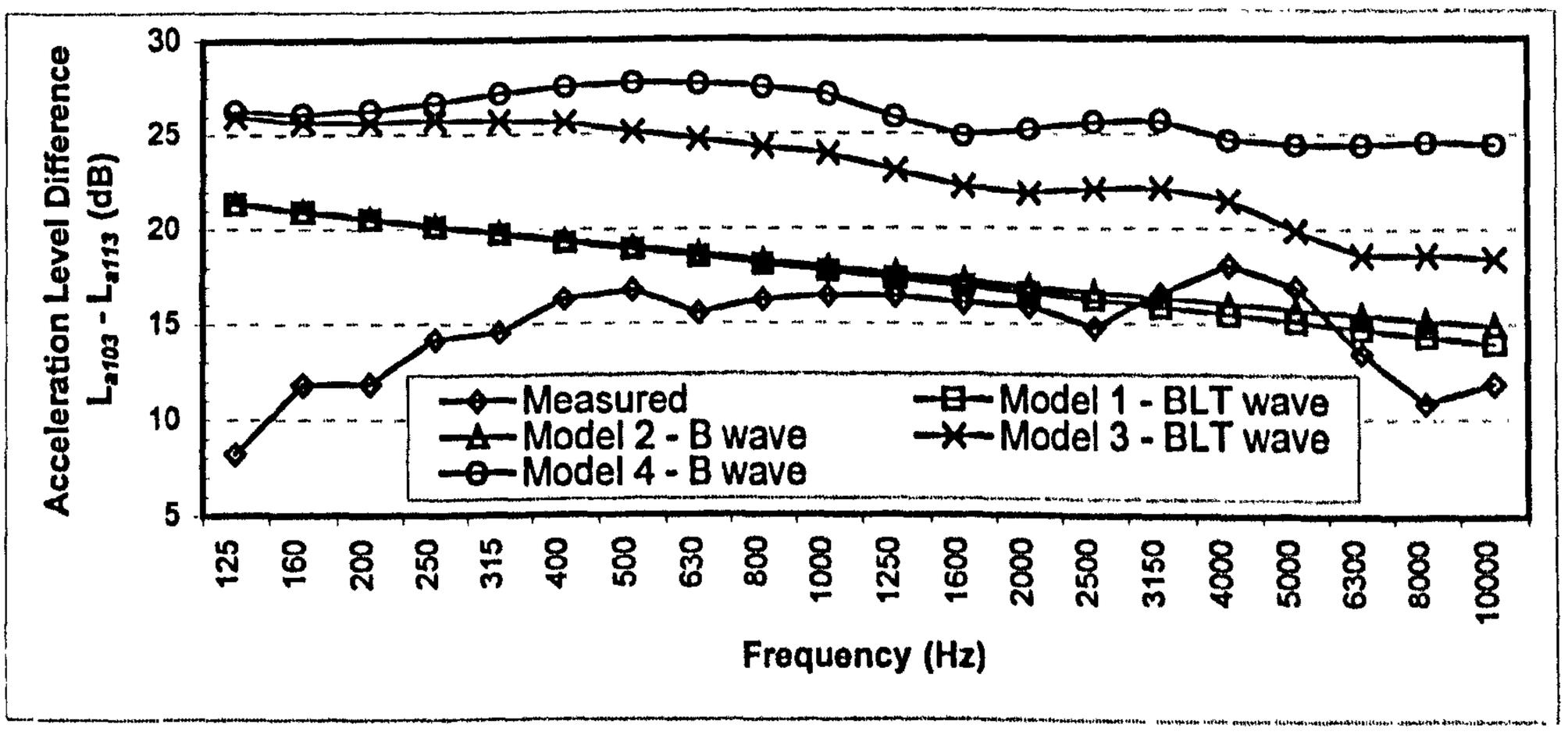

Figure 6.35 Comparison of predicted and measured attenuation L_{a103}-L_{a113}

results are presented in the higher frequency bands because the input power to the structure was insufficient to get above the background noise level. The predictions from the coarse BLT and B wave SEA models show good agreement with the measured acceleration level difference in the 400 Hz to 3.15 kHz frequency bands. Below the 400 Hz frequency band, the measured attenuation decreases and although there is reasonable agreement in the 200 Hz and 250 Hz bands, this is probably due to chance. The predicted acceleration level difference from the detailed SEA model is 4 to 5 dB higher than the coarse SEA prediction.

In figure 6.34 the measured acceleration level difference between subsystem 103 and transverse bulkhead subsystem 400 is shown. The predictions from the coarse BLT and B wave SEA models show good agreement with the measured acceleration level difference in the 400 Hz to 10 kHz frequency bands. Below the 400 Hz frequency band the measured attenuation decreases with frequency while the predicted attenuation increases. The predicted acceleration level difference from the detailed model is 5 to 8 dB higher than the coarse results.

In figure 6.35 the measured acceleration level difference between subsystem 103 and side shell subsystem 113 is shown. The predictions from the coarse BLT and B wave SEA models show good agreement with the measured acceleration level difference in the 400 Hz to 10 kHz frequency bands. Below the 400 Hz frequency band the measured attenuation decreases with frequency while the predicted attenuation increases. The predicted acceleration level difference from the detailed model is at best 4 to 6 dB higher than the coarse results.

The results presented in this section are typical of all the superstructure results when comparing the measured and predicted attenuation from the SEA model i.e. good agreement in the 400 Hz to 10 kHz frequency bands, but below 400 Hz the measured attenuation reduces as the frequency decreases. The poor performance below 400 Hz is surprising given the predicted modal density, mode count and modal overlap of the centre bulkhead, deck plates and main side shells will be of a similar order. The mode count and overlap of the other subsystems fall between those shown in figures 6.30 and

6.31 for subsystem 103 and 113. The measured attenuation shows a clear difference below 400 Hz and therefore the SEA model of the superstructure does not represent the model in the 125 Hz to 400 Hz frequency range. The results from the detailed modelling approach gave poor agreement with the coarse prediction and measured data.

The other feature is that the predicted attenuation from the BLT and B wave SEA models are very similar. This was expected given the differences between the bending-bending and the bending-in-plane coupling loss factors. Therefore for the SEA models of superstructure sections an SEA model consisting entirely of bending wave subsystems is probably sufficient.

A double tier section of ship superstructure was also analysed using the same modelling strategy employed for the single superstructure. Similar results were found for that structure as well with the coarse, BLT wave model giving the best agreement with the measured vibration level, although no results are presented here.

6.4 Section of Ship Hull

In the section 6.2 , the attenuation across a large ribbed plate was studied. In this section a part of the ship hull is examined, a substantially more complex ribbed structure. The hull section weighs approximately 45 to 50 tonnes, is 13 metre long, 15 metres wide and 5 metres high. Figure 6.36 shows a half section of the hull structure being modelled. It can be seen that the hull structure consists of a series of approximately periodically spaced transverse frames, continuous longitudinal stiffeners and a deck structure. The structure as shown is considerably simplified as the equipment mountings and small intermediate stiffeners (1L, 2L, 4L, 6L, 9L, 10L, 11L) have been neglected. In addition to this there are cut-outs and man holes in areas of the deck plate and the frames and longitudinal stiffeners between the deck and hull plate .

Because of the large size of the structure a full set of measurements were not performed and therefore the survey was restricted to examining the attenuation in the longitudinal direction and the attenuation around the hull. For practical reasons the source subsystem

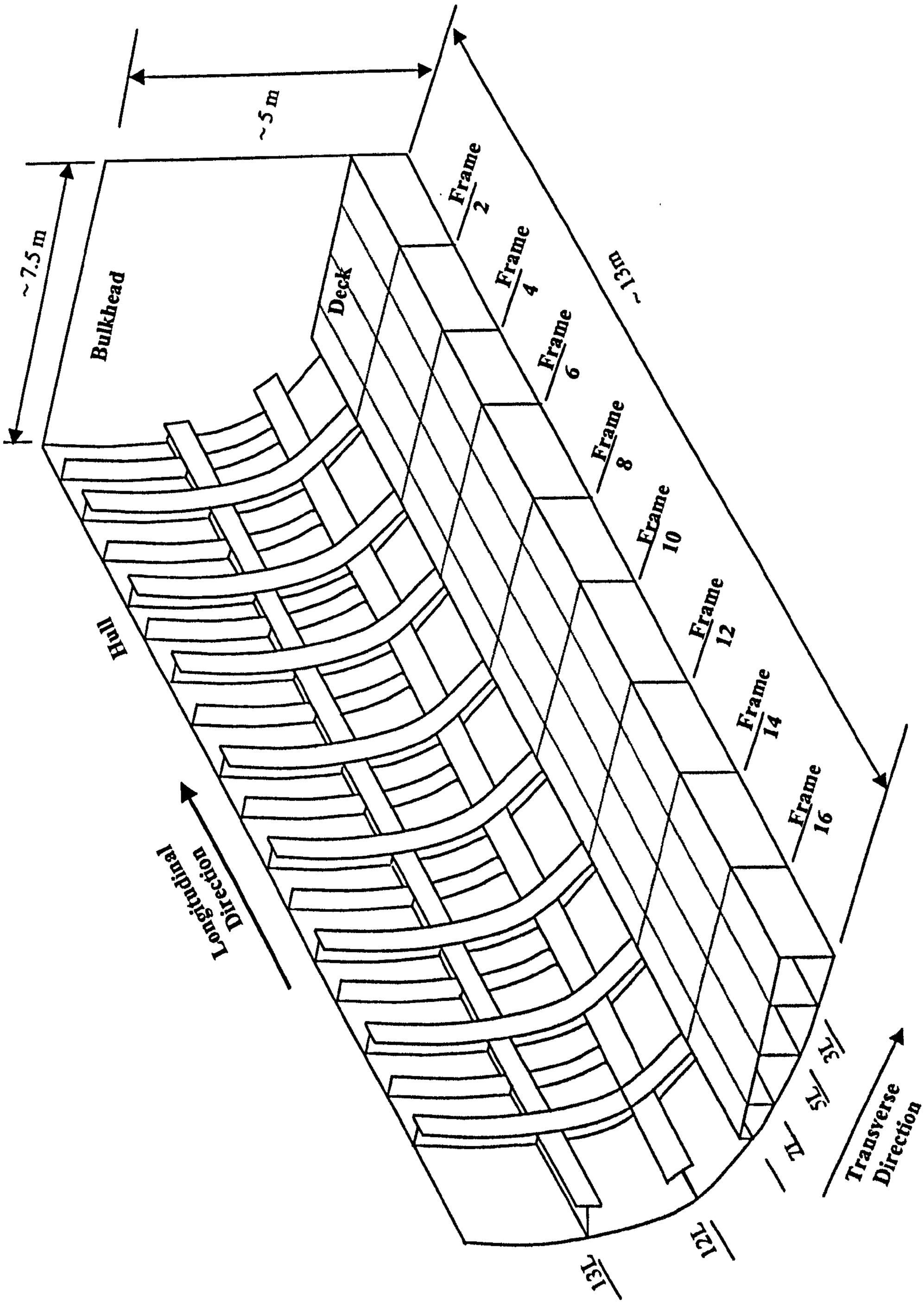

Figure 6.36 Half section of ship hull

was selected on the hull plate. The preferred option would have been to apply the excitation at the equipment mountings on the deck plate, however it would not have been possible to input sufficient power with the hammer to obtain excitation at the deck plate and the hull plate.

In the next section the SEA modelling of the hull section is discussed with regard to subsystem selection and joint modelling. As the results from the superstructure and ribbed plate studied previously show that detailed modelling does not improve the accuracy of the predictions, a coarse SEA model will be implemented.

6.4.1 The SEA Model of the Hull

The SEA modelling of the hull section presents a number of modelling problems that were not seen in the large laboratory test structure and the ribbed plate studied previously.

In figure 6.37 a cross section of the hull is shown with the longitudinal stiffeners. For the transverse joints, i.e. around the hull, the first assumption is that the singly curved hull plates can be approximated to a flat plate so that the stiffeners 12L and 13L can be modelled with the theoretical model given in chapter four. The radius of curvature of the hull is between 5 m and 7.5 m which gives an equivalent ring frequency of 110 Hz. Above the ring frequency the curvature of the hull plate can be ignored and the assumption of a flat plate is valid. The keel plate and longitudinal stiffeners 3L, 5L, 7L and the margin plate can not be modelled using the hull frame joint. Instead the joint developed by Smith [78] for two parallel plates connected by a perpendicular plate is used for the deck/hull structure. For the keel plate and joints 3L and 5L this is justifiable because the curvature of the hull plates is small. For joint 7L and the margin plate the curvature of the hull makes the use of the parallel plate joint difficult to justify, instead a dynamic a stiffness matrix modelling approach may be better for these joints as it would accommodate the angle between the hull plate and stiffener. Figure 6.38 shows the joint representation for the main transverse joints.

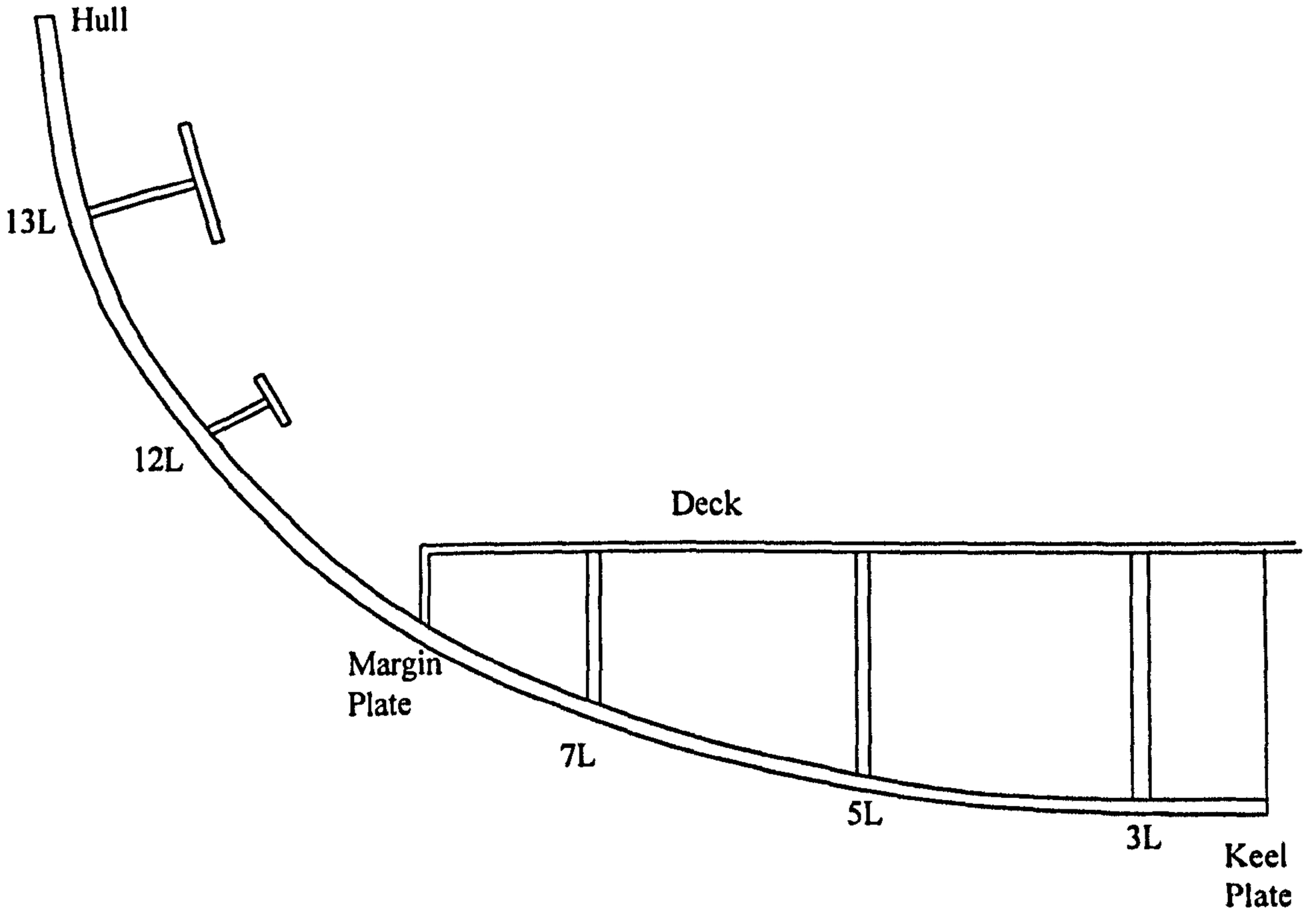

Figure 6.37 Cross section through ship hull

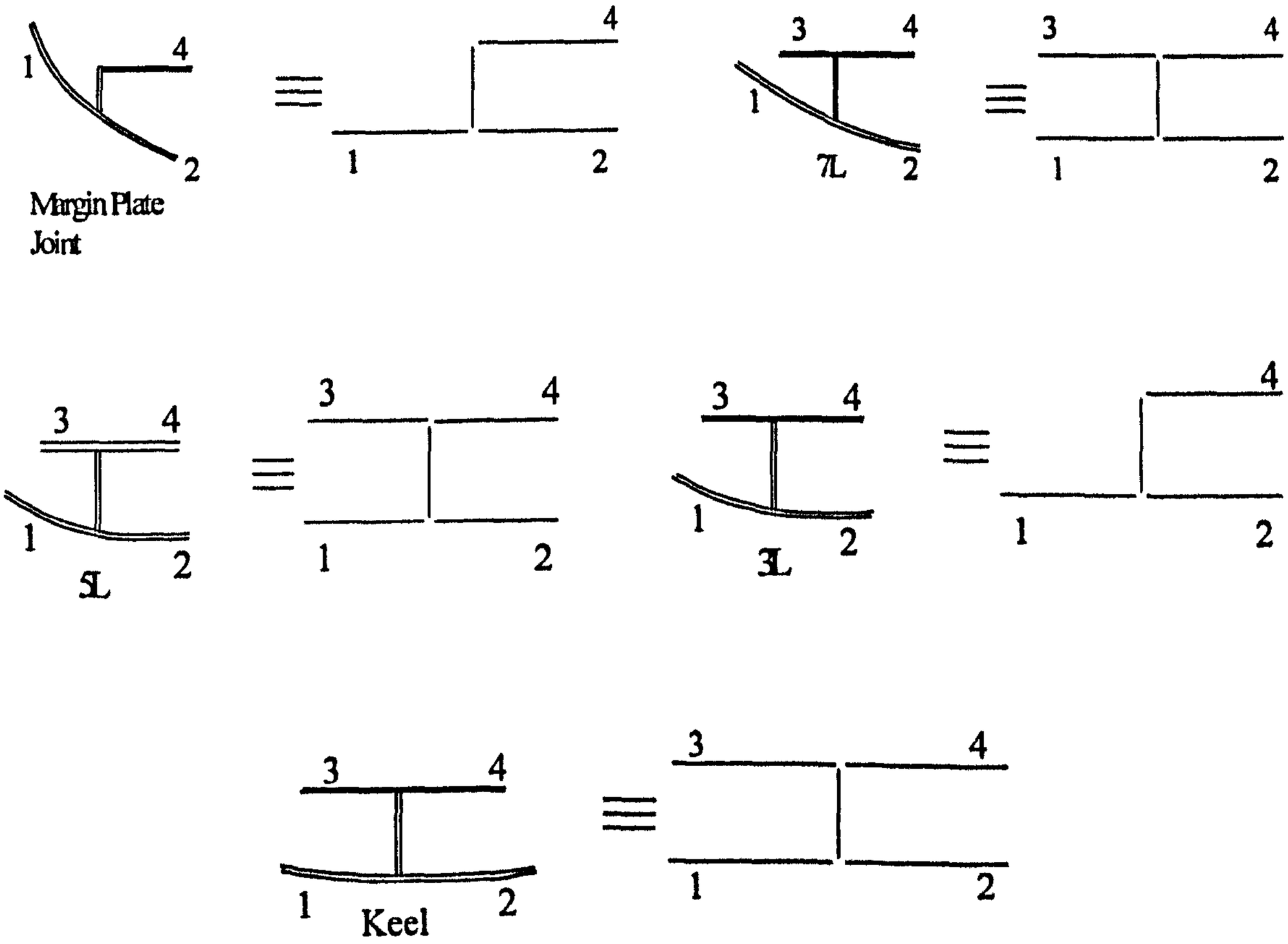

Figure 6.38 Transverse joint models

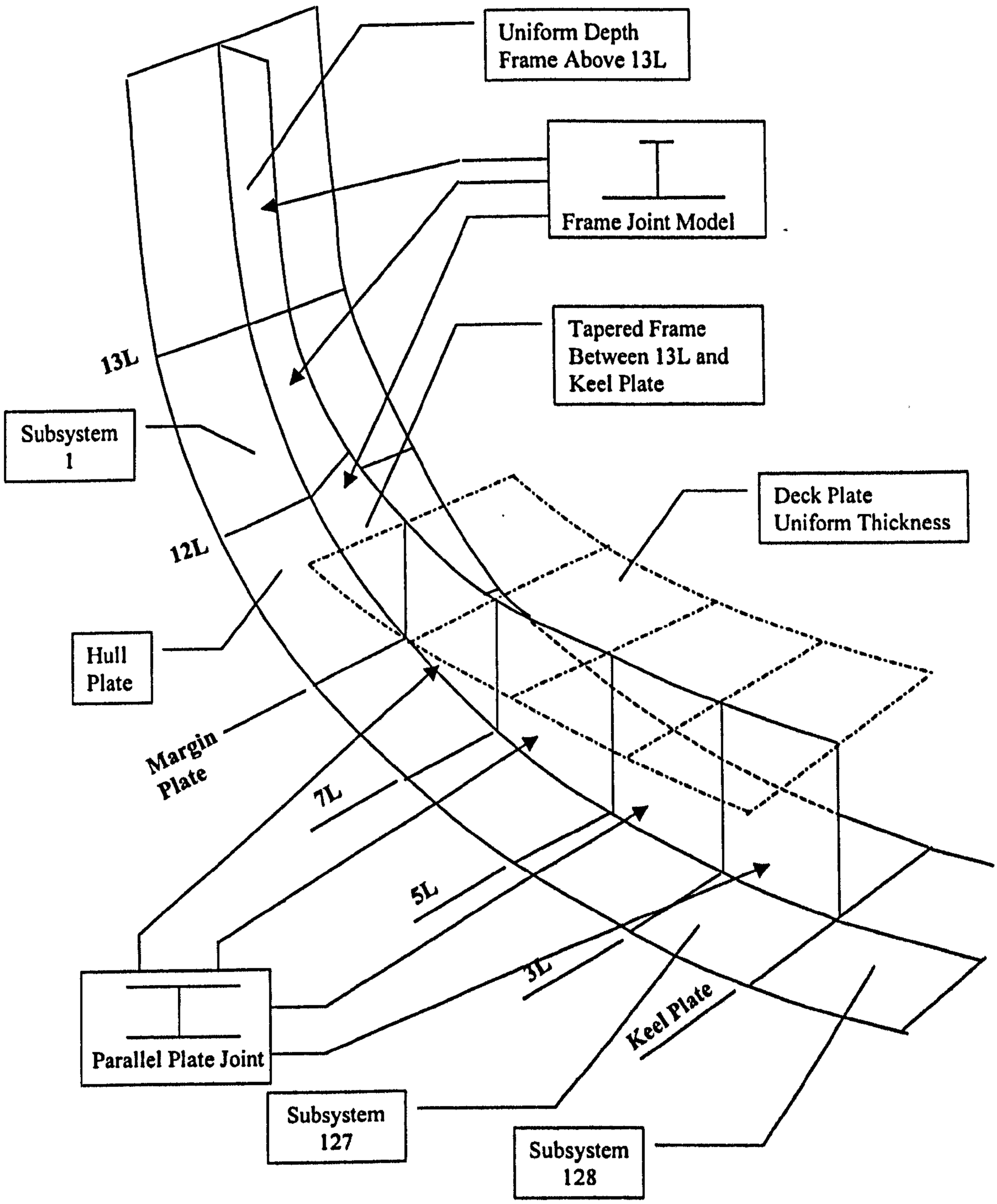

Fig 6.39 Longitudinal joint details for even numbered frame sections.

(Flange plates have been omitted for clarity)

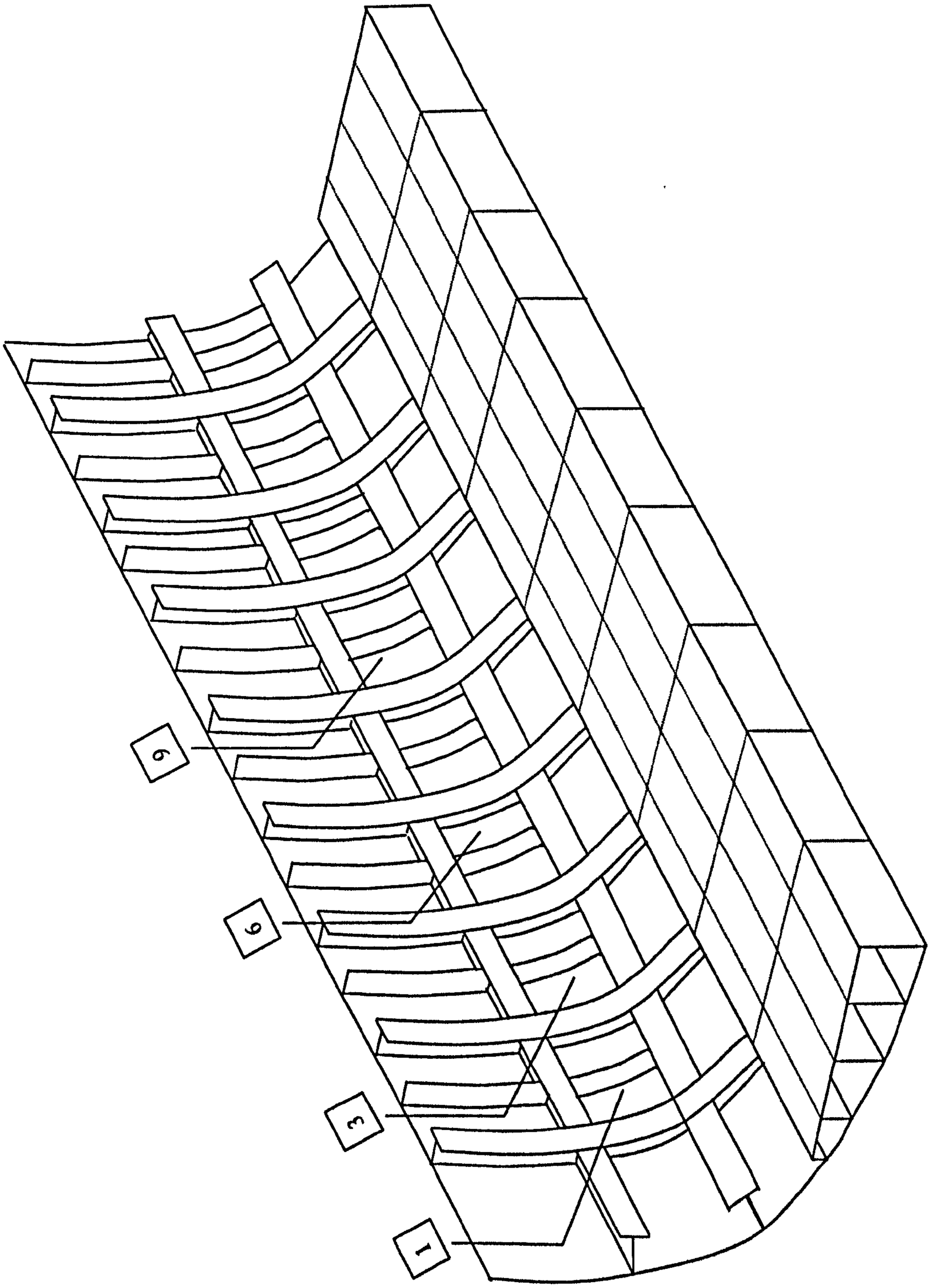

Figure 6.40 Hull section SEA subsystem numbers

Figure 6.39 shows a typical frame section with the longitudinal stiffeners, deck and hull plates. For the longitudinal joints it is again assumed that the singly curved hull plates can be approximated to a flat plate so that the stiffeners 13L, 12L and the margin plate can be modelled with the frame joints. The joints between the deck plate and hull plate can be modelled with the parallel plate joint. The one feature that is common to all the frames is that between 13L and the keel plate the frame depth is continuously increasing. In the analysis model the average depth of the frame plate between longitudinal stiffeners has been used.

Figure 6.26 shows the numbers of the subsystems of the SEA models where the attenuation with distance results are presented in this section. Figure 6.25 also shows the location of the subsystems around the hull relative to the source subsystem for which results are presented. The bulkhead at frame 0 shown in figure 6.22 is remote from the source subsystem and has not been included in the SEA model. The SEA models of the hull created for analysis are as follows:

(a) Model 1: The SEA model of the structure consists of bending, longitudinal and transverse wave subsystems. The frame stiffeners in the x and y directions are modelled without flange plates and all other rib stiffeners are modelled as web plate joints. The SEA model has approximately 24,900 coupling loss factors and 338 subsystems.

(b) Model 2: The SEA model of the structure consists of bending wave subsystems only. All rib stiffeners on the deck plate are modelled as web plate joints. i.e. the flanges of the frame stiffeners are ignored. The SEA model has approximately 2126 coupling loss factors.

(c) Model 3: The SEA model of the structure consists of bending, longitudinal and transverse wave subsystems. The frame stiffeners in the longitudinal and transverse directions are modelled with flange plates and all other rib stiffeners are modelled as web plate joints.

(d) Model 4: The SEA model of the structure consists only of bending wave subsystems. The frame stiffeners in the longitudinal and transverse directions are modelled with flange plates and all other rib stiffeners are modelled as web plate joints.

Theoretically it would be expected that model with the full frame model with flange plates would give the best results. From the complex laboratory structure in chapter 5 and the ribbed deck plate in section 6.2 it has been shown that a full bending, longitudinal and transverse wave model with web plate joints will give the most accurate results. Therefore model 1 would be expected to give the most accurate prediction.

6.4.2 SEA Model– Subsystem Properties

In figure 6.41 the predicted statistical mode count for the source subsystem 1 is shown and the longitudinal and transverse subsystems 1001 and 2001. It can be seen that there is one mode in the 125 Hz band and 10 modes in the 1 kHz frequency band. For the longitudinal subsystems the first mode occurs in the 4 kHz frequency band and for the transverse subsystem the first mode occurs in the 2.5 kHz frequency band. From the predicted mode count it would be assumed that below 1 kHz the predictions from SEA model will not be accurate. The low in-plane mode count would also indicate the in-plane modes are relatively unimportant and therefore the B wave and BLT wave SEA models will give similar results. The properties are similar to those of the large flat plate analysed in section 6.2.

In figure 6.42 the predicted modal overlap M_b, M_l and M_t is shown for subsystems 1,1001 and 2001 respectively. It can be seen that for the bending subsystem the modal overlap exceeds unity in the 200 Hz frequency band even though there is a low mode count. The modal overlap indicates that the SEA model should theoretically be accurate down to the 200 Hz frequency band. The longitudinal modal overlap M_l for 1001 exceeds unity in the 5 kHz frequency band and the transverse modal overlap M_t for 2001

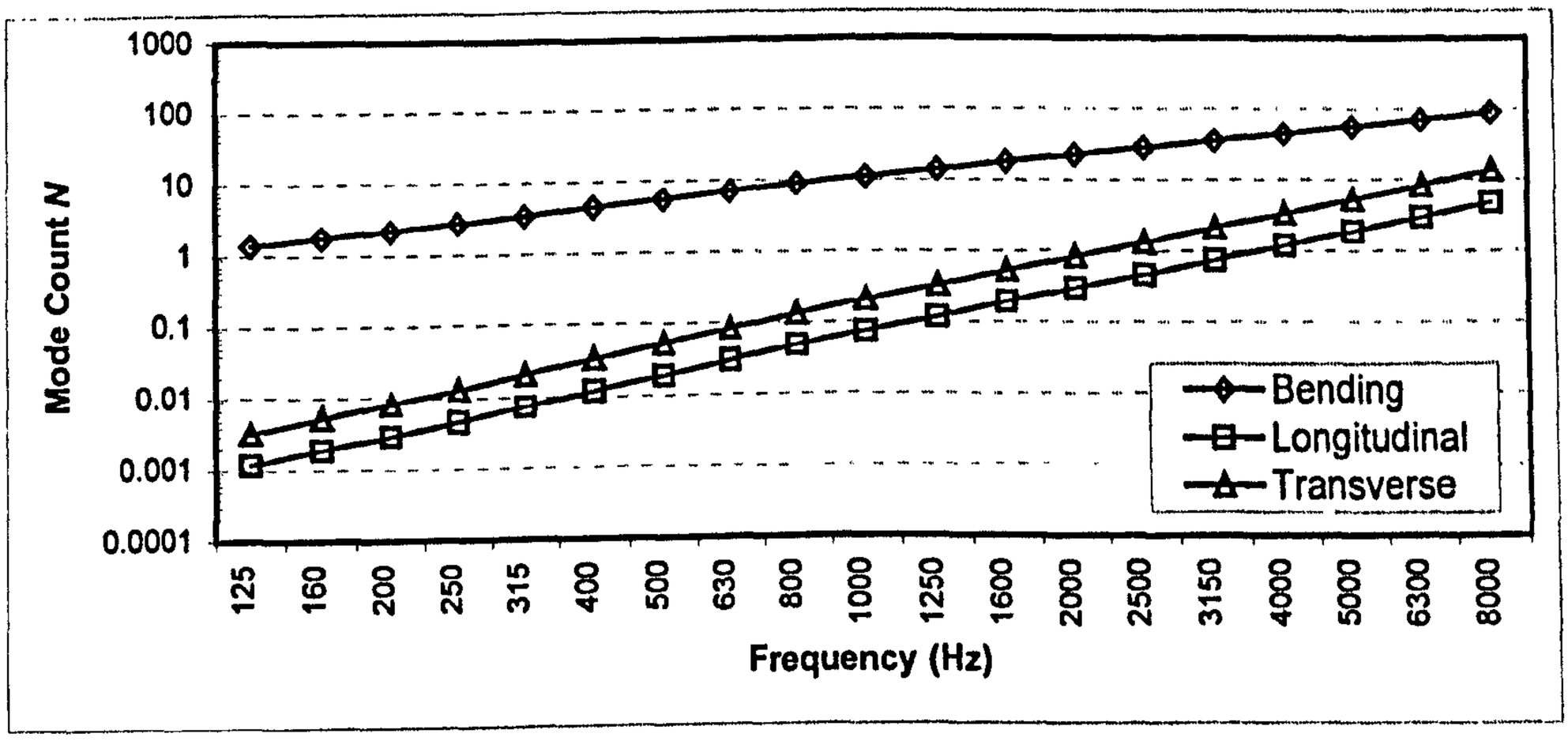

Fig 6.41 Predicted statistical mode count for source subsystem 1

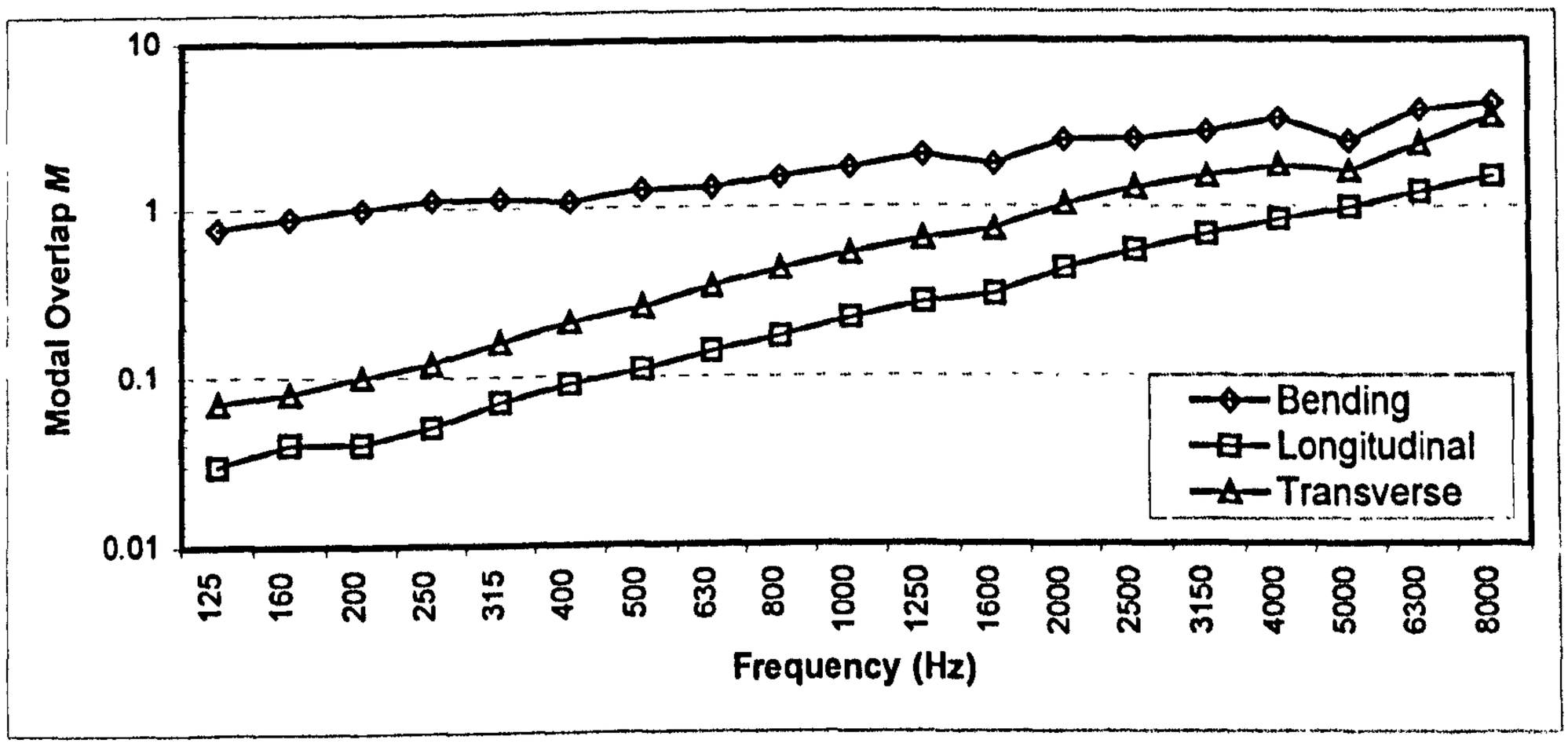

Fig 6.42 Predicted modal overlap for source subsystem 1

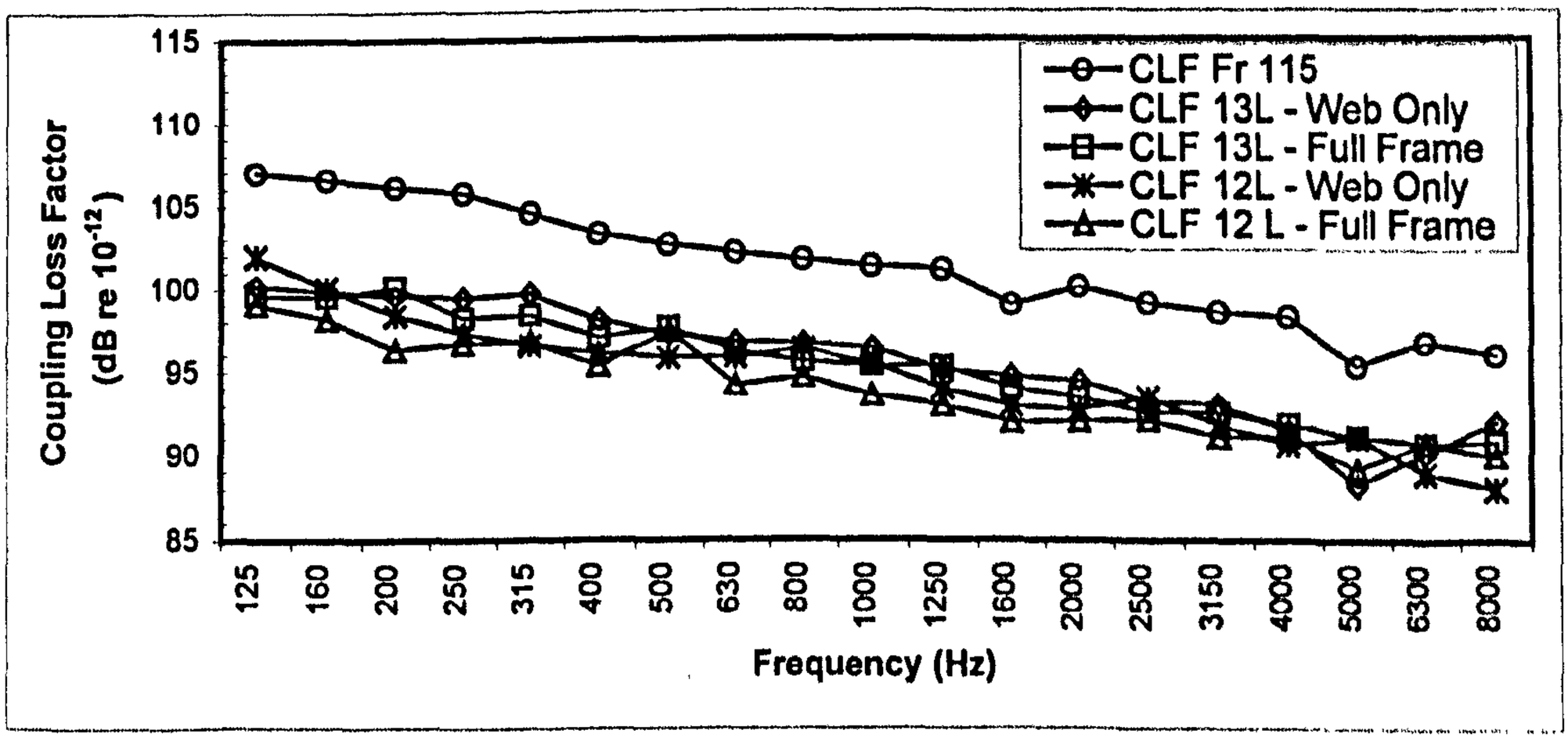

Fig 6.43 Comparison of predicted CLF's for source subsystem 1

exceeds unity in the 2 kHz frequency band. The in-plane subsystems should not be significant until the higher frequency bands.

In figure 6.43 the coupling loss factors for the longitudinal stiffeners *12L* and *13L* are plotted for the web plate and full frame models. It can be seen that the predicted coupling loss factors for the two stiffener sizes and modelling approaches are very similar across the frequency spectrum, with a difference of 1 to 2 dB. In contrast the coupling loss factor in the longitudinal direction, $\eta_{1\text{-}2,}$ for frame 15 is shown. It can be seen that the coupling loss factor is 4 to 5 dB higher than the transverse coupling loss factors and therefore more power will be transmitted in the longitudinal direction.

6.4.3 SEA Model – Comparison Of Predicted And Measured Attenuation

In this section the measured and predicted attenuation from the four SEA models of the hull is presented. The results are given between the 160 Hz and 8 kHz frequency band. Figure 6.44 shows the results for the measured attenuation between source subsystem 1 and subsystem 3. The results from the four SEA models are very similar in all frequency bands and the SEA predictions show good agreement over all frequency bands.

Figure 6.45 shows the results for the measured attenuation in the longitudinal direction between subsystem 1 and subsystem 6 on the hull. It can be seen that predicted attenuation from the BLT wave SEA models 1 and 3 show good agreement between the 500 Hz to 8 kHz frequency bands, generally the prediction is within 1 to 2 dB. The predicted attenuation from the B wave SEA models is approximately 1 dB higher than the BLT predictions. Below the 500 Hz band there is a dip in the measured attenuation at 250 Hz which the SEA models do not predict.

Figure 6.46 shows the measured attenuation in the longitudinal direction between subsystem 1 and subsystem 9 on the hull plate. The results from the four SEA models are very similar with the difference between the B and BLT models is approximately 1 to 1.5 dB in all frequency bands. The agreement between the measured and predicted

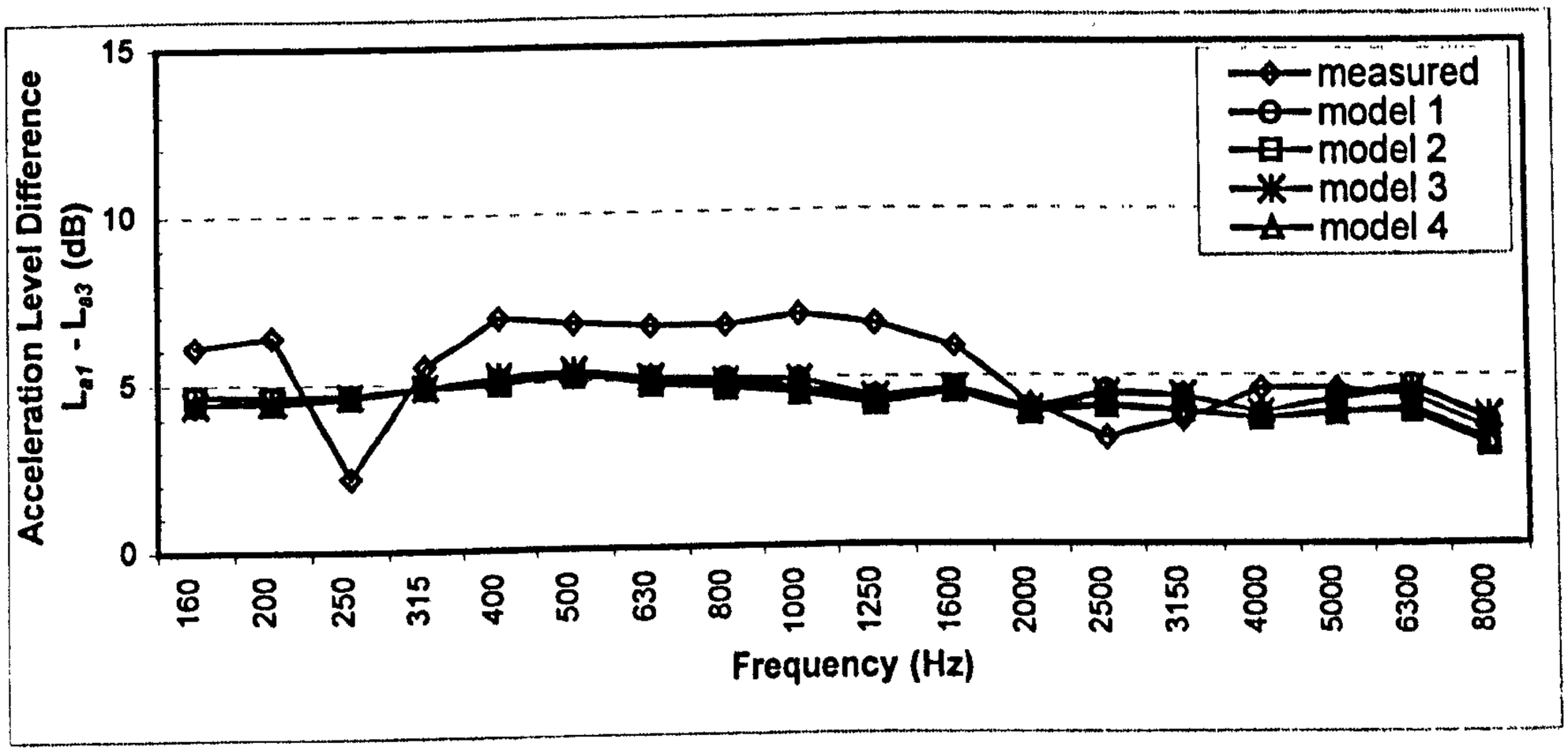

Fig 6.44 Comparison of predicted and measured attenuation L_{a1}-L_{a3}

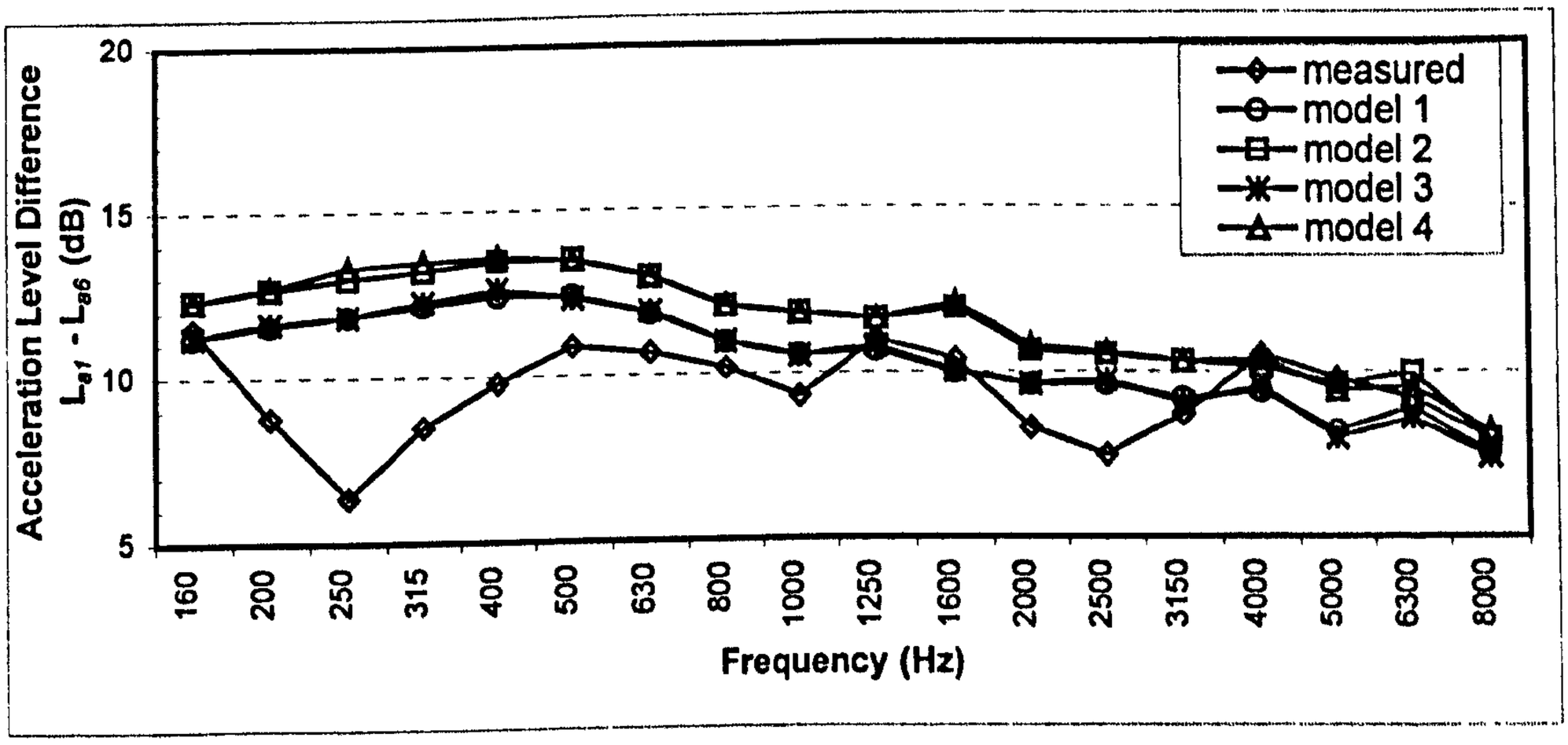

Fig 6.45 Comparison of predicted and measured attenuation L_{a1}-L_{a6}

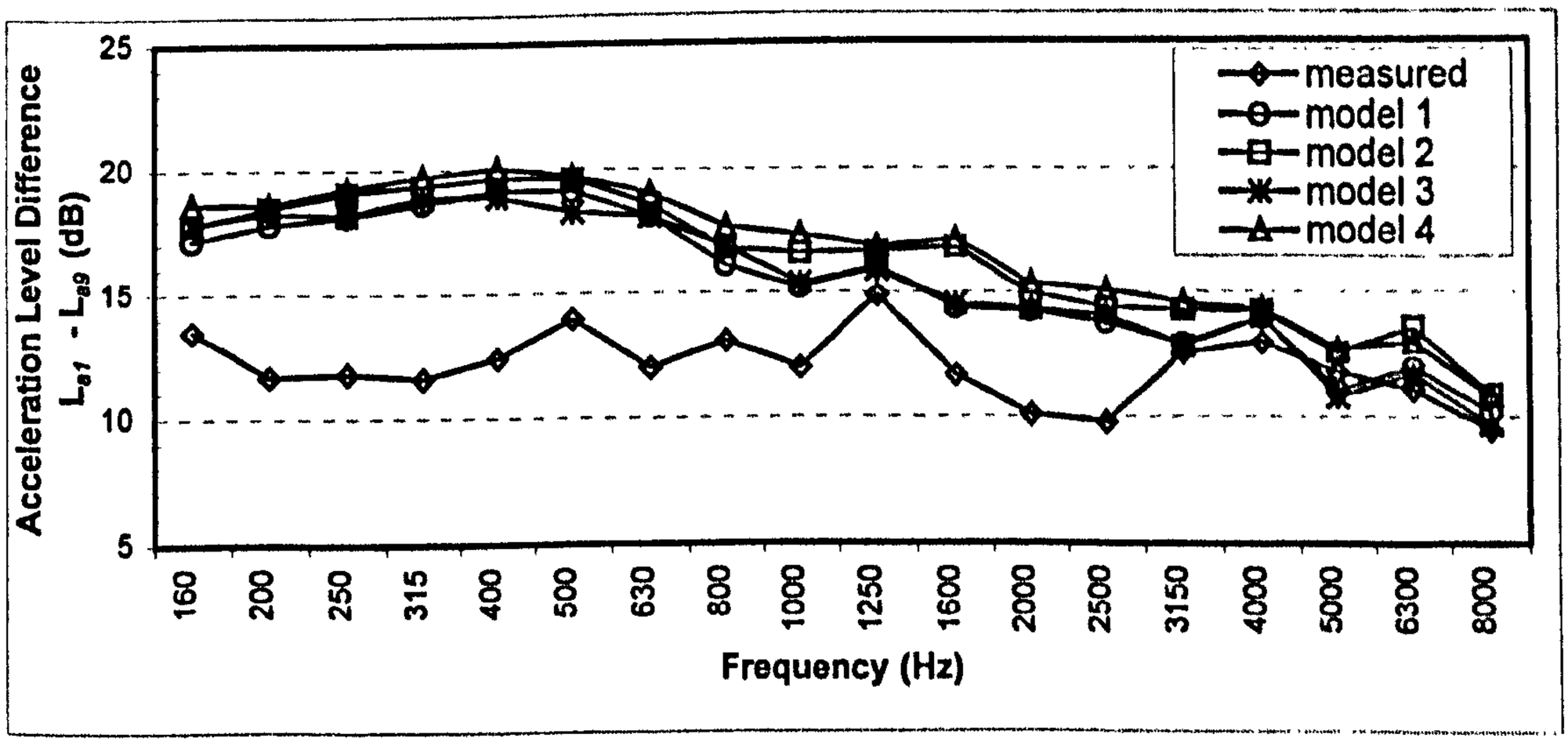

Fig 6.46 Comparison of predicted and measured attenuation L_{a1}-L_{a9}

attenuation is reasonably good from 1.25 kHz to 8 kHz. Below the 1.250 kHz frequency band the agreement is not particularly good a difference between 3 to 6 dB between the measurement and the prediction. The 95% confidence level of the measured attenuation is ± 3.7 dB in the 200 Hz band and ±2.1 dB in the 800 Hz frequency band, and therefore there could be better agreement in the lower frequency bands.

In figure 6.47 the measured attenuation from subsystem 1 to subsystem 127 (see fig 6.39) on the hull between the keel plate and the longitudinal stiffener 3L is plotted from the 160 Hz to 5 kHz frequency bands. The prediction from all four SEA models show excellent agreement with the measured attenuation over the entire frequency spectrum.

In figure 6.48 the measured attenuation from subsystem 1 to subsystem 128 on the hull between the keel plate and the longitudinal stiffener 3L is plotted from the 160 Hz to the 5 kHz frequency bands. It can be seen that in the 160 Hz to 2 kHz frequency bands there is good agreement with the measured attenuation. Above 2 kHz the measured attenuation is 4 to 5 dB higher than the predicted attenuation from the BLT wave SEA models. Above 2.5 kHz the measured attenuation is 2 to 3 dB higher than the predicted attenuation from the B wave SEA models which show a gradual divergence with frequency from the BLT results.

In figure 6.49 the measured attenuation from subsystem 1 to subsystem 132 on the opposite side of the hull between the margin plate and the 12L is plotted from the 160 Hz to 8 kHz frequency bands. It can be seen that in the 160 Hz to 2.5 kHz frequency bands there is poor agreement with the predictions from the B wave SEA models and the measured attenuation. Above 2.5 kHz the predicted attenuation is in good agreement with the measured attenuation. For the BLT wave SEA models there is good agreement from 315 Hz to 4.0 kHz with the difference between the measured and predicted attenuation being less than 5 dB. The 95 % confidence level on the measured data is approximately 2.5 dB at 315 Hz to 1.5 dB at 1 kHz, therefore the agreement between the predicted and measured attenuation could be better than shown.

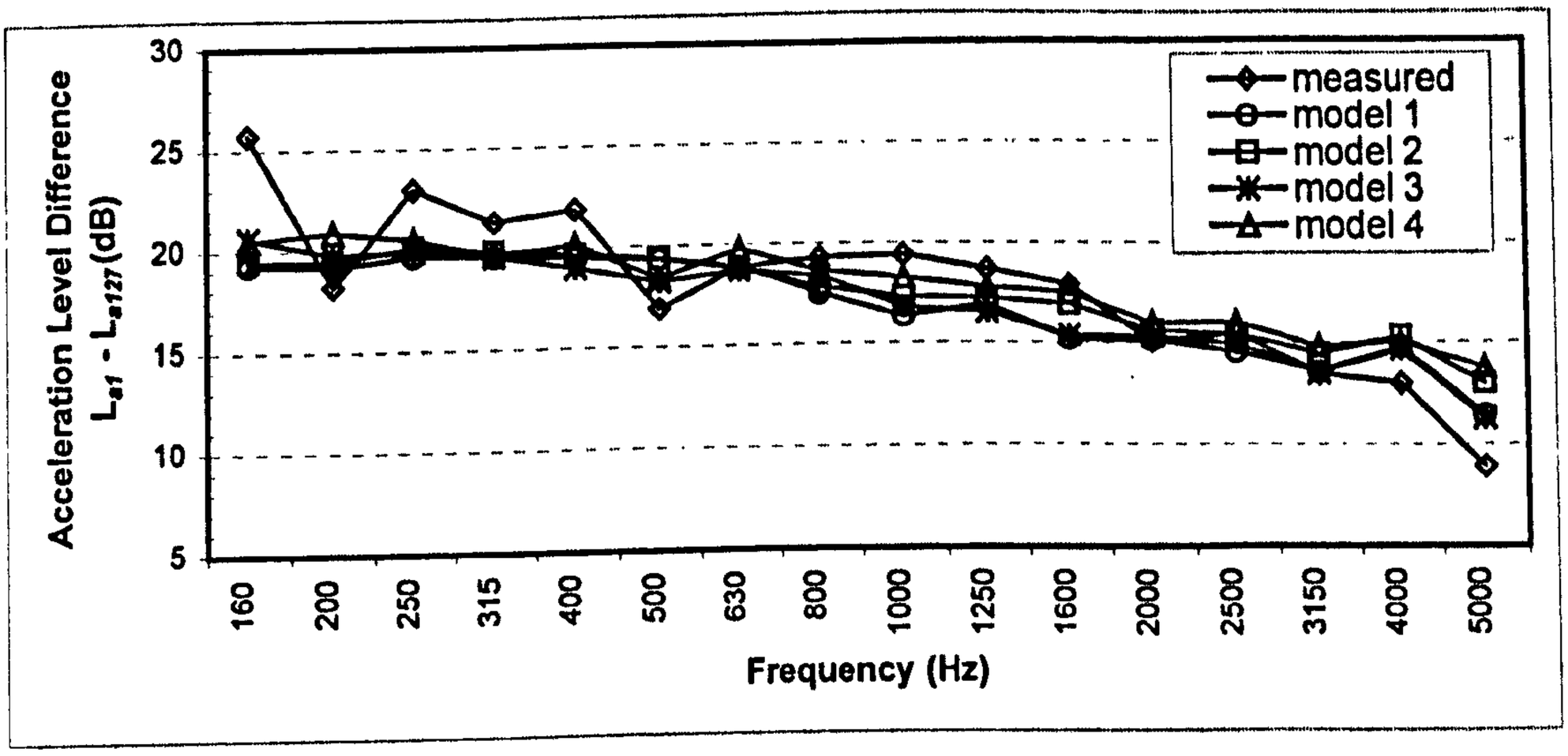

Fig 6.47 Comparison of predicted and measured attenuation L_{a1}-L_{a127}

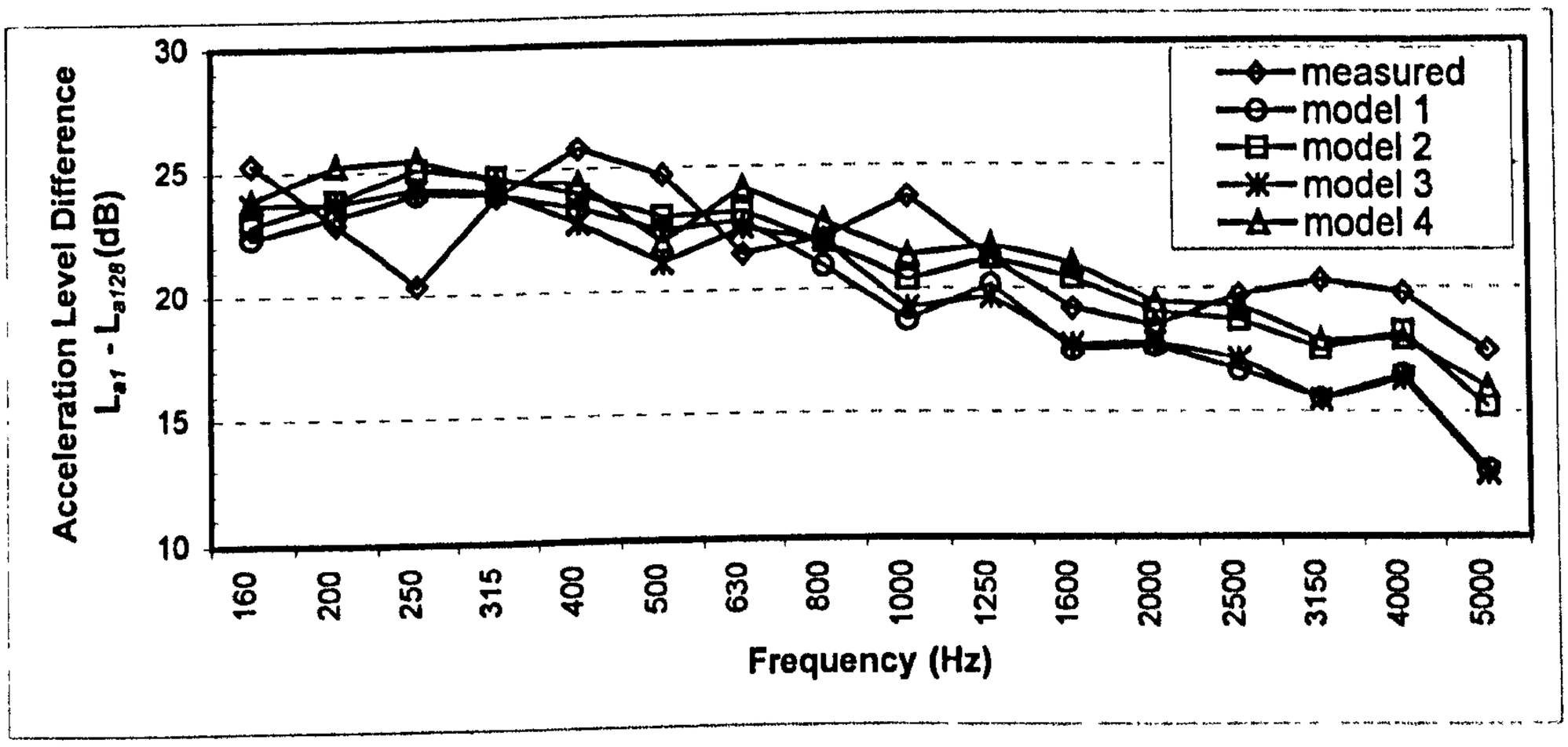

Fig 6.48 Comparison of predicted and measured attenuation L_{a1}-L_{a128}

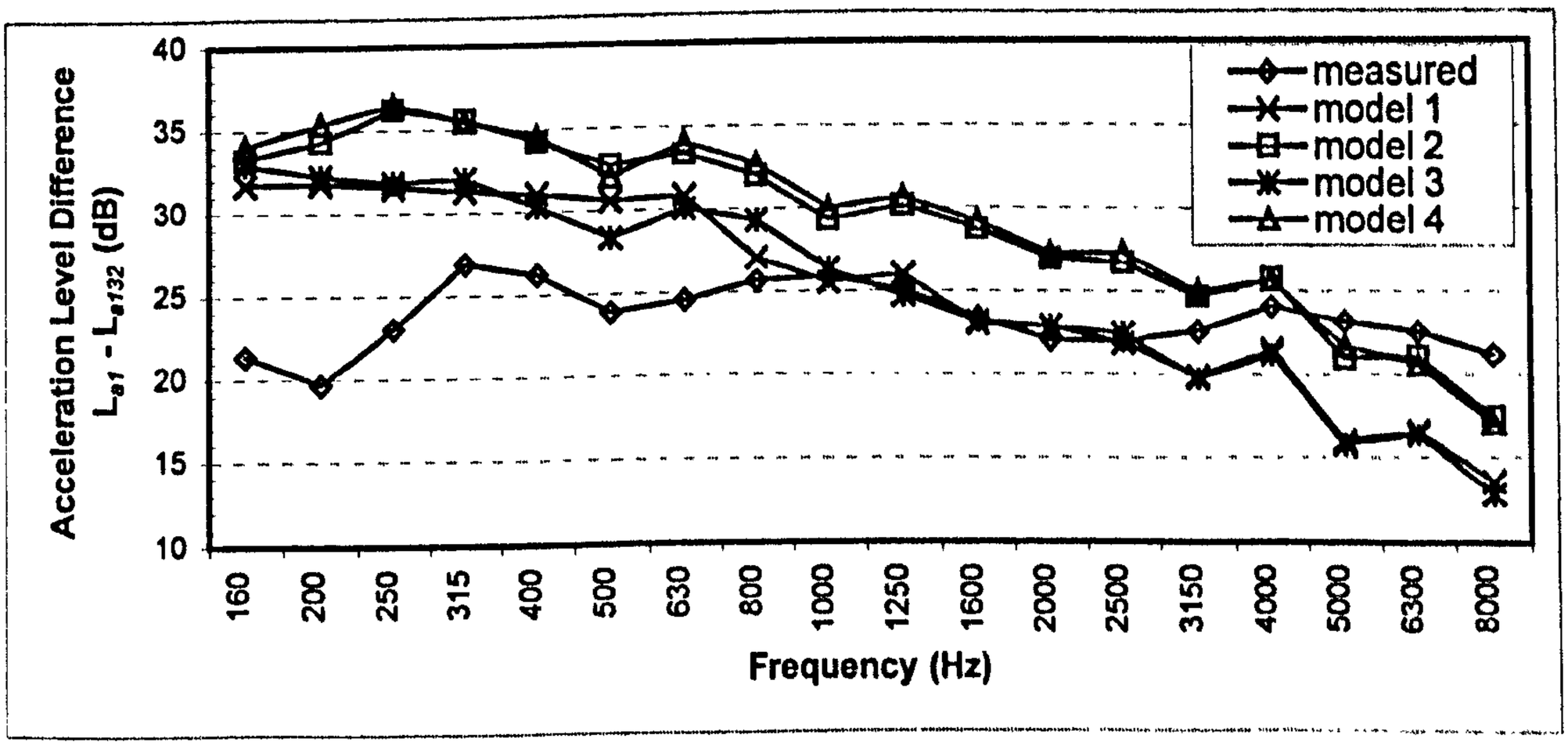

Fig 6.49 Comparison of predicted and measured attenuation L_{a1}-L_{a132}

Above 4 kHz the attenuation is underpredicted, which could be due to the effect of the small intermediate longitudinal stiffeners on the measured data but which have been neglected for the SEA model. These small stiffeners will not have any significant effect on the attenuation on the low frequency structure-borne noise, but will increase the attenuation in the higher frequency bands.

The results from the SEA models show good agreement for the predicted attenuation around the hull and for attenuation with distance over the first 6 frames. However as was observed with the detailed SEA model of the large ribbed plate, as the number of joints between the source and receiving subsystems increases the difference between the prediction and measurement increases, with the attenuation being overpredicted in the lower frequency bands.

6.5 Discussion

The results presented in this chapter raise a number of issues regarding the application of SEA to ships for discussion. The first point relates to the theoretical model developed in chapter 4 of this thesis. The best predictions were obtained from the web joint models which was also found the complex laboratory structure the results presented in chapter 5,. Including the flange plates does not significantly improve or detrimental to the results when considering the complex hull section, however for the simpler large ribbed plate the accuracy of the prediction at low frequencies is improved by omitting the flange plates. It has also been shown that the curved plates of the hull can be considered as flat plates because the ring frequency is low. In fact the radius of curvature in most ships will be large and consequently the ring frequency will always be low. Therefore the flat plate assumption will be valid for most ships.

The predicted SEA properties have shown that the modal overlap for bending wave subsystems is generally above unity in the 125 Hz to 160 Hz frequency bands. It has been argued by Nilsson [14,15,16] that SEA could not be applied to ships below 250 Hz because of the low mode count of structural elements such as the deck and hull. The analysis has indicated a mode count of 3 to 4 modes typically in the 125 Hz for the

coarse SEA models. The analysis of subsystem properties suggests that an SEA model can be valid down to this frequency.

The predicted modal properties for the in-plane subsystems indicate that in-plane subsystems should not be significant until the higher frequency bands, typically above 2.5 kHz. This would not indicate that there should not be any significant difference between the B and BLT wave SEA models until the higher frequency bands. However errors in the SEA model due to a low mode count in the longitudinal and transverse wave subsystems are not important if the coupling loss factor between the B and LT subsystems and the LT and B subsystems is low and all sources excited are bending waves. For the experimental measurements, hitting the structure with a hammer will principally excite bending waves but in practice the engines, prop shaft and gearboxes will excite bending and in-plane waves.

The subsystem properties such as mode count and modal overlap are based on the area of the subsystem, and indicate that in-plane subsystems should only be important in the higher frequency bands for the SEA models. In practice the deck and hull will support in-plane waves across the entire deck plate, along and around the hull, therefore there will be in-plane waves in the low frequency bands. The BLT wave SEA model gives the better prediction of attenuation because all the joint models are based on the assumption of transmission on semi-infinite plates which will therefore support in-plane waves in low frequency bands and this gives a good approximation to the real structure, even though the calculated subsystem properties indicate there are no modes in the low frequency bands. The presence of the tee joints formed between the deck and bulkheads and the bulkhead and the side shell are important as bending waves will be converted to in-plane waves and vice versa and this energy exchange is not represented in the B wave SEA model, hence it's poorer performance. Therefore in-plane waves are important when predicting attenuation with distance.

The analysis results presented in this chapter for the complex laboratory structure have shown that the most accurate predictions are obtained for models that include all bending, longitudinal and transverse wave types. The models based exclusively on

bending wave only models were found to consistently predict a higher acceleration level difference than measured, this was particularly clear in the attenuation with distance results e.g. figs 6.16, 6.17 and 6.18. The analysis of the structures in this section has shown that detailed modelling of the structure does not improve the accuracy of the predicted attenuation. The coarse modelling strategy has been shown to give the most accurate prediction of the attenuation. This is advantageous since it will reduce modelling time and the overall size of the model. The major disadvantage is that this means it will not be possible to apply automatic sub-structuring to generate SEA models without implementing some modelling criteria\rules in the creation of an SEA model.

The ability to predict the attenuation in vibration level distance is the most important aspect for a ship. It has been shown in section 6.2 for a large ribbed deck plate that reasonably accurate predictions have been achieved. In the more complex hull section the attenuation with distance results in the longitudinal and transverse hull sections are reasonably accurate. The predictions are however extremely sensitive to the damping level of the model and small changes can have a significant effect on the attenuation level, particularly over several structural joints. The results presented in this chapter have used the same damping value for all subsystems based on the loss factor data described in chapter three, section 3.2 which can be taken as a minimum damping level for plain steel plates. In practice on the finished vessel there will be damping throughout the structure such as cement/polymer floor coverings and floating floors applied to the deck and damping layers applied to the hull. The measured attenuation with distance results on the finished vessel could be very different from those measured in this work.

The approach used in this thesis has been referred to as classical SEA by Heron [60] where each subsystem and joint is defined. From the data presented it is not possible to rule out classical SEA in favour of methods such as the dynamic stiffness matrix or wave intensity analysis as the most suitable modelling approach. It is interesting to note that difference between the measured and predicted attenuation in real ship sections is considerably less than that reported by Langley et al [59,96] and Heron [60] for simple one-dimensional periodic laboratory structures, who report errors as large as 40 to 50 dB over five to six subsystems.

From the results presented in section 6.2 it can be seen for the detailed model that as the number of joints between the source and receiving subsystems increases the difference between the predicted and measured attenuation increases. The results presented for the full frame model shows increasingly poor agreement with the measured attenuation for each joint crossed. Comparing the results with the coupling loss factor curves shown in figure 6.9, it can be seen that good agreement is observed only in the frequency bands where the coupling loss factor for web plate and full frame joint model are very similar e.g. 630 Hz, 2.5 kHz, 3.15 kHz bands etc. In the other frequency bands where there is a difference between the two predicted coupling loss factors, the difference in the predicted attenuation mirrors this, but it increases with each joint crossed. It does not require a large number of joints to be crossed before the predicted attenuation from the full frame joint model becomes inaccurate. The results for the full frame and web plate joint modelling approaches are very similar in the 400 Hz to 8 kHz frequency bands. The difference between the two modelling approaches in the 125 Hz to 400 Hz frequency bands is consistent with the difference seen in the coupling loss factor curves.

The agreement between the two joint modelling approaches is better in the detailed SEA model than in the coarse model where the differences between the coupling loss factor are amplified as the number of joints between the source and receiving subsystem increase. The better agreement between predictions in the detailed model is due to the 'smoothing' effect of the coupling loss factor for the small web plate stiffeners which reduces the difference between the two modelling approaches. Neither joint modelling approach in the detailed model gives an accurate prediction of the attenuation with distance. A small reduction in the damping model could improve the accuracy of the prediction.

The predictions from the coarse model were shown to be in good agreement the measured data but the actual plate may be considered too small with insufficient joints to verify the attenuation with distance. The results from the hull section also show reasonably good agreement with the measured data and a small reduction in the damping of the SEA model could improve the accuracy of the prediction and extend the range of the model. However as the number of joints crossed increases, the difference

between the predicted and measured results will increase if there is a systematic bias error in the assumed value of internal loss factor (Ref. Craik [97]).

A consequence with having to model all three wavetypes is that the size of the SEA model rapidly increases. For a single joint between two plates, a bending wave model has 4 coupling loss factors for the joint, but for a full wavetype model there are 36 coupling loss factors per joint. Given that an SEA model will have several thousand joints, the model will become extremely large. There are therefore practical benefits in using a bending wave and in-plane wave model where the longitudinal and transverse wave subsystems are combined to form one subsystem supporting both wavetype. This would give 16 coupling loss factors for a two plate joint. Craik [98] has investigated this approach for building structures.

From the coarse BLT SEA models analysed, some estimates of overall model size can be obtained. The large ribbed plate in section 6.2 weighed approximately 5 tonnes and the model had approximately 52 joints, 47 subsystems and 616 coupling loss factors giving an estimate of 10.5 joints, 9.4 subsystems and 123 coupling loss factors per tonne. The superstructure unit weighed approximately 6 tonnes and had approximately 49 joints, 67 subsystems and 2638 coupling loss factor giving an estimate of 8.2 joints, 11.2 subsystems and 440 coupling loss factors per tonne. The hull section weighed approximately 45 tonnes and had approximately 312 joints, 24,900 coupling loss factors and 338 subsystems, giving an estimate of 7 joints, 7.5 subsystems and 553 coupling loss factors per tonne. The average is then 8.6 joints, 9.4 subsystems and 365 coupling loss factors per tonne. For a ship weighing two thousand tonnes (a relatively small vessel !) then a coarse SEA model could be expected to have 17200 joints, 18800 subsystems and 730,000 coupling loss factors. This poses a serious problem in terms of modelling effort, joint computational time and solution of the loss factor matrix. A more computationally efficient solver could be employed for the solution of the power balance equations and loss factor matrix such as Irons frontal solver which is used in finite element codes instead of Gaussian elimination.

The remaining point this leads to is the proposed use of a finite element pre-processor to generate the ship model which is then input to a conversion program which interrogates the FE model database to create a complete SEA model of a ship. This approach was used by Kim et al [34] and Hynna et al [35]. The problem with using an FE model to create the SEA model is that the process is entirely dependant on the conversion software and its capability to interrogate the FE model database. This is an extremely complex problem and the potential to create an SEA model that is strewn with errors is high. It is questionable that any analyst would be able to rigorously check the input deck with confidence. Some of the problems that could be expected to be encountered are as follows.

(a) Identification of subsystems: Equating finite elements to subsystems is an obvious step but likely to create a large number of redundant joints and meaningless subsystems. e.g. two elements of the same thickness, same material and connected to each other in the same plane would be identified as two subsystems and a single joint in the conversion process, even though there is no attenuation ! In a ship FE model there could be thousands of such elements resulting in a large SEA model with thousands of meaningless subsystems and joints.

(b) Finite elements have a topological order that define a normal vector that gives the orientation of the top and bottom surfaces for plates and shell elements. This information would have to be correctly interpreted to correctly define the orientation of subsystems when defining SEA joint connectivity.

(c) For beam finite elements the orientation vector is used to define the principal bending axes of the beam. If beam subsystems are used then the conversion process must correctly interpret the beam orientation vector to correctly define the beam SEA subsystem and orientation for joint definitions.

(d) Beam elements are frequently used to represent stiffeners in finite element models. This work has shown that beam elements are unsuitable for modelling ship frames and a plate definition is better. It would therefore be necessary to convert beam elements to plate subsystems and correctly identify the frame when defining the joint.

(e) It has also been shown in this work that coarse modelling of the structure is sufficient and in some cases necessary. Small stiffeners can be disregarded and this is reasonably intuitive when examining structural drawings. For a conversion program some rules require to be incorporated to determine which size of stiffeners are to be modelled and which are to be discarded.

(f) If acoustic subsystems are required, then acoustic elements or solid elements will require to be defined in the finite element model. Without these elements it would be extremely difficult to generate acoustic subsystems. It would also be necessary to correctly identify which plate elements are coupled to the solid/acoustic element to ensure the walls and decks are correctly coupled.

One feature particular to the hull section is the tapering frame section (see figs 6.39 and 6.40). These are an interesting feature because of the constantly changing depth and it was shown in chapter four that the trace wavelength of incident waves which match the frame depth are important in determining the transmission characteristics. For a tapered web, there is therefore an infinite number of wave matching frequencies. In the hull model for analysis purposes the average web depth was used, however further research experimentally and theoretically on the transmission characteristics of tapered frames is merited.

6.6 Conclusions

In this chapter the SEA modelling of real ship structures has been studied. The results for two large, approximately periodic sections of the ship were investigated and a

section of the ship superstructure. The sections of the ships are in a physical sense near periodic in that they are connected in a regular, repetitive spatial pattern in two dimensions, however mathematically they are not since they do not consist of identical subsystems. The analysis has shown that all three wave types require to be included in the SEA model. The practical option would to use a bending wave and in-plane wave model, where the longitudinal and transverse wave subsystems are combined to form one subsystem. The analysis has shown that the full frame model developed in chapter four gives poor agreement in low frequency bands when applied to a large ribbed deck plate, but on other larger structures the inclusion of flange plates is not significantly detrimental. The best results were obtained with a web plate joint model ignoring the flange plates. This is consistent with the results for the complex laboratory structure presented in chapter 5.

Two different SEA modelling strategies were investigated, a coarse and detailed approach. It was found that the coarse modelling approach gave the best agreement with the measured data, as the detailed modelling approach predicts a higher acceleration level difference. This is advantageous as it will help reduce the model size. Model size statistics are given based on the measured data which allow the number of joints, subsystems and coupling loss factors to be estimated for a ship SEA model. However this also means that implementation of automatic sub-structuring to generate SEA models of ship sections is more problematic.

The results for the near-periodic structures of the large ribbed plate and hull section show good agreement for the coarse BLT wave SEA model with web plate joints. The results presented for large ribbed plate show excellent agreement with measured data. The hull section results show good agreement for attenuation around the hull and in the longitudinal direction. The difference between the measured and predicted attenuation is good accounting for the 95 % confidence level in the low frequency bands. The results are however sensitive to the damping level and these results do not allow for the increased damping in a finished vessel due to floating floors, damping layers on the hull, polymer\cement floor coverings. The measured attenuation therefore may be quite

different to the results presented in this chapter. This requires further work to quantify the effect of ship damping treatments and it's implication for the SEA modelling.

It was shown for sections of the superstructure that a coarse modelling approach gave better agreement with the measured data than the detailed modelling approach. The superstructure can be simplified to an assembly of flat plates and stiffeners neglected. Given that the superstructure is remote from the principal noise sources on a ship, this is not unreasonable.

Chapter Seven

Conclusions and Recommendations

7.0 Conclusions

In this thesis the prediction of structural vibration transmission in ships by statistical energy analysis has been investigated. The thesis examined wave transmission models to predict the transmission coefficients for ship hull frame joints. Measured and predicted vibration results for simple single joint structures, complex multi-joint laboratory structures and sections of a ship were presented. From this work the following conclusions are drawn.

The analysis of the vibration transmission across a single frame joint in chapter five compared the measured and the predicted acceleration level difference for different sizes of hull frame stiffener. The frame stiffener was modelled as a beam subsystem, a single plate and an assembly of plates. It was shown that modelling the frame as a beam subsystem gave poor agreement with measured data because the predicted coupling loss factor is too low. The model developed in chapter four representing the frame as an assembly of plates was shown to be a better modelling approach for a single joint. Modelling the web plate of the frame only and ignoring the flange was also shown to give an accurate prediction for a single joint.

From the parametric survey of the hull frame model in chapter four it was shown that, for deep frames joints, the predicted transmission loss was very similar for wide flanges, narrow flanges or completely omitting the flange plates. The extra effort in modelling the flanges therefore does not significantly affect the accuracy of the predicted transmission loss. For small frames it was shown that the predicted joint transmission

loss is higher if the flange plates are included by 1 to 3 dB, and the choice of joint modelling approach is therefore important. It was also shown that for transmission models including longitudinal and transverse waves there is significant variation of transmission loss within frequency bands. The transmission loss can vary by 50 to 60 dB between the maximum and minimum values. Rather than rely on the transmission loss calculated at the centre frequency it would therefore be prudent to average the transmission loss at 4 to 5 frequencies between the lower and upper frequencies of a frequency band.

The analysis models of the complex multi-joint laboratory and ship structures have shown that the extra effort involved in modelling the flange plates does not result in a more accurate prediction. The results for the web plate joint models gave a consistently better prediction of the attenuation in vibration with distance. This is because the web plate model predicts in the lower frequency bands that there are more incident waves that give total transmission. There are several advantages in being able to omit the flange plates. The joint modelling, definition and data entry is considerably simplified, the analysis time is reduced as there are only 16 unknown transmission coefficients for the web plate model instead of the 32 unknown transmission coefficients in the full frame model. If there are a large number of joints and joint types this can significantly reduce the analysis time. The full frame model also requires a higher number of integration points to ensure the consistency relationship is satisfied.

From the complex laboratory structure and the ship sections, it has been shown that bending, longitudinal and transverse waves need to be included in the model even if all the excitations and measured response are associated with bending waves. The predicted modal overlap and mode count of the in-plane wave subsystems show that in-plane subsystems should not be important until the higher frequency bands. The in-plane mode count and modal overlap are based on the dimensions of the subsystem, however in practice there will be in-plane waves in the lower frequency bands that propagate across the entire structure, which will be un-attenuated by the rib stiffeners. Such modelling was not carried out as it is not clear what boundaries should be used.

Including separate bending, longitudinal and transverse wave types will result in a large number of subsystems and coupling loss factors in a ship SEA model. To reduce the size of the ship SEA model, the optimum approach may be to combine the longitudinal and transverse wave subsystems into a single in-plane subsystem. As an example the bending, longitudinal and transverse wave SEA model of the hull section in chapter six had approximately 25,000 coupling loss factors and the use of combined in-plane wave subsystems would significantly reduce the overall size of the SEA model.

Damping measurements taken on the experimental laboratory structure, bulkheads, deck plate, hull plate and a complete ship have shown good agreement with the Irie equation for the internal loss factor (η_{id}) of steel given in equation *3.4*. This equation can reliably be taken as a minimum value of the internal loss factor of plain undamped steel for bolted and welded steel construction. In a finished vessel there will be floor coverings, bulkhead cladding, damping treatments on the hull and fluid loading on the hull, all of which will increase the damping of the steel. The internal loss factor of these subsystems requires to be increased above the Irie prediction in the SEA model.

From the analysis of the large ribbed plate and the hull section it was shown that the SEA approach of defining the individual joints and subsystems works close to the source subsystem. As the number of joints between the source and receiving subsystems increases, the SEA model predicts a higher attenuation than measured. However small errors in the damping can introduce a systematic bias error in the predicted attenuation that can significantly change the predicted attenuation with distance.

It has been assumed by other researchers that the ribbed plating on ships can be assumed to be periodic and that the wave filtering effects of the stiffeners render SEA ineffective. In real ships the manufacturing variation in welding, changes in section size, stiffener spacing reduce wave filtering effects of the stiffening. Also the geometry of the structure exhibits some periodic features but it is not mathematically periodic as the joints and subsystems are not identical. In this thesis it has been shown that in real structures the agreement between the measured and predicted vibration level with SEA is much better than the results presented for simple one-dimensional periodic structures,

where methods such as wave intensity analysis are advocated. Therefore SEA is capable of modelling real stiffened plates, however the level of detail in the SEA model is important in determining the accuracy predicted attenuation.

For the sections of the ship studied it was shown that a coarse modelling approach is necessary to give an accurate prediction and that small bulb plate stiffeners, angles and flat bar stiffeners can be omitted to give an accurate prediction from the SEA model. This has implications for automatic substructuring and generation of SEA models from an FE model. The development of coarse modelling strategy for ships requires further investigation.

7.1 Recommendations for further research

In this section recommendations for future ship related and general SEA work is presented.

Current shipbuilding practice favours modular construction, where stiffened plates are welded together to form units and several units are then assembled together into a module. A module is typically a complete section of the ship encompassing the hull, decks and part of the superstructure. The modules are then welded together to form the complete ship structure. Several units have been analysed in this thesis, however it is recommended that the SEA modelling of complete modules be investigated as it increases the magnitude and complexity of the structures in this thesis. Such a study of a full ship would require several years and close collaboration with a ship builder.

The main problem found in this work has been that of predicting the attenuation in vibration level with distance as the number of joints between source and receiving subsystems increases. The analysis has shown that on the hull section and large ribbed plates of real ship structures the classical SEA approach of defining individual joints can work but the predicted attenuation with distance is sensitive to damping level. This is limitation of all models, not only SEA.

The range can be extended by a coarse SEA modelling approach by omitting stiffeners but as the distance between source and receiving subsystems increases the tendency will be to predict higher attenuation than measured. Further research is required to develop coarse modelling strategy for 2D structures, such as the large ribbed plate and hull section analysed in this thesis, to determine which sizes of stiffener to include in the SEA model, which to ignore and the determination of subsystem sizes.

The one aspect not covered in this thesis is the effect of fluid loading on the transmission characteristics and this is a significant problem that has to be overcome if SEA is to be applied successfully to real ships. Theoretical research has been undertaken on the basic problems presented by a dense fluid medium and the basic effects of mass loading can be incorporated fairly easily into the SEA framework. No one as yet has attempted to incorporate the effects of fluid loading on the bending wave equation into wave transmission models for standard joints. The bending wave equation changes from a fourth to a fifth order equation which can only be solved numerically and the nature and physical interpretation of the wave types becomes more problematic. This is an area that requires further development. It is also necessary to examine if the radiation equations presented in chapter two which were developed for a low density fluid medium such as air can be used for radiation into a dense fluid medium such as water.

One of the features of ship construction found is the use of tapered beams at the hull bottom i.e. the beam continually varies in depth. It may be useful to examine experimentally and analytically the transmission characteristics of tapered beam sections to establish if the use of the average beam depth is satisfactory for joint models. Because of this change in depth, the beam will have a large number of wave matching frequencies and therefore the transmission characteristics could be quite different. There has not been any work on this type of joint to date.

In the structures tested, the source subsystem where power was input was taken at a convenient location, however vibration data measured throughout the structure of different vessel types in operation and with real noise sources is required. This would allow an estimate to be made to the proportion of the actual structure that requires to be

included in an SEA model, since modelling an entire ship structure is very time consuming. Operational vibration measurements would also for vibration due to power input to in-plane subsystems from the principal noise sources such as the engines, something which is difficult to achieve by impacting the structure with a hammer.

A detailed study of ship damping for typical floor coverings and hull damping layers used in ship construction is required. In addition measured vibration data requires to be gathered on typical sections of ribbed ship structure, such as those presented in this work, with applied damping treatment to verify if the structure-borne vibration level changes significantly and the accuracy of SEA models of the damped structure. The damping of fluid loaded plates requires to be determined to include the effects on hull plates.

1 **International Maritime Organisation**
Code on noise levels on board ships and recommendations on methods of measuring noise levels at listening posts.
1982.

2. **ISO standard 6954 - 1984 (E)**
Mechanical vibration and shock - Guidelines for the overall evaluation of vibration in merchant ships

3. **E.Jantunen M.K.Hakala S.Rintala,**
Integrated vibration analysis of a Baltic passenger ship,
Proceedings of the 5th international symposium on practical design of ships and mobile units V1 p818-827 1992.

4. **R.Nagamoto K.Kagawa T.Hara K.Yanagi,**
Vibration study on superstructure of LNG carrier,
Proceedings of the 5th international symposium on practical design of ships and mobile units V1 p828-834 1992.

5 **J.H.Janssen J.Buiten,**
On acoustical designing in naval architecture,
Inter-Noise 1973 p349-356.

6 **J.Plunt,**
Laboratory Measurement Of Acoustical Properties Of Accommodation Systems On Ships,
Inter-Noise 1977 p 668-673.

7 **J.Plunt,**
Empirical Formulas For Structure-Borne Sound Levels Of Ship Machinery,
Inter-Noise 1978 p795-798.

8 **J.Plunt,**
Methods for predicting noise levels in ships. Part I: Noise prediction for ships based on empirical data,
Ph.D Thesis, Chalmers University of Technology 1980.

9 **E.Szczerbicki A.Szuwarzynski,**
Prediction of octave noise spectra in accommodations in the superstructure of a ship,
Archives of acoustics, 1983, p119-130.

10 **P.Calcagno R.Maltese F.Pinazzi,**
Applications of two mathematical approaches to predict airborne noise levels in ship superstructures,
Shipboard acoustics, 1986, p245-263.

11 **F.J.Fahy E.Lindqvist,**
Wave propagation in damped stiffened structures . characteristic of ship construction,
Journal of sound and vibration 1976 V45 p115-138.

12 **A.C.Nilsson,**
Wave-propagation in simple hull-frame structures of ships,
Journal of sound and vibration 1976V44 p393-405.

13 **A.C.Nilsson,**
Attenuation of structure borne sound in super structures on ships,
Journal of sound and vibration 1977 V55 P71-91.

14 **M.Heckl,**
Wave propagation on beam-plate systems,
Journal of acoustical society of America, 1961 V33 p640.

15 **A.C.Nilsson,**
Reduction of structure-borne sound in simple ship structures: results of model tests,
Journal of sound and vibration 1978 V61 P45-60.

16 **A.C.Nilsson,**
A method for the prediction of noise and velocity levels in ship constructions,
Journal of sound and vibration 1984 V94(3) p411-429.

17 **R.J.Sawley,**
The evaluation of a shipboard noise and vibration problem using statistical energy analysis,
ASME, Symposium on stochastic process in dynamical problems, Los Angeles 1969,

18 **M.Chernjawski C.Arcidiacono,**
Simplified method for the evaluation of structure borne vibration transmission through complex ship structures,
Shock and vibration bulletin 1972 V42 p235-243.

19 **J.O.Jensen,**
Structure borne noise transmission in ship,
Inter-noise 74 p403-406.

20 **J.O.Jensen,**
Calculation of structure borne noise transmission in ships using the statistical energy analysis approach,
Proceedings of the international symposium on shipboard acoustics, 1976.

21 **Y.Irie S.Takagi,**
Structure borne noise transmission in steel structure like a ship,
Inter-noise 78 p789-793.

22 **K.Fukuzawa C.Yasuda,**
Studies On Structure-Borne Sound In Shi,p
Inter-Noise 79 p1-6.

23 **J.Plunt,**
Methods for predicting noise levels in ships. Part II: Prediction of structure-borne sound transmission in complex structures with the SEA method,
Ph.D Thesis, Chalmers University of Technology 1980.

24 **T.Yoshikai K.Hattori T.Sato,**
Prediction of noise level on board ship using statistical energy analysis,
Inter-Noise 1981 p1049-1052.

25 **Y.Irie T.Nakamura,**
Prediction of structure-borne sound transmission using SEA,
Bulletin of the marine engineering society in Japan V13 p60-72 1985.

26 **R.H.Lyon J.Tratch,**
The role of in-plane vibration on structure-borne sound,
Inter-noise 1985 p697-700.

27 **J.Tratch,**
Vibration transmission through machinery foundation and ship bottom structure,
M.Sc. Thesis, 1985, MIT.

28 **Y.S.Shimomura,**
The effect of a liquid storage tank on sound transmission through ship structures,
M.Sc. Ocean Engineering Thesis, 1985, MIT.

29 **Y.S.Shimomura R.H.Lyon,**
Noise reduction in a ship structure by a liquid storage tank,
Inter-Noise 1986 p655-658.

30 **K.Iino I.Honda,**
Total noise prediction for a passenger cruise ship,
Proceedings of the 5th international symposium on practical design of ships and mobile units, V1 p1648-1661 1992.

31 **M.I.Taroudakis D.V.Lyridis K.Pliatsikas,**
Study of the effect of the plate stiffeners on the structure-borne noise transmission on board ships using the SEA,
Inter-noise 1993 p1205-1208.

32 **H.S.Kim H.J.Kang J.S.Kim,**
Bending wave transmission in multi-connected plates,
Inter-noise 1993 p1209-1212.

33 **H.Kang H.S.Kim J.S.Kim Y.C.Lee,**
SEA Modelling Of Ship Structures,
Noise Con 1993 p583-588.

34 **J.S.Kim H.J.Kang H.S.Kim S.Y.Hahn Y.C.Lee J.H.Chung,**
Shipboard noise prediction package based on statistical energy analysis,
Proceedings of the 6th international symposium on practical design of ships and mobile units,V2 p1151- 1162 1995.

35 **P.Hynna P.Klinge J.Vuoksinen,**
Prediction of structure-borne sound in large welded ship structures using SEA,
Journal of sound and vibration 1995 V180 P583-607.

36 **R.H.Lyon and R.G.DeJong,**
Theory and application of statistical energy analysis.
Second edition,Butterworth and Heinemann 1995.

37 **R.J.M Craik,**
Sound transmission through buildings using statistical energy analysis,
Gower 1996.

38 **R.H.Lyon and G.Maidanik,**
Power flow between linearly coupled oscillators,
Journal of the acoustical society of America 1962 V34 (5) p623-639.

39 **P.W.Smith,**
Response and radiation of structural modes excited by sound,
Journal of the acoustical society of America 1962 V34 p640-647.

40 **T.D.Scharton and R.H.Lyon,**
Power flow and energy sharing in random vibration,
Journal of the acoustical society of America 1968 V43 p1332-1343.

41 **R.H.Lyon and E.Eichler,**
Random vibration of connected structures,
Journal of the acoustical society of America 1964 V37 p623-639.

42 **R.H.Lyon,**
Statistical analysis of power injection and response in structures and rooms,
Journal of the acoustical society of America 1969 V45 p545-565.

43 **R.H.Lyon and T.D.Scharton,**
Vibrational energy transmission in a three element structure,
Journal of the acoustical society of America 1965 V38 p253-261.

44 **E.Eichler**
Thermal circuit approach to vibrations to coupled systems and the noise reduction of a rectangular box
Journal of the acoustical society of America 1963 V37 p995-1007.

45 **G.Maidanik,**
Variations in the boundary conditions of coupled systems,
Journal of sound and vibration 1976 V46 P585-589.

46 **G.Maidanik,**
Response of coupled dynamic systems,
Journal of sound and vibration 1976 V46 P561-583.

47 **G.Maidanik,**
Some elements in SEA,
Journal of sound and vibration 1977 V52 P171-191.

48 **J.E.Brooks G.Maidanik,**
Loss and coupling loss factors of two coupled dynamic systems,
Journal of sound and vibration 1977 V55 P315-332.

49 **J.Woodhouse,**
An approach to the theoretical background of statistical energy analysis applied to structural vibration,
Journal of the acoustical society of America 1981 V69(6) p1695-1709.

50 **E.K.Dimitriadis A.D.Pierce,**
Analytical solution for the power exchange between strongly coupled plates under random excitation: a test of statistical energy analysis concepts.
Journal of sound and vibration 1988 123(3) p397-412

51 **J.E.Manning,**
Formulation of SEA parameters using mobility functions,
Phil. Transactions of the royal society of London A(1994) 346 p477-p488.

52 **R.S.Langley,**
A general derivation of the statistical energy analysis equations for coupled dynamic systems,
Journal of sound and vibration V135 p499-508.

53 **R.S.Langley,**
A derivation of the coupling loss factors used in statistical energy analysis,
Journal of sound and vibration V141 p207-219.

54 **B.R.Mace,**
The statistical energy analysis of two continuous one dimensional subsystems,
Journal of sound and vibration 1993 V166(3) p429-461.

55 **B.R.Mace,**
On statistical energy analysis hypothesis of coupling power proportionality and some implications of it's failure,
Journal of sound and vibration V178(1) p95-112.

56 **H.Kishimoto D.S.Bernstein S.R.Hall,**
Energy flow modelling of interconnected structures : a deterministic foundation for statistical energy analysis,
Journal of sound and vibration 1995 V186(3) p407-445.

57 **R.J.Pinnington D.Lednik,**
Transient statistical energy analysis of an impulsively excited two oscillator system,
Journal of Sound and vibration 1996 V189(2) p249-264.

58 **R.J.Pinnington D.Lednik,**
Transient energy between two coupled beams,
Journal of Sound and vibration 1996 V189(2) p265-287.

59 **J.C.Sun C.Wang Z.H.Sun,**
Power flow between three series coupled oscillators,
Journal of Sound and vibration 1996 V189(2) p215-229.

60 **R.S.Langley and A.N.Bercin,**
Wave intensity analysis of high frequency vibrations,
Phil. Transactions of the Royal Society of London A(1994) 346 p489-p499.

61 **K.H. Heron,**
Advanced statistical energy analysis,
Phil. Transactions of the Royal Society of London (1994) 346 p511-p524.

62 **F.J.Fahy,**
Statistical energy analysis: a wolf in sheep's clothing ?,
Inter-Noise 1993 p13-26.

63 **F.J.Fahy,**
Statistical energy analysis: a critical overview,
Phil. Transactions of the Royal Society of London A(1994) 346 p431-p447.

64 **B.R.Mace,**
Wave coherence, coupling power and statistical energy analysis,
Journal of sound and vibration 1997 V199(3) p369-380.

65 **M.Beshara A.J.Keane,**
Statistical energy analysis of multiple, non-conservatively coupled systems,
Journal of sound and vibration 1997 V198(1) p95-122.

66 **L.Cremer M.Heckl E.E.Unger,**
Structure-Borne Sound,
Second edition, Springer Verlag,

67 **T. Kihlman,**
Transmission of structure-borne sound through buildings,
Report 9, national Swedish institute for building research.

68 **P.G.Craven and B.M.Gibbs,**
Sound transmission and mode coupling at junctions of thin plates, part I: Representation of the problem,
Journal of sound and vibration 1981 V77 p417-427.

69 **B.M.Gibbs and P.G.Craven,**
Sound transmission and mode coupling at junctions of thin plates, part II: parametric problem,
Journal of sound and vibration 1981 V77 p429-435.

70 **W. Wohle, T.H. Beckmann and H. Schreckenbach,**
Coupling loss factors for statistical energy analysis of sound transmission at rectangular structural slab joints, part I,
Journal of sound and vibration 1981 V77 p323-337.

71 **W. Wohle, T.H. Beckmann and H. Schreckenbach,**
Coupling loss factors for statistical energy analysis of sound transmission at rectangular structural slab joints, part II,
Journal of sound and vibration 1981 V77 p335-344.

72 **P. Mees and G. Vermeir,**
Structure-borne sound transmission at elastically connected plates,
Journal of sound and vibration 1993 V166 p55-76.

73 **J.A. Steel,**
Sound transmission between plates in framed structures,
Journal of sound and vibration 1994 V178(3) p379-394.

74 **I. Bosmans., P. Mees and G. Vermeir,**
Structure-borne sound transmission between thin orthotropic plates: analytical solutions,
Journal of sound and vibration 1996 V191(1) 75-90.

75 **M.C.Battachayra**
The response of structures to acoustic excitation and the transmission of sound and vibration,
Ph.D thesis, University of Liverpool, 1970.

76 **R.D.Sullivan**
Sound insulation of brick diaphragm walls,
Ph.D thesis, University of Liverpool, 1994.

77 **R.Wilson**
Sound transmission through double walls,
Ph.D thesis, Heriot-Watt University, Edinburgh 1992.

78 **R.S.Smith,**
Sound transmission through lightweight parallel plates,
Ph.D thesis, Heriot-Watt University, Edinburgh 1997.

79 **R.S. Langley K.H. Heron,**
Elastic wave transmission through plate/beam junctions,
Journal of sound and vibration 1990 V143 P241-253.

80 **R.S. Langley,**
Elastic wave transmission coefficients and coupling loss factors for structural junctions between curved panels,
Journal of sound and vibration 1994 V169 P297-317.

81 **G. Maidanik,**
Response of ribbed panels to reverberant acoustic fields,
Journal of the acoustical society of America 1962 V34 N6.

82 **C.E.Wallace ,**
Radiation resistance of a rectangular panel,
Journal of the acoustical society of America 1972 V51(3) p946-52.

83 **F.G.Leppington E.G.Broadbent K.H.Heron,**
The acoustic radiation efficiency Of rectangular panels,
Phil. transactions of the royal society of London A(1984) A382 p245-p271.

84 **F.G.Leppington E.G.Broadbent K.H.Heron,**
Acoustic radiation from rectangular panels with constrained edges,
Phil. transactions of the royal society of London (1984) A382 p67-p84.

85 **F.G.Leppington E.G.Broadbent K.H.Heron S.M.Mead,**
Resonant and non-resonant acoustic properties of elastic panels. I. The radiation problem,
Phil. transactions of the royal society of London (1986) A406 p139-p171.

86 **G.Maidanik,**
Energy dissipation associated with gas-pumping in structural joints,
Journal of the acoustical society of America V40(5) p1064-1072.

87 **R.J.M.Craik J.A.Steel and D.I.Evans,**
Statistical energy analysis of structure-borne sound transmission at low frequencies,
Journal of sound and vibration 1991 V144(1) P95-107.

88 **Jensen and Holm**
Noise reduction in the accomodation of ships by means of constrained layer damping
Inter-noise 1979, I5-C

89 **T.Kihlman and J.Plunt**
Prediction of noise levels in ships
Proceeding of International symposium on shipboard acoustics, 1976, Elesvier

90 **R.J.M.Craik**
Study of sound transmission throug buildings using statistical energy analysis
Ph.D thesis, Heriot-Watt University, Edinburgh 1980.

91 **M.R.Spiegel**
Theory and problems of Statistics
Schuam's outline series 2nd edition, McGraw-Hill

92 **R.Taggart,**
Ship design and construction,
Edited by society of naval architects, 1980

93 **CETENA,**
Noise and vibration and shock on board ships, 16th graduate school,
CETENA and university of Genoa volume 1 and 2, March 1992.

94 **G.Fraser**
Structure-borne sound in motor vehicles using statistical energy analysis
Ph.D thesis, Heriot-Watt University, Edinburgh 1998.

95 **CIRIA underwater engineering group,**
Dynamics of marine structures: methods of calculating the dynamic response of fixed structures subject to wave and current action,
Report UR8, 2nd Edition, 1978.

96 **R.S.Langley, J.R.D.Smith and F.J.Fahy**
Statistical energy analysis of periodically stiffened damped plate structures
Journal of sound and vibration, 1997, V217(3) p407-426

97 **R.J.M.Craik,**
The effect of design changes on sound transmission through a building.
Journal of building acoustics 1996 V3 No 3 p145-185.

98 **R.J.M.Craik and A.Thancanamootoo,**
The importance of in-plane waves in sound transmission through buildings,
Applied acoustics 1992 V37 No 1 p85-109.